Research and Technology

1989

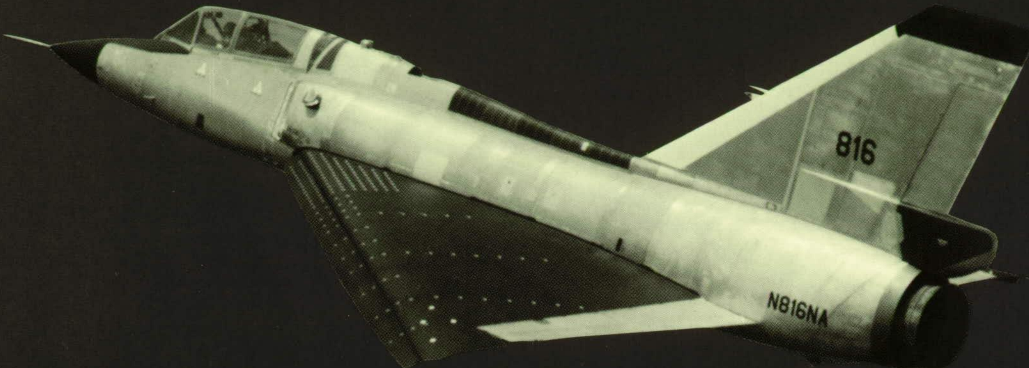

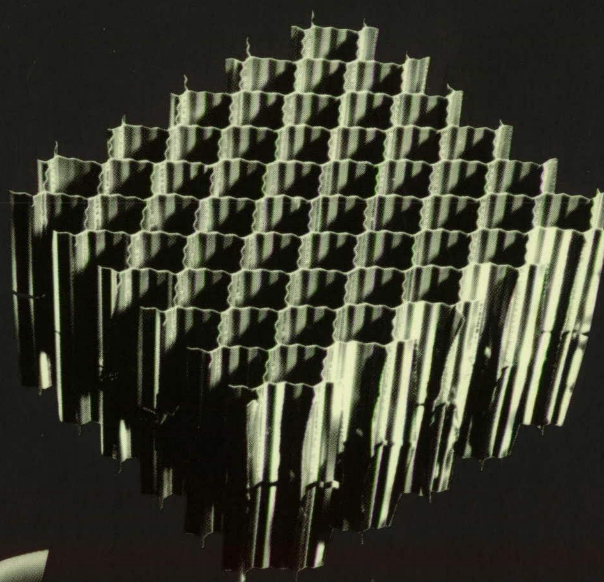

Langley Research Center

NASA Technical Memorandum 4150

Research and Technology *1989*

Langley Research Center

NASA Technical Memorandum 4150

NASA
National Aeronautics and
Space Administration

Langley Research Center
Hampton, Virginia 23665

Foreword

The mission of the NASA Langley Research Center is to increase the knowledge and capability of the United States in a full range of aeronautics disciplines and in selected space disciplines. This mission will be accomplished by performing innovative research relevant to national needs and Agency goals, transferring technology to users in a timely manner, and providing development support to other United States Government agencies, industry, and other NASA centers. This report contains highlights of the major accomplishments and applications that have been made during the past year. The highlights illustrate both the broad range of the research and technology activities at NASA Langley Research Center and the contributions of this work toward maintaining United States leadership in aeronautics and space research. For further information about the report, contact Dr. Richard W. Barnwell, Chief Scientist, Mail Stop 105-A, NASA Langley Research Center, Hampton, Virginia 23665, (804) 864-6062.

Richard H. Petersen
Director

Availability Information

The NASA program office and the corresponding Agency-wide Research and Technology Objectives and Plans (RTOP) work breakdown structure are listed in the Contents for each research and technology accomplishment. OAST designates the Office of Aeronautics and Space Technology; OEO designates the Office of Equal Opportunity; OSSA designates the Office of Space Science and Applications; AA designates the Associate Administrator; OCE designates the Office of the Chief Engineer; OCP designates the Office of Commercial Programs; OEXP designates the Office of Exploration; OSF designates the Office of Space Flight; and OSS designates the Office of the Space Station.

For additional information on any summary, contact the individual identified with the highlight. This individual is generally either a member or a leader of the research group submitting the highlight. Commercial telephone users may dial the listed extension preceded by (804) 86. Telephone users with access to the Federal Telecommunications System (FTS) may dial the extension preceded by 928.

Contents

Electronics Directorate

Flight Systems Directorate

Space Directorate

Structures Directorate

Systems Engineering and Operations Directorate

Technology Utilization Program

Aeronautics Directorate

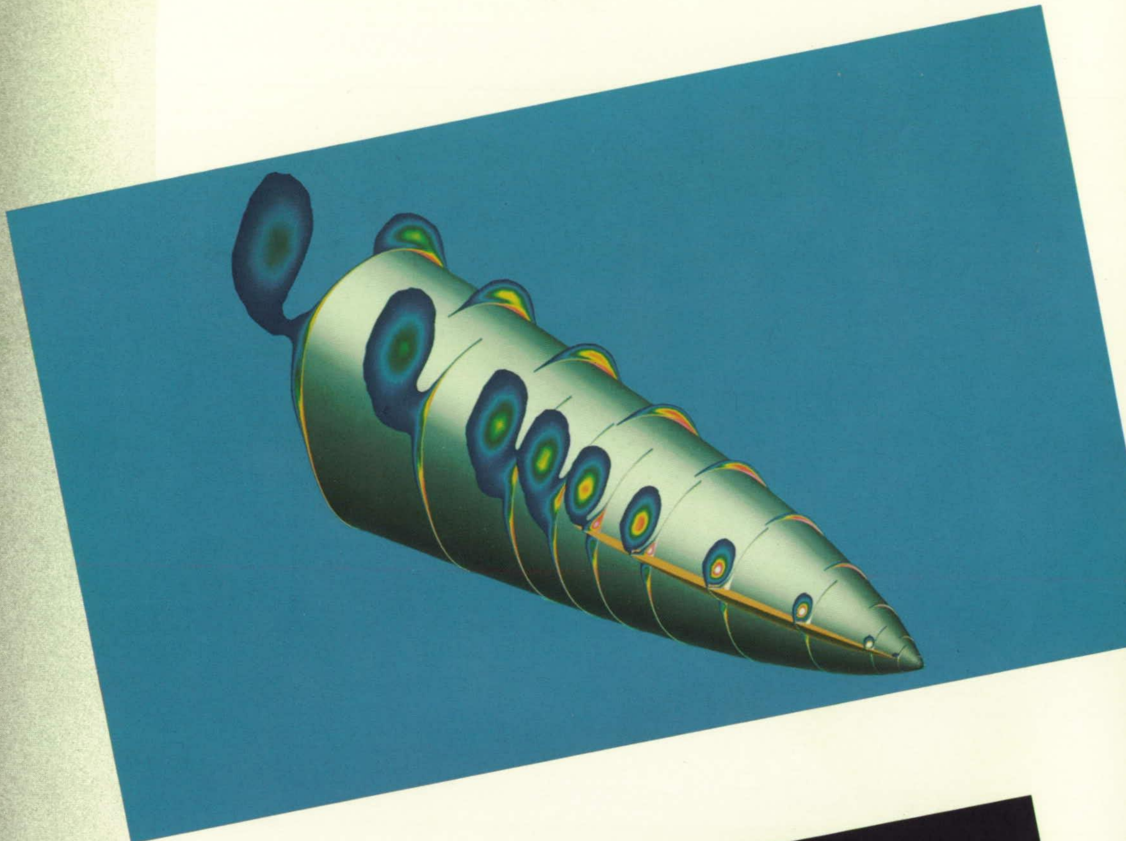

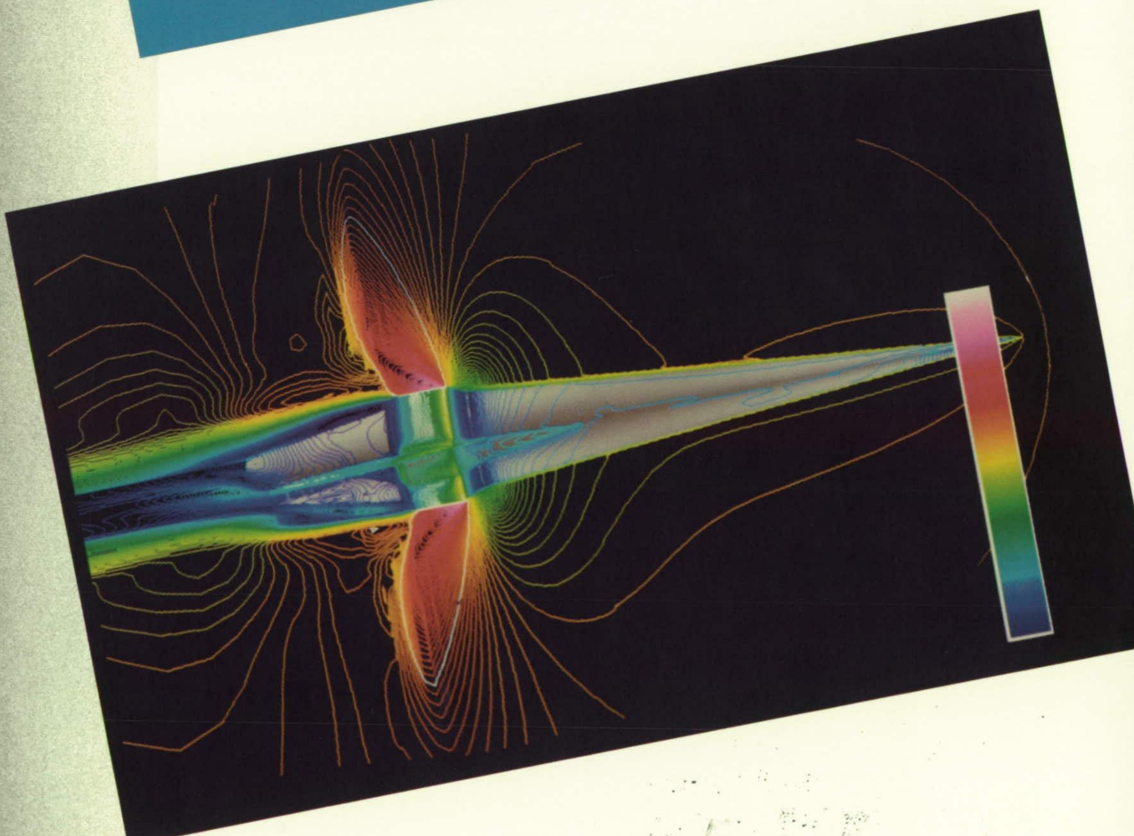

The Aeronautics Directorate is composed of approximately 330 scientists and engineers engaged in basic and applied research in the various aeronautics disciplines. The directorate is organized into four research divisions, a facilities planning office, and a program office, which conduct aeronautical research to advance the state of the art throughout the complete aerodynamic speed range.

The Hypersonic Technology Office coordinates broad-scope hypersonic vehicle research and technology programs including those involving the National Aero-Space Plane (NASP) and conducts design studies of various hypersonic vehicle concepts.

The Advanced Vehicles Division conducts multidisciplinary advanced aeronautical vehicle studies to assess the benefits of discipline research advances and to identify potential new research thrusts. In particular, the vehicle classes of long-haul subsonic and supersonic transports, advanced military aircraft, and general-aviation and commuter aircraft are addressed. The primary emphasis is on high-risk, far-term application of integrated research results from primary aeronautical disciplines.

The Applied Aerodynamics Division is responsible for advancing the state of the art of aircraft and missile technology from subsonic to hypersonic speeds in all areas of fundamental aerodynamics. The research emphasis is on developing advanced aerodynamic technology for future aerospace vehicles. These technologies include such concepts as active flight controls, thrust vectoring, laminar flow and turbulent drag reduction, closely coupled propulsion/airframe integration, and flexible composite structures. Research information is generated using analytical techniques and a variety of wind tunnels including the Langley 14- by 22-Foot Subsonic Tunnel, Langley 7- by 10-Foot High-Speed Tunnel, 8-Foot High-Temperature Tunnel, Langley 0.3-Meter Transonic Cryogenic Tunnel, National Transonic Facility, supersonic Langley Unitary Plan Wind Tunnel, 20-Inch Supersonic Wind Tunnel, 20-Inch Mach 6 Tunnel, and Mach 8 Variable-Density Tunnel. The division is also responsible for developing improved experimental techniques including adaptive-wall test section concepts and cryogenic wind tunnel technology.

The Flight Applications Division conducts research in the areas of basic and applied aerodynamics with an emphasis on flight experiments, flight dynamics, aircraft operations, aviation safety, laminar-flow control, and improved test methods. Research aircraft are used to conduct experiments that complement the ground-based research effort of the Center. The division specializes in high-angle-of-attack technology including stall/spin behavior, automatic spin prevention, and the operation of unique facilities including the only operational spin tunnel in the Nation.

The Fluid Mechanics Division conducts theoretical, computational, and experimental research to advance the state of knowledge in fluid mechanics as it applies to the design of advanced aircraft and missiles across the speed range and hypersonic propulsion systems. Particular areas of emphasis include boundary-layer transition, turbulence, and vortical flow physics and control; supersonic laminar-flow physics and control; supersonic laminar-flow control; viscous drag reduction; separated-flow control; wave drag reduction; flow diagnostics; and theoretical and computational techniques for analyzing and predicting complex flows about aircraft and missiles. The propulsion research focuses on developing an enhanced understanding of the effects of turbulence, mixing, chemistry, fuel injection conditions, and geometry on ignition and combustion at both subsonic and supersonic speeds. Innovative concepts for engine components (including airframe-integrated inlets and nozzles, combustors, and fuel injectors) and integrated engine flow paths are developed and analyzed.

A hypersonic, two-dimensional, real-gas stability theory, which predicts transition onset, has had a major impact on the knowledge of hypersonic boundary-layer transition. The first NASP engine tests were conducted in the scramjet test facilities, and Langley Research Center significantly impacted the contractor's design through suggested improvements in critical engine components. Major improvements in hypersonic analysis capability provided an independent government in-depth analysis to support the NASP Technology Maturation Plan decision process. The hybrid

laminar-flow control wind tunnel experiment demonstrated high potential and paved the way for a full-scale flight experiment. Major enhancements in the National Transonic Facility were completed and demonstrated. Computational, experimental, and conceptual research has set the pace for the High-Angle-of-Attack Technology Program. Inhouse High-Speed Civil Transport system studies indicate potential directions to alleviate environmental concerns.

Real-Time Measurements of Natural Rain Intensity

Presently, the National Weather Service data base for rainfall is averaged over long time constants. This averaging can result in a misunderstanding of the short-duration rainfall characteristics. Hence, an investigation is under way to obtain measurements of high-intensity, naturally occurring rainfall at ground level. These results will provide a data base for the categorization of natural rain by variables such as rain rate, downpour duration, and frequency of high rain rate occurrence. This information will then contribute to the ongoing investigation into the influences of heavy rain on the aerodynamic performance of airplanes.

Three instruments are being used to provide the rain rate information. One, referred to as the load cell collector, uses a 1 ft^2 rain collector mounted on a platform scale transducer or load cell that utilizes four load-bearing strain gauges. A computer is used for sampling and converting the voltages into engineering units of in./hr or mm/hr.

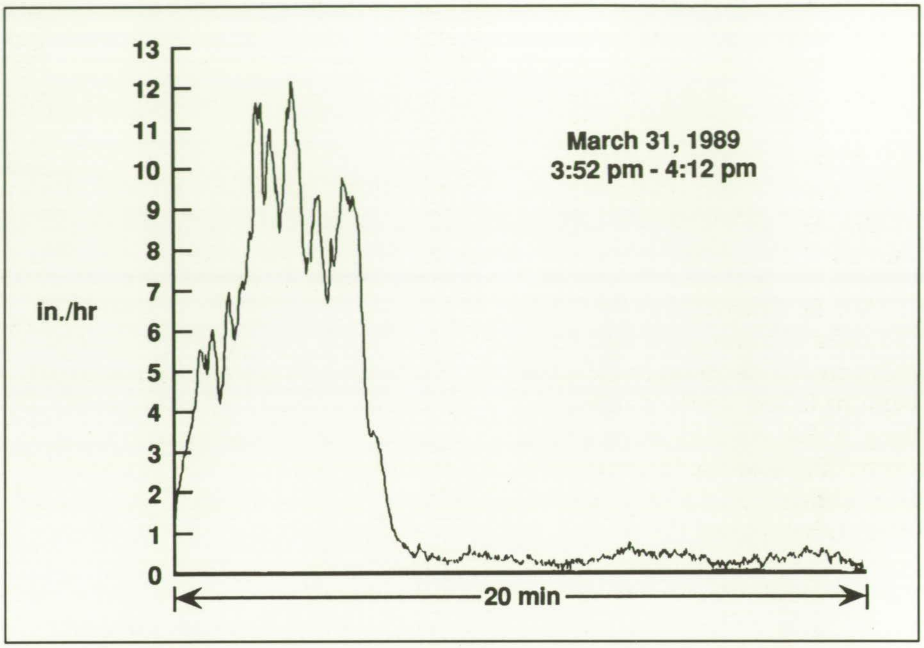

Natural rain measurement at Wallops Flight Facility using load cell collector.

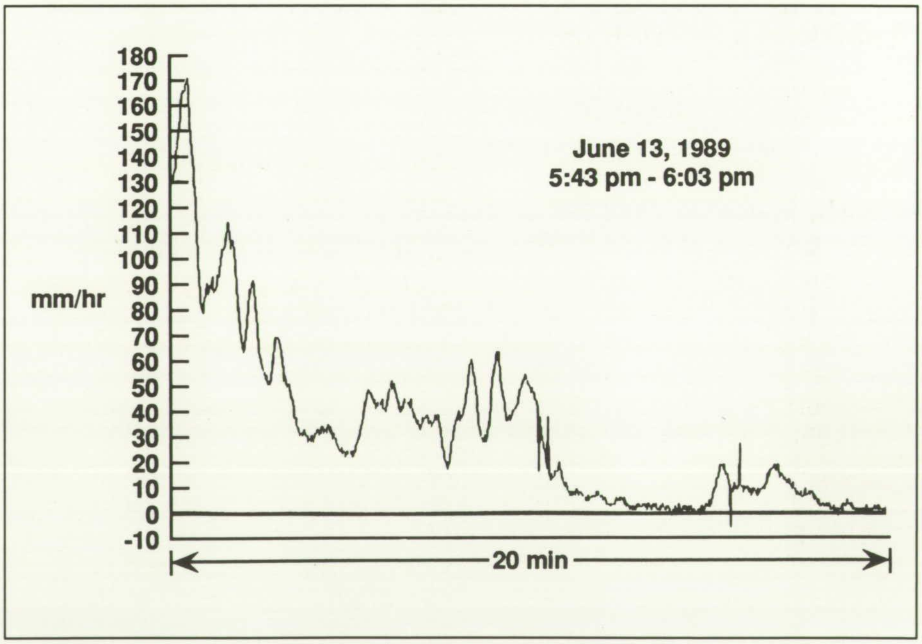

Natural rain measurement at Langley Research Center using load cell collector.

The second instrument is an optical rain gauge that uses an infrared light-emitting diode as a light source. As raindrops pass through the light beam, they induce scintillations that can be detected by the receiving optics. The intensity of the scintillations provides the rain

rate values. The third instrument is a commercially available 8-in. tipping bucket rain gauge. Field measurements are being done at the Langley Research Center and the Wallops Flight Facility using all three sensors; the Kennedy Space Center uses only the load cell collector and the tipping bucket.

Thus far, maximum rain rates of 12 in./hr (305 mm/hr) and 7 in./hr (173 mm/hr) were recorded at the Wallops Island Flight Facility and Langley Research Center, respectively. The data show that rain rates above 5 in./hr (127 mm/hr) seem to be of rather short duration (60 sec to 90 sec); whereas, those below 5 in./hr may continue for much longer durations (3 min to 5 min). Based on these measurements, it appears that short-duration rain rates on the order of 10 in./hr are more frequent during storms than previously thought.

These results verify that intense, short-duration rainfall is a frequently occurring phenomenon that experimentally has proved to be a potential hazard to airplanes during the landing and takeoff phases. Also, considering the dispersion (due to winds) of rain as it falls, the rain intensity or mass of liquid water per unit volume of air at altitude would be significantly higher, thus posing more of a threat.
(Bryan A. Campbell, 45069, W. Edward Melson, Jr., and R. Earl Dunham, Jr.)

Distributed Processing With Networked Computers

Many compute-bound jobs, such as graphics processing of large data sets, can be divided into a large number of relatively independent tasks, such as computing individual streamlines or surfaces or computing the color of individual screen pixels. The rapid processing of such compute-bound jobs requires either a single fast computer, such as a CRAY, or multiple slower computers to process the individual job tasks in a coordinated fashion. The approach taken here has been to develop software to enable such coordinated processing of job tasks across multiple networked computers. The goals of the approach included fully dynamic load balancing (to allow processors with different performance levels and job mixes to contribute any available resources to the distributed job); event-driven task scheduling (to allow processors to join or leave the distributed job asynchronously); fault tolerance (to allow individual processors to fail without "killing" the distributed job); and ease of use (to enable a researcher to use the distributed technique without being burdened with the details of task scheduling).

A pilot code has been developed to implement the distributed processing approach; this code has been tested successfully using up to 15 VAX workstations and minicomputers. The code is separated into task management routines and task execution routines. The user of the distributed processing approach need only supply the task execution routines, which are called by the task management routines to get a new task, to execute a task or to return task results, respectively. The task management routines send individual tasks to separate processors as the processors become available to compute new tasks. The routines are implemented such that task processing can begin as soon as a single processor is available, rather than having to wait for all processors to respond before starting the job tasks. Similarly, if a processor fails or becomes unresponsive, its tasks are diverted to other processors. Tasks are allocated to processors in a pipelined fashion, so that a processor does not sit idle between sending a completed task and waiting to receive a new task.

As an initial test, the code has been used to compute elements of the Mandelbrot set, which is a compute-bound job that takes approximately 30 min to compute on a single VAX 750 minicomputer. The same job takes only approximately 1 min to compute when distributed across the VAX 750 and 14 additional VAX workstations and minicomputers of varying processor capabilities. The aggregate processing capability of the 15 VAX's is approximately 30.5 times that of the single VAX 750, so for this problem the 30:1 job speedup yields a processor utilization efficiency of >95 percent. Such job speedups can often be approached even when the workstations are in production use, because interactive use of workstations leaves many unused workstation processor cycles that can be dynamically applied to distributed job tasks.

Work is under way to extend this distributed processing approach to other problems of interest and to other network architectures. The possibility of distributing tasks across multiple networked supercomputers is also being investigated.
(James P. Chamberlain, 42147)

Johnson-King Turbulence Model for 3-D Flows

It is a well-known fact that an equilibrium type of turbulence model, such as the Baldwin-Lomax model, is inadequate for accurate prediction of separated flows. In order to increase the reliability of computational methods, it is essential to develop turbulence models that are suitable for predicting flows with separation. A nonequilibrium type of turbulence model, namely the Johnson-King model developed originally for two-dimensional flows, has been extended to three-dimensional (3-D) flows and incorporated in a three-dimensional Navier-Stokes code.

Calculations have been performed for transonic flow over an ONERA (Office National d'Etudes et de Recherchers Aérospatiales) M6 wing. The computed pressure distributions using the Baldwin-Lomax and Johnson-King models are compared with the experimental data in the first figure. Based on these comparisons, it is clear that the Johnson-King model results in a significant improvement compared to the Baldwin-Lomax model. The surface streamline patterns corresponding to these computations are shown in the second figure. It is observed from this figure that the Johnson-King model results in a much larger reverse flow region, particularly on the outboard portion of the wing. Also, the separation line, which lie near the shock, moves upstream when the Johnson-King model is employed. The movement in shock position and increase in the reverse flow region improve the pressure correlation with the data, as seen i the first figure.

(Veer N. Vasta, 42236, Ridha Abid, and Bruce W. Wedan)

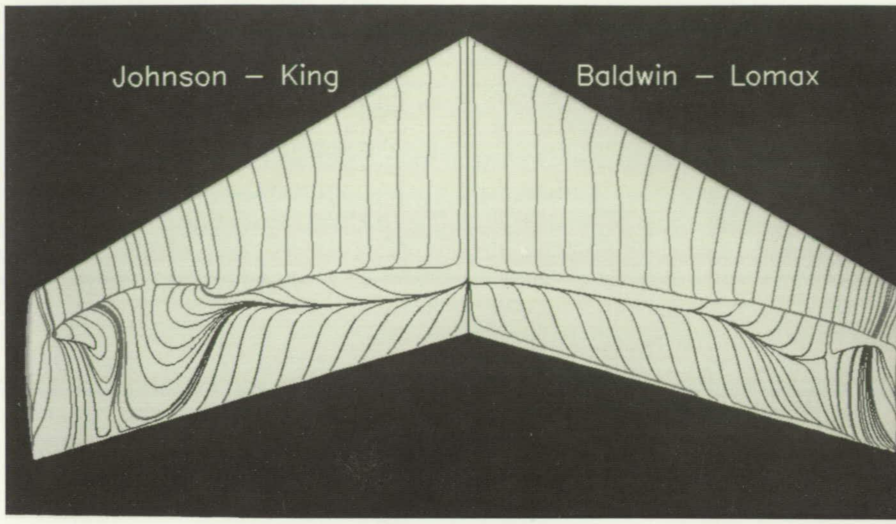

Particle traces on ONERA M6 wing using different turbulence models ($M_\infty = 0.84$, $\alpha = 6.06°$, and $R_e = 11.7 \times 10^6$).

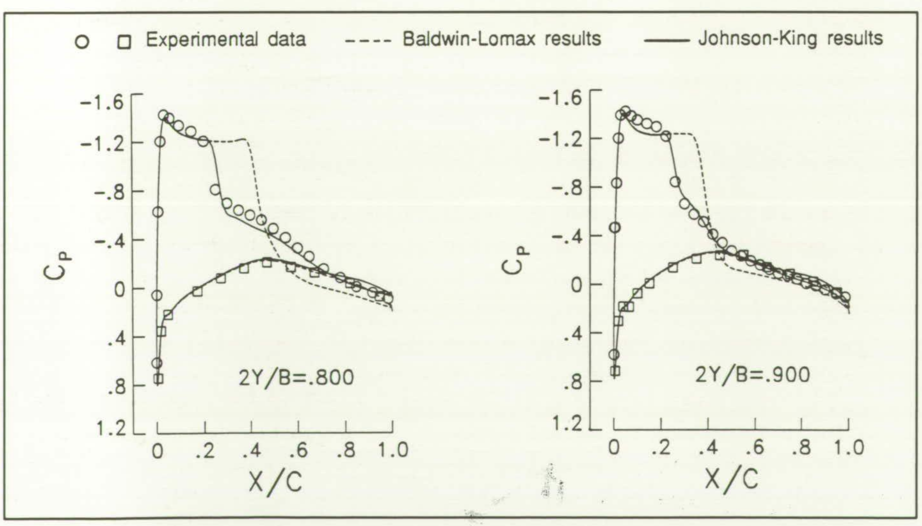

Effect of turbulence model on calculated pressure distributions ($M_\infty = 0.84$ and $\alpha = 6.06°$; $289 \times 65 \times 49$ grid computations).

Computation of Hypersonic Compression-Corner Flows

The design and the analysis of the National Aero-Space Plane (NASP) rely heavily upon the development of computer codes with appropriate physical models and geometric flexibility because many of the high Mach number, high enthalpy flow conditions that the vehicle may encounter in flight

cannot presently be simulated in ground-based facilities. However, before such a code can be used with confidence, the range of validity of the solution procedure and physical modeling must be known. This information can be determined by comparing computed solutions with benchmark experimental data. Such a comparison has been made for four different codes that solve the compressible Navier-Stokes equations for hypersonic flow over the compression corner formed by the intersection of a stream-aligned flat plate and a compression ramp. Flows of this type occur within scramjet engine inlets. Three of the four codes use upwind, finite-volume algorithms, and the fourth uses a central finite-difference algorithm.

For a 15° wedge with fully attached flow, two-dimensional calculations with the four codes gave virtually identical results for a sufficiently refined grid. For a 24° wedge with a highly separated flow, two-dimensional calculations overpredicted the size of the separated flow region. A three-dimensional computation, which included the finite-span effects of the experiment, was required in order to obtain agreement with the data. The figure shows the computed three-dimensional flow field. Pressure contours are shown for the center plane and the outflow plane, and the separated flow region is defined by forward and backward particle traces near the surface. The finite-span effects were important in determining pressure and heat transfer distributions, as well as the extent of separation. In addition, the three-dimensional calculation correctly determined the time required to establish steady-state flow, which was much shorter than for the two-dimensional calculation.

The study demonstrated that the four codes are capable of accurately representing, both qualitatively and quantitatively, the types of complex hypersonic flows with strong viscous-inviscid interactions considered.

(David H. Rudy, 42297, James L. Thomas, Ajay Kumar, Peter A. Gnoffo, and Sukumar R. Chakravarthy)

Computed flow field for Mach 14 flow over 24° compression ramp.

Parabolized Navier-Stokes Code for High-Speed Chemically Reacting Flows

Work has been going on for a number of years at Langley Research Center to develop a supersonic combustion ramjet (scramjet) engine that is capable of propelling a transatmospheric vehicle to hypersonic speeds. The present research has been directed toward the development of computational techniques for the efficient modeling of high-speed chemically reacting flows typical of those found in scramjets. A computer code has been developed to solve the parabolized governing equations for three-dimensional chemically reacting flows with finite-rate chemistry. A test case to demonstrate its capabilities involves streamwise hydrogen injection at sonic velocity into a Mach 2.44 vitiated airstream and the subsequent turbulent mixing leading to chemical reaction. The configuration for the case is shown in the figure.

Comparisons were made with available experimental data, and the computed flow quantities (such as mole fractions of hydrogen, oxygen, nitrogen, and water) were observed to possess all the essential trends exhibited by the experimental data. As an example, the total

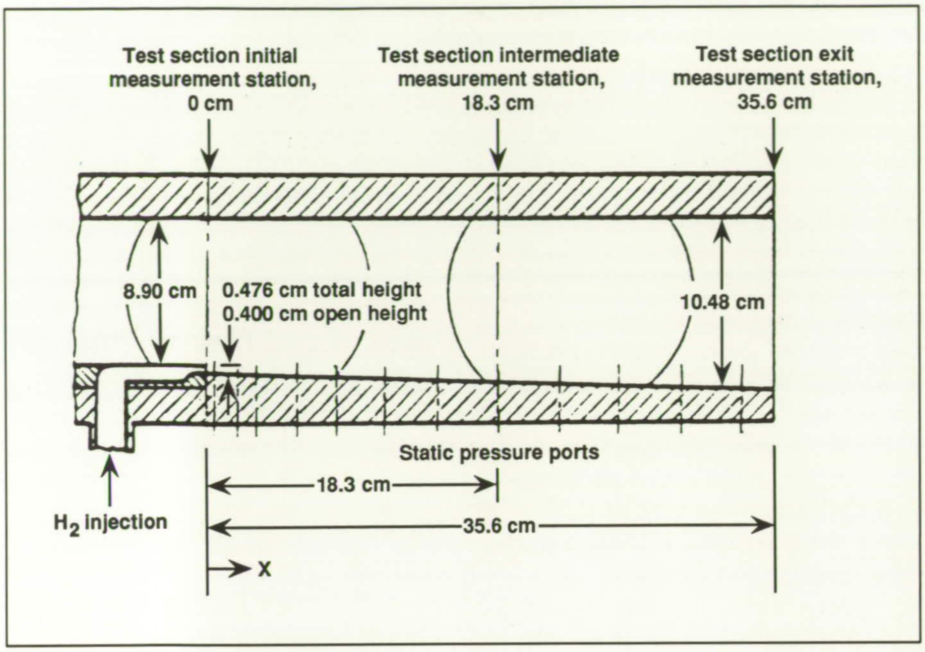

Schematic diagram of test section.

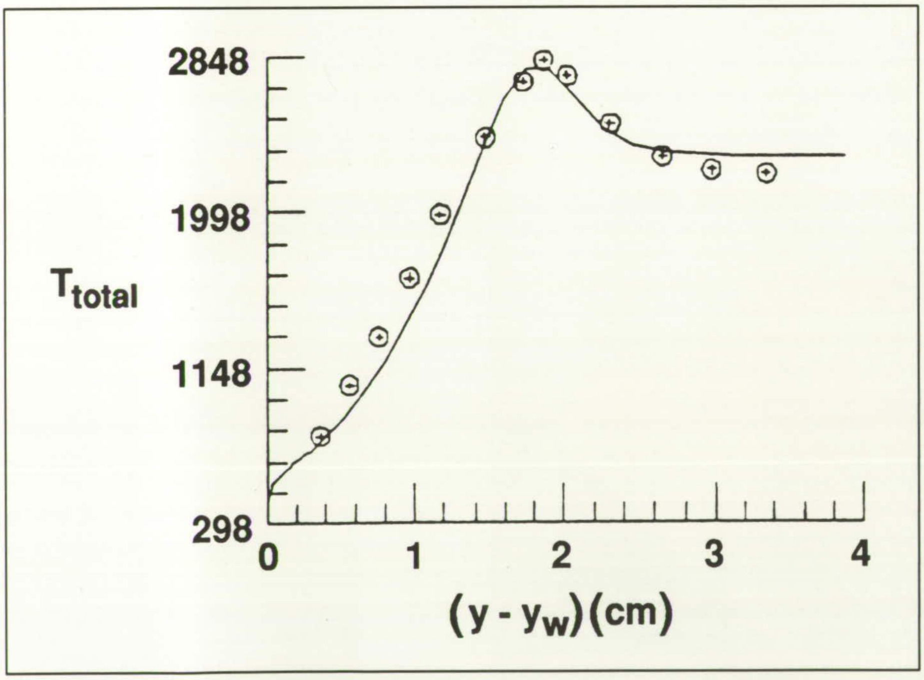

Total temperature comparison.

temperature comparison is shown in the figure, plotted as a function of the distance from the lower wall at the $x = 0.356$ m location. For the total temperature, the quantitative agreement between the computed and experimental profiles is reasonable. However, for the water mole fraction it was observed that the computed profile underpredicts the peak when compared with the experimental data (which exhibit a noticeable scatter).

The use of parabolized governing equations instead of the full unsteady governing equations results in a significant reduction in computer memory requirements and execution times. The parabolized solver can be used in conjunction with the existing elliptic version of the code for accurate and efficient computation of scramjet flow fields, leading to improvements in combustor design.
(Hemant Kamath, 42321 and J. Philip Drummond)

Direct Simulation of Compressible Turbulence

Much research has been conducted on turbulence from the physical, numerical, and experimental points of view. However, most of this research has been confined to incompressible flows although many flows of interest are compressible. In the present work, compressible homogeneous turbulence was studied numerically both to better understand the physics and to generate accurate data bases against which new and old turbulence models can be evaluated. The time-dependent Navier-Stokes equa-

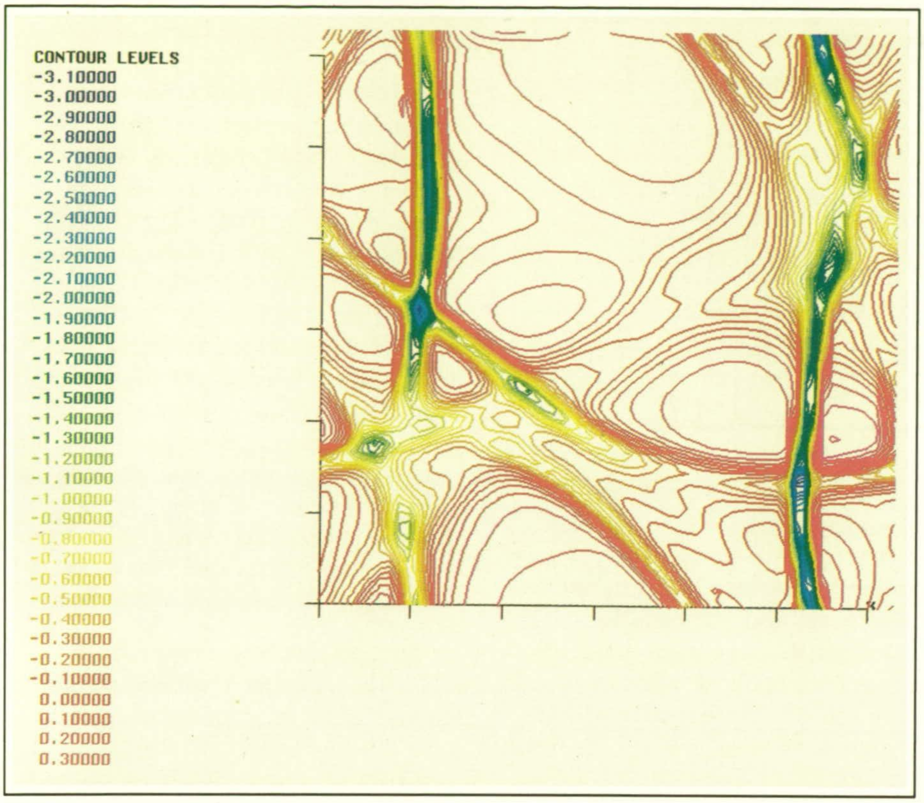

Divergence of velocity in 2-D compressible turbulence ($M = 0.028$ *and* $R_e = 150$; *computed on* 256×256 *grid).*

tions were solved numerically, using a fully spectral algorithm, in a periodic two-dimensional box. A new implicit algorithm was developed to treat the acoustic terms. This algorithm resulted in a factor of 10 speedup on the NASA Numerical Aerodynamic Simulation (NAS) CRAY-2 computer at the NASA Ames Research Center when the fluctuating Mach number is <0.05.

Specifically, the effect of the initial conditions on the evolution of decaying isotropic turbulence was studied at a very low fluctuating Mach number. It was found that where the rms (root mean square) density fluctuations are large compared to the fluctuating Mach number, weak shock waves appear in the system and propagate at the sound velocity. These shocks are vorticity amplifiers and sound generators, as evidenced by time-dependent flow visualization of vorticity and pressure contours. Where shocks occur, there is a transfer of energy from the solenoidal to the irrotational components of velocity. Most of the kinetic energy eventually lies in the compressible velocity modes. Random spot checks confirmed that local regions of vorticity are enhanced by the passage of a shock and that a pressure pulse is emitted when a shock wave hits the center of a vortex region. The figure shows the divergence of velocity at a frozen time level. The shocks are characterized by local regions of strongly negative velocity divergence (green to dark blue contours).

Further simulations of two- and three-dimensional turbulent shear flows will be conducted to assess whether the presence of weak curved shocks can enhance mixing when the convective Mach number is supersonic. These direct simulations improve our understanding of turbulence and can provide a good foundation upon which to build advanced turbulence models.
(Gordon Erlebacher, 42308 and Thomas A. Zang)

Embedded Grids Applied to Delta Wings

The flow over a highly swept delta wing is a focal point for the current interest in high-angle-of-attack aerodynamics. The flow is characterized by two counterrotating primary vortices that form over the wing due to separation at the leading edge. The primary vortices induce adverse pressure gradients that can lead to secondary and tertiary vortices. A coordinated computational/experimental program is under way to provide detailed information concerning the areas in which computational methods can be improved. Computational results from a three-dimensional Navier-Stokes code for the flow over a 75° swept delta wing at an angle of attack of 20.5° have been compared to detailed experimental data obtained in the Basic Aerodynamics Research Tunnel. The comparison revealed that the computation predicted quite well the overall physics of the flow. For instance, the lift and moment, as well as the positions and sizes of the shed vortices, were similar between computation and experiment. However, detailed comparisons of off-body measure-

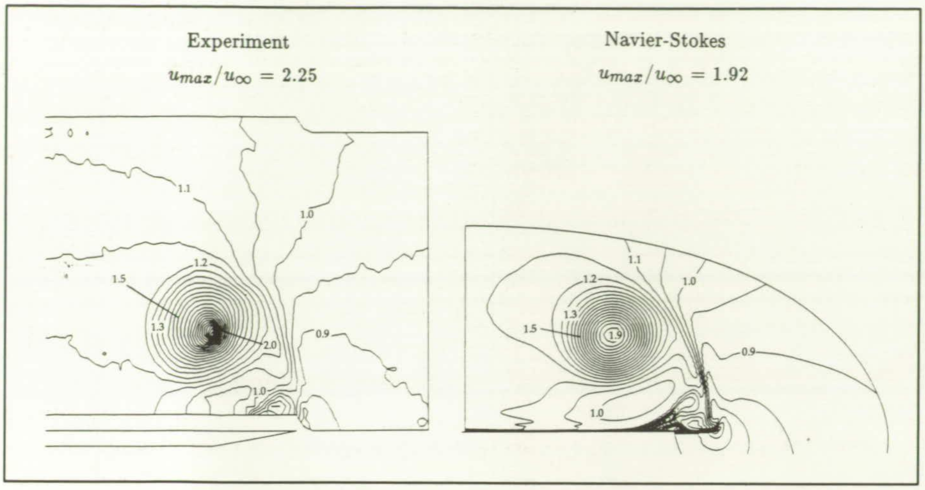

Streamwise velocity contours, $x/L = 0.7$ *and* $\alpha = 20.5°$.

ments of velocity and pressure indicated substantial differences between computation and experiment in the vicinity of the vortex core.

The computational grids are clustered near the surface to resolve the boundary layer, and this leads to coarser grid spacing in the vortex core regions. An embedded grid scheme was implemented into the Navier-Stokes code to improve the local resolution of the vortex core. With the grid embedding scheme, the number of grid points in the core region can be increased without refining the grid throughout the entire physical domain. Thus, for example, the resolution of a grid with 1,214,793 points can be obtained with far fewer points using the embedded grid scheme at a substantial savings in computer time.

Streamwise velocity contours for experimental (left) and computational (right) results at a chord location of 0.7 are shown in the figure. The computational results were obtained using a global grid with one level of embedding. Both the primary and secondary vortices are similar in size and location between experiment and computation. The experimental data show a maximum primary vortex core velocity of 2.25, while the computational method predicts a value of 1.92. This result is a significant improvement over the value of 1.55 obtained without grid embedding. Although the regions of embedding are currently chosen based on knowledge of the flow characteristics and experimental findings, the placement of the embedded grids ultimately will be automatically determined based on the local truncation error.
(S. L. Krist, J. L. Thomas, 42163, and S. O. Kjelgaard)

Application of Generalized Patched-Grid Algorithm to F-18 Forebody With Actuated Strake

Confidence in Navier-Stokes solvers has grown considerably in recent years. This increase in confidence, coupled with ever faster computational speeds, has generated considerable interest in the application of these codes to aircraft geometries. For complex configurations, grid generation is a major consideration; unstructured grids are quite promising, but experience with structured grids is much broader. If structured grids are employed on a complex configuration, then multiple grid blocks are a virtual necessity. To this end, a general grid-block patching algorithm has been developed for use with the Navier-Stokes code CFL3D. The computational grid for a complex geometry may contain as many arbitrarily shaped blocks as are needed to make the grid generation problem tractable and to model accurately the physics of the flow.

The general block patching algorithm has been applied to the computation of the flow around an F-18 forebody with an actuated strake positioned 120° from bottom dead center. The purpose of the strake is to provide yaw control at high angle of attack, a condition under which the rudder loses effectiveness. The figure shows total pressure contours for a laminar-flow solution obtained using CFL3D. A strong vortex forms along the strake and is shed into the flow field above the starboard side; the much weaker vortex arising from boundary-layer cross flow separation is evident on the port side. A significant yawing force is generated in the direction opposite to the strake. Seven grid blocks were used, one on the port side and six on the starboard (strake) side, giving a total of approximately 220,000 points. Patching occurs across eight longitudinal, eight circumferential, and two radial surfaces.

Work is under way to include the F-18 leading-edge extension aft of the forebody strake for estimates of

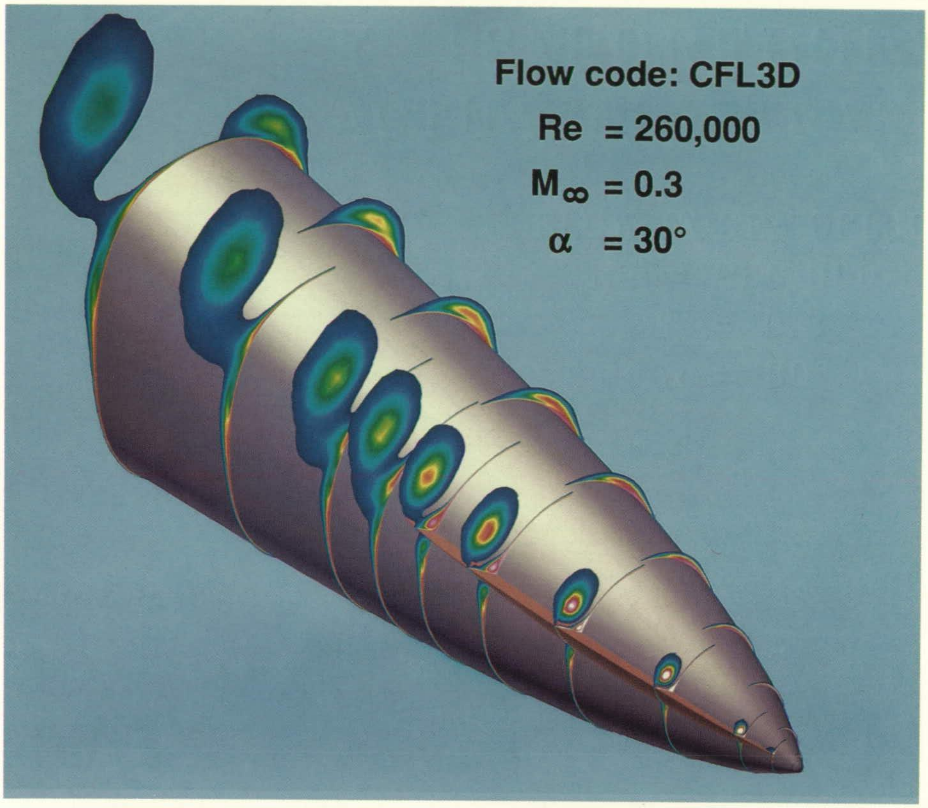

F-18 forebody actuated strake.

flight loads and Reynolds number effects. The code will be calibrated with both flight and wind tunnel data.
(Robert T. Biedron and James L. Thomas, 42163)

Graphical Display of Fluid Flow Results on Unstructured Grids

Software has been developed using the X-windows graphics protocol on inexpensive color workstations for the display of computational fluid dynamics results on two- and three-dimensional (2-D and 3-D) unstructured as well as structured flow field grids. Unstructured grids have gained increasing research focus, driven by the need to generate computational grids for more complex configurations. In contrast to structured grids, the unstructured-grid cells do not necessarily have their nearest neighbors stored contiguously in computer memory. Existing fluid dynamics graphics workstation software, such as the PLOT3D software developed for the NASA Numerical Aerodynamic Simulation (NAS) project, is designed for the more broadly used structured-grid computational solutions.

In addition to providing unstructured-grid graphics capabilities, another goal is to provide a researcher with an easily learned interactive ability to examine rapidly the details of computational flow field results. The software employs a convenient mouse-driven user interface with pulldown menus for feature selection, and other mouse-button/motion combinations for

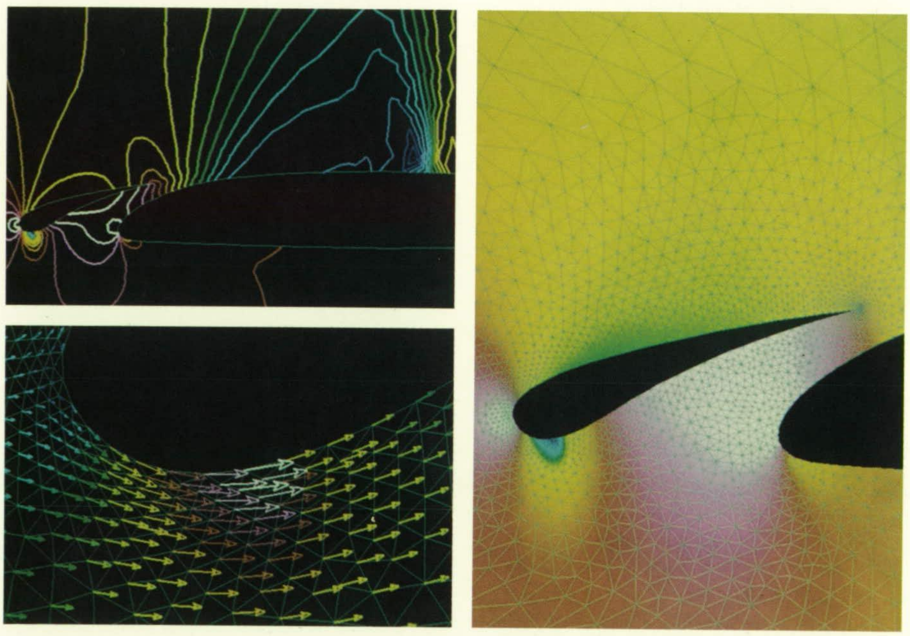

Sample workstation display for unstructured 2-D flow field results (cool colors: low values; warm colors: high values).

ORIGINAL PAGE
COLOR PHOTOGRAPH

rapid manipulation of the image. Since typical inexpensive color workstations have graphics hardware for drawing only constant-color 2-D lines, curves, and polygons (filled and unfilled), software is used to emulate smooth shading and 3-D drawing. This emulation is also necessary with current X-windows functionality. The graphics software has been implemented initially on VAX workstations with 256-color capability. The productivity of researchers is enhanced by the ability to use the inexpensive workstations on their desks for the routine display of computational grids and flow field solutions as an alternative to competing for time on the scarce and expensive resources of a sophisticated and more expensive 3-D graphics workstation shared by many users.

The figure shows some typical window displays that a user can select for viewing a set of 2-D unstructured results. Additionally, a gray-scale rendition of the color image can be generated for output to a PostScript laser printer.

Work is under way to provide 3-D hidden-surface removal in the workstation software. Additional features will be added for improved display control, color manipulation, labeling, and extended functionality. **(Robert P. Weston, 42149)**

Detection of Shock-Induced Separation Using MEDS^3 Technique

The objective of this research is to develop a reliable flow diagnostic tool to detect accurately the shock-induced separation on airfoils at transonic speeds.

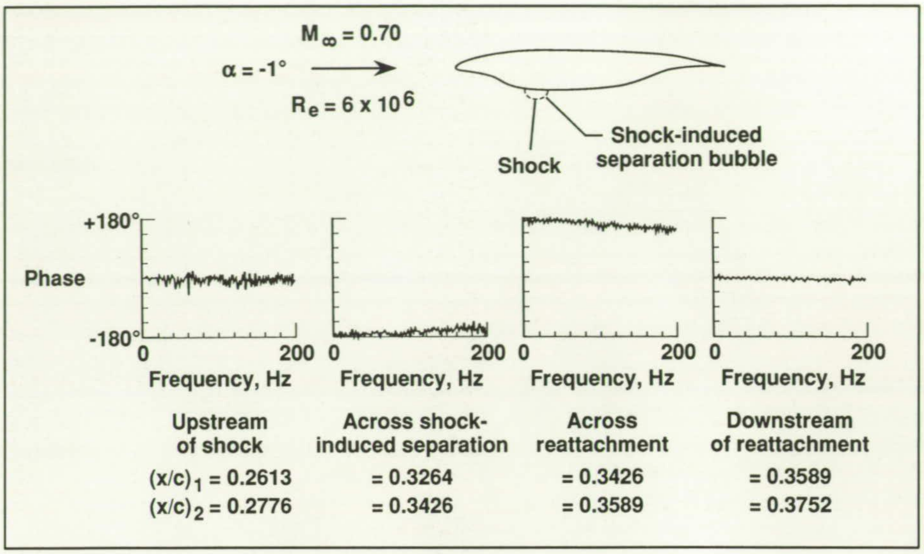

Phase shifts at separation and reattachment.

The Multielement Dynamic Shear Stress Sensor (MEDS^3) technique is used to detect shock-induced separation on a supercritical airfoil model at transonic speeds in the Langley 0.3-Meter Transonic Cryogenic Tunnel. Shock-induced separation is clearly detected by phase reversal in low-frequency dynamic shear stress signals using the MEDS^3 technique (as shown in the figure). When shear stress fluctuations from adjacent surface hot-film sensors are compared, a $-180°$ phase shift is observed across the shock-induced separation, a $+180°$ phase shift is observed across the reattachment, and no phase shifts are obtained upstream and downstream of the separation bubble.

The MEDS^3 technique now can be used not only at low speeds but also at transonic speeds to accurately locate flow separation. Since the phase-reversal phenomenon appears to be independent of the speed regime, there is reason to believe that the technique may also be applicable to supersonic and hypersonic flows.

Future plans include efforts to apply the MEDS^3 technique in flight tests and conduct more detailed fundamental experiments to understand the physical significance of the phase-reversal phenomenon. **(John P. Stack, 41050)**

Supersonic Transition on Cones and Flat Plates

Boundary-layer transition can alter dramatically the drag and heating loads of high-speed vehicles. Despite the importance of this phenomenon and more than three decades of research, large discrepancies between theoretical predictions and wind tunnel measurements still remain. For example, transition has been shown experimentally to occur at much lower Reynolds numbers on flat plates than on cones in conventional, supersonic wind tunnels. The opposite behavior is predicted by linear stability theory. Because conventional super-

sonic/hypersonic wind tunnels are known to be noisy, an investigation was conducted to determine if wind tunnel noise could account for the observed discrepancy between theory and measurement. With the development and successful operation at Langley Research Center of a Supersonic Low-Disturbance Pilot Tunnel, these previously dominant facility disturbances can now be essentially eliminated in the upstream sensitive regions of the cone and flat-plate boundary layers.

Measurements of transition on flat plates and cones in the Supersonic Low-Disturbance Pilot Tunnel show transition Reynolds numbers are approximately an order of magnitude higher in this tunnel than in conventional noisy tunnels (as shown in the figure). The ratio of cone-to-flat-plate transition Reynolds numbers is approximately 0.6 compared with approximately 2 to 2.5 at this Mach number in conventional tunnels.

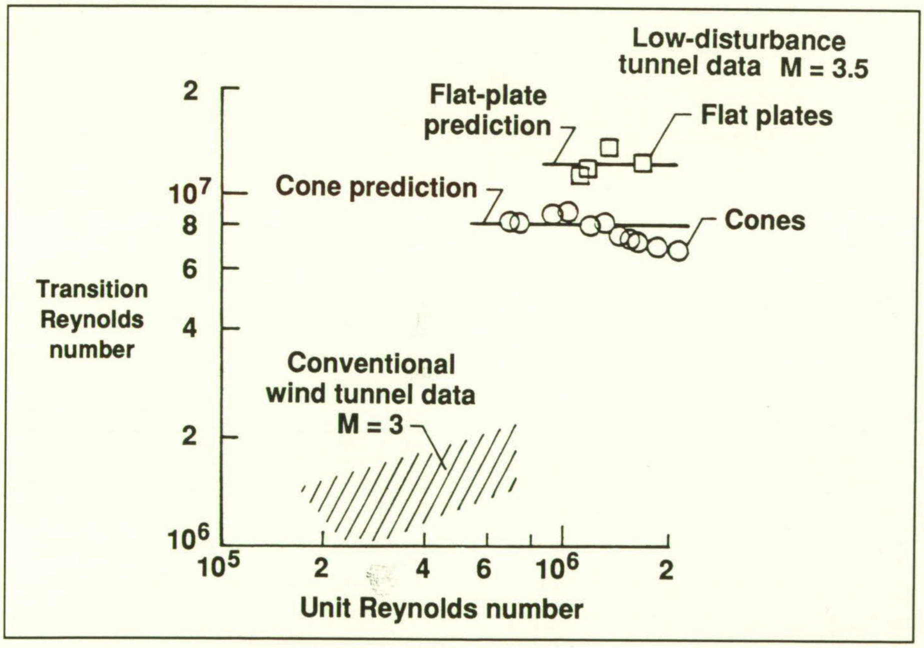

Comparison of transition Reynolds numbers.

Transition predictions based on the e^N method with $N = 10$ are in excellent agreement with both the cone and flat-plate data (as shown in the figure).

These results account for the lower transition Reynolds numbers obtained in conventional tunnels on flat plates and cones and reinforce the importance of using quiet tunnels for high-speed transition studies and the apparent usefulness of the e^N method for transition prediction.
(Ivan E. Beckwith, 45544)

Submerged Vortex Generators

Vortex generators have long been the method of choice for controlling boundary-layer separation on aircraft. Conventional generators are typically vanes set at an angle to the flow and are approximately equal to the boundary-layer thickness in height. This configuration, although effective, imposes a significant device-drag penalty. The objective of the present research was to develop effective, low-drag vortex generator designs.

The Langley 20- by 28-Inch Shear Flow Control Tunnel was used to evaluate various passive and active methods of controlling turbulent boundary-layer separation over a two-dimensional, downstream-facing ramp. Surface oil-flow visualizations and pressure distributions were used to document the effectiveness of the control techniques. Wheeler-type vortex generators with heights of only 10 percent of the boundary-layer thickness were found to be effective separation control devices. The figure shows pressure distributions in the separated flow region with and without the Wheeler vortex generators. Reattachment length, i.e., the distance from the base of the ramp to reattachment (peak pressure point), was reduced by 66 percent over the baseline case.

Submerged, Wheeler-type vortex generators perform almost as well as conventional, vane-type generators for reducing the extent of widely separated flows, and they impose a device-drag penalty of only 10 percent of that for vane-type generators. These characteristics are important for applications

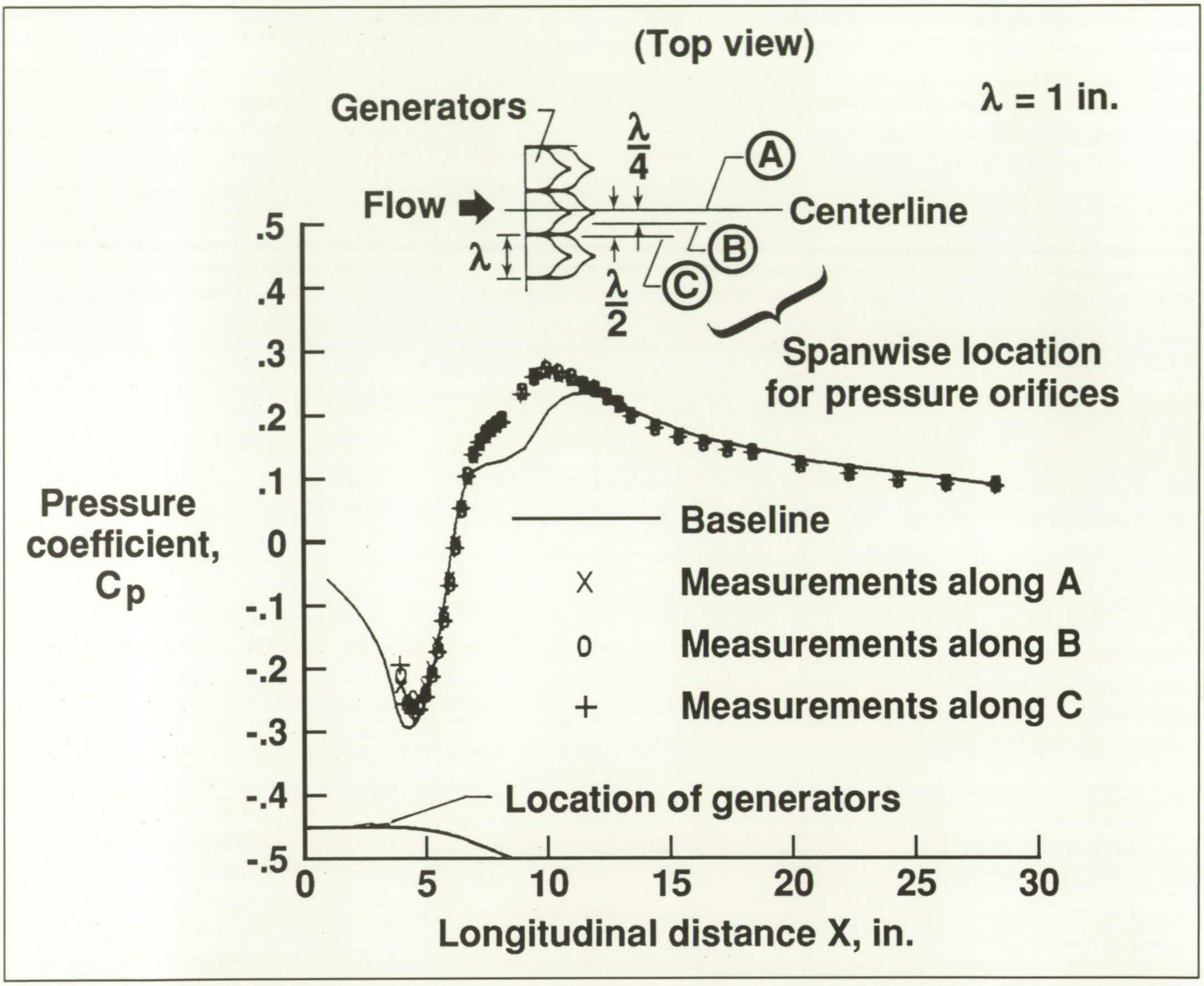

Wheeler vortex generators.

in which device drag is critical (e.g., standby separation control system). **(John C. Lin, 45556)**

Application of Laminar-Flow Control to Supersonic Transport Configurations

Under contract to the Langley Research Center, Boeing Commercial Airplane Company has conducted a study to investigate the feasibility and impact of implementing a laminar-flow-control (LFC) system on a supersonic transport configuration. On the inboard part of the wing, suction was applied over the first 10 percent chord, and laminar flow was predicted to extend to 30 percent chord. On the outboard part of the wing, by using two suction strips, laminar flow was predicted to extend to 40 percent chord (as shown in the figure). In addition, a 20-percent chord natural laminar flow was predicted for the horizontal and vertical tails. This

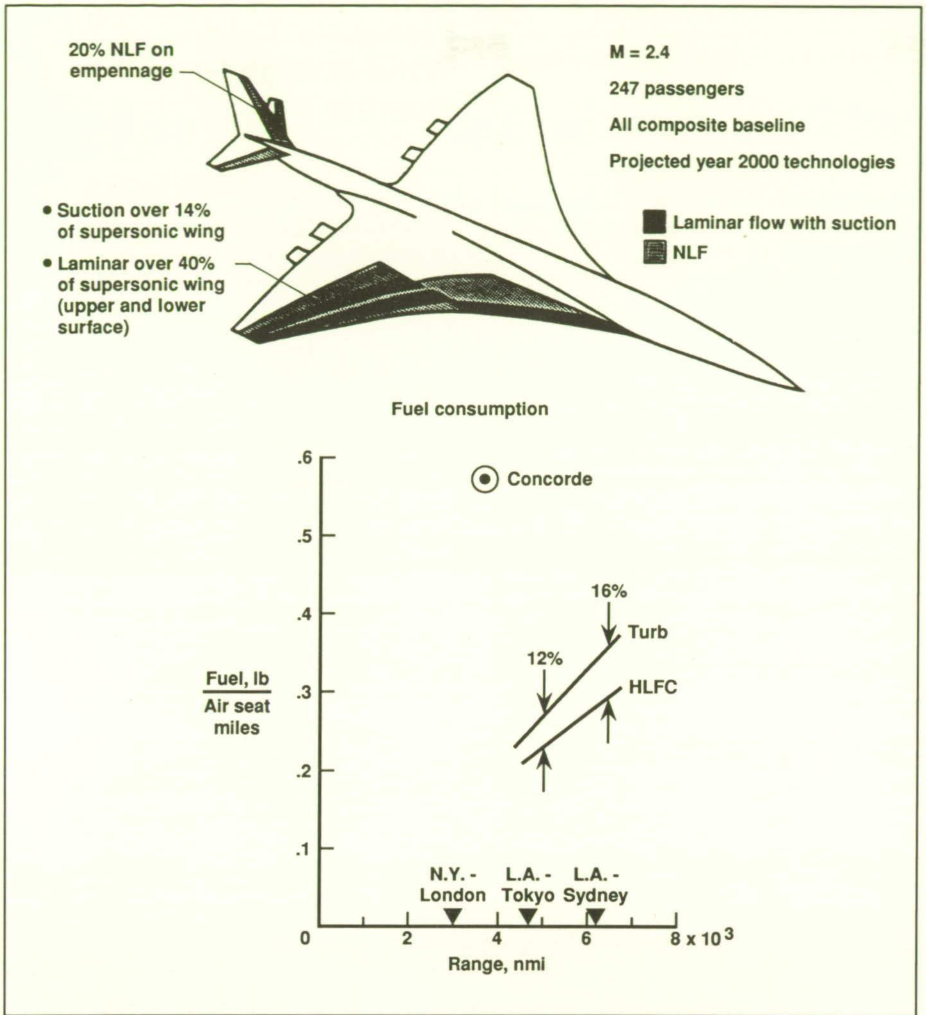

Fuel consumption benefits of hybrid laminar-flow-control (HLFC) supersonic transport configuration as compared to fully turbulent (Turb) configuration.

amount of laminar flow on the wing and empennage resulted in an 8.2-percent reduction in total cruise drag.

The aerodynamic benefit of reduced drag due to the amount of laminar flow (as shown in the figure) was weighed against the penalties of suction system weight, fuel volume displacement, and engine power extraction. At a range of 5000 nmi, the cycled laminar-flow configuration showed a reduction in fuel consumption factor (pounds of fuel/air-seat miles) of 12.0 percent and a reduction in takeoff gross weight of 8.5 percent when compared to the fully turbulent baseline configuration. At a range of 6500 nmi (i.e., Los Angeles, California to Sydney, Australia), the reductions in fuel consumption factor and takeoff gross weight increase to 16.0 percent and 12.9 percent, respectively. Therefore, the aerodynamic benefits afforded by LFC significantly outweigh the LFC system weight, volume, and power requirement penalties, and these benefits improve with increasing range. However, the present study also identified critical areas in aerodynamics, structures, and systems technologies in which significant research and development will be needed in order to realize these potential benefits in a practical application.

(Dennis W. Bartlett, 41916)

Application of Transonic Design Method to Complex Geometries

During the past 5 years, the Langley Research Center has been involved in several research programs that had the requirement of designing or modifying a wing to achieve a given pressure distribution at transonic speeds. In order to meet this requirement, a design method was developed which modifies the surface curvatures and slopes of an initial airfoil geometry so that a target pressure distribution is matched. The Direct Iterative Surface Curvature (DISC) Method was then extended to wings and found to be robust and efficient. This method, which has been useful in designing wings in the presence of other aircraft components (such as winglets, fuselages, and nacelles), can be used to achieve a given pressure distribution and thus reduce or eliminate undesirable flow characteristics or adverse interference effects between different components.

The surface curvature method has been used in a number of design exercises involving complex

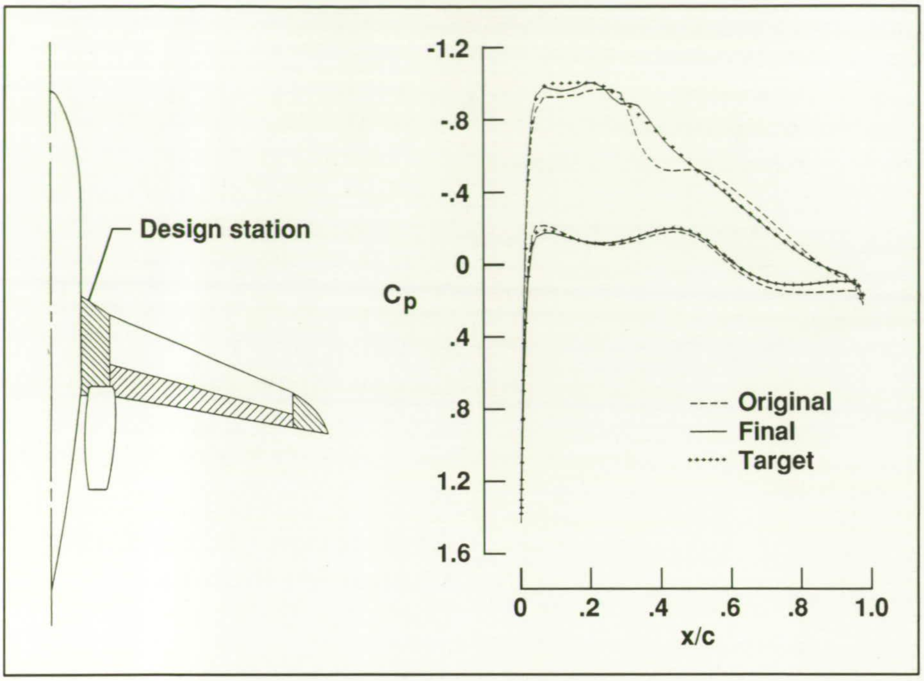

Wing root design to eliminate shock, $M = 0.74$.

geometries. Results for an executive transport with fuselage-mounted nacelles are shown in the figure. The sketch on the left shows a wing root plug (the cross-hatched area ahead of the nacelle) to be added to the existing wing. The flow in this region is strongly influenced by both the fuselage and nacelle. The original wing plug has a fairly strong shock near 40 percent chord (the right half of the figure). The design method was used successfully to modify the wing to eliminate this shock and to give a more uniform isobar pattern in this region.
(Richard L. Campbell and Leigh A. Smith, 42872)

Construction and Transonic Testing of Thin Wing at High Reynolds Number

Airfoils used in supersonic fighter aircraft are typically very thin. Building thin airfoil models with pressure instrumentation for cryogenic testing is unusually difficult. However, a technique that uses chemically etched pressure channels in the bond planes between multiple sheets of metal has been developed at the Langley Research Center. The canard of the X-29 fighter aircraft was chosen as a proof-of-concept model to build. This configuration has a maximum thickness of only 5 percent of chord, and it is highly tapered from root to tip, making pressure instrumentation very challenging.

The first figure is a photograph of the X-29 canard upper surface.

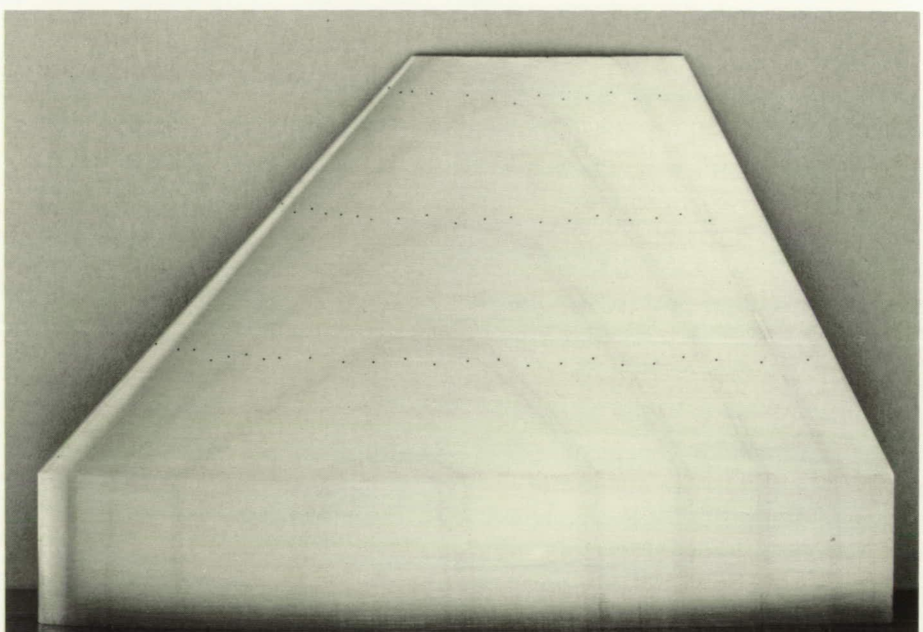

Upper surface of canard model showing bond planes and orifice rows.
L-88-3055

ORIGINAL PAGE
BLACK AND WHITE PHOTOGRAPH

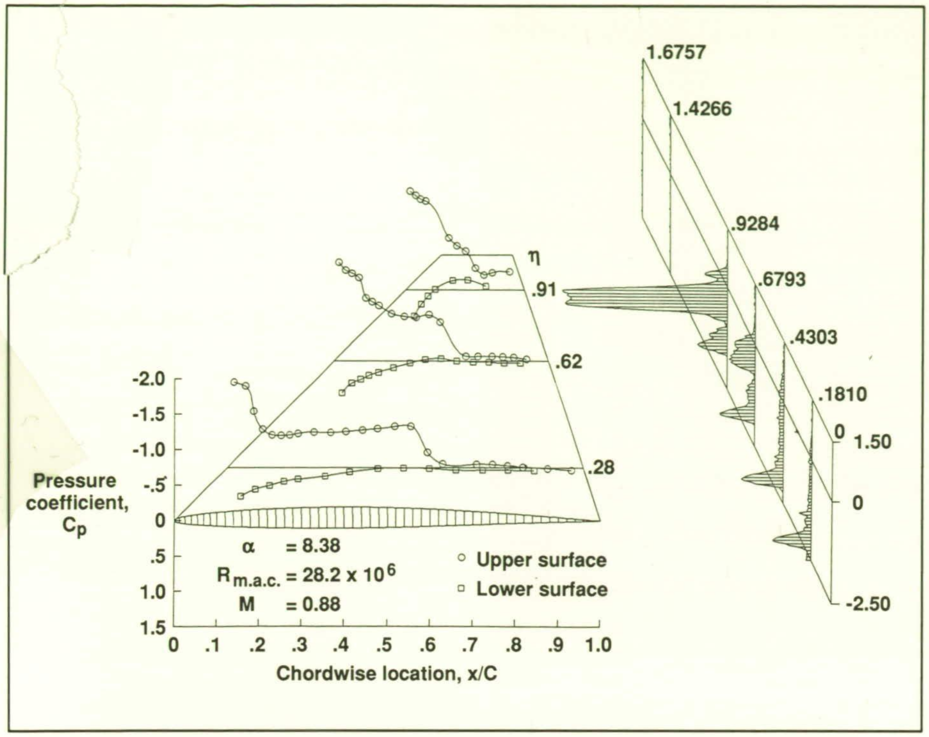

Sample of surface pressure and wake data on X-29 canard model.

Three rows of orifices with a total of 56 orifices on the upper surface exist, and six thin plates form the upper surface of the airfoil. The outcrop of the five bond planes is clear in the figure. There are 37 additional orifices on the bottom surface; these orifices are deliberately staggered to minimize any buildup of boundary-layer instabilities. The choice of model size to test resulted in a root chord of 14.5 cm and a corresponding maximum thickness of only 0.725 cm.

The model, which was mounted on the sidewall turntable in the adaptive-wall test section of the Langley 0.3-Meter Transonic Cryogenic Tunnel, was tested in May 1988. Testing took place over nearly the full range of conditions available with the adaptive-wall test section. For testing this semispan three-dimensional model, a special computational method was used to adapt the flexible test section floor and ceiling for minimum interference. Aerodynamic data were taken for the airfoil (surface pressures and wake survey) at Mach numbers from 0.3 to 1.07. At most Mach numbers, a 10-to-1 range of Reynolds number was covered, and Reynolds number flight values were obtained easily. The second figure shows an example of the airfoil data at an angle of attack of 8.38°, a Mach number of 0.88, and a Reynolds number (based on mean aerodynamic chord) of 28.2×10^6. **(Pierce L. Lawing, 45137)**

Navier-Stokes Simulation of Wind Tunnel Choke

The Langley 8-Foot Transonic Pressure Tunnel (TPT) is presently being converted from the special-purpose configuration of the laminar-flow-control experiment back to a general-purpose configuration for transonic performance testing. A two-wall sidewall choke located downstream of the test section is also being considered to further improve test section flow quality. As part of the choke design effort, computational fluid dynamics (CFD) is being utilized to assess the feasibility of the proposed choke design and to provide design load estimates.

Initial computations have been performed for the sidewall geometry of the tunnel, both with and without the choke, using a method that explicitly solves the two-dimensional compressible Navier-Stokes equations by a multistage Runge-Kutta integration technique. An H-topology grid of approximately 37,000 points was generated with sufficient clustering to resolve the wall turbulent boundary layer, where the turbulence is represented by the Baldwin-Lomax algebraic eddy-viscosity model. Solutions were obtained using mesh sequencing and required approximately 10 min of CRAY-2 time to achieve a residual reduction of four orders of magnitude.

Mach contours for two turbulent solutions are shown in the figure for a test section Mach number of 0.70 and a Reynolds number of 12×10^6 based upon a choke chord of 4 ft. The upper half of the figure is for the sidewall simulation of the empty tunnel; the lower half of the figure includes the sidewall choke.

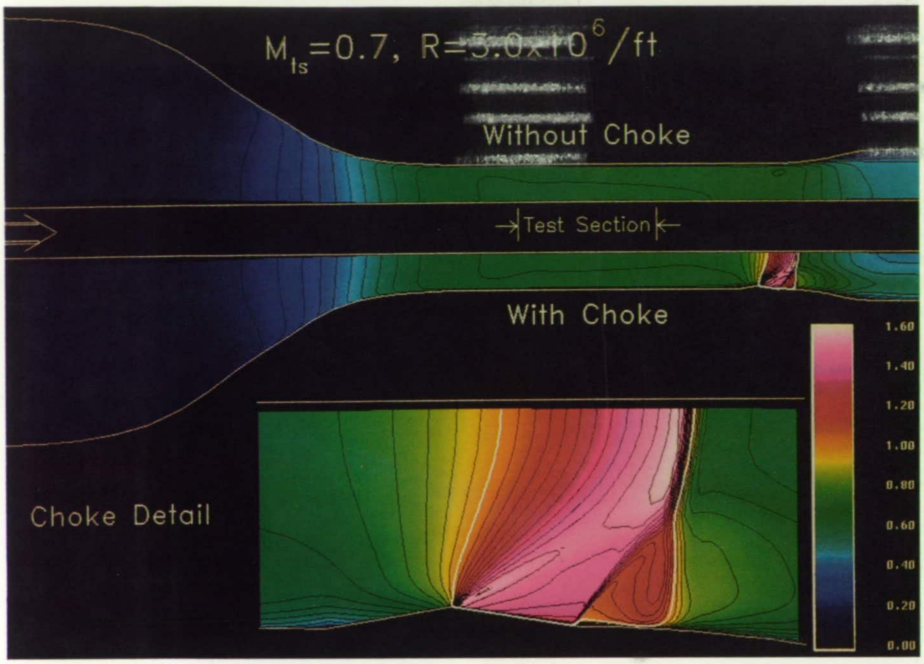

Sidewall simulation, Mach contours.

The results indicate that the upstream perturbation of the choke was minimal. Details of the flow over the choke are also shown in the figure with the sonic line highlighted; they illustrate the supersonic expansion over the crest of the choke followed by a combination of oblique and normal shocks in a λ-pattern. This result also demonstrates that the flow remained attached over the choke with only a minor separation pocket at the foot of the oblique shock where the choke meets the tunnel sidewall. Additional computations have indicated that meaningful simulations of the sidewall flow in the wind tunnel can be accomplished with the two-dimensional formulation by modifying the boundary conditions to account for certain three-dimensional effects.

(J. M. Luckring, 42869, B. L. Bates, and R. C. Swanson, Jr.)

Navier-Stokes Solutions for Asymmetric Vortical Forebody Flows

Asymmetric vortex shedding arises when slender bodies, typical for missiles and fighter aircraft noses, are set at large angles of attack (typically $\alpha \geq 30°$). Under these conditions, side forces occur which become so large that they dominate the lateral stability of these vehicles. Experimental surface pressure data suggested that small geometric imperfections (such as an out-of-round tip of a sharp-nosed wind tunnel model) control such vortex asymmetries along the entire body. This control mechanism is confirmed in the present computational study, in which the surface geometry of a 3.5-caliber tangent-ogive cylinder is perturbed into slightly elliptic cross sections just at the nose tip.

Steady-state solutions for vortical flows with $0.2 \times 10^6 \leq Re_D \leq 3.0 \times 10^6$ (D is the maximum diameter) and $20° \leq \alpha \leq 40°$ have been obtained using FMC1, a time-implicit upwind method for the three-dimensional, incompressible Navier-Stokes equations. This solver, which comprises flux-difference splitting (an upwind discretization of the inviscid fluxes)

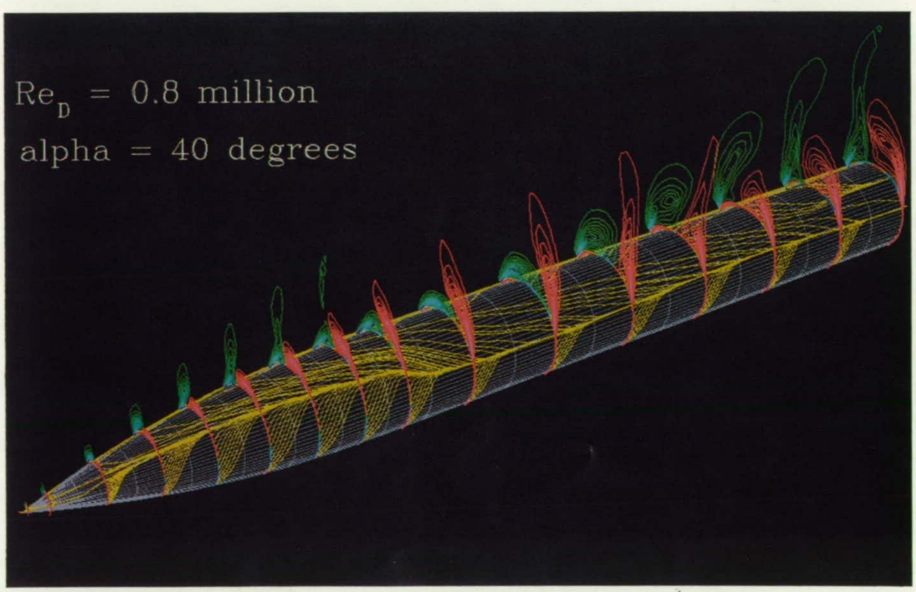

Helicity density contours.

ORIGINAL PAGE
COLOR PHOTOGRAPH

and an extension to the algebraic turbulence model by Baldwin-Lomax, allows, for the first time, computational modeling of transitional cross flow separation (i.e., flows with three-dimensional, laminar, equatorial separation bubbles, and subsequent transition in the separating shear layers that roll up into two primary vortices).

By rotating the perturbed nose tip, the computed surface pressures indicate an almost sinusoidal variation of side force with roll angle while the vortex shedding frequency remains close to a fixed value. These two integral properties and the computed surface pressure distributions themselves agree well with experimental data. A typical result is shown for $\alpha = 40°$ and $Re_D = 0.8 \times 10^6$. The computed flow field is visualized by means of helicity density contours (helicity density is defined as the scalar product of the local velocity and vorticity components), which are superimposed on a surface flow pattern. This plot discloses four vortex shedding events and their spatial frequency. Further analysis using computational flow visualization techniques disclosed that maximum local side force is associated with one dominant primary vortex in the wake and an asymmetric arrangement of the lateral primary separations. Minimum local side force is distinguished by primary vortices of approximately equal strength and an almost symmetric separation pattern.

(Peter-M. Hartwich, Robert M. Hall, 42881, and Michael J. Hemsch)

Reynolds Number Effects on Boeing 767 Airplane Model

A Memorandum of Agreement between NASA (Langley and Ames Research Centers) and the Boeing Commercial Airplane Company calls for testing an 0.03-scale model of the Boeing 767-200 airplane in the National Transonic Facility (NTF) at Langley, the 11-foot transonic leg of the Unitary Plan Wind Tunnel at Ames, and the Boeing Transonic Wind Tunnel. The agreement calls for low Reynolds number testing in the three facilities for tunnel comparison. No significant difference has been observed in the data from the three facilities. High Reynolds number testing is being conducted in the NTF (as shown in the first figure) to determine Reynolds number effects on the aerodynamic characteristics; to obtain data at full-scale Reynolds number for comparison with available flight test data; and to obtain data for the development and enhancement of Reynolds number scaling techniques.

Data have been obtained at Reynolds numbers ($R_{N,\bar{c}}$), based on mean aerodynamic chord, from 4.5×10^6 (conventional wind tunnels) to 40.0×10^6 (cruise flight). The data shown are the Reynolds number effect on the drag polar for the tails-off configuration. Also shown are the 4.5×10^6 Reynolds number data corrected for Reynolds number effects on skin friction at 40.0×10^6; the difference between the high Reynolds number data and the low Reynolds number corrected data can be attributed to uncorrected drag contributions such as interference drag and aeroelasticity. The results are typical of the other configurations

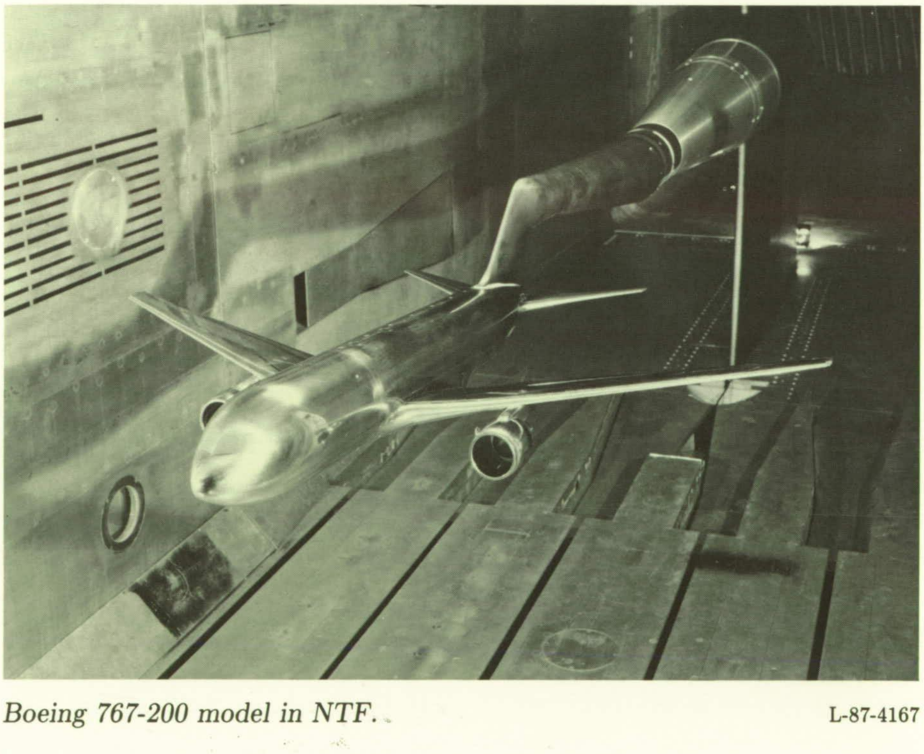

Boeing 767-200 model in NTF. L-87-4167

ORIGINAL PAGE
BLACK AND WHITE PHOTOGRAPH

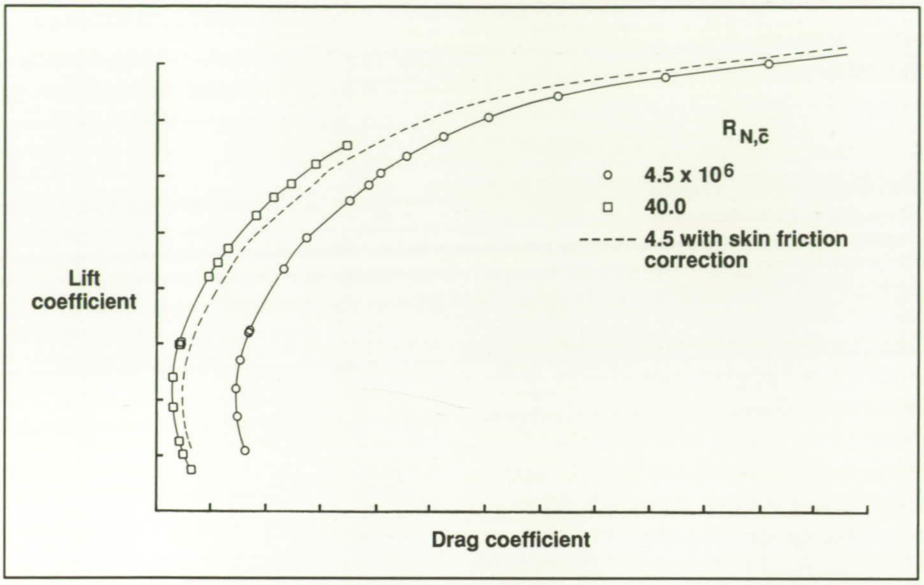

Reynolds number effect on Boeing 767-200 model (tails off; $M_\infty = 0.80$).

and conditions. The data were shown to be very repeatable.
(Stuart G. Flechner, 45108 and Blair B. Gloss)

Transonic Wind Tunnel Wall Interference Prediction Code

The influence of wind tunnel walls on the flow in a test section and the resulting effects on the wind tunnel data have long been the subject of concern for experimentalists. More recently, there has been an increased emphasis on computationally determining wall interference effects. In response to this need, a small disturbance transonic wall interference prediction code has been developed to analyze the influence of wind tunnel walls on a configuration mounted in a test section. Wall boundary conditions that can be modeled by this code include solid, open, perforated, and slotted walls as well as slotted and solid walls with viscous effects. This code, which evolved from the Wing-Body-Pod-Pylon-Winglet (WBPPW) code developed by Charles Boppe of Grumman Corporation-Aircraft Systems Division, is capable of modeling WBPPW configurations. Modifications were made to the Cartesian grid system and to the outer boundary conditions of the WBPPW code to implement the various wall models.

An example of results obtained with the wall interference prediction code can be seen in the figure for a Mach number of 0.826 and a lift coefficient of approximately 0.18. The experimental data were taken in the High Reynolds Number Channel 1 Tunnel at Ames Research Center on an untapered, swept semispan wing. This model is swept 20°, has an aspect ratio of 3, and an NACA 0012 airfoil section. The Channel 1 Tunnel is 10 in. by 15 in. with solid walls. The blockage ratio for this case is approximately 2 percent.

Significant differences between the computations modeling the wind tunnel walls and free-air conditions can be seen in the pressure coefficient C_p distributions at an inboard station (similar results were seen at all span stations). The changes in the level of pressures on the upper and lower surfaces and in the shock location resulting from simulating free air and solid wind tunnel wall boundary conditions are indicative of the strong interference effects of the tunnel walls. For example, one influence of the solid wall on the tunnel flow properties is to increase the effects of blockage, thereby yielding an apparent increase in the free-stream Mach number. This increase is evident in the pressure distribution presented by the increase in the level (i.e., more negative pressure coefficients) of upper surface pressure coefficients and by the more aft shock location relative to the free-air results.

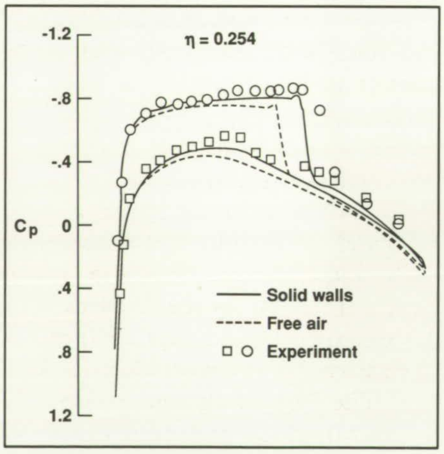

Comparison of computation and experiment on swept NACA 0012 wings.

Good agreement exists between experimental results and computational results when the solid wind

tunnel walls are modeled. As illustrated in the figure, reasonable agreement between experiment and computations could not have been obtained without accounting for the influence of the tunnel walls.
(Pamela S. Phillips, 42880 and Edgar G. Waggoner)

General-Aviation Easy-to-Fly Concepts

New flight control and display concepts are being developed through the use of the General Aviation Simulator. These systems, which are intended to reduce initial training and recurring practice requirements for pilots and thus make general-aviation airplanes a safer and more practical transportation system, are as user friendly as possible. To emphasize the instinctive reactions of the test subjects, no practice or training simulator runs are given and only two runs are made with any one test subject. Test subjects range from NASA research pilots to nonpilots. Both test runs are made using a head-up display (HUD), which is a pictorial display of a "highway in the sky" designed to resemble a road marked with lane stripes as shown in the figure. The display also includes a horizon line and telephone poles to provide a more realistic altitude cue. The first run is made with a fly-by-wire decoupled control system (Ez-Fly) which has responses designed to resemble those of an automobile. The second run is made with a conventional control system (baseline) which is typical of current airplanes.

A comparison of one nonpilot's control activity and performance

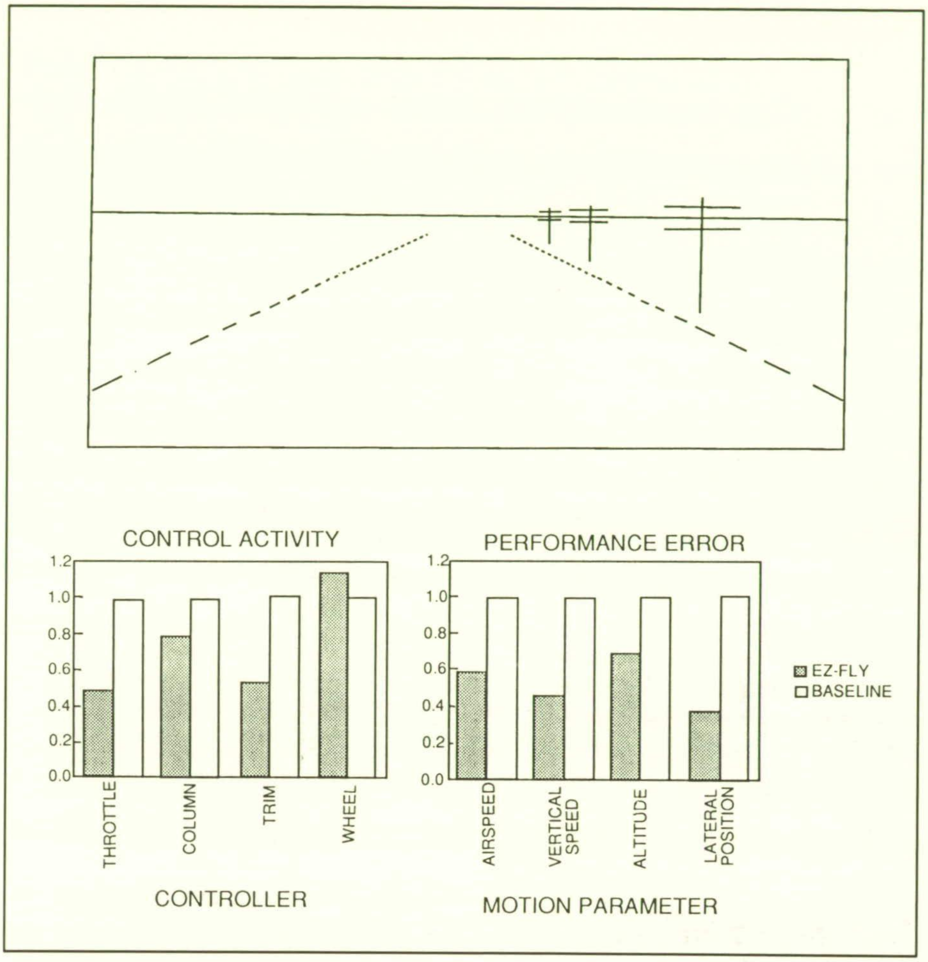

"Highway-in-the-sky" display format.

(shown in the bottom of the figure) indicates smaller controller activity and much better performance with the Ez-Fly system. In fact, the test subject was able to fly (without training and on the first attempt) a complete maneuver from takeoff, around a race-track-shaped path in simulated clouds, to an acceptable landing. Using the baseline conventional control system and the experience gained on the first run, the test subject was able to complete approximately 75 percent of the maneuver using the "highway-in-the-sky" display, but crashed short of the runway. Refinements to the display format and further tests are planned.
(Eric C. Stewart, 43939)

Natural Laminar Flow Certification Program

For the past decade, Langley Research Center has contributed to the development of natural laminar flow (NLF) technology for application to business, commuter, and transport aircraft. Application

Natural laminar flow research airplane. L-88-13,090

of this technology to new airplane designs has brought into question the adequacy of the existing Federal Aviation Regulations (FAR) Part 23 for certification of new general-aviation-type aircraft having significant NLF. In a joint NASA, Cessna Aircraft Company, and Federal Aviation Administration program, a Cessna T210 airplane is being tested in accordance with FAR Part 23 with a modified wing incorporating a NASA-designed NLF airfoil section, an NLF horizontal stabilizer, and a smoothed vertical stabilizer. Research flights address the aircraft performance, stability, controllability, and stall characteristics with combinations of laminar and turbulent boundary-layer configurations on the aircraft wing and tail surfaces.

Flight test results to date show that the fully turbulent configuration degrades airspeed 15 knots compared to the fully laminar configuration without degrading handling characteristics. For both boundary-layer configurations, stall maneuvers show the absence of both prestall buffet and wing roll-off tendency at a stall entry rate of one knot per second at idle power. **(Gregory S. Manuel, 43864)**

Flight Testing of Strakes on Helicopter Tail Boom

A flight test program has been completed at Langley Research Center to evaluate the benefits of using strakes on a helicopter tail boom. A strake is a spoiler mounted along the upper left side of a tail boom to beneficially change the air loading on the tail boom of single main rotor helicopters in low-speed flight. Generally, helicopters can experience tail rotor power and yaw control limitation in right sideward flight or in hovering in winds from the right. By changing the air loading on the tail boom, the thrust and power required of a tail rotor are reduced. A second strake mounted on the lower left side augments the benefits. The concept was first evaluated with a two-dimensional test apparatus in the Langley 14- by 22-Foot Subsonic Tunnel. The flight testing was conducted with a Bell Helicopter 204B at the Wallops Flight Facility. Testing was conducted for wind speeds of up to 35 knots and wind azimuths of 0° to 330°. At the critical wind speed and azimuth, tail rotor power was reduced and yaw control was improved. Tests at higher flight speeds disclosed no problems introduced by the presence of the strakes. The results demonstrate that strakes are an economical way to improve helicopter low-speed flight handling qualities, particularly in right sideward flight. **(Henry L. Kelley, 45088, John C. Wilson, and C. Cook)**

Flight test of Bell Helicopter 204B with tail boom strakes. L-88-4857

Dynamic Stall Research

Future fighter aircraft probably will incorporate advanced controls technology that will provide a very high degree of agility and maneuverability. These capabilities will allow aggressive maneuvering in the high-angle-of-attack flight regime that is typically dominated by unsteady vortex flows. A broader understanding of the complex mechanisms involved in such flows is of great importance in developing methods for improving the high-angle-of-attack, stall/poststall combat maneuverability of modern fighter aircraft. As part of an ongoing research program in high-angle-of-attack unsteady aerodynamics, wind tunnel studies have been conducted in the Langley 12-Foot Low-Speed Tunnel to explore effects of large-amplitude pitch motions on aerodynamic force and stability characteristics of an F-18 model. This model was tested using a computer-controlled, hydraulically actuated dynamic pitch rig, which is schematically shown in the figure. Oscillation and ramp motions were tested at various rates and amplitudes. Smoke flow visualization was conducted to aid in the analysis of the data, and simulation studies are being made on the Langley Differential Maneuvering Simulator to obtain insight into the potential effects of dynamic stall phenomena on aircraft maneuvering capability.

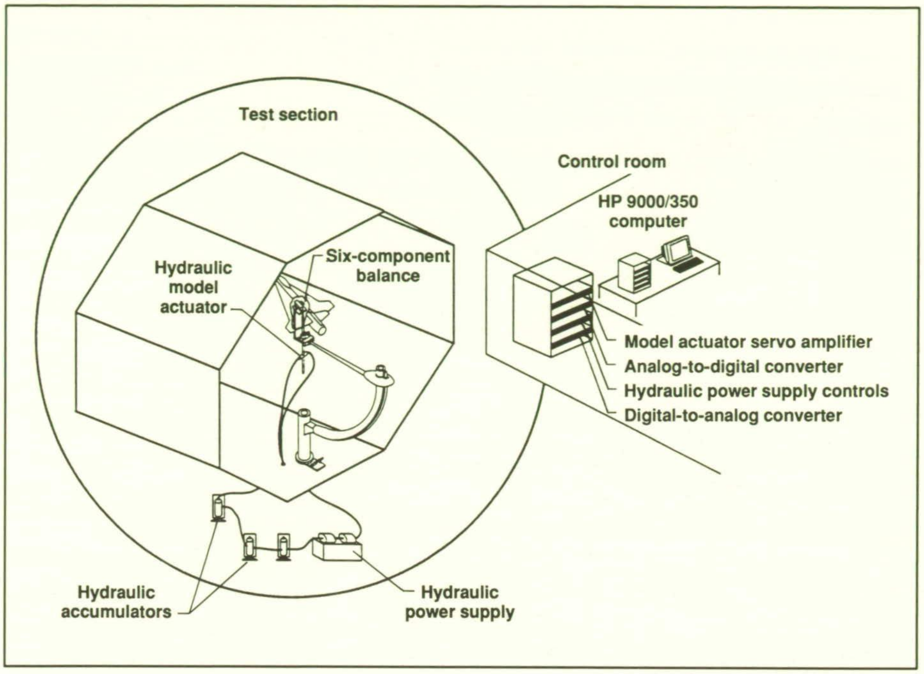

Dynamic stall test setup.

Results of the study show large effects of pitch rate on aerodynamic coefficients. Lags in the vortex burst location and separation/reattachment of flow on the upper surface of the wing produced large overshoots and hysteresis in the force-and-moment data. A major consideration when evaluating the impact of observed dynamic effects on the high-angle-of-attack maneuverability of an aircraft is the persistence of the dynamic effects once the airplane motion stops. The data show that the duration of dynamic stall effects is strongly dependent on both pitch rate and angle-of-attack range. Persistence times of up to approximately 45 convective times (the time needed for an air particle to travel across the chord of the wing) were obtainable at realistic pitch rates. Further testing is continuing to develop methods to control and exploit high-angle-of-attack unsteady aerodynamic effects for maneuvering enhancements.

(Jay Brandon, 41142 and Gautam Shah)

Euler Analysis of High-Speed Civil Transport Concept

A High-Speed Civil Transport concept for Mach 3 cruise has been defined to identify the technology requirements for this class of aircraft. This particular concept was sized to carry 250 passengers over a range of 6500 nmi based on technologies that are expected to be available in the 1995 to 2000 time period. The preliminary aerodynamic studies were performed using state-of-the-art linearized potential methods. As the concept matured, it became appropriate to apply the emerging computational fluid dynamics (CFD) technology. The GEM3D Euler solver, developed by Dr. Michael J. Siclari of Grumman Aerospace Corporation, was chosen for this study.

The GEM3D analysis was performed on the wing and body at a

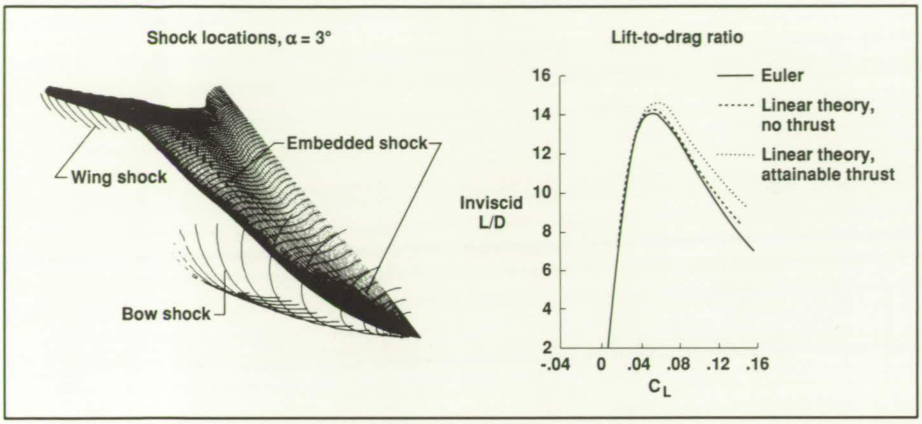

High-Speed Civil Transport Euler analysis (Mach 3).

typical cruise condition of Mach 3 and an angle of attack of 3°. The lift coefficient is approximately 0.1 for this condition. The figure shows that the Euler analysis predicts embedded cross flow shocks on the wing upper surface at cruise. These shocks are sufficiently strong to separate a turbulent boundary layer according to a simple static pressure criterion. The integrated forces from the GEM3D code were compared with those from the linearized potential theory. The lift and drag forces define the lift-to-drag ratio, which is an important aircraft performance parameter. The GEM3D Euler method predicted lower inviscid lift-to-drag ratios than the linearized potential theory. Therefore, the range estimates based on linearized potential theory are optimistic because range depends directly on lift-to-drag ratio.
(James L. Pittman, 45585 and Daryl L. Bonhaus)

Incipient Leading-Edge Separation

In supersonic wing design, the aerodynamicist would like to have control over the formation of leading-edge separation in order to make optimum use of both separated- and attached-flow conditions at the leading edge. Thus, it becomes important to be able to predict and understand the effects of certain geometric parameters on the initial formation of leading-edge separation. A computational study was conducted to determine the effects of leading-edge radius and camber on the initial formation of leading-edge separation on the leeside of a 65° conical delta wing at Mach 1.6. Conical Navier-Stokes solutions were obtained on geometries that varied in leading-edge radius and/or spanwise camber.

A summary of the results is shown in the figure. The test conditions were Mach 1.6, a local Reynolds number of 1×10^6, and a turbulent boundary-layer condition. The computational data are presented in the form of cross flow Mach number contours and surface-pressure distributions. The data show that at an angle of attack $\alpha = 4°$, the leading-edge separation observed on the sharp leading-edge geometry is prevented through the use of leading-edge radius. At the higher angle of attack of 8°, the rounded leading-edge geometry has a leading-edge separated flow pattern that can be prevented through the use of spanwise camber. Based on this study, three wind tunnel models are being designed to verify these results.
(S. Naomi McMillin, 45581)

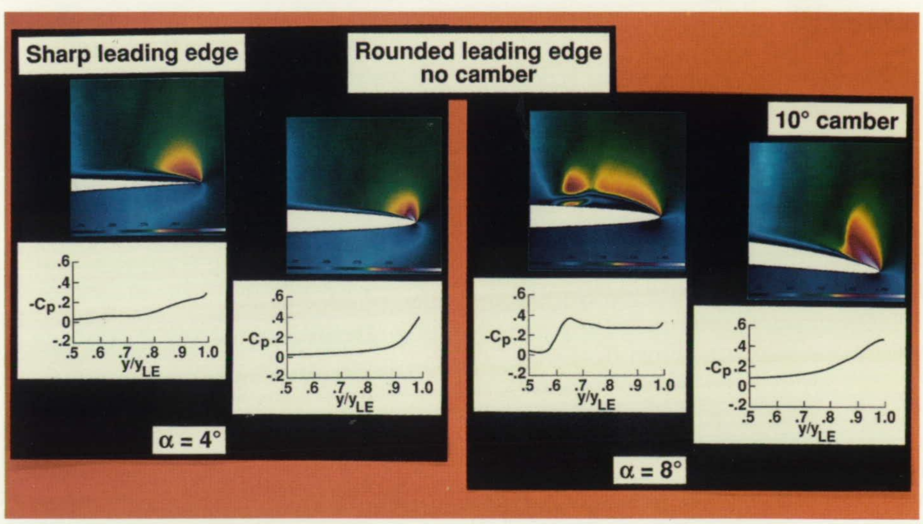

Incipient separation computational study ($M = 1.6$, $\Lambda = 65°$, and $R_e = 1 \times 10^6$). L-89-2520

CARS and LDV Measurements in Supersonic Reacting Flow

A laboratory-scale supersonic burner (SSB) has been constructed and installed in the Nonintrusive Diagnostics Laboratory (NDL). The SSB is an axisymmetric device that produces a hot, Mach 2 flow of vitiated air with centerline injection of hydrogen at the SSB exit plane. Simultaneous measurements of temperature, nitrogen density, and oxygen density have been made in the supersonic exhaust of the SSB using a Dual Stokes Coherent Antistokes Raman Spectroscopy (CARS) system. The first figure shows the SSB with the laser beams

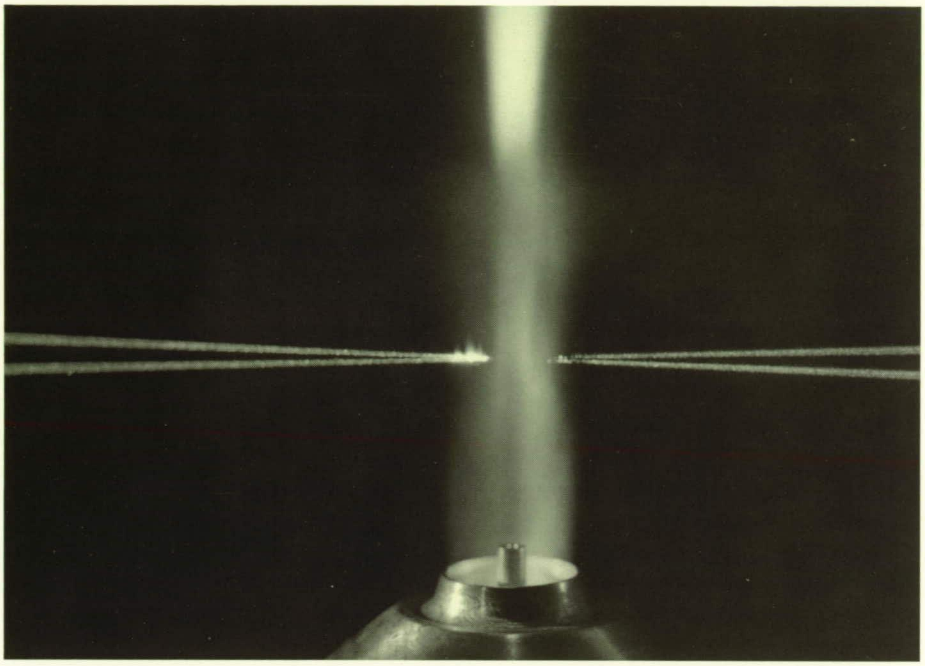

Supersonic burner with CARS laser beams focused in flow for simultaneous generation of nitrogen and oxygen signals. L-87-262

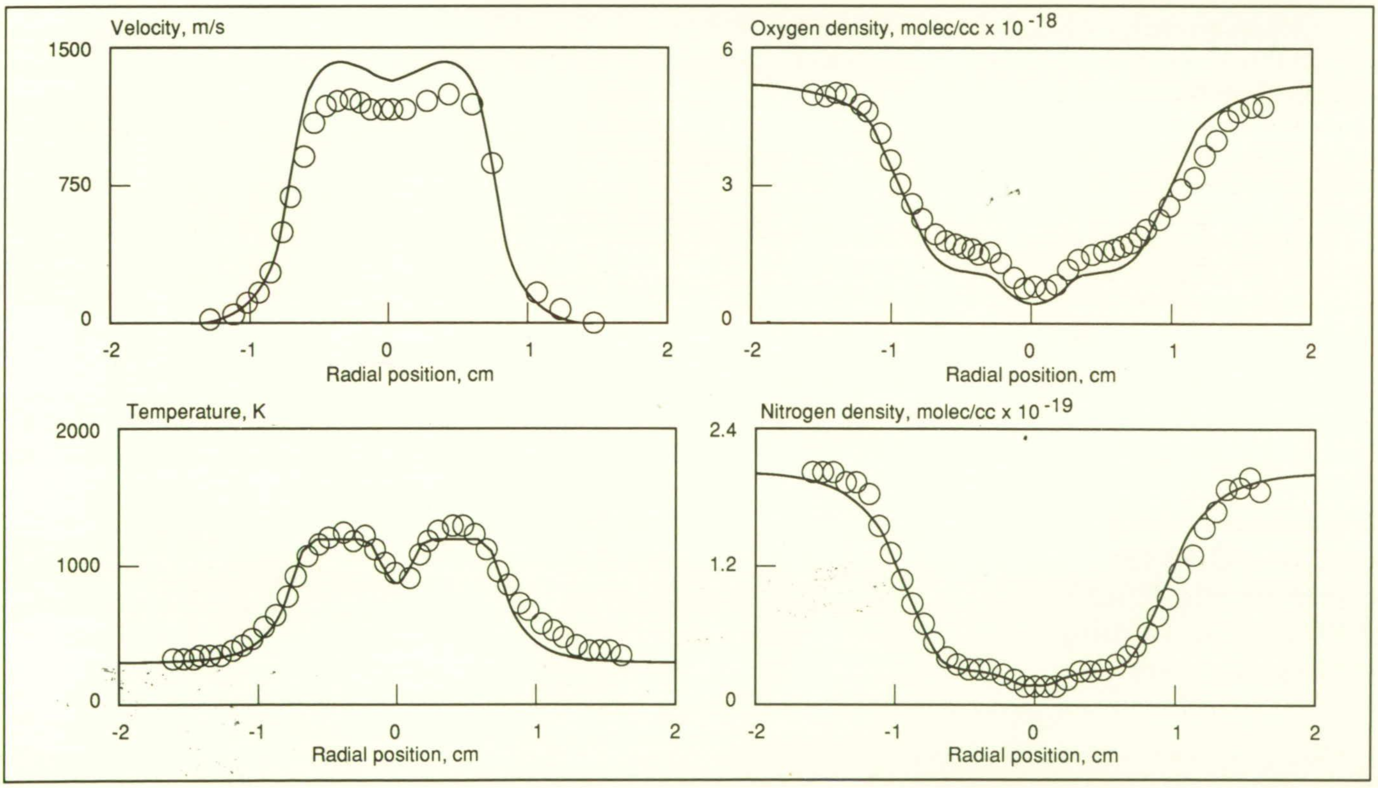

CARS temperatures, nitrogen and oxygen densities, and LDV velocity profiles 5.08 cm above supersonic burner exit plane compared with CFD (line) results.

used to generate the CARS signals in the flow field. Laser Doppler velocimeter (LDV) measurements of velocity in the SSB flow were made under a grant with Virginia Polytechnic Institute and State University (VPI&SU). These data have been collected to provide a data base for comparison with the results of computational fluid dynamics (CFD) modeling of the supersonic flow. The code used for initial comparisons was a modified SPARK code.

Examples of CARS and LDV measurements are shown in the plots. These data are radial profiles of the SSB flow 5.08 cm from the nozzle exit plane. The averages of one thousand LDV samples and one hundred simultaneous temperature, nitrogen, and oxygen measurements are presented at each radial location. The LDV data were not simultaneous with CARS. The CFD-CARS/LDV comparisons are shown in the second figure.

Currently, a hardened CARS system is being assembled to function in the hostile (sound level > 150 dB) environment of the Scramjet Test Complex Test Cell #2, a vitiated test facility.
(Olin Jarrett, Jr., 46320)

Application of New Adaptive Grid for Aerodynamic Predictions of Shock Containing Supersonic Jets

Future propulsion systems for fighter aircraft must be designed for maximum maneuverability over a wide range of flight Mach numbers. This feature can be achieved with rectangular or nonaxisymmetric nozzles. A few codes are available to predict the aerodynamics of three-dimensional shock containing single and twin jets. However, nonaxisymmetric jet and twin jets always go through very complex shock-cell structure and evolution of cross-sectional shapes. A need exists for a good adaptive grid technique that allows the grid point positions to change as the jet problem is calculated.

An efficient adaptive grid-generation method providing high grid density for the jet shear layer and the internal shock system has been developed. The grid adaptation strategy is based upon the monitoring surface concept established by Peter R. Eiseman. The grid-generation system is algebraic and computationally efficient. The system achieves a close approximation to grids generated through the Euler-Lagrangian differential equations.

Computations for a single circular supersonic jet are chosen as an example to validate this adaptive grid approach. A Cartesian grid adapted to a polar pattern is generated to provide high-density coverage of the jet plume cross section. The simplified Reynolds-averaged Navier-Stokes equations are solved using space marching in the streamwise direction and the van Leer flux splitting scheme in the cross plane. Mach surfaces at different streamwise locations are

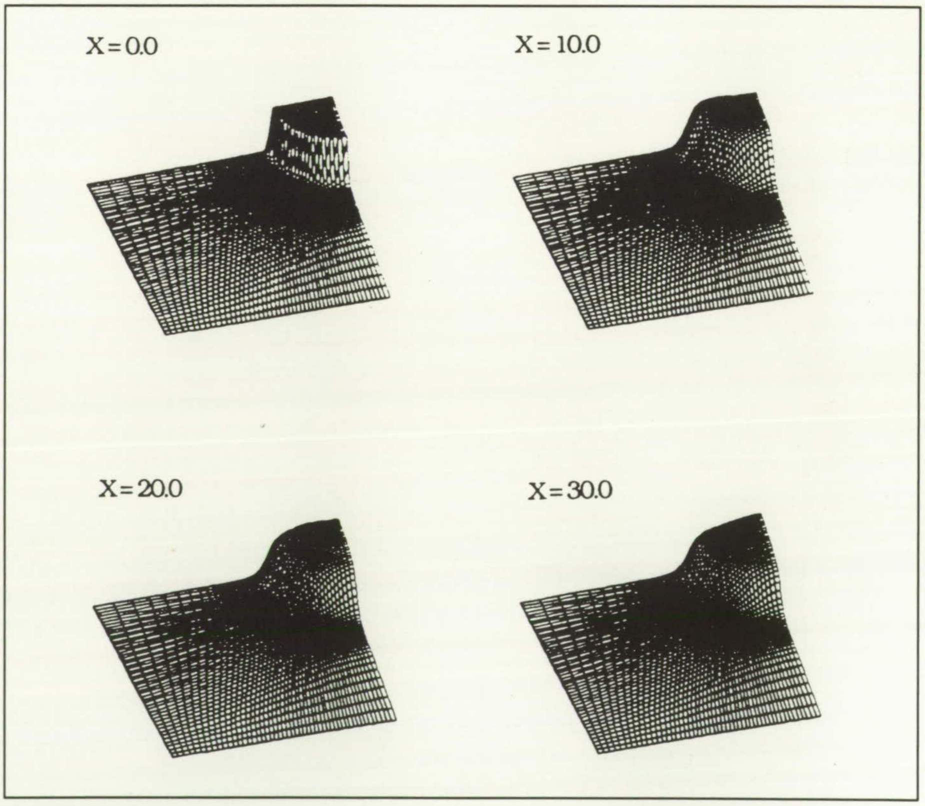

Computed Mach surfaces of underexpanded round nozzle at different stations.

shown in the figure. The Mach surface started with a top hat profile that subsequently evolved to a bell shape at $X = 30$, where X is the downstream distance divided by the jet radius. The flow solver preserved the circular shape of the jet in this adapted Cartesian grid. Other plume flow properties are found to have complete agreement with earlier polar grid results. Further applications to single and twin vectored-thrust nozzles are in progress.
(S. Paul Pao, 43044 and Khalid S. Abdol-Hamid)

External Flow Effects on Thrust-Vectoring Vanes

Several full-scale flight research aircraft that use external nozzle vanes for thrust vectoring are being developed. The intent is to use thrust vectoring for control augmentation in flight regimes in which conventional aerodynamic control surfaces are ineffective, namely, at very low flight speeds and very high angles of attack. Tests have been conducted at static conditions (no external flow) on these and other thrust-vectoring concepts. However, because external vanes will be exposed to external flow during flight, static test results will provide only a partial answer for thrust-vectoring vane performance.

An investigation has been conducted on a generic research model to determine the effects of external flow on nozzle external-vane, thrust-vectoring capability. This investigation was conducted at Mach numbers from 0.2 to 0.9, angles of attack up to 14.5°, and nozzle pressure ratios up to 7.0.

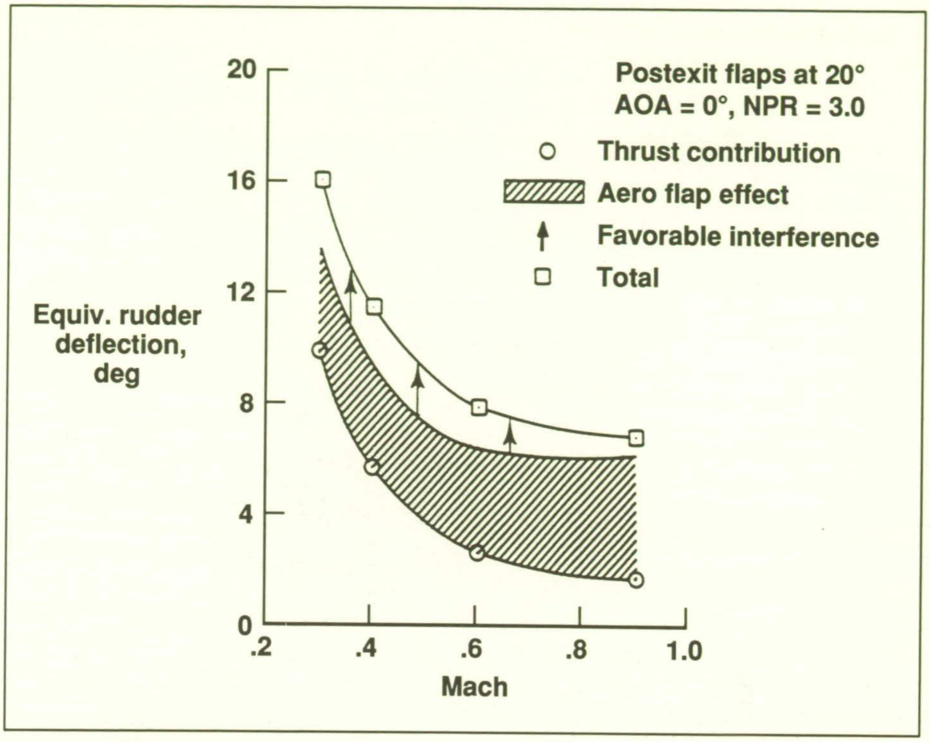

Effect of external flow on external-vane-type thrust-vectoring concept.

The results of this investigation indicate that very large favorable external flow effects occur on nozzle external-vane, thrust-vectoring concepts. External flow effects consisted of an aerodynamic flap effect (similar to a rudder deflection) and an interference (interaction of internal and external flows) effect. The external flow effect increased with increasing Mach number and contributed over four times the thrust contribution to yawing moment (shown as an equivalent rudder deflection angle) at a Mach number of 0.9.
(B. L. Berrier, 43003, M. L. Mason, and J. G. Taylor)

Supersonic Navier-Stokes Simulations of Turbulent Afterbody Flows

The performance of three turbulence models in predicting the supersonic flow past a nonaxisymmetric nozzle has been investigated. The investigation was conducted at free-stream Mach numbers of 1.2 and 1.3 and at an angle of attack of 0.0°. The Reynolds numbers for this investigation ranged from 20.5×10^6 to 21.5×10^6 based on the model length. The calculations are compared with experimental wind tunnel data.

The three different algebraic turbulence models are the Baldwin-Lomax, the nonequilibrium model of Johnson-King, and the Goldberg modification for the separated flow region. These models are in-

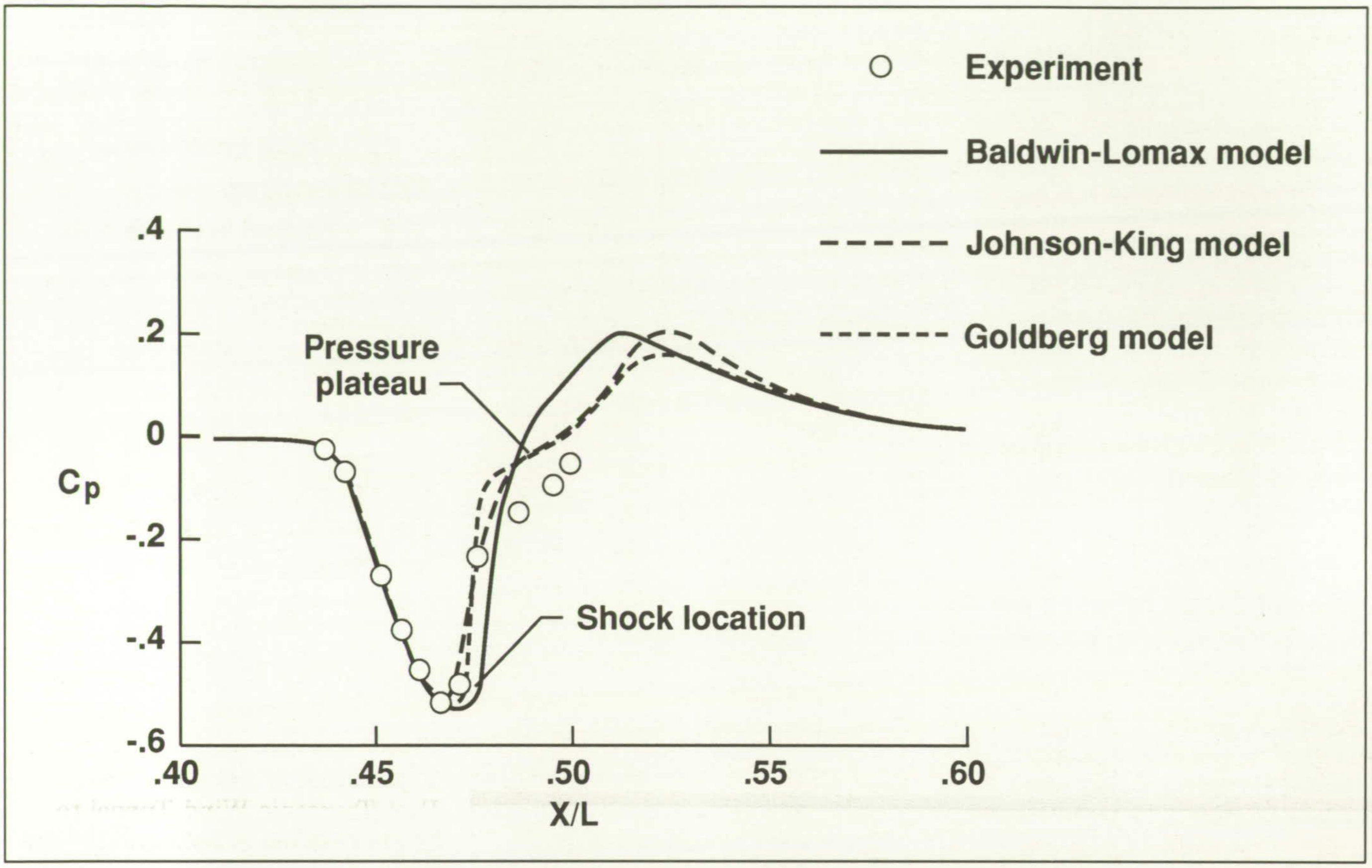

Effect of turbulence model on pressure distribution predictions (free-stream Mach number = 1.2, angle of attack = 0°, and Reynolds number = 20.5 × 10^6).

corporated in a three-dimensional Navier-Stokes code (PAB3D) using a solid plume to simulate the jet exhaust flow. The governing equations are solved using the finite-volume principle in conjunction with implicit third-order approximate factored upwind-biased numerical algorithms.

The Baldwin-Lomax model gives good agreement with the data up to the shock location (point of flow separation). On the other hand, the Johnson-King and Goldberg turbulence models give a much better prediction of the shock location and pressure plateau in the separated region than does the Baldwin-Lomax model. The Johnson-King model requires an additional 2 percent of computational time per time step, and the Goldberg model takes an extra 1 percent per time step over that taken by the Baldwin-Lomax model. It is expected that the inclusion of jet exhaust in the numerical simulation will help to improve the present prediction. **(K. S. Abdol-Hamid and W. B. Compton III, 43048)**

Simulation Studies of Enhanced Combat Maneuvering Using Advanced Controls

A simulation program is being conducted in the Langley Differential Maneuvering Simulator (DMS) to evaluate the enhancements in maneuverability provided by advanced control concepts under realistic combat conditions and to define the technology requirements to maximize these benefits. Recent research efforts have focused on two classes of concepts which maintain a high level of control effectiveness at high angles of attack; these two

View of DMS cockpit and visual display. L-87-8822

classes include multiaxis vectoring of the engine thrust and unconventional aerodynamic control devices such as movable forebody strakes. The results to date show significant enhancements in maneuver performance across an expanded angle-of-attack envelope for the airplane equipped with the advanced controls.

Design methodologies to satisfy technology requirements for maximizing these potential enhancements are also being studied. Control law concepts have been developed to take advantage of the additional control power to maximize the maneuver enhancements and incorporate the two fundamental requirements of proper blending of the aerodynamic and propulsive controls, and provision for high angular rate capability while maintaining acceptable levels of controllability. In addition, concepts for pilot information systems to aid the pilot in making correct decisions on when and how to use the enhanced maneuvering capability are being investigated. The results from these studies will be carried to full-scale flight tests and validation on the High Alpha Research Vehicle (HARV).

(Marilyn Ogburn, 41175 and Keith Hoffler)

Significant Impact to Vortex Flow Field by Small Changes to F-16 Geometry

An experimental investigation of the vortex flows about the F-16C was conducted in the David Taylor Research Center 7- by 10-Foot Transonic Wind Tunnel to explore the impact of adding small nose-probe chines to the baseline configuration. During this joint program involving Langley Research Center, Ames Research Center, General Dynamics Corporation (Fort Worth Division), and the Air Force Wright Research and Development Center, force-and-moment data were taken as well as off-body flow visualization using a laser vapor-screen technique. Both the baseline and modified configurations were tested at free-stream Mach numbers M_∞ from 0.3 to 0.8, angles of attack α from 0° to 60°, and angles of sideslip β from $-10°$ to $+10°$. The geometry differences between the baseline configuration with the nose probe alone and the modified configuration with the chines added are shown in the figure. Note the small size of the nose probe and the chines, which are approximately

ORIGINAL PAGE
BLACK AND WHITE PHOTOGRAPH

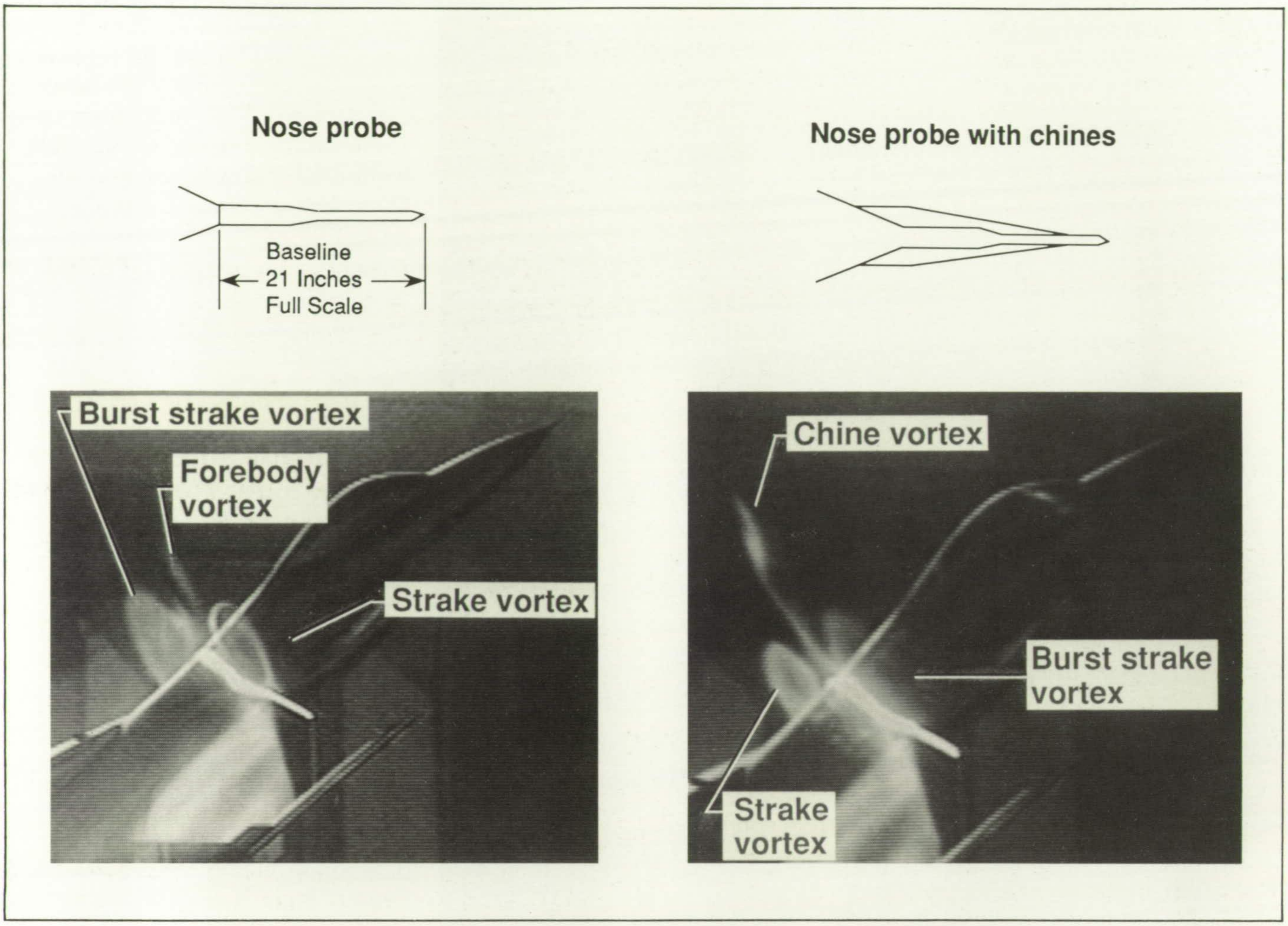

Altered vortex flow field and stability characteristics by addition of chines to existing nose probe. ($M_\infty = 0.60$, $\alpha = 35°$, and $\beta = 2°$.)

0.1 percent of the wing reference area.

A comparison of off-body flow fields for the two configurations at $M_\infty = 0.6$, $\alpha = 35°$, and $\beta = 2°$ is also shown in the figure. Both off-body flow patterns are illustrated at the same longitudinal station by the laser light sheet, which is illuminating the water condensation that has occurred within the vortices. For the baseline configuration, the wing-body strake vortex on the leeward (left) side has burst (there is no clear structure or core region) while the windward strake (right side) vortex still has not burst. There is evidence of a weak forebody vortex above and between the two strake vortices. For the chines-on configuration, the flow field has dramatically changed; in this case, the windward strake vortex has burst while the leeward vortex has not. Furthermore, there is now a strong vortex that is shed from the leeward nose-probe chine that dominates the region above the strake vortices. As would be expected, these large flow field changes significantly influence the lateral-directional stability characteristics of the configurations.

The present results demonstrate that perturbations to the flow near the nose are greatly amplified downstream by the highly coupled nature of the F-16C forebody and wing-body strake vortices. Consequently, very small geometry changes to the nose region of this configuration can impact the global aerodynamics.
(R. M. Hall and G. E. Erickson, 42886)

Vortex Flows at Transonic Speeds

An experimental investigation was conducted of leading-edge vortex flows with emphasis on identifying the vortex structure and vortex-shock interactions at high angles of attack and transonic speeds. The testing was conducted in the Ames Research Center 6- by 6-Foot Transonic/Supersonic Wind Tunnel using a 65° cropped delta wing model. Off-body and surface flow visualizations, wing upper surface static pressures, and six-component forces and moments were obtained at free-stream Mach numbers M_∞ of 0.40 to 1.60, Reynolds numbers based on the wing centerline chord of 2.4×10^6 to 5.3×10^6, and angles of attack α of 0° to 24°.

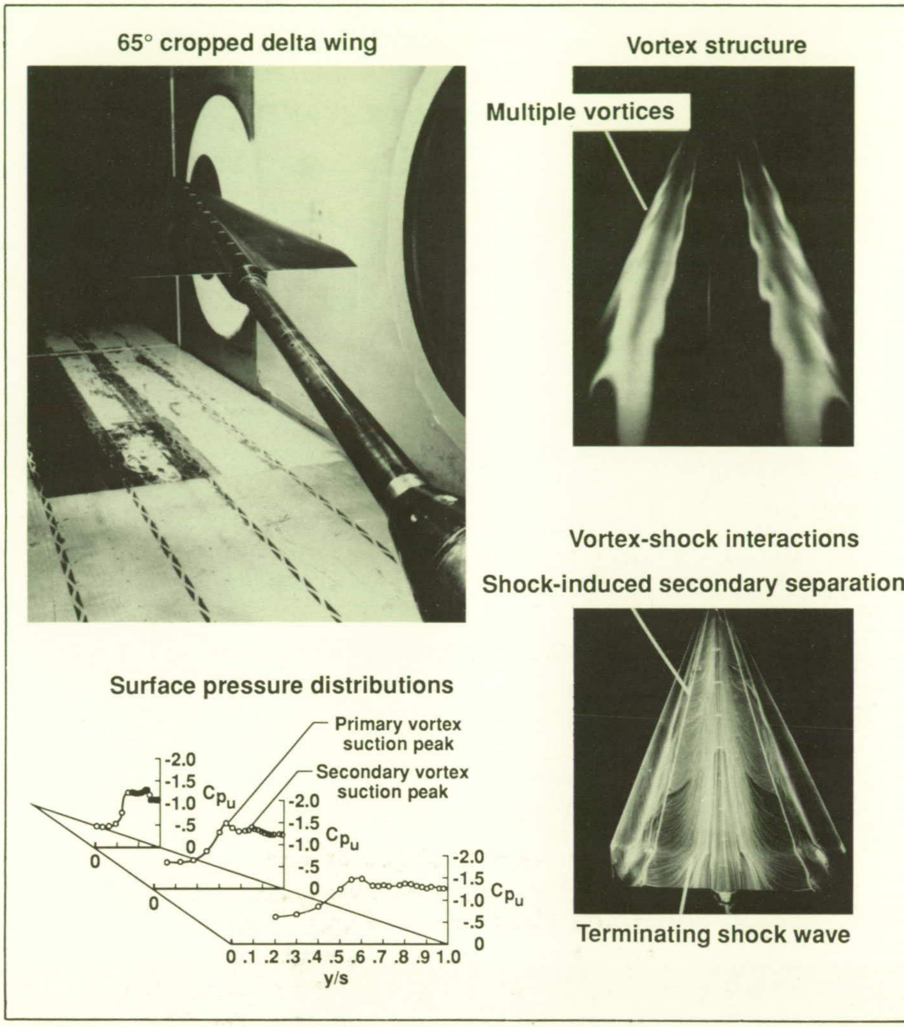

Transonic vortex flows about 65° cropped delta wing model.

Multiple vortices were shed along the length of the wing leading edge that combined to form the primary vortex at the high angles of attack. This flow structure is a departure from the single, continuous feeding sheet that has been assumed to exist on slender wings. The primary vortex was highly compressible, and the vortex signature in the wing surface pressures diminished at $M_\infty > 0.40$. The flow about the cropped delta wing model transitioned from the low-speed, classical vortex regime to the transonic regime, beginning at $M_\infty = 0.60$, where the vortices coexisted with shock waves. A cross flow shock formed between the vortex and wing surface that was of sufficient strength at $M_\infty \geq 0.80$ to separate the boundary layer. The shock-induced boundary-layer separation promoted a strong secondary vortex that was of comparable strength to the wing primary vortex. A normal (terminating) shock wave developed along the rear portion of the wing that extended through the leading-edge vortex. The vortex-shock interaction did not affect the onset of vortex breakdown over the wing or its progression with the angle of attack. At free-stream Mach numbers approaching 1, the wing vortex breakdown was delayed due to the diminished upstream influence of the trailing edge and the associated reduction in the adverse longitudinal pressure gradient.
(G. E. Erickson, 42886)

Wind-Tunnel-to-Flight Correlations of F/A-18 Vortex Flows

Correlations have been made of the vortex flows visualized in wind tunnel and flight experiments of the United States Navy/McDonnell Douglas Corporation F/A-18. This work was conducted to establish the degree to which the vortical flows in wind tunnel testing of subscale fighter models represent the flow field behavior in flight at full scale. The wing leading-edge

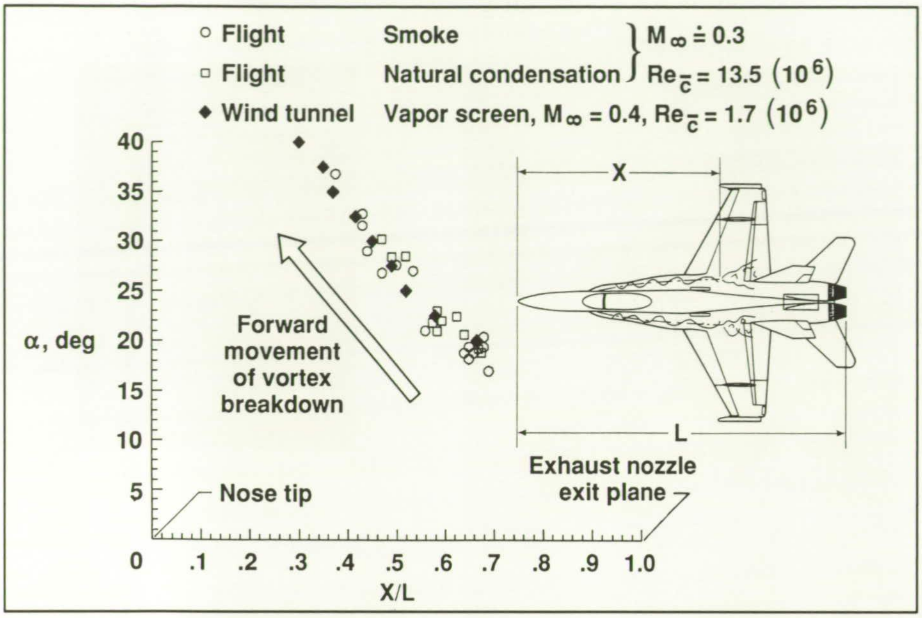

F/A-18 LEX vortex breakdown characteristics (wind tunnel and flight).

extension (LEX) vortices about a 6-percent-scale model of the F/A-18 were visualized in the David Taylor Research Center (DTRC) 7- by 10-Foot Transonic Wind Tunnel using a laser vapor screen technique. The vortex structure, trajectories, and breakdown characteristics observed at subsonic speeds (M_∞ = 0.30 and 0.40) in the wind tunnel were compared to the off-body flow visualizations obtained on the full-scale F-18 High Alpha Research Vehicle (HARV) at the Ames Research Center/Dryden Flight Research Facility. The Reynolds number based on the wing mean aerodynamic chord was approximately 1.7×10^6 in the wind tunnel and 13.5×10^6 in flight. The experiments were conducted as part

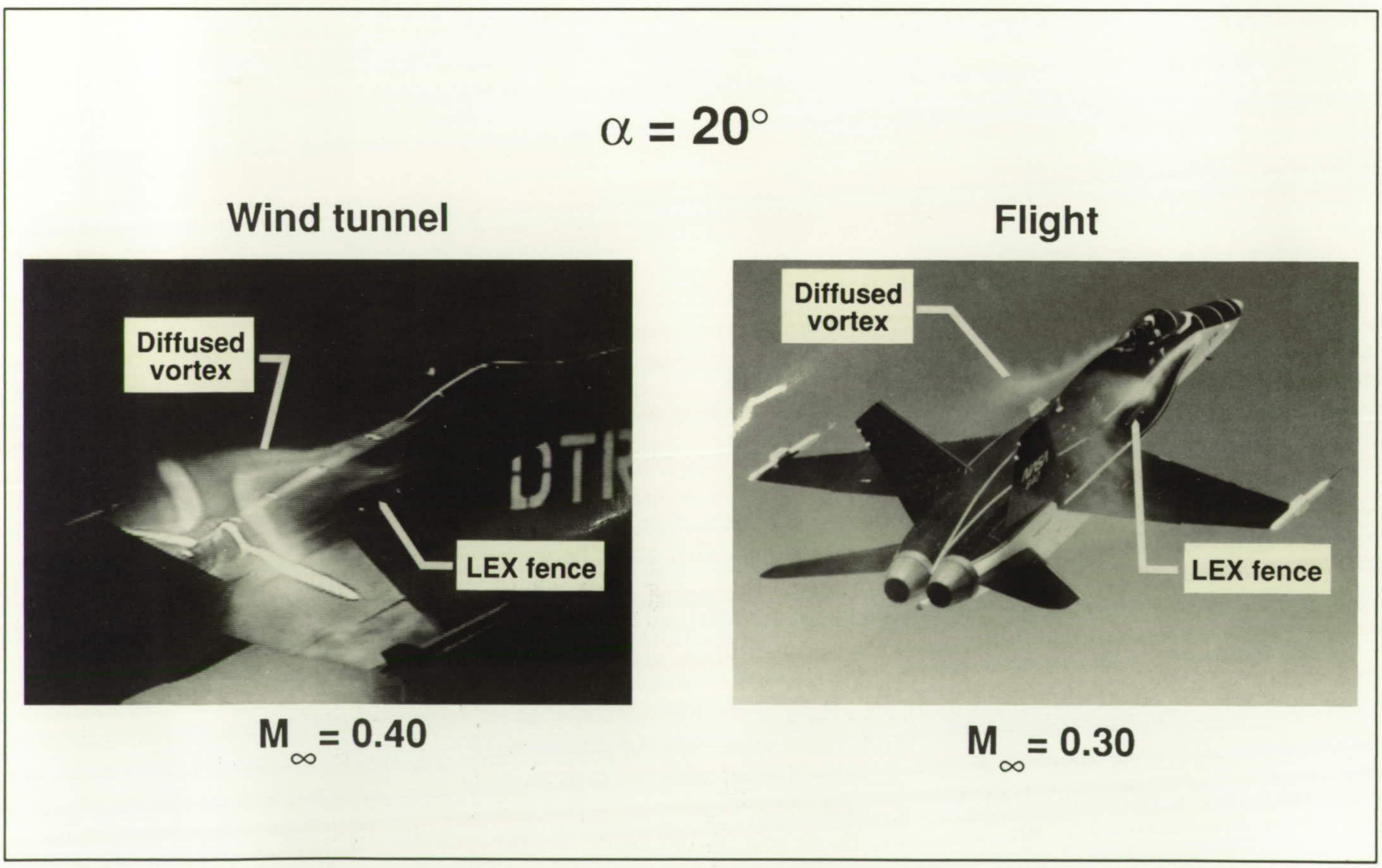

F/A-18 LEX vortex flows with LEX fences on (wind tunnel and flight).

of the NASA High-Angle-of-Attack Technology Program.

The present study showed a high degree of correlation of the vortex flows about the small-scale wind tunnel model and the F/A-18 aircraft. The structure and location of the LEX vortical flows were similar. The onset of vortex breakdown, its forward progression with increasing angle of attack, and the interaction of the burst vortex with the twin vertical stabilizers compared well in the wind tunnel and flight experiments. The physical mechanism for the effectiveness of LEX upper surface fences in reducing the vertical tail buffet was first identified in the wind tunnel testing and subsequently confirmed in the flight experiments. The off-body flow field observations on the 6-percent-scale model and the F-18 HARV showed an upward displacement and restructuring of the LEX vortices with the fences on. The test results also demonstrated the usefulness of applying different flow visualization techniques to improve the understanding of complex vortical flows. For example, the diffuse nature of the LEX vortex downstream of the fence resembled the classical vortex breakdown phenomenon due to the rapid increase in the size of the vortical region. However, illumination of the vortex cross flow with the intense sheet of laser light in the wind tunnel revealed a weakened system of corotating vortices that had not burst.

(G. E. Erickson, 42886)

Multigrid Solutions of Navier-Stokes Equations on Overlapped Grids

One of the limitations in solving the partial differential equations of the fluid flow is the adequate discretization of the physical domain about complex configurations. One method of avoiding this limitation is to decompose the global flow domain into overlapped subdomains, which can accept easily generated, fairly smooth, and curvilinear component grids with no singularities. The Multi-Geometry-Grid Embedder (MaGGiE) computer code is developed, based on the Chimera code of the Ames Research Center and the Calspan Corporation (Arnold Engineering Development Center). This code generates overlapped composite grids at sequentially coarser levels for a multigrid and finite-volume solution scheme. Regions of a component grid common to the others are removed (thus creating holes) to avoid excessive interpolation.

The CFL3D computer code is modified to solve the complete Navier-Stokes equations and perform multigrid convergence acceleration despite the existence of holes and overlapped regions. Hence this CFL3D based computer code (VUMXZ3) solves the viscous flow equations using an upwind, multigrid scheme on Chimera-type overlapped grids and zonal grids. The VUMXZ3 code combines the advantages of an efficient, geometrically conservative, and minimally dissipative solution algorithm with the flexibility of the domain decomposition using overlapped or nonoverlapped grids.

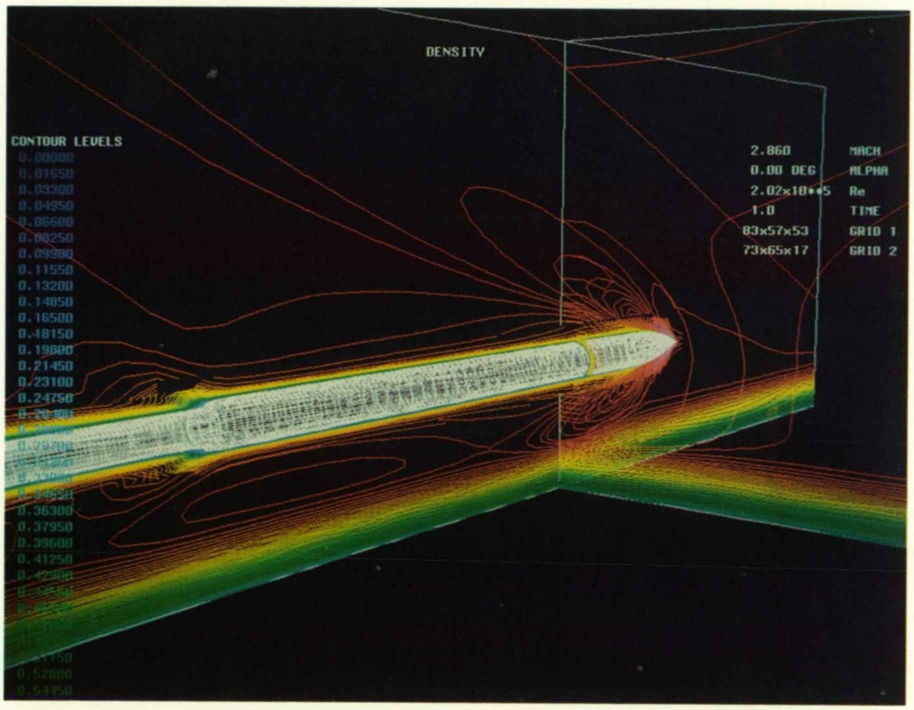

Density contours of flow ($M = 2.86$, $R_e = 2 \times 10^6/ft$) past ogive-nose cylinder ($L/D = 18$) near flat plate.

The supersonic flow past an ogive-nose cylinder in the proximity of a flat plate has been simulated to test the applicability, accuracy, and convergence attributes of MaGGiE and VUMXZ3 codes (as shown in the figure). Currently, the flows past an ogive-nose cylinder with an L-shaped sting in and near a rectangular cavity are being simulated. Wind tunnel tests have been conducted for this configuration for the validation of these computer codes.
(Oktay Baysal and Robert L. Stallings, Jr., 45590)

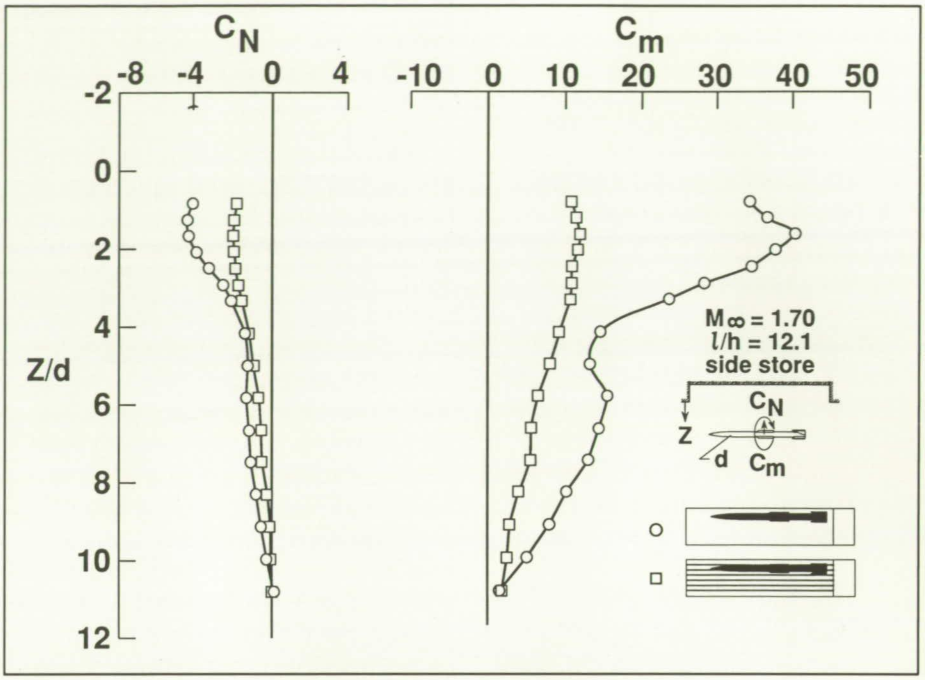

Effect of vent pipes on aerodynamic characteristics of generic store separating from cavity. (Z is distance from plate to store; d is store diameter.)

Passive Venting Technique to Facilitate Store Separation From Shallow Cavities

A study was recently completed in the Langley Unitary Plan Wind Tunnel to evaluate the effectiveness of a passive venting technique for improving the aerodynamic characteristics of stores separating from shallow cavities. The large pressure gradients and flow turning angles that normally occur for shallow cavity flow fields can create large pitching moments on a store during separation and make it pitch up and, in some cases, fly back into the cavity. A characteristic pressure distribution for shallow cavities consists of low pressures occurring over the forward part due to the flow expanding into the cavity, and large pressures occurring over the rear part due to the flow compressing as it leaves the cavity. The existence of this pressure difference led to the passive venting concept investigated in this study. This concept consists of small pipes installed on the cavity floor which permit high pressures at the rear to vent to the low-pressure region at the front of the cavity. The resulting increase in pressure at the front will then reduce the extent of flow expanding into the cavity and decrease the local flow turning angles that should reduce the store pitching moments.

Typical pitching moment coefficients C_m and normal force coefficients C_N from the present study for a store separating from a shallow cavity having a length-to-height ratio l/h of 12.1 are presented in the figure and show that the store pitching moments at a free-stream Mach number M_∞ of 1.70 were significantly reduced with the vent pipes installed as indicated by the square symbols. These results are for the case of the store separating from a side carriage position in the cavity. Similar results were also obtained at this Mach number with the store separating from the center carriage position.
(Robert L. Stallings, Jr., 45590)

Effect of Real Gas on First- and Second-Mode Instability in Hypersonic Boundary Layers

At high temperatures, air departs from the perfect gas behavior due to vibrational excitation and gas dissociation. Since high Mach number flows at flight conditions are generally associated with high temperatures, the effect of a real gas on hypersonic boundary-layer transition is considered in a newly developed spatial stability analysis code

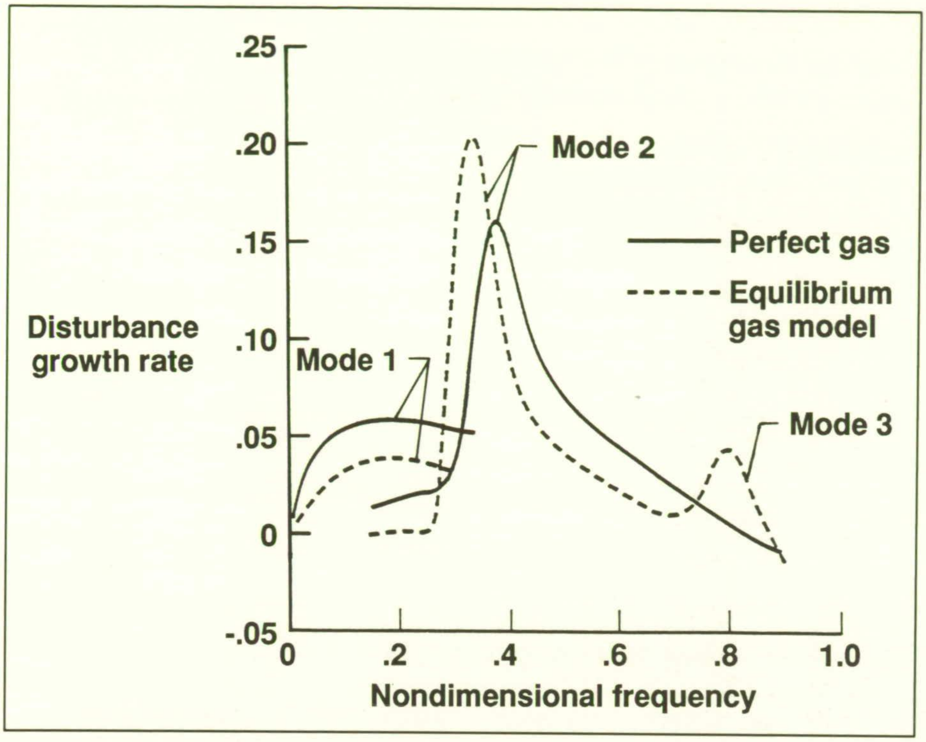

Effect of equilibrium gas chemistry at Mach 10.

(e^{Malik}) for transition prediction. This code uses linear stability theory and incorporates an equilibrium real-gas model. The calculations have been made for an adiabatic wall boundary layer in which the local edge Mach number is 10 and the edge temperature is 500°R. The adiabatic wall condition is chosen to generate sufficient temperature to observe any effect of real gas on the mean flow and its stability. For a perfect gas and an equilibrium real gas, stability results for a Reynolds number R of 2000 are presented in the figure where the spatial growth rate is plotted as a function of nondimensional frequency ω/R. Three instability modes are identified in the calculations, and the curves show that the equilibrium gas growth rates are less (more stable) for mode 1 and mode 3 disturbances and enhanced (less stable) for mode 2 disturbances.

Even though the effect of chemical reactions is to increase the second mode growth rate, it lowers the growth rate of the first and third modes as evidenced in the figure. The overall effect of a real gas on the first- and second-mode growth rate is very similar to the effect of wall cooling, as previously observed both computationally and experimentally for a perfect gas. That is, in high Mach number flows, second-mode disturbances can dominate, and real-gas effects can have a significantly destabilizing influence and may lead to early transition. **(Mujeeb R. Malik and Ivan E. Beckwith, 45564)**

F-106 Vortex Flap Flight Experiment

The 60°-swept wing of an F-106B has been modified to incorporate a leading-edge vortex flap for enhanced transonic maneuver performance. Flight tests are providing pressure distributions, incremental drag measurements, and flow visualization to enable validation of the flap design technique and verification of the predicted improvement in lift-to-drag ratio in transonic maneuvering flight. The baseline F-106B performance has been established, the flap-equipped airplane's flight envelope has been

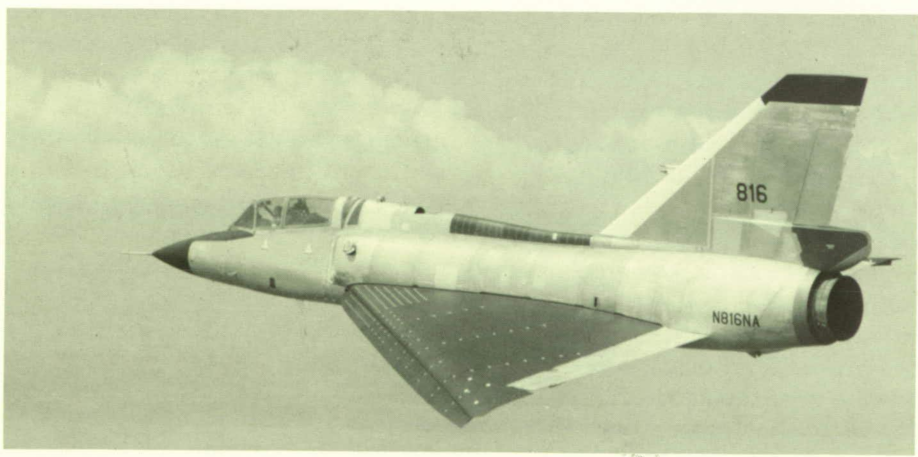

F-106B with vortex flap.

L-88-8200

cleared, and performance measurement testing is in progress. Thus far, the vortex flap has worked as expected based on wind tunnel model tests and simulation studies. A significant improvement in transonic maneuvering performance has been demonstrated at the 40° flap deflection design condition. Flow cones attached to the wing have been used to locate the position of the vortex on the flap and wing. Tests later in 1989 and 1990 will use a light-sheet system to visualize the vortical flow above the surface of the flap and wing.

Designers of proposed High-Speed Civil Transports have become interested in the application of vortex flaps for improvement in takeoff and landing performance. Additional research with the modified F-106B is being planned to address this interest.
(Ronald H. Smith, 43871)

Blade Surface Pressures Measured on Pusher Propeller in Flight

Unsteady blade surface pressure measurements were made on a pusher propeller in flight by the University of Kansas under a NASA grant. The pylon that connects the nacelle to the fuselage provides a one-per-cycle wake encounter for the instrumented blade. The pylon wake profile is also measured via a 20-port rake. Miniature pressure transducers mounted on a 75-percent and a 90-percent radii of the instrumented blade provided a chord- and spanwise time history of the unsteady pressure signals. Twenty-two pressure transducers were used; 14 transducers were mounted at the 75-percent radius, and the remaining 8 were mounted on the 90-percent radial location. An advanced turboprop test bed aircraft configured as shown in the figure performed flight test operations at 26 different flight conditions.

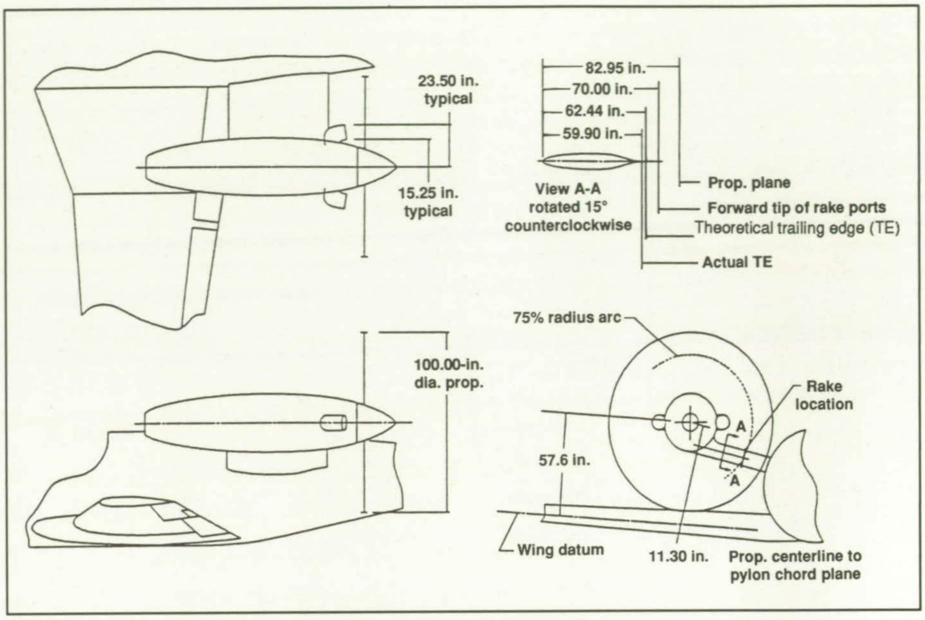

Flight configuration of advanced turboprop test bed aircraft.

Detailed investigation of the blade surface pressure fluctuations caused by the wake momentum deficit on the propeller tip operating in the transonic regime provides the necessary understanding of the flow physics involved in aeroelasticity and aeroacoustics of advanced turboprops. The primary goals of the present research are unsteady aerodynamic code validation, model development for the unsteady response of a three-dimensional lifting surface to inflow distortions, and aeroacoustics of a pusher propeller.
(D. Dunham, 45061)

Superfan Nacelle/Pylon Interference Study on Low-Wing Twin-Engine Transport Model

The evolution of commercial transport aircraft over the past decade has resulted in tremendous nacelle-size growth relative to wing chord length. This growth is due to increased wing aspect ratio (reduction in wing chord relative to wing span and area) and to increased turbofan bypass ratio (increase in nacelle diameter relative to thrust). This relative size growth increases the potential for much larger interference effects of the nacelle on the wing. In addition, the new supercritical wing airfoils are more sensitive to small flow disturbances that can cause premature shock formation and flow separation.

To learn more about high bypass turbofan nacelle installation effects, a generic twin-engine, low-wing,

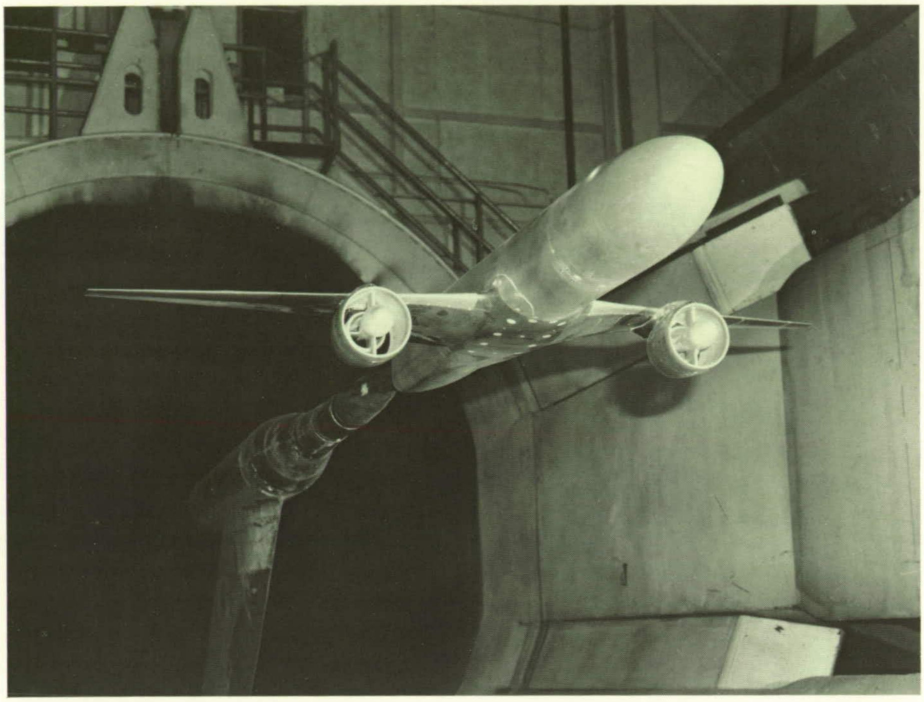

L-89-3315

1/17-scale low-wing transport model with superfan nacelles installed.

supercritical airfoil transport model has been investigated at the Langley Research Center at Mach numbers from 0.50 to 0.80. The wing, which had a design cruise Mach number of 0.77, a design lift coefficient of 0.55, an aspect ratio of 10.8, and a quarter chord sweep of 21°, was extensively instrumented with pressure orifices. Three flow-through nacelle designs were investigated; one represented an advanced turbofan nacelle, and the other two represented the so-called superfan nacelles. The nacelles were installed at the 0.40 semispan location and set at a range of incidence and toe angles relative to the fuselage centerline. The advanced turbofan nacelles were also tested at the 0.34 semispan location.

The increase in model drag resulting from replacement of the advanced turbofan nacelles with either of the superfan nacelles was approximately 6 percent at the design Mach number and lift coefficient. Since the superfan engines should yield approximately 12 to 15 percent improvement in specific fuel consumption over the advanced turbofans, they should, therefore, produce significant improvement in direct operating cost for the airlines.

(O. C. Pendergraft, Jr., 43008, R. J. Re, A. M. Ingraldi, and T. T. Kariya)

UDF Wing Mount Location Studies

A parametric study to identify the interference effects between a General Electric Unducted Fan® (UDF) and a large-scale semispan wing has recently been com-

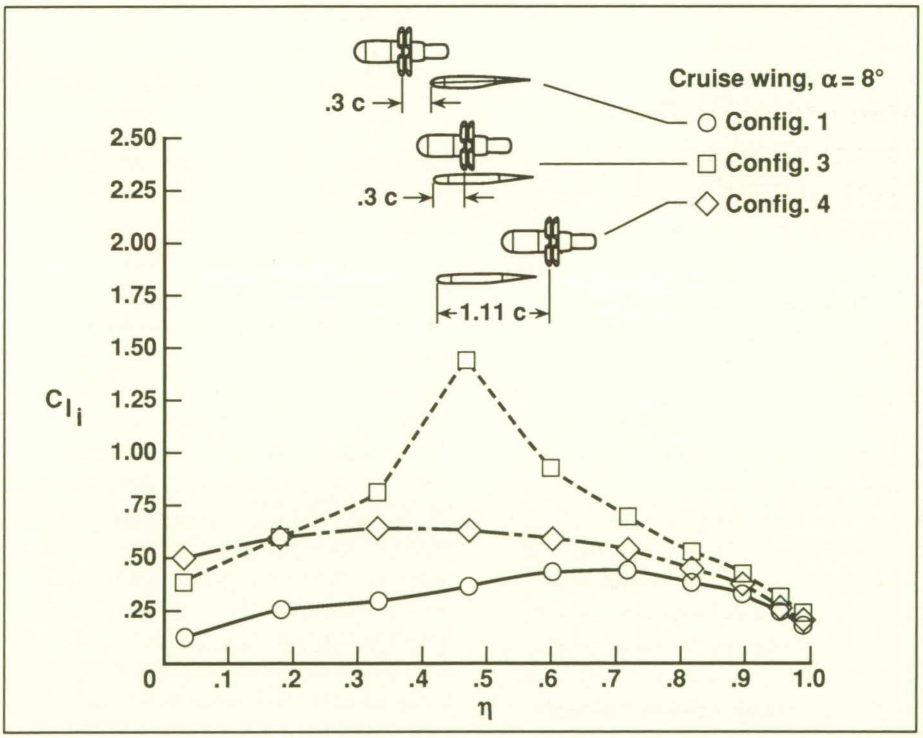

UDF/semispan wing, power-on data.

pleted in the Langley 14- by 22-Foot Subsonic Tunnel. Overall aerodynamic loads and discrete blade stresses were measured on each blade row of the 2-ft UDF simulator. Overall aerodynamic loads and chordwise pressures at 10 span locations were measured for the straight 0012 section wing. A limited number of acoustic measurements were also made. A total of seven different propeller/wing positions were tested for angles of attack from −4° to 20°. For each position the wing was configured for cruise, takeoff, and landing flap settings, and the blades were removed to determine nacelle influence. Results provide a valuable addition to the propulsion/airframe integration data base for advanced turboprop concepts.

The figure shows the section lift from the integrated wing pressures for three streamwise variations in propeller location. The large increase in lift from placing the propeller over the wing is clearly seen. The data are being used for comparison with predictions to determine needed improvements in predictive techniques. Such validated analytical methods provide the designer with the ability to extend the present experimental results to specific design problems.
(Z. Applin, 45062)

Scramjet Exhaust Simulation Studies

Hypersonic, airbreathing vehicles require careful integration of the scramjet propulsion system and the airframe because the airframe afterbody also serves as an external nozzle surface for the scramjets. The exhaust flow pressure field yields a large thrust and a pitching moment that affect the total vehicle performance. It is impractical to perform combustion tests in a small-scale wind tunnel model; therefore, other means of simulating the scramjet exhaust pressure field must be used.

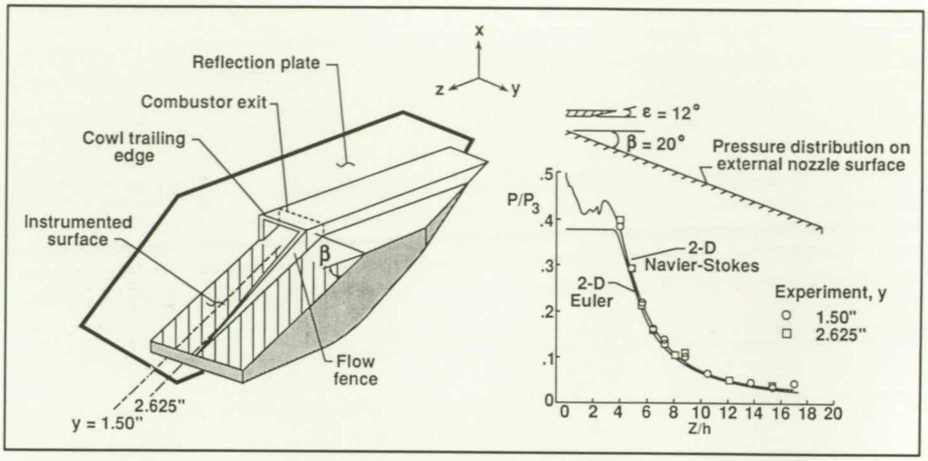

Two-dimensional computational fluid dynamics pressure prediction on external nozzle, argon/Freon exhaust simulation (M_∞ = 6 and NPR (nozzle pressure ratio) = 120).

A study was performed at Grumman Aerospace Corporation (under NASA contract) to identify cold gases that correctly simulate the pressure field of a hot scramjet exhaust. This study showed that a mixture of argon and Freon correctly matches the inviscid exhaust simulation parameters of combustor exit Mach number, static-pressure ratio, and the ratio of specific heats. These findings were validated experimentally against hydrogen-air combustion products in a shock tunnel at Mach 6 and 8. Subsequently, the argon/Freon scramjet exhaust simulation technique was adopted for use in long-duration conventional hypersonic tunnels. A sketch of a generic hypersonic vehicle afterbody model that uses substitute gases is shown on the figure. The cross-hatched area on the external nozzle surface indicates the area instrumented with pressure ports. Experimental surface-pressure data are shown compared with computed results from a two-dimensional Euler code, SEAGULL, and a two-dimensional full Navier-Stokes code developed by Dr. Oktay Baysal of Old Dominion University. At the free-stream condition of Mach 6, the surface pressures inside the flow fence are well predicted by both computational methods.
(James L. Pittman, 45585 and William J. Monta)

Test Technique Demonstrator Forebody Redesign

The design of scramjet-powered hypersonic vehicles is driven mainly by the necessity of obtaining good propulsion/airframe integration. The airframe must provide efficient compression and expansion surfaces for the scramjet propulsion system. In support of the National Aero-Space Plane Technology Maturation

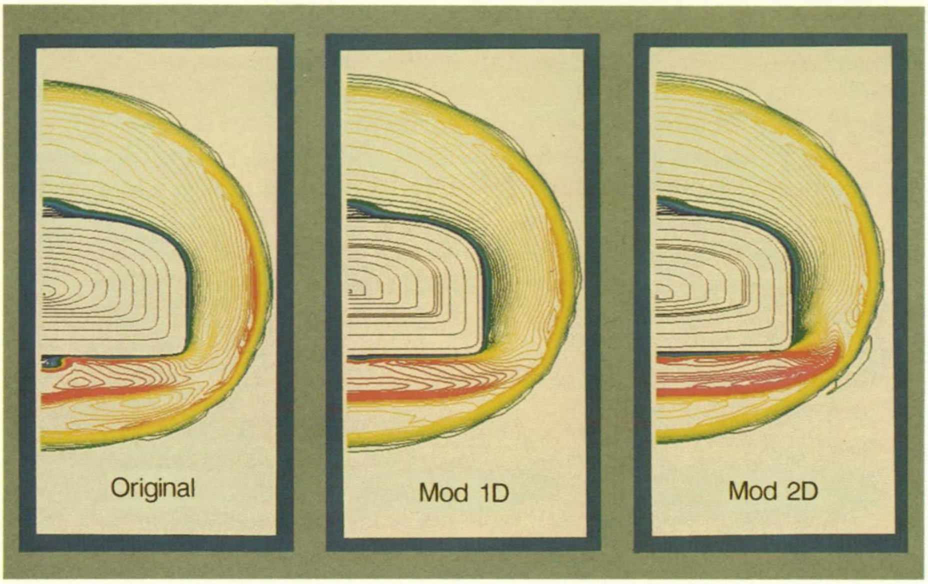

Computational redesign of TTD forebody, TTD computational inlet-face x-momentum ($M_\infty = 6$, $\alpha = 0°$, and $R_{e_\infty} = 10^6$/ft, laminar).

Plan (NASP TMP), the Langley Research Center Test Technique Demonstrator (TTD) was designed to address these issues. Unfortunately, studies of the original TTD geometry revealed undesirable forebody flow characteristics. Therefore, an effort was undertaken to computationally redesign the TTD forebody to eliminate or minimize the undesirable characteristics.

The flow characterization study of the original TTD geometry identified three undesirable characteristics that include unexpected forebody shocks, significant lower-surface inflow, and substantial centerline boundary-layer accumulation. To address these problems, geometry modifications to the TTD were parametrically evaluated using the CFL3DE parabolized Navier-Stokes (PNS) computational method. As shown in the figure, the geometry modifications that were incorporated influenced the x-momentum and resulted in a more uniform boundary layer at the inlet face. Furthermore, examination of particle trace, surface pressure, mass flow, and drag data indicates that the geometry modifications (Mod 2D) eliminate the undesirable forebody shocks, as well as significantly increase inlet-face mass flow and reduce forebody drag. Wind tunnel models of the modified TTD were fabricated, and a validation test was conducted in the 20-Inch Mach 6 Tunnel. Oil-flow, schlieren, and inlet-face pitot-pressure data were obtained and compared with similar data for the original TTD. Comparison of these data validated the modified TTD redesign, which greatly enhances the TTD inlet-face flow quality, making it more representative of NASP TMP goals and more suitable for conducting scramjet propulsion/airframe integration studies.

(Davy A. Haynes, 45584 and Lawrence D. Huebner)

Transonic Navier-Stokes Solution for High-Speed Accelerator Configuration

The design of the proposed National Aero-Space Plane (NASP) will inevitably rely heavily on computational fluid dynamics (CFD) to complement and extend information

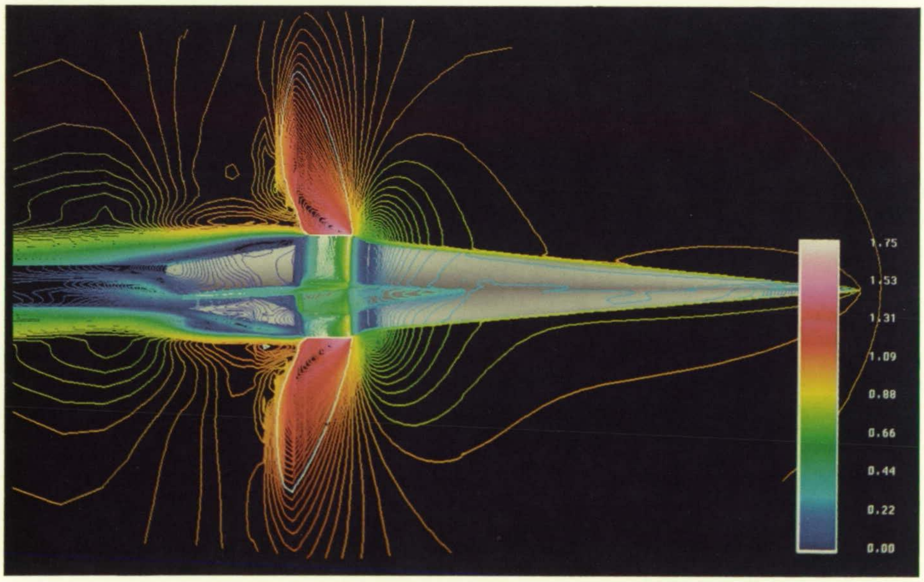

Navier-Stokes Mach contours, $M_\infty = 0.9$, $R_\ell \approx 30 \times 10^6$, and $\alpha = 2°$.

ORIGINAL PAGE
COLOR PHOTOGRAPH

obtained in ground test facilities. The present investigation is directed toward applying an advanced CFD code to a generic NASP-like configuration at transonic flow conditions that may be conducive to flow separation.

An accelerator configuration recently tested in the Langley 16-Foot Transonic Tunnel was selected for the study. This model was comprised of a cone-cylinder-frustum body, a wraparound engine nacelle, forebody and aftbody engine fillets, and a 70° delta wing at incidence. The configuration surface was represented analytically; a blocked flow field domain of approximately 373,000 points was then constructed with hybrid topologies using established transfinite interpolation methodology. Steady-state solutions to the compressible thin-layer Navier-Stokes equations were obtained with an implicit finite-volume algorithm (CFL3D) developed at Langley Research Center.

These solutions were achieved using van Leer's upwind-biased, flux-vector-splitting technique and an extended version of the Baldwin-Lomax algebraic turbulence model.

Turbulence results have been obtained at an angle of attack of 2°, a Reynolds number of approximately 30×10^6 (based upon the total body length), and a Mach number of 0.9. These flow conditions were included in the recent wind tunnel tests just mentioned. Mach contours on the surface and in the plane of symmetry demonstrate a smooth solution in the figure for the blocked representation of this configuration. After a subsonic and mainly attached forebody flow, the flow accelerates supersonically at the cowl lip of the faired-over engine inlet and subsequently shocks down at the exhaust cowl lip. (The sonic line is represented with a white contour line in the plane of symmetry to highlight the supersonic flow region.) The shock produces an adverse pressure gradient that causes the flow to separate massively and envelop the boattail region. Predicted forebody pressures agree with experimental data reasonably well; a qualitative prediction of the separated boattail flow is also achieved.

(Farhad Ghaffari and James M. Luckring, 42856)

Finite-Element Sizing Tool for NASP Structural Weight Prediction

Structural weight predictions for hypersonic vehicles such as NASP require resolution of structural loads resulting from complex thermal and mechanical environments. The NASSIZER code, a structural sizing computer code, was developed to predict weight of detailed aerospace structures based on elemental loads obtained with MSC/NASTRAN, a finite-element analysis code from the MacNeal-Schwendler Corporation; MSC/NASTRAN is widely used in the aerospace industry.

The NASSIZER code establishes minimum dimensions for each element in the finite-element model (FEM) by resizing element geometry to resist element forces with factors of safety selected by the user. Resulting element geometries are reentered into the FEM, and a new MSC/NASTRAN solution and an element sizing it-

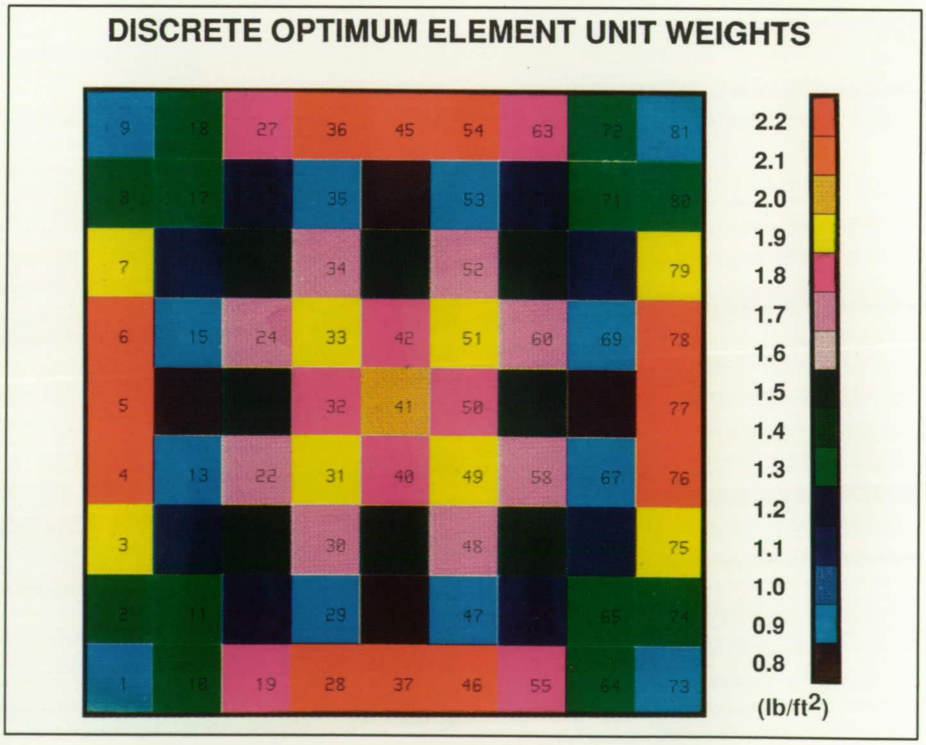

Element unit weights that closely follow element forces at second iteration of NASSIZER test case.

eration are performed. This process is repeated until the element geometries no longer change. Element weights are then summed to produce a fully stressed, minimum weight prediction for the complete model. Specific capabilities of NASSIZER include the use of temperature-dependent material properties and element forces computed from mechanical and thermal loads, including in-plane and through-thickness temperature gradients. Several standard beam and panel sections are represented, but any structural architecture for which stiffness and strength relations can be written may be added to NASSIZER's section library.

The figure shows unit weight results for the second iteration of a square plate test case composed of a nine-by-nine element FEM. The model was restrained on all edges and loaded with a uniform pressure load. Results indicate that element unit weights follow element forces very closely.

Recently, NASSIZER was used to evaluate engine designs from NASP engine contractors during a program review. This analytical assessment was conducted by Langley Research Center in support of the NASP Joint Program Office.
(Paul L. Moses and James L. Hunt, 43732)

Thermal Management Analysis for NASP

High-speed aircraft must endure surface heating that is often beyond the capability of state-of-the-art insulated structures. A solution to this problem for hypersonic aircraft such as NASP is to use the fuel for

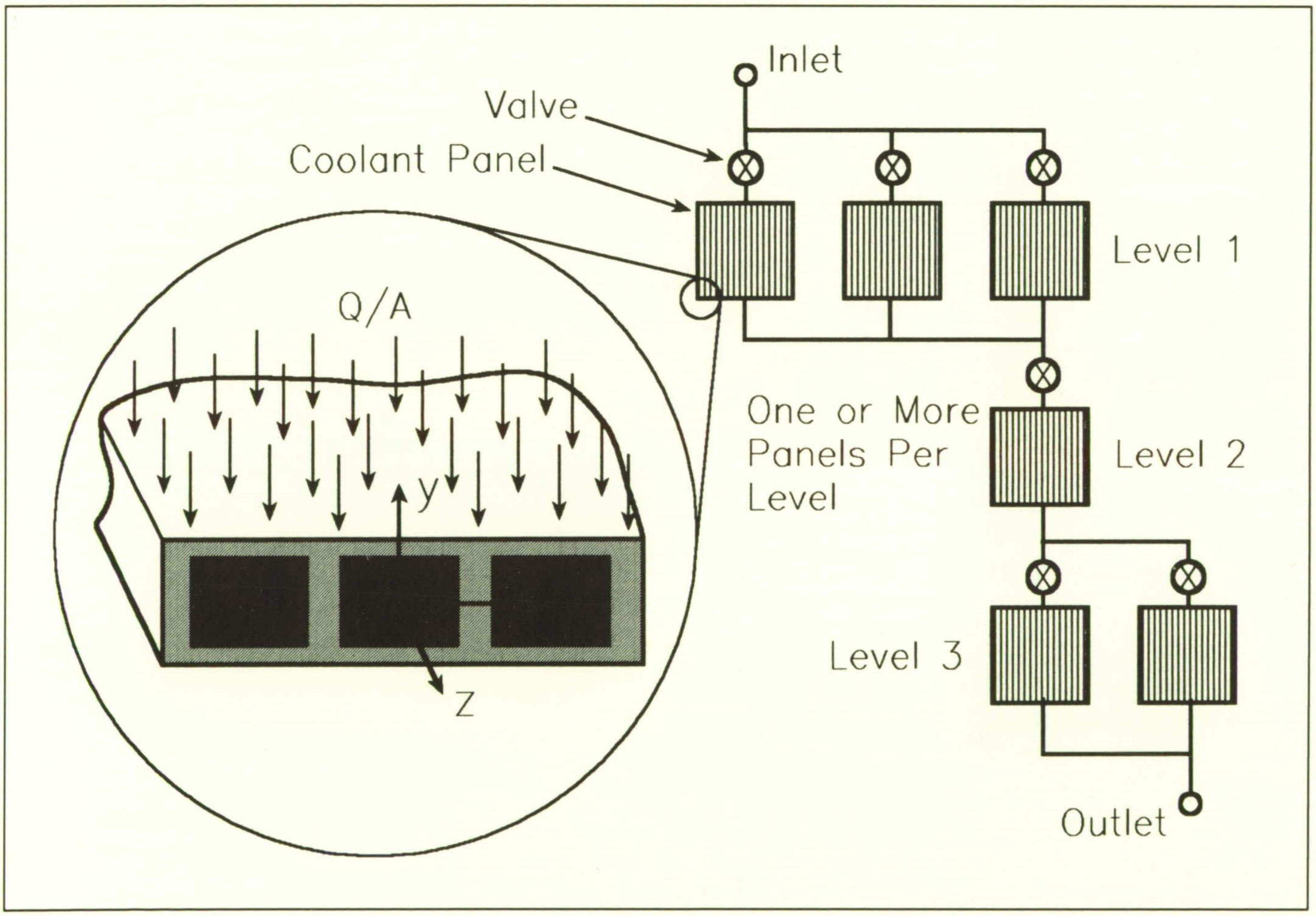

Submodel of coolant panel network.

cooling before it is injected into the engine. The design, analysis, and sizing of this cooling system is the major concern for the discipline called thermal management. Langley Research Center has developed a modified version of the SINDA-85 finite-difference code, NASP/SINDA-85, to model these cooling systems.

The NASP/SINDA-85 computer code has been used extensively to evaluate thermal management for NASP airframe and engine concepts. Complete cooling systems have been modeled. Inputs to the program are cooling system design, panel geometry, heat flux distribution Q/A, coolant inlet temperature and pressure, and coolant outlet pressure. The program calculates through-the-thickness panel temperature distributions at each panel exit and the coolant conditions throughout a cooling system. Fluid properties are obtained from subroutines within the code which are based on accurate equations of state. Custom software is used to model coolant panel networks as submodels in the NASP/SINDA-85 code. A submodel consisting of six panels is shown in the first figure. One or more panels can be specified in parallel on each level for any number of levels in series. Each panel has an optional valve on the inlet to allow corrections for pressure losses. A complete temperature distribution is calculated in the x-y plane at each panel exit. Fluid properties are calculated in the z direction at the entrance and exit of each panel and valve. Submodels are modeled in a system in the same way that panels are modeled in a submodel; a system of submodels is analogous to a submodel of panels. The modeling of panels is based on internal compressible flow through channels with any degree of roughness. Heat addition, friction, and area change are included in the flow calculations. Pumps, turbines, manifolds, and/or mass removal may be specified at any point in the system. Capabilities for film cooling and heat load calculation soon will be added to the code. Calculated panel temperatures for a typical network are shown in the second figure. The hydrogen flows from the lower numbered panels to the higher numbered panels in this network.

(Dennis H. Petley, 43759)

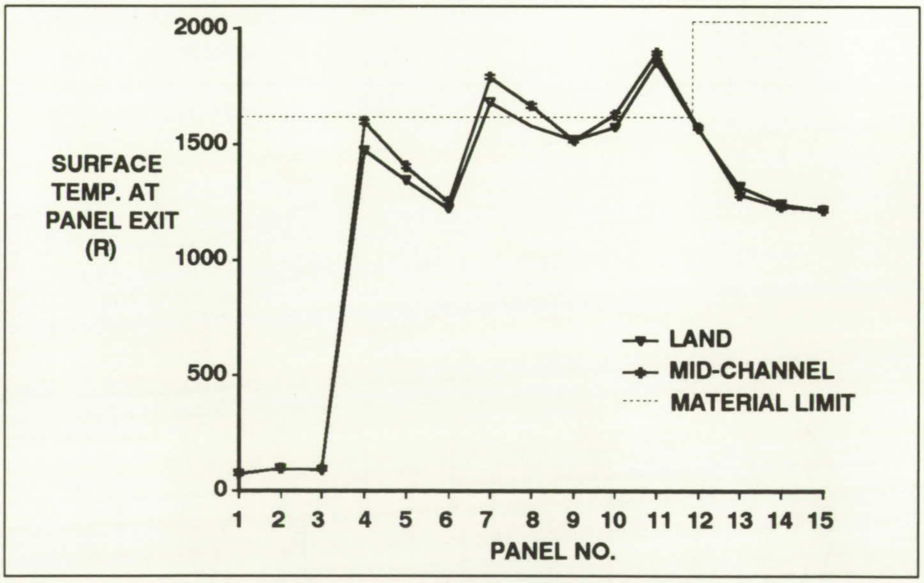

Typical network panel temperatures.

Electronics Directorate

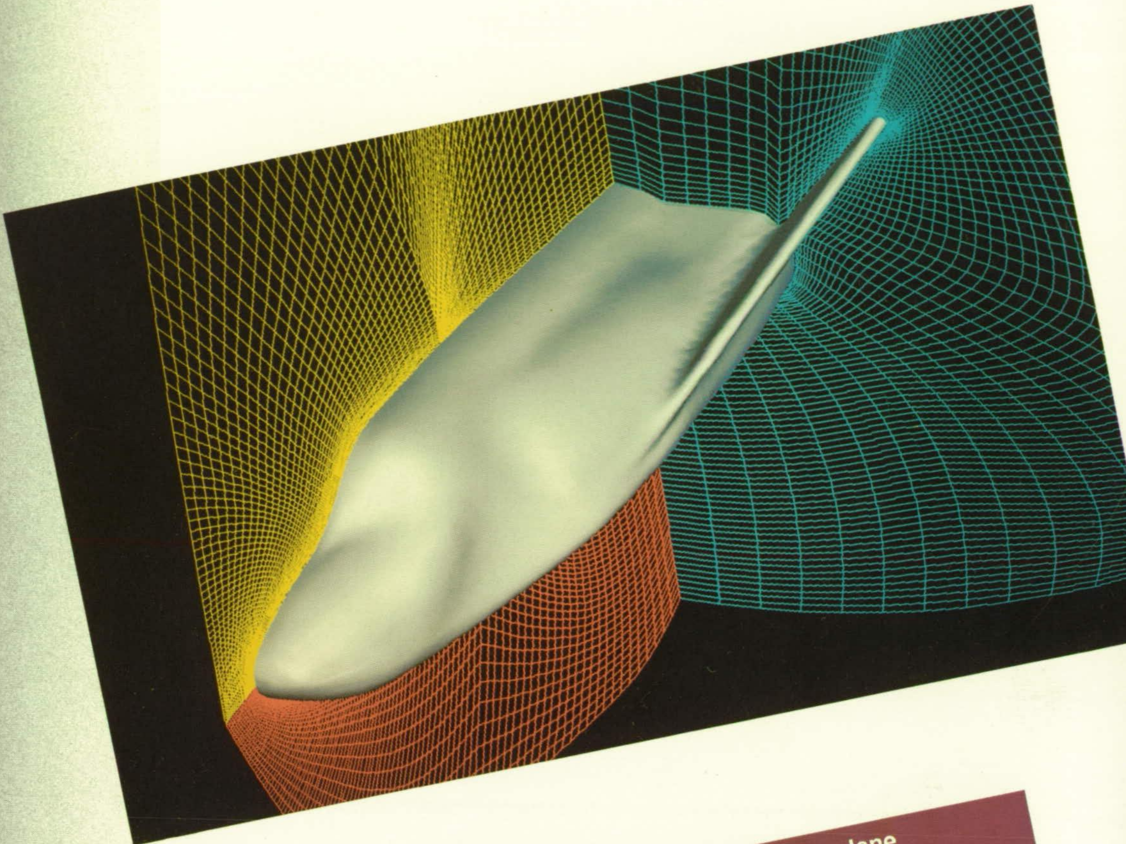

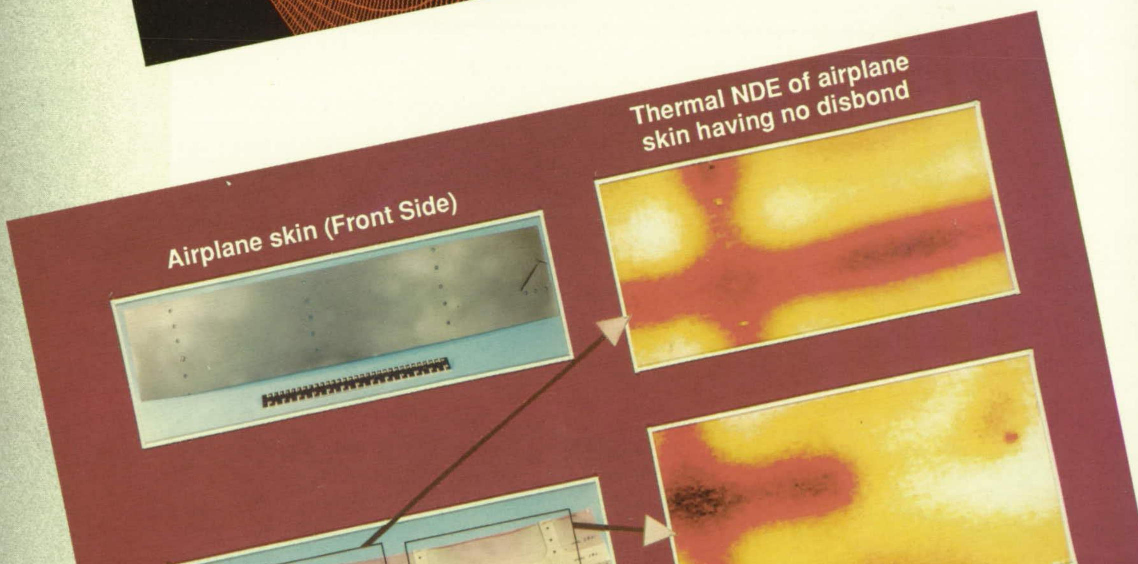

PRECEDING PAGE BLANK NOT FILMED

ORIGINAL PAGE
COLOR PHOTOGRAPH

41 INTENTIONALLY BLANK

The Electronics Directorate is responsible for planning, directing, and evaluating research and applications programs in the areas of measurements and computer science which will potentially benefit the Center's aerospace activities. This directorate also manages the Center's instrumentation, data acquisition, and data processing resources through the four divisions, each of which has specific support functions.

The Analysis and Computation Division is responsible for the development and application of mathematical and computer theory to the solution of computational problems arising from theoretical and experimental aerospace research activities performed at Langley Research Center. Additional responsibilities include conception, design, implementation, and management of advanced centralized data processing systems, flight software systems, and flight simulators, as well as providing consultation on Langley Research Center application of computer technology.

The Instrument Research Division provides instrumentation and measurement support for experimental aerospace research activities performed at Langley Research Center, with primary responsibility for the instrumentation of ground-based facilities. This division conducts research and development programs in instrument areas in which present measurement capabilities are deficient or nonexistent to satisfy both current and future aerospace test program requirements. Additional responsibilities include providing engineering and application expertise to support computer-based data acquisition and control requirements, developing and maintaining measurement standards, calibrating and repairing instruments, and managing an instrument pool.

The Flight Electronics Division is responsible for the development and application of electronic and electro-optical systems for aerospace flight and flight-related projects. This division conducts research and development programs in electronics, optics, lasers, and related disciplines to provide measurement, communication, and data processing systems. Additional responsibilities include design, fabrication, testing, and operation of ground and flight electronic equipment and instrumentation for approved flight projects and applications.

The Projects Division is responsible for the implementation and management of the Langley Research Center participation in major projects. These projects include the four Earth Observing System (Eos) proposals (currently in the definition phase), the Dynamic Scale Model Technology (DSMT) project, and the Microgravity program. In addition, this division is responsible for mature projects, such as the Scout launch vehicle, which can place a 400-lb class payload in a low-Earth orbit, and retrieval of the Long-Duration Exposure Facility (LDEF), scheduled for December 1989.

The accomplishments of the Electronics Directorate over the past year are as diverse as the directorate itself. Significant advances have been realized in applied research for remote sensing of the Earth's atmosphere and nonintrusive diagnostic measurements for Center-wide ground facilities. Some examples of these advances include research that led to greater than a 43-percent conversion efficiency of green laser light to tunable infrared light in titanium-doped sapphire, extension of pressure and strain sensors to 1,000° C, and nondestructive evaluation (NDE) techniques applied to Space Shuttle rocket motors. The NDE research has led to strong cooperative programs with several aerospace companies.

In addition, the directorate installed and made fully operational a new supercomputing capability (based upon the CRAY-2), which is utilized to full capacity by Langley Research Center research personnel. The successful award of four Eos proposals to Center Principal Investigators was strongly supported by engineering and project management personnel. The directorate also is leading the Eos definition studies.

Magnetoacoustic Emission Residual Stress Measurement Technique

To compensate for a weakness in the magnetoacoustic (MAC) residual stress measurement technique, a new method called the magnetoa-

coustic emission (MAE) technique has been developed. The MAC technique, which uses an active transducer (transmitting/receiving) and a dc external magnetic field, provides a negative initial slope of the acoustic natural velocity curve taken as a function of net magnetization induced parallel to the compressive uniaxial stress applied to an iron-like ferromagnet. The MAC technique, however, has a limited capability in detecting the presence of residual stress other than compression because the slope of acoustic natural velocity is positive when a material is either unstressed or under tension.

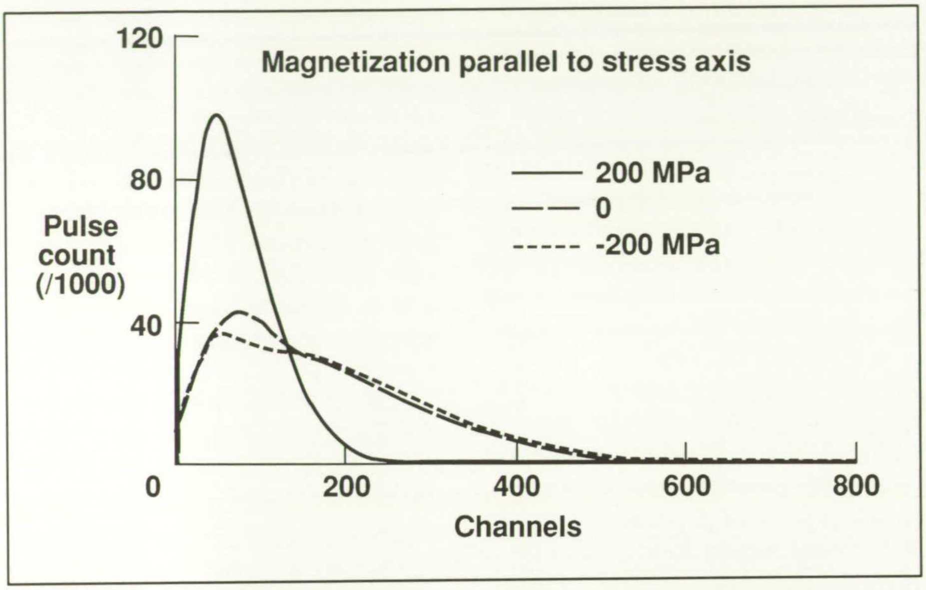

MAE histograms for HY80 steel rod sample under ±200 MPa and in unstressed state with ac magnetic field applied parallel to uniaxial stress axis.

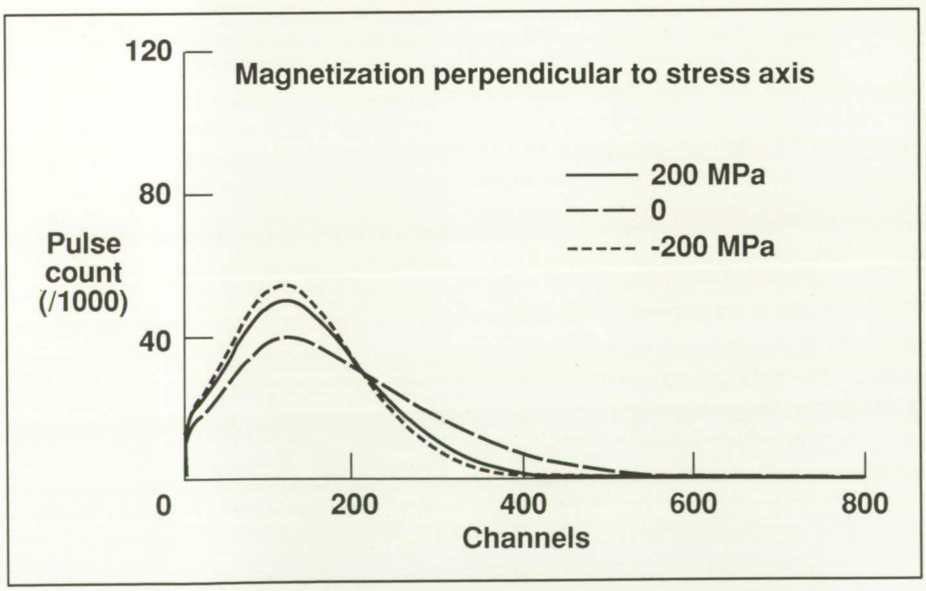

MAE histograms for HY80 steel rod sample under ±200 MPa and in unstressed state with ac magnetic field applied perpendicular to uniaxial stress axis.

The MAE technique, which uses a passive acoustic transducer (receiving only) and an ac external magnetic field, detects acoustic noise generated by the external field-induced magnetic domain wall motion. The spectral characteristics of such an acoustic noise pattern show the stress effects because the availability of acoustic noise-generating domain walls is controlled by the stress state. The most effective method of inspecting spectral characteristics of this type is pulse height analysis. This analysis results in histograms representing the counting rate of pulses as a function of their amplitudes. To ensure statistically stable histograms, approximately 10^6 acoustic noise pulse events are typically collected and processed using a multichannel analyzer. The first figure shows three histograms taken in a rod-shaped HY80 steel sample with an ac external magnetic field of 20 Hz applied to the cylindrical axis (which was also the uniaxial stress axis). The significant narrowing of the histogram under tension is due to suppression of a 90°-domain wall motion responsible for MAE. As predicted, no significant stress effect has been seen in other cases including when the external field was applied perpendicular to the stress axis. These results show that the presence of tensile residual stress in iron-like ferromagnets can be detected unambiguously. As in the case of the MAC technique, the amplitude of residual stress can be estimated by the MAE technique when proper calibration data are available.

(M. Namkung, 44962 and W. T. Yost)

High-Performance Airborne CO and CH_4 Sensor

The Differential Absorption Carbon Monoxide Measurement (DACOM) instrument is a laser-based, in situ, airborne sensor that, during several Global Tropospheric Experiment (GTE) expeditions, has made important contributions to our present understanding of atmospheric CO. Recently a capability to simultaneously measure CH_4 was added to DACOM in order to investigate the CH_4 source strength of the arctic and subarctic tundra. This study was a primary objective of the GTE Arctic Boundary-Layer Experiment (ABLE-3A). During ABLE-3A, DACOM exhibited unprecedented performance including high precision (0.2 percent CH_4 and 2 percent CO) and fast response (< 70 msec) while providing more than 100 hours of flight data over a variety of arctic terrain.

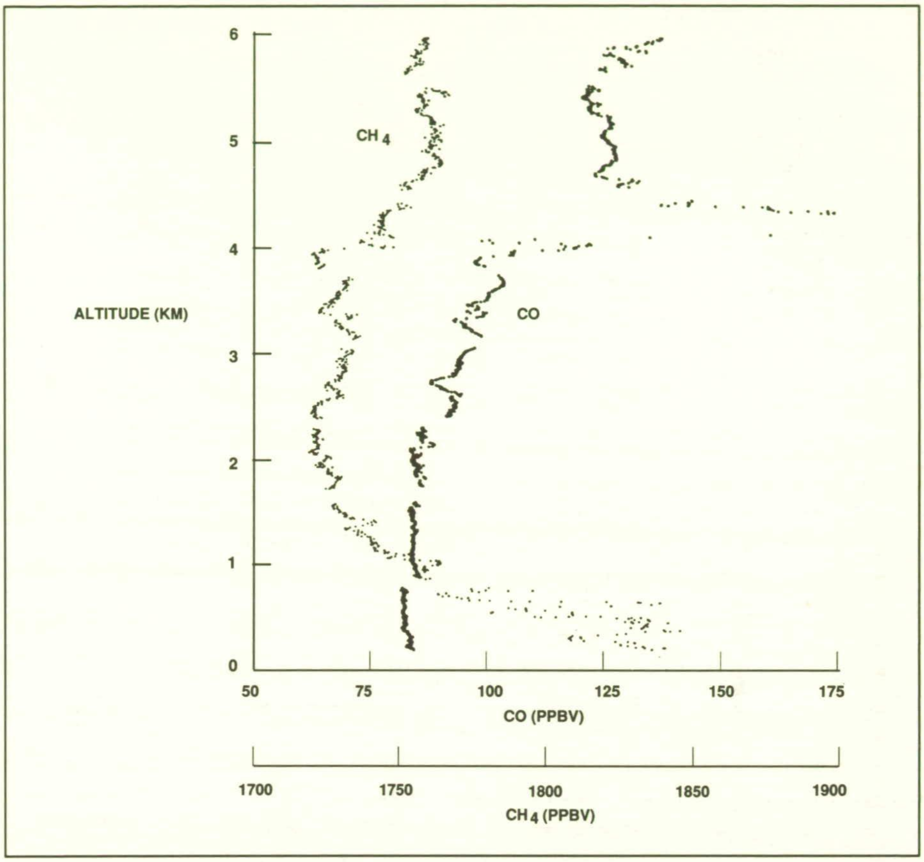

Methane and carbon monoxide profiles over Alaskan tundra.

An example of high-resolution vertical profiles of CO and CH_4 over the Alaskan tundra is shown in the figure. The CH_4 production by the tundra is evidenced by the large CH_4 enhancement found in the mixing layer (below 1 km). The flat CO distribution in the mixing layer suggests that the tundra is not a significant source or sink of CO. The CO layer at $\approx$ 4.5 km was due to long-range transport from a region of forest fires. By combining DACOM's rapid concentration measurements with fast response vertical wind velocity data from the Langley-developed Turbulent Air Motion Measurement System (TAMMS), the flux of CO and CH_4 from the tundra was directly measured during low-level flights in the mixing layer. These so-called "eddy correlation" flux measurements have substantially improved the flux estimates from tundra and indicate that the vast tundra regions of the Northern Hemisphere are a major global source of CH_4.
(Glen W. Sachse, 41566)

Venturi Air Jet Vacuum Ejectors for Atmospheric Sampling Onboard Wallops Electra Aircraft

The GTE program includes many trace gas sensing experiments that require ambient air sampling from aircraft platforms. These experiments require some form of air flow system, which generally includes mechanical vacuum pumps. These vacuum pumps collectively create a heavy payload, utilize many kilowatts of aircraft electrical power, and generate a large heat load that is often impossible to satisfactorily dissipate. An alternative type of vacuum pump that has many desirable characteristics for aircraft application is the venturi air jet vacuum ejector. This type of venturi pump is lightweight, requires no electrical power, will not contribute to the aircraft heat load, and can provide high pumping speeds at moderate vacuum pressures. The high-pressure motive gas that this type of pump requires is generally available in ample supply from air-

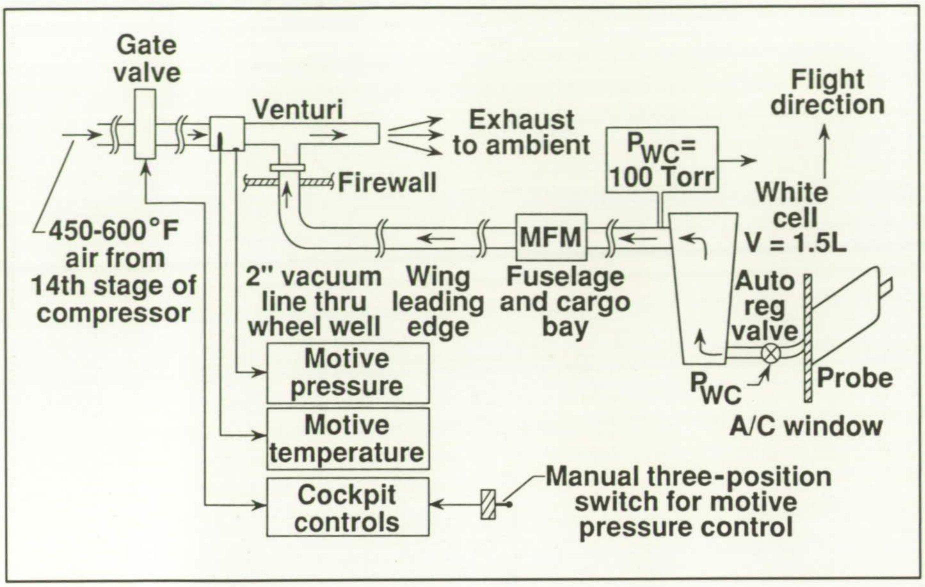

NASA GTE-ABLE-3A DACOM venturi fast flow system. L-89-2968

craft engine compressors. Venturi operation is tested both on the aircraft and in the 20-Inch Mach 6 Tunnel.

The NASA Differential Absorption Carbon Monoxide Measurement instrument has flown successfully on more than 50 missions (over 200 hours) onboard the Wallops Electra aircraft using venturi pumps during the GTE/ABLE-2B expedition (Brazil, 1987) and the GTE/ABLE-3A expedition (Alaska, 1988). Other experimenters also have used venturi pumps mounted onboard the Wallops Electra to solve their pumping requirements during CITE (Chemical Instrumentation Test and Evaluation) and ABLE expeditions.
(Gerald F. Hill, 41559)

Characteristic Ultrasonic Behavior of $YBa_2Cu_3O_7$ and Tl-Ca-Ba-Cu-O at Superconducting Transition

Ultrasonic attenuation of longitudinal and transverse waves has been measured on polycrystalline samples of Tl-Ca-Ba-Cu-O and $YBa_2Cu_3O_7$ as a function of temperature at various frequencies. A frequency-independent attenuation anomaly is observed at temperatures close to the superconducting transition temperature T_c (103 K) of Tl-Ca-Ba-Cu-O for both wave modes. This anomaly is more pronounced in the case of transverse waves. Furthermore, the attenuation decreases with temperature exponentially below T_c. The $YBa_2Cu_3O_7$ also has an attenuation peak at its T_c (90 K), when the relaxation-type attenuation is subtracted from the experimental data. In addition, the temperature derivatives of sound velocity of both

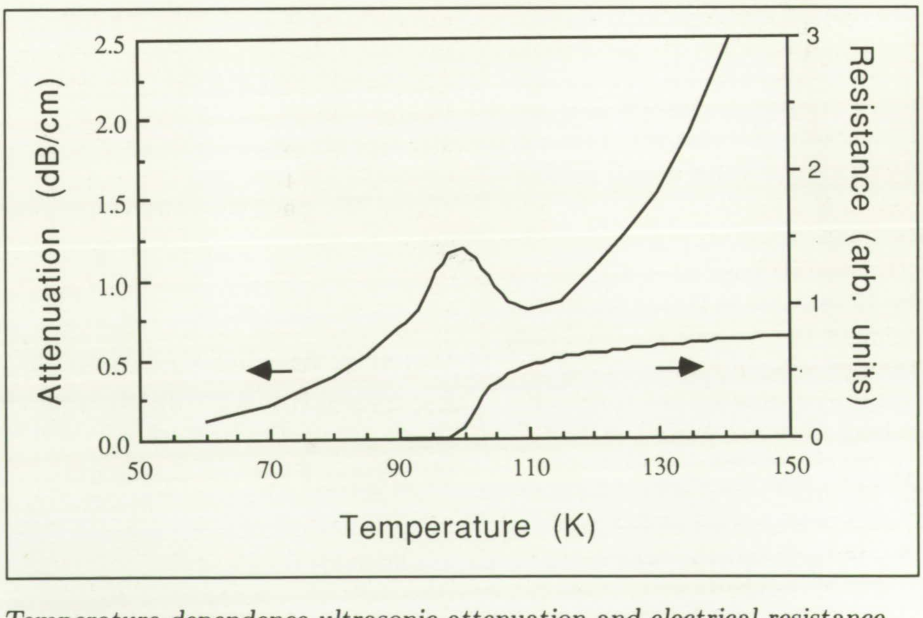

Temperature dependence ultrasonic attenuation and electrical resistance of Tl-Ca-Ba-Cu-O.

these two high T_c systems show a discontinuity around T_c.

Recently, exchange-type interactions between spins of copper ions and charge carriers as well as between the spins of copper ions were proposed to explain several experimental observations. It is predicted that a possible lattice distortion that involves the displacement of oxygen ions along the c axis will occur below T_c if the superexchange interactions between Cu-O planes play an important role. The unusual variations of ultrasonic attenuation and velocity near T_c may provide evidences for this magnetism mechanism which are responsible for the electron pairing in high-temperature superconductivity. **(Keun J. Sun, 44974)**

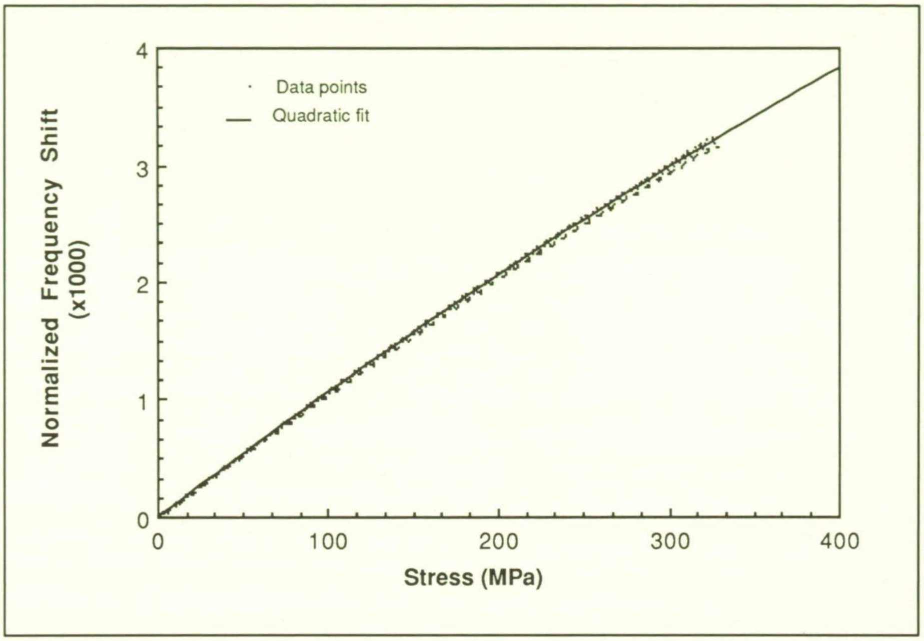

Normalized frequency change of ultrasonic shear wave propagating perpendicular to fiber direction with polarization along fiber direction and tensile stress along fiber direction.

Tensile Stress Acoustic Constants of Unidirectional Graphite/Epoxy Composites

Composites, because of their high strength, stiffness, and light weight, are useful materials for the aerospace industry. However, there remains a need to quantitatively characterize important material properties and develop applicable nondestructive evaluation techniques for composites. Research at Langley Research Center has been carried out to determine the linear and nonlinear elastic properties of unidirectional graphite/epoxy composites. These properties are of great importance in conventional materials and may be useful in further understanding composites.

The nonlinear elastic properties of a material can be determined by measurement of a parameter known as the stress acoustic constant (SAC). The SAC is a measurement of the changes in ultrasonic wave speed with applied stress in a material. If the material were perfectly linear elastic, the ultrasonic wave speed would not change as a function of stress. Previous measurements of SAC's in composites were made under compressive stress. Compression was used so that measurements could be made with the stress direction other than along the fiber direction without premature failure of the sample.

However, because composites are most often used under tensile loading because of their high tensile strength along fiber directions, it is important to evaluate their properties under this mode of loading. In this research, the SAC's for longitudinal and shear waves propagating perpendicular to the fiber direction were measured while tensile stress was applied in the direction of the fibers. The ultrasonic wave speed change was monitored with a pulsed-phase-locked-loop ultrasonic interferometer that records them as changes in frequency of the signal. The figure shows a typical plot of the normalized change in ultrasonic frequency versus tensile stress. In this case the ultrasonic wave was a shear wave with polarization along the fiber direction.

This study provides the first measurements of tensile SAC's in unidirectional graphite/epoxy composite materials thus yielding further information on the mechanical behavior of fiber-reinforced composite materials. These measurements, which may be useful in developing nondestructive techniques to monitor applied and residual stresses in

composites, may also be helpful in nondestructively determining other important engineering properties such as ultimate strength and fiber-matrix interfacial properties.
(W. Prosser, 44960)

Thermal Diffusivity Measurements in Carbon-Carbon Composites for Porosity Evaluation

In recent years, carbon-carbon (C-C) composite materials have come into widespread use in aerospace industries. These materials are particularly attractive for high-temperature applications due to their thermal and mechanical behavior. Few quantitative measurements, however, have been made to characterize these materials. One problem encountered with C-C composites is porosity. Materials engineers have determined that the degree of porosity is correlated to interlaminar shear strength in C-C composites. Since repetition of the C-C processing cycle reduces porosity, a technique for assessing porosity between processing cycles which is noncontacting and does not contaminate the material would be of value. A material property that is related to density and therefore to porosity is thermal diffusivity. Thermal diffusivity is easily measured remotely with infrared techniques and is therefore an attractive candidate measurement for assessing porosity between processing cycles of C-C composites.

A noncontacting technique for measuring thermal diffusivity which utilizes an Nd-YAG (yttrium, aluminum, garnet) laser as a thermal wave source and an infrared camera detector has been developed in the NDE Research Laboratory. Thermal diffusivity is extracted from the phase delay between the thermal wave source and a spatially offset detection region. Diffusivity can be determined for three orthogonal directions to indicate the variation of diffusivity with structural anisotropy of the material or to account for local variations in the fiber direction due to fiber weave in the composite lay-up. In the figure, results are given for diffusivity measurements of a series of samples which have undergone varying numbers of processing cycles, thus producing a range of porosity levels. A strong correlation of diffusivity in the through-ply direction with the bulk density and therefore with the level of porosity of the composite material is shown.
(D. M. Heath, 44964 and W. P. Winfree)

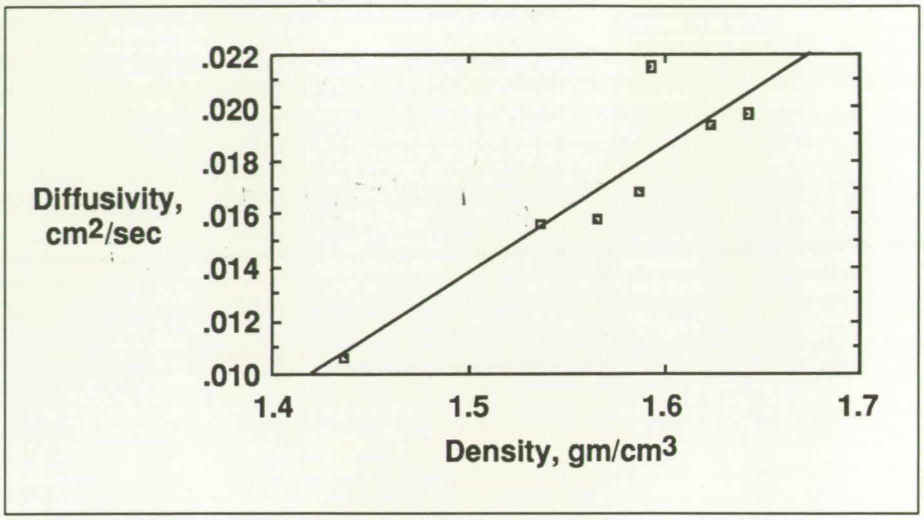

Thermal diffusivity versus density of C-C composite material.

Fabrication of Lightweight Si/SiC Lidar Mirrors

Space-borne lidar systems, with applications to aeronomy and tropospheric/stratospheric research, require large collecting optics to obtain reasonable signal levels for accurate measurements. Large aperture mirrors require tight fabrication tolerances, high thermal conductivity, low thermal expansion coefficient, high stiffness, and low areal mass. Additionally, the mirror material also must be capable of fabrication to the shape, figure, and size of interest in a cost-effective manner.

The technology for fabricating lightweight Si/SiC lidar mirrors (by a scalable chemical vapor deposition (CVD) process) which meet these previously mentioned requirements has been developed. The feasibility of producing mirrors by CVD has been demonstrated successfully for small diameter (7.5-mm) mirrors, and the process has been scaled to produce a 40-cm-diameter, spherical mirror. The process is scalable to

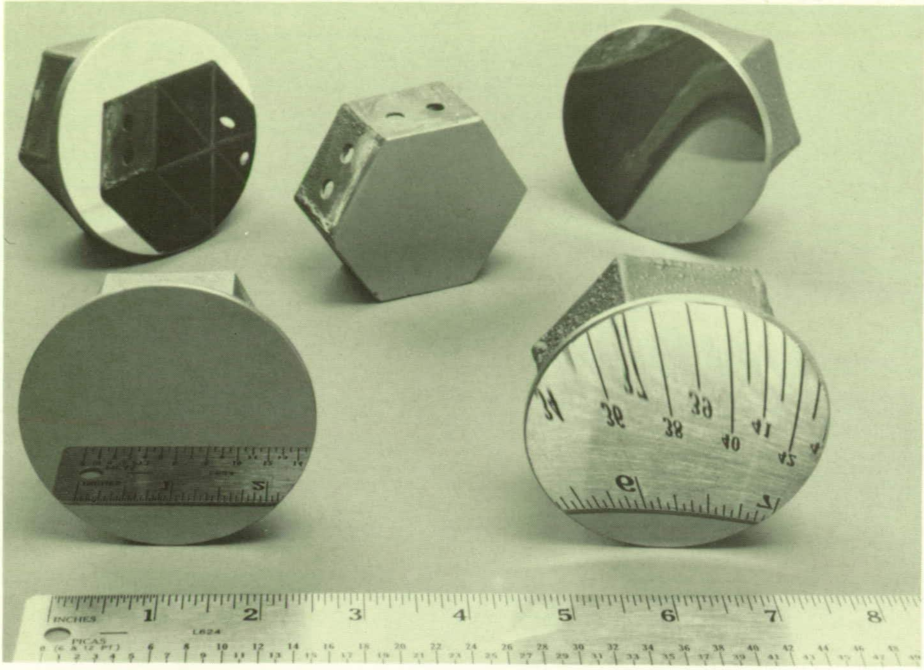

Samples of lightweight mirrors by CVD.

much larger (meter to a meter-and-a-half diameter) mirrors.

Mirrors are produced in a high-temperature furnace by depositing, to a predetermined thickness, SiC onto a master mandrel of graphite having a surface figure that is the negative of the actual mirror figure. A lightweight honeycomb, graphite structure is bonded to the substrate, and the combination is reloaded into the CVD furnace in which SiC is deposited onto the structure. The SiC bonds to the SiC substrate and the exposed surfaces of the honeycomb to form a rigid and lightweight backup structure. The combination is removed from the furnace and separated from the mandrel. It is then turned around and remounted in the CVD furnace for chemical vapor deposition of a thin faceplate of Si on the substrate. After removal from the furnace, the Si faceplate can be polished to the desired accuracy to produce a high-quality, very lightweight mirror.
(Dwayne E. Hinton, 41646)

Cloud Particle Effects on Laminar Flow

Statistical analyses have been reported for the first time of the effects of cloud particle concentrations on the maintenance of laminar flow on a laminar-flow control (LFC) research aircraft, and of the effectiveness of particle measurement instrumentation for the detection of particle concentrations affecting laminar flow.

A NASA Lockheed JetStar airplane, modified with modern LFC wing leading-edge test articles, was flown during the period 1983 to 1987 in a joint Langley Research Center/Ames Research Center/Dryden Flight Research Facility LFC research program. Two particle detection instruments were flown on a ventral pylon above the airplane (see the figure). One instrument is an experimental charging patch, mounted on the pylon's lead-

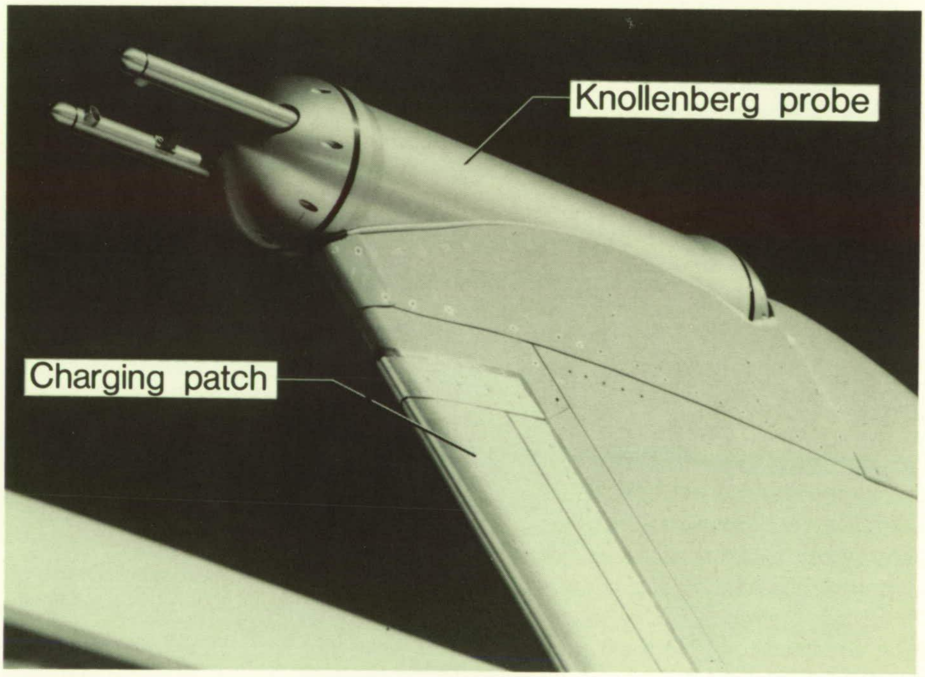

Cloud particle detectors on JetStar pylon.

L-89-18

ing edge. This instrument operates by a triboelectric principle, wherein the aircraft surface is charged by an encounter with ambient particles; the existence of a reading from the patch implies the presence of cloud particles. The patch instrument is a prototype of a simple, rugged sensor that could be flown on operational LFC aircraft to give warning of the presence of particle concentrations deleterious to the maintenance of laminar flow. The other instrument, mounted atop the pylon, is a standard commercial laser cloud particle spectrometer (Knollenberg probe). This probe instrument gives size/concentration spectra and is used mainly as a truth instrument for the experimental patch device.

Use of these instruments and correlation of the data with the degree of laminar flow obtained have resulted in the first statistical data base and comprehensive analysis of the variability of laminar flow in both clear and unclear air conditions. This analysis has also shown that the charging patch is more than 90 percent effective in detection of cloud particle concentrations causing loss of laminar flow and that the probe is more than 84 percent effective. **(Richard E. Davis, 41647)**

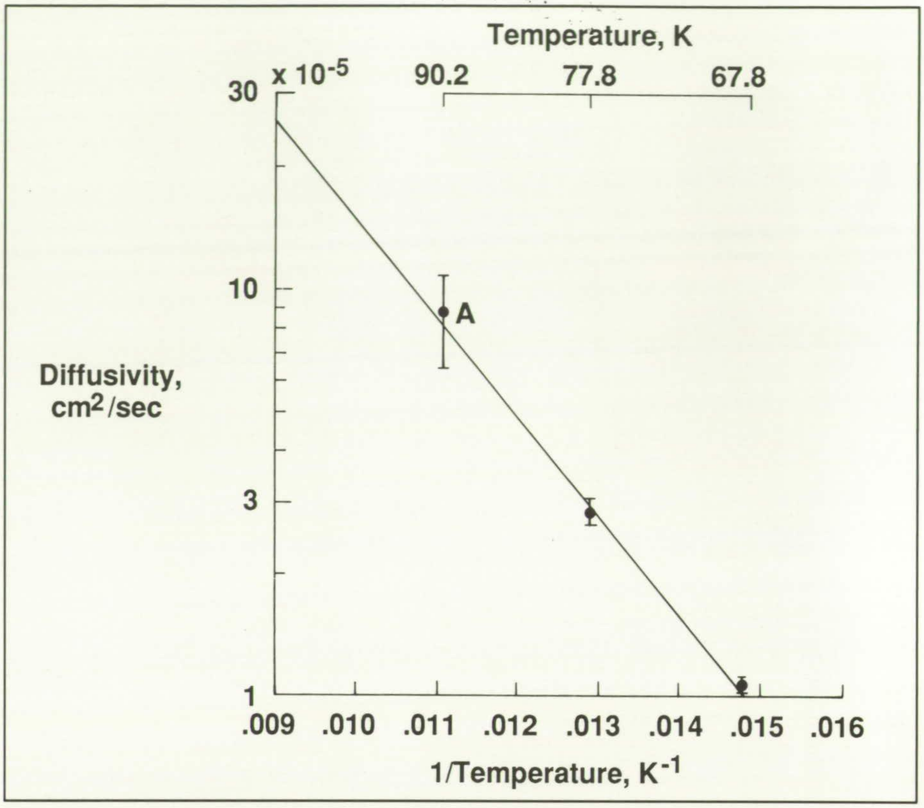

Arrhenius plot of diffusion of N_2 into LOX (point marked "A" was measured in this study).

Diffusion of Nitrogen Into Liquid Oxygen

The modified 8-Foot High-Temperature Tunnel will utilize pressurized gaseous nitrogen (GN_2) at approximately 2000 psig to transfer liquid oxygen (LOX) from a run tank to the tunnel combustor. Since the GN_2 liquifies when the pressure reaches 67 psig, it contaminates the LOX through molecular diffusion. A novel measurement technique, based on a method known as differential flash vaporization, was used to study the penetration of the liquid N_2 into the LOX in the 7-Inch High-Temperature Tunnel. After the run tank was filled with LOX to a specified level, GN_2 was admitted to a pressure of 1700 psig, held for 15 min, and blown down to 0 psig. The vapor from the evaporating LOX was passed through an oxygen analyzer to determine the N_2 content.

The time history of the N_2 content permitted the diffusion coefficient of LN_2 into LOX to be determined. The result is shown as the point marked "A" on the Arrhenius plot of the figure, and the remaining points were taken from the literature. The activation enthalpy for the diffusion process was determined to be 1.08 kcal/mol. Under the operating conditions of the modified 8-Foot High-Temperature Tunnel, the N_2 penetration into the LOX to a 1-percent contamination level is expected to be no more than 0.9 cm, indicating a negligible loss of LOX due to contamination. **(Allan J. Zuckerwar, 44658)**

Automated Inlet Mass Flow Control System

A new automated feedback controller for the Inlet Mass Flow Sys-

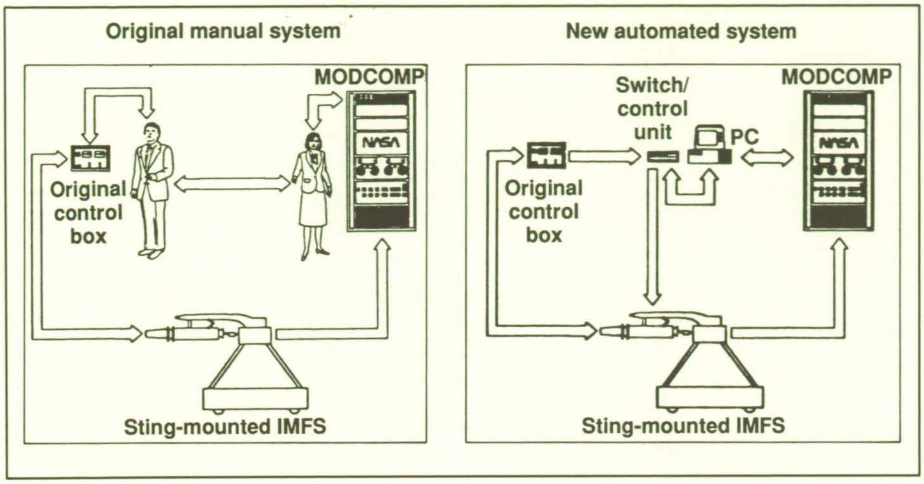

Inlet Mass Flow System.

tem (IMFS) has been successfully designed and installed at the Unitary Plan Wind Tunnel (UWT). The IMFS is a device that measures the mass air flow of aircraft engine air intake models. This PC-based control system promises a savings in both manpower and tunnel running time.

The original system used a manually controlled electric actuator for positioning a cone-shaped plug within the IMFS. This plug, positioned at various stations, is used to simulate the back pressure seen in an actual jet engine. In the original open-loop system, an operator was required continually to manually position the plug by operating a toggle switch, while monitoring the plug position readout. This tedious manual operation frequently produced data errors during a typical test that lasts more than several weeks duration and requires hours of continuous tunnel operation.

The new controller is an easy-to-use, menu-driven, PC-based, closed-loop system. During wind tunnel tests, it automatically sets the plug position and initiates recording of data. Once a sequence of plug positions is entered into the computer, the computer, which takes over the testing procedure, swiftly and precisely moves the plug to its designated position, pauses a sufficient time for the flow to settle out, then cues the tunnel mainframe computer to initiate the data recording process. Upon data acquisition completion, the automated system sets the plug to its next sequential position. After completion of the specified sequence of plug positions, the plug is returned to its initial position, and the system is ready to accept a new set of test parameters.
(P. Tcheng, 44717 and F. H. Supplee, Jr.)

High-Temperature Skin Friction Measurement

A specially modified skin friction balance was used for the first time at Langley Research Center to make high-temperature skin friction measurements in Test Cell #2 of the Scramjet Test Complex.

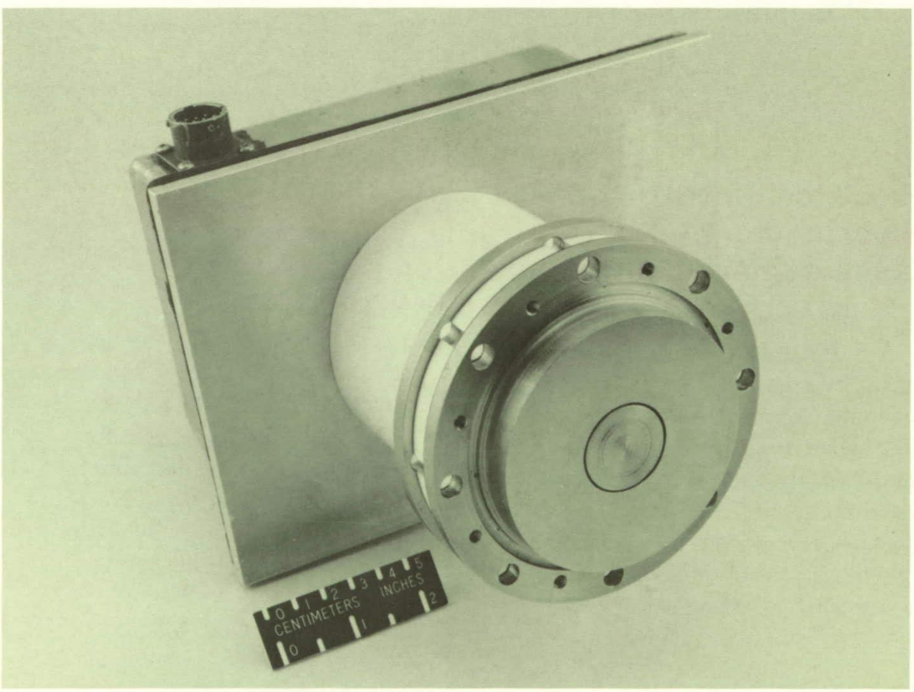

High-temperature skin friction balance. L-88-13,564

A ceramic standoff was added to the skin friction balance, originally developed in-house for a flight research program, to provide thermal insulation for high-temperature operation. The modified balance functioned satisfactorily over a series of test runs, each lasting 20 sec at flow temperatures well over 1000°F. The tests verified that the balance configuration design is robust and that the insulation is adequate to withstand the high-temperature environment without active cooling.

The electromechanical design of the balance includes a mechanical suspension configuration that is inertially balanced. A closed-loop servo system electromagnetically maintains the movable mechanical components of the balance in a null, or zero load, position. The load, or skin friction force, is proportional to the electromagnet current required to hold the balance in its null position.
(P. Tcheng, 44717 and F. H. Supplee, Jr.)

Precision Electro-Optical Displacement Measurement System

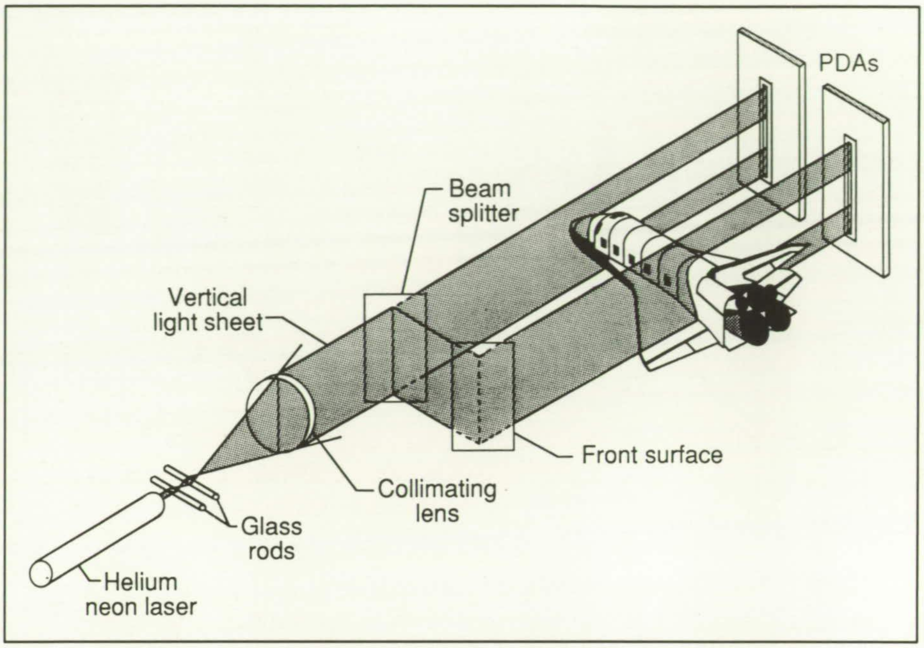

Optical layout of electro-optical displacement measurement system.

A nonintrusive method of measuring wind tunnel model position or angle of attack (AOA) is desirable when the physical size of the model limits the use of conventional instrumentation. A two-channel electro-optical system has been developed for AOA measurements at the 13-Inch Magnetic Suspension and Balance System (MSBS) at Langley Research Center. The system senses the attitude of the magnetically suspended wind tunnel model and provides feedback signals for control.

Laser light sheets are used to illuminate two linear photodiode arrays (PDA's) containing 4096 elements each. When a wind tunnel model obstructs the light sheets, a shadow is formed on each of the arrays. The resulting shadow is used to sense the position of the model. Custom electronics detect the location of the shadow edges on each of the PDA's. The AOA of the wind tunnel model is then computed from these data and updated at a rate of 256 Hz. The system, which was fabricated and calibrated in the laboratory, displayed a linear displacement precision of ±0.0005 in. (12.7 μm) and an angular position precision of less than ±0.015°. The angular rate of calibration was ±17°.
(T. D. Schott, 44715 and P. Tcheng)

Model Deformation Measurements With Improved Video Photogrammetry System

Charge Coupled Device (CCD) cameras and computer-controlled video frame digitization boards have been incorporated into a system to photogrammetrically measure wing deflection and twist at the National Transonic Facility (NTF). This system is an improved version of an earlier system that included high-resolution tube-type cameras. The new system eliminates both the vibration-induced distortion associated with tube cameras and the manual processing of video hard copy images necessary in the earlier system.

The new system was used to acquire data on a targeted Boeing 767 model during recent tests at the NTF. In the figure the Mach number M was 0.8, the angle of attack

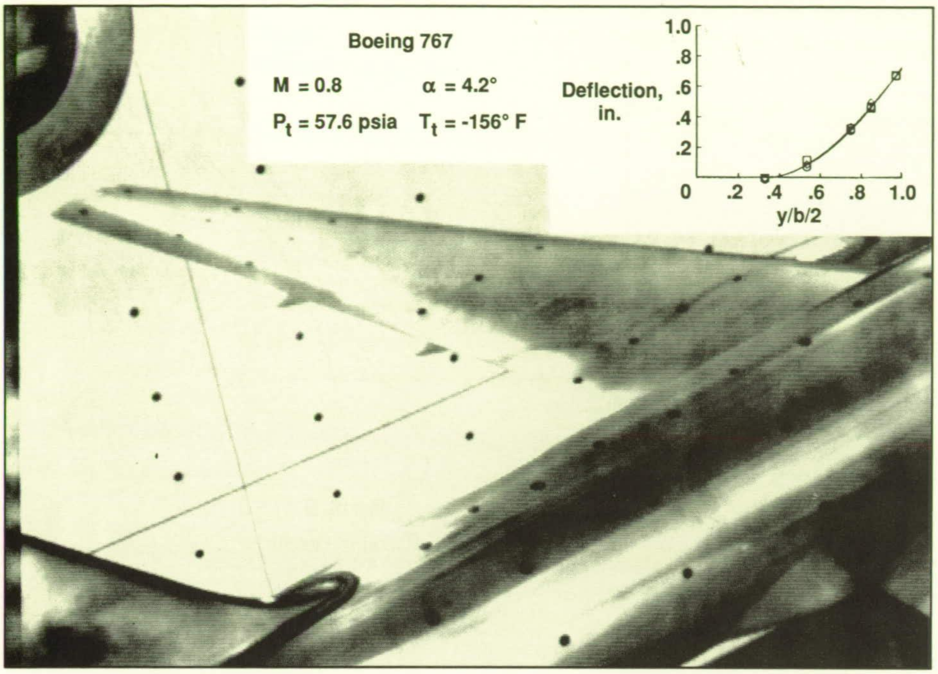

Hard copy of video image recorded at National Transonic Facility.

α was 4.2°, the total pressure P_t was 57.6 psia, and the total temperature T_t was −156°F. The maximum wing tip deflection for this condition was found to be 0.71 in. The maximum wing twist was less than 1°. The wall targets that surround the wing on the figure were used to check for image jitter, which could affect the accuracy of the measurement, by comparing the repeatability of the image coordinates for this condition to the repeatability without flow at ambient conditions. The image jitter was found to be small enough not to appreciably affect the accuracy. In addition, image motion of the fuselage and wing targets was found to be consistent with rigid-body lateral motion.
(A. W. Burner, 44635, W. L. Snow, and W. K. Goad)

Monitoring Dynamic Loads on Wind Tunnel Force Balances

The heavily filtered strain-gauge force balance output has always been closely monitored during wind tunnel tests to ensure that the design loads of the model, balance, or tunnel support system were not exceeded. More stringent safety regulations coupled with concern for the higher costs that may be incurred in the event of a failure have led to the need for dynamic monitoring as well. Two instruments have been designed at Langley Research Center to monitor the dynamic loads incurred during wind tunnel testing. The first, the Balance Dynamic Display Unit (BDDU), monitors and displays the combined static and dynamic forces and moments in the three orthogonal model axes. The second, the Balance Critical Point Analyzer (Balance CPA), scales and sums each normalized signal from the BDDU to obtain combined static and dynamic signals representative of the dynamic loads at high-stress points that were determined during balance design. A typical display of each instrument is shown in the figure. Each display is a multiplex of six analog signals such that each channel is displayed sequentially as one-sixth of the horizontal axis on a single oscilloscope trace.

This display format allows the operator to monitor quickly, easily, and simultaneously the average static load as well as the amplitude

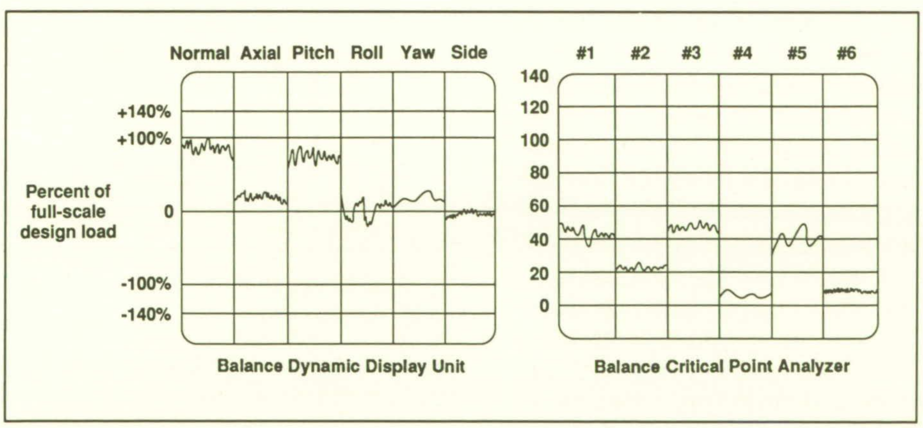

Typical displays.

and frequency of the dynamic loads of each of the six channels. To further assist in monitoring peak loads, a two-level visual alarm and a high-level audible alarm are incorporated in each instrument. Nine of the BDDU's are in use in Langley Research Center facilities. The National Transonic Facility has both the Balance CPA and the BDDU in use.

(Alice T. Ferris, 44702)

Evaluating Laser Transit Anemometry Performance Capabilities

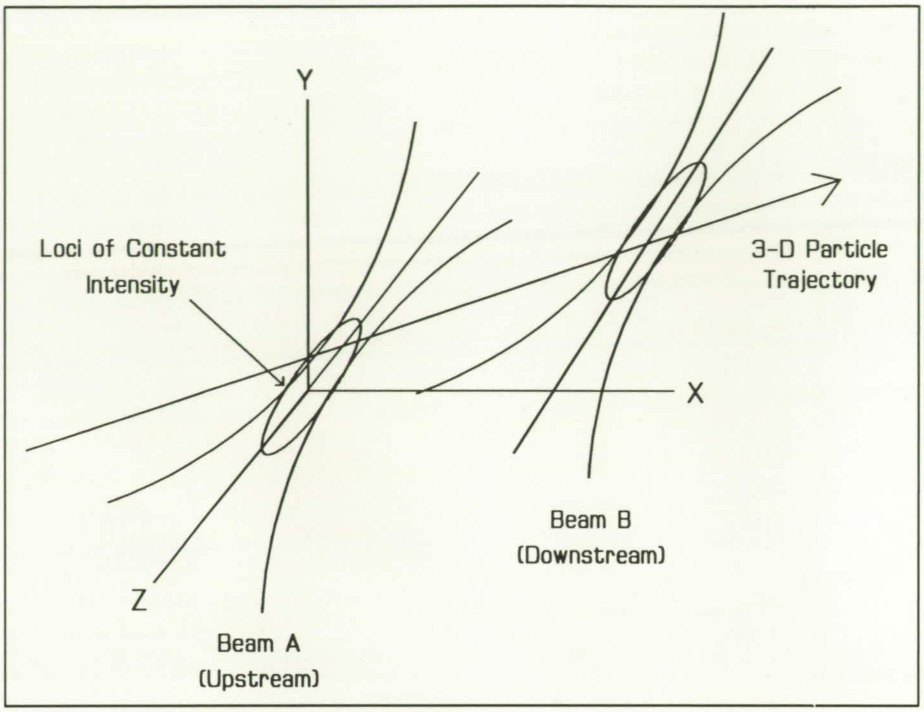

Monte Carlo simulation beam geometry model.

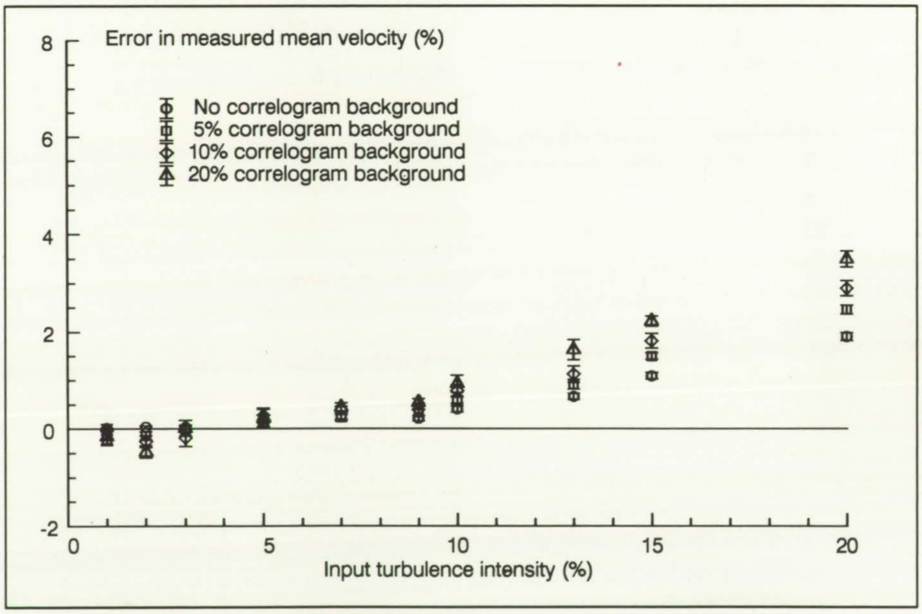

Typical analysis results from simulation system with input correlation coefficient = 0.4.

A Monte Carlo based simulation system has been developed to evaluate the performance capabilities of a laser transit anemometry (LTA) data processing system. The LTA data describe the flow field characteristics obtained in a plane normal to the optical axis of the instrument. The process system extracts from the LTA data set two components of velocity, turbulence intensity, and the related correlation coefficient. The simulation system generates typical data sets as formed by the instrument which are processed with the analysis system. These analysis results are then compared with input parameters from the simulator to obtain quantitative values of measurement accuracy and precision. The simulator modeling includes the flow field characteristics as well as the three-dimensional geometry of the LTA laser beams (see the first figure). Individual measurement events are simulated by assigning to each Mie scattering partiele a velocity magnitude and trajectory based on an assumed two-dimensional flow field probability distribution. Groups of particles are used to generate ensembles of transit time histograms which are assumed to be analogous to correlograms produced by the instrument and which correspond to various angular orientations of the LTA system beams with respect to the flow field. Poisson-distributed

background noise is added to these histograms to simulate noise levels commonly encountered when using the instrument. An analysis of test matrices generated with this simulation system indicates an ability of the LTA processing algorithms to measure mean flow parameters to less than a 1.0-percent error for turbulence intensity levels of up to 10.0 percent and signal-to-noise ratios as low as 5.0. Turbulence intensities are measurable to within 5.0 percent over the same turbulence and noise ranges. A typical analysis plot is shown in the second figure. These results indicate that the processing algorithms have application to fluid flow surveys with acceptable accuracy and robustness. **(William M. Humphreys, Jr., 44601 and William W. Hunter, Jr.)**

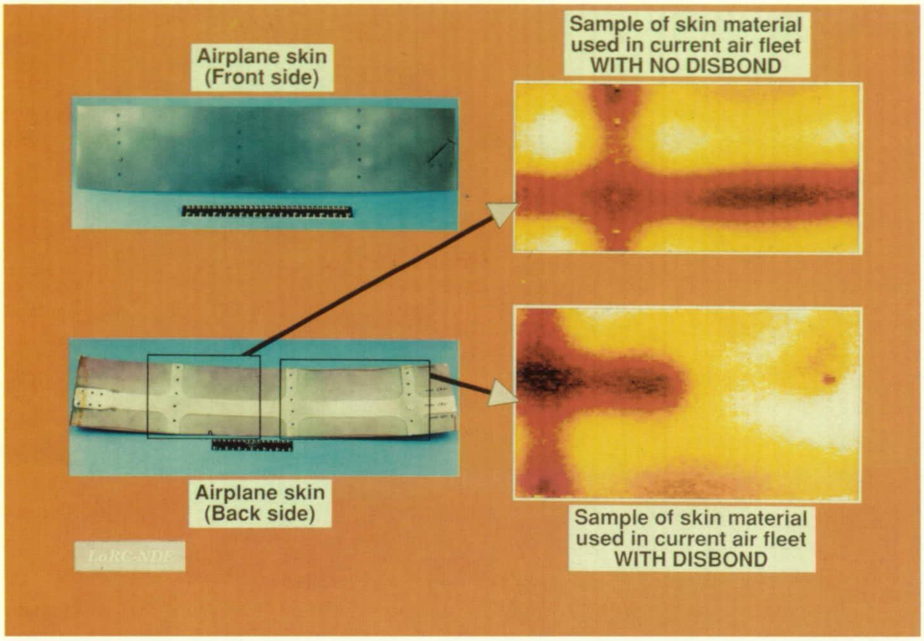

Thermal image indicating disbond in aircraft skin. L-89-4986

Thermal NDE for Aging Aircraft

Aircraft (particularly those in the commercial fleet) which have been subjected to many thousands of flight cycles are at risk for damage to the outer skin due to extended environmental stress factors. This damage, which is often progressive in nature, originates at weak points and propagates subsequently within the structure. The outermost skin of aircraft is difficult to inspect for corrosion damage and bond integrity using current techniques because inspections are generally done from the inside out. Obtaining access to the critical points requires complete disassembly of the interior, and even then, the bonds in question are difficult to inspect because of the complexity of the monocoque structure. If inspections can be found to detect this damage at low levels, corrective measures are available which can halt and repair the damage long before structural integrity is compromised.

An NDE (nondestructive evaluation) technique using computer analysis of thermal image data has been developed to provide an inspection of the outermost bond in an aircraft skin. The figure shows a sample of aircraft skin (supplied by an aircraft manufacturer) which includes a disbond. The two panels on the left show a sample of aircraft skin with the rivets removed. The front side is smooth, and the back side is bonded to a "doubler" reinforcement. The upper panel on the right side shows a processed thermal image over a region, indicated by the hollow box, where the bond is secure. The lower panel on the right side shows a similar image over a region where the doubler is partly unbonded, the disbond being indicated by the missing red horizontal pattern. The inspection is performed completely from the outside of the skin, and it clearly shows the difference between the normally bonded joint and the damaged, disbonded area. The inspection protocol and analysis algorithm both lend themselves to rapid and accurate inspections of complete aircraft skins in the hangar environment. **(William P. Winfree, 44963)**

Grid Generation About Crew Emergency and Rescue Vehicle

Computational fluid dynamics (CFD) is being used to study the aerodynamic and heating characteristics of a Crew Emergency and Rescue Vehicle (CERV). Grid generation is a necessary part of CFD. Described here is grid generation about a winged-lifting

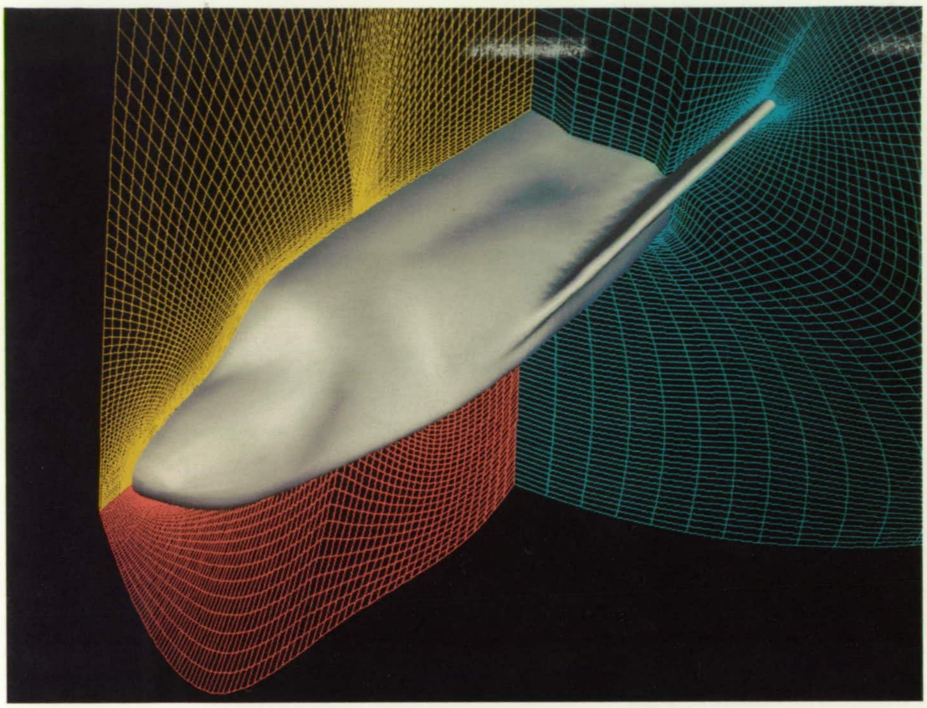

Grid surfaces about CERV.

CERV that consists of a fuselage and swept, high-dihedral wings.

The first step in grid generation is choosing a suitable topology for the configuration and the flow conditions. A dual-block topology, having an inner grid block that covers the rearward wing-fuselage region and an outer grid block that covers the front of the fuselage and the inner grid, has been chosen. This topology allows the inner grid to be computed and held fixed while the outer grid is adjusted to capture the remainder of the active flow field.

Once the topology is chosen, the intermediate boundary surface, separating the inner and outer grid blocks, and the far-field boundary surface are computed. These surfaces are determined by considering a curve in two dimensions whose shape is controlled with user-defined parameters. The curve is discretized, translated, and rotated about the vehicle's windward axis. In the case of the far-field boundary, two curves are used and blended into each other during the rotation about the vehicle; this allows the outer surface to have different characteristics below and above the vehicle, dependent on the Mach number and angle of attack.

The interior grid of each block is computed using transfinite interpolation. Hermite cubic blending functions are used for the inner block, and quadratic Lagrangian blending functions are used for the outer block. Hermite cubics afford a high degree of control and orthogonality around the wings, and the quadratics allow first-order continuity between the blocks. The grid is concentrated at the wing tip, toward the vehicle surface and toward the nose of the vehicle.

This procedure has been coded as an interactive program that runs on an IRIS 3030 workstation. Parameters are adjusted to control the intermediate and far-field boundaries and the concentrations of grid points. The figure shows the vehicle surface and the surrounding grid structure for flow computation at Mach 10 and an angle of attack of 25°.
(Robert E. Smith, 45774)

Sensitivity of Ultrasonic Polar Backscatter Technique to Fiber Orientation in Presence of Porosity

The existence of porosity in composites is an undesirable problem in the manufacture of composite components. For NDE (nondestructive evaluation) scientists, the detection of porosity in composites is also a challenging problem. Ultrasonic polar backscatter has been investigated to assess its sensitivity to the quantitative measurement of porosity. In one study, a uniaxial graphite/epoxy composite sample with ~4 percent volume fraction of hollow carbon spheres as inclusions to model porosity was investigated. The polar backscatter measurements were performed by transmitting ultrasonic energy in the sample at a polar angle of 30° from normal and where the azimuthal angle was varied with respect to the fiber orientation. Polar backscatter was measured using a 10-MHz center frequency transducer. Integrated polar backscatter was obtained by averaging over the useful bandwidth (4 MHz to 12 MHz). The figure shows a series of images made at

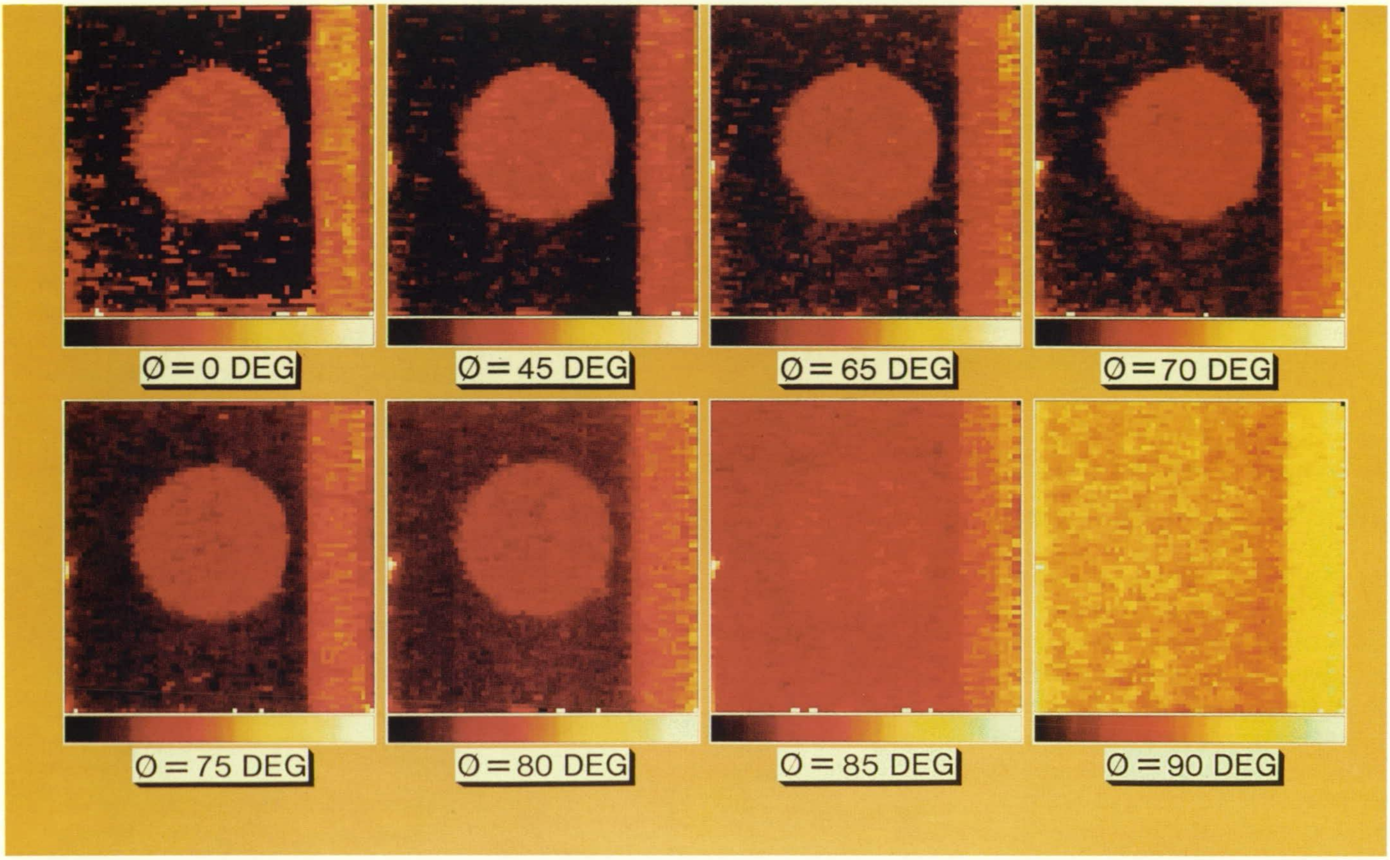

Contrast variation with respect to azimuthal angle variation of integrated polar backscatter in uniaxial graphite/composite sample with ~4 percent porosity.

various azimuthal angles. As could be expected, the strong scattering from the fibers in the composite when the ultrasound energy is incident from a direction perpendicular to the fiber's axis ($\Phi = 90°$) masks the effects of porosity, even at this high level of porosity. As the ultrasound beam direction becomes oblique to the fiber orientation, the porosity readily becomes visible. Results of these investigations suggest the potential value of this ultrasonic technique for the nondestructive characterization of porosity in graphite/epoxy composites. **(Eric Madaras, 44993)**

Slow Positron Beam Generator for Lifetime Studies in Thin Polymer Films

Polymers are finding increasing applications in aerospace industry. Some of the more challenging applications often call for polymers in the form of thin films. The properties of these films are strongly dependent on their molecular morphology. It is therefore necessary to develop a technique that can give information concerning the internal structure of thin polymer films. It was decided to adapt conventional positron lifetime spectroscopic techniques for the study of thin films. This, however, required developing a variable-energy slow positron generating assembly.

A 250-μCi Na^{22} source, deposited between the folds of a 2.54-μm-thick aluminized mylar film, is sandwiched between two 2.54-cm × 2.54-cm × 0.0127-cm tungsten pieces. Two thin test polymer films insulate the two tungsten moderator pieces from the aluminized mylar source holder. The figure shows a schematic diagram of the slow positron generator test assembly. Thermalized positrons diffusing out of the moderator pieces are attracted to the aluminized mylar source foil held at an appropriate potential with respect to the moder-

ORIGINAL PAGE
COLOR PHOTOGRAPH

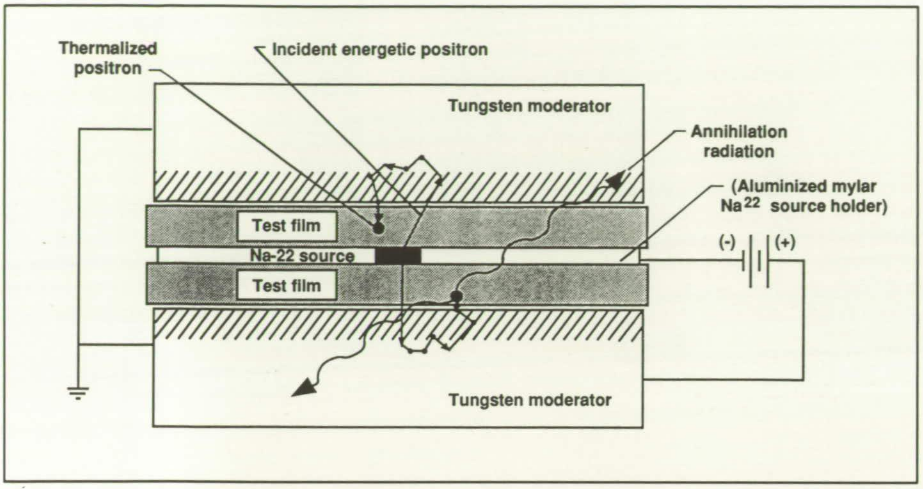

Schematic diagram of slow positron generator assembly.

ator pieces. These positrons have to pass through the test polymer films before they can reach the source foil. The potential difference between the moderator pieces and the source foil is so adjusted as to force the positrons to stop and annihilate with electrons in the test polymer films. Based on the observed annihilation spectrum, the generator efficiency is calculated to be 6 percent, which is in excellent agreement with the Monte Carlo calculation for the test assembly. **(Jag J. Singh, 44760)**

Advanced Infrared Detector Technology

Infrared detector technology to meet NASA mission requirements for the 1990's and beyond will require detectors in linear and area array formats having unprecedented sensitivity and resolution covering the mid-infrared (3 μm to 5 μm) and the far-infrared (8 μm to 20 μm) spectral bands. These detectors will be expected to operate unattended for periods of 5 or more years. The objective of this program is to develop advanced infrared materials and detectors having improved robustness and reliability for remote sensing applications from satellite platforms.

The HgZnTe materials covering the far-infrared bands have been developed with electro-optical properties equivalent to or better than current state-of-the-art HgCdTe materials. The relative response of HgZnTe as a function of wavelength and operating temperature is shown in the figure. Also, the HgZnTe materials system has demonstrated increased strength (hardness) and greater resistance to thermal drift. The increased robustness leads to reduced process-induced damage and results in more uniform materials properties and a higher device yield. The longer operating lifetime in the HgZnTe devices is achieved as a result of the increased resistance to thermal drift. Theoretical calculations and analysis have verified results thus far obtained and have further indicated that the HgZnTe materials/device systems offer important advantages in lower tunneling currents and higher operating temperature.

Presently, prototype (270 by 1) linear arrays are being processed from the 17 μm to 20 μm HgZnTe material for characterization and measurement of lifetime parameters. **(William E. Miller, 41720)**

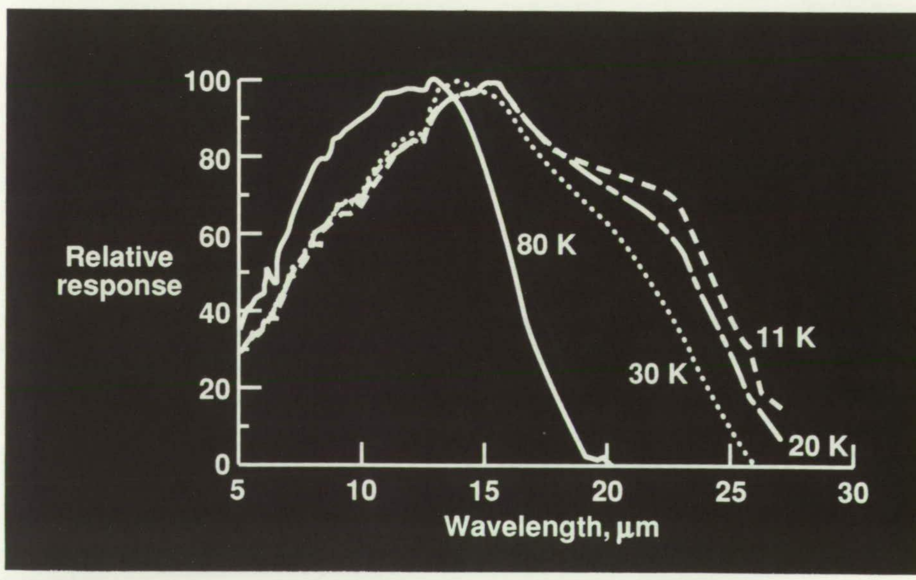

Relative spectral response of HgZnTe as function of operating temperature.

F-106 Vortex Flap Instrumentation and Personal Computer Monitor

Flights of the F-106 aircraft modified with the experimental vortex flap were conducted throughout 1989. Following the first flight on August 2, 1988, a series of envelope expansion test flights were completed to investigate structural dynamic and static loading limitations. After loading maneuvers to 2.9 *g*'s and speed increases to Mach number 1.1 (40,000 ft), the flight envelope was cleared to proceed with dedicated performance research flights.

Instrumentation for the ultimate evaluation flight tests was built in stages. The first figure summarizes the instruments used during the envelope expansion phase. Three-dimensional flow effects were observed through two video cameras observing flow cones on the surface of the left wing. An extensive array (68) of wing strain gauges was used to assure nonexceedance of predicted, allowable structural loads throughout the wing. The first figure also shows the initial phase of pressure belts (two) near the wing tip and the thin-film dynamic transducers for fluctuating pressures.

Six structural dynamics accelerometers were arrayed through the wing and tail to measure onset of structural dynamic phenomena (flutter, buffet, and vibration). A real-time power-spectral analysis was performed on the telemetered data during flight tests to assure flutter-free test conditions.

A new personal computer (PC) monitor system was developed for real-time analysis and display of

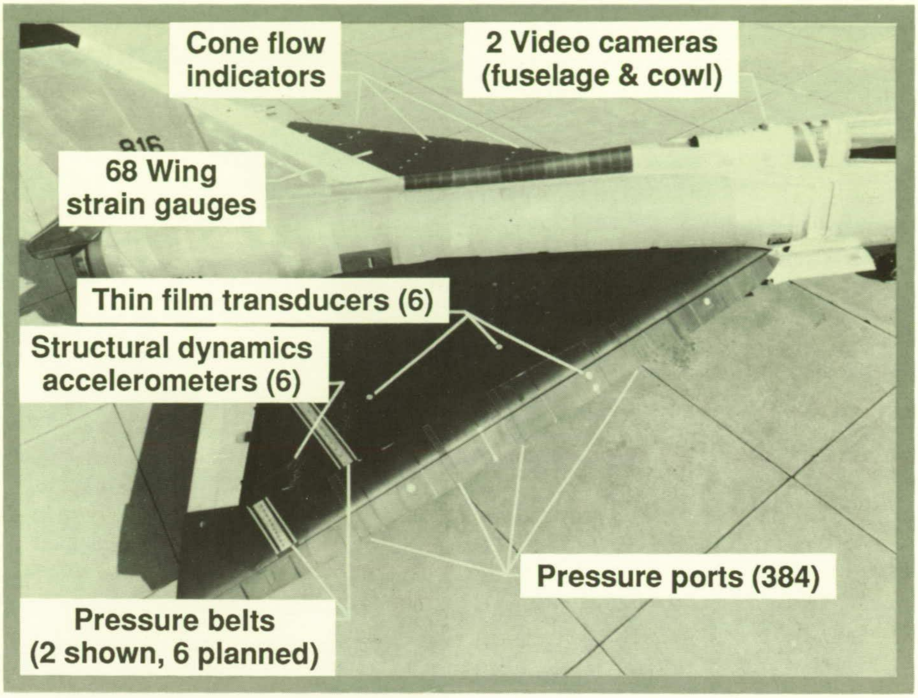

Vortex flap experiment research instrumentation. L-89-3052

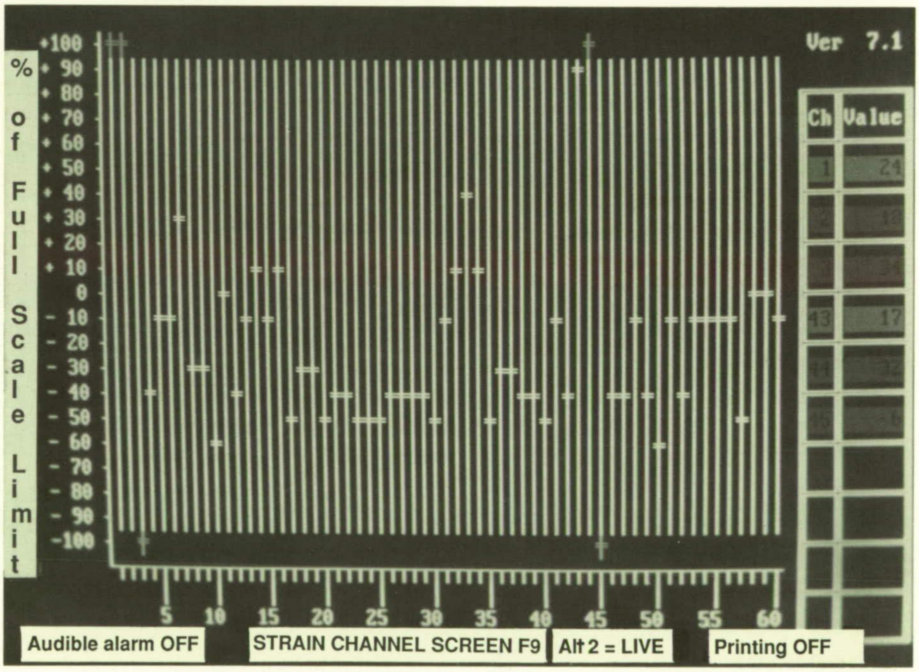

Display of real-time strain-gauge data. L-89-3749

the strain-gauge data during flight. The second figure shows a black and white photograph version of the computer-generated color display of 60 structural strain channels during the load expansion flights. The ordinate indicates strain values in percent of allowable limits, and the abscissa indicates the number of each individual strain gauge. The screen pictured indicates exceedances of three preset limits on the high side indicated by the data crosses and also two on the low side (compressive) limits. One strain value is in the caution region between +85 percent and +100 percent. The values in micro-strain of the exceeding strain gauges are shown on the right-hand side table display.

In a condition near the limits, such as this display indicates, an alarm sounds, automatic printing of all data occurs, and the ground-based test engineer calls a caution to the test pilot to abort the maneuver-strain.

Using the monitor greatly enhanced the ability to visualize structural loading conditions and to avoid onset of any excessive loads during the envelope expansion flights of the F-106.
(J. Otis Riggins, Jr., 43807, R. Smith, and J. R. Elliott)

Quantitative Anisotropic Stiffness Images Measured in Carbon-Carbon Composites

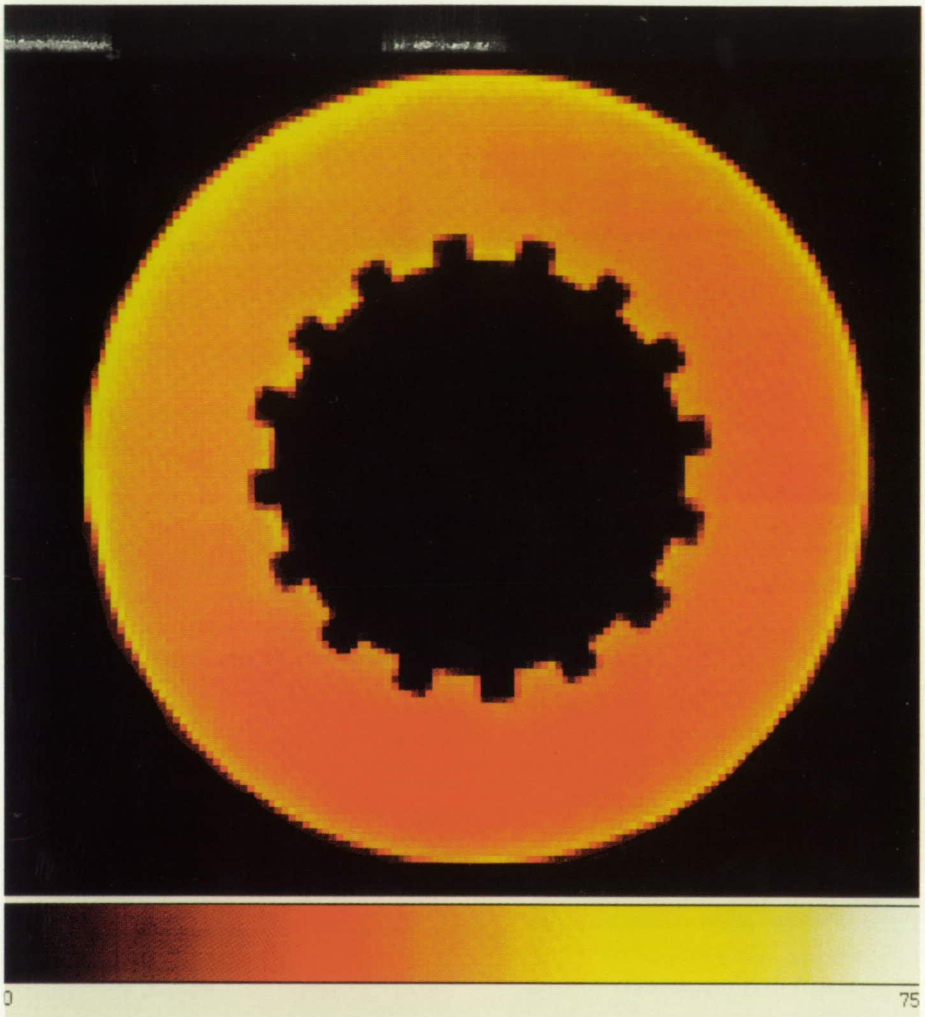

Digitized X-ray radiograph of carbon-carbon brake stator.

The introduction of high-strength, low-weight composite materials is dramatically changing aircraft designs. New materials are constantly being introduced to meet ever-increasing demands on performance. These new materials are requiring more advanced nondestructive evaluation considerations; this is particularly true for high-temperature applications for which carbon-carbon composites are one possible material choice.

A technique to measure quantitatively the anisotropic stiffness moduli in an orthotropic material nondestructively has been developed. This technique has been demonstrated in a carbon-carbon brake shoe stator. In this work, local material anisotropy was characterized with an ultrasonic velocity analysis technique. Orthotropic material symmetry was assumed; hence, nine independent velocity measurements (using multiple angles of incidence) were required. Due to the large amount of attenuation present in these materials, a low-frequency (500-kHz) tone burst technique was used along with a pulsed phase-locked-loop detection system to ensure accurate velocity

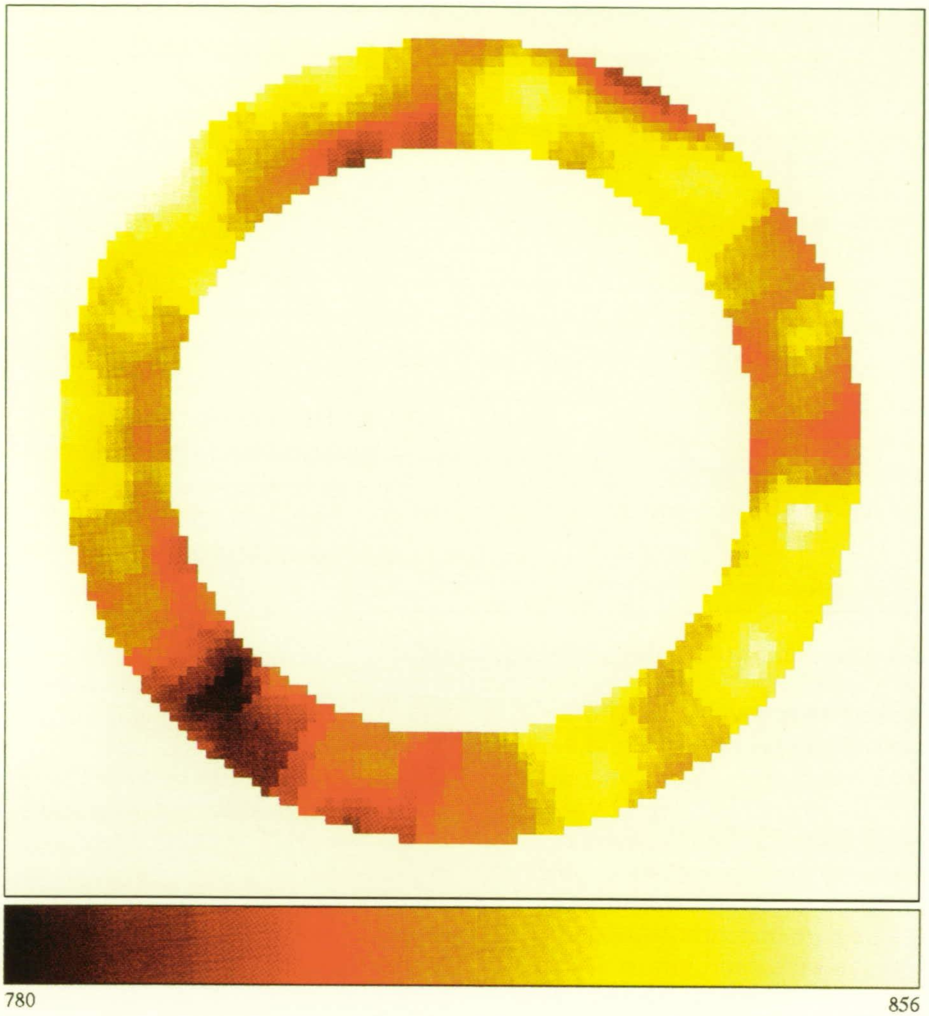

One of nine stiffness moduli measured in carbon-carbon brake stator.

measurements. The data were then processed with a computer program that could solve the resulting system of nonlinear equations.

The first figure is a digitized X-ray radiograph of a carbon-carbon brake stator. The quantitative X-ray image is relatively uniform indicating approximately a 1-percent density variation. The density variation for this component is considered acceptable. For the ultrasonic work reported here, a ring-shaped area of this stator was measured. The second figure shows an image of one of the nine measured stiffness moduli. This modulus represents the tensile stiffness in the tangential direction around the brake stator. The quantitative values indicate an almost 20-percent loss in stiffness in the one dark region. That region will of course exhibit a different strain behavior under the loading conditions to which the stator will be subjected.
(Eric Madaras, 44993)

Active Laser Sensors for Wind Shear Detection

Detection of hazardous wind shears is being pursued aggressively by Langley Research Center. Various technologies are being investigated which will detect the presence of potentially fatal wind shear hazards for civilian aviation including Doppler radar, passive radiometry, and laser radar. Each technique has strengths and weaknesses depending on the local weather conditions. The NASA/industry studies have identified 2-μm coherent laser radar as a promising new technology for civilian wind shear measurements. The thrust of this research effort is to demonstrate key laser performance features in the laboratory which will enable successful deployment of the 2-μm laser sensors.

Two-μm laser research has concentrated on development of the master oscillator that determines the laser wavelength and bandwidth. Continuous wave operation has resulted in output powers of 60 mW and wall plug efficiency of 10 percent. In general, 2-μm lasers operate with 10 GHz to 50 GHz bandwidths. Single longitudinal mode operation of the 2-μm laser has been achieved by NASA researchers and overcomes one of the major obstacles associated with coherent radar. Careful bandwidth measurements using heterodyne techniques are expected to verify 1 MHz or less lasing bandwidth.
(Mark Storm, 41635)

Simulation of Diode Laser Array Pumping of Tm-Ho or Tm-Doped Lasers With High-Power Long Pulse Lasers

A flashlamp-pumped Cr:GSAG laser has been developed in-house for pumping of Tm-Ho and Tm-doped YAG (yttrium, aluminum, garnet) and YLF (yttrium, lithium, fluoride) lasers to simulate pumping with high-power diode laser arrays that are still under development. The output of the Cr:GSAG laser peaks at room temperature in the $\approx 0.782\,\mu$m to $0.787\,\mu$m range of the Tm absorption band, and, when operated with $\approx$ 1 msec pulses, it approaches the several msec upper state lifetimes beneficial to energy storage with diode laser pumping. Potential color center formation due to ultraviolet absorption must be carefully controlled for Cr:GSAG lasers. The peak output achieved so far for the Cr:GSAG laser is $\approx$ 200 mJ, which, considering a somewhat less than msec pulse, simulates more than 200 W quasi-cw diode laser power.

For an initial demonstration, the Tm-Ho crystal with a 3-mm length, 3-mm diameter, and $\approx$ 1-mm mode diameter has been pumped at $0.784\,\mu$m at a reduced energy of 90 mJ with an absorbed energy of 46 mJ. A Tm-Ho laser output of 14 mJ (the pulse energy requirement for airborne wind shear Doppler lidar is 10 mJ) has been obtained with a slope efficiency of 33.6 percent in terms of the absorbed input energy. The Cr:GSAG pumped Tm-Ho, Tm-doped YAG, or YLF laser will be evaluated for production of pulses for DIAL (differential absorption lidar) and Doppler lidars (through Q-switching and other techniques), and its laser bandwidth will be controlled through injection locking with low-power diode laser pumped Tm-Ho lasers. Further, the rate coefficients for Tm-Ho energy transfers and up-conversion losses in these lasers will be evaluated for a range of concentrations, temperatures, and power densities for incorporation in the laser rate equation.
(K. H. Kim, 41555)

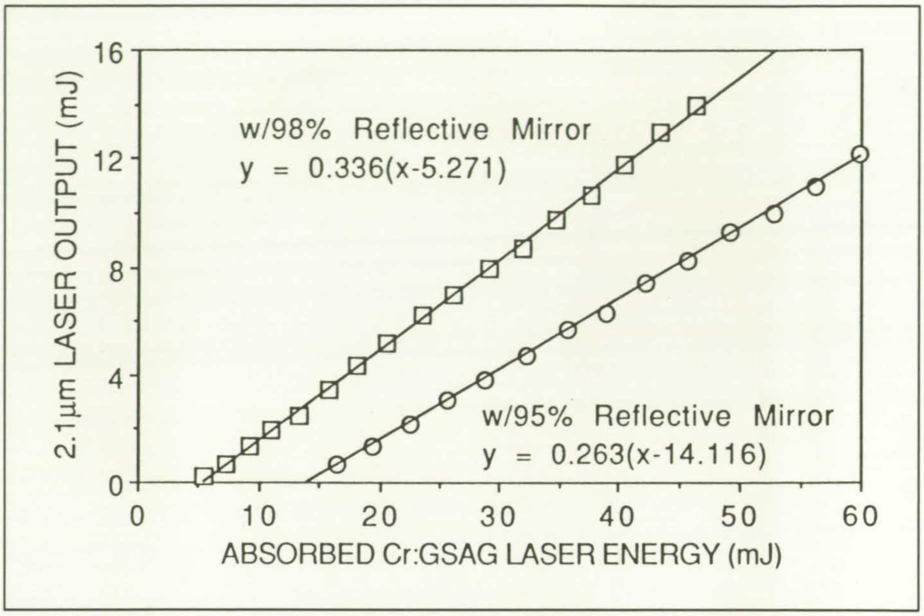

2-μm laser output versus absorbed energy.

Theoretical Modeling of Normal Mode and Q-Switched Cr-Tm-Ho-Doped $\approx$2 μm Solid-State Lasers

A rate equation model using our experimentally determined spectroscopic and laser parameters has been developed to optimize the energy transfer in laser-pumped Tm-Ho or flashlamp-pumped Cr-Tm-Ho-doped lasers for efficient $\approx$ 50 nsec pulse (DIAL) and $\approx 1\,\mu$sec pulse (Doppler lidar) laser operation. The differing time scales in the laser rate equations required development of a new computer algorithm for the solution of a series of stiff differential equations. The results of modeling have been compared with normal mode and Q-switched operation of a flashlamp-pumped Cr-Tm-Ho:YAG laser.

The figure displays normal mode operation, resulting from the $\approx 200\,\mu$sec long quasi-cw flashlamp pulse, and shows the expected clamping of the population inversion at its threshold. The photon energies show a series of spikes which are also observed in the experiment. The delay of the Q-switch opening to extract the energy from the Cr-Tm-Ho energy transfer, in a single pulse rather than a series of spikes, has been obtained from the model and shows similar trends as the

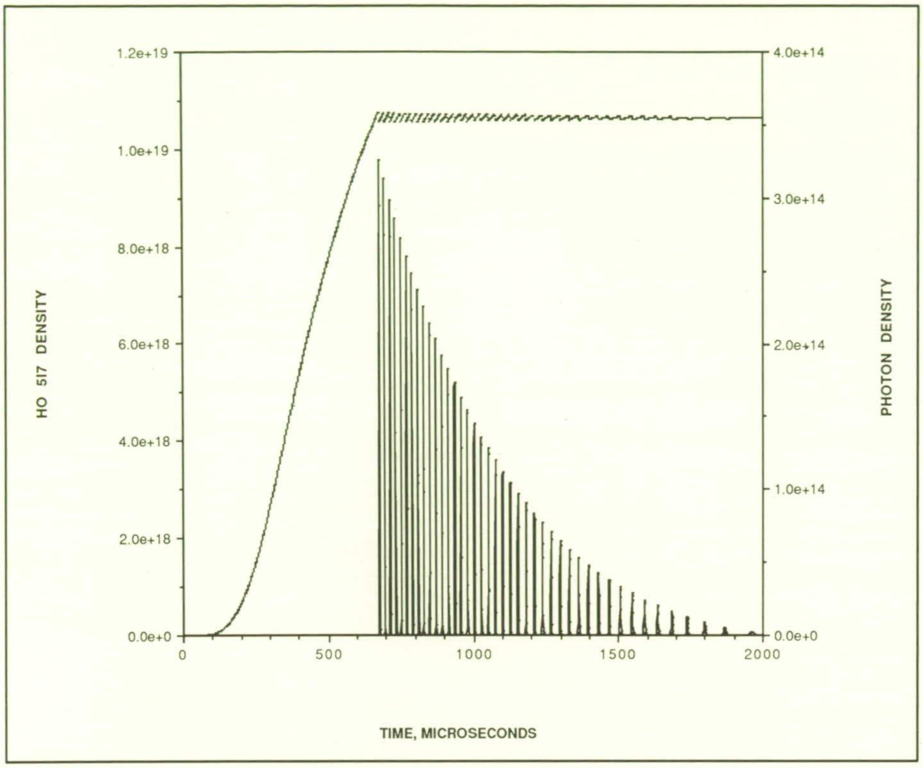

HO 517 state and photon densities versus time.

experiments. The coefficients in the rate equations are being further refined through experiments in spectroscopy and laser-pumped Tm-Ho and flashlamp-pumped Cr-Tm-Ho lasers.
(C. H. Bair, 41556)

Data Base for Solid-State Laser Design

Models for designing solid-state lasers require data for laser, optical, and nonlinear materials. Depending on the particular concern being addressed by a specific model, absorption or emission spectra and crystalline, optical, thermal, and mechanical properties of materials may be needed. Hundreds of materials have been investigated as potential laser or nonlinear materials; new materials continue to be developed. Topical concerns, such as ion-to-ion energy transfer and up-conversion, force laser researchers to reassess old data in a new light. The extensive variety of data, the large number of materials, the necessity for future expansion, and the changing analytical requirements warrant a systematic, versatile, and flexible approach to data storage and retrieval.

A two-part, computerized, interactive data base that retrieves materials data in a way that is useful to the laser designer has been developed to run under a commercially available data base manager. One part of data base LASERS contains laser material absorption and emission spectra and laser diode emission spectra; the other part contains tabulated physical properties of laser, optical, and nonlinear materials. Crystalline, optical, thermal, and mechanical properties reside in approximately 25 tables with approximately 190 unique columns of data. The tabulated portion of data base LASERS currently contains approximately 10,000 rows of data. Macros, programs written in the data base language, retrieve information for the laser designer in a user friendly, relevant fashion. Among other things, data base LASERS and associated data base macros and laser models can be used to quantify the absorption efficiency, the spatial distribution of absorbed energy, the sensitizer to active ion transfer rate, and the population distributions of the various laser levels for many laser materials. By predicting the relative performance of various laser materials before actually building the lasers, the long and costly process of experimentally optimizing a laser design can be reduced.
(Patricia L. Cross, 41633, Elizabeth D. Filer, and Norman P. Barnes)

Heat Transport in Solid-State Lasers

The design of laser systems for the remote sensing of the atmosphere from space requires laser sources that are efficient, stable, and long lived. Solid-state lasers, pumped directly or indirectly by semiconductor diode lasers, satisfy these requirements. Optimal design of these laser systems requires an understanding of thermal dissipation rates as a function of

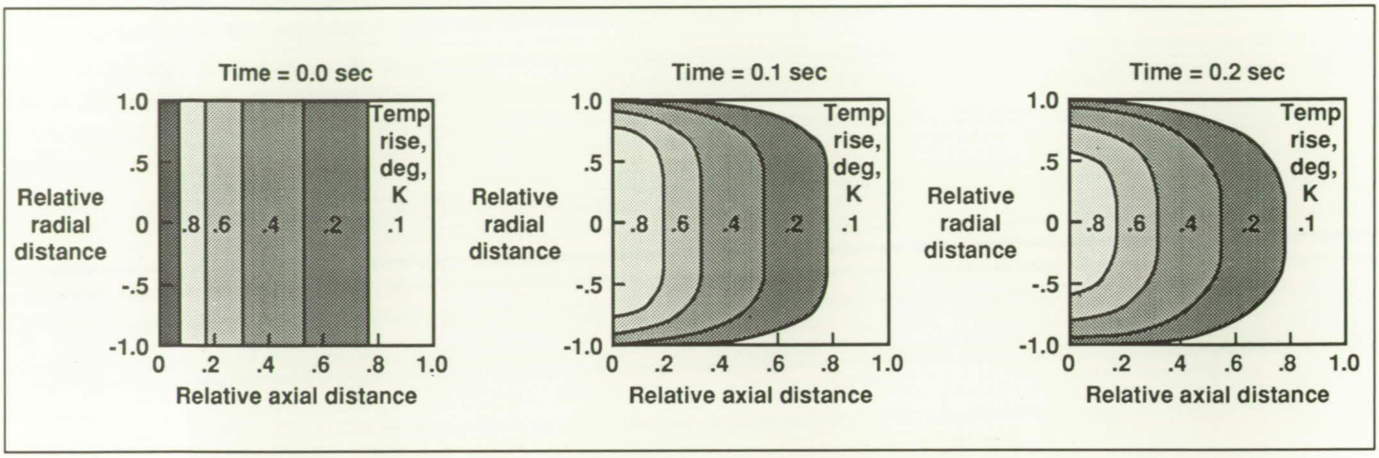

Heat propagation in laser rod, end-pumped single pulse, uniform cross section.

pump configuration, pulse energy, and pulse rate. To address these requirements, a technique was developed to analyze the heat transport in laser rods.

This technique takes into consideration the finite size of the laser rod, the pumping configuration, and the method of active cooling. An expression that predicts the time evolution of temperature in finite laser rods was derived for various specified pumping and active cooling schemes. The model was used to calculate the evolution of temperature in laser rods including titanium-doped sapphire and neodymium YAG, which are candidates for an all-solid-state laser remote sensing system. Localized thermal hot regions in laser rods lead to thermal lensing effects that lower the output from these systems and decrease their efficiencies. In addition, this model, which can predict the time evolution of temperature for various pumping configurations and estimate the probable duty cycles of such systems, can be used to evaluate different thermal management schemes for optimum operation. The model will be used to evaluate thermal effects as a step in the optimization of specific systems in remote sensing applications. For example, current and new laser materials can be evaluated for suitability under various pumping and cooling configurations.

(U. Farrukh and P. Brockman, 41554)

Development and Construction of Airborne Autonomous Wavemeter

One experiment to make water vapor DIAL (differential absorption lidar) measurements from a down-looking airborne platform is the

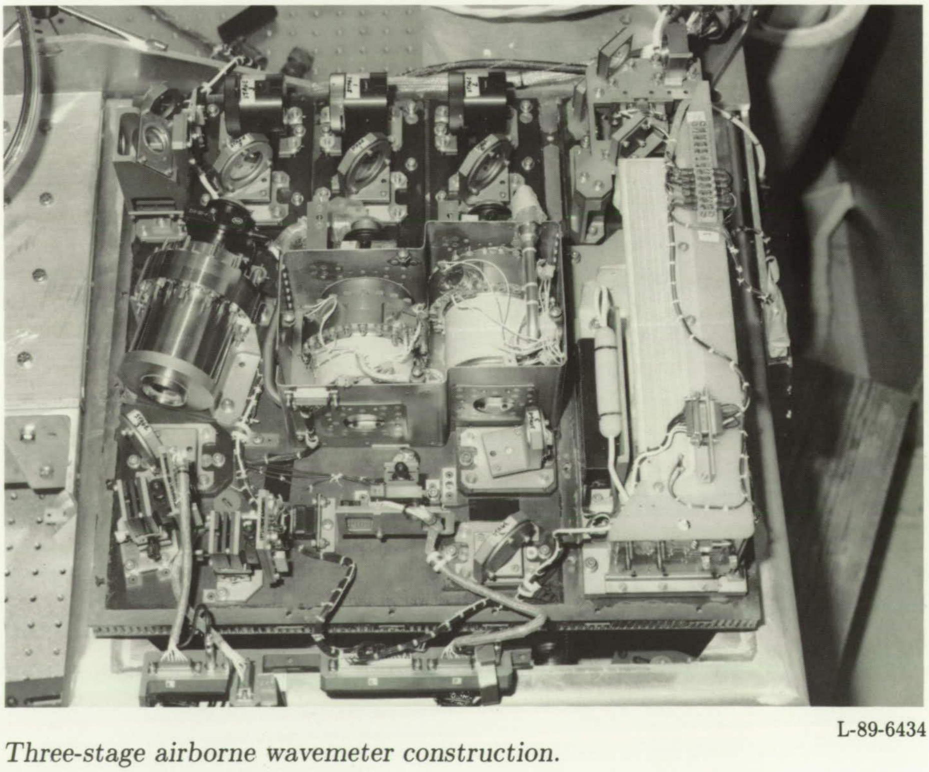

L-89-6434

Three-stage airborne wavemeter construction.

NASA-LASE (Lidar Atmospheric Sensing Experiment) Project instrument to be flown on a NASA ER-2 aircraft. Breadboard results have been obtained that predict that a wavemeter can be built to survive the harsh airborne environment of low temperatures and low pressures that exist in high-altitude flight.

Based on the breadboard results, the airborne wavemeter consists of three stages of Fabry-Perot interferometers. Stages one and two give the necessary information to provide laser wavelength centroid measurements to the required accuracy of < 0.25 pm. This accuracy provides the real-time information necessary for tuning the two tunable alexandrite lasers for the water vapor measurement. A high-resolution stage number three interferometer provides the laser spectral profile measurement with an instrumental profile < 0.5 pm full width at half-maximum amplitude for the post-flight science data reduction. To maintain interferometric stability, the first two stages are thermally controlled and contained in a vacuum chamber. A two-level control approach is used to stabilize the interferometers above the highest ambient temperature.
(Joseph H. Goad, Jr., 41636)

PC-Based Interface Simulations of Flight Systems

As flight experiments become more complex, simulation of data interfaces between subsystems becomes more critical in the design. The subsystems usually are developed independently requiring simulators to represent data interfaces. The Lidar Atmospheric Sensing Experiment (LASE), a major Langley Research Center lidar remote atmospheric sensing program, has distributed processing among five microcomputer-based subsystems. An effective solution is to design to an interface standard, such as the RS-232-C standard, which enables the use of inexpensive IBM PC/AT computers to simulate the interfaces. A single AT was used to simulate all the real-time data interfaces in the LASE Control and Data Subsystem (CDS), using commercial timing and multiport RS-232-C cards with a minimum of customizing.

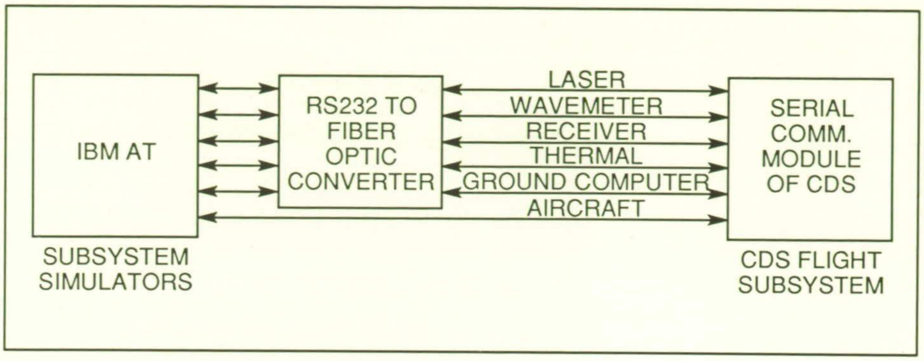

Flight hardware interface simulation.

User-friendly menu-driven display screens enable the user to exercise different command sequences through keyboard entry during real-time operation. The simulator software program for the CDS was written in Turbo C, and, with minor modifications, was used for the other subsystems. The use of standard interfaces has allowed the parallel development of subsystems at different locations with a high degree of confidence for a successful instrument integration.
(Kevin Brown, 41856)

Flight Systems Directorate

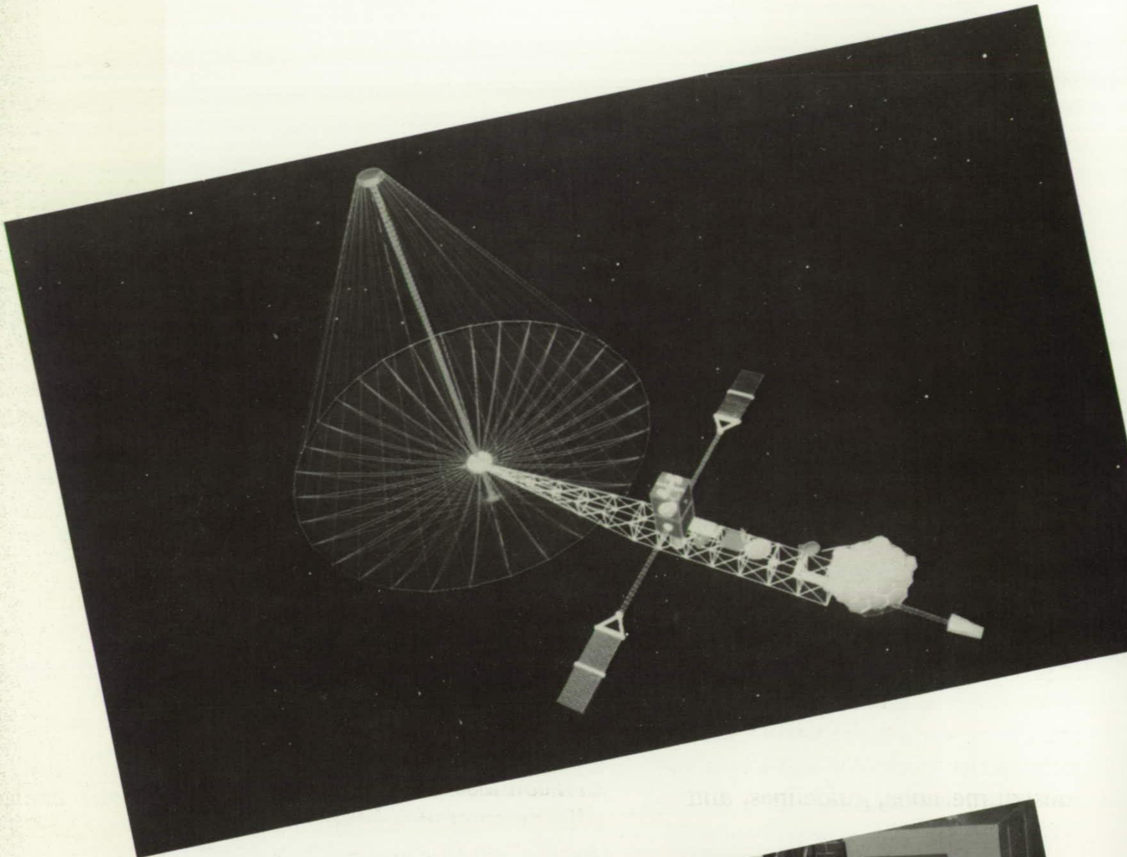

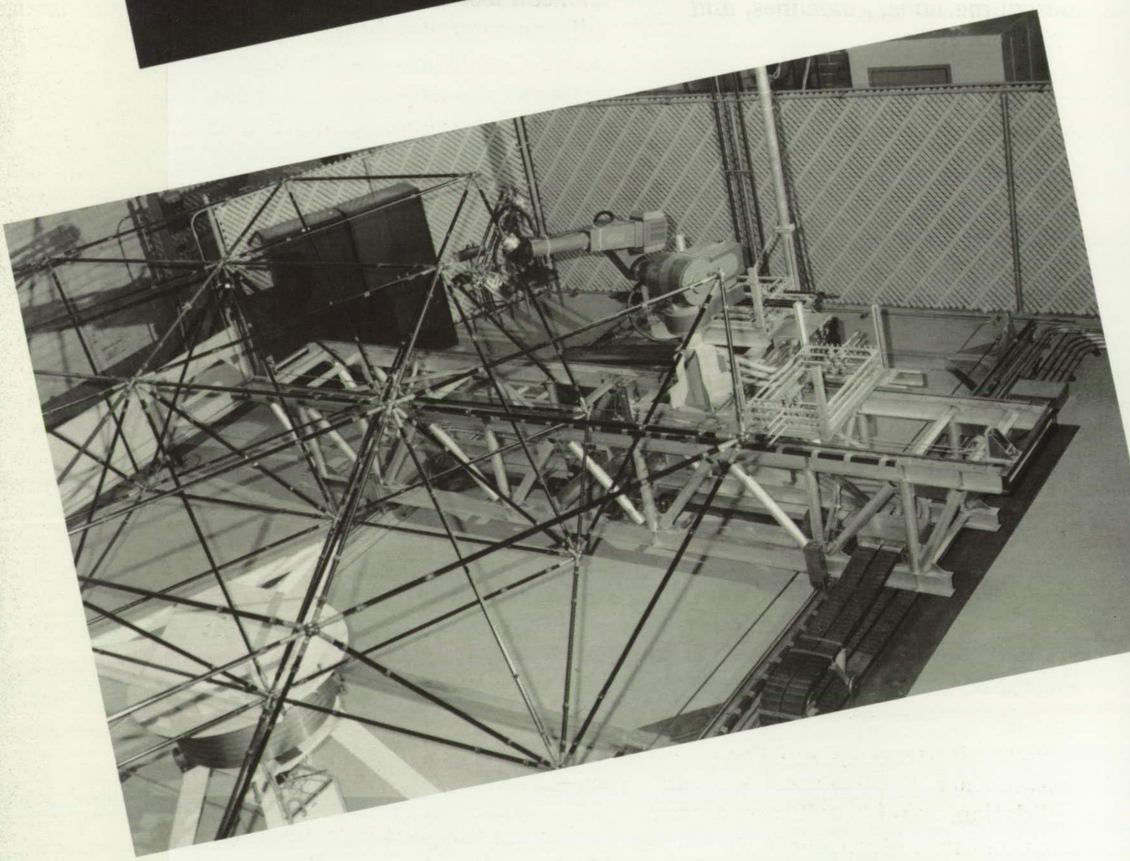

ORIGINAL PAGE
BLACK AND WHITE PHOTOGRAPH

The Flight Systems Directorate conducts basic research and development in the broad, multidisciplinary area associated with aerospace flight systems. This includes systems hardware and software architecture concepts and design guidelines, validation and verification methods for reliable flight control systems, advanced cockpit interfaces, advanced airborne systems technology, aircraft operating procedures, fundamental electronics research, automation and robotics technology, and aircraft and spacecraft guidance and control system design methods, guidelines, and criteria.

The Advanced Transport Operating Systems Program Office coordinates a wide-scale focus technology research and development effort aimed at developing and improving the technology base for transport aircraft operating systems and the integration of these systems with the current and future air traffic control environments. The office also provides a focus for research and development of improved airborne operations and procedures and operates the NASA Boeing 737 aircraft and associated simulator.

The Information Systems Division conducts research to provide an advanced technology base for future spacecraft and aircraft systems. Specifically, the division performs research in the areas of robotics and automation, fault-tolerant systems validation, reliable software, system architectures, electronic/optical subsystem technology, and software engineering. The scope of activities is broad and ranges from the highest level systems considerations to the investigation of solid-state physics phenomena.

The Guidance and Control Division conducts generic and applied research on aircraft and spacecraft guidance, control, and antenna systems. The research is directed toward the development of a technology base for advanced aircraft and spacecraft systems analysis and design methods, including validation and verification demonstrations of advanced concepts. The division also develops multidisciplinary computer-based tools and techniques that allow appropriate guidance, control, and antenna design issues to be considered through all stages of aircraft and spacecraft design.

The Flight Management Division conducts research to provide a viable technology base for future aircraft and spacecraft flight management systems. Specifically, the division provides technologies required by designers of crew station systems; defines and evaluates improved guidance and control procedures; and studies advanced airborne systems technology, traffic control strategies, and operating procedures for improving the efficiency of air traffic control operations. In addition, the division provides methodologies and criteria for measuring crew work load and stress.

During the past year the Flight Systems Directorate achieved and documented a significant number of technical accomplishments in a wide range of technical areas. Among these accomplishments were the establishment of a new robotics assembly laboratory (the Automated Structures Assembly Laboratory) and the completion of the first truss structure construction tasks in that facility. A number of manned simulator studies were completed; these studies were aimed at determining the benefits of having three-dimensional stereo in aircraft cockpit displays. Initial investigations of the use of helmet-mounted displays to provide fighter aircraft pilots with critical information were also conducted. Important research was continued to understand better the airborne wind shear phenomenon and how to detect wind shears and safely avoid or fly through them. A new, versatile uncluttered engine-monitoring and control system (E-MACS) was developed, patented, and evaluated. E-MACS, which offers promise of early acceptance by aircraft manufacturers, won the 1989 Research and Development 100 Award, which is presented annually by Research and Development magazine to 100 scientists or engineers who have contributed the most significant products for advancing science and technology during the year.

Expanded efforts in the controls and displays for superagile fighter aircraft were undertaken in preparation for a new program to investigate fighter aircraft performance at high angles of attack. Research in the use of artificial intelligence or knowledge-based systems in vari-

ous aspects of aircraft system monitoring, flight management, and control continued to be emphasized. The past year again was an active year of flight testing in the Transport Systems Research Vehicle (TSRV) with tests on the Takeoff Performance Monitoring System (TOPMS), the E-MACS, the microwave landing system (flying complex paths), and data links. A number of studies associated with software and hardware reliability and fault tolerance were completed as part of a continuing effort. Research also continued in analytical and laboratory studies associated with the control of large space structures.

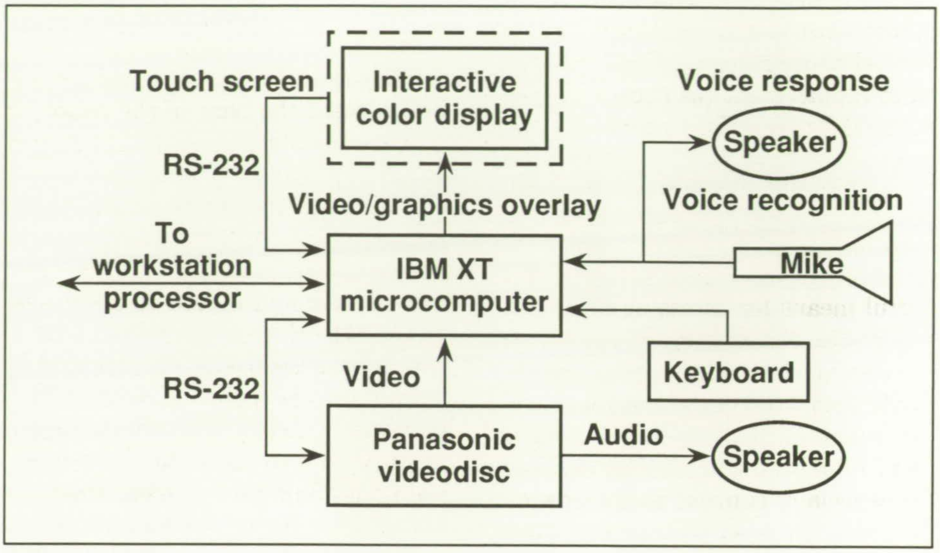

Interactive videodisc system architecture.

Interactive Videodisc System Application for Space Station Freedom Workstation

Interactive videodisc technology has demonstrated the capability to increase human productivity with reduced work load. Because of its inherent capability for high-density storage and its characteristic of being highly interactive, this technology offers a significant reduction of size and weight and more effective presentation of information as opposed to conventional paper manuals used for training and maintenance applications. The goal of this effort has been to evaluate potential advantages of such a capability in a space station workstation environment using a representative application.

An interactive repair and maintenance application for an Environmental Control and Life-Support Subsystem (ECLSS) was conceived and produced on videodisc for assessment within the Space Station *Freedom* workstation environment. The application was then implemented on an IBM XT with an embedded voice recognition system and interfaced to a Panasonic videodisc player and a color monitor with an interactive touch screen capability (as shown in the first figure). This application not only gives operators the choice of an overview of the ECLSS and associated subsystems, but also leads them through logic branches to iso-

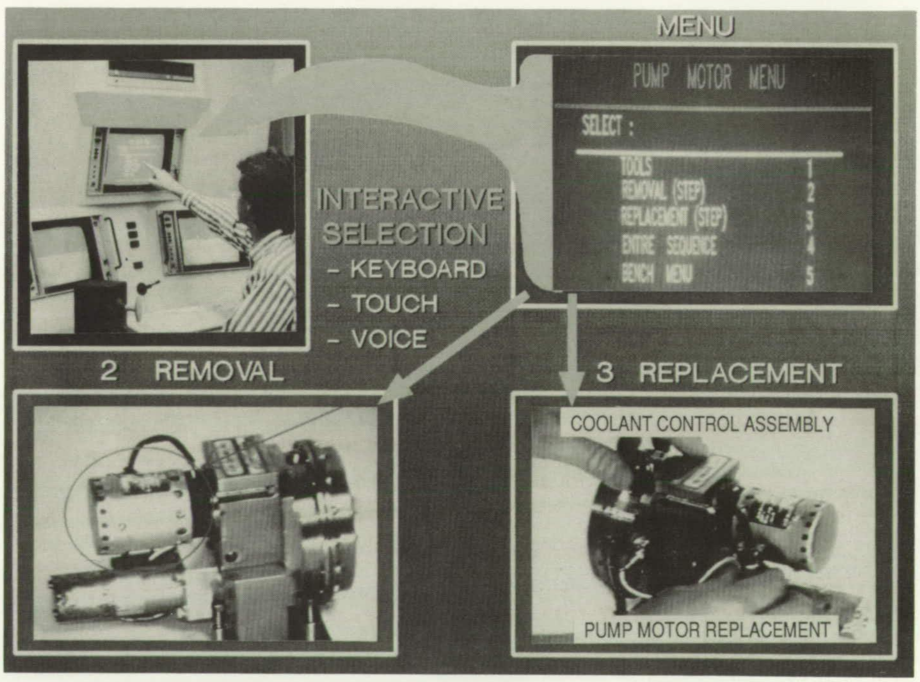

ECLSS maintenance application example.

late the defective Orbital Replacement Unit (ORU) and provides self-paced procedures for ORU removal and replacement (as shown in the second figure). This process is accomplished via menu selections, image motion sequences, auditory explanations, prompts, and queries.

This application provides a powerful means for assessing interactive videodisc technology, which is proposed to replace myriads of manuals that would otherwise have to be taken aboard for on-orbit repair and maintenance. This capability is especially convenient for Space Station *Freedom*, which consists of innumerable subsystems that will remain aloft for long periods of time and must be serviced by a limited crew with only generalized subsystem knowledge.
(A. M. Busquets, 46652, T. W. Hogge, F. McWilliams, and R. V. Parrish)

Automated Assembly of Large Space Structures

A cooperative research program between structures and robotics has been developed to evaluate technology and demonstrate the potential for automated in-space assembly of large space structural platforms. A test facility has been constructed to perform assembly studies on a two-ring model of a regular tetrahedral truss with 2-m-long members. The structural assembly is accomplished using a commercial robot arm to place the struts in the truss in a totally automated manner. The robot arm is moved into the various assembly positions on an *X-Y* carriage that is designed to minimize base positioning errors, and the truss is mounted on a rotating motion base.

The truss struts are stored in pallets near the base of the robot, and a specially designed end-effector picks the strut from the pallet and places it in the truss locking it in position. As the pallets are emptied, they are picked up by the end effector and moved to a storage rack at the side of the robot. The complete truss has 102 struts and 31 nodes. The strut tubes are graphite/epoxy, and the strut joints are designed to accurately position the nodes and have a linear load and displacement response.

Assembly operations are driven by two computers that are serially connected and controlled by a third computer that serves as an executive system. The operator monitors system execution from both computer operation prompts and a video surveillance system. The video surveillance system consists of two cameras with programmable pan tilt drive controllers and two fixed mounted cameras attached to the end effector. The operator may terminate assembly at any time if an error occurs.

Initial tests indicate that the proposed approach for automated structural assembly is a viable option for erecting large space truss structures. Also, tests indicate that computer control of assembly operations is very desirable and that it will be difficult for even an experienced operator to remember every sequence and state required to assemble a simple planar truss.
(Ralph W. Will, 46672 and Marvin D. Rhodes)

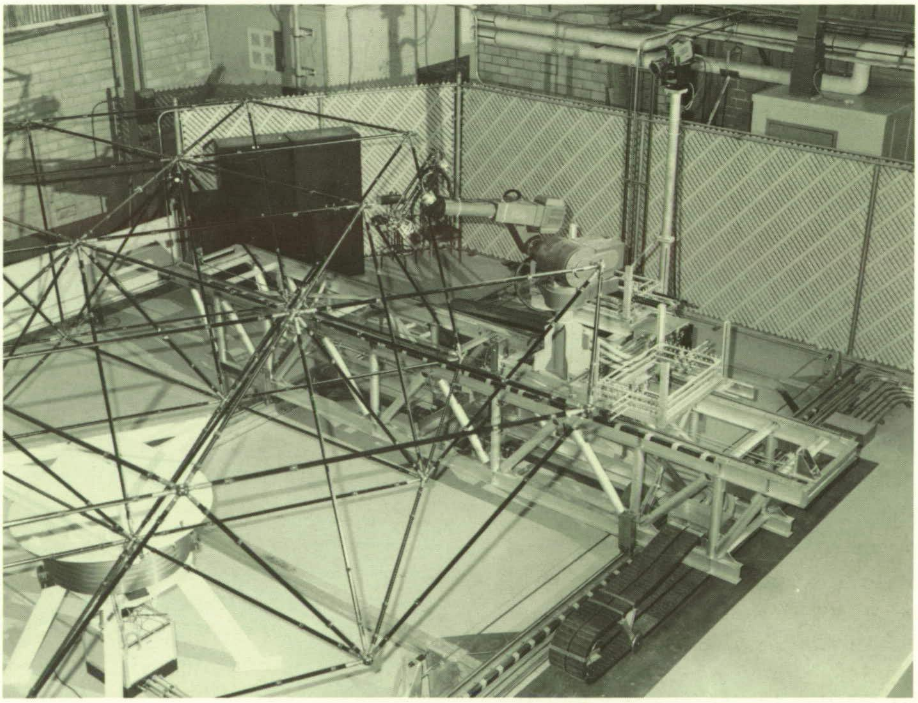

8-m-diameter truss in assembly facility. L-89-03427

Mentat: An Object-Oriented Macro Data Flow System

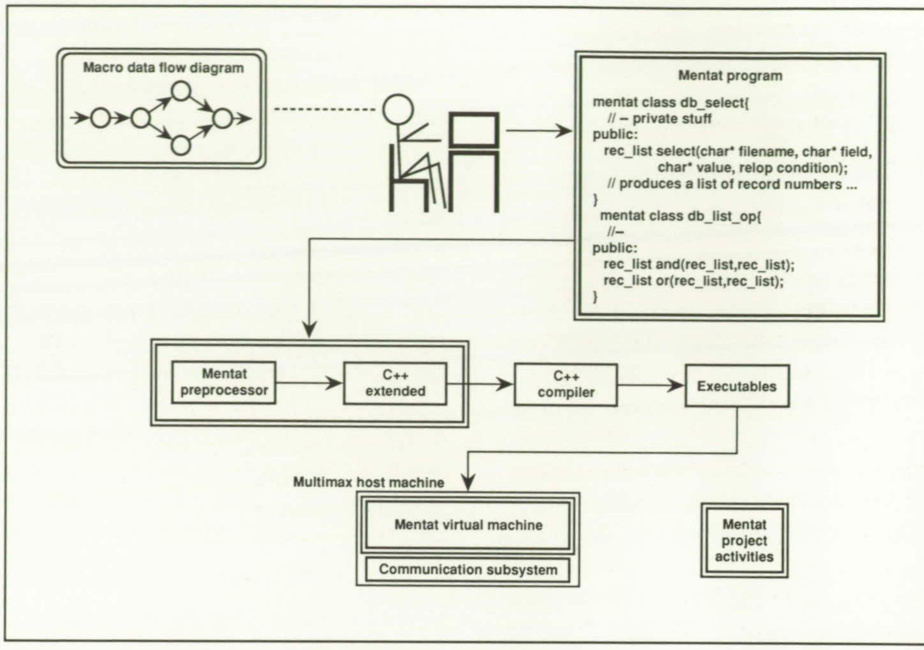

Application of Mentat macro data flow system.

In recent years, distributed systems and multiprocessor systems containing large numbers of interconnected processors and computers have been used to support a broad spectrum of applications. Efforts to increase parallelism and performance have concentrated on load balancing via remote procedure call and process migration. Mentat, which was designed and developed under the Illinois Computer Laboratory for Aerospace Systems and Software (ICLASS) block grant at the University of Illinois Urbana-Champaign, combines the object-oriented paradigm with the macro data flow model of computation. The objective of this work was to create a system to support an easy-to-use, transparent mechanism to increase parallelism in distributed and multiprocessor systems. Object-oriented languages have the ability to define abstract types (objects) which hide implementation and data structure details from other objects that use them. Data flow models are used to increase parallelism in tightly coupled systems; here a program is represented as a directed graph in which the nodes are computation primitives (actors) and the arcs represent dependencies between actors.

The Mentat data flow language was developed as an extension to the C++ programming language. The macro data flow model in Mentat differs from the traditional model in two ways: some actors are persistent (retain state information), and the data flow graphs are dynamic. The Mentat preprocessor detects data dependency, generates data flow graphs, and converts Mentat programs into standard C++ programs augmented with calls to library routines. These routines provide the interface to the Mentat virtual macro data flow machine. A prototype Mentat virtual machine was implemented on a 10-processor Encore Multimax Computer. This prototype allows different hardware architectures to be simulated.

The results from an evaluation of Mentat indicate the following: The combined data flow and object-oriented approach allows the programmer to specify the desired degree of parallelism. The use of persistent actors provides an effective means for interprogram communication. The use of dynamic graphs eliminates the need for small granularity control actors. Experimental results show that the overhead of graph construction is approximately an order of magnitude less than the overhead of control actor execution. Performance data collected from executing several benchmarks demonstrated that the total communication and graph construction overhead is kept sufficiently low in Mentat for it effectively to support large-grain parallel execution of distributed programs.
(Kathryn A. Smith, 41699)

Robust Eigenstructure Assignment Techniques for Multivariable Control Systems

One of the major performance issues in control synthesis centers around robustness (sensitivity) of design to parameter variations. For multi-input/multi-output systems, many alternative definitions of robustness can be postulated, depending upon the formulation of the synthesis problem. The objective of this research was to develop quanti-

tative robustness metrics based on the system eigenstructure geometry in order that eigenstructure assignment synthesis techniques could be employed to derive minimum sensitivity solutions.

For a linear time-invariant state variable system, a new fundamental relationship between eigenvalue/eigenvector (eigenstructure) robustness and eigenspace geometry has been derived. The volume V of the parallelepiped, formed with the normalized eigenvectors as sides, is shown to directly relate to eigenstructure robustness (as shown in the figure). Furthermore, the determinant of the matrix of eigenvectors represents this volume and constitutes an analytical robustness metric. The system has perfect robustness when the volume attains its upper bound of unity. In this case, the parallelepiped becomes a cube with the eigenvectors forming an orthonormal system.

Using this new robustness metric, an optimization algorithm, based on eigenstructure assignment theory, has been developed to compute both robust eigenvalues and eigenvectors of the feedback system. Use of the determinant as a robustness measure in the optimization scheme substantially reduces the computational overhead when compared to the use of a traditional eigensystem robustness measure of minimizing the condition number of the matrix of eigenvectors. The iterative and interactive nature of the design procedure, coupled with the direct control of the feedback system eigenstructure, provides a powerful synthesis tool to the designer for deriving realizable, minimally sensitive feedback solutions using physical insight of the system.
(S. Srinathkumar, 44004)

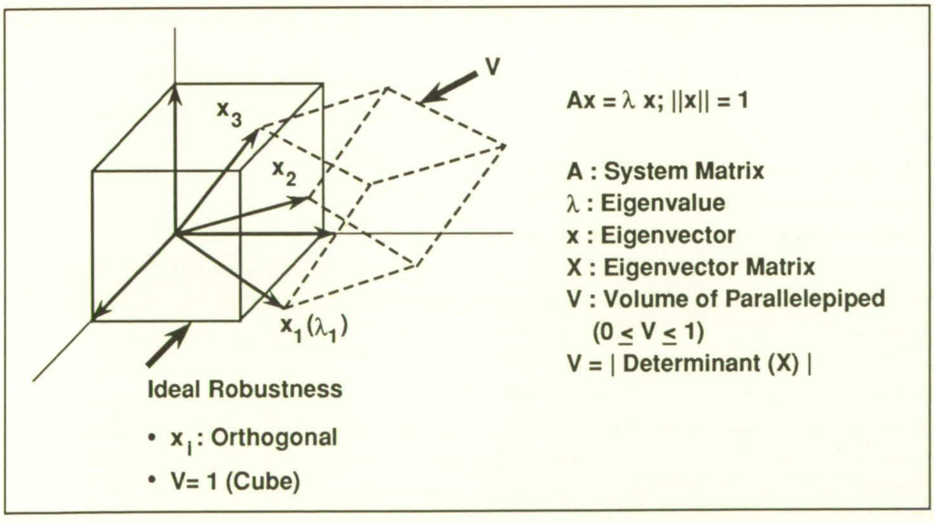

Robustness relationship to eigenspace geometry.

Increased Control of Depth-Viewing Volume by New Stereo 3-D Algorithms

Advanced flight display concepts that embody true 3-D images of synthetic objects or scenes (i.e., computer-generated examples) are being conceived and evaluated at Langley Research Center. Current technology can provide high-fidelity pictorial displays under flicker-free conditions which incorporate stereopsis or depth in the display elements. The goal of this research has been to provide the display designer with higher performance software tools than are presently available in the research community in order to exploit stereo display hardware. The specific objectives were to provide more complete control of the stereopsis effect within the depth-viewing volume and to expand the stereo field of view to allow full exploitation of stereopsis cueing in advanced flight display concepts.

Stereo displays are created by generating both left- and right-eye views of the display. The presently available computational techniques rely on asymptotic transformations (to map the visual scene to the viewpoint of the eye) and symmetric clipping algorithms (to limit the view to the display screen boundaries). The approach used in this research was to develop and employ two new and innovative computational techniques, a piecewise linear transformation and an asymmetric clipping algorithm, to increase the control and field of view of the stereo-viewing space. The conventional asymptotic transformations, which are used to map the visual scene into the stereo-viewing volume, allow the display designer to

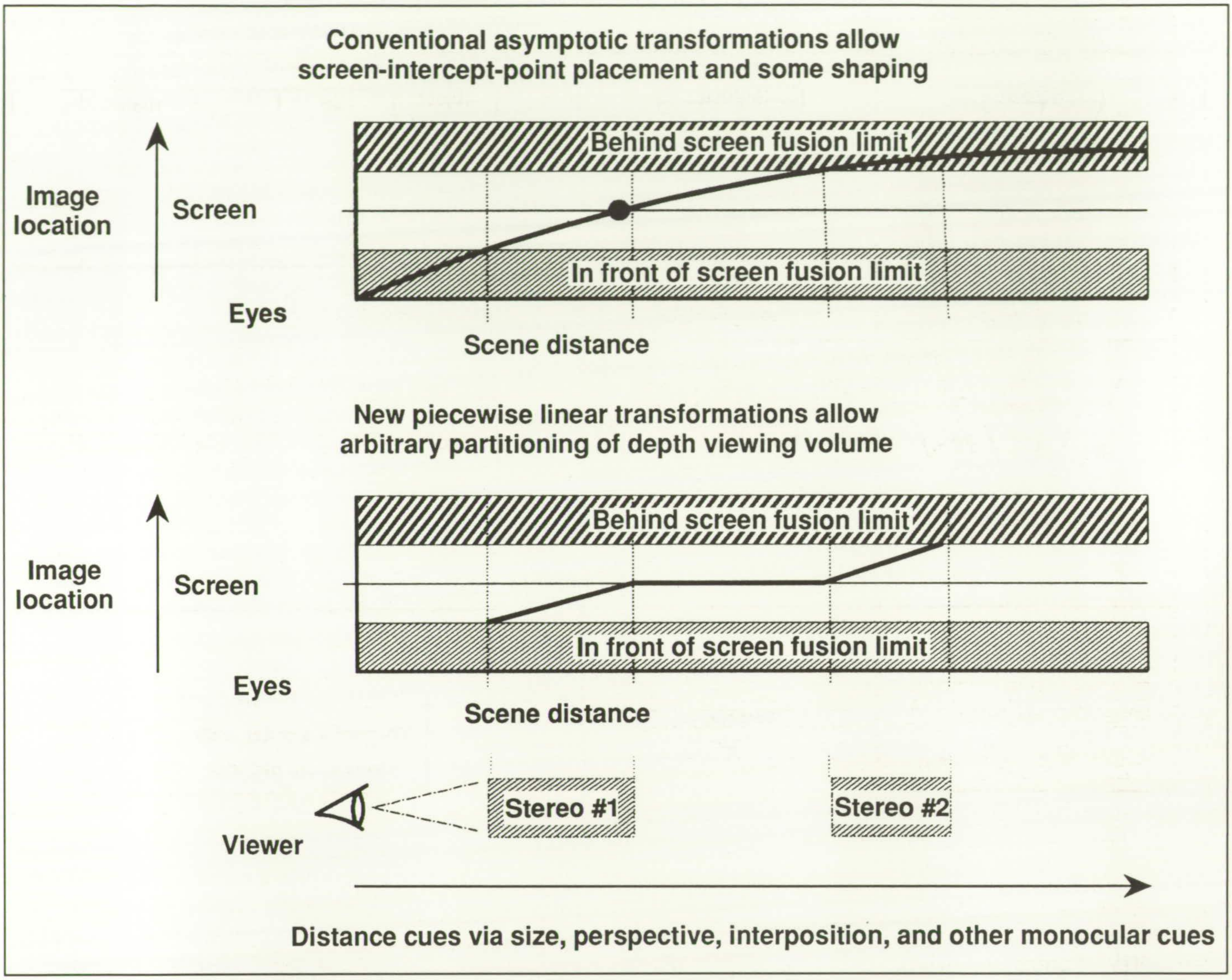

Visual scene mapping to stereo 3-D viewing volumes.

fix a specific scene distance at the screen location in the viewing volume (as shown in the first figure). The new piecewise linear approach (also shown in the first figure) allows the designer creatively to partition the depth-viewing volume with the freedom to place depth cueing at the various scene distances at which emphasis is desired. The second figure presents an illustration of the conventional symmetric and the new asymmetric clipping, as well as the effects of using each algorithm. Symmetric clipping dictates a smaller field of view (FOV) for each eye (shown in the second figure as a top view for the left eye). Combining the FOV's for both eyes results in different stereo overlap regions and single-eye viewing regions at different scene distances for the two clipping approaches. The perceived FOV's for the stereopsis regions (and also the total horizontal FOV's) provided by the asymmetric clipping algorithm

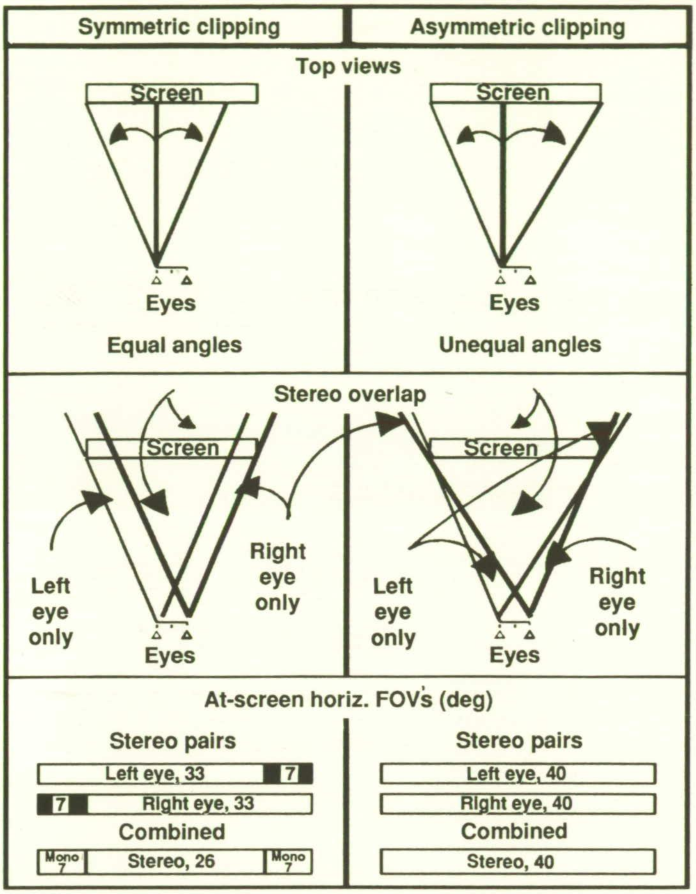

Symmetric clipping*

Scene object distance	Perceived horizontal field of view (deg)			
	Left monocular	Stereo	Right monocular	Total
Nearest	30.8	0	30.8	61.6
Screen	7.0	26.0	7.0	40.0
Infinity	0	33.2	0	33.2

Nearest = location of nearest visible object on centerline

Asymmetric clipping*

Scene object distance	Perceived horizontal field of view (deg)			
	Left monocular	Stereo	Right monocular	Total
Nearest	36.0	0	36.0	72.0
Screen	0	40.0	0	40.0
Infinity	6.65	33.2	6.65	46.5

* Screen distance = 19 in.
Horizontal monitor width = 12.4 in.
Interocular distance = 2.5 in.

Stereo 3-D clipping algorithms.

are greater throughout the scene-viewing envelope than those of the symmetric clipping algorithm. **(Steven P. Williams, 46650 and Russell V. Parrish)**

Stereopsis Cueing in Display Enhancements for Simulated Rotorcraft Precision Hover Tasks

Advanced flight display concepts that embody true three-dimensional (3-D) images were conceived and evaluated in order to assess the supposition that stereopsis cues could be used in 3-D pictorial displays to enhance the situational awareness of pilots conducting precision tasks in a simulator environment.

The efficacy of stereopsis cueing in 3-D pictorial display enhancements was assessed in a real-time piloted simulation experiment of a rotorcraft precision "hover-in-turbulence" task. The experiment utilized the Visual/Motion Simulator (VMS) in a fixed-base mode. Seven pilots endeavored to fly to and maintain a hover by visually aligning inner and outer wickets (shown in the first figure), thus attaining the desired hover position. The display conditions examined included the presence or absence of a velocity display element (see the first figure), as well as the stereopsis cueing conditions of nonstereo (no stereopsis depth cues), stereo 3-D, and hyperstereo. The latter condition represented the case of the

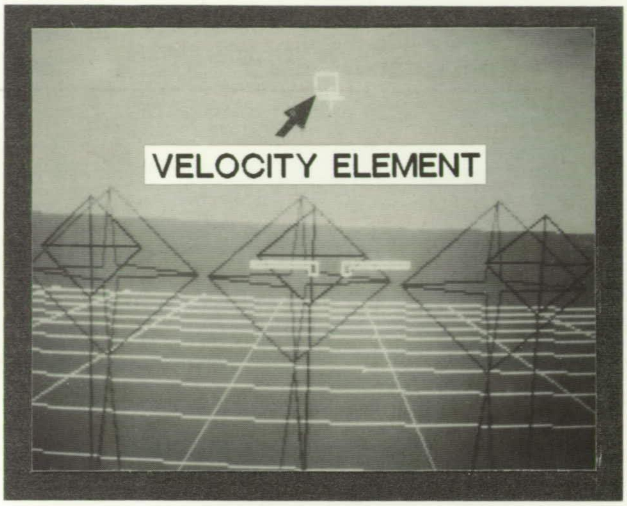

Pictorial flight display format

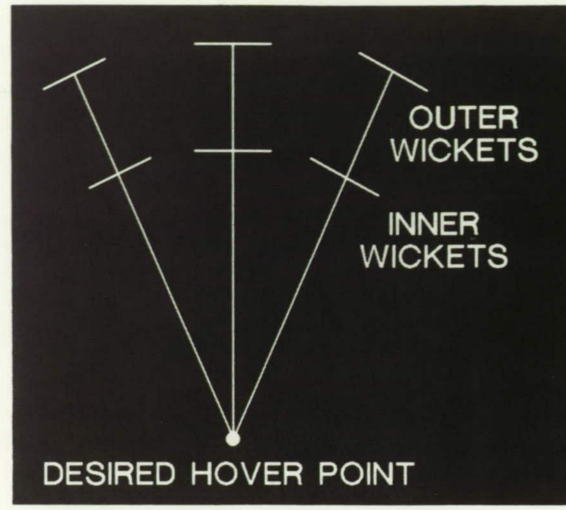

Top view-of-task geometry

Rotorcraft precision hover task.

pilot's eyes (image sources) being located 6 ft apart (as might be encountered with forward-looking infrared [FLIR] cameras mounted on each side of a cockpit for a binocular display), rather than the usual 2 in. This hyperstereo condition provided exaggerated depth cues in the display. The performance metrics for the study included not only root mean square values of the displacement from the desired hover point, but also pilot control inputs and subjective pilot comments.

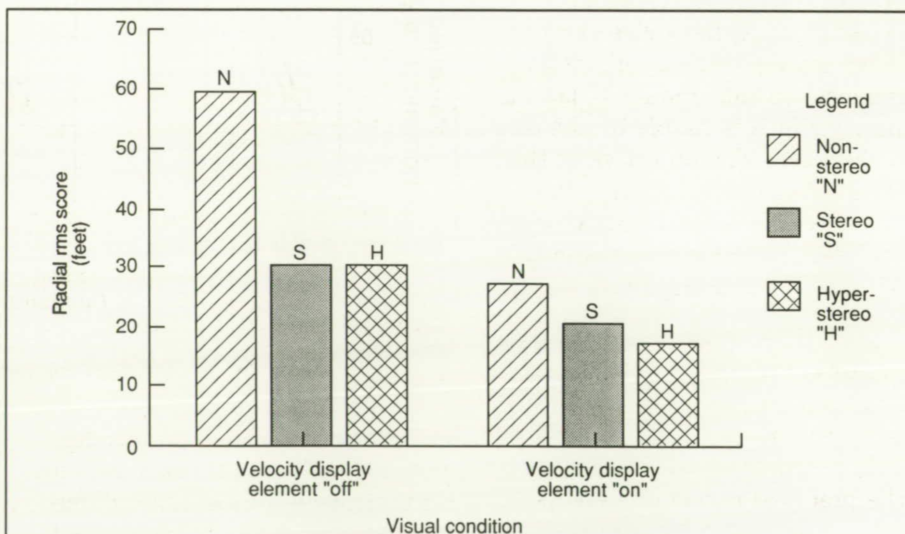

Effectiveness of stereopsis and velocity display element in rotorcraft precision hover (task performance of seven army pilots).

Both the objective and subjective results indicated that the depth cues provided by the stereo displays enhanced the situational awareness of the pilot. The enhancement was particularly effective when the velocity information element was absent from the display (as shown in the second figure), implying that velocity information, as well as positional information, can be extracted more readily from the stereo presentation. Pilot control input data revealed that 12 percent to 21 percent less control action was required to attain the improved hover performance using the stereo displays.

(Steven P. Williams, 46650 and Russell V. Parrish)

Practical Depth-Viewing Volumes for Stereo 3-D Graphic Displays

In ordinary displays of real-world scenes, depth information is provided by such cues as perspective, relative size, shape, interposition, and motion. Stereoscopic displays of such scenes add lateral disparity and muscular cues associated with vergence. In these displays, the distance that affects accommodation (focus) is screen distance, which remains constant. Thus, the major depth cue missing in synthetic generation of stereo 3-D displays is the change in accommodation with fixation-point depth; this is, indeed, a major lack, for accommodation and convergence are highly associative. For a fixed accommodation distance, a limited range of vergence conditions exists which will result in comfortable, clear, fused, single vision. Thus, for a given screen distance for a stereoscopic display, limits exist to the amount of lateral disparity which is usable by the display designer. The objective of this effort has been to determine these limits of lateral disparity and make appropriate guidelines available to designers of stereo displays.

A knowledge of where and how accurately subjects perceive depth cues placed within the depth-viewing volume is essential to the display designer. A determination of the practical region of stereopsis cueing for a stereoscopic display system was formed empirically. Data were gathered comparing perceived depth (via subject-controlled probe placement) against computed depth (disparity calculations), as presented via a stereo computer graphics display, throughout the viewing volume of several subject-to-CRT (cathode-ray tube) screen distances (see the first figure). Eight hundred trials with four repetitions at each of three different distances between the subject and the screen were performed, with results from four subjects. For objects placed in front of the screen, occurrence of double vision limited the usable volume. For objects placed behind the screen, perceived depth became increasingly larger than that presented. The second figure presents perceived depth error versus computed depth, with both normalized to screen distance. If one accepts criteria of comfortable single vision in front of the screen, with less than a 10-percent perceived depth error behind the screen, the usable viewing-volume falls between −0.25 and +0.6 of the screen distance.

(Russell V. Parrish, 46649, Steven P. Williams, and Lawrence E. Gupton)

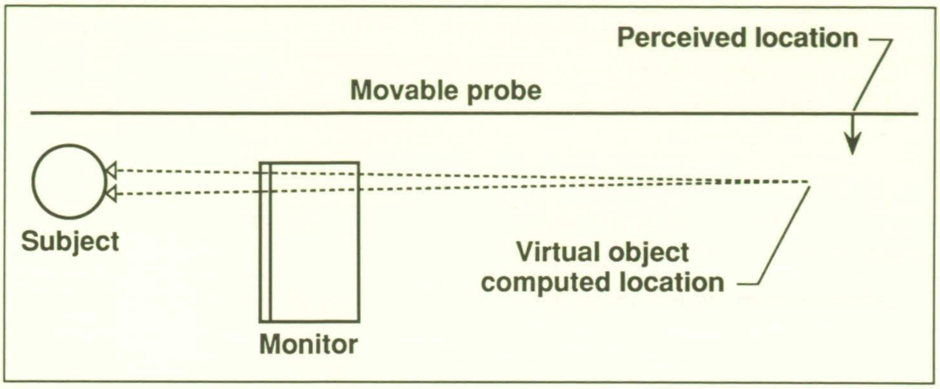

Experimental apparatus (top view).

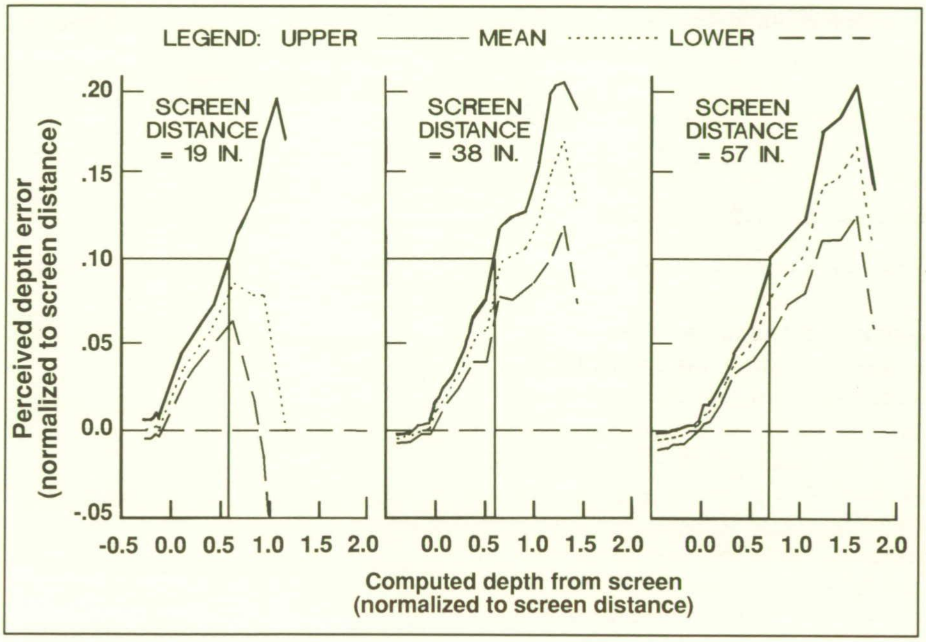

95-percent confidence intervals for perceived depth error.

Experimental Investigation of Validation Requirements for Multiversion Software

Reliability is a pressing concern in the development of software for modern systems. Executing multiple versions of independently developed software has been proposed as a technique for tolerating residual software faults. This technique has been used in software to control aircraft and railroads and has been proposed for nuclear power plants. A growing tendency, however, exists to reduce software validation of the multiple versions and rely on multiversion testing in order to reduce the software development costs. An experiment, conducted at the University of California, Irvine, provides empirical data that address the appropriateness of reducing standard testing procedures for multiversion software (on the assumption that voting of redundant software achieves a high degree of fault-tolerance in operational software) and using voting of redundant software as a test oracle in the software validation process.

A problem specification, adapted from the aerospace industry, formed the basis for multiple implementations by senior-level computer science students working in two-person teams. Eight versions of moderately sized programs (1186 to 2489 lines of code) were independently designed, coded, and debugged to a state that is typical of software immediately prior to unit testing. The software was subjected to five different testing methods: code reading by stepwise abstraction, static data reference analysis, embedded assertions, functional testing, and triple-version voting. Software error data were accumulated for each technique, and the software faults were identified.

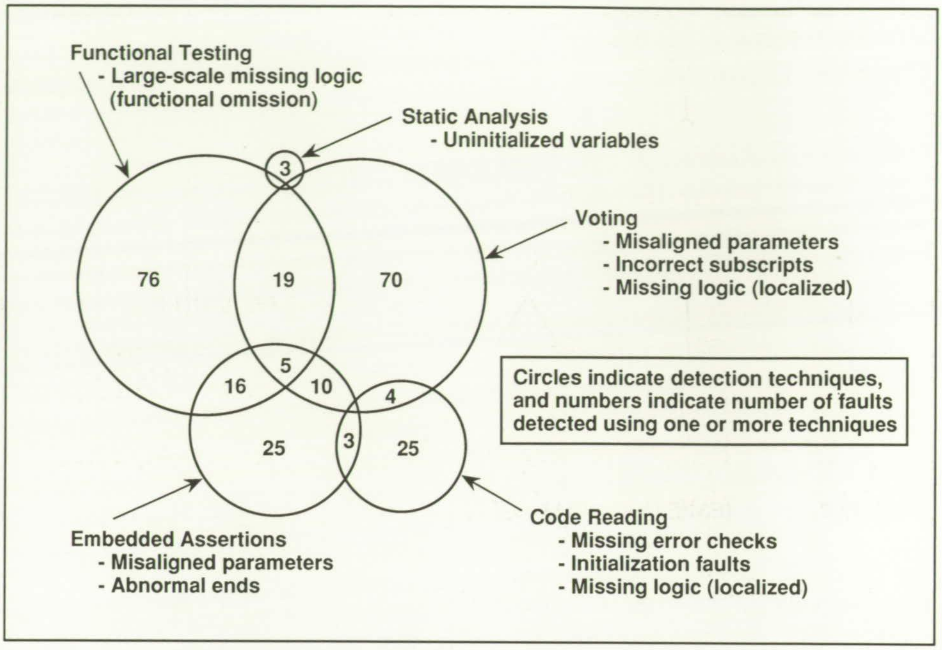

Fault sets and detection techniques.

The experimental activity of applying five different fault detection techniques to eight versions of independently developed software produced the first software error data directly comparing standard testing techniques with multiversion voting. Analysis of the data resulted in significant findings concerning current proposals for validating multiversion software; that is, the data do not support proposals that normal software validation can be reduced for multiversion software or that multiversion voting is a substitute for functional testing. A surprising result was the disjoint nature of the fault sets detected by each of the test techniques indicating that the software testing techniques are complementary and all should be considered for use in critical applications.
(Dave E. Eckhardt, 41698)

Fault-Tree Compiler: High-Level Language-Oriented Fault-Tree Program

Fault trees have been used to compute the reliability of complex systems for approximately 30 years. Although many computation techniques have been developed, a single superior algorithm has not been discovered. Some algorithms are superior for some problems but inferior for others. Also many of these algorithms are not available in the form of a computer program with a language-oriented user interface.

At Langley Research Center, a new algorithm for solving fault trees and an expressive and readable language for them have been developed. A computer program has been developed based on the new algorithm and input language. A rigorous error bound has been

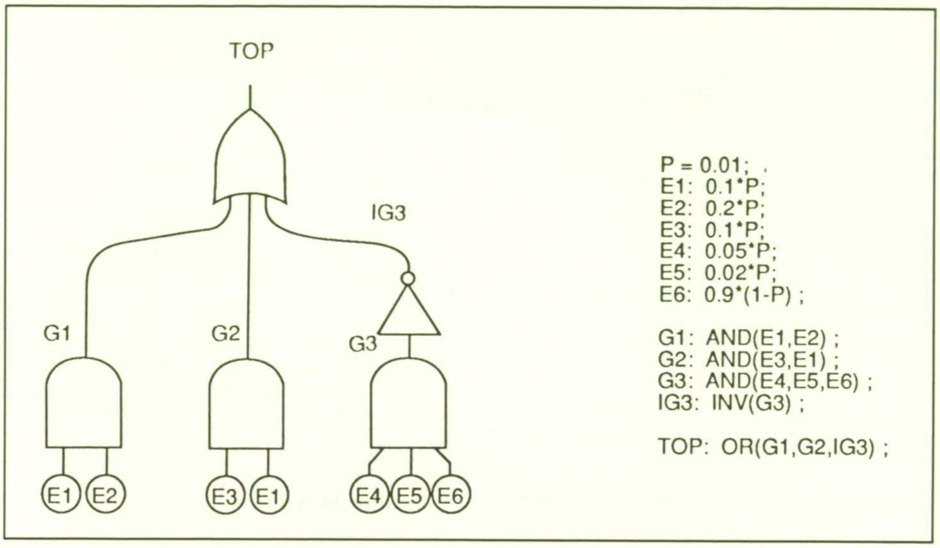

Fault tree and corresponding FTC input.

derived for the solution technique which enables the program to supply an answer to within a user-specified level of accuracy. The program's solution technique is tailored for the analysis of fault trees used to model fault-tolerant architectures, in particular, fault trees in which the dominant failure modes contain a small number of basic events (e.g., one, two, or three events). A hierarchical modeling capability is provided which can simplify the preparation of the fault-tree input file and significantly reduce the program execution time. The program is named the Fault-Tree Compiler (FTC) and is available on VAX VMS machines and machines that run Berkeley UNIX.
(Ricky W. Butler, 46198)

Parallel Processor Reliability Study

A study was conducted to examine the impact of a 5-year space mission environment on fault-tolerant parallel processor architectures. The target application required 256 parallel computations with a probability of system failure less than 10^{-7} while performing at full operational capability for one-half hour. Additionally, the system was required to have full operational capability after 5 years of inactivity with 0.99 probability and with no provision for repair of failed processors.

With the average lifetime of a processor built today estimated at 20,000 hours, most of the processors in the system would be expected to fail during a mission of 5 years, or 43,500 hours. Thousands of spare processors and tens of thousands of interconnecting communication links would be required for any of the fault-tolerant parallel processor architectures currently under development. Two solutions were explored: use of more reliable processors, and use of reconfiguration at a lower level than the processor level common in fault-tolerant architectures today.

The use of processors five times as reliable as those available today was shown to decrease the number needed by 71 percent, and the use of processors 10 times as reliable resulted in an 83-percent decrease. The effectiveness of reconfiguration of faulty components at lower than the processor level is shown in the figure. Varying the reconfigurability of each processor from one to five subcomponents reduces the number of processors needed by 54 percent.

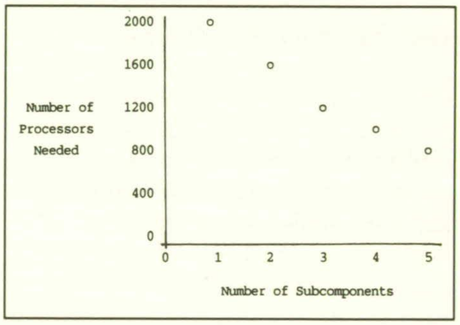

Reconfiguration of processor subcomponents.

The use of both these solutions in combination could result in up to a 92-percent reduction in components.
(Sally C. Johnson, 46204)

Simple, 3-D Analytic Microburst Model for Piloted Simulations

A math model of a wind shear environment that emulates real-world conditions is a requirement for simulation studies of airplane performance in the presence of wind shear. Numerical models based on radar data from actual events require large computer storage capacity and are not suitable for use on personal computers. The objective of this task was to develop a simple analytic model of a microburst, maintaining realistic physical characteristics and fluid mechanics requirements, for the purpose of fast-time simulation studies on a personal computer and real-time piloted simulations.

A set of four functions, which comprises a solution to the mass conservation (continuity) equation of fluid mechanics, was used as a starting point. These functions were chosen to approximate the shape of the vertical and horizontal wind velocity profiles from the NASA Terminal Area Simulation Study (TASS) microburst model. Four key parameters were identified as inputs to the algorithm for the purpose of changing the size and strength of the microburst in real-time simulations.

Results from fast-time simulation studies indicated that altitude dependence in this model, specifically the boundary-layer effects near the ground, had a significant effect that was not present in the very simple model used for previous guidance studies. The model has been implemented in the Visual/Motion Simulator for piloted studies of guidance laws in wind shear. Additionally, the analytic model has been used as the wind environment for studying distribution of the hazard index (F-factor), and the effectiveness of first- and second-order wind rate estimators. The figure shows dimensionless altitude distributions for the horizontal velocity components of a jet impinging on a wall, field data from the Northern Illinois Meteorological Research on Downbursts (NIMROD), and the analytic model. The analytic microburst model exhibits the effects of altitude and radial distance found in real-world data. The model is easily implemented and can be placed at any location relative to the airplane flight path.

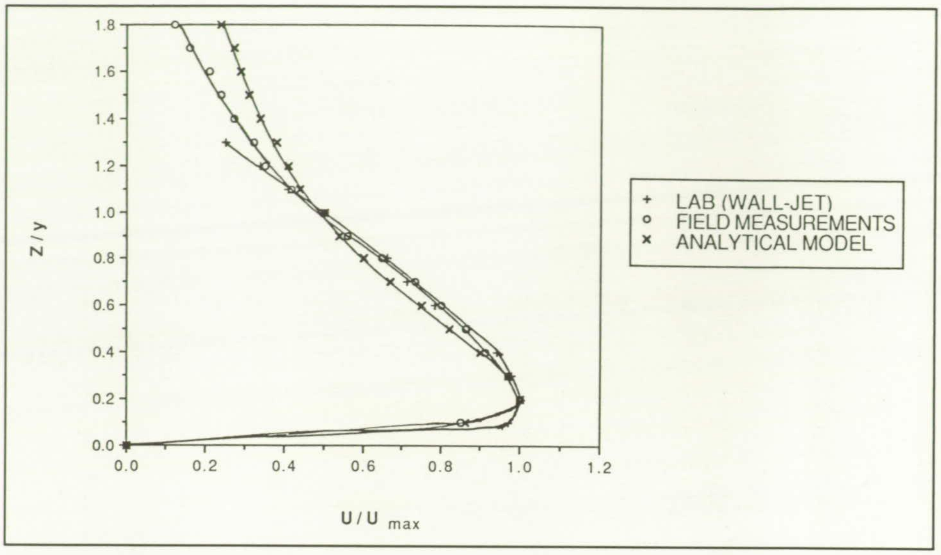

Comparison of wind model velocity distributions.

(Rosa M. Oseguera, 42029)

Helmet-Mounted Display Synthetic Visibility System

The helmet-mounted display (HMD) project defined, developed, and evaluated a synthetic visibility system for performing safe, accurate, and consistent manual approaches and landings under visual meteorological conditions using video cameras and the HMD in lieu of a traditional cockpit windscreen.

The project was a joint Langley/McDonnell Douglas Corporation (MDC) effort in which MDC provided a proprietary state-of-the-art HMD system, augmented by Langley-developed supplementary symbology. Langley installed the system in the Advanced Transport Operating Systems (ATOPS) Boeing 737 aircraft and conducted flight evaluations. The system included forward-looking television cameras covering a field of regard 80° wide and 30° high mounted behind a window in the radome. A 40° by 30° portion of the field of regard was displayed on a helmet-mounted eyepiece, depending on the direction in which the pilot looked. Superimposed on the scene was supplementary symbology, including airspeed, altitude, heading, flight path angle, longitudinal acceleration, airspeed error, flare cue, flight

Dispersion statistics

	Visual	HMD
X, mean	97 ft	97 ft
σ	202 ft	212 ft
Y, mean	2 ft	3 ft
σ	6 ft	10 ft
Sample	58	67

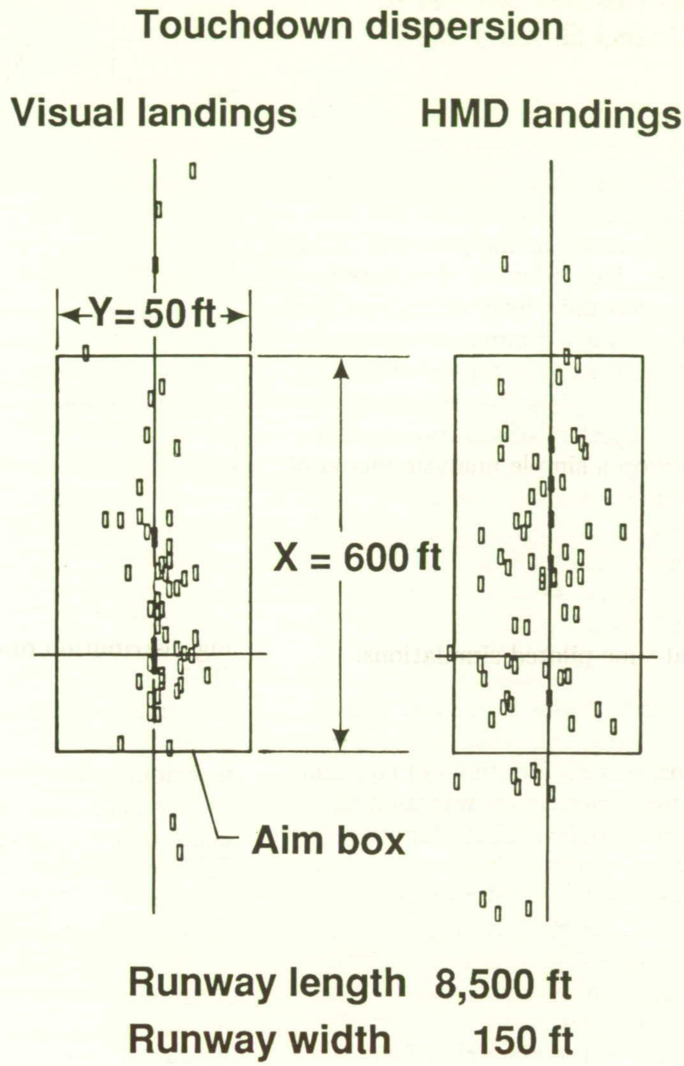

Helmet-mounted display.

path reference line, waterline, and a pitch ladder, felt to be necessary to conduct a visual approach and landing.

Flight evaluation of the system in over 200 landings was completed by two NASA and two MDC pilots. Results indicated the feasibility of HMD's for landing high-performance aircraft. Touchdown dispersions using the HMD were comparable to the dispersions for visual landings. Thus, a synthetic visibility system may provide a suitable alternative in hypersonic vehicles to a traditional cockpit windscreen during approach and landing. **(James R. Hall, 43851)**

Data Link ATC Message Exchange Concept

The data link message exchange for Air Traffic Control (ATC) offers the prospect of increasing system safety and efficiency by reducing communication errors, enabling more data to be exchanged between aircraft and ground facilities, and relieving congested ATC voice radio frequencies.

A study (NASA CR-2859) previously completed at Langley Research Center concluded that data link ATC information transfer appears to be highly beneficial to flight deck operations although the effects on pilot instrument monitoring and out-of-the-window vigilance need additional study. Also, pilot test subjects expressed concern about the reduced party line effect in the data link environment. In the voice radio environment, the party line, sharing a common frequency, normally allows the pilot to receive lead situation information by overhearing ATC communications with other aircraft.

A follow-up study using a touch-sensitive CRT (cathode-ray tube) as the data link interface, illustrated in the figure, is currently nearing completion. This study is intended to acquire some objective measures of party line benefits in the conventional voice ATC communication system and provide missing lead information by supplementing data link communications required for ATC instructions with situation information. The follow-up study also explores the use of a synthetic voice to speak messages arriving in the flight deck to lessen the impact of alphanumeric information display on flight crew vigilance. The airline pilots who were test subjects were favorably impressed by the crew-initiated automatic entry of radio frequencies, route changes, and autopilot commands into the aircraft systems, a capability enabled by the data link operation. Preliminary results indicate significant flight deck crew benefits from these added features in the data link environment.
(Marvin C. Waller, 42025)

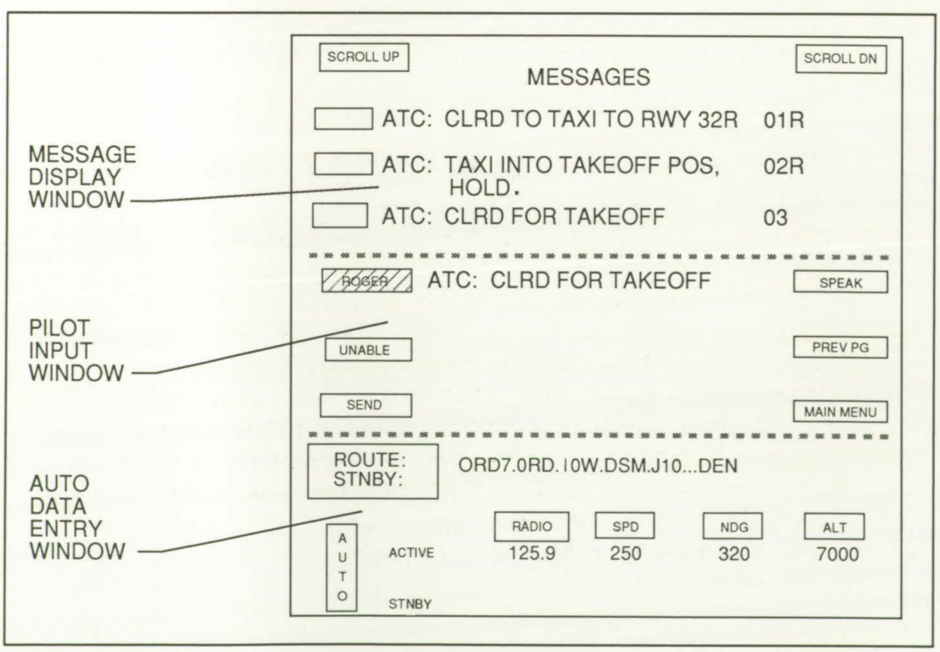

Three-window, touch-sensitive data link interface.

Validation of Knowledge-Based System Implementation of Optional Flight Information Display Manager

The objective of this study was to validate the implementation of a system that uses artificial intelligence (AI) programming techniques to control the presentation of optional flight information on the primary flight display (PFD) of a glass cockpit. A knowledge-based system approach was used in this study to simplify the complex reasoning necessary for the Task-Tailored Flight Information Manager (TTFIM) and to provide an architecture more adaptable to frequent modifications.

Pilot verification of the information presentations on the PFD during flight tests aboard the Advanced Transport Operating Systems (ATOPS) Transport Systems Research Vehicle aircraft validated the correct implementation of the TTFIM decision logic. The flight test also validated the successful integration of an AI system with more traditional systems already aboard the TSRV. During the flight test, the knowledge-based system operated in interpreted-LISP mode on an 86386 CPU provided by the Gold Hill Computers Humming-Board card. The TTFIM software communicated with the other flight computers through a communications card that was provided in the host PC-AT. The communications card provided the knowledge-based system with the aircraft flight parameters from various flight computers and data recording stations and gave the knowledge-based system a means of communicating its decisions (as shown in the figure).

c-2

ORIGINAL PAGE
BLACK AND WHITE PHOTOGRAPH

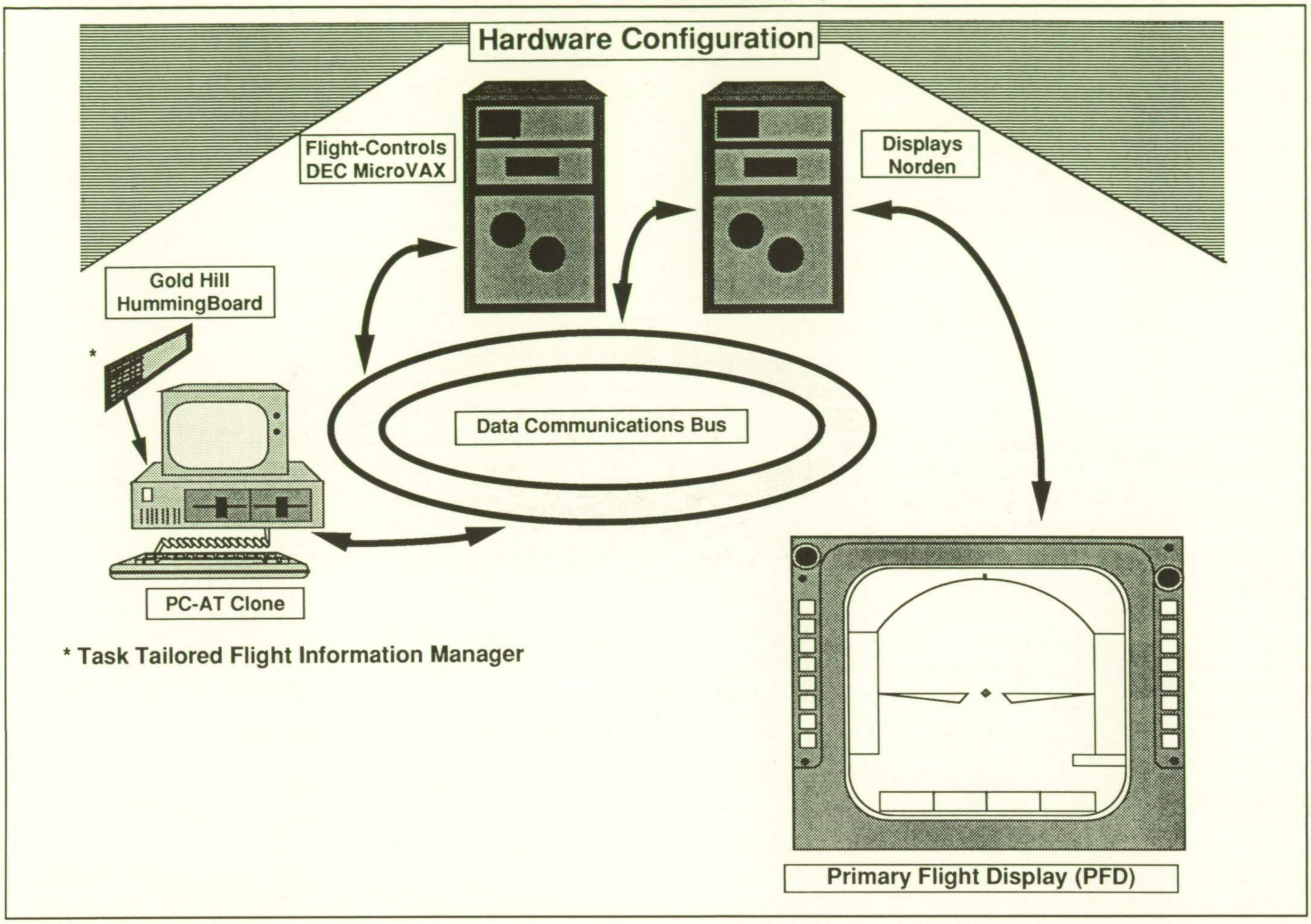

Hardware configuration.

The TTFIM knowledge-based system had an average of 60 to 70 rules during its development period. Most of the knowledge-based system consisted of data-driven rules with more advanced reasoning to activate overhead operations. The knowledge-based system was developed with Gold Hill Computers GoldWorks expert system shell. The many utility functions of the expert system shell and the versatile inference engines greatly eased the construction of the knowledge-based system. Frequent changes during the development of the TTFIM decision logic validated the ability of the knowledge-based system to be easily modified.

The results of this study validated the implementation and integration of a knowledge-based system that controls the presentation of optional flight information on the primary flight display of a glass cockpit. The knowledge-based system produced in this effort has provided a flexible platform that will ease the future testing of various display philosophies (e.g., task-tailoring).
(Wendell R. Ricks, 46733)

Flying Complex Paths With Microwave Landing System

As part of the joint Federal Aviation Administration/NASA Microwave Landing System (MLS) Advanced Applications Program, one research objective has been to determine guidance requirements for flying jet-transport-type airplanes equipped with electronic flight displays and advanced flight control systems for manually controlled flight along complex, curved paths.

A study was conducted with particular issues addressed that included flight director (FD) requirements, electronic map versus standard horizontal situation indicator (HSI) displays, and effects of various path geometries, including length of the final approach segment and consecutive turns.

A real-time piloted simulation was used for test runs made along six complex, curved paths with final approach segments between 1.25 nmi and 0.25 nmi and a standard instrument landing system (ILS) approach. Eight subject pilots (six airline pilots and two NASA pilots) each flew approximately 78 data runs with various wind and moderate turbulence conditions.

Analysis (see the attached figure) along the complex paths indicates that lateral path-tracking performance is slightly improved with the map display versus the HSI display (both using the FD), although tracking accuracy at the decision height (200 ft above the ground) where visual contact was established is about the same. Vertical tracking accuracy was unaffected by the HSI and map display options. Tracking data indicate that the FD is required for precision complex approach paths with low decision heights. While the tasks were more demanding to fly, even the shortest final approach paths were judged, by the subjects, to be acceptable with FD guidance. In addition, although pilot work load is slightly higher for the curved paths as compared to the ILS path, the data and pilot comments indicate that these operations are acceptable for normal airline operations. The results of these tests show that airplanes equipped with the proper guidance may be flown on highly complex, curved paths within the MLS signal coverage. The use of MLS will result in more airplanes attaining the benefits of curved paths, including increased airport capacity, safety, and noise abatement capabilities. **(Charles E. Knox, 42038)**

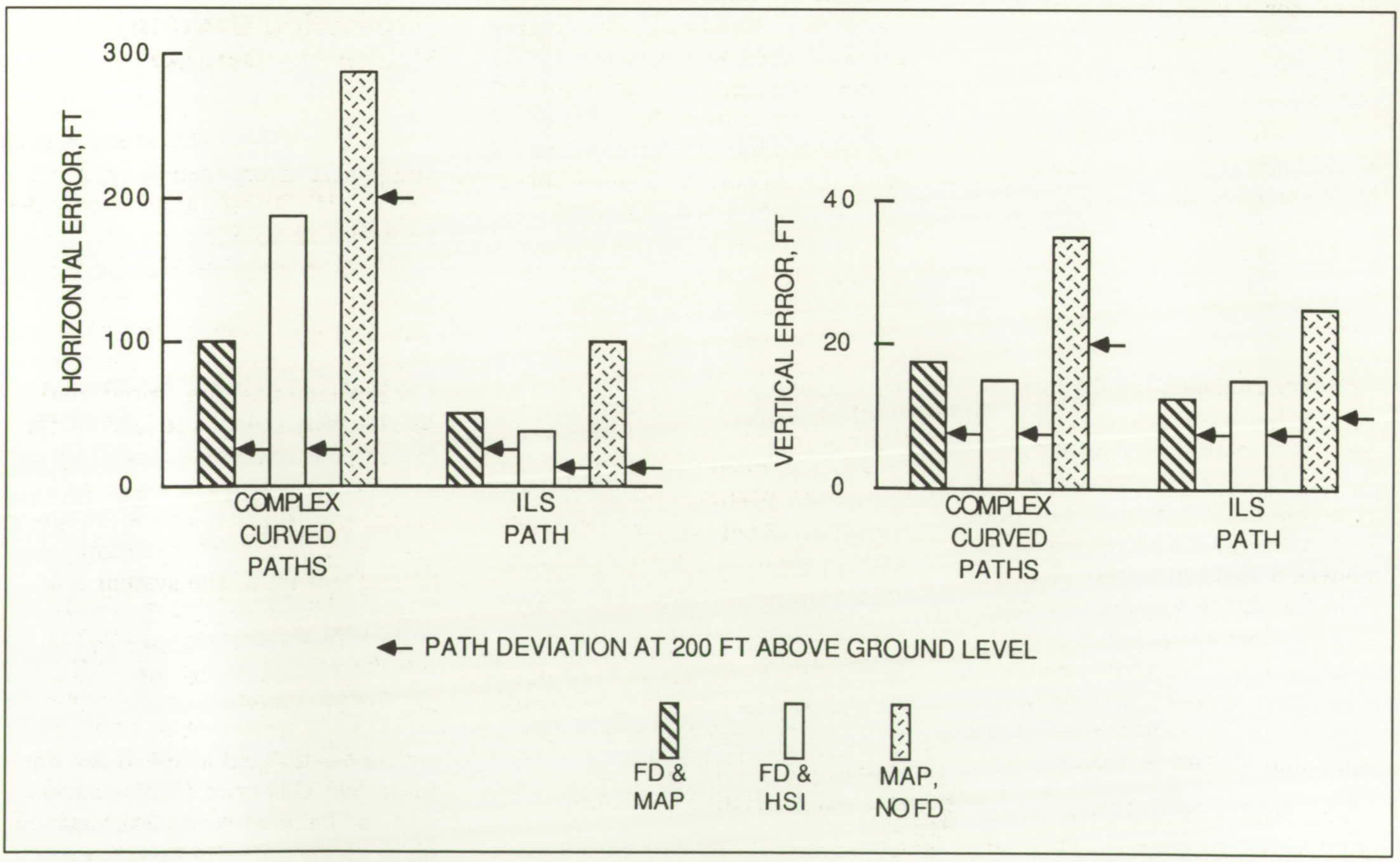

Guidance comparison path tracking errors (root mean square).

Forward-Look Wind Shear Detection for Aircraft Landing Approach

Microburst wind shear poses a significant threat to aircraft during takeoff and landing. Among the issues concerning the aviation industry are how to recover from an inadvertent microburst encounter, what safety benefits can be achieved from forward-look sensing, and how far ahead of an airplane must a sensor see to ensure successful escape from a microburst? The objective of this research was to provide answers to these questions in a piloted-simulation environment.

Three strategies were chosen and implemented as flight director guidance in the Visual/Motion Simulator, programmed with a Boeing 737 math model. The three recovery strategies that were chosen for implementation were rotate to an initial pitch of 15° then control sink rate; track the glide slope to a preset altitude at full thrust to preserve airspeed, then fly level until exiting the shear; and manage the flight path angle to avoid obstacles and unnecessary climb. The first strategy, used as a baseline, is accepted by the industry and is currently being taught to crews. Both reactive and forward-look detection and warning capabilities were programmed. Two wind shear models, a numeric model of the Dallas/Fort Worth microburst and an advanced analytical model, were implemented. A total of 455 microburst encounters were made by seven pilots, including research pilots and air carrier pilots.

The results showed that, when given only a reactive warning, the difference in recovery performance between the three strategies was not statistically significant. When given a forward-look warning, the advanced strategies showed improved characteristics over the baseline, but had similar minimum altitudes. With the forward-look detection scanning only 10 sec ahead of the airplane, however, the improvement in recovery performance was very significant compared to a reactive alert. The results (see the figure) show that the factor that has the greatest improvement on microburst recovery is the time at which the recovery is initiated. All pilots provided very positive comments about the recovery capabilities achieved with forward-look sensing.

This effort is the first to provide a basis for quantifying the benefits of forward-look sensing and has implications for the possible modification of recent Federal Aviation Administration regulatory activity.
(David A. Hinton, 42040)

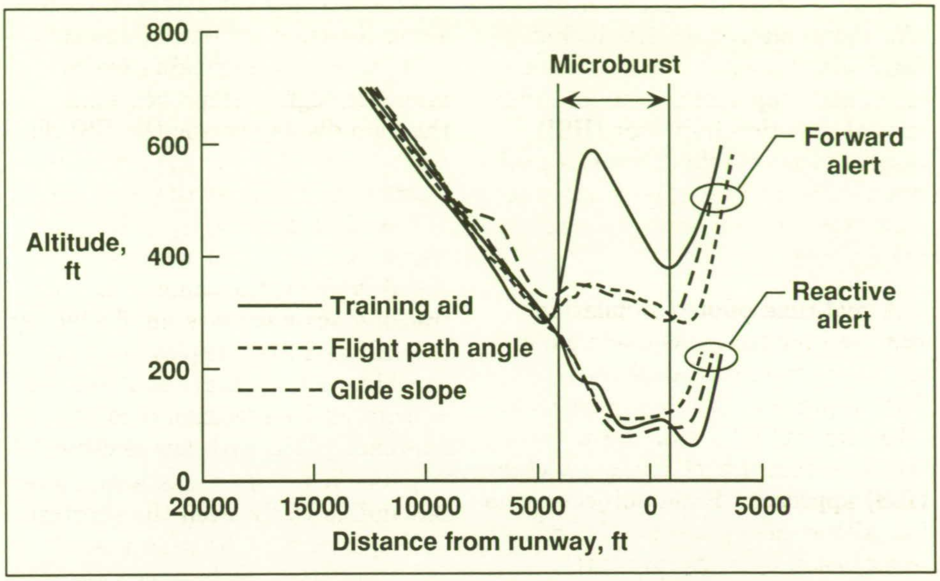

Effect of forward-look capability on wind shear recovery (piloted simulation, landing approach).

Takeoff Performance Monitoring System Heads-Up Display

The objective of this study was to design and incorporate a heads-up display (HUD) into a previously developed Takeoff Performance Monitoring System (TOPMS) that contained a heads-down display only. The TOPMS provides the following advisory information: engine status; airplane position, speed, and acceleration error; locations on the runway where decision speed V_1 and rotation speed V_R are expected to occur; and location where the airplane can be braked to a stop. A special feature of the system is a "situation advisory flag" (SAF) that recommends whether the pilot's best option is to continue or to abort the takeoff.

The design goal of the HUD was to project this type of information into the fields of view of the takeoff pilots as they looked down the runway. The figure shows the left

TOPMS displays during normal takeoff. L-89-6440

side of a Boeing 737 simulator with the heads-down TOPMS display on the navigation screen (lower of the two CRT's (cathode-ray tubes)) and the simpler HUD superimposed on the out-the-window runway scene. The situation pictured shows that an airplane has reached 100 knots and is progressing satisfactorily down the runway. If an abort situation were to develop, the vertical wedge-shaped indicator (acceleration error) centered at the end of the HUD runway graphic would move to the left until the error became unacceptable; when this occurred, the indicator would be replaced by a prominent SAF advising an abort. An abort flag would also appear in the heads-down display.

Comments by evaluation pilots on the usefulness of the HUD have been very favorable. They have found the HUD to be a significant enhancement to the TOPMS and, in turn, to takeoff flight safety. The HUD format and symbology were judged to be highly satisfactory and noninterfering in that they did not mask any significant information from the runway visual scene.
(David B. Middleton, 44034)

Tactical Decision Generator (TDG) for Superagile Aircraft

The increased complexity of the air combat environment, combined with the expanded capabilities of high-performance aircraft, has changed the future of air combat engagements. To support the study of superagile aircraft, the Tactical Decision Generator (TDG) is being developed using artificial intelligence (AI) programming techniques. The objective of this research is to identify tactical decision generation techniques and combat maneuvers that effectively exploit agility in the tactical environment.

The TDG, consisting of several knowledge-based systems (KBS) hosted on a symbolic computer, generates air combat maneuvering commands based on the tactical status of a one-versus-one engagement. As shown in the figure (a

situation assessment module), an integrated, active throttle management system and trial-maneuver scoring algorithms have been implemented in the TDG as highly specialized KBS. The situation assessment module was developed to determine the tactical mode of operation, either aggressive, defensive, neutral, or evasive. Information concerning the current mode of operation is used by the throttle management system and the maneuver evaluation and scoring algorithms to determine the best maneuver. Control commands to execute that maneuver (load factor, bank angle, and thrust) are then passed to the aircraft simulation. The use of the KBS situation assessment module and unique modes of operation allow the TDG to adequately replicate the complex decision-making process of the pilot. Thus, the TDG is capable of responding to rapidly varying combat situations.

The AI-based TDG has been evaluated in batch simulation and in real-time simulation against NASA test pilots. Comprehensive batch simulations against the Adaptive Maneuvering Logic, an earlier guidance logic, have shown the TDG to achieve highly favorable exchange ratios. In real-time simulation using the Langley Differential Maneuvering Simulator, the TDG equals the performance of its test pilot opponents. The TDG is currently being modified to accommodate two-versus-one engagements and poststall maneuver options. **(Kenneth H. Goodrich, 44009 and John W. McManus)**

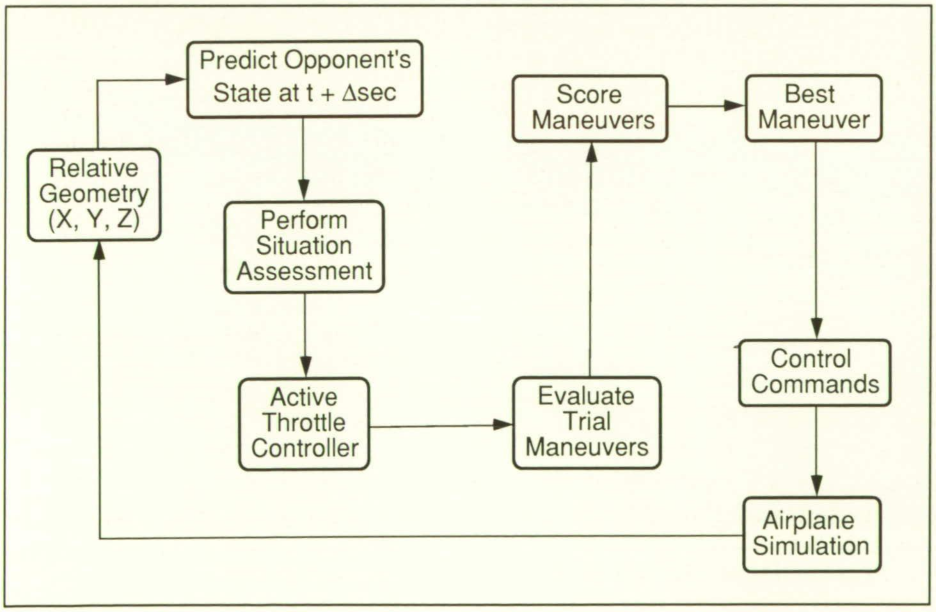

Operational flow diagram of TDG.

Approach to Nonlinear Output Feedback for High-Alpha Control

The objective of this research is the design of practical control laws for high-performance aircraft that can operate over a large nonlinear flight envelope such as the angle-of-attack α range from low α to poststall. This research is based upon a direct-digital, optimal, output feedback control design technique.

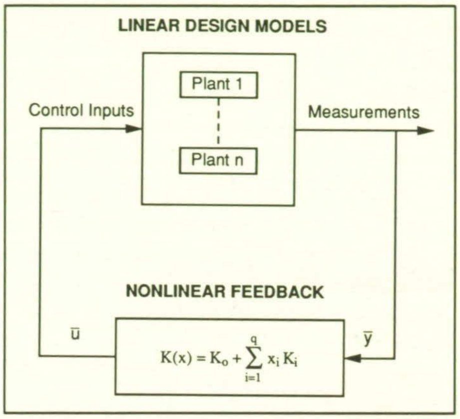

Closed-loop system with nonlinear feedback.

An ensemble of linear models (see the figure), representing the aircraft at different parts of the nonlinear flight envelope, is used in a control synthesis algorithm that generates variable output feedback gains by minimizing a performance index of weighted states and controls. These output feedback gains $K(x)$ are a linear function of gain-scheduled parameters x_i, which are themselves linear or nonlinear functions of some variables such as α and α^2. During the design process, the x_i are assumed constant for each trim condition, whereas during implementation the x_i are time varying. The implemented control law thus contains both linear and nonlinear terms due to the dependence of K on x and the fact that the control vector $\bar{u}$ is generated by multiplying the time-varying variables x_i and $\bar{y}$.

Results for a high-performance aircraft demonstrate that the control design methodology is

feasible for a highly nonlinear flight envelope when using one gain scheduling parameter, namely α. Four linear models, representing the aircraft from low α (5°) to poststall (60°), were used to obtain feedback gains that vary with α. Additionally, a procedure was developed for simultaneously designing a two-mode system that includes a pitch-rate command system at low α, an α-command system at stall and beyond, and a transition region between the two. The design was evaluated in a nonlinear six-degree-of-freedom batch simulation. Simulation results showed smooth transition between modes, the ability of the controller to regulate at commanded values with zero steady-state error, and the ability of the controller to hold a high α in the presence of lateral maneuvers.

(Aaron J. Ostroff, 44025)

Hot-Bench Simulation of Wind Tunnel Model to Support Active Flutter Controls

The purpose of this work was to develop a tool to validate the implementation of digital control laws in a computer actively controlling the elastic modes of a wind tunnel model. While real-time simulation using rigid-body aircraft dynamic models is a frequently employed, well-understood step in the validation of flight control laws, the implementation of the more complex, aeroelastic vehicle equations to support wind tunnel testing of active

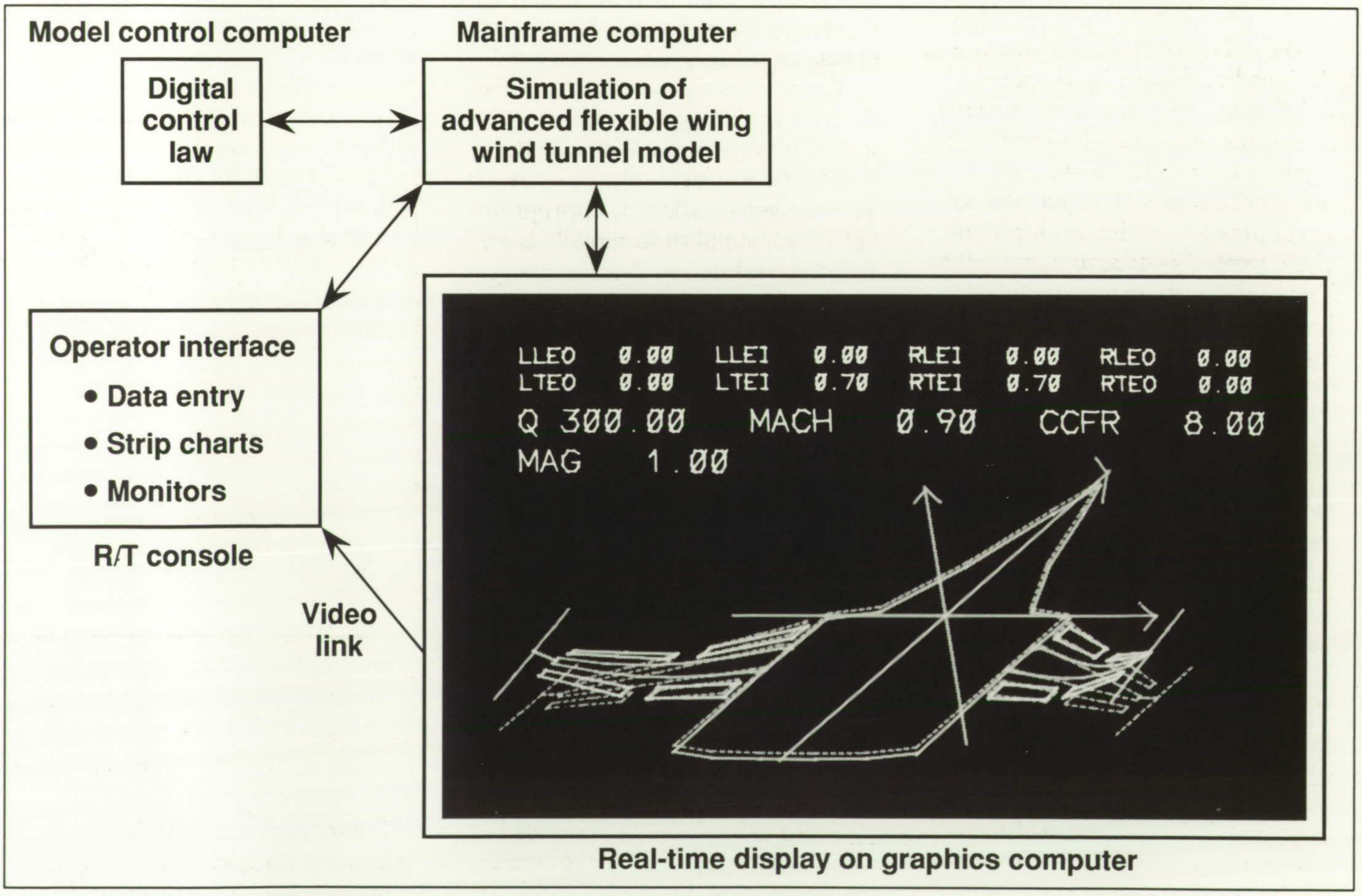

Overview of hot-bench simulation.

structural control laws is less common in the simulation community. This work was conducted in support of a joint NASA/Rockwell International Corporation Active Flexible Wing Wind Tunnel Test Program.

Future airplanes will require integrated digital control of flight path, attitude, and structural response. Fighter aircraft, in particular, with multimission, aggressive performance requirements will push the limits of active control technology. In order to apply and extend active control concepts, a joint program involving Rockwell International Corporation and Langley Research Center was initiated in 1987. The program calls for two wind tunnel tests (1989 and 1990) in the Transonic Dynamics Tunnel (TDT). The test article, which was designed and built by Rockwell, is a full-span, free-to-roll dynamically scaled model of an advanced tailless fighter. One of the most aggressive applications of active control is suppression of flutter, a potentially explosive dynamic instability that can occur when a sufficiently flexible wing begins to extract energy from the airstream. The wind tunnel model has been designed to flutter within the TDT operating envelope. Flutter suppression and load alleviation during a rapid roll maneuver will be independently investigated during an early 1990 tunnel entry.

End-to-end verification of the digital controller as a total system is essential. The primary flutter mode of the model is predicted to be violently unstable at the highest anticipated test dynamic pressures. The digital controller has been coupled to a near real-time hot-bench simulation (HBS) of the model/wind tunnel system using the advanced real-time simulation system at Langley. The components of the coupled system are shown in the figure. The HBS dynamic model was developed from scratch using data bases generated by existing aeroservoelastic analysis tools. The dynamic model is complex. In addition to a roll mode, symmetric and antisymmetric elastic modes, unsteady aerodynamic states, third-order actuator dynamics, hinge moment effects, and turbulence are included. The resulting size of the simulation model and the high-frequency dynamics involved prevent it from being run in real time. Instead, both the digital controller and the HBS are run in synchronized slow time while maintaining dynamic validity. A benefit of running in slow time is that the critical model dynamics, which would otherwise be a blur, can be observed on the graphics display in slow motion. Real-time graphic displays were developed to assist in understanding relevant dynamic behavior. The implementation of appropriate hot-bench simulation models is an enabling technology for the design of highly integrated airplanes with active structural control.
(Carey Buttrill, 44016 and Jacob Houck)

Active Flutter Suppression Via Feedback of Synthesized Modal Velocity

The need for techniques for synthesis of active flutter suppression systems (FSS) is becoming more critical as the design of aircraft moves toward lighter, more flexible configurations. In this research, a previously developed novel FSS synthesis methodology for blending the outputs of an available sensor set to produce a synthesized scalar signal that approximates the velocity $\dot{z}$ in the critical flutter mode has been extended to include multiple control degrees of freedom (see the figure). The methodology was then applied to develop an FSS for an advanced tailless fighter configuration. The sensors and control surfaces used for flutter mode control are shown in the figure. Constrained optimization techniques are employed to determine optimum values for the sensor blending matrix B; the control distribution matrix D; and free parameters in the compensator $K(s)$. The compensation matrix $T(s)$ is fixed during the optimization. Feedback of the resulting signal adds damping that stabilizes the flutter mode.

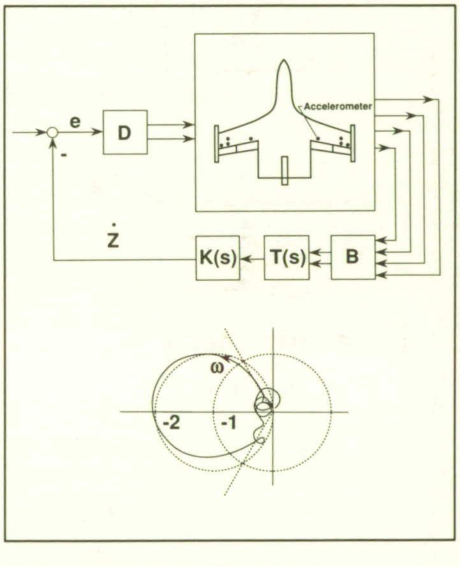

FSS control law structure and robustness, controller block diagram for advanced fighter (top) and Nyquist stability diagram (bottom).

Robustness characteristics obtained by applying the synthesis procedure to the symmetric degrees of freedom of an aeroelastic

model representative of the advanced fighter configuration are shown as a polar (Nyquist) plot of the transfer function $\dot{z}/e$. The design point, at a Mach number of 0.8, is at a dynamic pressure of 300 lb/ft^2, which is approximately 25 percent above the flutter point. For the closed-loop system to be stable at this point, the Nyquist path must encircle the critical point (−1) in a counterclockwise direction. The ideal, minimum energy controller that could be achieved if the modal velocity synthesis were exact is indicated by the dashed circle centered at the critical point (−1). Increasing the system gain, which corresponds to more control effort, expands the diameter of the circle; whereas, uniformly changing the phase rotates the circle. In the ideal case, the gain could be increased without limit or reduced to one-half its nominal value before the critical point would be encountered indicating instability; likewise, the path could be rotated ±60° before encountering instability. The solid curve shows the Nyquist path achieved for a specific case using four symmetric accelerometer signals and two symmetric commands into the trailing-edge control surfaces. Blending and distribution design variables were selected for optimization. These results show that the ideal case is closely approximated with satisfactory margins of stability in both gain and phase. For an otherwise nominal system, the gain can be divided by a factor of 2.2 or multiplied by a factor of 3.4 before instability occurs; phase errors between −50° and 47° can be tolerated. Other results show that levels of control deflection and rate required are satisfactory for reasonable design disturbances.

(William M. Adams, Jr., 44013 and David M. Christhilf)

New Engine-Monitoring and Control System (E-MACS) Display Concept

The objective of this research was to provide an advanced aircraft engine display system designed to exploit the capabilities of electronic display media for increased pilot understanding of system performance while simultaneously reducing pilot mental work load and error. The underlying concept was that a reduction in the mental work load may require that information be provided in a form that is more directly oriented to the user's task. The area of interest for this study was secondary flight display formats, with engine instruments as the specific application. This application area was chosen because it provided both a control task, engine power with throttle, and a systems monitoring task. A part-task evaluation in the Transport System Research Vehicle (TSRV) simulator was used to compare the E-MACS display with a modern, current-generation engine display format (see the first figure).

The E-MACS display provides an innovative interface for reduced pilot work load and increased situational understanding. The E-MACS display format, shown in the first figure, provides unique display elements tailored to the pilot's task. Display elements were based on a model of engine performance characteristics. The display element for the control task provided a direct indication of engine thrust

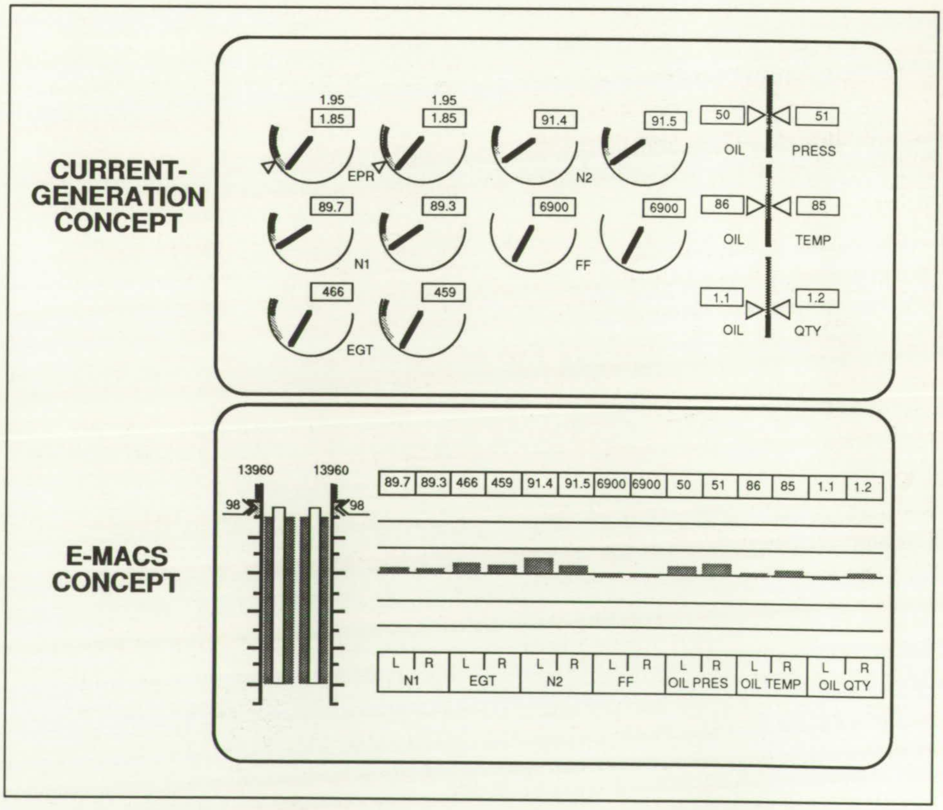

Comparison of current-generation engine display with E-MACS display.

- $\frac{1}{2}$ were fault situations (32 per format).
- 4 data runs / format / pilot (64 per format).

UNDETECTED FAULTS			
	degraded	out-of-tolerance	TOTAL
Conventional format	10	4	43 %
E-MACS format	0	0	0

E-MACS quantitative results.

relative to a computed maximum-available-thrust value. For the monitoring task, quantitative information was presented in a form that may be cognitively processed in a qualitative manner. Column-deviation indicators were used as the display elements for monitoring, where the deviation was between the actual and a computed ideal value.

Sixteen pilots participated in a simulator evaluation of E-MACS; this evaluation compared E-MACS with a traditional electronic engine display format. The test included takeoff and in-flight conditions with both normal and fault (degraded and out-of-tolerance) conditions. As part of the evaluation, each pilot was presented four different scenarios for each of the two display formats. Half of the scenarios involved fault situations. The subjective results of this test showed an overall preference for the E-MACS display relative to the traditional display. Additionally, the monitoring display elements seem to allow holistic viewing of the system information. The most significant result is that with the E-MACS display no faults were undetected; with the conventional display, 43 percent of all faults went undetected.

(Terence S. Abbott, 42009)

Physiological Measures Useful in Boredom Detection

The performance and safety of crew/vehicle systems may be threatened as increased automation changes the role of the pilot from controller to that of monitor, producing a mental state such as "boredom." This state can be exacerbated by long-duration missions such as transoceanic flights. The goal of this research is to detect the mental states of the pilot which are predictive of performance degradation and, then, to intervene to restore acceptable pilot/system performance. The first step toward this goal is to establish the sensitivity of physiological measures, as parameters of a boredom detection model, to operator mental state in a task underload environment.

The study was designed to establish the sensitivity of electrocardiogram (ECG), electroencephalogram (EEG), and pupil diameter (PD) measures to operator mental state. An underload condition was created by having subjects perform a fault-acknowledgment task (shown in the first figure) characterized by simple repetitive responses with minimal novelty, complexity, and uncertainty. This task consisted of monitoring faults presented on a jet engine "fault" pictorial and acknowledging the fault with minimal response time. Performance parameters recorded included response time and response accuracy. Physiological measures were monitored over a 1-hour test session for each of 11 subjects.

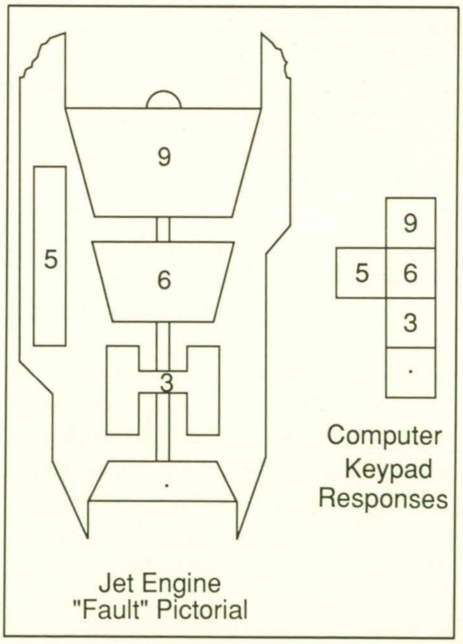

Fault acknowledgment task.

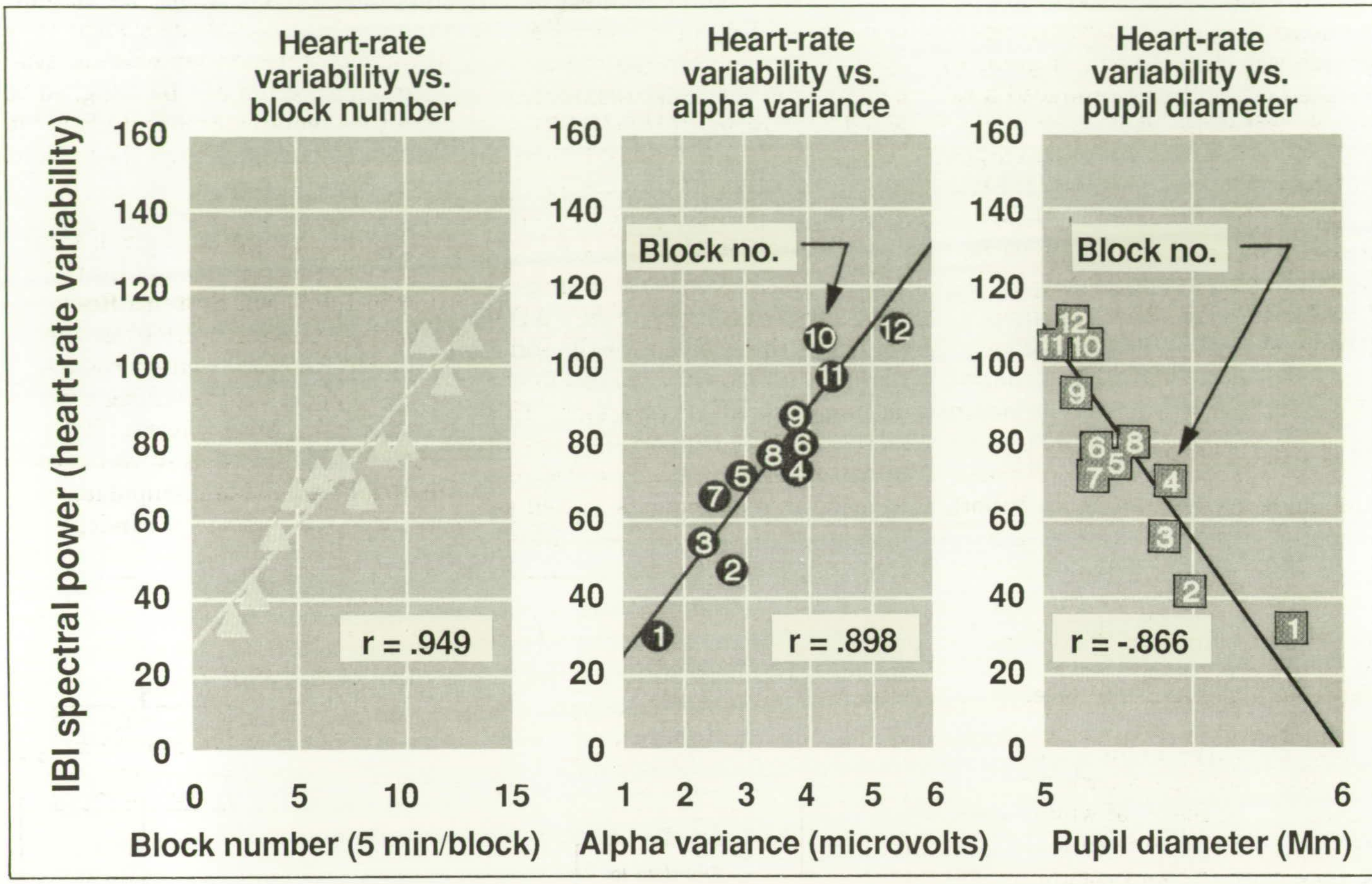

"Boredom" model parameters with averaged data from 11 subjects which show correlation of 3 physiological measures.

Heart rate variability (HRV), alpha variance (EEG component), and PD each exhibited changes indicative of decrements in subject arousal level (as shown in the second figure). Concurrently, response time increased over the test session. The second figure shows HRV (spectral power of the inter-beat interval (IBI) versus test session block number). Correlations among heart rate variability, alpha variance, and pupil diameter, with block number, were high (0.949, 0.855, and –0.864, respectively). The second figure also shows high correlations between heart rate variability and alpha variance (r = 0.898) and heart rate variability and pupil diameter (r = 0.866).
(J. Raymond Comstock, Jr, 46643, Randall L. Harris, and Alan T. Pope)

Automation of FAA Wind Shear Training Aid Using Expert System

The objective of this study was to explore the fusion of different types of wind shear detection information with corroborating weather information to produce a more reliable estimate of the wind shear hazard than each of the wind shear detection methods could have produced independently. Such an increase in reliability could increase the probability of wind shear detection and reduce the number of nuisance warnings.

The FAA has developed a training aid to help pilots recognize and avoid wind shear. This training aid instructs the pilot to collect data from different weather sources and combine that information with their own visual and tactile information. The first step toward the objective was to automate the information integration outlined in the train-

ing aid using an expert systems approach. An expert systems approach was then chosen. A grant to Princeton University produced a research prototype wind shear recognition expert system that attempted to detect and classify wind shears based on various sources of input data (e.g., Automatic Terminal Information Service (ATIS) reports, Low-Level Wind Shear Alerting System (LLWAS), air data, pilot visual sightings, and Pilot Reports (PIREPS)). The prototype, containing 140 rules, produced a rudimentary assessment of the wind shear and guidance selection (e.g., "abort takeoff"). The study also identified issues that will need to be explored, such as the usefulness and availability of certain inputs, the effects of false alarms on flight crew confidence, and the user interface.

The prototype produced in this effort provides a basis for exploring the fusion of wind-shear-related information to provide a more complete and accurate assessment of hazardous wind shear. The lessons learned from this exploration can aid in the development of a system that can help reduce the number of inadvertent encounters with wind shear while minimizing the number of false/nuisance alarms. Such systems could lead to improved safety and have a minimal impact on airport operational efficiency. **(David A. Hinton, 42040 and Paul C. Schutte)**

Computer-Aided Design Tools for Tele-Operated Robotic Control Systems

The objective of this study was to verify and apply an approach to the design and assessment of tele-operated robotics control systems through the use of two computer-aided design/computer-aided engineering (CAD/CAE) tools: Team*work* and ADAS (Architecture Design and Assessment System). The Team*work* tool provides the capability to graphically specify data flow and control flow of the system software, while ADAS simulates the behavior of the software when mapped onto candidate hardware configurations. This method will allow robotics engineers to formally specify a design to meet its requirements as well as to simulate its behavior on various resource configurations. By simulating the behavior of the system prior to implementation, an efficient system architecture can be designed to meet its requirements and allow for growth of the system as the system evolves.

During the initial phase of this study, the control system hosted in the Intelligent Systems Research Laboratory (ISRL) at the Langley Research Center was described and evaluated using the Team*work*/ADAS toolset. The ISRL system consists of two commercially available manipulator arms capable of working indepen-

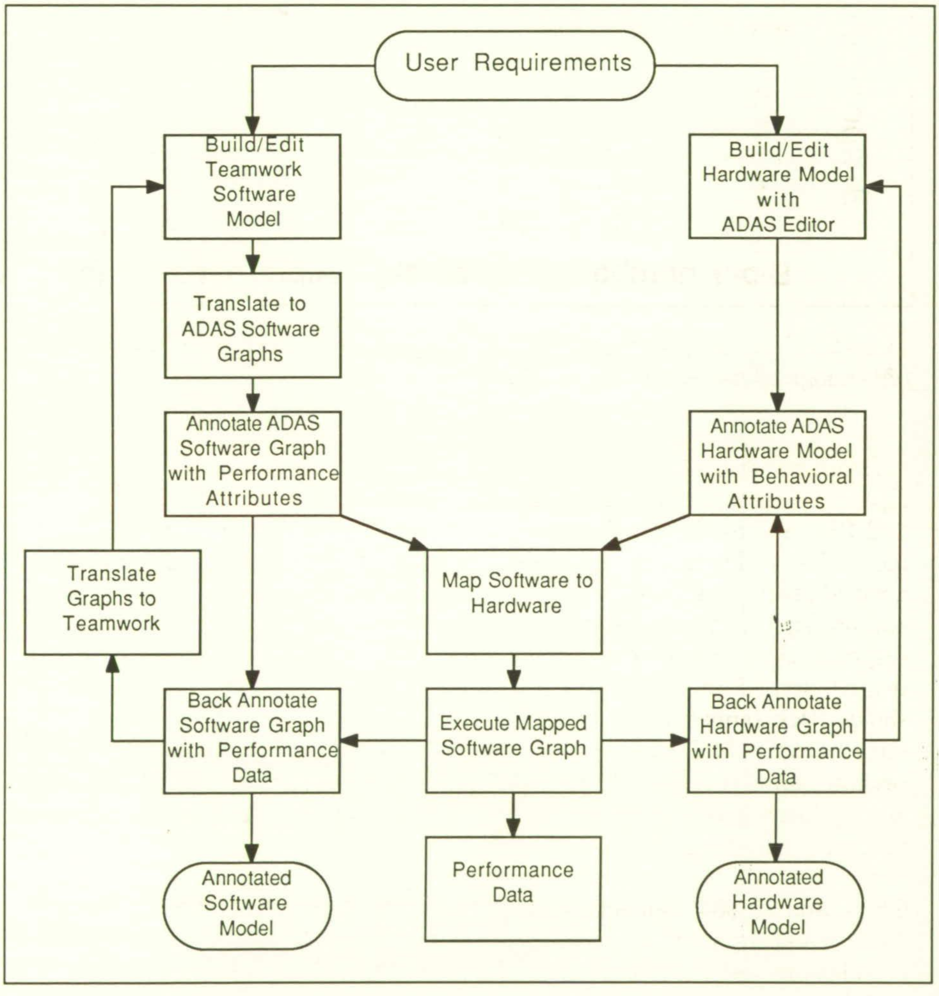

Team*work/ADAS design process.*

dently or in a coordinated fashion. The arms are controlled by a distributed system consisting of two MicroVAX II computers, two PDP-11 computers, and an OCTEK image processing device. For this experiment, a Team*work* model representing the data and control flow of the system software was completed. This model graphically and textually described the functions required of the system and specified how they would be implemented. This model, along with the necessary performance parameters, was then used to create a set of ADAS models that could be used in the simulation studies. Performance parameters (software execution times) were measured by accesses to an external timer located on the backplane of the host computer. The ADAS simulations revealed a 40-percent utilization of the MicroVAX II central processing unit during real-time processing. In addition, ADAS revealed how much of this 40 percent was consumed by each subprocess executing on the machine. In each case, the ADAS results agreed with the run-time performance monitor executing on the host machine.

These initial findings provide evidence that these tools are capable of representing teleoperated systems during the initial stages of the design. By using the Team*work*/ADAS toolset, designers are given quantitative information that can aid in making critical design decisions at the conceptual stage of the design; this eliminates not only extensive prototype/testing costs, but also provides a system specification that can be constantly updated during the life-cycle of the system.

(Steven D. Young, 41709 and F. Wallace Harrison)

Electromagnetic-Plasma Analysis Model for Spacecraft Entry Plasma Sheath Investigation

Future NASA missions may require the use of aerodynamic braking for orbital transfer. The development of such Aeroassisted Space Transfer Vehicles (ASTV) requires an improved understanding of the flight regime that will be encountered. The principal objective of the Aeroassist Flight Experiment (AFE) is to provide flight data to be used in the design of future ASTV. The data will be a benchmark to be used in the verification of present prediction methods and computational techniques in the nonequilibrium chemistry flight regime. The Microwave Reflectometer Ionization Sensor (MRIS) will be one of the instruments onboard

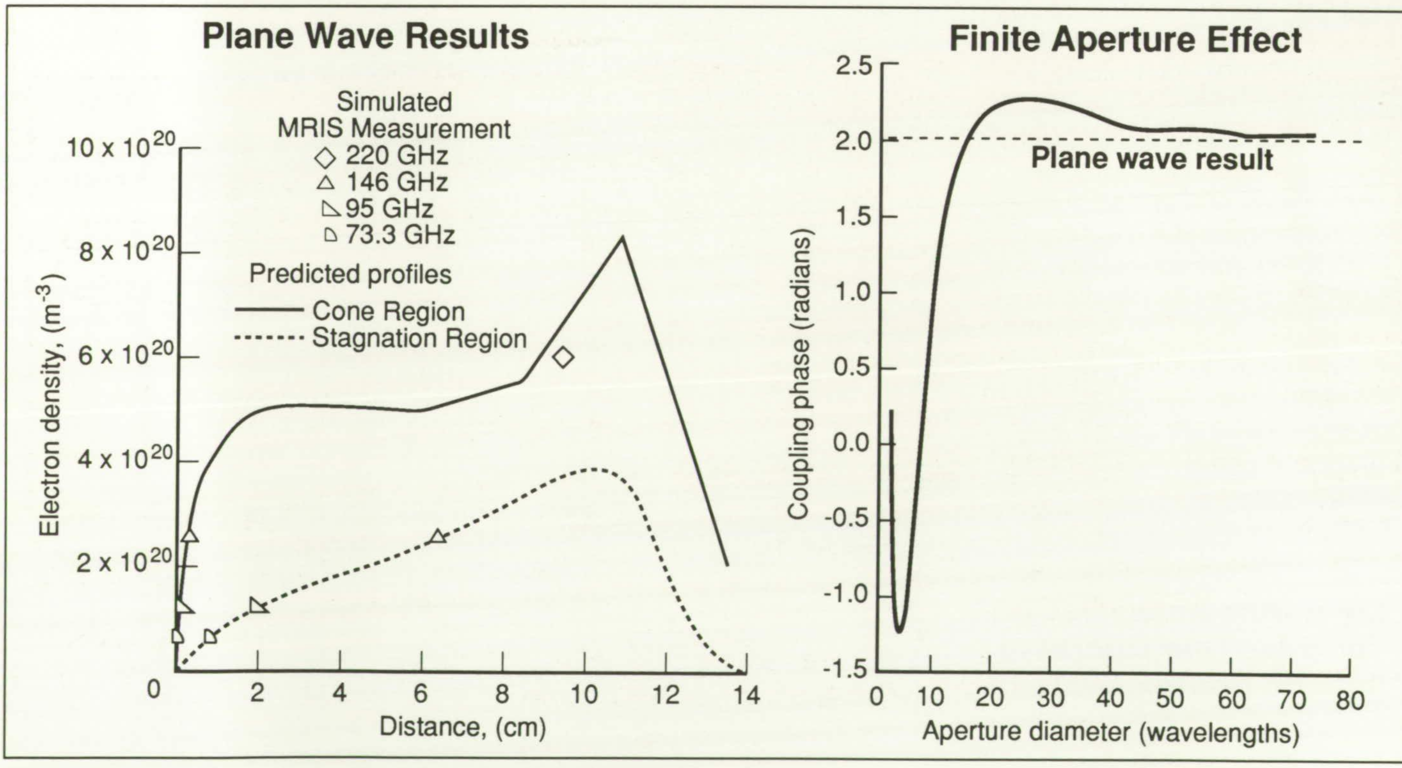

Electromagnetic-plasma analysis development for MRIS.

ORIGINAL PAGE
BLACK AND WHITE PHOTOGRAPH

the AFE to provide these data. The MRIS is intended to use the reflective properties of the ionized flow field at microwave frequencies to nonintrusively estimate the electron density profile in the shock layer. This measurement is accomplished by measuring the effect on the phase of the coupling coefficient between two apertures. The data from the MRIS will provide information concerning wall catalysis, radiative heating, and flow field dynamics.

In order to predict the performance of the MRIS and to develop data inversion techniques, a model for the electromagnetic coupling between apertures in the presence of a plasma has been developed. This model is based on an existing aperture coupling code (NASA TM-101614) with the addition of a model to include the electromagnetic interaction with the plasma. This model is now being used to investigate the coupling between two circular apertures in the presence of an inhomogeneous plasma with a gradient in the direction normal to the aperture plane. The model is also being used to develop a data inversion technique to estimate the electron density profile from coupling data.

This model has been used to demonstrate the ability of a data inversion algorithm to infer distance from MRIS coupling measurements. A comparison of the simulated MRIS measurement based on a plane wave solution (infinite aperture) and the predicted electron density profile is shown in the figure. In addition, the figure includes the modeled effects of reduced aperture size on the MRIS coupling measurement. The model is presently being used to study the inclusion of the aperture effects in the data inversion technique.
(Roland W. Lawrence, 41821)

Distributed Optical Sensing and Processing for Control of Flexible Structures

The purpose of this research is to develop a new technology of distributed sensing and computation for vibration and shape control of large, flexible spacecraft. Crystal mediums are used with real-time holography to gather and store images that can yield vibration and instantaneous

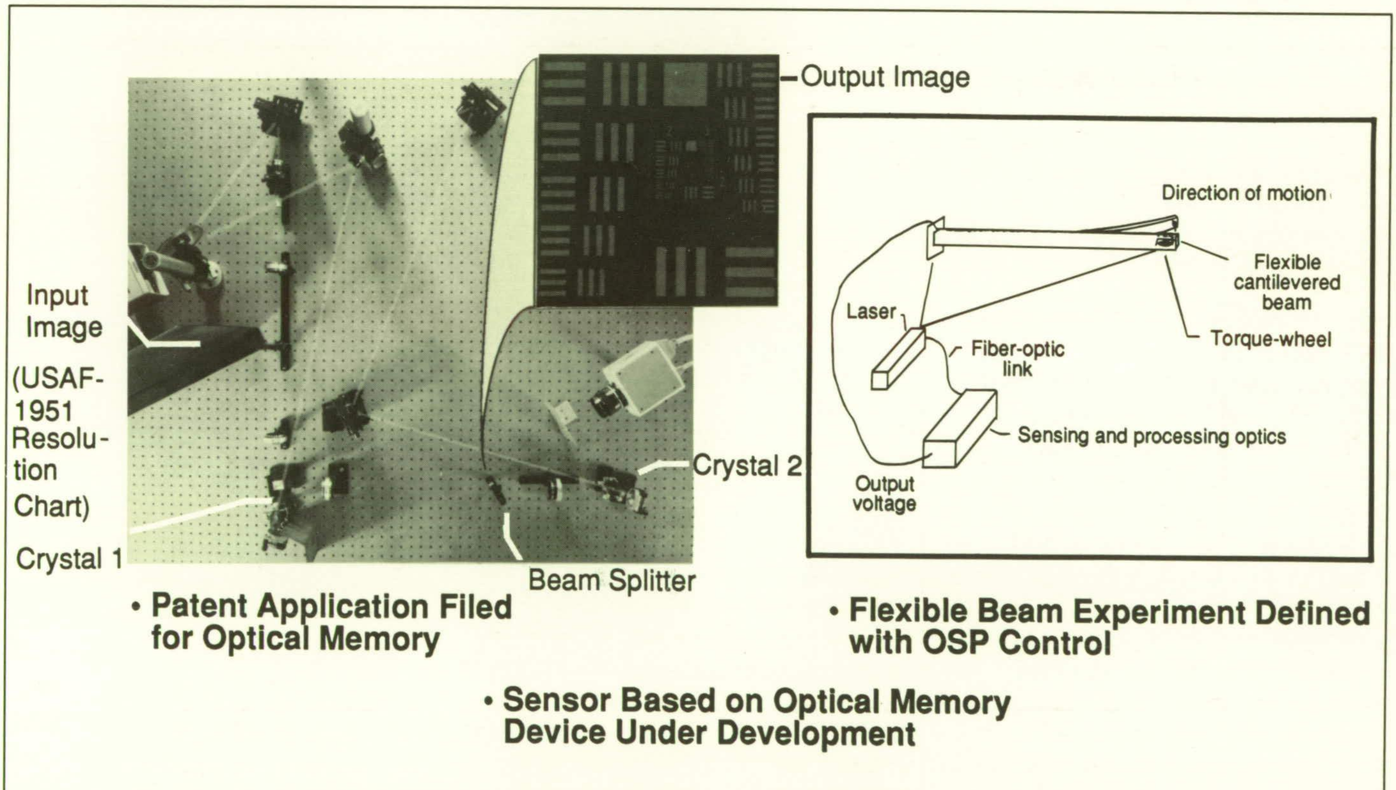

Integrated optical sensor/processor.

geometry data for a structure. Optical computation techniques are employed to process the image data and to compute commands to actuators located on the structure. Currently, the focus of the research is the development of a laboratory demonstration of the technology using a flexible cantilevered beam.

The figure shows a laboratory setup of the basic element of a distributed optical sensor/processor, a dynamic holographic memory, and a schematic diagram of the flexible beam experiment. The dynamic memory element provides the means to record and erase holographic images in real time. To generate the stored image shown in the photograph, a hologram of an Air Force Resolution 1 test pattern was initially recorded in one of two photorefractive crystals. Simultaneously, this hologram was read, and the reconstructed wave was used to form a hologram in a second crystal. When the second hologram was read, the reconstructed wave was directed back into the first crystal to rerecord the original hologram. Image information oscillates between the two photorefractive crystals and thus remains stored.

In the flexible beam experiment, the beam is illuminated with coherent laser light, and the wave front reflected from the surface of the beam is sampled in time. During each sampling interval, the reflected wave front is collected by the sensing optics, focused, and stored in a dynamic holographic memory. When the stored hologram is subsequently read, an image of the beam is generated which contains information concerning the position of the beam at the time the hologram is recorded. This information is processed, using analog image processing techniques, to yield a control signal to drive a torque wheel actuator located on the tip of the beam.
(Sharon S. Welch, 46611)

Optimal Integrated Control-Structure Design for Spacecraft

Future missions utilizing large space structures will have stringent requirements for performance, reliability, and cost, and these requirements will necessitate further advances in the design methodology. The performance of advanced spacecraft will depend heavily on both the structural design and the control systems design; thus, the two disciplines can no longer be considered independently, but must be addressed in an integrated manner. An optimization-based approach has been developed for performing integrated control-structure design for large spacecraft. The basic formulation consists of an objective function to be minimized (such as the total mass, or the root-mean-square (rms) pointing error at a specified location) and a set of structure-, control-, and performance-related constraints. A new software test bed (entitled Control-Structure Simulation Software (CS^3)) has been developed to implement the integrated approach for computer-aided design of future spacecraft.

The software test bed consists of three modules as shown in the first figure: a structural modeling and analysis module, a control synthesis processor (based on the software package ORACLS), and a versatile optimization package. The in-core architecture is designed so that all required structure, control, and optimization analyses are

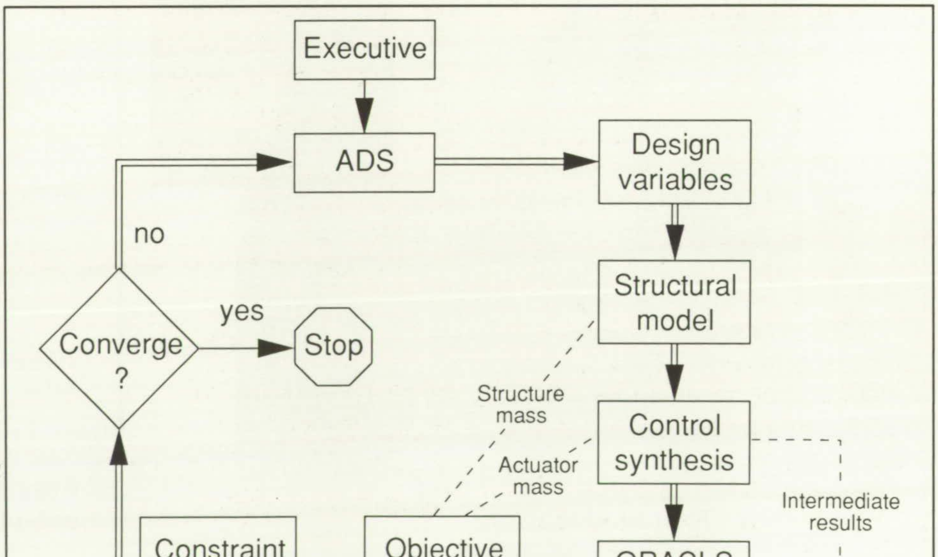

CS^3 flowchart.

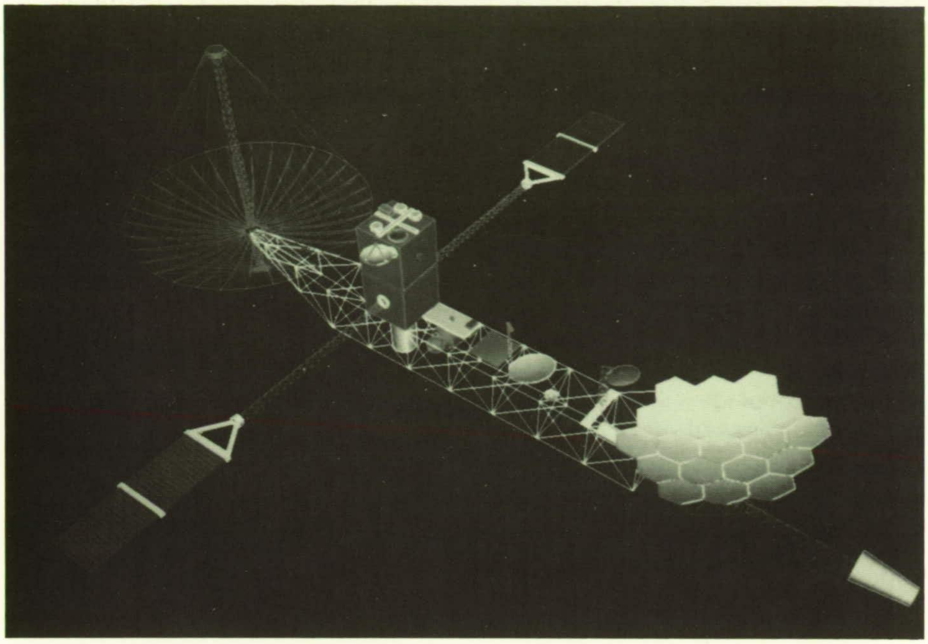

CS^3-generated model of EPS. L-89-10225

performed within one executable program. Several advantages exist in using the in-core architecture versus the conventional off-line data base approach. First the computational speed is improved by eliminating duplicate calculations in the controls and structures modules. Second, the architecture provides an environment conducive to interdisciplinary design by allowing engineers and scientists from both controls and structures disciplines to use the same software tool. Finally, the architecture provides flexibility in studying different design methodologies because a great deal of freedom exists in the selection of optimization criteria. An example of a computer-generated model of an Earth pointing satellite (EPS) provided by the structural modeling and analysis module is given in the second figure.

By incorporating codes from separate disciplines within a single executable program, optimization of the control-structure, coupled-field problem can be solved as easily as a single-field problem. Hence, much insight can be gained by the optimization-based objective and constraint sensitivity calculations. The integrated design approach and the software test bed should promote increased understanding of proper control-structure design for future spacecraft.

(W. K. Belvin, 44319, S. M. Joshi, and E. S. Armstrong)

Maximization of Single-Stage-to-Orbit Payload Via Trim Drag Reduction

An important technical objective in the development of a horizontal takeoff, single-stage-to-orbit (SSTO) vehicle is reduction of the aerodynamic drag during ascent. Drag is directly related to fuel consumption and, inversely, to payload mass capability. The objective of this research was to investigate ways to reduce the drag of SSTO vehicles and increase payload mass capability.

Examination of experimental data and theoretical estimates for a generic SSTO configuration indicates that forward migration of the aerodynamic center (AC) exceeds 35 percent of the mean aerodynamic chord (MAC) or 20 percent of fuselage length as the Mach number increases to orbital values. The AC migration and center of gravity (CG) travel are shown in the figure. The aerodynamic lift and distance between the AC and CG cause a large pitching moment that must be balanced. Traditionally, this trim moment would be generated by deflecting control surfaces.

The drag increase due to moderate deflections of aerodynamic controls at hypersonic speeds can be significantly large and can exceed the drag of the entire vehicle. As shown in the figure, at Mach 20 the drag increment due to 20° (trailing edge down) deflection of partial span elevons δ_e for the configuration above is approximately equal to the drag of the vehicle (with elevons undeflected). For elevon deflections in the 25° range, the drag increase exceeds that of the basic vehicle.

The migration of the AC and high drag due to elevon deflections suggested design of a CG management system to track the vehicle AC to minimize the pitch trim moments and, thereby, to reduce the trim elevon deflections, associated drag, and excessive fuel consumption. A second approach was to investigate vectored thrust for trim moment generation as a means of reducing trim drag.

An SSTO simulation study was completed for the generic vehicle having a takeoff gross weight of 300,000 lb. (A stability augmentation system was designed to ensure desirable dynamic response characteristics.) For the baseline vehicle, pitch-trim elevon deflections were large, reaching 16° trailing edge down at hypersonic speeds, and the associated drag caused an extra 15,000 lb of fuel to be burned. A rudimentary CG management system was implemented resulting in substantially reduced elevon deflections and consequent loss of lift resulting in a need for increased trim angle of attack. The overall result was that 6,000 lb less fuel than the baseline was consumed. The thrust-vector trim system also nearly centered the elevon deflections resulting in a savings of 4,000 lb of fuel over the baseline.

The results of this study suggest that use of aerodynamic controls such as elevons for pitch trim moment generation for SSTO vehicles should be avoided because of significant trim drag penalties. Use of a CG management system to minimize lift-induced moments (and use of stability augmentation to provide desired vehicle response characteristics) can reduce the ascent fuel consumption. Fuel consumption can also be reduced via vectored thrust for pitch-trim moment generation. Use of both systems together should result in the minimum trim drag and maximum increase in vehicle payload mass capability.

(John D. Shaughnessy, 44014)

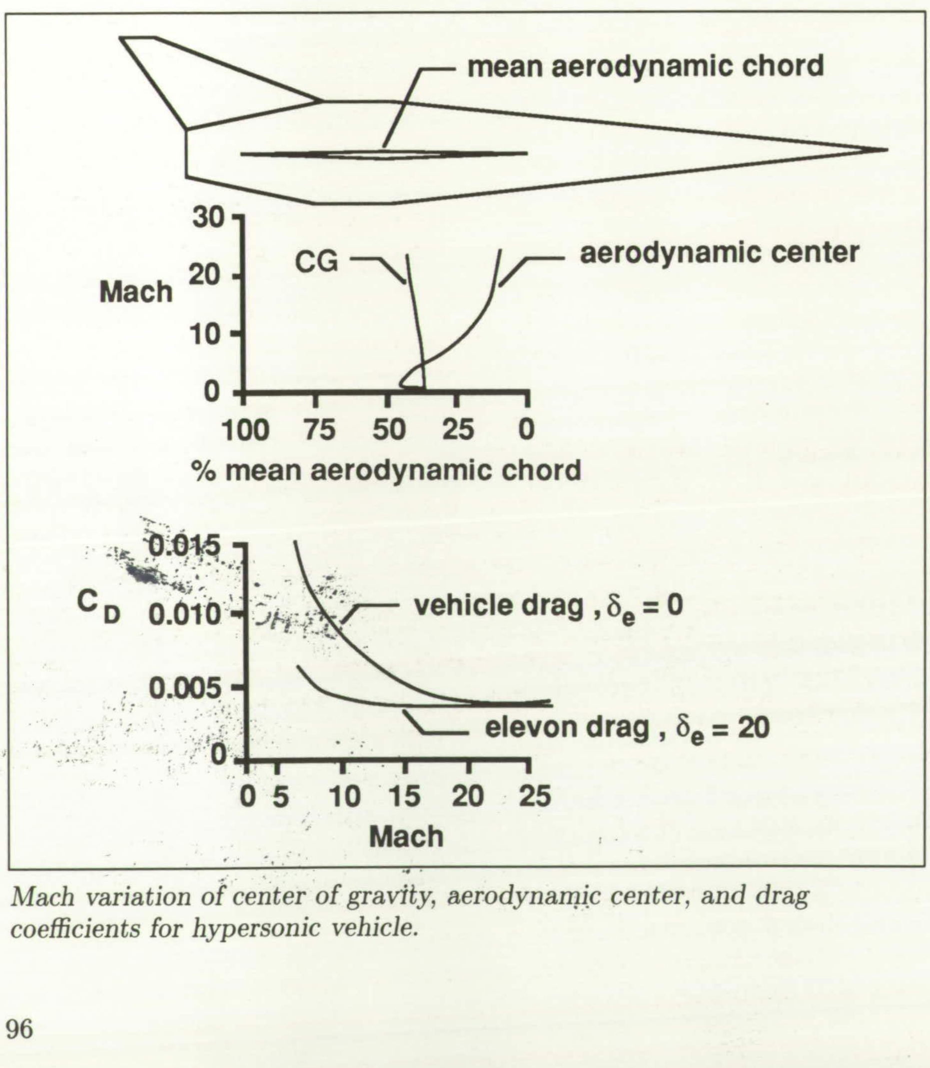

Mach variation of center of gravity, aerodynamic center, and drag coefficients for hypersonic vehicle.

Space Directorate

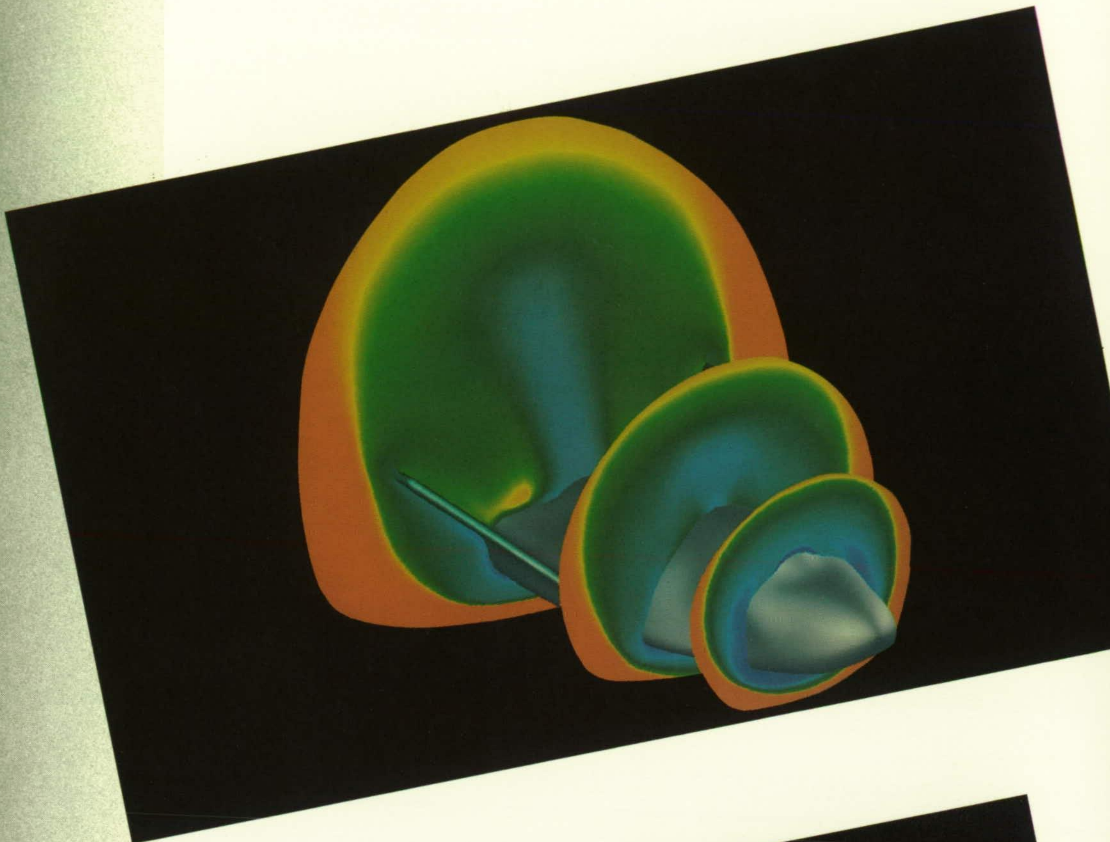

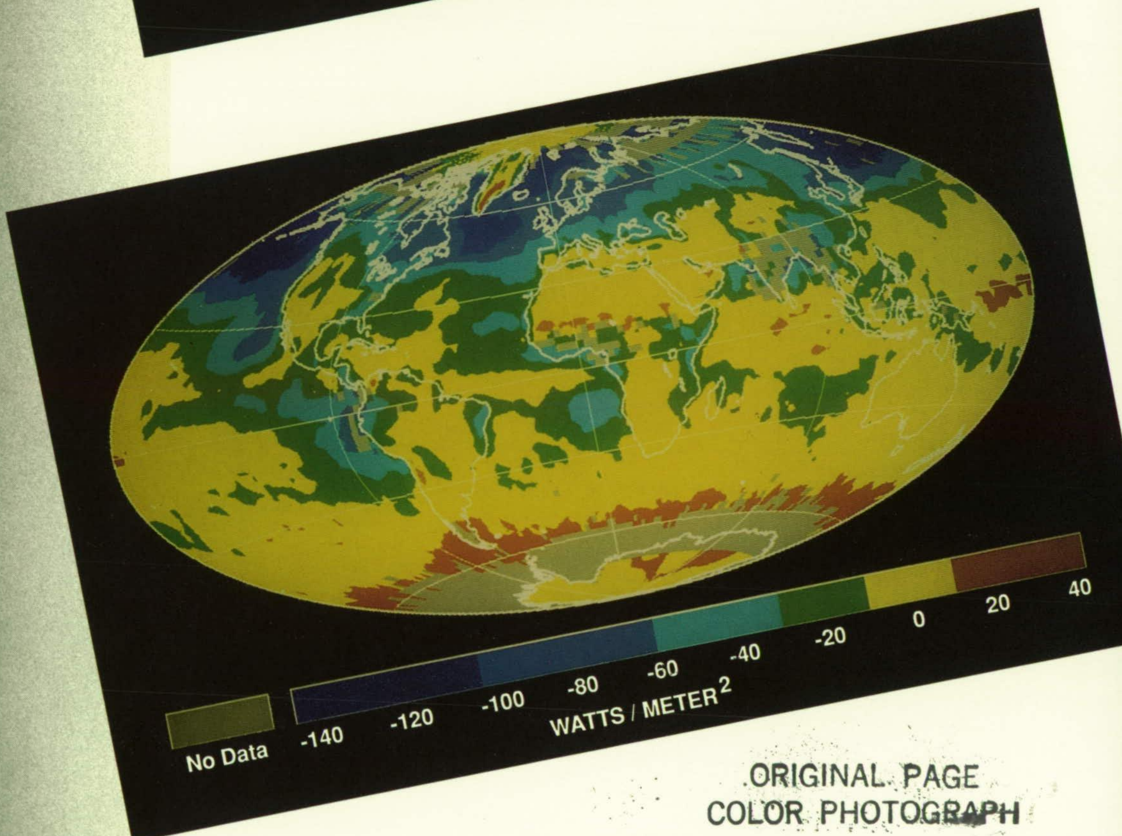

The Space Directorate conducts research in atmospheric and Earth sciences, identifies and develops technology for advanced transportation systems, conducts research in energy conversion techniques for space applications, and provides the focal point for conceptual design activities for both large space systems technology and space station activities.

The Atmospheric Sciences Division is a leader in the area of atmospheric sciences. Its researchers are involved in seeking a more detailed understanding of the origins, distributions, chemistry, and transport mechanisms that govern the regional and global distributions of tropospheric and stratospheric gases and aerosols, and in the study of the Earth radiation budget and its effect on climate processes. The research seeks to understand better both natural and anthropogenic processes and covers a wide spectrum of activities, including the development of theoretical and empirical models; collection of experimental data from in situ and remote-sensing instruments designed, developed, and fabricated at Langley Research Center; organization of extended field experiments; and development of data management systems for the efficient processing and interpretation of data derived from airborne and satellite instruments.

The Space Systems Division conducts research and systems analysis studies of advanced transportation systems, large space systems, and space station concepts; analytical and experimental research in hypersonic aerodynamics and aerothermodynamics; hypersonic computational fluid dynamics code development and studies; and basic research on energy generation and conversion techniques for potential use in space. The division is a leader in the development of highly interactive computer-aided design tools that enable rapid conceptual design and evaluation of space vehicles and spacecraft and identification of technologies needed to develop these space systems. Space systems such as Earth-to-orbit launch vehicles, utility vehicles, and space transfer vehicles are developed and evaluated. Flight experiments are developed which use the Space Shuttle orbiter as an orbital platform and as a reentry research vehicle and which use entry vehicles launched from the Space Shuttle to study aerothermodynamic and aerodynamic characteristics. The results provide a data base for development of advanced vehicle systems.

The Space Station Freedom Office is the focal point for Langley Research Center's involvement in the Agency-wide Space Station Program and is responsible for the implementation and coordination of Langley's direct support of this program. The Space Station Freedom Office is NASA's lead office for the identification, definition, and evaluation of the evolutionary space station capabilities and for the identification of technology and advanced development required for long-term evolutionary development. The office represents the engineering community as technology users of the space station. It also advocates flight experiments on future Space Shuttle flights that contribute to space station technology use as well as flight experiments from technology programs that can contribute to both the initial operational capability and the evolutionary space station. The office provides Langley Research Center support to the NASA-wide in-house space station systems engineering and integration in areas consistent with demonstrated Langley capabilities and expertise.

The Space Directorate has had a significant number of major accomplishments this year. Several important experiments designed to provide new insights into chemical and dynamical processes in the atmosphere have been accomplished by the Atmospheric Sciences Division. The Global Tropospheric Experiment, which was conducted over the Alaskan tundra, used surface, tower, and aircraft trace gas flux measurements to show that the tundra is a major source of the greenhouse gas methane. The NASA/NSF/NOAA (National Science Foundation/National Oceanic and Atmospheric Administration) 1989 expedition to the Arctic used real-time data from SAM II (Stratospheric Aerosol Measurement II) and SAGE II (Stratospheric Aerosol and Gas Experiment II) satellite experiments and Langley airborne lidar systems on the NASA DC-8 aircraft to characterize aerosol and ozone concentrations that produce polar stratospheric clouds and the resulting holes in the ozone layer. Earth radiation budget research has produced an analysis of the first 4

months of processed and archived ERBE (Earth Radiation Budget Experiment) data to show that clouds have more of a cooling effect than a greenhouse warming effect on the Earth/atmosphere system.

The Space Systems Division has conducted extensive system studies in the areas of advanced transportation systems and large space systems. A lifting-body concept has been developed for application to the Assured Crew Return Capability mission for the Freedom *Space Station and the assured manned access to space mission called the Personnel Launch System. This concept has evolved from early studies in the 1960's by NASA and the United States Air Force concerning reentry vehicles through wind tunnel aerodynamic and heating tests; computational fluid dynamic predictions for real-gas phenomena; and performance, stability, and control simulation of reentry, cross range, and landing. Results have shown that the concept requires a simple flight control system to accomplish all flight missions, and it provides low acceleration forces for crew return and several opportunities daily for landing sites. Radiation protection studies related to the proposed manned Mars mission have been conducted. Significant advancements have been made in aerothermodynamic computational techniques with thermal and chemical nonequilibrium effects, for both continuum and rarefied flow regions. In addition, experimental data were obtained and assessed for expanding the heating and aerodynamic data base for the Aeroassist Flight Experiment, and new hypersonic wind tunnel testing techniques were developed.*

The Space Station Freedom *Office developed requirements and representative configurations for a number of alternative evolutionary paths for the space station that included research and development growth and growth into a transportation node in support of human missions to the Moon and Mars. Based on these analyses the evolutionary space station resource, capability, and "scar" (a hardware design accommodation to enable and/or enhance the addition or update of systems and capabilities at some future time) requirements were established. The Space Station* Freedom *Office conducted a technical and economic analysis for a Commercially Developed Space Facility (CDSF) in response to a congressional request. The study included science mission definition scenarios, quantified the concept system performance parameters, developed benchmark operation scenarios, provided Space Shuttle interface descriptions, assessed development schedule activity, and provided a cost and economic assessment for the endeavor. In addition, the Space Station* Freedom *Office led the Office of Aeronautics and Space Technology (OAST) outreach program to develop new technology experiments in industry and academia. Details of the accomplishments of the Space Directorate follow.*

Detection of Stratospheric HBr

Emission features of HBr isotopes have been identified in high-resolution far-infrared emission spectra obtained in 1979 with a balloon-borne Fourier transform spectrometer. The constant volume mixing ratio retrieved from the average spectrum of six single-scan interferograms is 20 pptv (10^{-12} in volume) above 28 km with an uncertainty of 35 percent. This new finding has a significant meaning for the bromine chemistry in the Earth's atmosphere. The previously proposed bromine chemistry for the ozone destruction in the stratosphere (as much as a 2- to 3-percent ozone loss) and in Antarctica is based on the catalytic scheme and partitioning of total bromine concentration into its major components, BrO and HBr. The direct measurement of BrO and HBr is, therefore, required to verify the catalytic scheme. The current level of organic bromine compounds observed in the troposphere is 25 pptv. Prior to these spectroscopic measurements, no direct measurement of BrO or HBr in the stratosphere had ever been made. The retrieved HBr amount of 20 pptv of this work suggests that HBr could be the major stratospheric bromine species and that reevaluation of stratospheric bromine chemistry should be undertaken. Shown in the figure are spectral fittings of the observed spectra using a nonlinear least-squares fit technique. The shaded portion shown in the figure is the emission attributed to HBr with the signal-to-noise ratio of 2.5. The top panel is the difference between the observed and simulated spectra. The

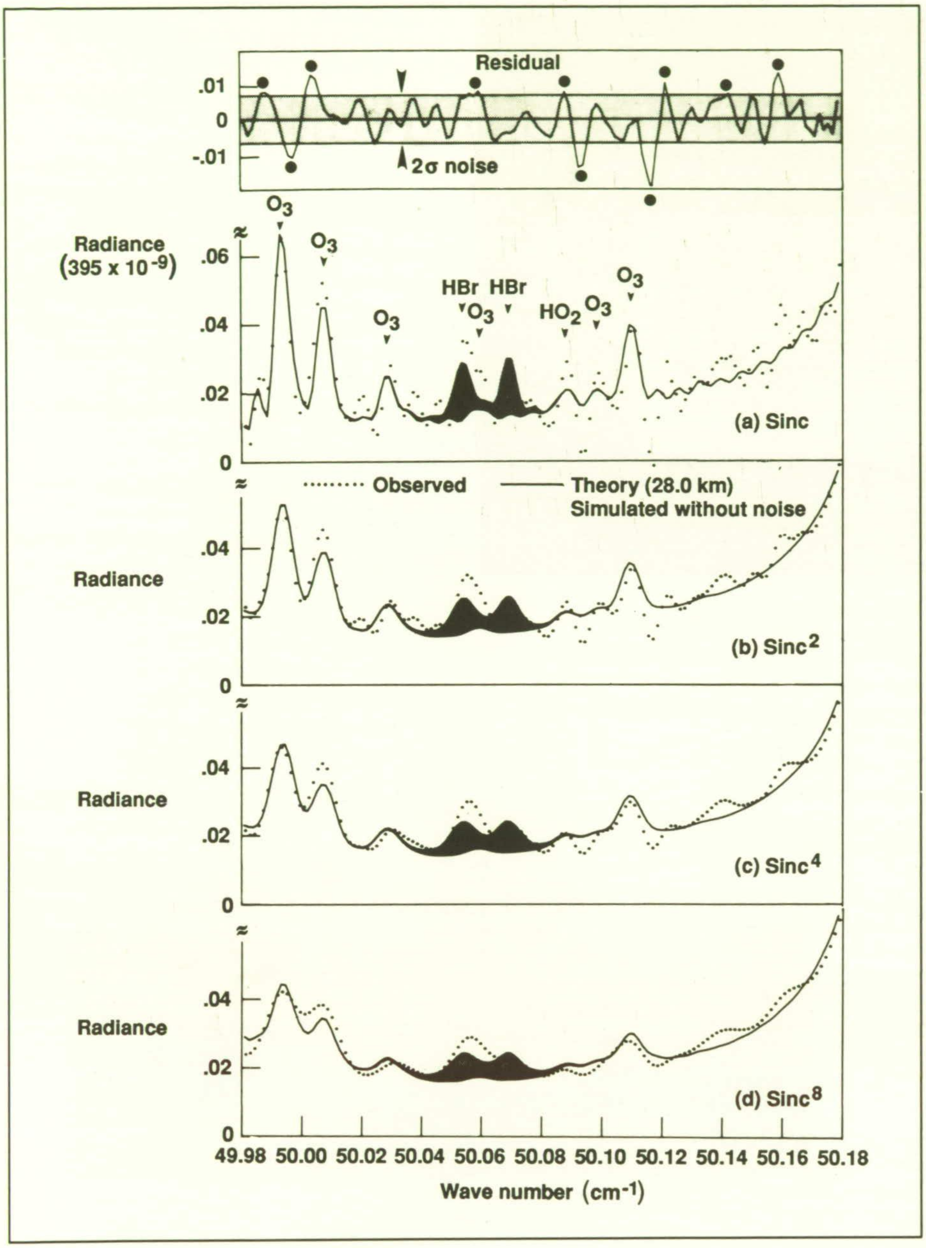

Simulation of observed spectra for four different apodizations. (After Park, Carli, and Barbis, Geophysical Research Letter, vol. 16, 1989.)

noise features (solid circles) and 2-σ noise level are indicated.

(Jae H. Park, 45811)

Airborne Lidar Observations of Stratospheric Ozone and Polar Stratospheric Clouds Over Arctic Region

The Langley Research Center airborne differential absorption lidar (DIAL) system was operated from the Ames Research Center DC-8 aircraft to obtain profiles of ozone and polar stratospheric clouds (PSC's) in the lower stratosphere during the 1989 Airborne Arctic Stratospheric Experiment (AASE). A total of 15 long-range flights were made over the Arctic from Stavanger, Norway, from January 6 to February 15, 1989. Simultaneous transmission of six laser beams provided the DIAL system with profile measurements of ozone concentrations and multiple-wavelength PSC scattering ratios and depolarization ratios between the altitudes of 12 km to 24 km along the DC-8 flight track.

An example of the ozone distribution obtained by the airborne DIAL system over the Arctic is shown in the figure. During the winter, the ozone distribution clearly indicated the edge of the polar vortex, and it was also an effective tracer of dynamical processes in the stratosphere. Near the end of the AASE experiment, the DIAL data showed that ozone concentrations had been reduced by 10 to 15 percent in the same region perturbed by $C\ell$ chemistry. These data may be the first evidence of ozone destruction due to $C\ell$ chemistry found during this experiment. The PSC's were observed on all missions through February 3 in regions of low temperatures ($\leq -78°C$). Two types of PSC's, thought to be predominantly nitric acid trihydrate, were observed

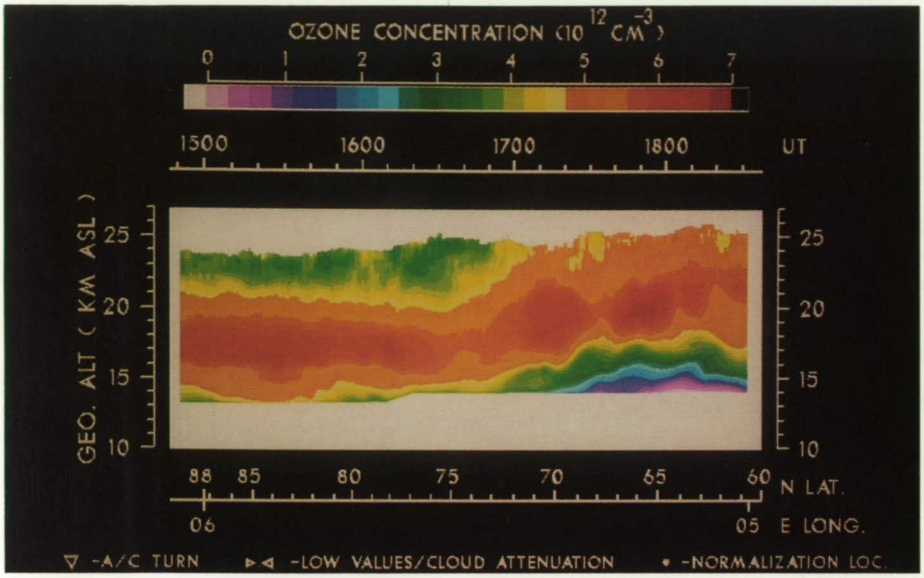

Airborne lidar measurements of stratospheric ozone inside wintertime Arctic polar vortex (latitudes > 71°N) and outside polar vortex (latitudes < 71°N) on February 9, 1989. Ozone concentrations are mapped according to color scheme given on top of figure. Evidence of ozone depletion was found near 75°N latitude between 19 km to 23 km.

to have very different scattering and depolarization characteristics. Water ice PSC's were observed in limited regions having lower temperatures (approximately -85°C). The PSC's play a critical role in freeing Cℓ to permit the subsequent catalytic destruction of ozone. The lidar measurements of the PSC's have led to a better understanding of their formation, physical properties, and spatial extent. The region in which the ozone reduction was observed with the DIAL system was spatially correlated with previously detected PSC's and the chemically perturbed region found by instruments on the ER-2 aircraft inside the vortex.

(Edward V. Browell, 41273)

Satellite Studies Reveal Continental Ozone Pollution Plumes

Analysis of data obtained from two independent sets of satellite measurements has been used to determine the global distribution of ozone in the troposphere. This technique uses data obtained from the Total Ozone Mapping Spectrometer (TOMS), which measures the amount of ozone in both the stratosphere and the troposphere, and the Stratospheric Aerosol and Gas Experiment (SAGE) instrument, which measures vertical profiles of ozone in the stratosphere. By subtracting the amount of ozone in the stratosphere determined from the SAGE measurements from the total amount of ozone measured by the TOMS instrument, the derived distribution of the tropospheric residual shown in the figure is ob-

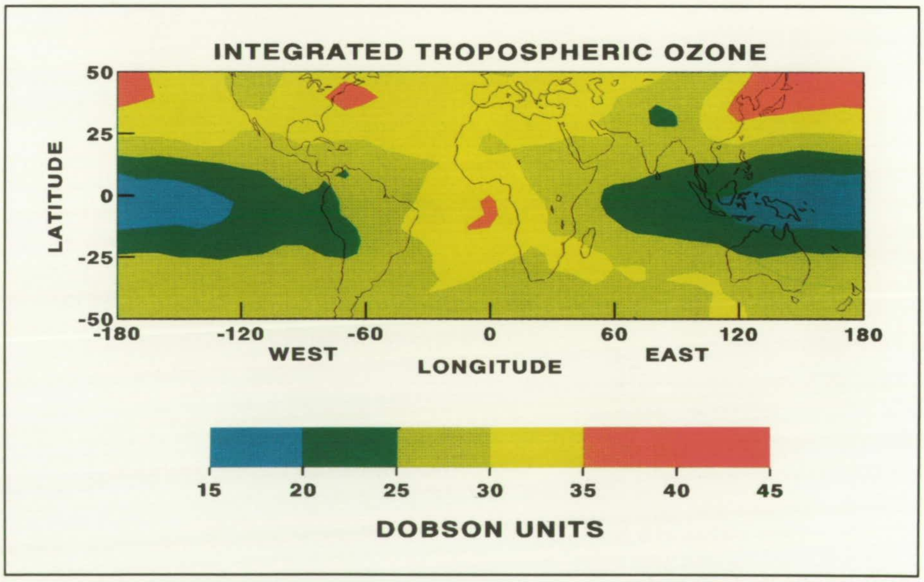

Integrated amount of ozone in troposphere (determined from analysis of TOMS and SAGE measurements) shown in Dobson units (2.69×10^{16} molecules ozone/cm^2).

tained. This residual has been derived from more than 18,000 coincident TOMS and SAGE observations taken between 1979 and 1987.

Of particular interest are the high levels of tropospheric ozone which are observed downwind (east) of Asia and North America, and west of Africa. The plume, found off the coast of Africa, is a result of widespread biomass-burning practices that are commonly used in tropical and subtropical cultures to clear land for agricultural purposes. The plumes found downwind of North America and Asia are probably the result of smog generated from industrialized activities. In all three cases, these plumes, which are a result of man's activities on this planet, may have a significant impact on climate (because tropospheric ozone is an important greenhouse gas) and on the photochemistry of the troposphere.
(Jack Fishman, 42720)

Long-Term Trend in Atmospheric Chlorodifluoromethane ($CHC\ell F_2$)

Concern that emissions of fully halogenated hydrocarbons such as chlorofluorocarbons 11 and 12 (CFC-11 and CFC-12) may deplete stratospheric ozone through chlorine-catalyzed destruction has promoted a search for safer chemicals. Chlorodifluoromethane $CHC\ell F_2$ (CFC-22) is a promising substitute because it contains only a single chlorine atom and is partially removed in the troposphere by reactions with hydroxyl radicals (OH). Recognizing these facts, CFC-22 has been excluded from controls under the Montreal Protocol. The possibility of rapidly increasing use of CFC-22 suggests the need for careful atmospheric measurements, especially because the atmospheric lifetime of CFC-22 is long ($\sim$ 20 years) but uncertain, and absorption by the strong CFC-22 infrared bands could contribute to greenhouse warming.

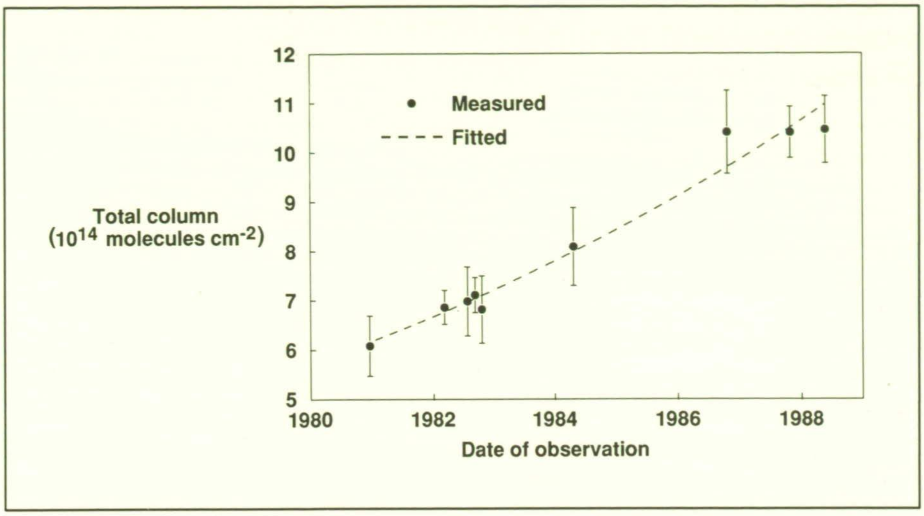

Total column amount of CFC-22 ($CHC\ell F_2$) above Kitt Peak, Arizona.

To derive the long-term trend in the total column of atmospheric CFC-22, Langley researchers have analyzed absorption by the 829.05-cm^{-1} Q branch of CFC-22 in high-resolution solar absorption spectra recorded between December 1980 and May 1988 at the National Solar Observatory on Kitt Peak, near Tucson, Arizona. The results, which are shown in the figure, indicate a 7.8 percent ($\pm$0.8 percent 2 σ) per year average rate of increase in the CFC-22 total column above Kitt Peak. Because of the long lifetime of CFC-22, the measured increase rate should be representative of the global trend; it is substantially higher than corresponding rates for the two most abundant chlorofluorocarbons, CFC-11 and CFC-12 ($\sim$5 percent per year).

Published analyses of surface air samples from the mid to late 1970's and early 1980's yielded average CFC-22 increase rates of 10 to 13 percent per year. The lower rate, derived from solar spectral data up to May 1988, suggests a recent decrease in the percent rate of atmospheric CFC-22 accumulation. This conclusion is supported by the slower growth of CFC-22 industrial production estimated for the present decade ($\sim$8 percent for 1981 to 1984, or approximately one-half that for the 1970's). The declining rate of CFC-22 atmospheric accumulation noted in this work may reverse in the future as CFC-22 is substituted for CFC-11 and CFC-12 in response to the Montreal Protocol.
(Curtis P. Rinsland, 42699 and Joel S. Levine)

GTE/CITE-2 Intercomparison Results: Nitrogen Family

The Global Tropospheric Experiment (GTE)/Chemical Instrumentation Test and Evaluation (CITE-2) focused on the measurement capability for nitric oxide (NO), nitrogen dioxide (NO_2), nitric acid (HNO_3), and peroxyacetyl nitrate (PAN). Results establish the level of measurement uncertainty for the major daytime nitrogen species and are important to photochemists and modelers investigating nitrogen budgets in the troposphere. Three NO, four NO_2, three HNO_3, and two PAN techniques were intercompared. Instrumentation included a laser-induced fluorescence system (NO and NO_2), two NO plus O_3 chemiluminescence techniques for NO and NO_2 (one using the $FeSO_4$ conversion of NO_2 to NO, the other using the arc-lamp photolysis of NO_2 to NO), a tunable-diode laser method (configured either for NO_2 or HNO_3), a filter collection system (HNO_3), a denuder technique (HNO_3), and two separate gas chromatographic techniques (PAN).

The nitric oxide results show a level of agreement of approximately 30 percent at the higher mixing ratios. Below 20 pptv, the level of agreement is 15 to 20 pptv. For the nitrogen dioxide, results show that the $FeSO_4$ converter is not specific to NO_2. The remaining techniques show good correlation at mixing ratios of >100 pptv with levels of agreement of 30 percent. At mixing ratios <50 pptv, however, little correlation in the measurements is noted, the tunable-diode laser tends to be high, and agreement between the two chemiluminescence techniques is at a 20-pptv level.

The nitric acid results suggest that the laser system is high (a factor of 2) compared to the other methods. The denuder and filter methods agree to better than 10 percent for mixing ratios of 300 pptv to 600 pptv, but the agreement deteriorates as the mixing ratio range is decreased. For mixing ratios <150 pptv, the correlation coefficient is less than 0.1. For the peroxyacetyl nitrate, at mixing ratios of 100 pptv to 300 pptv, agreement is of the order of 25 percent. At mixing ratios <100 pptv, agreement is, on the average, 17 pptv with a 95-percent confidence interval of 9 pptv.

(Gerald L. Gregory, 45834, James M. Hoell, Jr., and Richard J. Bendura)

Turbulent Transport of Trace Gases Important for Understanding Climate

An understanding of the chemical and dynamical interactions within the planetary boundary layer (PBL), the depth of which ranges diurnally from several tens of meters to a few kilometers, is fundamental to the discipline of tropospheric chemistry. With an aircraft that is capable of making measurements of both mean and turbulent quantities of the ambient three-component wind field and scalar species distribution (such as temperature, humidity, and trace gases), the rate of deposition of these quantities to the surface, the rate at which they escape from the PBL to the free troposphere (or vice versa), or even the net internal source strength (photochemical production minus loss) in a volume

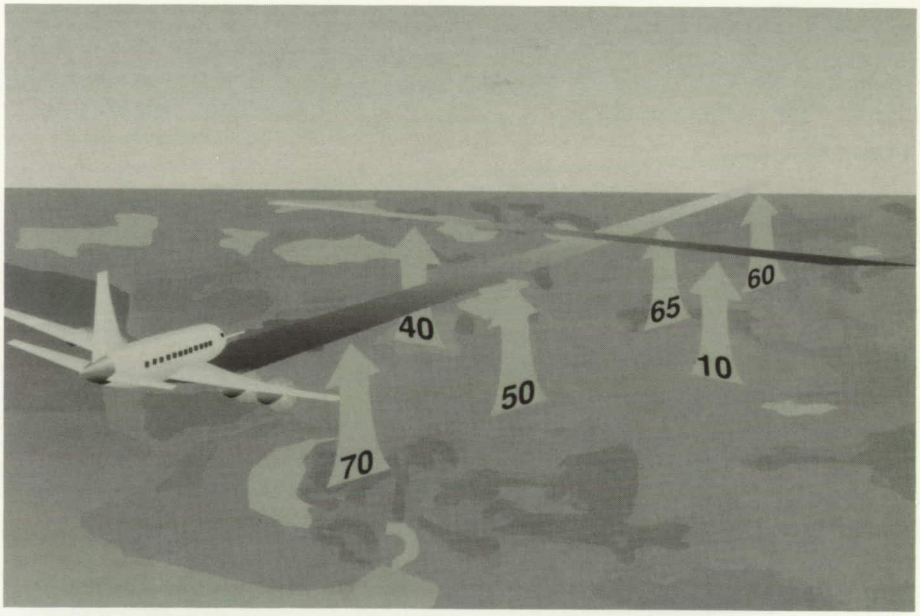

Methane surface flux distribution (mg m^{-2} day^{-1}) over Alaska's Yukon-Kuskokwim delta as measured by TAMMS aboard NASA Electra aircraft. Data were obtained during NASA-GTE Arctic expedition (July to August 1988).

of air can be determined. The Langley Turbulent Air Motion Measurement System (TAMMS) has been developed over the last several years with these and other purposes in mind.

The TAMMS platform was used in NASA-sponsored expeditions to the Amazon Basin (April to May 1987) and the Arctic (July to August 1988) as part of the Global Tropospheric Experiment (GTE) to investigate the role that tropical forests and wetlands play in the global budgets of ozone, carbon monoxide, and methane. Results from the Amazon indicate that the rain forest offers a very low resistance to O_3 destruction by deposition to the canopy (0.1 sec cm^{-1}), thus offering concrete data for tropical deforestation scenarios. While the PBL was seen to be a significant sink for tropospheric O_3, a coincident production of CO was detected which may have resulted from photochemistry acting on the hydrocarbons emitted by the trees. During the Arctic expedition, CH_4 was the key species of interest due to its important role as a greenhouse gas and because the Arctic wetlands are globally significant natural sources for this species. The figure gives the CH_4 surface flux distribution over the Yukon delta obtained during one of the Arctic missions. The numbers shown are the CH_4 flux values in mg m^{-2} day^{-1}. These first-ever data sets have provided the scientific community invaluable information regarding the natural sources and sinks of these important trace gases that impact global climate.
(John A. Ritter, 45693, John D. W. Barrick, and Mary A. Woerner)

Emissions From Biomass Burning: Correlation With Global Ecosystem

An increased public awareness of the relationship of man's and nature's activities in governing the habitability of planet Earth has been seen during the present decade. One process that is currently receiving much attention involves the global burning of forests, fields, and grasslands. Both natural and man-induced fires potentially are leading to changes in the composition of the atmosphere. Major emissions from such burning include carbon dioxide (CO_2), carbon monoxide (CO), methane (CH_4), hydrocarbons (HC's), and nitrous oxide (N_2O). These gaseous emissions, all of which are produced during biomass burning, have the potential to alter atmospheric chemistry and climate. Biomass-burning research at Langley Research Center has focused on determining whether burn emissions vary as a function of ecosystem and vegetation, and if such differences can be correlated to the ecosystem type.

Helicopters and light aircraft have been used to collect smoke samples over large fires in boreal forests, chaparral, and grassy wetlands. While emissions of CO, H_2, CH_4, HC's, and N_2O (based on CO_2-normalized emission ratios; $\Delta X/\Delta CO_2$; V/V; ΔX = specific trace gas species) were found to be nearly the same during the flaming stages of combustion for each ecosystem studied, emissions during smoldering combustion (see the figure) were found to differ substantially. Characterizations such as these should improve assessment of biomass-burning emissions, and thus atmospheric impact, based on global ecosystem and vegetation parameters.
(W. R. Cofer III, 45835 and J. S. Levine)

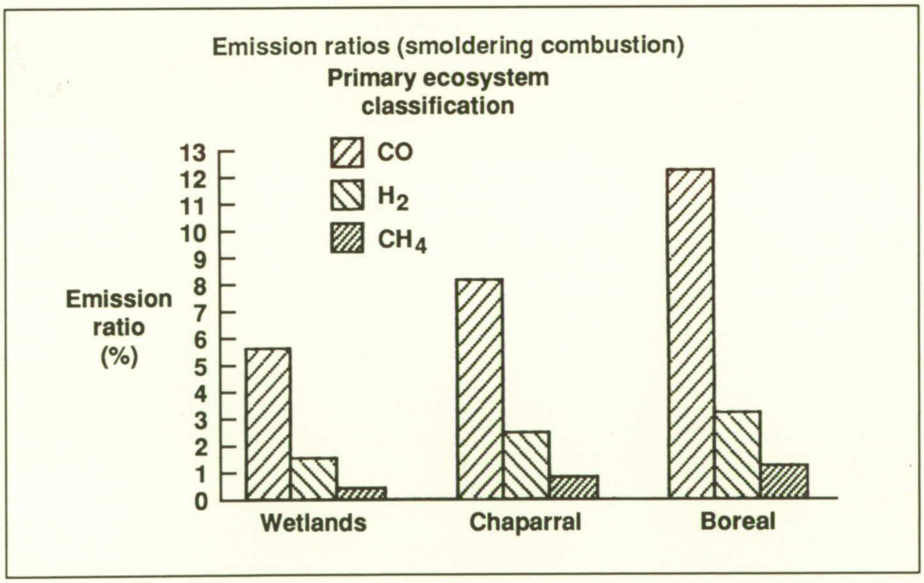

Mean emission ratios from primary ecosystems.

Fertilization Effects of Fire on Biogenic Emissions of Gases

On a global scale, two of the most important sources of environmentally significant trace gases to the atmosphere are biogenic emissions (a source of nitrous oxide (N_2O), nitric oxide (NO), and methane (CH_4)) and biomass burning, i.e., the burning of trees, grasslands, and vegetation. Both N_2O and CH_4 are greenhouse gases that will lead to a global warming. In addition, N_2O leads to the destruction of ozone in the stratosphere, and CH_4 is chemically active in the troposphere. Nitric oxide is chemically transformed to acid rain in the troposphere. Langley researchers have found that burning results in significantly enhanced biogenic emissions of N_2O, NO, and CH_4. The connection between burning and biogenic emissions of gases is that the combustion products of biomass burning are the substances needed by bacteria in the production of these biogenic gases. Ammonium, acetate, and formate were found to be produced in large quantities during biomass burning. Ammonium is the raw material required by nitrifying bacteria to metabolically produce N_2O and NO. Similarly, acetate and formate are needed by methanogenic bacteria to metabolically produce CH_4.

On a global basis, fire is a very common phenomenon. The National Academy of Sciences has estimated that as much as 5 percent

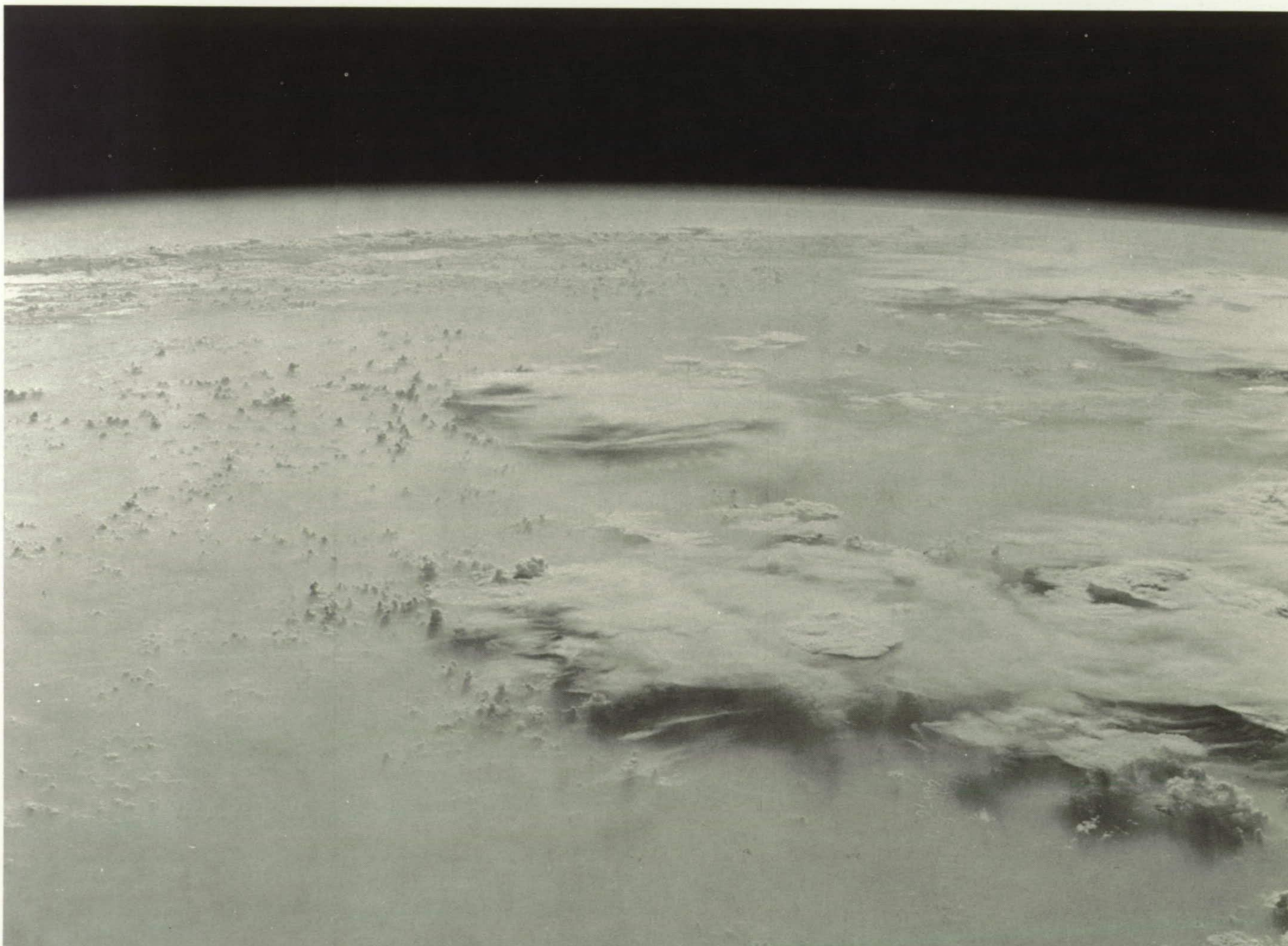

Smoke from human-initiated fires for land clearing in Amazon Basin obscures Earth's surface in photograph taken by Space Shuttle (STS-26) astronauts in September 1988. This smoke cloud represents the largest ever photographed from space.

of our planet's land area burns each year. Recent photographs taken by the Space Shuttle (STS-26 in September 1988) showed the largest and densest smoke cloud ever seen from space. A smoke cloud more than three times the size of Texas was photographed from fires over the Amazon Basin. The vast majority of this burning is human initiated, such as burning for deforestation and land clearing and to remove agricultural stubble after harvest. The new results of Langley Research Center indicate that in addition to being an instantaneous source of environmentally significant trace gases resulting from combustion, burning has a long-term fertilization effect on the production of biogenic gases.

(Joel S. Levine, 45692 and Wesley R. Cofer III)

Carbon Dioxide and Methane Flux Measurements in Arctic Tundra

Carbon dioxide and methane are trace gases that play important roles in the chemistry and radiative transfer of the atmosphere. Both gases are produced and consumed in large quantities by natural environments, but techniques for measuring the gas flux rates over large areas are in an early developmental stage.

Estimates of the surface exchanges of trace gases in tundra environments of Alaska were made using three different measurement approaches based on small enclosures, on a micrometeorological tower, and on aircraft during the summer of 1988. The objective of the experiment was to compare the magnitude and spatial trends of exchange estimates made by the different measurement approaches over these varying spatial scales.

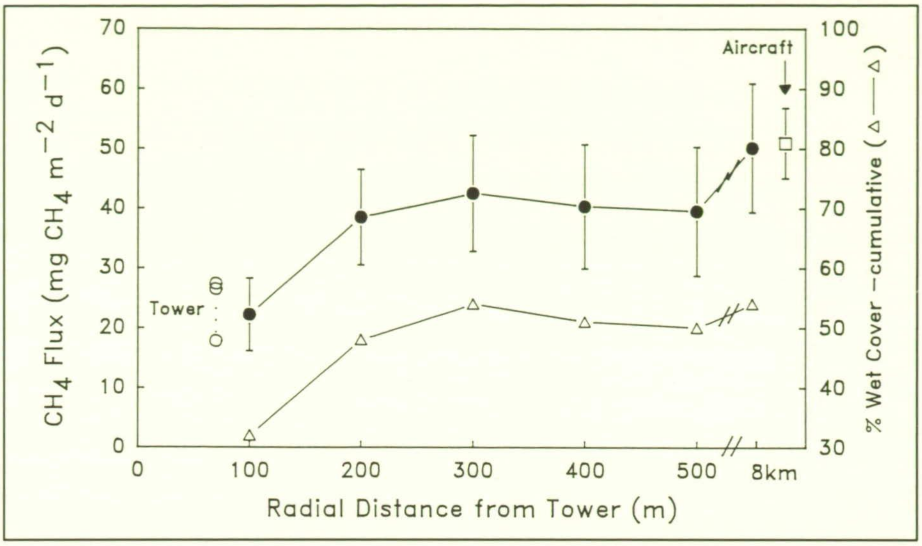

Methane flux at Lake Able site.

SPOT (a French satellite) imagery with 20-m ground resolution was used to map the landscape units "upland tundra," "wet meadow tundra," and "open water" in the vicinity of the tower. Characteristic magnitudes of flux in the three landscape units, determined using enclosures, ranged over an order of magnitude for methane and over a factor of 2 for carbon dioxide. Fluxes for areas having different radii were made by extrapolating chamber measurements based on the proportion of each cover type within that area. The estimates of flux for the different areas are shown as closed circles (• — •), and the proportion of wet cover type is shown by open triangles (△—△). Comparisons are shown with tower measurements (open circles (o....o)) and with aircraft measurements (open square (□)). Mean summer methane flux measured by the tower closely matched the estimates made by extrapolating enclosure measurements to the area around the tower (see the figure). Estimates of carbon dioxide flux also show excellent agreement.

Area-weighted methane flux estimates for a tower-centered circle (approximately 8 km in radius) were compared with the mean of 10 aircraft flux estimates made over the tower. Fluxes derived from the two approaches corresponded very closely and indicated that aircraft measurements provided an accurate estimate of surface methane flux integrated over large areas (see the figure). Extrapolation of the area-weighted flux to the entire 8×10^6 hectare test site resulted in an estimated summer methane flux of more than 4×10^6 kg per day.

(David S. Bartlett, 45850)

Hydrogen Transport Properties of NASP Materials

The transport properties of hydrogen in candidate materials for the National Aero-Space Plane (NASP) must be characterized in order to determine the parameters that affect the mechanical strength of the materials and the hydrogen loss rate in containment volumes. Titanium aluminide alloys have been identified as candidate materials for NASP because of their high strength-to-weight ratio at elevated temperatures, but, unfortunately, these materials are highly reactive to hydrogen. Continual adsorption of hydrogen at the surface and subsequent dissolution into the bulk can substantially affect the mechanical strength depending on the exposure conditions. Further, there is concern that the hydrogen permeation rate may be too severe for acceptable containment integrity.

Currently, a significant interest exists in the Ti-14Al-21Nb alloy. Permeation studies of hydrogen through membranes of this material have shown repeatable data only above 600°C and severe time-dependent behavior below this temperature. Data (presented in the figure) show the dramatic change in surface composition of this alloy as a function of temperature. The data indicate a high carbon and oxygen concentration at the surface at low temperatures, but when the temperature is increased to approximately 400°C, the oxygen and carbon begin to dissolve into the bulk. These original concentrations are virtually eliminated from the surface at higher temperatures. It appears that at temperatures >600°C, the carbon and oxygen dissolution rate exceeds the surface adsorption rate for the carbon and oxygen partial pressures generated by secondary processes (e.g., $p \sim 10^{-5}$ torr CO) resulting in no significant barrier to hydrogen permeation. When the temperature is below 600°C, however, the surface concentration of titanium carbides and oxides is thick enough to noticeably inhibit permeation. The permeation rate K clearly reflects this behavior (see inset in the figure) above and below 600°C.

(R. A. Outlaw, 41433)

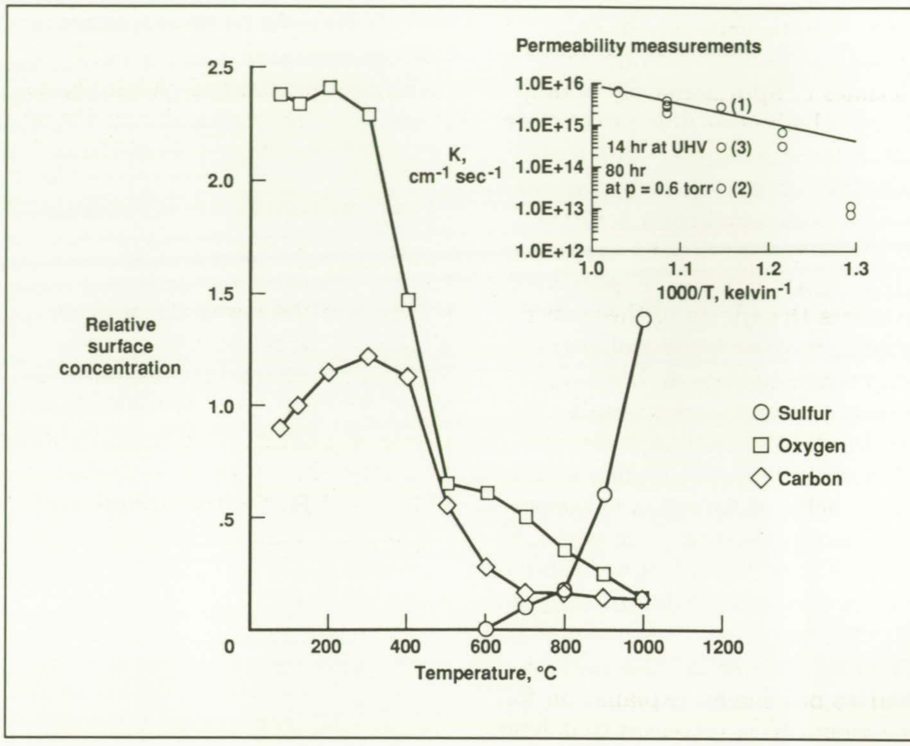

Surface compositional variation as function of temperature for Ti-14Al-21Nb. (Note hydrogen permeability K decrease at temperatures below 600° C (873 kelvin) in inset.)

Global Odd Nitrogen Increases Due to Precipitating Relativistic Electrons

Recently published observations of relativistic electrons (1 to 15 MeV) at geostationary orbit (6.6 Earth radii) indicate that the flux of these energetic particles has increased sevenfold between 1979 and 1985, with sharp declines thereafter. It is well known that many of these energetic particles are lost from the magnetosphere to the atmosphere through precipitation (downward penetration) at latitudes of 50° to 70° in both hemispheres. As these particles interact with the atmosphere, ion chemistry occurs with the for-

mation of nitrogen oxides (with lifetimes of approximately months to years) and hydrogen oxides (with lifetimes of approximately hours). Due to the long residence time of odd nitrogen, it may accumulate in the atmosphere. Calculations have been carried out with the Langley Research Center two-dimensional photochemical and transport model to assess the effects of these energetic electrons on the global tropospheric and stratospheric odd nitrogen. The figure presents the ratio of hemispheric odd nitrogen with the effects of energetic electrons included to values without these effects. Increases of odd nitrogen of up to 40 percent are shown with significantly different temporal variations in the two hemispheres. These odd nitrogen variations appear to provide an explanation for the global NO_2 increases that have been reported in the open literature and are thought to be the principal cause for the anomalously large and currently unexplained global O_3 declines reported in the *Ozone Trends Panel Report* (NASA RP-1208, 1988). The results also appear to establish the existence of the first climatologically important coupling mechanism between the magnetosphere and the lower atmosphere. This research is a collaborative effort with personnel from Goddard Space Flight Center, the Aerospace Corporation, Los Alamos National Laboratory, and STX Corporation. **(Linwood B. Callis, 45806 and Robert E. Boughner)**

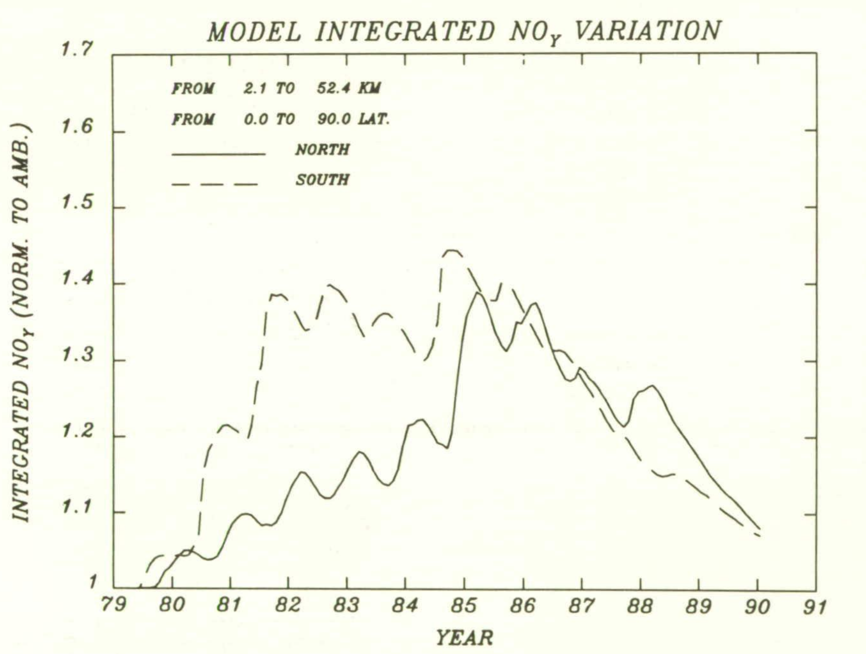

Relative variation with time of hemispherical odd nitrogen due to precipitating relativistic electrons.

Analysis of Cosmic Ray Doses for Conceptual Mars Transit Vehicles

The NASA Office of Exploration has recently promulgated a series of case study activities which are directed toward future manned exploration of the solar system. The earliest scenarios include missions to the Moon and Mars. The problems involved in sustaining human life for extended periods in interplanetary space are numerous and challenging. One such problem pertains to the rather hostile ionizing radiation environment outside the Earth's magnetosphere. The radiations of most importance in interplanetary space with respect to human exposure are the steady flux of high-energy cosmic rays, augmented occasionally by large solar proton flares. Because the earliest exploration missions have rather severe mass constraints, radiation shielding predictions must be as accurate as possible. This accuracy is particularly needed for an envisioned expedition to Mars, because transit times can be 1 year or more.

The Langley cosmic ray transport code has been used in recent studies to provide estimates of shield requirements for a typical Mars expedition scenario. In order to assess radiation exposures for given shield configurations, the transport of the various primary cosmic ray heavy ions as well as all secondary particles generated as a result of nuclear interaction processes must be included. The resultant particle fluxes at a given target point within the shielded volume may then be used to determine the corresponding radiation dose at that point. The incoming radiation from various directions encounters different atten-

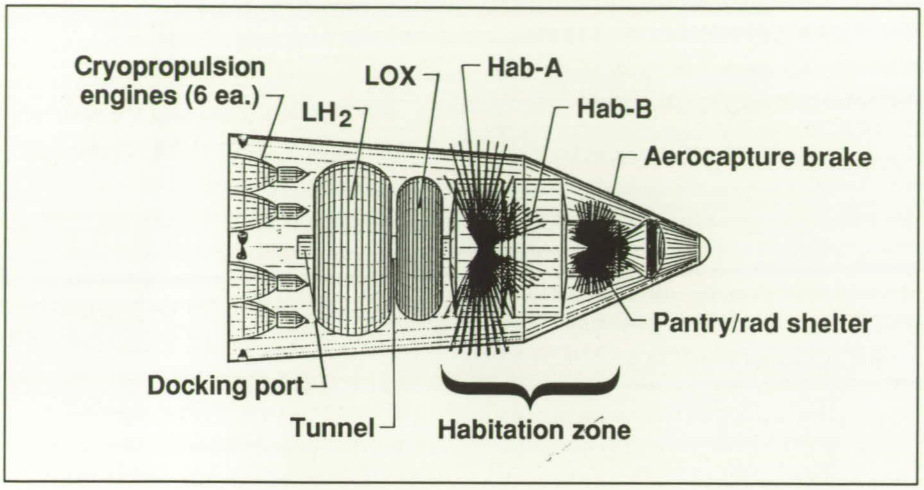

Configuration of Mars Piloted Vehicle (Martin Marietta concept) with sample directional dose patterns for two points: center of habitation module (integrated dose = 29 rem/yr) and center of shielded compartment (integrated dose = 18 rem/yr). Current astronaut dose limit is 50 rem/yr.

Ionizing Radiation Environment in Low Mars Atmosphere

A future goal of the United States space program is a commitment to the exploration and habitation of Mars. Once space travelers leave the protective Earth environment, the hazards of space become an important consideration of such missions. One major concern is the effect of ionizing radiation from high-energy galactic fluxes and solar proton flares.

The Langley cosmic ray transport code and the Langley nucleon transport code (BRYNTRN) were used to quantify the transport and attenuation of the galactic cosmic rays (GCR) and solar proton flares

uating media, and even though the external radiation is isotropic, the internal directional distribution may be highly anisotropic. This effect is illustrated in the figure, which depicts directional dose patterns at two locations within a conceptual piloted Mars vehicle. The lengths of the vectors compromising the patterns around a point are proportional to the incurred doses due to radiation coming from the direction of the vectors. The total dose at the target point may then be evaluated by the appropriate solid-angle integration. Since approximate exposure predictions for such missions approach (or exceed) astronaut dose limits, more detailed calculations that account for specific geometries and materials effects become critical. Proper accounting of the radiation transport and directionality is certain to be of value in the design of adequate radiation protection shields for advanced manned missions.

(John E. Nealy, 44412)

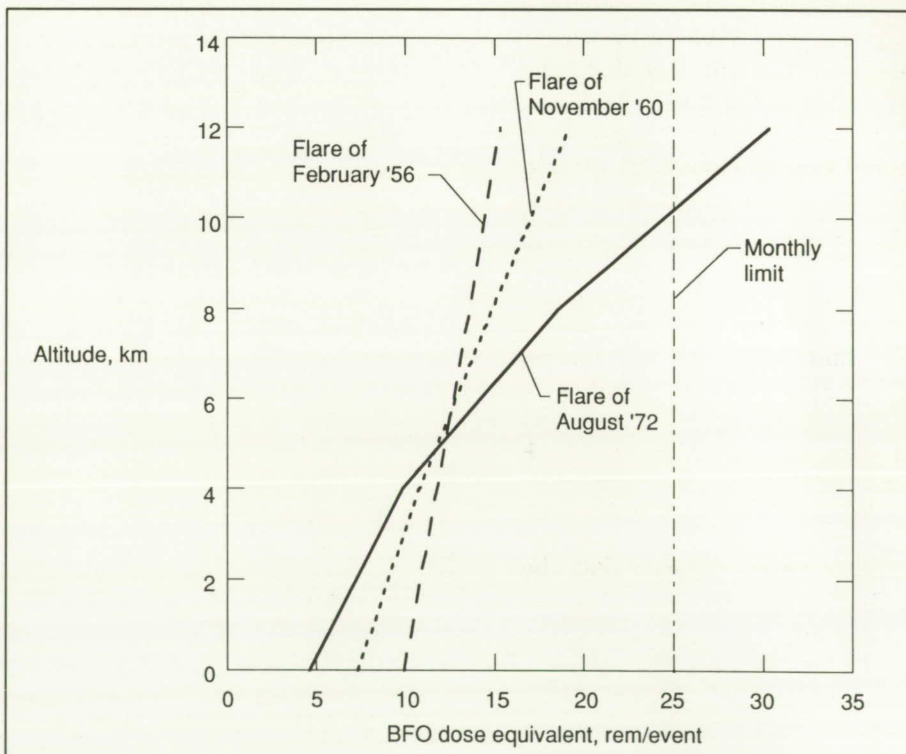

Blood-forming organ dose equivalent versus altitude above Martian surface for three largest solar flares (in terms of dose potential) in last 50 years.

through the Martian atmosphere. Without the atmosphere's protection, the dose incurred from GCR fluxes would be 58 rem/yr, and the doses per event incurred from the solar flare protons would be 411 rem, 110 rem, and 62 rem for the August 1972, November 1960, and February 1956 events, respectively. Conservative results were obtained using a low-density carbon dioxide model of the atmosphere which provided a total of approximately 16 g/cm^2 of protection. At the Mars surface during the solar minimum cycle (maximum GCR flux), a blood-forming organ (BFO) dose equivalent of 12 rem/yr due to galactic cosmic-ray transport and attenuation was calculated. This dose is well below the 50 rem/yr astronaut limit. These GCR doses do not vary significantly at low altitudes because of their penetrating high-energy fluxes; however, the solar flare doses can vary significantly in this altitude regime. The BFO dose equivalents for three solar-flare events were calculated at various altitudes above the Martian surface. Results indicate surface BFO dose equivalents of approximately 4, 7, and 10 rem per event, which is below the 25 rem per month astronaut limit. However, at relatively high (mountain-top) altitudes in the upper atmosphere, the decreased solar flare radiation attenuation may result in doses that require special shielding.

These results indicate that the Mars atmosphere can provide substantial shielding from GCR and solar-flare radiation. The characterization of this radiation environment is valuable in assessing the radiation protection requirements for an extended manned presence on the Martian surface.
(Lisa C. Simonsen, 44432)

Control Moment Gyroscope Attitude Control Law for Space Station Freedom Simulation

Various Space Station *Freedom* system studies have identified the need to simulate the operation of control moment gyroscopes (CMG's) for attitude control. A CMG control law, steering law, and model have been implemented into the Interactive Design and Evaluation of Advanced Spacecraft (IDEAS**2) to meet the simulation and systems analysis need. The control law generates a torque command that provides continuous closed-loop control of the spacecraft attitude, attitude rate, and CMG angular momentum via state feedback and disturbance rejection. The CMG peak angular momentum is minimized, and the CMG secular angular momentum is driven to zero to prevent CMG saturation. Given a torque command, the steering law for parallel-mounted CMG's generates appropriate gimbal rate commands that distribute the CMG momentum vectors such that all inner gimbal angles are equal and all outer gimbals are equally spread out. The double-gimballed CMG's are modeled as error-free actuators that deliver the gimbal rate command subject to user-defined gimbal freedom and gimbal rate limits. All results are written to a project relational data base and made available for output plotting.

As an example, the first plot in the figure illustrates a typical Space Station *Freedom* attitude response to the orbit environment starting from a local vertical, local horizontal (LVLH) attitude. The control

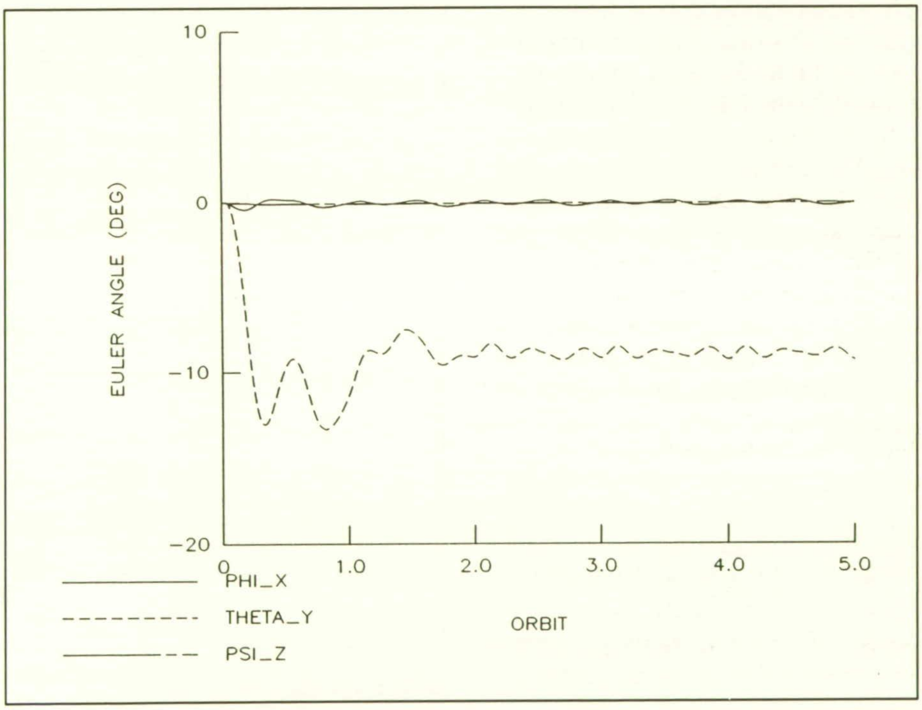

Euler angles versus true anomaly for Space Station Freedom phase 1.

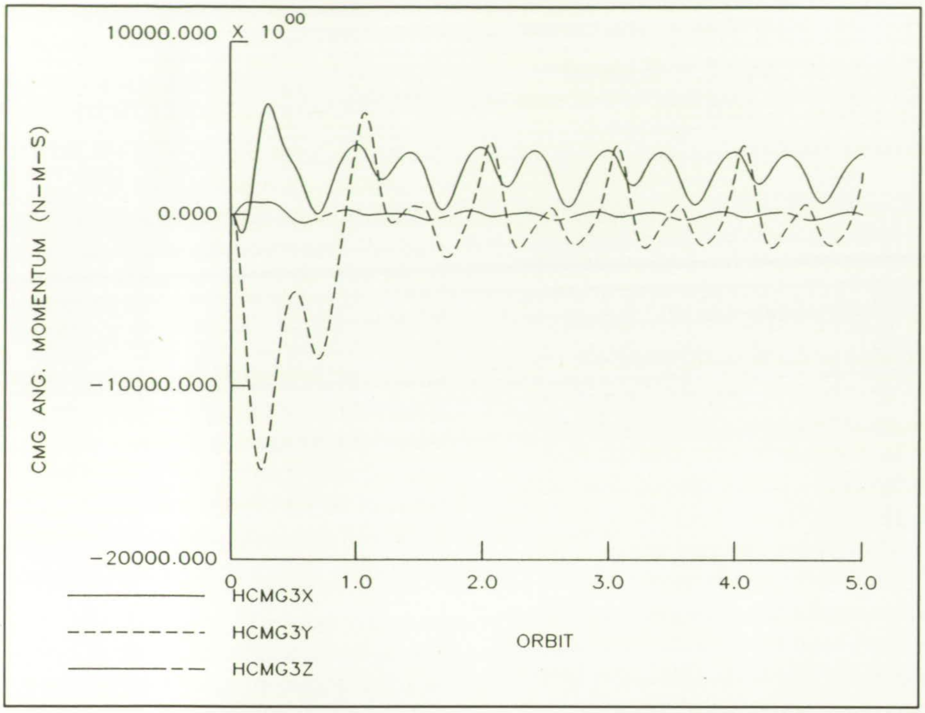

CMG angular momentum (body) versus true anomaly for Space Station Freedom phase 1.

law drives *Freedom* to a steady-state pitch torque equilibrium attitude (TEA) of approximately −8°. Note the low-amplitude nonzero roll rate required to prevent CMG angular momentum accumulation. The second plot illustrates that the CMG angular momentum is bounded with a peak of approximately 14,000 N·m·s over five orbits.

(Brent R. Robertson and Leonard J. DeRyder, Jr., 41946)

Space Station Freedom Reference R&D Evolutionary Configuration

Space Station *Freedom* (SSF) will provide a permanently manned facility in space for conducting scientific research and pursuing commercial space endeavors. The Phase I configuration must evolve over the 30-year operational lifetime to meet growth in user demands for increased resources and capabilities. The Space Station *Freedom* Office at Langley Research Center has developed evolutionary configurations for the space station as a function of future evolution paths or options and has selected one to serve as a reference for the Space Station *Freedom* Program (SSFP). This reference configuration addresses the continued growth of the space station as a research and development (R&D) facility and will support the design-for-growth process at the space station development centers leading to the Preliminary Design Review in 1990.

The reference R&D evolutionary configuration, shown in the figure, meets the growth requirements recommended by Langley Research Center at the SSFP Preliminary Requirements Review in 1988. Dual keels and upper and lower booms are added to the Phase I space station to support attached payloads and provide volume for new facilities and large structures assembly. The configuration provides 275 kW of power in its mature operations phase with solar dynamic power generation added to the baseline

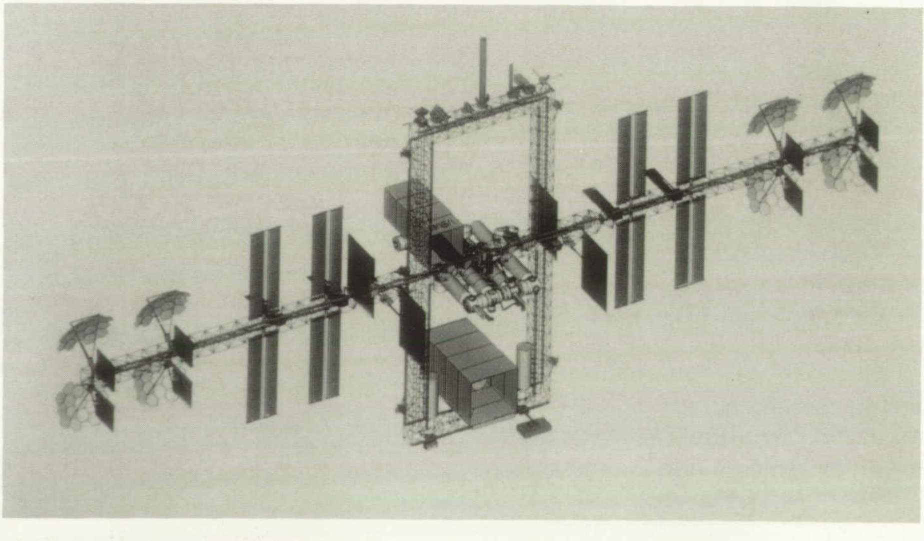

R&D evolutionary configuration.

photovoltaic systems. Three habitation modules support a crew of up to 24 people, and five laboratory modules accommodate pressurized payloads for both the United States and international partners. In addition, provisions exist for up to four "pocket" labs for attached, pressurized payloads.
(Barry D. Meredith, 41960)

Use of Space Station Freedom as Transportation Node for Exploration Missions

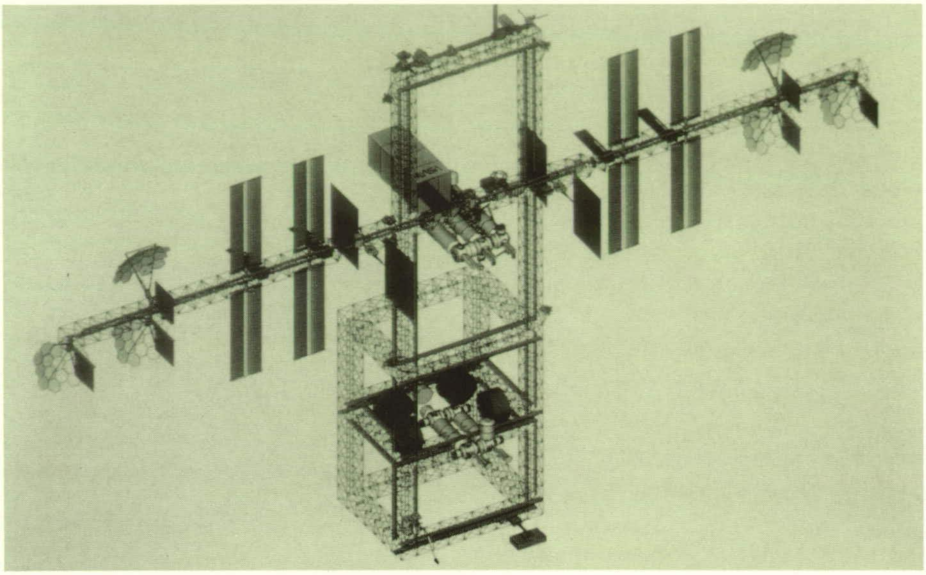

Transportation node for lunar missions.

Space Station *Freedom* will evolve from its baseline, initial configuration to an orbital facility capable of supporting many different categories of users. One potential use of a growth space station is as a facility for the in-space assembly, test, servicing/refurbishment, and fueling of space transfer vehicles for manned lunar and Mars missions.

In support of the Office of Exploration, the Evolutionary Definition Office (EDO) of the Space Station *Freedom* Office has been studying various concepts for adapting Space Station *Freedom* to a facility that could accommodate the in-space vehicle assembly and processing requirements of both lunar and planetary missions. The figure is one concept of a space-station-based transportation node configured to support a manned lunar mission.

The configuration depicted has been analyzed for its controllability, orbital lifetime characteristics, and the effects on the space station's microgravity environment. Results to date indicate that the concept is viable. Analysis of the dynamic behavior of the configuration, resulting from the addition of the large hangar/service bay and accommodation of the massive vehicles, is under way. Additional analyses will be conducted in a number of areas (e.g., on-orbit propellant handling, storage, and transfer).
(Charles P. Llewellyn and Karen D. Brender, 41942)

Vehicle Processing Operations Data Base

In order to perform manned exploration missions, it will be necessary to use Space Station *Freedom* to perform assembly and refurbishment operations on the exploration vehicles. Exploration operations studies have shown that the volume of data to be analyzed and the number of data manipulations that must be performed demonstrate the need for an automated method to assist the operations analyst. The Vehicle Processing Operations Data Base (VPOD) has been developed as the first of a set of tools which can aid the operations analyst in studying the assembly and refurbishment operations requirements and can perform trade studies between various vehicle configurations and operational methods.

The VPOD has the capability to accumulate and manipulate the operations data needed for the analysis of exploration missions. Specifically, for a given mission, the VPOD can maintain a list of the events that need to be performed for a vehicle assembly or refurbishment. This event list is a hierarchical list of data records which can be set up at any level of detail desired. Each event record contains a name field, duration fields, cost fields, crew requirements fields, ground support requirements fields, pointers to assembly and equipment data records that are used to perform the event, and other useful supporting information fields. The assembly

records describe the vehicle element that is being assembled, and the equipment records describe the support equipment that is required to perform the work. Both assembly and equipment records contain a name field, part number field, physical description fields, active and housekeeping resource requirement fields, cost fields, pointers to hierarchically related records, and other useful supporting information fields.

Once the event, assembly, and equipment table data for a mission have been entered and the mission scenario has been defined, the VPOD will produce reports that permit operations analysis of the impact that on-orbit exploration vehicle processing will have on Space Station *Freedom* resources and on on-orbit crew and ground support personnel requirements. The analyst is also able to use VPOD to derive estimates of vehicle processing costs and resource loads that must be accommodated by the Space Station *Freedom* and to perform trade studies, such as automation and robotics versus extravehicular activity or differing on-orbit processing procedures. **(George G. Ganoe, 41940)**

NASA/ONERA Cooperative Study in Hypersonic Aerothermodynamics: Aerodynamic Tests at Mach 6 and Mach 10 in Air

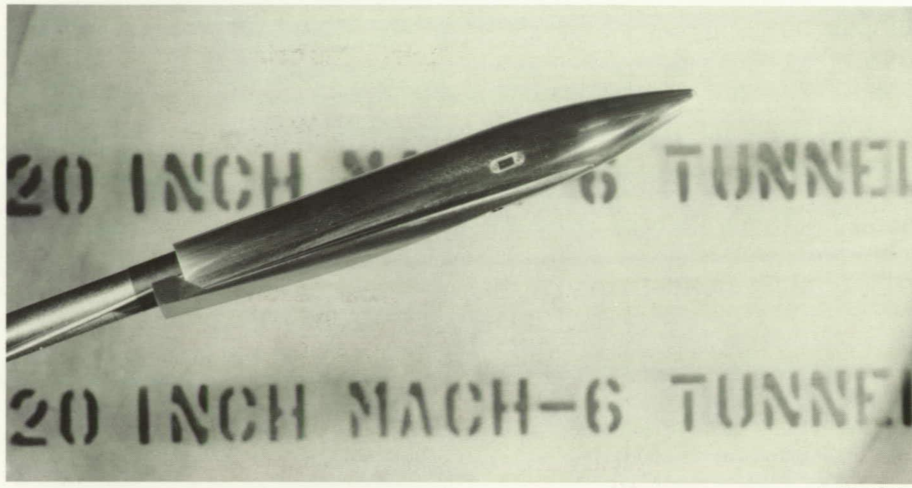

L-88-12,817

Winged reentry configuration installed in 20-Inch Mach 6 Tunnel.

Aerodynamic tests at Mach 6 and 10 have been completed in support of an agreement with the French Aerospace Research Organization ONERA (Office National d'Etudes et de Recherches Aerospatiales) to test the same model in the Langley Research Center and ONERA hypersonic wind tunnels. Under this agreement, force-and-moment tests as well as thermal mappings will be conducted for Mach numbers of 6 and 10 in air and Reynolds numbers from 0.5×10^6 to 7.6×10^6/ft. The purpose is to compare the data obtained and the test techniques used by both organizations for aerodynamic and aerothermodynamic testing.

Force-and-moment tests were conducted in the 20-Inch Mach 6 Tunnel and the 31-Inch Mach 10 Tunnel. Data were taken through an angle-of-attack range from −2° to 45°, at Reynolds numbers from 0.5×10^6 to 7.6×10^6/ft. At Mach 6, a maximum lift-to-drag ratio of 2.7 was achieved at an angle of attack of 11°. The vehicle trimmed at an angle of attack of 21° with no control surface deflections, with a lift-to-drag ratio of 2.2. No significant effects due to Reynolds number were seen other than an increase in drag. At Mach 10, the maximum lift-to-drag ratio was 2.2 at an angle of attack of 15°. The vehicle trimmed at an angle of attack of 24° with a lift-to-drag ratio of 1.9. **(Gregory J. Brauckmann, 45234)**

Flow Quality in 31-Inch Mach 10 Tunnel

A recalibration of the 31-Inch Mach 10 Tunnel was necessary after extensive repair to the square nozzle throat section. The approach was to use survey rakes to measure detailed lateral and longitudinal pitot pressure and total temperature profiles to determine free-stream flow uniformity and conditions over a range of reservoir pressures. Tests were conducted on a 4-in.-diameter hemispherical model (a representative blunt shape) to explore potential blockage effects and to verify the calibration. As the reservoir pressure was increased and the corresponding unit Reynolds number increased from 0.25×10^6/ft to 2.5×10^6/ft, the inviscid test core increased in size from approximately

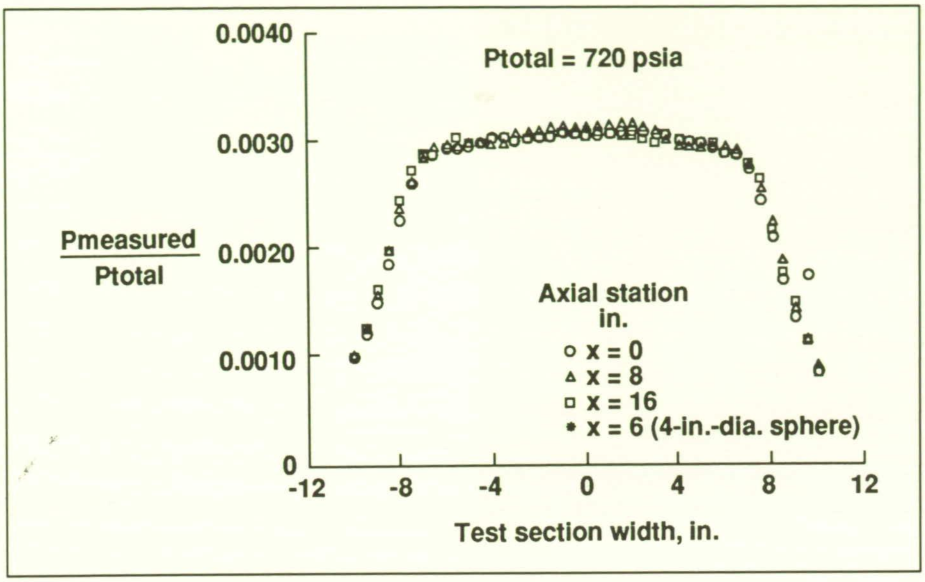

Pitot pressure profile across width of test section.

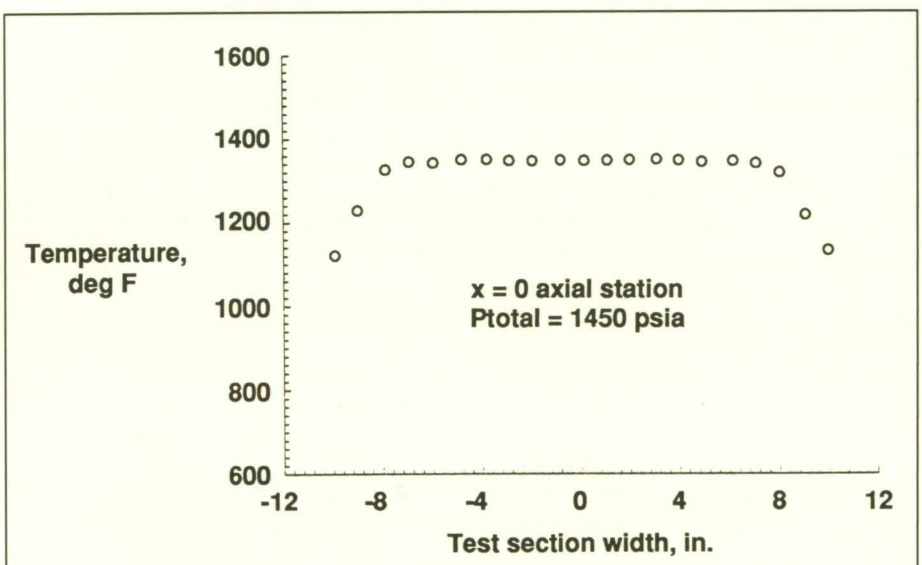

Total temperature profile across width of test section.

10 by 10 in. to 14 by 14 in. At a given axial station, the pitot pressure variation across the inviscid test core was less than 3.5 percent. Within ±3 in. of the nozzle centerline (6-in. core), where most models are tested, the pitot pressure variation was less than 1.5 percent. The smallest variations were observed at a reservoir pressure of 350 psia, where pitot pressure variation was less than 2 percent across a 12- by 12-in. test core and less than 1 percent in the center 6 in. of the test core.

Excellent axial flow uniformity is shown in the first figure in which the longitudinal variation in pitot pressure (averaged over a 6-in. test core) was less than 2 percent for 16 in. of the test section. Stagnation pressure measurements on the hemispherical pressure model agreed to within ±0.5 percent of the center pitot probe on the rake. This indicates absence of model blockage effects and verifies the pitot pressure rake results. Total temperature profiles showed that temperature variation was less than 0.5 percent in the test core for the range of reservoir pressure. These highly uniform total temperature profiles, shown in the second figure, indicate flow symmetry about the test section centerline and substantiate the test core size deduced from the pitot pressures. Together these results indicate that the square nozzle of this facility provides excellent flow uniformity, particularly within the center 6 in. of the test core.
(W. F. Hinson, 45231 and T. P. Dye)

Hypersonic Investigation of 5° Winged-Cone Configuration

One proposed generic transatmospheric vehicle (TAV) concept will utilize a large number of annularly arranged air-breathing engines to accelerate into low-Earth orbit. The configuration shown in the figure represents this vehicle type without engines; this configuration was tested to provide force-and-moment data to calibrate the computational fluid dynamic codes required to predict the aerodynamics of TAV concepts. The configuration incorporates a 5° conical

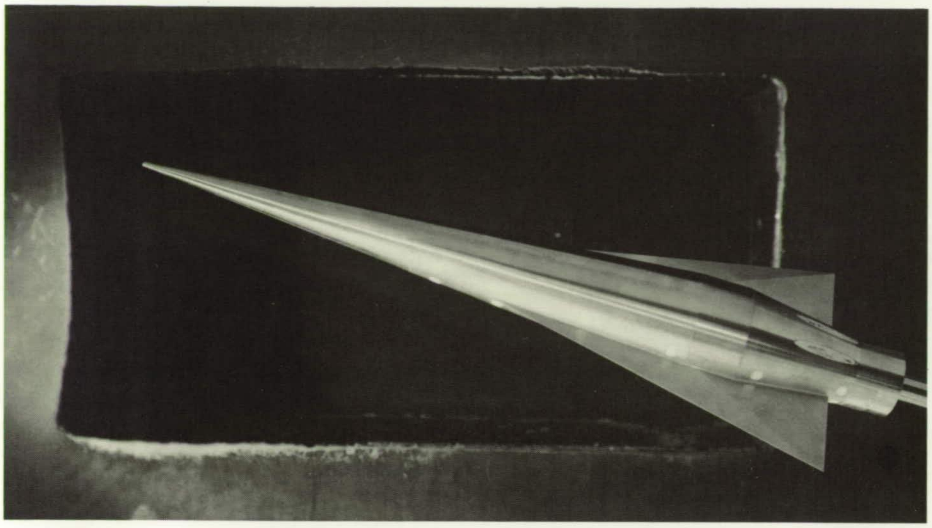

5° winged-cone model mounted in Hypersonic Helium Tunnel. L-88-8646

fuselage forebody, a wing with an aspect ratio of 1.0, and a truncated cone/cylinder afterbody. Longitudinal aerodynamic investigations were made in the 20-Inch Mach 6 Tunnel and the Hypersonic Helium Tunnel (Mach 20) at angles of attack from –4° to 20°. Test Reynolds numbers based on fuselage length ranged from 3.5×10^6 to 5.0×10^6 in air at Mach 6 and from 3.1×10^6 to 23.0×10^6 in helium at Mach 20. Aerodynamic effects of nose bluntness, wing longitudinal position, and wing incidence were determined during these studies.

Preliminary Mach 6 results indicate that the longitudinal center of pressure is at 65 percent of the fuselage length for the zero-incidence, mid-located wing configuration. The corresponding maximum lift/drag ratio was approximately 2.8 and occurred at an angle of attack of 7°.

These data obtained for the 5° winged-cone configuration provide the experimental hypersonic aerodynamic characteristics for Langley Research Center studies of the accelerator TAV concept that will encompass the flight Mach number range.
(W. Pelham Phillips, 45239)

Aerodynamic Characteristics of Systematic Series of Irregular Planform Wings at Mach 10

Tests have been conducted in the 31-Inch Mach 10 Tunnel on a systematic series of irregular planform wings. For this study, the planforms were referred to as wing-fillet combinations with the inboard, more highly swept portion of the planform being defined as a fillet. This study is directed toward improving the aerodynamics of aircraft as well as advanced aerospace vehicles.

The present series consists of five basic planform shapes of constant area and aspect ratio; the variables include leading- and trailing-edge sweep. The basic wings have leading-edge sweeps of

Basic 35° swept wing in combination with various fillets Λ_f. L-89-2137

25°, 35°, 45°, 53°, and 60°. The irregular planforms were formed by extensions to the basic wings in 5° or 10° increments up to a maximum of 80°. Also included for the 45° wing series were the effects of wing thickness ratio. The angles of attack ranged from approximately -4° to 56°; this range was sufficient to cover the angles for maximum lift-to-drag ratio $L/D_{\max}$ (for maximum cross range) and maximum lift coefficient $C_{L,\max}$ (for minimized aerodynamic heating) at 0° of sideslip. Results of this investigation indicate that the addition of fillets resulted in increases in $L/D_{\max}$ primarily by reducing the minimum drag coefficient $C_{D,\min}$ with large increases in $C_{L,\max}$ for each wing. Increasing wing thickness ratio resulted in large reductions in $L/D_{\max}$, small reductions in the value of $C_{L,\max}$, and little or no effect on the center-of-pressure location variation with angle of attack for a given wing.

(Bernard Spencer, Jr., 45245)

Experimental Investigation of Proposed Lifting-Body Assured Crew Return Capability Vehicle

NASA is considering the use of one or more crew return vehicles docked at Space Station *Freedom*. These vehicles must provide speedy, dependable return of the astronauts to Earth in the event of an accident or crew emergency. Configurations varying from ballistic shapes to winged reentry vehicles are under study. One concept proposed by Langley Research Center has a lifting-body shape that produces moderate lift/drag L/D values over the speed range, provides some cross range performance, and offers the possibility of a conventional landing.

A series of wind tunnel investigations has been performed to define the aerodynamic/aerothermodynamic characteristics from low-subsonic to hypersonic speeds. Tests have been conducted in the Calspan 8-Foot Transonic Tunnel, the Langley Unitary Plan Wind Tunnel, and the Langley 31-Inch Mach 10 Tunnel. A summary analysis of the vehicle's aerodynamic performance over the test Mach range with controls undeflected is presented in the figure. The vehicle was stable and trimmed at near maximum lift/drag values at subsonic and hypersonic speeds thus maximizing reentry cross range capability and producing favorable landing characteristics. For the Mach range 1.5 through 2.7, pitch control deflection is needed to trim the vehicle to higher angles of attack where lift, lift/drag ratio, and directional stability C_{n_β} are positive.

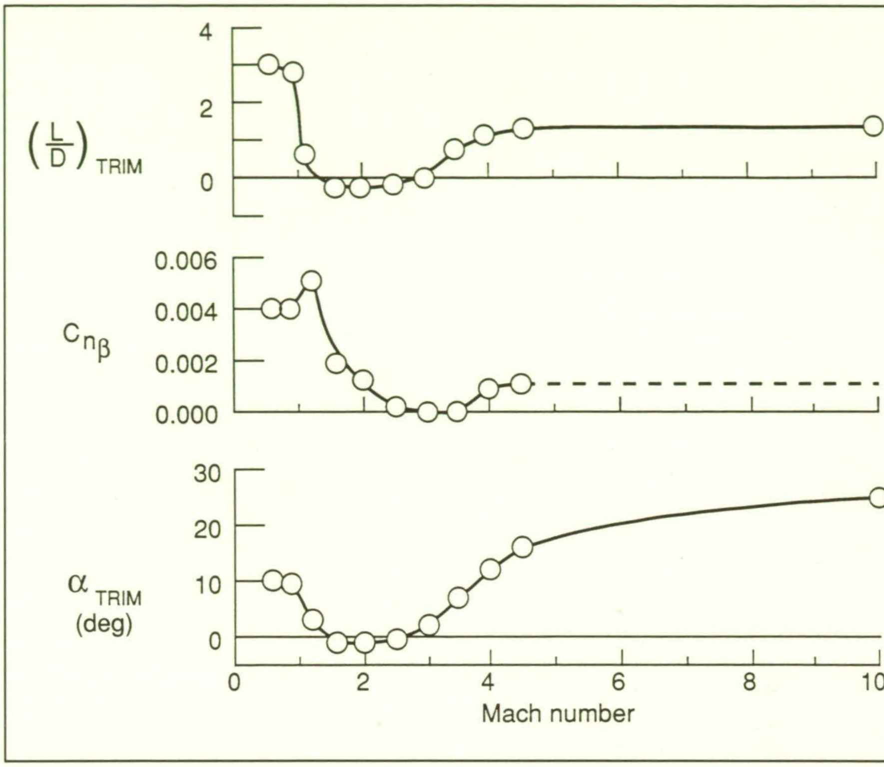

Aerodynamic performance of lifting-body with controls undeflected.

Thermal mapping patterns were obtained in the 31-Inch Mach 10 Tunnel using the phase-change paint technique. The tests were performed over a range of angles of attack from 0° to 45° at unit Reynolds numbers of 0.5×10^6/ft and 2.0×10^6/ft. The effects of angle of attack α on thermal mapping patterns indicated significant leeward heating over the canopy and streak heating on the fuselage sides. As expected, heating over the canopy decreased with increasing angle of attack or effective leeward

shadowing; however, fuselage streak heating remained for all angles of attack. For this factor-of-4 increase in unit Reynolds numbers, no effect of Reynolds number on thermal mapping patterns was noted.
(George Ware, 45246, John Micol, and Thomas Horvath)

Confirmation of Low-Density Flow Environment in Hypersonic CF_4 Tunnel

The Hypersonic CF_4 Tunnel uses tetrafluoromethane (CF_4) as a test gas, which allows a partial simulation of real-gas effects for hypersonic entry vehicle aerodynamic and aerothermodynamic research. This facility is usually operated with a reservoir pressure of approximately 1500 psia, which produces a postshock unit Reynolds number of 18,600/in. Tests on vehicles that fly at high altitudes require a lower density, lower Reynolds number test environment. (An example of a class of high-velocity, high-altitude flight vehicles with blunt configurations is the Aeroassisted Space Transfer Vehicle.) The facility has been successfully operated at a reservoir pressure of approximately 100 psia and a corresponding postshock unit Reynolds number of 1700/in. Computed free-stream quantities in the test section were based on measured temperature and pressure in the reservoir and pitot pressure in the test section.

To verify that the equations and the range of CF_4 properties used to describe the expansion of flow through the nozzle with a reservoir pressure of 1500 psia were still valid at 100 psia, the distribution of pressure over the face of a 1.77-in.-diameter hemisphere was predicted by a computer code. In a parallel effort, pressure distributions over an identical body were measured in the tunnel with operation over a range of reservoir pressures and were compared with the computed distributions. Agreement between the computed and measured pressure distributions over the hemisphere indicates that the computed test section free-stream quantities are valid in the low-density, low-Reynolds-number environment.
(William L. Wells, 45237, Raymond E. Midden, and Hubert H. Senter)

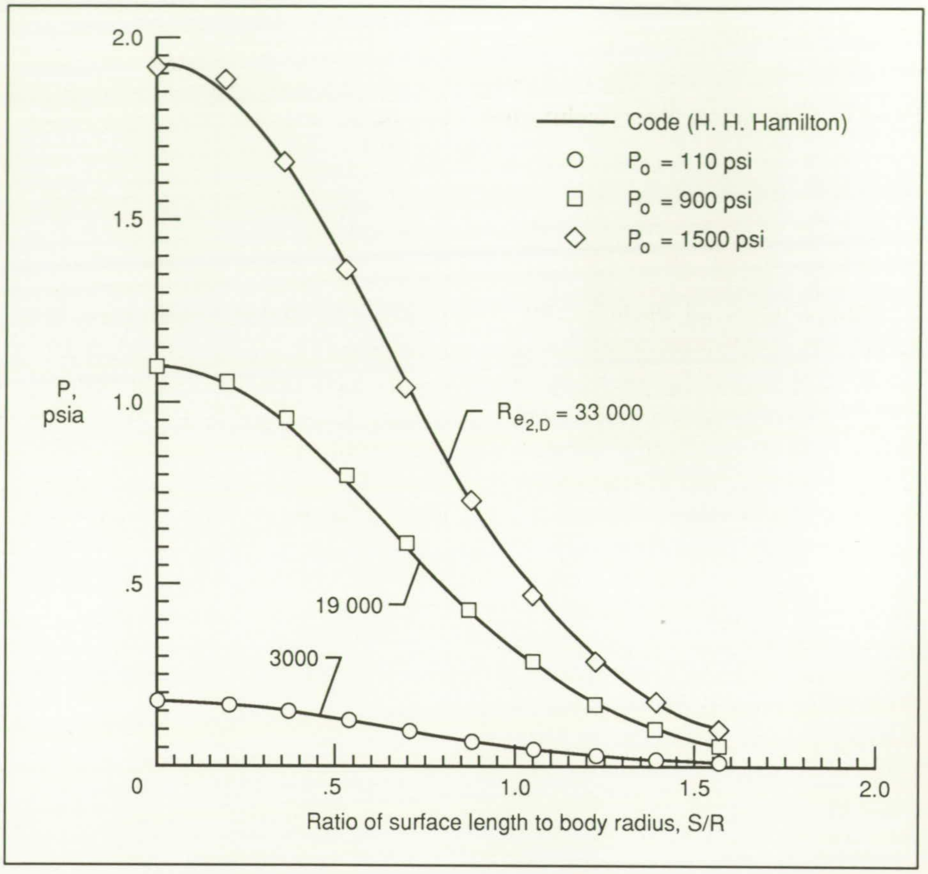

Measured and computed pressure distributions on hemisphere at three reservoir pressures (P_o) in Hypersonic CF_4 Tunnel. Hemisphere stagnation point is at $S/R = 0$.

Upper Atmosphere Density Measurements From Accelerometry

A region of the Earth's atmosphere exists in which limited data can be gathered due to this region's inaccessibility by ordinary means. This region is below orbiting spacecraft altitudes and above altitudes of typical meteorological sounding rockets and ground lidars. The Space Shuttle orbiter, however, passes through this region upon each reentry and, with adequate onboard accelerometry, can provide important atmospheric data

heretofore unobtainable under most practical circumstances.

Atmosphere density can be calculated in this region using techniques developed from planetary entry science investigations for Mars and Venus. The combination of acceleration and pressure measurements from flight, aerodynamic force coefficients from wind tunnels, and computational studies provides the necessary ingredients to calculate density values along the Space Shuttle orbiter's flight path.

The High-Resolution Accelerometer Package (HiRAP), which is a research experiment on the Space Shuttle orbiter with a 10^{-6} g resolution (where g is the acceleration due to gravity), provides reliable acceleration measurements for the first time from approximately 160 km down to approximately 90 km, thereby covering most of this inaccessible region. In addition, the Space Shuttle orbiter's inertial navigation measurement unit (IMU) provides acceleration values from approximately 90 km to touchdown, thereby providing overlap and connecting with the region regularly assessed by earlier researchers. Over a period of 3 years, data from 10 flights have been collected and analyzed, thus providing a significant gain in the data base for this region. The data from these flights are similar to satellite observations in that they cover a very wide horizontal distance, thus providing a component not available to the near-vertical profiles collected by sounding rockets and ground lidars. The ground tracks for each of the 10 flights can be seen in the figure.

Also shown are the density measurements normalized by the 1976 United States Standard Atmosphere model. As seen, the data exhibit wave features that are not predicted by the current atmospheric models in this region. The exact nature of these waves and their causes are not fully understood at this time. However, based on the limited sample of data collected, the amplitude has a dependence on solar activity and time of year, and the wavelength is nearly constant (~ 37 km vertically), but the wave phase is independent of altitude.

These findings are of significance because the deviations of measured

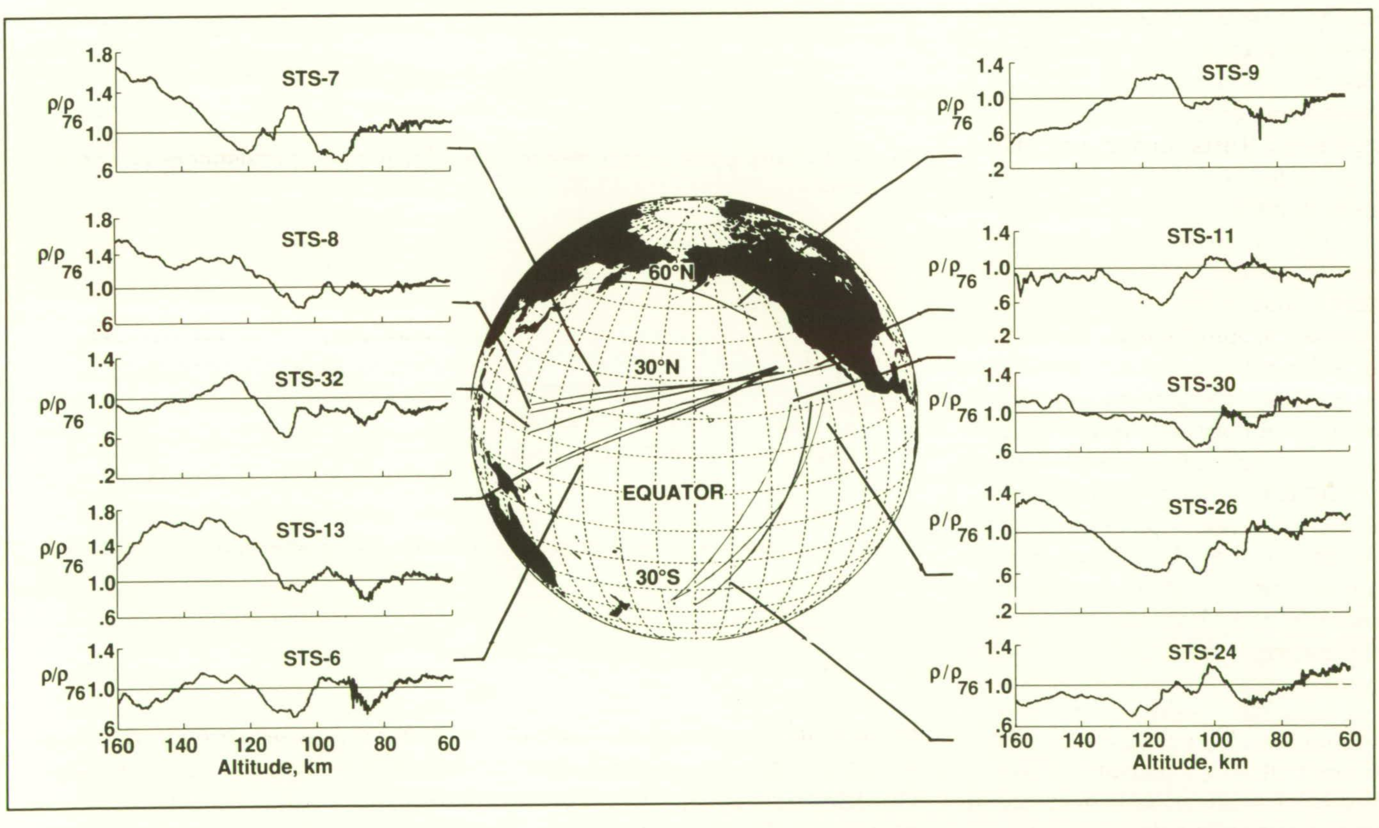

Space Shuttle accelerometry (HiRAP/IMU) density measurements.

density from current atmosphere models on any given flight are large (more than 50 percent). Thus, these measurements, although limited in number, provide some insight for improving atmosphere models in this altitude regime. Furthermore, a potential exists for having an impact on decisions regarding design of and applications to future NASA missions, such as an aerobrake.

(R. C. Blanchard, 44391)

Code Calibration in Support of Aeroassist Flight Experiment

The Aeroassist Flight Experiment (AFE) is a project designed to obtain critical flight data that will be used in the validation of computational fluid dynamics (CFD) approximation methods. These CFD codes require flight data for validation because of the complexity of the important physical processes that must be modeled in order to accurately predict aerodynamic forces and convective and radiative heating for planned Aeroassisted Space Transfer Vehicles (ASTV's). Until validation-quality flight data become available, the codes must be calibrated with available experimental data sets that include some elements of the intended application. The objective of this research is to conduct calibration runs of the Program LAURA (Langley Aerothermodynamic Upwind Relaxation Algorithm) to assess its strengths and weaknesses with regard to eventual AFE and ASTV applications.

Calibration runs have been made using perfect-gas wind tunnel tests over a scale model of the AFE and on both flight and ground tests that challenge some aspect of the thermochemical nonequilibrium model. In the first case, the gas model is simple, but the grid-related problems of defining the real vehicle are present. In the second case, the vehicle geometries are simple, but nonequilibrium processes must be modeled correctly in order to compare with the experimental data. These tests of the thermochemical nonequilibrium model include ballistic range data for shock shape, shock tunnel data for shock shape and interferograms, project FIRE

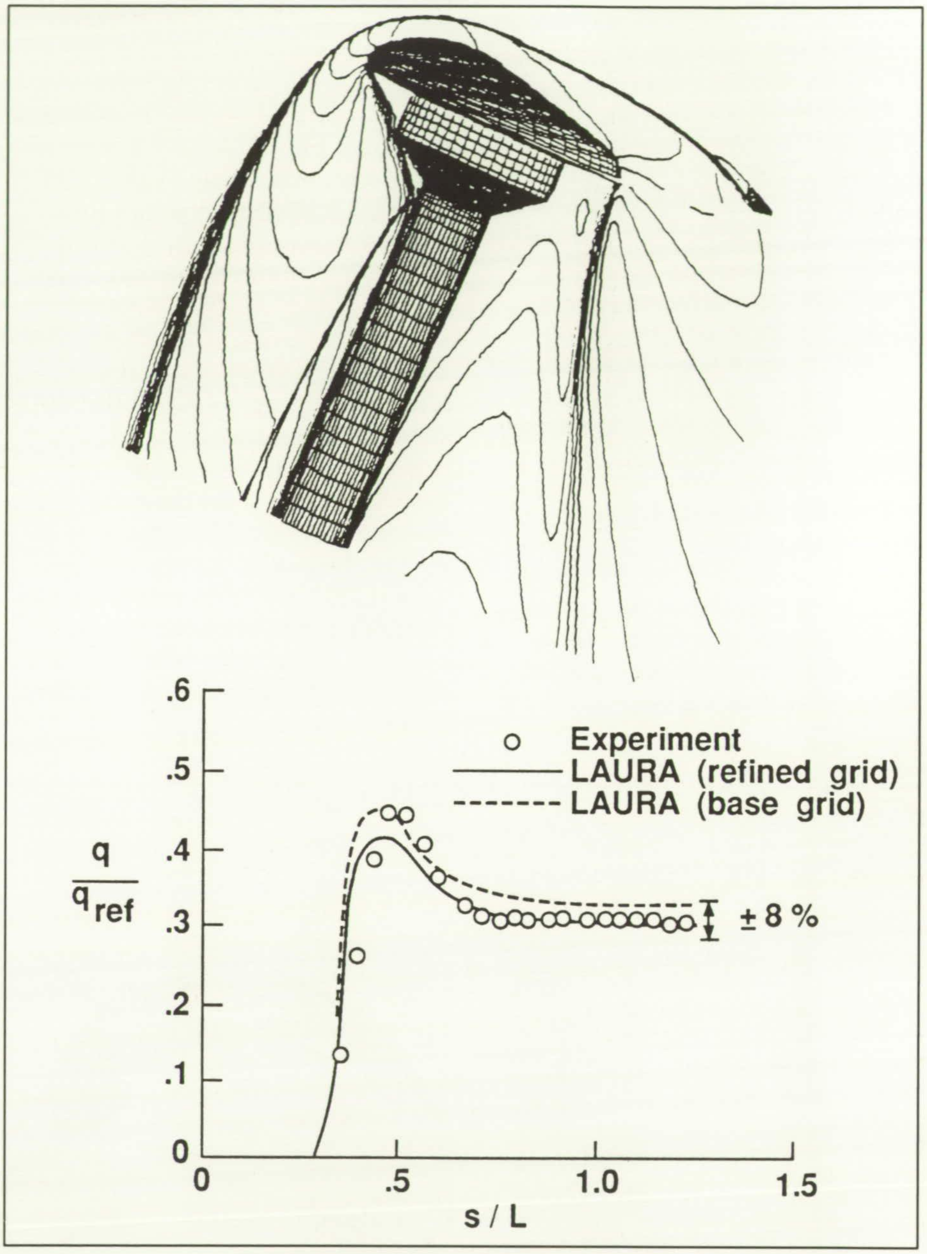

Mach number contours over AFE in wind tunnel test at Mach 10 and associated heating on wind side of sting as predicted by Program LAURA.

(Flight Investigation Reentry Environment) data for surface heating, and project RAM C (Radio Attenuation Measurement C) data for electron number density. Comparisons are generally good, except for some anomalies in the predicted electron number density profiles which are still under investigation. (The results are documented in AIAA Paper 89-1673.) The calibration data sets provide necessary, but not sufficient, check points in the code validation process for AFE and ASTV applications.

In the figure, Mach number contours over the AFE in a wind tunnel test at Mach 10, as predicted by Program LAURA, show sharply captured shock waves over the aerobrake and sting as well as the free shear layers flowing off the aft corner of the brake. The corresponding heating on the wind side of the sting (behind the shock), as obtained by experiment and calculation using a nominal and a refined grid, is presented at the bottom. The predictions are within the experimental error, which is given as 8 percent. Some thickening of the peak heating region near the shear layer impingement point is believed to be caused by an inadequately resolved shear layer in an oblique, transverse direction to the high-gradient region near the separation point.
(Peter A. Gnoffo, 44387)

Flight Stagnation-Point Heating Calculations on AFE

Calculated total stagnation-point heating rates (both convective and radiative) have been obtained along the nominal flight trajectory for the Aeroassist Flight Experiment (AFE) vehicle. Calculations were performed on a sphere with an effective radius of 2.16 m, which has been shown to produce stagnation-point heating rates that match those obtained using a three-dimensional Navier-Stokes code on the full-scale AFE vehicle. Most of the convective heating rates were obtained using a Viscous Shock Layer (VSL) code with a five-species nonequilibrium chemical model and a surface catalytic efficiency similar to that used for the Space Shuttle thermal protection tiles. The VSL code was used because it greatly reduced the computational time required to compute points along an entire trajectory. The nonequilibrium radiative heating rates were estimated from a correlation developed from the results of detailed calculations.

The free-stream conditions used in the computations correspond to selected points along the entry, aerobraking, and exit phases of the AFE trajectory, where the altitude and velocity ranges considered are 122 km to 75 km and 9.9 km/sec to 7.5 km/sec, respectively. Peak heating occurs at approximately 117 sec (76 km) and produces a radiative equilibrium wall temperature of approximately 1785 K, which is near the upper limit of the surface tile.

For times greater than 325 sec where the altitude is above 90 km, the heating rates calculated by the VSL code level off. In this region, the atmospheric density is dropping rapidly, and the VSL equations are no longer completely valid. In an effort to extend the heating results to higher altitudes, a stagnation-region Navier-Stokes code has been used both without (N-S) and with (N-S ws) wall slip.

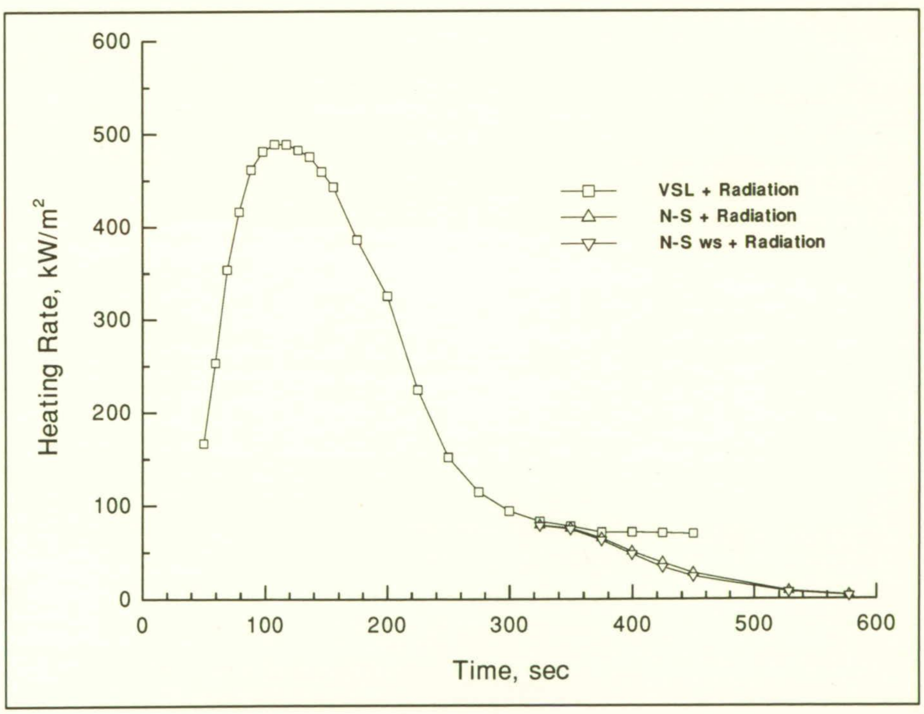

Total stagnation-point heating rates on AFE.

The heating rates obtained from this code match the VSL results at the lower altitude and decrease with increasing altitude as would be expected. It can also be seen that including wall slip for this case has little effect on the heating rates.

These calculations are the most complete set of continuum stagnation-point heating rates that have been obtained over the high heating portion of the AFE trajectory and are being used to define the aerothermodynamic environment needed for the heat shield design. **(Harris Hamilton, 44365, Roop Gupta, and Jim Jones)**

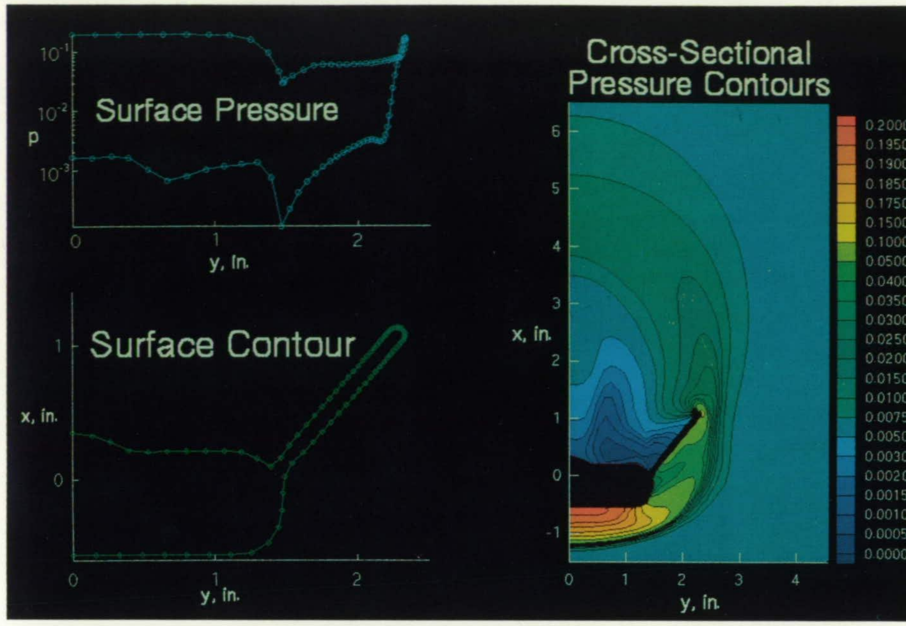

Lifting-body pressure distributions in outflow plane at $M_\infty = 10$ *and* $\alpha = 25°$ *(x and y dimensions in in.).* L-89-6538

Lifting-Body Flow Field Analysis

Currently within NASA, an ongoing activity exists to define candidate approaches for crew return from Space Station *Freedom*. A number of ACRC (Assured Crew Return Capability) concepts have been identified for study over the next 2 years. Interest at Langley Research Center has focused on a lifting-body shape derived from work initiated by NASA and the United States Air Force in the late 1960's in studying the Dyna-Soar, HL-10, X-24, and M2-F2 vehicles.

Refinement of the operational characteristics of the lifting body requires a detailed analysis of its aerodynamic and aerothermodynamic characteristics through the use of CFD (computational fluid dynamics) techniques. The CFD analysis of this complex shape requires not only robust CFD software, but also state-of-the-art surface definition, grid generation, and data presentation techniques. The surface was defined using spline interpolations of measured cross sections taken from a wind tunnel model. The surface and volume grids were constructed by a combination of algebraic techniques and transfinite interpolation. An inviscid version of the Program LAURA (Langley Aerothermodynamic Upwind Relaxation Algorithm) code was used for the CFD analysis.

The pressure field at the aft end of the vehicle for a free-stream Mach number of 10 and an angle of attack of 25° is shown in the figure. In the lower left corner is a plot of the surface contour in the outflow plane; this plot indicates the complexity of the surface geometry. The symbols on the contour show the location of surface grid points. In the upper left corner is a log plot of nondimensional pressure as a function of the same axis as the surface contour plot; the axis similarity allows a direct comparison between surface pressure and surface location. On the right is a contour plot of the nondimensional pressure field in the outflow plane with its corresponding color bar. Surface pressures derived from CFD computations can be used directly in structural analysis, whereas the computed velocity fields can be combined with approximate boundary-layer techniques to determine surface heating. **(K. J. Weilmuenster, 44363)**

Approximate Three-Dimensional Inviscid Hypersonic Flow Field Method

Engineering methods that calculate surface heating rates are important tools in the preliminary design of reentry vehicles. One approach in determining the aerothermal loads is to couple an inviscid

flow field solution with a viscous boundary-layer technique. For this purpose, an approximate solution technique has been developed for three-dimensional, inviscid, hypersonic flows using an inverse Maslen method.

Simplifications to the exact inviscid flow for hypersonic speeds include using an algebraic expression for the pressure and assuming approximate stream surfaces in the shock layer. The solution procedure involves iteratively changing the shock shape in the subsonic-transonic region until the correct body shape is obtained. Beyond this area, the shock surface is determined using a marching scheme. Surface pressures in the planes of symmetry are shown for a paraboloid at an angle of attack of 8° and a free-stream Mach number

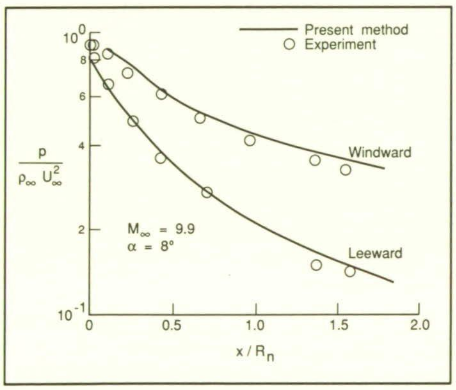

Axial surface pressure distribution on paraboloid.

of 9.9 in air. Note that the pressures are referenced to the free-stream dynamic pressure and are presented as a function of the axial distance from the nose of the paraboloid. Good agreement is observed between results from the present method and the experimental data in both the windward and leeward planes of symmetry. In addition, the speed of the calculations makes the procedure attractive for engineering design applications. **(Christopher J. Riley, 44387)**

Direct Simulation Monte Carlo Analysis on Parallel Processors

The direct simulation Monte Carlo (DSMC) method has proved to be an extremely useful tool for analyzing the aerothermodynamic environment of entry bodies in rarefied and transitional flow regimes where traditional Navier-Stokes methods are invalid. However, at the lower altitudes of these flight regimes, the computational times required can be quite large. One approach for speeding up the calculations is through the use of parallel processing in which the computational work is distributed among many individual processors. Because the DSMC method is based on a probabilistic simulation of the behavior of thousands of individual molecules, the calculations are quite amenable to this approach. This study represents an initial attempt to study the potential benefits of parallel processing applied to DSMC analysis.

A parallel DSMC algorithm was developed which uses domain decomposition of the simulated physical space to distribute the work load among the individual processors (called nodes) of a hypercube. Message-passing software was then used to send and receive information between nodes on molecules that cross node boundaries. Two simple problems were tested on a commercially available hypercube (Intel Corporation iPSC/2). Results for these benchmark problems show speedups over single-processor computing rates of approximately 4 for a one-dimensional problem and approximately 12 for a two-dimensional problem. (Speedup is defined as the single-processor computing time divided by the computing time with parallel processing.) Although the results show that the

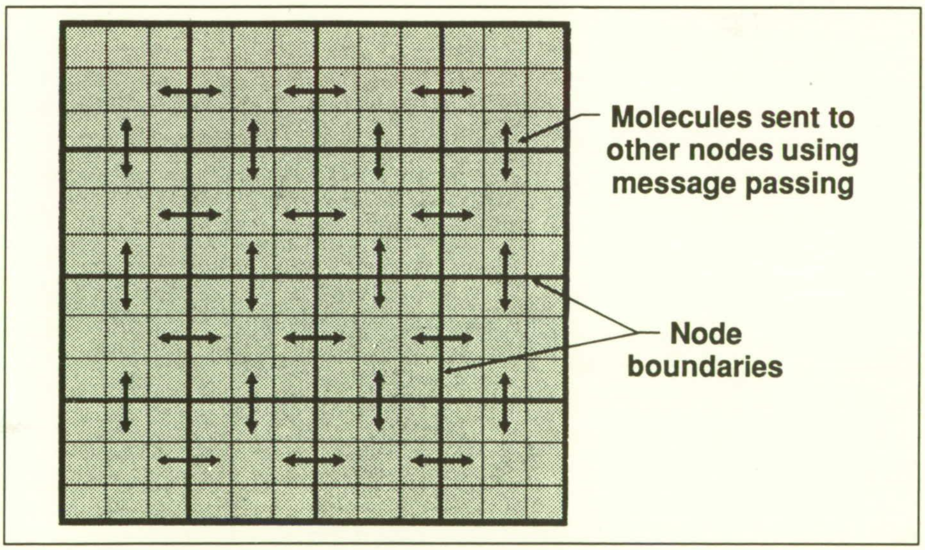

Domain decomposition used for parallel processing.

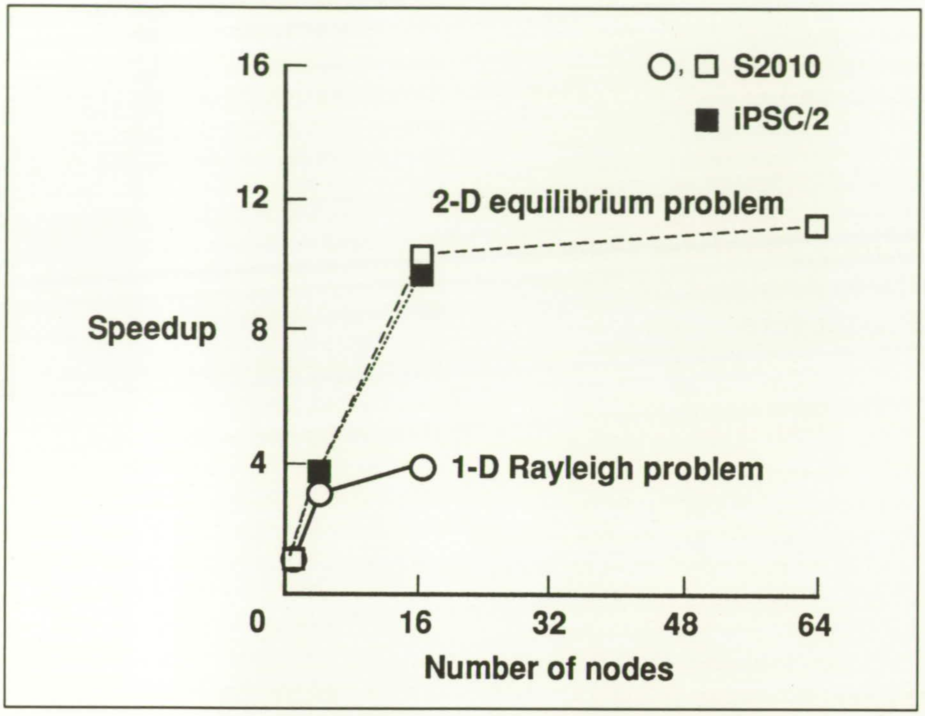

Speedup measured on hypercubes for two benchmark problems.

maximum speedup achievable for a given problem is limited by the communications time required for message passing, increasing the size of the problem actually increases the maximum speedup that can be obtained. Therefore, by properly sizing the problem to the number of available processors, the parallel method can achieve performance levels comparable to and even exceeding those obtained on modern supercomputers.
(R. G. Wilmoth, 44368)

Efficient Solar-Pumped Iodine Photodissociation Laser for Space Power Beaming

A key element in the choice of a laser system for beamed power transmission and conversion in space is the solar-to-laser efficiency, which affects the area of the solar collector. One promising candidate is the iodine photodissociation laser, the efficiency of which depends on the availability of a suitable organic iodide having good solar energy utilization, favorable laser kinetics, and chemical reversibility to minimize the need for lasant renewal. A survey of potential iodides has revealed that iodoperfluoro-tert-butane (t-C_4F_9I) best satisfies these requirements.

Comparison of spectrophotometric absorption data with the air-mass-zero solar spectrum shows that the solar energy utilization of t-C_4F_9I is a factor of 3 better than that of the commonly used iodide n-C_3F_7I.

Favorable laser kinetics are achieved because of the unusually small rate coefficient for the combination of two C_4F_9 radicals into the relatively stable molecule R_2 ($R = C_4F_9$). More free radicals are thus available in the system for combining with ground-state iodine atoms, thereby depleting the lower laser level and simultaneously blocking the formation of molecular iodine, the major quencher of the upper laser level. Since the action of I_2 is less important for this lasant, a high lasant flow rate to remove the I_2 from the laser cavity is less important. This factor should simplify the design and alleviate the cost of space laser systems.

Finally, the ready recombination of C_4F_9 and ground-state iodine atoms into the original iodide, with only small amounts of R_2 to be broken up and recombined with iodine, means minimal chemical recycling in a closed, flowing system and therefore a simpler and much lighter overall laser system.

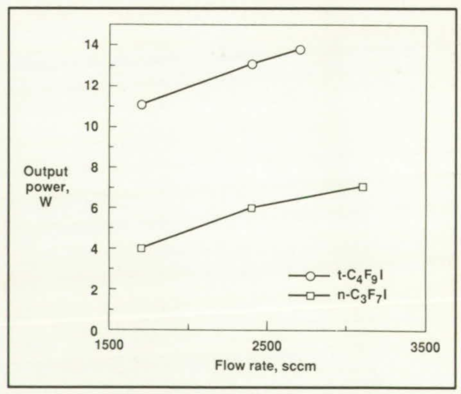

Laser output power.

Experimental research also included the first laboratory demonstration of a solar-pumped (solar simulator) continuous wave iodine laser using t-C_4F_9I. As shown in the figure, 14 W of output was achieved from a 15-cm tube at the flow rate and vapor pressure of 2700 sccm and 17 torr, respectively, when

pumped at a solar concentration of approximately 1,000. The superiority of t-C_4F_9I over n-C_3F_7I is immediately apparent and suggests strong consideration for its use in high-power laser systems for space applications.
(Ja H. Lee, 41473)

Orbit Lifetime Prediction for Long-Duration Exposure Facility

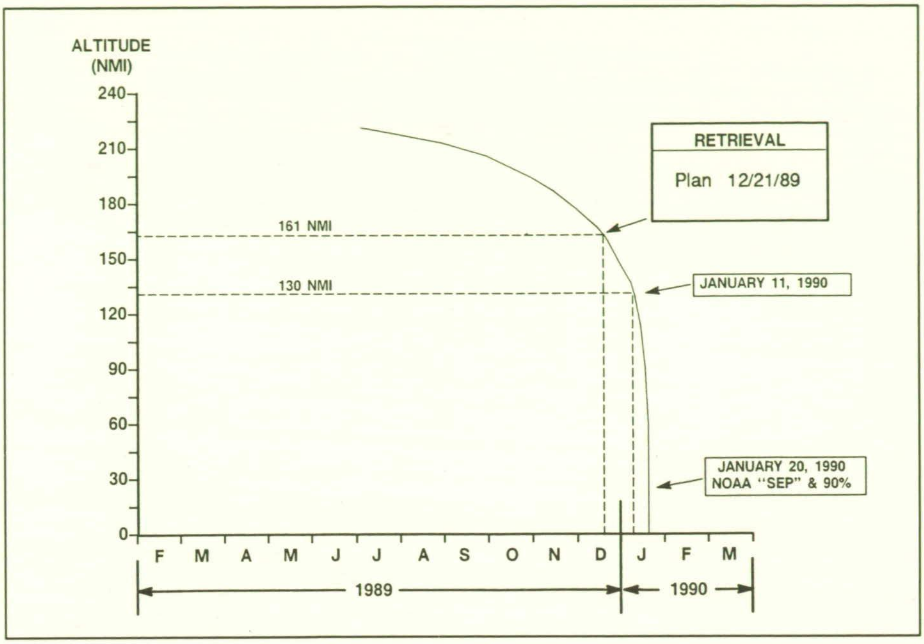

LDEF lifetime prediction (NOAA solar data, July 4, 1989, NORAD) with C_D = 2.16.

The Long-Duration Exposure Facility (LDEF) launched from the Space Shuttle in April 1984 at an altitude of 257 nmi accommodates a variety of experiments of interest to scientists, engineers, and researchers worldwide. Based on the then best estimate of atmospheric density profile, the predicted lifetime for LDEF was in excess of 10 years. However, two unrelated events placed the LDEF retrieval mission in jeopardy. First, the actual atmosphere encountered by LDEF was denser than anticipated, close to a $+2\sigma$ profile, statistically speaking. Compounding this, the occurrence of the peak solar activity (which increases atmospheric density) nominally associated with an 11-year cycle was observed to occur approximately 20 months earlier than expected, subjecting LDEF to maximum aerodynamic forces and orbit decay rates. The second event that focused community concern about LDEF retrieval was the untimely Space Shuttle *Challenger* accident and the resultant delays in all scheduled orbital science, including LDEF retrieval.

The Langley Space Station *Freedom* Office has been utilizing the Orbital Lifetime Computer Program (OL) module of the integrated multidisciplinary computer-aided engineering analysis code IDEAS**2 (Interactive Design and Evaluation of Advanced Spacecraft) for predicting LDEF altitude profiles. The prediction process consists of four components; these components include obtaining the latest LDEF orbit solutions as tracked by the North American Aerospace Defense Command (NORAD) for use as initial conditions and obtaining the latest and best solar flux and geomagnetic activity as determined by either the Marshall Space Flight Center or the National Oceanic and Atmospheric Administration (NOAA) for use in the atmospheric density models. Two other components include estimating and refining the effective LDEF aerodynamic drag coefficient obtained by matching observed decay rates with predicted values and utilizing the three components with OL to predict an LDEF reentry date. As of July 4, 1989, propagation of the current NORAD orbit solution yielded an estimated drag coefficient C_D of 2.16 and a predicted LDEF reentry date of January 20, 1990. As a result of these studies, NASA designated the December 1989 Space Shuttle *Columbia* mission for LDEF retrieval. The figure depicts the LDEF altitude profile during the retrieval mission time frame.
(G. Mel Kelly and Leonard J. DeRyder, 41946)

Space Station Structural Characterization Experiment

A study has been conducted during 1988 for OAST (Office of Aeronautics and Space Technology) to determine the feasibility of

the Space Station Structural Characterization Experiment (SSSCE) and to define a preliminary conceptual design for the experiment. The SSSCE objective is to collect on-orbit data to characterize the structural dynamics of Space Station *Freedom* and to develop modeling techniques for large space structures. The *Freedom* Space Station offers a unique opportunity for conducting this research on multiple structural configurations during its assembly.

The conclusion has been reached, based on a McDonnell Douglas Space Systems Company study, that the SSSCE is feasible with minimal impact to Space Station *Freedom* configuration, resources, and operations. The proposed experiment concept, pictured in the figure, requires the excitation derived from RCS (reaction control system) thruster firing during reboost, the measurement of acceleration response at approximately 100 points on the structure, and the use of free-decay modal identification methods to characterize the system. Selective signal-to-noise enhancement, as required to resolve relatively weak modes, may be achieved with the careful modulation of reboost pulses. The station data management system will be used for data acquisition and storage. It has been determined that the proposed system enables a feasible experiment and offers low technical risk. Preliminary system design has begun.
(J. W. Johnson, 41963 and J. P. Raney)

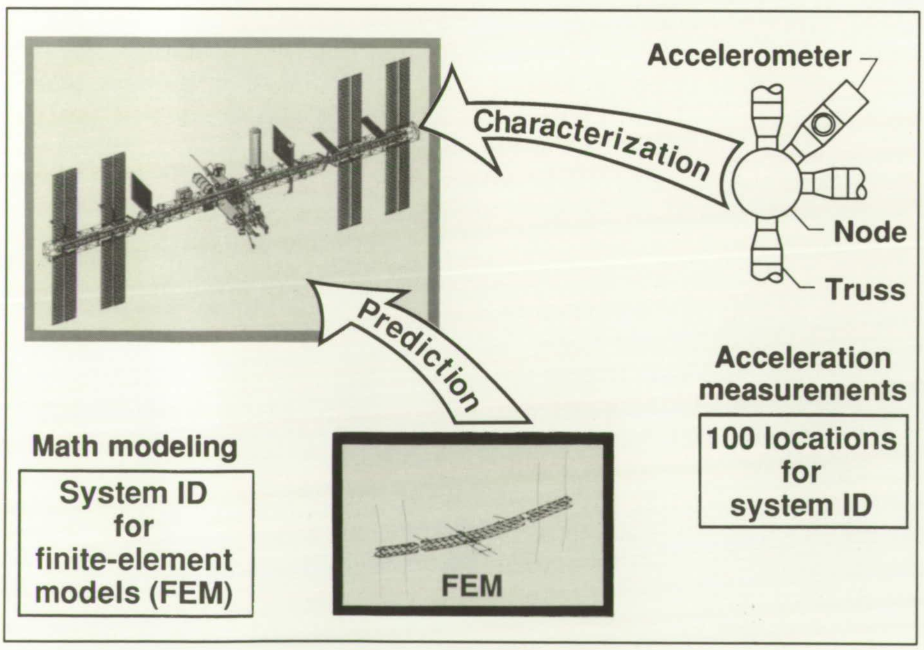

On-orbit structural dynamics.

Solid Modeling Aerospace Research Tool

The SMART (Solid Modeling Aerospace Research Tool) system has been developed at Langley Research Center to generate both external and internal geometry for the conceptual and preliminary analysis of advanced aerospace vehicles. This geometry is used as input to various engineering discipline analyses such as aerodynamics, aerothermodynamics, structures, weights, and mass properties. State-of-the-art computer graphics hardware and bicubic parametric functions for surface definitions have been integrated to develop an easy-to-use geometry system that can be utilized by all design and analysis codes that require geometric coordinates, derivatives, and/or properties.

A second-generation SMART has been completed for generating geometry, creating photo-realistic images, computing geometric properties, and generating finite elements for wings. Interfaces exist for the Aerodynamic Preliminary Analysis System (APAS), the PATRAN finite-element system, the Langley Wireframe Geometry Standard (LAWGS), and the Integrated Geometry Exchange Standard (IGES), which is a standard for the computer-aided design/computer-aided manufacturing industry.

The system has been used to create external and internal geometry for the Advanced Manned Launch System configurations, the Space Station *Freedom* Assured Crew Return Capability vehicle, and government and industry National Aero-Space Plane configurations. Shown in the figure are a geometry and grid that were produced for a computational fluid dynamic solution of a winged reentry vehicle. With the SMART system, productivity and quality of analysis have been dramatically improved through reduced

ORIGINAL PAGE
BLACK AND WHITE PHOTOGRAPH

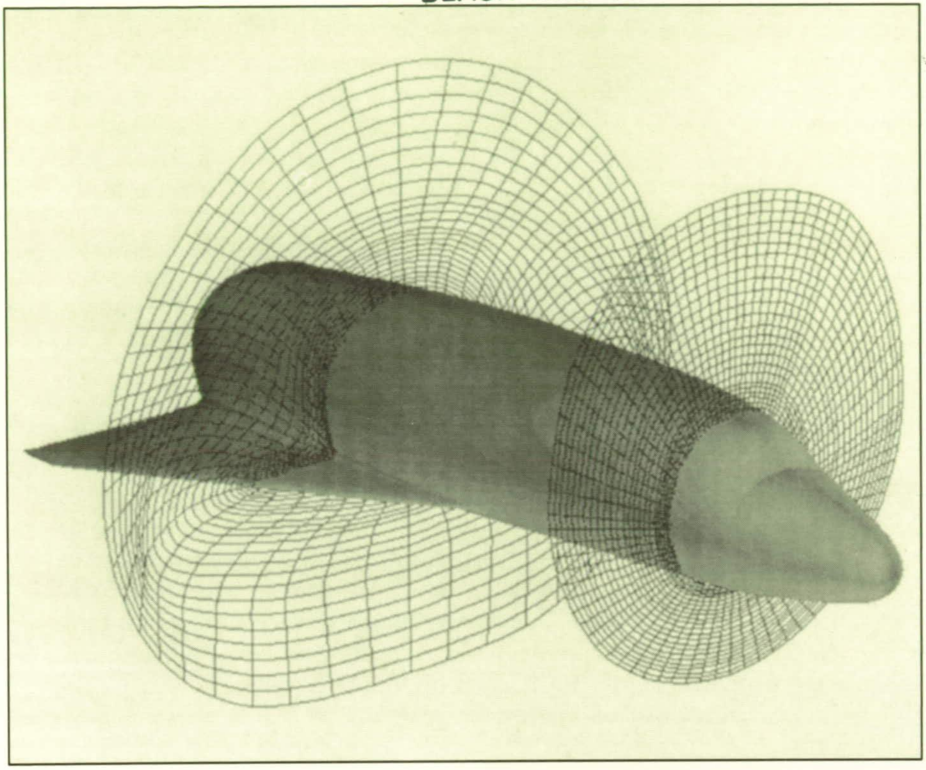

Computational fluid dynamics grid planes about winged orbiter.

applying regression analysis techniques to historical weight data. This approach is appropriate for vehicles whose properties closely resemble those of a number of existing vehicles, but it is inadequate for concepts that will include advanced technologies or innovative construction techniques. A finite-element analysis approach has been developed which permits the accurate analysis of advanced vehicle concepts. This more rigorous approach lends a greater degree of accuracy to the conceptual level analysis and reduces the overall analysis time of a vehicle through the preliminary level design phase while increasing fidelity.

The structural analysis technique includes a solid geometry modeler, a finite-element pre- and post-processor, and a finite-element sizing routine. The solid geometry modeler SMART (Solid Modeling Aerospace Research Tool) can

modeling time, increased surface fidelity, and integrated design and analysis functions.
(Mark L. McMillin, 44521)

Structural Analysis and Weights for Advanced Space Transportation Vehicles

With an aging Space Shuttle fleet and new space exploration initiatives, the aerospace community is assessing new launch systems. Most of the systems needed to fulfill future requirements are currently in the conceptual or preliminary design phase. In the conceptual phase of vehicle design, structural weights typically have been estimated by

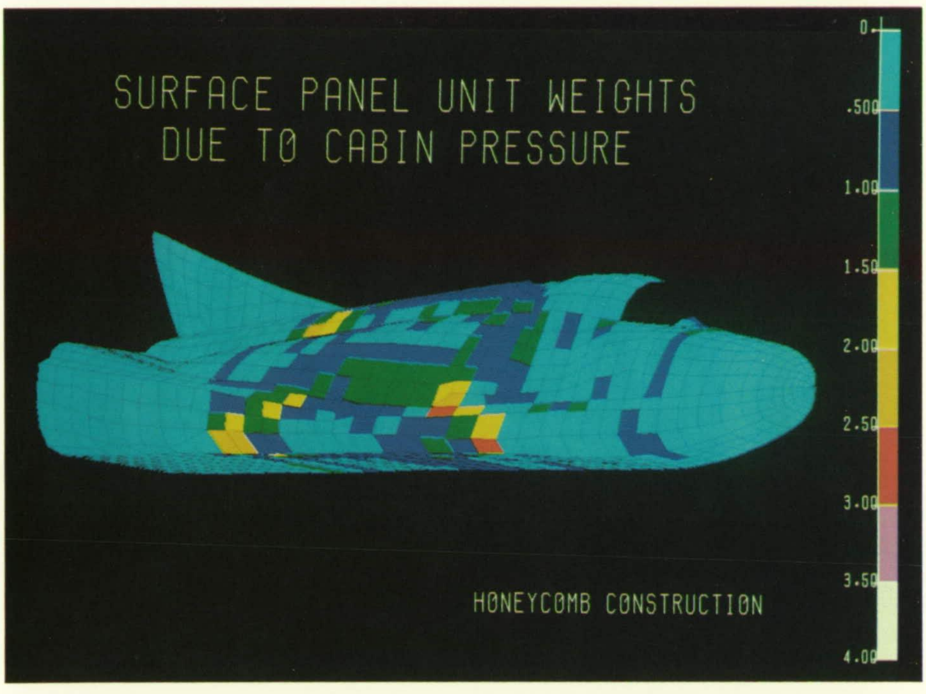

Structural analysis of lifting-body candidate for personnel launch system.

create a complex space transportation vehicle geometry within a day. The finite-element modeling is completed in PATRAN (developed by PDA Engineering) which includes the introduction of aerodynamic and inertial loads and the definition of the physical and material properties of the finite elements. Then the Langley-developed finite-element sizing code (EZDESIT) sizes the elements to withstand the resultant loads without failing. If no sizing is needed, the panel remains at minimum gauge. The sizing methodology depends on the type of construction (honeycomb, hat stiffened, or membrane) chosen. The results of the analysis and sizing are a vehicle structure capable of withstanding the static loads incurred during assembly, transportation, operations, and missions, and a corresponding structural weight. The results of the analysis for a lifting-body candidate for a personnel launch system are shown in the figure in which the surface panel unit weights due to cabin pressure are indicated.
(Lance B. Bush, 44514)

Thermal Distortion of High-Frequency Microwave Radiometer Antenna

Thermal structural distortions of a 7.5-m microwave radiometer antenna for global change Earth science research have been estimated. The antenna, designed to measure precipitation and atmospheric moisture over land and ocean, operates in the 60-GHz to 183-GHz frequency range. Its resolution ranges from 10 km to 30 km. This antenna is one of several instruments on a proposed geosynchronous Earth science platform. The reflector design of this antenna is based on Precision Segmented Reflector Technology being developed at Langley Research Center and the Jet Propulsion Laboratory and is supported by a tetrahedral truss structure composed of graphite composite tubes and aluminum end fittings.

In geosynchronous orbit, the reflector support structure is subjected to a severe and diverse thermal environment. Individual truss elements are exposed to direct solar heating for long periods combined with intermittent periods of extreme cold resulting from shadows caused by the antenna reflector or Earth. Truss element temperatures range from 130°C to −160°C depending on orbit position and on the truss element surface radiative properties. Three different truss element surfaces that were examined include bare graphite with a solar absorptivity/thermal emissivity α/ε ratio of 0.9/0.8 and two types of anodized aluminum coating, with α/ε ratios of 0.3/0.65 and 0.3/0.2. The element temperatures for the three surfaces varied throughout the orbit between 110°C and −160°C for the bare graphite, between 35°C and −160°C for the lower α/ε ratio coating, and between 130°C and −100°C for the higher α/ε ratio coating.

The complex heating and cooling of the truss elements lead to quasistatic dimensional changes in the antenna reflector surface. These distortions are directly related to the effective coefficient of thermal expansion (CTE) of the truss elements, which depends on the design of both the graphite tubes and aluminum end fittings. Initial structural analysis indicated that the resulting root-mean-square (rms) reflector surface distortions (shown in the figure) exceeded the maximum allowable surface accuracy specification. The worst distortions occurred during periods of partial shadow when both cold shadowed elements and hot exposed elements simultaneously existed in the truss structure. The options that exist to reduce these distortions include development of better surface coatings, tailoring the structural design

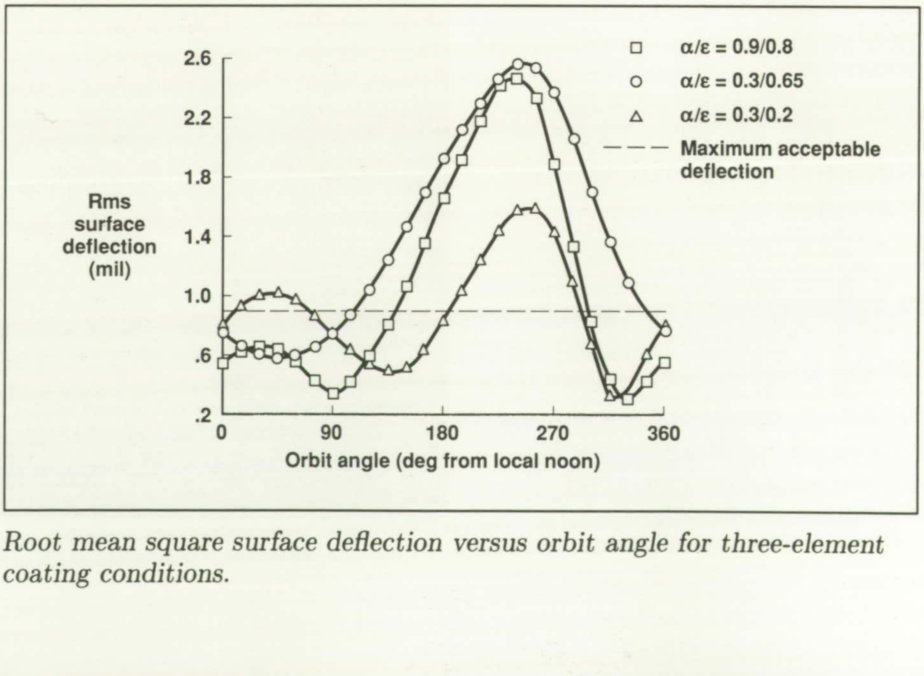

Root mean square surface deflection versus orbit angle for three-element coating conditions.

of the truss elements (tubes and end fittings) to lower effective CTE's, or utilization of insulation around the entire structure.
(Jeffery T. Farmer, 44422)

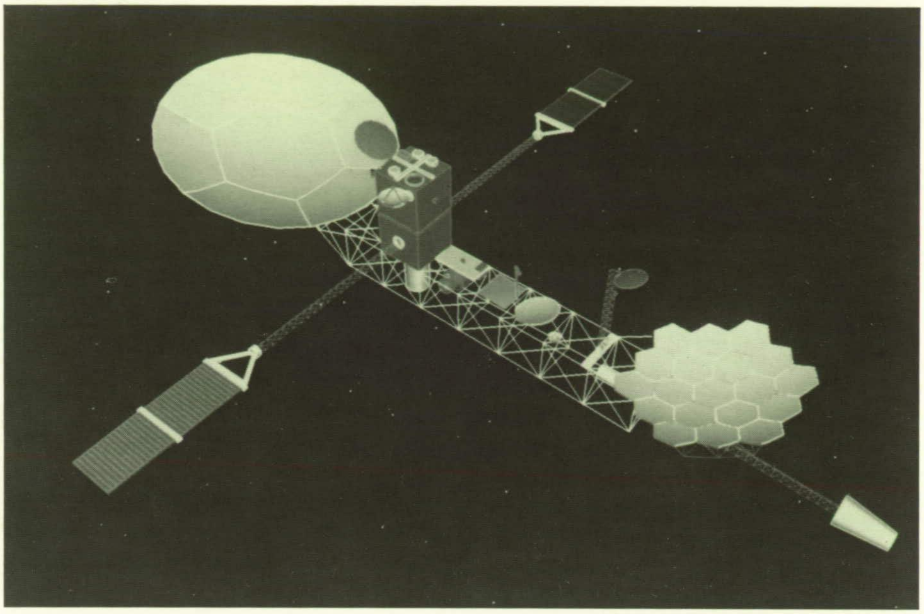

Second-generation Earth sciences geostationary platform concept. L-88-5881

Earth Sciences Geostationary Platform Systems Analysis

The Mission to Planet Earth envisions a complement of spacecraft in low and geosynchronous Earth orbits for monitoring the Earth's land, oceans, and atmosphere. The data that will be gathered will allow development and validation of models for predicting future environmental trends resulting from natural and manmade events. To reduce the number of costly geostationary spacecraft needed and to allow correlation of data among numerous sensors, large multi-instrument platforms are being proposed. These spacecraft will be the largest yet to occupy the geostationary orbit, and their complexity and stringent pointing requirements may require enabling or enhancing advanced technologies. Therefore, a systems study of second-generation geostationary Earth sciences platforms was conducted in order to evaluate the performance of the baseline concept shown and to identify advanced technology opportunities and benefits.

The approach was to develop solid and finite-element models for the baseline platform concept; to conduct structural, thermal, and controls analyses; and to develop subsystem designs and packaging strategies. In addition, assessments were made of the platform pointing performance and antenna radio frequency performance during on-orbit disturbances, and these were compared with mission requirements.

Structural forced-response analysis indicates that spacecraft pointing does not violate requirements for disturbances stemming from scanning by a Geostationary Operational Environmental Satellite sounder-type instrument. However, initial estimates of the disturbances resulting from antenna scanning are more severe, and compensation and isolation techniques may be required. Analyses have shown that thermal deformation of the bus does not violate pointing requirements but that thermal distortion of the antenna dish support structure does exceed surface roughness specifications for several thermal coatings evaluated. Subsystem trade studies have identified that geostationary stationkeeping requirements, typically dominated by north-south corrections, show increasing east-west corrections due to the large area-to-mass ratios of this class of spacecraft. Analyses have shown that the assembly version of this spacecraft can be packaged for a single Space Shuttle flight.
(Lawrence F. Rowell, 44459)

Rocket Versus Air-Breathing Propulsion for Single-Stage-to-Orbit Vehicles

This study was conducted to determine the effect of applying the materials, structures, and subsystem technologies of the National Aero-Space Plane (NASP) Program to a rocket-powered single-stage-to-orbit (SSTO) vehicle. The SSTO rocket-powered vehicle was designed to the same mission requirements and technology of the NASP configurations to compare vehicle size, weight, performance, heating, and operations.

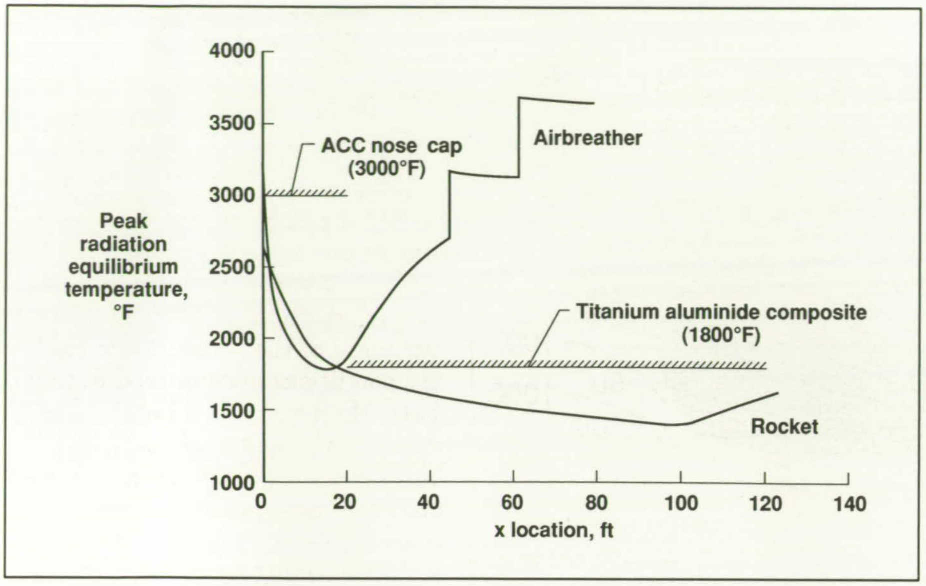

Windward centerline peak heating distribution.

The rocket vehicle was analyzed for aerodynamics and trim; ascent, reentry, and abort performance; heating; finite-element structural analysis; weights; and operations. A qualitative operations analysis was also performed. Results showed that the rocket vehicle as compared with the air-breathing NASP vehicle had one-fourth the maximum dynamic pressure and one-sixth the maximum heating rate, was 20 percent shorter and 24 percent lighter in dry weight, but was two times heavier in gross weight. As shown in the figure, using the advanced carbon-carbon (ACC) and the titanium aluminides from the NASP materials consortium, the rocket vehicle needed no surface tiles (such as the ones that are necessary for the Space Shuttle or for active cooling such as for the NASP configurations). Neither vehicle showed a superior operational advantage because operations from a launch pad for the rocket vehicle were traded with the maintenance of the additional subsystems required by the air-breathing vehicle.

This study shows that the NASP technology development has broad applications to aerospace vehicles. With this technology, the Nation will have a number of options for the development of future space transportation vehicles.
(Alan W. Wilhite, 44497)

High-Energy Aerobraking Studies

Through the Pathfinder Program, several analyses pertaining to the manned exploration of Mars are currently being performed. The feasibility of such a mission hinges primarily upon minimizing the initial vehicle mass in low-Earth orbit (LEO). For a vehicle that utilizes a high-thrust propulsion system (such as a chemical rocket), a majority of the initial mass is propellant; therefore, an effective means of decreasing the initial LEO mass is to reduce the propulsive requirements. By using the decelerating effects of atmospheric drag, the propulsive needs are diminished. In the case of an interplanetary transfer, enough energy must be lost so that the vehicle is captured into orbit about the target planet. Because of the large energy losses associated with this atmospheric maneuver, it is termed high-energy aerobraking.

Preliminary findings have shown that compared with an all-propulsive scenario, aerobraking in an interplanetary mission yields a potential weight reduction on the order of 20 to 60 percent. However, by including aerobraking, additional mission constraints pertaining to the atmospheric pass must be fulfilled. These integrated requirements, which inherently couple the interplanetary and atmospheric trajectories, include the effects upon the overall mission feasibility of a range of potential atmospheric entry conditions during Mars entry and Earth reentry, the amount of aerodynamically induced control that can be exerted during the atmospheric pass, interplanetary navigation inaccuracies, aerothermal issues, and packaging concerns.

Analyses have identified several mission opportunities (with an LEO launch date between 2010 and 2025) in which the Mars atmospheric entry velocity ranges from 6 km/sec to 10 km/sec and the entry velocity upon Earth return varies from 11.5 km/sec to 12.5 km/sec. These entry conditions yield significant aerothermal and aerodynamic performance implications. Convective heating generally dominates the aerothermal environment for vehicles with small nose radii, whereas radiative heating is dominant over blunt bodies at high velocities. Through the results of several programs (including Apollo), the rela-

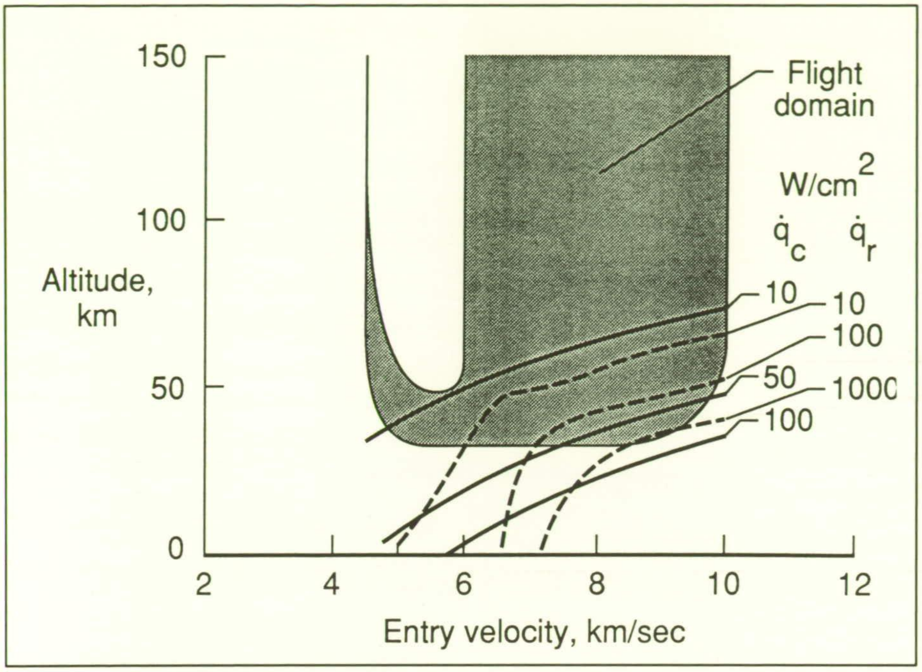

Flight domain and stagnation point heating rate during Mars atmospheric passage. (Convective heating $\dot{q}_c$ based on Sutton-Graves equation; radiative heating $\dot{q}_r$ based on Sutton's inviscid equilibrium method.)

tive importance of radiative heating over blunt shapes in the Earth's atmosphere is generally understood. However, two conflicting opinions currently exist pertaining to the significance of radiative effects (during Mars entry) over the range of potential atmospheric entry velocities (6 km/sec to 10 km/sec). One opinion is that because the entry velocities at Mars are low, radiation is only a second-order effect. The second opinion suggests that radiative heating over blunt vehicles is significant (even at these lower entry speeds) due to stronger radiation from the carbonaceous species that are not present in the Earth's atmosphere.

The second opinion is presented in the figure, which illustrates the predicted convective and inviscid equilibrium radiative heating rate at the stagnation point of a blunt configuration. For entry velocities of approximately 7.0 km/sec, this figure shows that the radiative and convective contributions to the total heating rate may become equal. In fact, if the vehicle flies near the lower bound of the flight domain, radiation can become the primary aerothermal concern. Hence, for a blunt shape, the effects of radiation should be accounted for in the stagnation region flow field analysis unless the atmospheric pass is performed at a very low entry velocity (below 6.2 km/sec). Additionally, as the entry velocity increases above 7.0 km/sec, the radiative effects may grow to dominate the aerothermal environment.

Other factors including aerodynamic performance, vehicle packaging requirements, Earth return aerothermal issues, and the effect of the Mars orbit selection are an integral part of an aerobraking mission analysis. Thus, if the LEO weight reduction associated with a high-energy aerobraking mission is desired, several additional requirements that depend upon both the interplanetary and atmospheric trajectories must be satisfied. With an understanding of the range and variation of the atmospheric entry conditions encountered during both Mars entry and Earth reentry, present studies are directed at improving our understanding of the relationship between the interplanetary and atmospheric trajectories and performing a detailed aerobraking analysis of several candidate design concepts.

(Richard W. Powell, 44506 and Robert D. Braun)

Three-Dimensional Powered Venus Swingby

In the 1960's, NASA examined the feasibility of a manned mission to Mars. Recently, interest in this mission has been renewed, and interplanetary analyses have been conducted to update the original data base and to include new mission concepts. Because one of the constraints on initial manned missions is a short total trip time, interest has focused on the use of a Venus gravity assist during one segment of the transfer to reduce trip time as well as total propellant usage. By incorporating a propulsive maneuver at the periapsis of the Venus swingby, the mission's overall propellant requirement, and thus the initial vehicle mass in low-Earth orbit, can be affected.

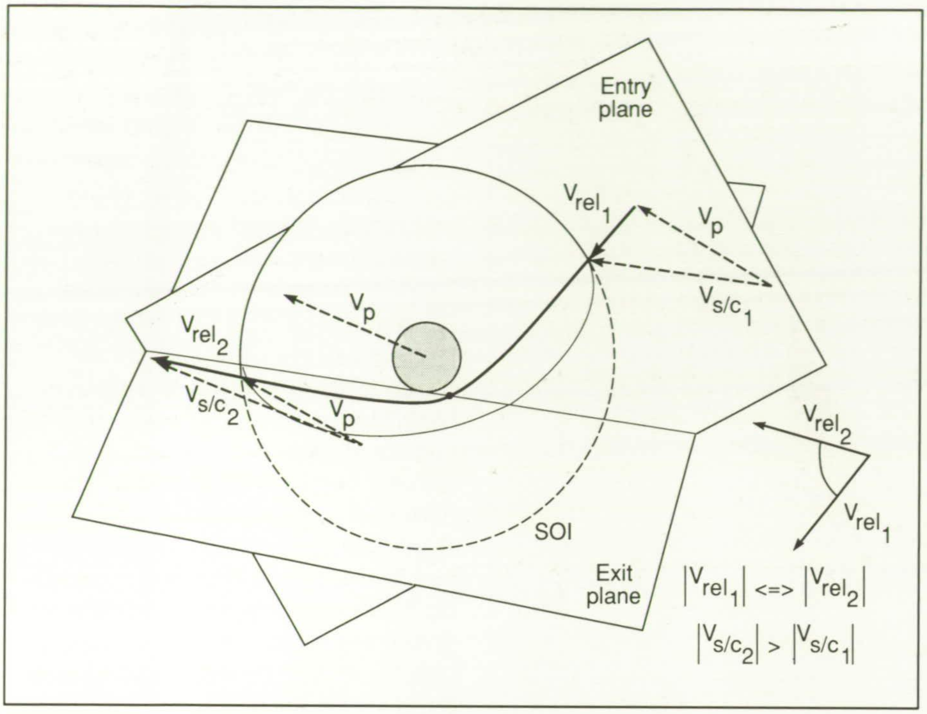

3-D powered swingby.

The gravity assist orbital maneuvering technique changes a spacecraft's interplanetary trajectory by altering its heliocentric velocity as it closely flies by a planet. Adding a propulsive maneuver during the swingby can allow a more efficient orientation of the relative velocity vector V_{rel} so that, when combined with the planet's heliocentric velocity V_p at its sphere of influence (SOI), the desired spacecraft heliocentric velocity vector $V_{s/c}$ is attained. For certain planetary orientations, moving the date of the swingby relative to the unpowered flyby date results in a lower required velocity change ΔV at Earth and Mars, while increasing the ΔV necessary at Venus. Therefore, by careful selection, an Earth/Mars trajectory can be found which requires less initial low-Earth orbit mass than for the unpowered swingby mission.

Early results have shown that the three-dimensional (3-D) burn allows an efficient reorientation of the relative velocity vector that is not always possible in the planar unpowered swingby option. Thus, a propulsive maneuver provides the trajectory designer with greater control over the spacecraft's heliocentric trajectory. Also, the periapsis burn can be in a direct or retrograde direction. When considered as part of the entire Earth/Mars trajectory, the 3-D powered swingby combined with more efficient Earth/Venus and Venus/Mars transfers can result in a lower initial low-Earth orbit vehicle weight. However, the mission's complexity is increased by the use of the extra burn. Additionally, the powered swingby seemed to have little effect, if any, on a very efficient unpowered swingby trajectory case. Thus, only less efficient missions will typically benefit from using the powered swingby option. **(Scott A. Striepe, 44512)**

Interannual Variability of Polar Stratospheric Clouds and Heterogeneous Chemistry During Antarctic Spring

Polar stratospheric clouds (PSC's) have been observed frequently in both hemispheres by the orbiting SAM II (Stratospheric Aerosol Measurement II) sensor since its launch aboard the *Nimbus 7* spacecraft in October 1978. The clouds form at very cold temperatures (below 195 K to 200 K) and, in Antarctica, often cover large areas and persist over the entire winter and into spring. Recent theoretical studies and experiments in the laboratory and field have established that PSC's play a major role in the development of the springtime Antarctic ozone hole through catalysis of heterogeneous (mixed-phase) chemical reactions that liberate ozone-destructive chlorine radicals from normally inert reservoir species.

An analysis of the 10-year SAM II record has shown that the number of PSC's sighted in the 14-km to 18-km altitude range during Antarctic spring (first figure) is modulated interannually according to the phase of the equatorial Quasi-Biennial Oscillation (QBO). The observed pattern conceptually matches those patterns reported previously for total ozone and minimum temperature in the Antarctic; years that coincide with the strong westerly phase of the QBO show

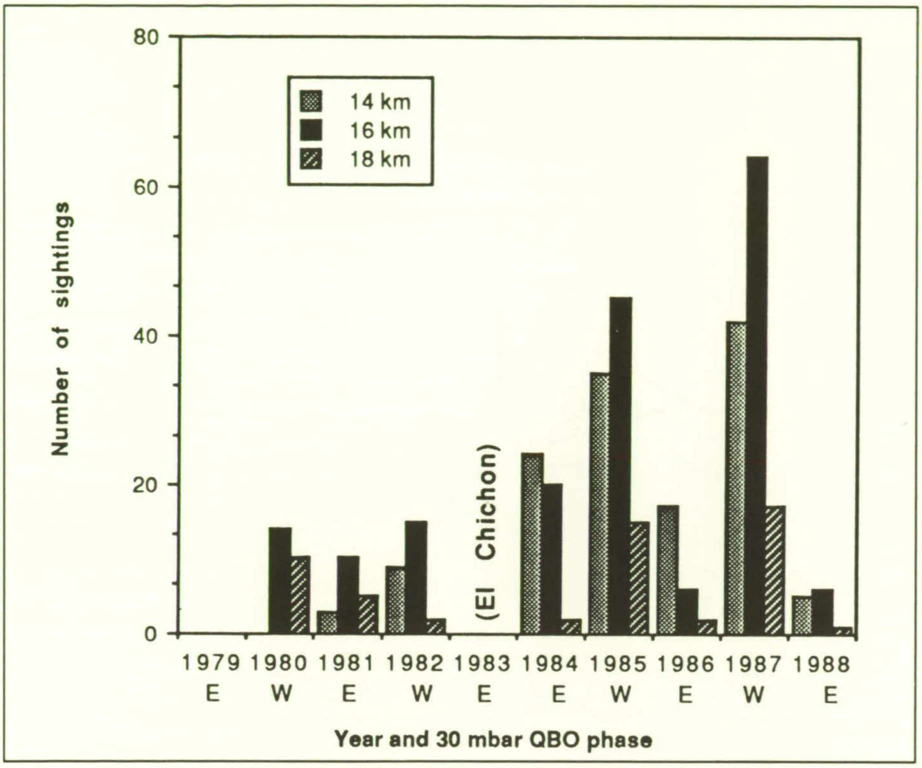

SAM II observations of Antarctic PSC's at 14 km, 16 km, and 18 km during October from 1979 to 1982 and 1984 to 1988, with 1983 excluded because of contamination by El Chichon aerosol.

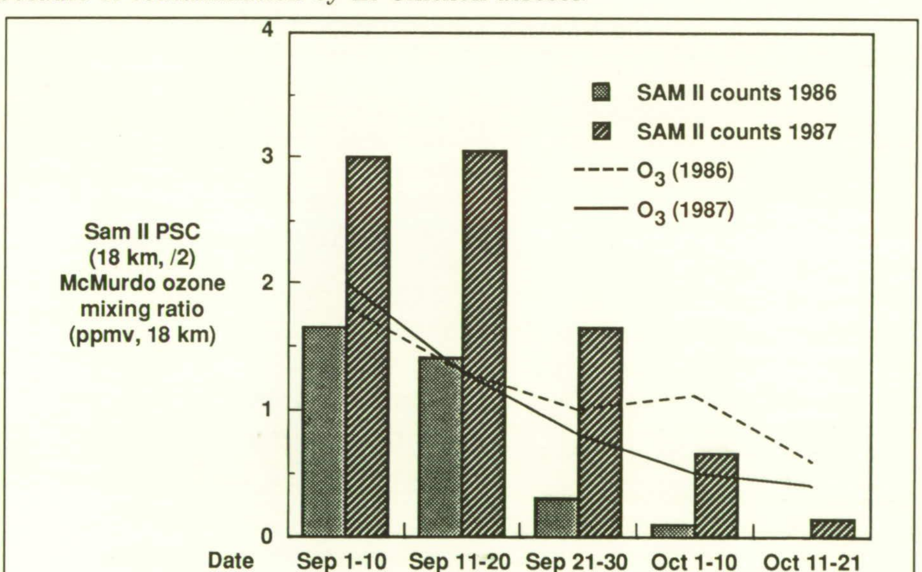

10-day averages of SAM II PSC sightings at 18 km and ozone volume mixing ratio at same level above McMurdo station (from Hofmann et al., J. Geophys. Res., vol. 93, 1989) for period September 1 to October 21 in 1986 and 1987.

maxima in PSC sightings and lows in minimum total ozone and minimum temperature. A comparison of 2 recent years of opposite QBO phase (1986 and 1987) shows that, in 1987, there were more PSC's at 18 km and that they persisted much later into the spring. Qualitatively similar behavior was observed in the 18-km ozone depletion observed at McMurdo Station during those 2 years (second figure), suggesting that in colder, westerly phase years, there may be an extension of the time period during which heterogeneous chemistry can drive ozone depletion and, hence, greater total depletion levels. October PSC sightings have also increased steadily over the past decade in years of the westerly QBO phase, a trend that likely is a result of the observed decadal ozone decline through its adverse effect on stratospheric heating rates. This trend suggests a positive feedback loop wherein ozone decreases lead to colder temperatures and more PSC's, which in turn produce even greater ozone losses. If confirmed by further measurements, this trend may amplify future ozone losses in the Antarctic well above those expected solely from increases in chlorofluorocarbon abundances.

(L. R. Poole, 42690)

Stratospheric Temperature Retrievals From SAGE II Solar Occultation Measurements

Air density contributes to the solar extinction observed by the stratospheric Aerosol and Gas Experiment II (SAGE II) satellite instrument, which is equipped with

seven wavelength channels centered at 0.385, 0.448, 0.453, 0.525, 0.600, 0.940, and 1.02 μm. In order to retrieve O_3, NO_2, H_2O, and multiwavelength aerosol extinction profiles, this air density contribution in the operational SAGE II data processing is removed at all channels by using meteorological data supplied by NOAA's (National Oceanic and Atmospheric Administration) National Meteorological Center (NMC). Recently, an attempt has been made to retrieve air density profiles from the SAGE II atmospheric extinction observations. Because the observed atmospheric extinction at a given SAGE II channel is a mixture of extinction of a particular species plus air molecules and because their relative contributions are different at different channels, a modified Levenberg-Marquardt algorithm has been adopted for retrieval of air density in the least-squares sense. The retrieved air density profile can then be used to derive the temperature profile.

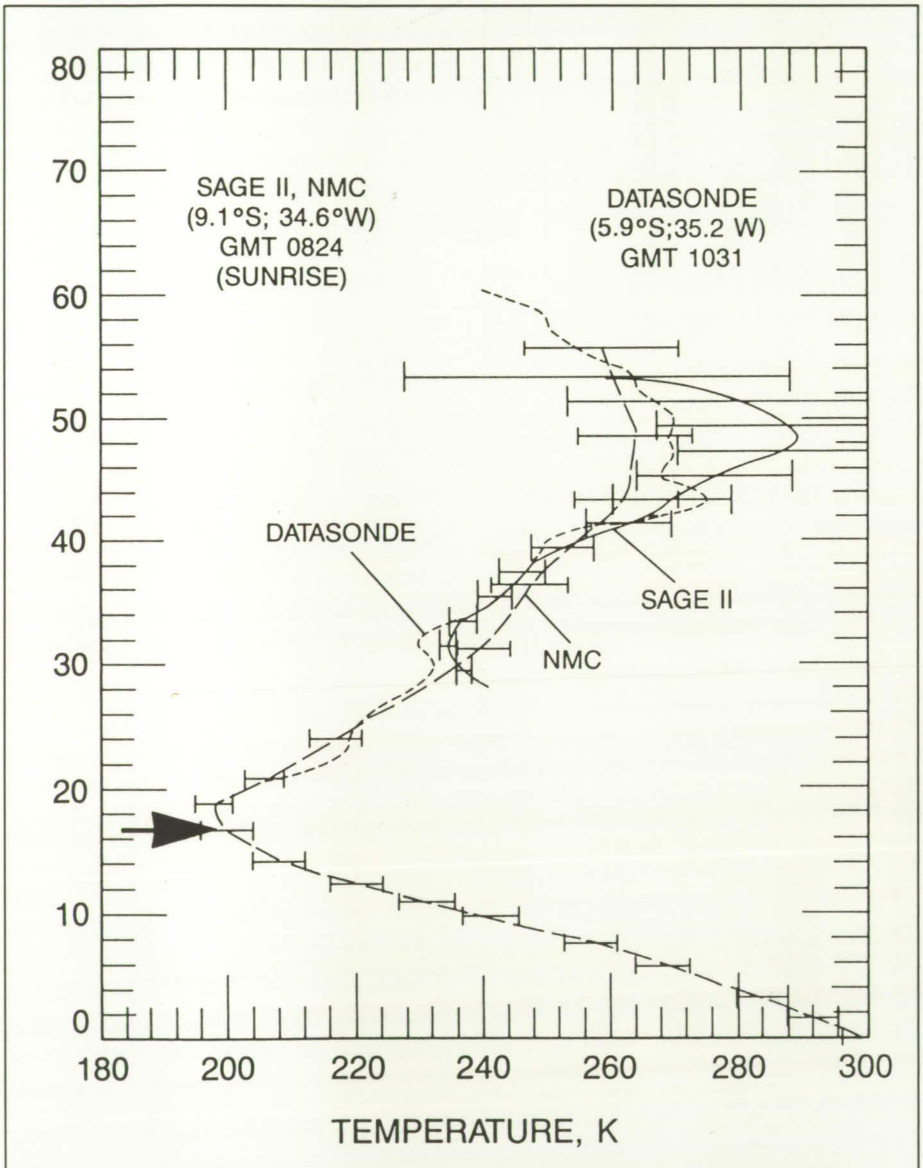

Temperature profile comparison between SAGE II (solid line), NMC (long dashed line), and datasonde (short dashed line); April 6, 1985.

A comparison of the SAGE II temperature with rocket and NOAA-NMC profiles is shown in the figure. This comparison indicates that the three different data sets show a general agreement within 12 K in the altitude range between 28 km and 45 km. Outside this range, the SAGE II data do not contain useful information. The agreement between SAGE II and datasonde is better than that between NMC and datasonde in the same altitude range, with the differences within 5 K between SAGE II and the datasonde and within 12 K between NMC and the datasonde.

Being able to infer stratospheric temperature makes SAGE II independent of external data sets and enhances the SAGE II observations, providing additional valuable long-term data sets to scientific communities for atmospheric studies.
(M. P. McCormick, 42669)

Cloud-Radiative Forcing and Climate: Insights From ERBE Data

Cloudiness is a pivotal variable for the balance of the Earth's radiant energy in our climate system. Clouds have two opposing radiative effects. They reflect incoming solar (shortwave) radiation and

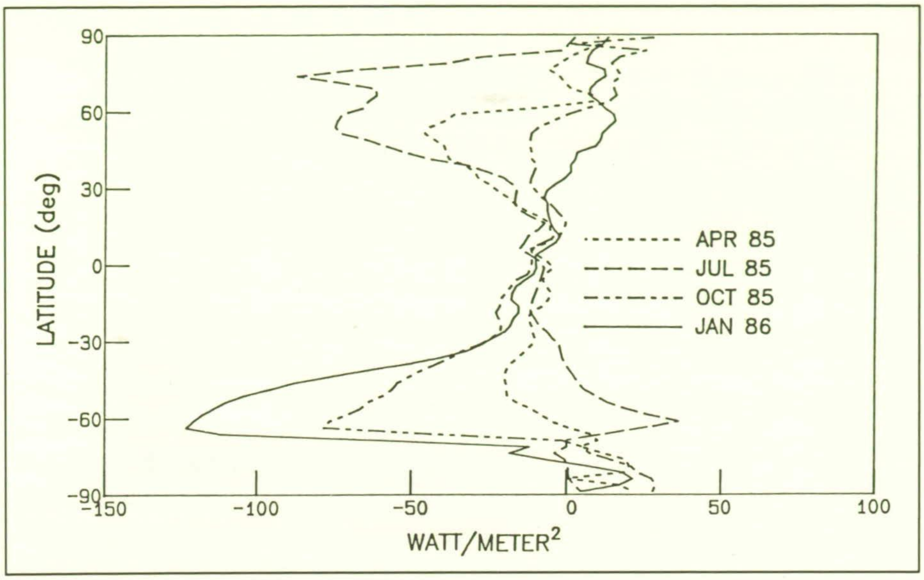

Seasonal variability of cloud-radiative forcing derived from ERBE observations.

therefore serve to cool the Earth-atmosphere system. On the other hand, they trap outgoing Earth-emitted (longwave) radiation and cause heating, which is referred to as the greenhouse effect. The net effect of clouds on climate is the combination of both of these radiation components.

The NASA multisatellite, Earth Radiation Budget Experiment (ERBE), is measuring the short-wave and longwave radiation over clear and cloudy scenes. The difference between the clear-sky and the total-scene radiation is defined as cloud-radiative forcing. As shown in the figure, the ERBE results indicate that clouds generally have more of a cooling effect than a greenhouse warming effect on the Earth-atmosphere system. The global net cooling varied from 14 Wm^{-2} to 21 Wm^{-2} between April 1985 and January 1986. Maximum net cloud forcing occurs over the storm tracks in the mid-latitude oceans of the summer hemisphere. The strong seasonal variation in net cloud forcing is driven primarily by the position of the Sun as well as by the physical and optical properties of the clouds. These results are being used to validate and improve general circulation models for climate studies.

(Edwin F. Harrison, 45663)

Stratospheric Aerosols Remain Perturbed From Volcanic Activity

A long-term data set on stratospheric aerosols is being produced using the 48-in. lidar system at Langley Research Center. Routine observations of the stratosphere have been made since 1974 and represent the longest data set of its kind in the world. Stratospheric aerosols, with their relatively long resident times, are important because they may directly affect the Earth's climate by scattering and absorbing both solar radiation and upwelling thermal radiation, and possibly by entering into heterogeneous chemical processes.

This long-term data set, shown in the figure, indicates that the major contributor to stratospheric aerosol enhancements has been of volcanic origin. Plotted in the figure is the lidar backscatter from stratospheric aerosols integrated from the tropopause to 30 km over the time period 1974 to 1988. A number of explosive volcanic eruptions, which are thought to have

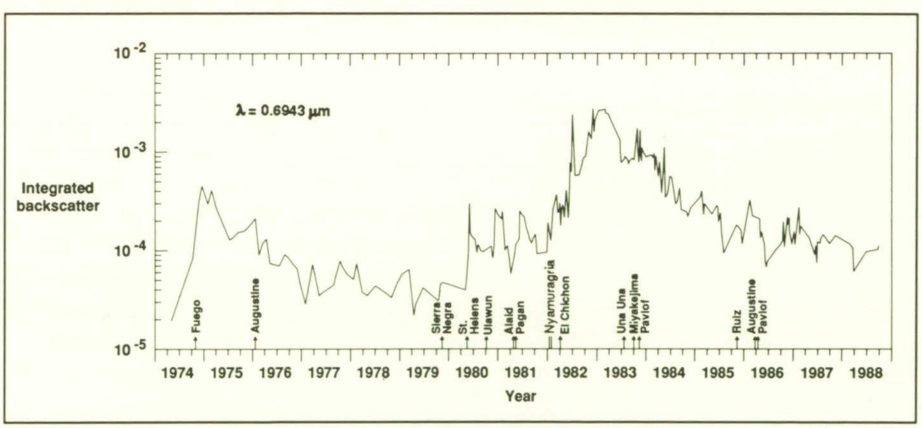

Integrated lidar backscatter measurements from stratospheric aerosols obtained at Langley Research Center (37.1°N, 76.3°W) by the 48-in. lidar operating at 0.6943 μm.

injected material into the stratosphere, are indicated at the time of their eruption. The integrated lidar backscatter is a measure of the relative column aerosol loading in the stratosphere, and by using optical models, can be converted to aerosol mass loading. The major perturbations to stratospheric aerosols due to the numerous volcanic eruptions are clearly evident, with the largest due to the April 1982 eruption of the El Chichon volcano in Mexico. This eruption is thought to have produced the largest perturbation in stratospheric aerosol loading to the Northern Hemisphere in this century. The largest recent perturbation was associated with the November 1985 eruption of the Ruiz volcano in Colombia, South America. The period from 1978 and 1979 is the lowest since measurements were begun and, therefore, is referred to as a background period for stratospheric aerosols. At the end of 1988, the integrated aerosol backscatter measurements were approximately twice these background values, although there is no reason to believe that the 1978 to 1979 values or even lower values will not be reached barring new volcanic perturbations.

(M. P. McCormick, 42669)

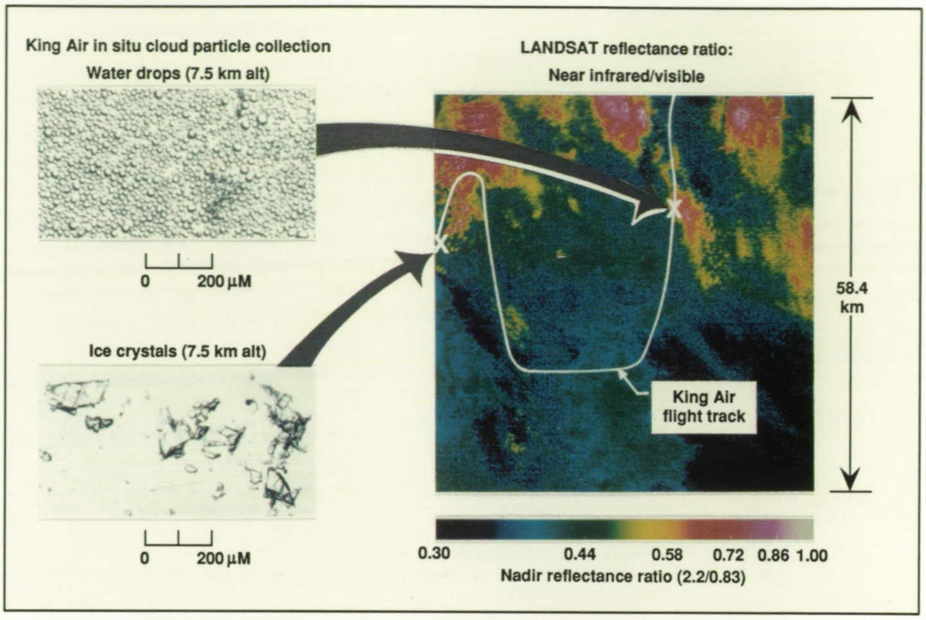

Sensing of cloud particle size (October 28, 1986).

Comparison of Satellite- and Aircraft-Observed Cirrus Cloud Particle Size

Cirrus clouds have the potential to either warm or cool the Earth's climate. One of the critical properties of cirrus clouds which control their effect on climate is cirrus particle size. The typical size of cirrus cloud particles has been a matter of debate over the last decade.

In a recent effort to examine this problem, the First ISCCP (International Satellite Cloud Climatology Project) Regional Experiment (FIRE) made observations of cirrus over Lake Michigan on October 28, 1986, from aircraft within and above the cirrus cloud, along with simultaneous Landsat satellite observations. The analysis region is shown in the figure, along with an image of the Landsat data and the superimposed King Air aircraft flight track.

The aircraft have two methods of observing cloud particle size. First, direct samples of cirrus particles were obtained on oil-coated slides. Second, particle size is measured using the Particle Measuring System (PMS) two-dimensional laser imaging probe (2D-C), which collects continuous 2-D images of cirrus particles along the aircraft flight track. The satellite estimates cloud particle size by comparing cloud reflectances in two spectral wavelength regions, 0.83 μm and 2.21 μm. As particle size increases, the reflectance at 2.21 μm decreases, while that at 0.83 μm is unaffected. A comparison of the Landsat reflectance ratios in the figure to the oil-coated slide cirrus particles gives good qualitative agreement with the aircraft data. The reflectance ratio is large (0.7) for the small water drops and is small (0.4) for the large ice crystals. Quantitative comparisons of effective cirrus particle radius along the entire King Air aircraft flight track showed good agreement for the size of the small water droplets, but poor agreement for the large ice crystals. The satellite data gave an effective mean particle radius of 60 μm versus the aircraft value of 200 μm. Examination of the size distributions of the aircraft data indicated that the distributions are dominated by the smallest particles measurable using the 2D-C probes (approximately 20 μm to 50 μm). These data imply the existence of even smaller cirrus particles that were missed by the aircraft 2D-C

probes, but were included in the satellite measurement.
(Bruce A. Wielicki, 45683)

Successful Post-Launch Satellite Calibration

NASA has established the Surface Radiation Budget (SRB) Satellite Data Analysis Center (SDAC) at Langley Research Center to coordinate the development of satellite methods for determining the SRB. A key element in the accurate determination of SRB parameters is the determination of in-flight calibration values for the operational satellites. Absolute calibration of satellites in flight is a complex process and requires confirming results from several different types of analysis. The figure presents SDAC calibration-team results that show the change in absolute calibration of the Advanced Very High Resolution Radiometer (AVHRR) instrument on the *NOAA-9* satellite over the first 1200 days of its lifetime. Results indicate that the satellite instrument is slowly deteriorating (increasing gain) and that calibration values must be updated from pre-launch values if accurate results are to be obtained.

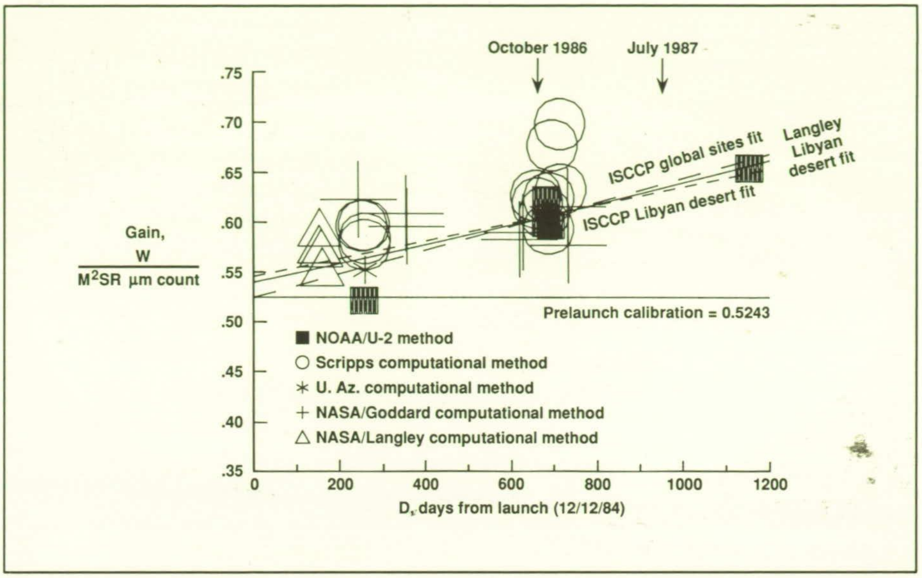

*NOAA-9 AVHRR channel 1 gain values with radiance = –22 plus (gain * 10-bit counts).*

These results have had a significant effect on several projects. As a direct result of the Langley Research Center multi-investigator in-flight calibration effort, the Goddard Space Flight Center has been requested to implement an improved high-altitude aircraft program for calibrating AVHRR every 3 months. Langley has been requested to study the feasibility of high-frequency (every 2 weeks), in-flight calibration of the GOES (Geostationary Operational Environmental Satellite) Visible and Infrared Spin Scan Radiometer. The European Center for Medium Range Forecasts has issued funding to several investigators to perform similar calibration studies on all AVHRR instruments on the *Tiros* satellite series from *NOAA-6* through *NOAA-11*. NOAA has decided to implement an approximate AVHRR calibration as part of its operational procedures. The International Satellite Cloud Climatology Project (ISCCP) has modified their procedures and directed all users to apply a 20-percent correction to their data dating back to July 1983. ISCCP is proposing to use the October 1986 calibration value from the SDAC study to establish a uniform calibration standard for five NOAA satellites, three GOES satellites, three GMS satellites, and three METEOSAT satellites for the period July 1983 through 1995. In addition, a Langley researcher has used the calibrated data to validate his satellite cloud retrieval algorithm, and an Oregon State University investigator has used the data to validate a Colorado State University cloud model.
(C. H. Whitlock, 45675)

New Capabilities for Estimating Earth Surface Radiation

The amount of solar and heat energy arriving at and leaving the Earth's surface is a vital factor in climate, safety, and economy. After nearly a decade of modeling research, techniques have been developed at Langley Research Center which allow estimation of the downward, upward, and net components of the Earth's surface radiation budget and knowledge of the variation of these components over the entire globe based on a surface resolution of 2.5°. The models used to produce the radiation

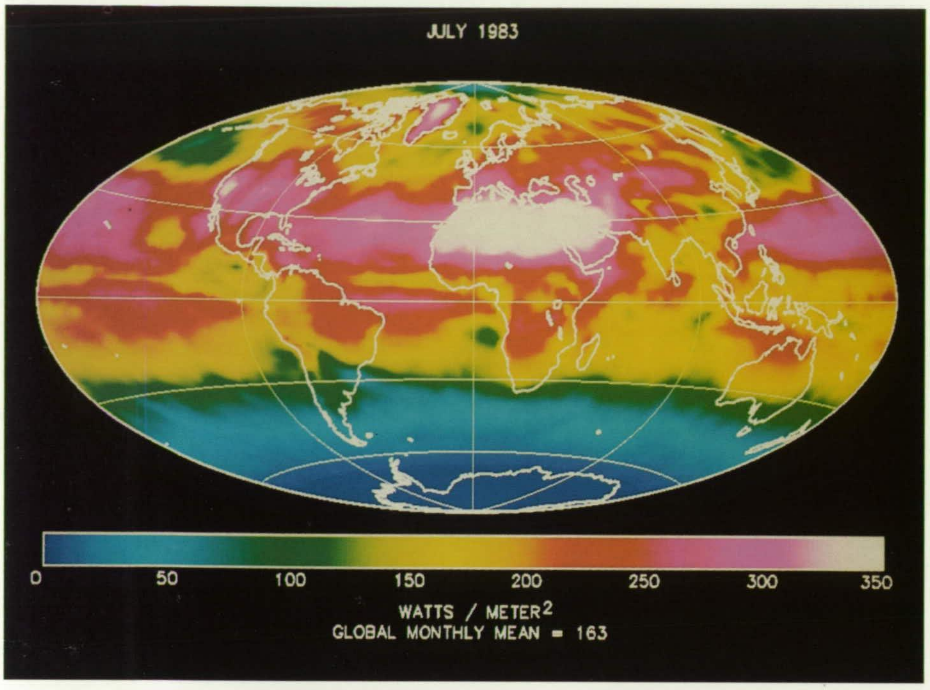

Distribution of radiation flux over the globe, downward shortwave.

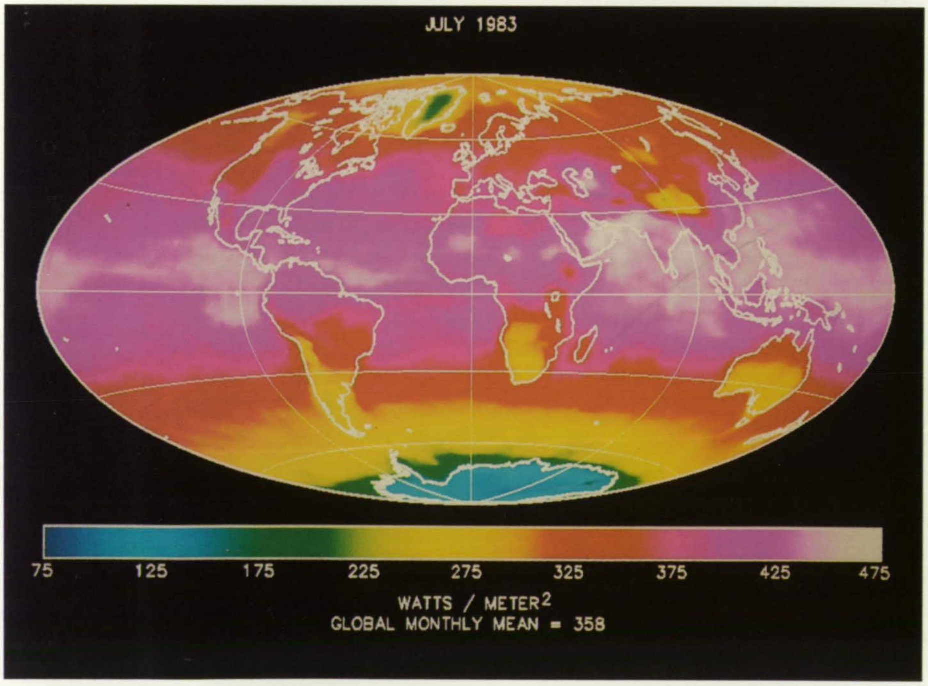

Distribution of radiation flux over the globe, downward longwave.

components rely on data from both Sun-synchronous and geostationary satellites. Basically, the geostationary satellites provide information concerning clouds, while the Sun-synchronous satellites provide meteorological data concerning atmospheric gas concentrations and atmospheric temperature profiles. Both types of satellites have operated for many years, but only recently have the data from all the geostationary satellites around the world been used together with a common format and common radiometric calibration.

These data are now being generated routinely by the International Satellite Cloud Climatology Project and allow global cloud parameters to be generated every 3 hours. A longwave and a shortwave physical model are the basic blocks in the overall algorithm, and they allow the satellite data to be transformed into surface radiation fluxes on a daily basis. The fluxes are time-averaged to obtain monthly results. The figures show estimated downwelling radiation fluxes for the solar (shortwave, first figure) and heat (longwave, second figure) radiative flux components of the Earth radiation budget for July 1983. The largest amounts of solar radiation during this month are in the Saharan and Saudi Arabian Desert regions. At the same time, downward longwave flux is greatest in the equatorial ocean regions, where large concentrations of atmospheric moisture and low clouds are found. **(W. L. Darnell, 45674)**

Temporal Studies of Earth-Emitted Longwave Radiation

Monthly averaged outgoing longwave radiation (OLR) results of a 10-year period from July 1975 through October 1985 have been used to study variability statistics. The data are wide field-of-view (WFOV) measurements taken from the Earth Radiation Budget (ERB) experiment that was flown on the *Nimbus 6* and *Nimbus 7* satellites. The data make it possible to study our changing climate over monthly, annual, and interannual scales in the time domain, and over regional, zonal, and global scales in the spatial domain.

The figure shows the standard deviation maps of the change in OLR for January and July over a 10-year period from 1975 through 1985. The maps represent the temporal change from year to year of averaged OLR about its 10-year mean. The maps are similar in that most of the variation is in the tropical and subtropical regions, especially over Indonesia and the western Pacific. Variations are larger in January where the standard deviation reaches 25 $W \cdot m^{-2}$ over the western Pacific Ocean. The January standard deviation map includes the peak of the 1982 to 1983 El Niño-Southern Oscillation (ENSO) time period, but even when ENSO was not included in the average, January still shows more variability than July. The increase in the interannual variability for January is most likely due to increases in cloud variability.

(T. D. Bess, 45688)

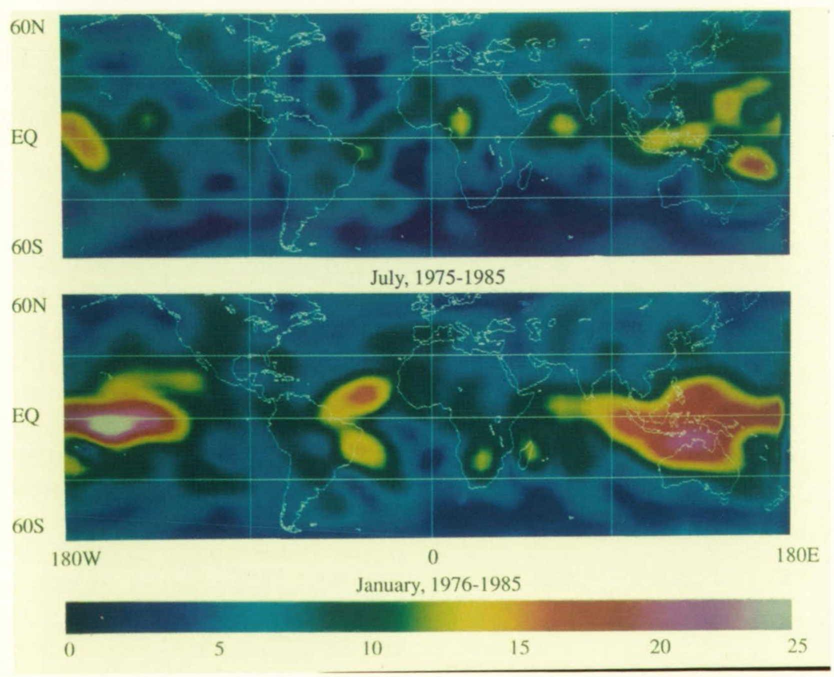

Monthly outgoing longwave radiation standard deviation for 10 years ($W \cdot m^{-2}$).

Detection of Atmospheric Temperature Response to Solar UV Variability

Knowledge of how temperatures in the middle atmosphere actually respond to solar ultraviolet (UV) variability is fundamental to our understanding of the radiative, dynamical, and chemical processes in the atmosphere. Studies have now been performed isolating the temperature response to short-term solar UV variability as a function of latitude and season. Four years of the highest quality temperature data from the *Nimbus 7* Stratospheric and Mesospheric Sounder (SAMS) were compared with the 205-nm solar variations. The component of the variation related to the 27-day rotation of the Sun was isolated in the study. Shown in the first figure is the response time (in days) of atmospheric temperature to the 27-day variations in solar UV radiation. A remarkably clear pattern of increasing response times is detected as one moves down from 90 km to 31 km. Response times are also found to increase with latitude in the winter hemisphere. Each latitude band has been determined independently, and yet the pattern of individual solutions is exceptionally smooth. One-dimensional chemical/radiative models indicate that response times to the 27-day UV variability near 43 km (2 mb) should be approximately 2 days as opposed to the observed response times shown here of approximately 7 days. This suggests that dynamical processes may play an important role in controlling the response times.

In the second figure, the change in temperature (in kelvin) corresponding to a 10-percent increase in 205 nm solar radiation is shown as a

PRESSURE, mbar												ALTITUDE, km
	WINTER							SUMMER				
0.002	0	0	0	0	0	0	0	0	1	1	1	90
0.005	0	0	0	0	0	0	0	1	1	1	1	84
0.007	1	0	0	0	0	0	0	1	1	1	1	82
0.010	1	0	0	0	0	0	0	1	1	1	1	80
0.015	1	0	0	0	0	0	0	1	1	1	1	78
0.020	1	1	0	1	1	1	0	1	1	1	1	76
0.030	2	1	1	1	1	1	1	1	1	1	1	74
0.040	3	2	1	2	1	1	1	1	2	1	1	72
0.050	4	3	2	2	2	2	1	2	2	1	1	70
0.070	7	5	4	3	3	3	3	4	4	2	1	68
0.100	9	7	5	4	4	4	5	5	5	3	1	66
0.150	12	9	6	5	4	4	5	5	5	4	-1	63
0.200	15	13	6	5	4	4	5	5	5	4	-2	61
0.300	18	17	6	5	4	4	5	5	4	1	-2	58
0.400	19	18	7	6	4	4	4	5	4	0	-2	55
0.500	19	18	7	6	5	4	4	4	3	1	-1	54
0.700	19	18	7	6	5	5	4	4	5	5	0	51
1.000	19	18	7	6	6	5	5	5	6	7	6	48
1.500	19	18	7	6	6	6	6	5	7	7	7	45
2.000	20	19	7	7	7	6	6	6	7	7	7	43
3.000	21	20	7	8	8	8	8	7	8	8	8	40
4.000	23	21	21	13	13	12	12	11	10	11	10	38
5.000	27	22	21	14	14	14	13	13	12	13	12	36
7.000	27	23	21	15	15	15	14	14	13	14	13	34
10.000	28	26	21	16	15	15	15	14	14	16	22	31
LATITUDE, deg	50		30		10		10		30		50	

Observed temperature response time (days) to solar UV variability.

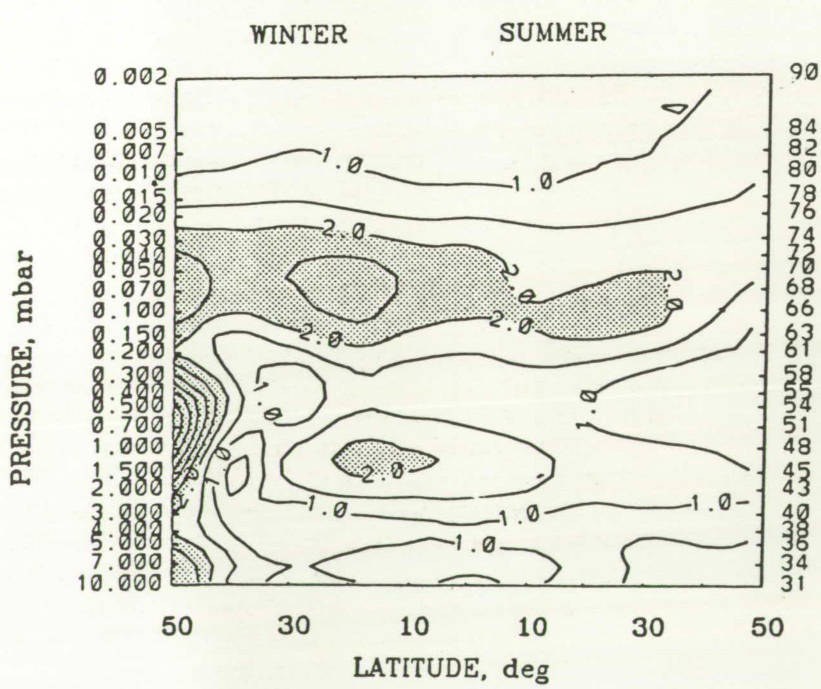

Change in temperature scaled to 10-percent increase in 205-nm solar variation. The shaded area indicates changes greater than 2 K.

function of latitude and season. In the stratosphere, the strongest 27-day heating occurs at high winter latitudes, the intermediate heating occurs near the Equator, and the weakest heating occurs at high summer latitudes. The maximum heating at high winter latitudes is, of course, also contrary to what would be expected from simple chemical/radiative models, and again it appears that dynamical processes may be important in establishing these 27-day variations. In the mesosphere, the strongest variations occur near 70 km. This observation is contrary to present-day theoretical models and may also require dynamical processes to induce the observed temperature variations. These first results on seasonal variations in the temperature response to solar forcing also give insight into the atmospheric response to the longer term 11-year solar variations.
(Gerald M. Keating, 45804 and Chaing Chen)

Analysis of Non-LTE Effects on Remote Sensing of Ozone

One of the most powerful techniques employed to remotely measure the ozone concentration in the stratosphere, mesosphere, and thermosphere is monitoring the infrared emission from ozone by scanning these regions of the atmosphere with a satellite-borne radiometer. The success of this technique depends on the ability to calculate accurately the infrared emission for specified conditions. The radiative emission from a molecule is determined by the distribution of energy among its various internal energy levels. The distribution of molecular

internal energy depends on how the molecule exchanges energy with its environment.

Atmospheric molecules are continually exchanging energy with their surroundings. In the troposphere and stratosphere (below approximately 50 km), the dominant mechanism by which molecules interact with their surroundings is through collisions with other molecules. In the mesosphere and thermosphere (above approximately 50 km), collisions, photochemical reactions, radiative absorption, and radiative emission may all be significant mechanisms by which a molecule interacts with its environment. If collisional processes dominate the energy exchange between a molecule and its environment, the condition of local thermodynamic equilibrium (LTE) is said to exist. Otherwise, non-LTE is said to exist. The radiative emission is strongly dependent on the processes affecting the molecular internal energy distribution and is, therefore, dependent on whether LTE or non-LTE exists in the emission bands to be observed.

Research is under way at Langley Research Center to quantify the effects of non-LTE processes on the infrared emission by ozone and other molecules. This research shows that non-LTE processes have a significant impact on the ozone emission. Failure to account for the non-LTE mechanisms will result in improper determinations of ozone concentration profiles. The figure shows an example of the radiance simulations for mid-latitude winter for LTE and non-LTE conditions. The non-LTE radiance is expected to be indicative of the actual ozone radiance for these conditions.
(Martin G. Mlynczak, 45695)

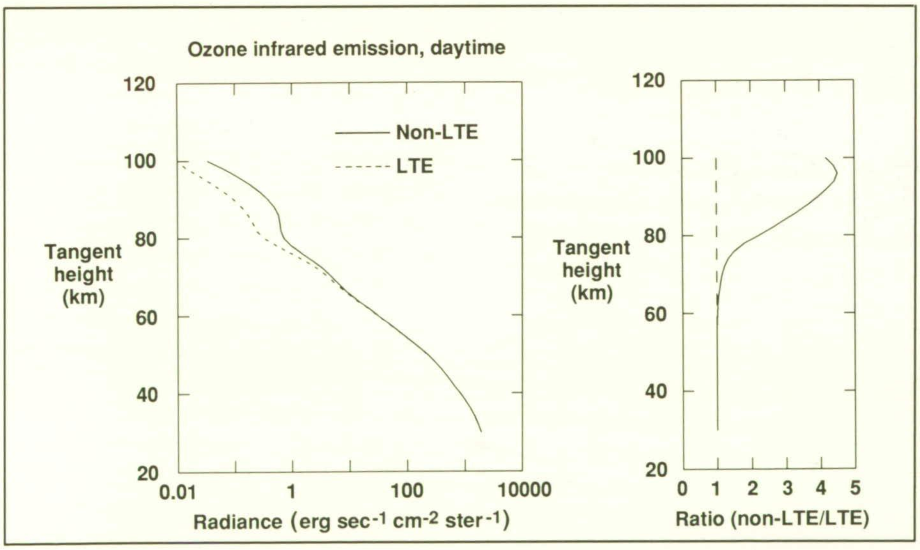

LTE and non-LTE radiance emitted by ozone as function of tangent altitude for mid-latitude winter conditions at noon.

Effect of Vibrationally Excited Emissions in LIMS Water Vapor

The *Nimbus 7* Limb Infrared Monitor of the Stratosphere (LIMS) experiment included channels centered at 6.9 μm and 6.2 μm to measure H_2O and NO_2, respectively. Because the photochemical lifetime of H_2O is several months, no diurnal variation in H_2O was expected; however, retrieved concentrations at mid-latitudes and low latitudes were larger in the daytime than in the nighttime in the upper stratosphere (by 20 to 30 percent at 1 mb). This result is attributed to a departure from local thermodynamic equilibrium of daytime emissions that had not been accounted for in the retrievals. Small changes in water vapor radiance represent significant changes in water vapor mixing ratio because of the inherent nonlinearity of the 6.3 μm H_2O band in the atmosphere.

Departures from nonlocal thermodynamic equilibrium (NLTE) have been evaluated in collaboration with Dr. Brian Kerridge of Rutherford Appleton Laboratory, England, and Dr. Susan Solomon of the NOAA (National Oceanic and Atmospheric Administration) Aeronomy Laboratory, Boulder, Colorado. It has been shown that excess radiance in the lower mesosphere can be explained by emission from the H_2O (020) $\rightarrow$ (010) hot band. In the stratosphere, there is also pumping of high vibrational states of NO_2 (v_3) by the chemical reaction $NO + O_3 \rightarrow NO_2 + O_2$ and by absorption of visible and near-infrared sunlight. The chemiluminescent emission from the vibrationally excited NO_2 occurs in the 6.9 μm H_2O channel. Estimates of the NLTE radiance contributions from both processes have been calculated and are shown in the figure. Because the measured total radiances increase rapidly with decreasing altitude, the NLTE radiances have their largest percentage effect in the upper stratosphere and lower

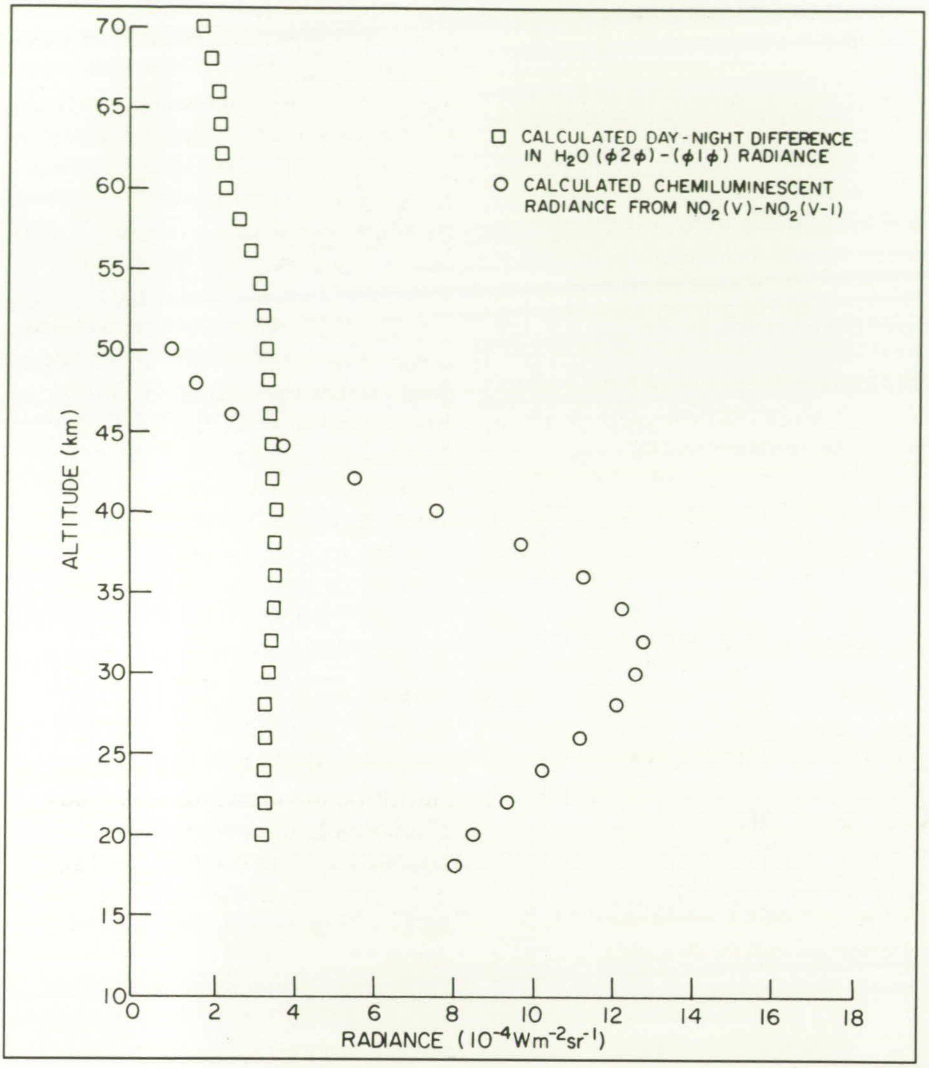

Calculated radiance contributions at 6.9 μm due to non-LTE effects.

mesosphere. The LIMS nighttime measurements of H_2O are not affected by these mechanisms, except in the polar night mesosphere.

The observation and interpretation of these enhanced radiances were possible because of the high precision of the LIMS radiances. More theoretical and laboratory studies of these NLTE effects are needed to assist with the exact identification of these processes. **(Ellis E. Remsberg, 45823 and James M. Russell III)**

Potential Effects of Antarctic Ozone Depletion on Global Ozone Budget

A growing consensus has developed within the scientific community that formation of the Antarctic ozone hole in the lower stratosphere during austral spring is largely a consequence of chlorine chemistry. Observed reductions of as much as 50 percent of the ozone column in polar regions have been observed. After the minimum is reached in late September to early October, the ozone column typically recovers within a few weeks. The recovery is a consequence of breakdown of the winter polar vortex with ozone-poor air exchanged with air masses with relatively higher ozone content from lower latitudes by large-scale quasi-horizontal transport.

It has been hypothesized that transfer of ozone-poor air from the polar regions to middle and low latitudes will create a deficit in the ozone (a "dilution" effect) which could persist for a long period because of the slow chemical replenishment time (months to a year), dependent upon latitude in the lower stratosphere. If the deficit in the ozone persists until formation of the ozone hole during the next spring, the effect may be cumulative with a permanent reduction in the global ozone budget.

A study of the dilution effect has been conducted with the Langley Research Center three-dimensional chemistry/transport model. Simulations were conducted in which an ozone hole was imposed in the polar region (69°S to the pole between 27 mb and 112 mb) by specifying a linear loss rate such that 90 percent of the ozone in that region was removed during September (5.75 percent of the total ozone in the Southern Hemisphere). One year later, a residual deficit of approximately 1.3 percent of the Southern Hemisphere ozone persists in the simulation (see the figure). Most of the residual ozone deficit in the simulation is below 100 mb and between latitude 30°S and the pole (approximately 1 percent of the column at 30°S and approximately 2 percent of the column from 60°S to the pole). The results are generally consistent with trends observed in the Total

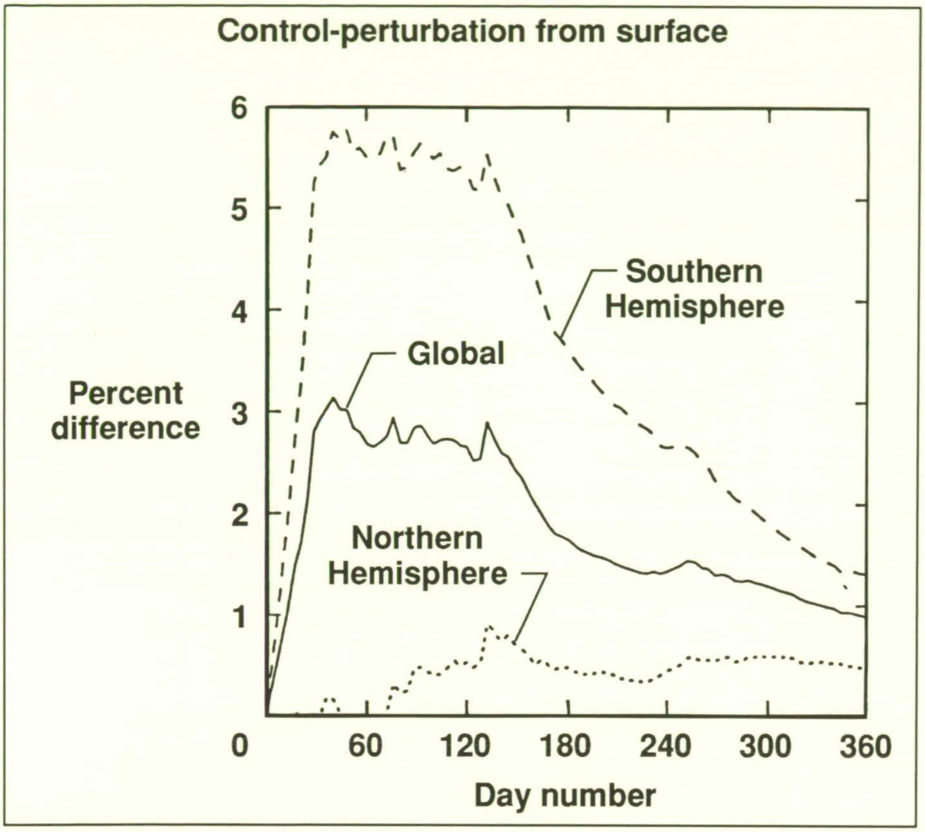

Percent difference in integrated global and hemispheric column for Antarctic ozone hole simulation relative to control simulation as function of time. (Day 0 is September 1.)

Ozone Mapping Spectrometer (TOMS) data. The simulation results suggest the possibility of a small, but cumulative, effect upon the global ozone budget.
(William L. Grose, 45820)

Six-Degree-of-Freedom ACRC Simulation Results

One of the concerns involved with the long-term use of Space Station *Freedom* is to provide an Assured Crew Return Capability (ACRC) in the event of an on-station emergency or the unavailability of the Space Shuttle. Studies have shown that the optimal method of providing this capability is by having dedicated vehicles docked at the station. If necessary, the crew would enter these vehicles, separate from the station, and deorbit. Two vehicle designs have been proposed to provide this capability. One is a capsule modeled after Apollo or Viking. The other is a lifting-body design based on the HL-10. A joint study effort by Lyndon B. Johnson Space Center and Langley Research Center showed that the total cost of the lifting body would exceed the cost of the capsule configuration by approximately 20 percent. However, the lifting body offers the advantages of runway landings, as opposed to ocean landings, and much lower accelerations during entry (1.5 g compared with 5 g).

One of the major questions that had to be answered for this study effort was how to control the lifting body during the high heating portion of the flight. The complexity and hence total cost would be

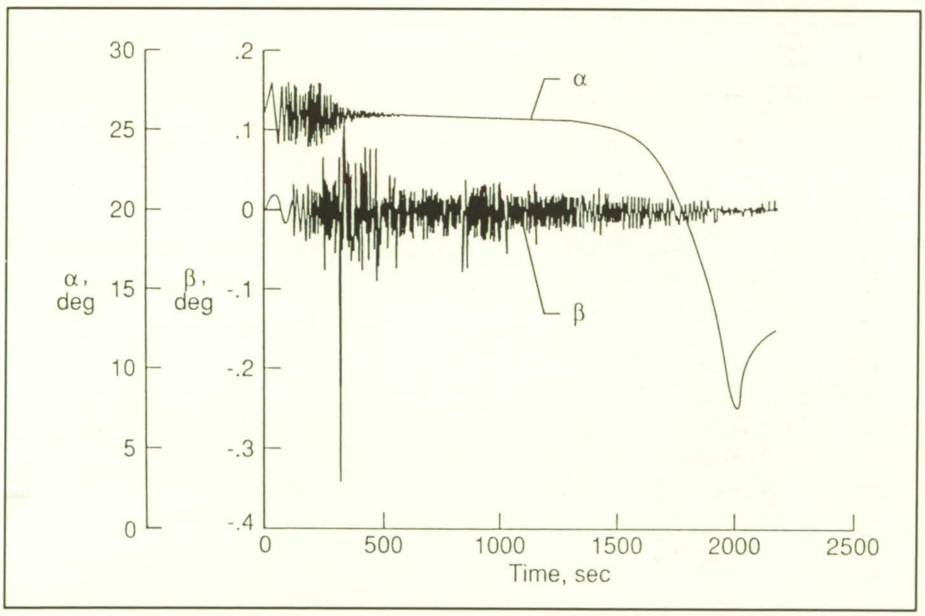

Complete six-degree-of-freedom entry.

reduced if the aerodynamic control surfaces were not used at hypersonic speeds. The reduction in complexity and cost would result from elimination of moving seals and reduction in required electrical power. To address this concern, a control and guidance system was designed for the lifting-body configuration that would fly the vehicle from the atmospheric interface to Mach 2. The proposed lifting-body control system used only the reaction control system, in contrast to the Space Shuttle, which uses both the reaction control system and the aerodynamic control surfaces. This reduction in control complexity is possible because the lifting body is directionally stable at these speeds, whereas the Space Shuttle is not. The figure shows the angle of attack α and sideslip angle β histories for this entry, which required only 30 lb of fuel for control.

(Richard W. Powell, 44506)

Lifting-Body Approach to Personnel Launch System

As part of a NASA Office of Space Flight study, three options are under consideration for the next manned space transportation system. One approach is the evolution of the present Space Shuttle through a series of upgrades and major changes. Another option is that of an all new Advanced Manned Launch System (AMLS) to replace the Space Shuttle at the end of its useful operational life. The third option is a small Earth-to-orbit personnel-only vehicle, the Personnel Launch System (PLS), to complement the Space Shuttle starting at the turn of the century. Several concepts for PLS are being investigated including ballistic capsules and lifting bodies.

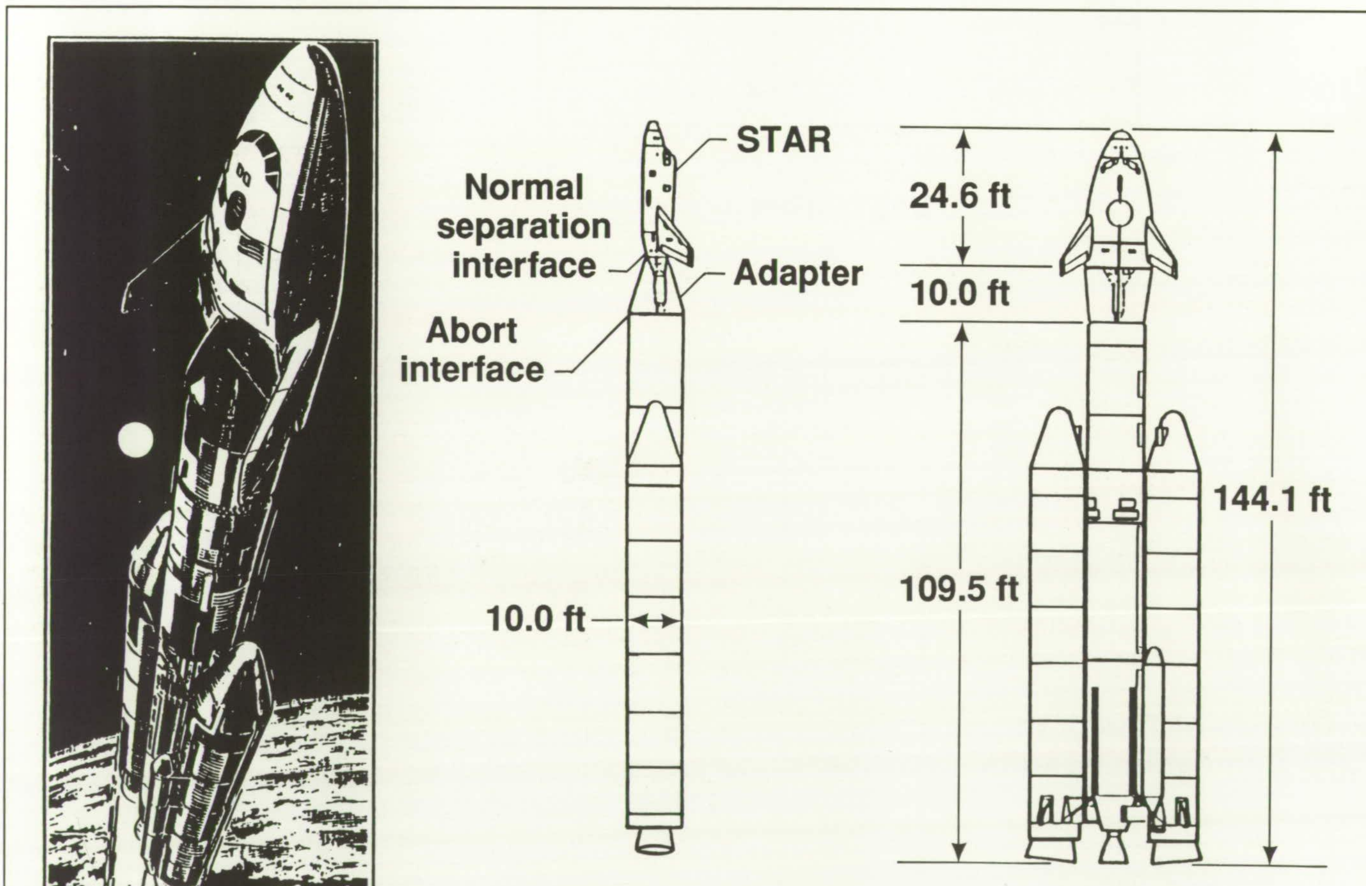

Personnel Launch System concept.

The Langley Research Center is examining a lifting-body approach to PLS called STAR (space taxi and return).

In conceptual design studies, the STAR lifting body is being scaled to carry from 8 to 10 people to Space Station *Freedom* and to return. The shape is a derivative of the X-24 and HL-10 lifting bodies flown during the 1960's. The use of the lifting-body concept permits a horizontal landing on a runway. Trajectory analyses have shown that entry loads are limited to less than 1.5 *g*. Extensive wind tunnel tests of this shape have demonstrated its good aerodynamic flying qualities throughout the range from subsonic through hypersonic flight. With an aerodynamic cross range exceeding 850 nautical miles, the lifting body has numerous landing opportunities available when returning to specified landing sites from orbit. Docked to the space station, the PLS may also function as an Assured Crew Return Capability (ACRC) vehicle for emergency return of stranded crew members.

Several launcher concepts are being explored for placing PLS in orbit. Use of existing expendable rockets, such as the *Titan III* and *Titan IV*, would lessen development costs and speed the initial operational readiness date of PLS. Also being considered are several operationally cost-effective launchers that use all-liquid propulsion.
(Theodore A. Talay, 44505)

NASA In-House Commercially Developed Space Facility (CDSF) Studies

Studies have been performed within NASA to develop a concept definition and a design, development, and operations cost estimate of a Commercially Developed Space Facility (CDSF). The premise of the CDSF concept is that the government would lease the capabilities of a low-Earth orbital space facility that is operated by a commercial venture company for the purpose of performing microgravity materials processing experimentation. NASA, through an anchor tenant

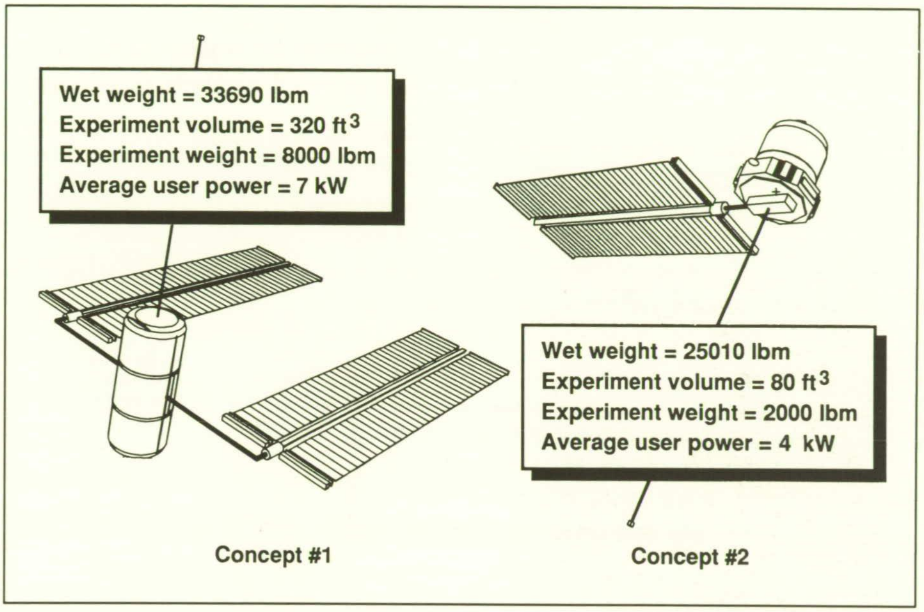

CDSF configuration concepts.

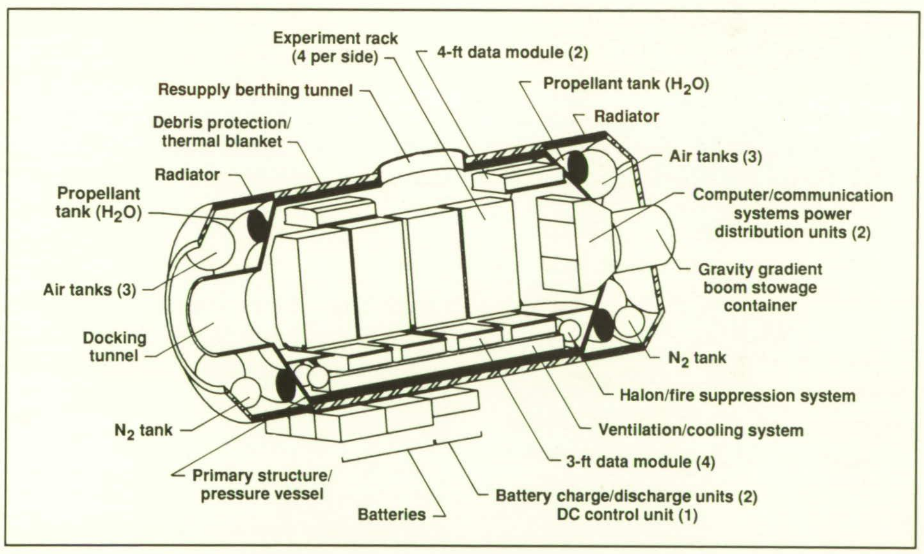

CDSF concept number 1, system configuration.

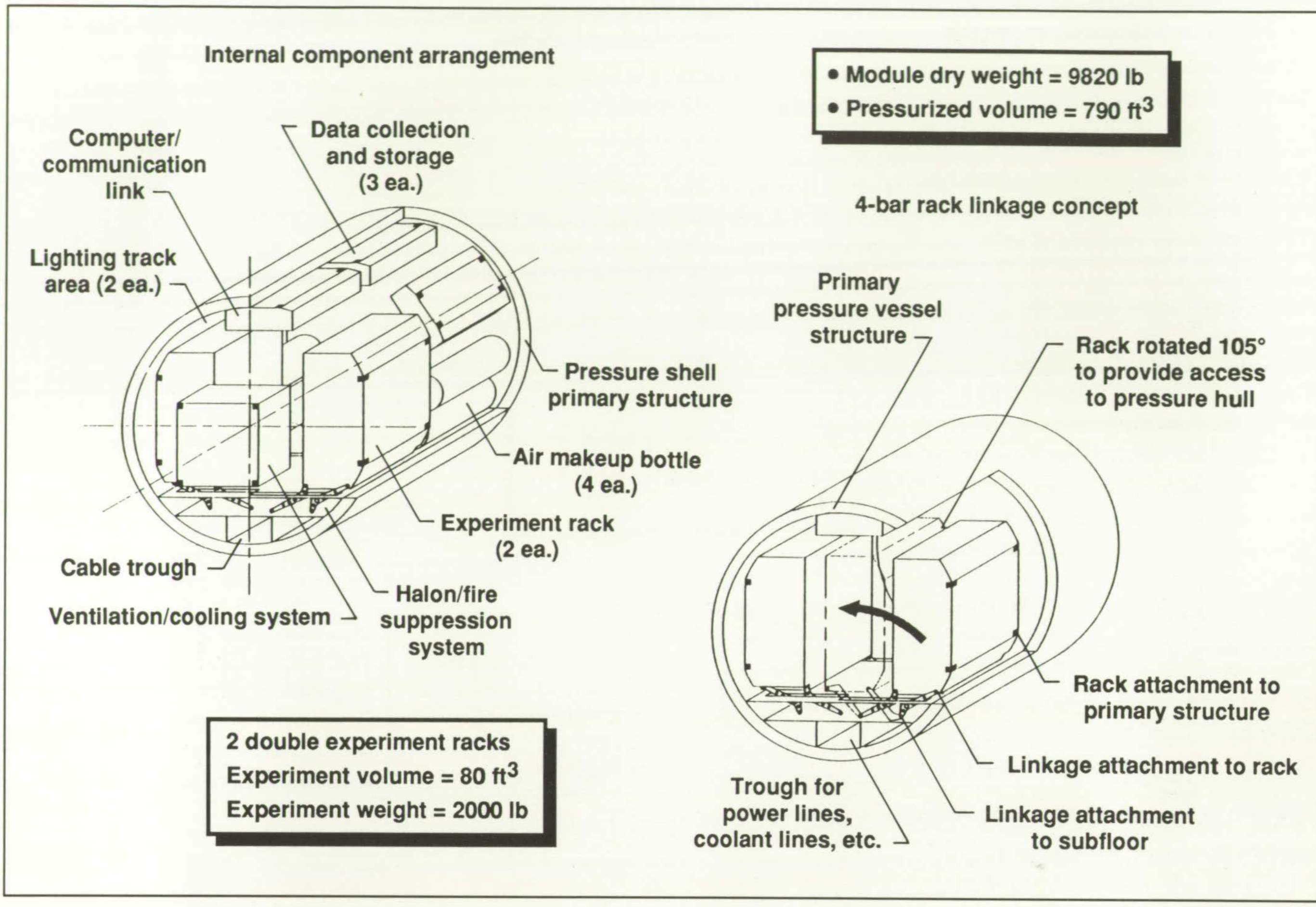

20-percent CDSF concept experiment module.

lease arrangement or through an initial space flight hardware purchase contract, would initiate the development process for such a facility that could be placed in orbit by the Space Shuttle in the 1993 time period.

These concept definition and cost estimation studies were directed by the NASA Administrator to be performed commensurate with studies performed by the National Research Council (NRC) to assess the national microgravity materials processing and manufacturing needs and goals, and by the National Academy of Public Administration (NAPA) to assess financial scenarios and fiscal year budgetary requirements. The specific objectives of the NASA in-house concept definition studies were to provide science mission utilization definition scenarios; quantify the conceptual configuration system performance parameters; establish benchmark operational scenarios; develop mission and flight control system concepts; provide Space Shuttle interface descriptions; estimate the design, development, and operations costs; and assess the development schedule. Two CDSF concepts were considered. The first concept is a baseline concept definition and cost estimation that incorporates 100 percent of the functional performance specifications. The second concept is a concept definition and cost estimation based on minimum assumed capabilities that would accommodate microgravity experimentation requirements. These concept definitions and cost assessments are documented in NASA TM-101586, volumes I and II, dated April 18, 1989. The resulting system configurations are shown in the figures.

(Leonard J. DeRyder, Jr., 41946)

Structures Directorate

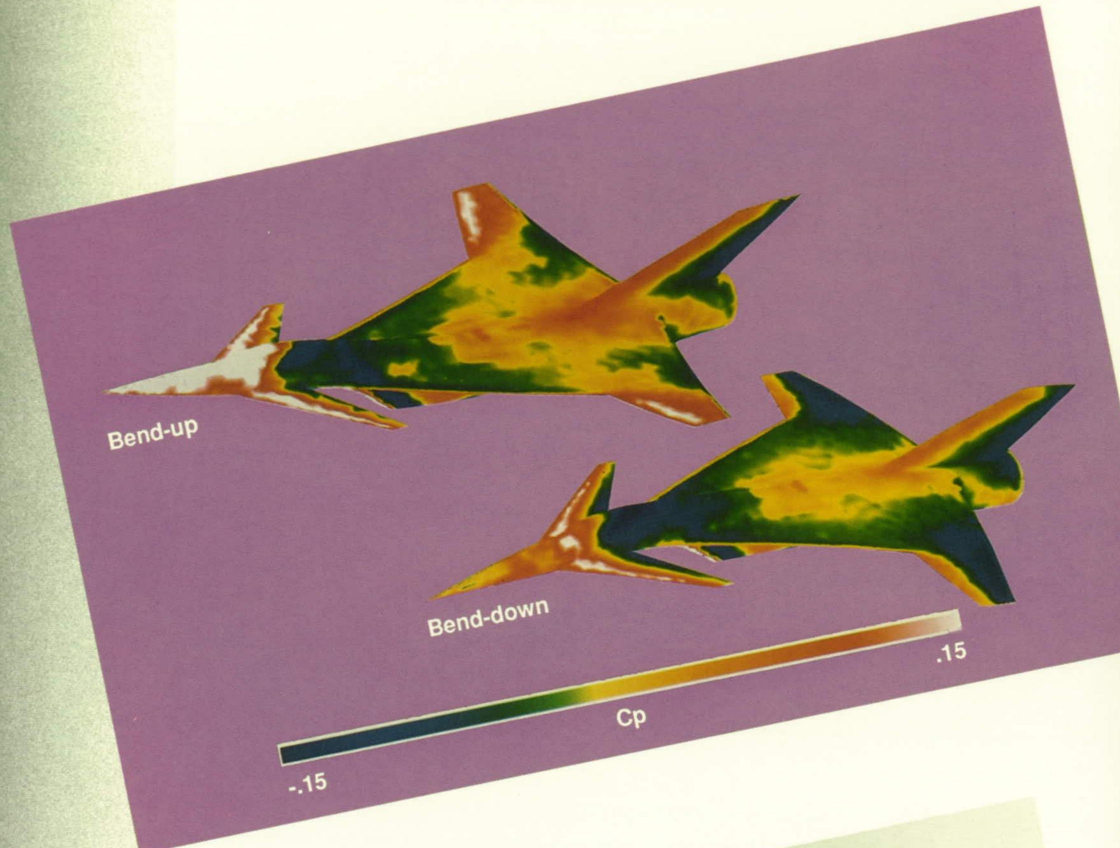

The Structures Directorate conducts basic research and develops technology in the areas of advanced aerospace materials and structures, structural loading and aeroelasticity, noise generation by aircraft propulsion systems and its interaction with structures, and methodologies for interdisciplinary design and optimization. This technology development is directed toward reduction in both weight and cost of aircraft and space structures along with an increase in their reliability and service life. The technology developed also provides improved design capability through more accurate prediction of aerostructural loads, vibration, and noise.

The Materials Division conducts research on advanced materials and their application to aircraft and space structures. The division also develops novel polymeric, metallic, and carbon-carbon materials for these applications. The materials processing and fabrication sciences are developed, and the application of materials to specific flight and space structures is demonstrated. The division conducts research on thermal protection materials and hot structure systems for application to hypersonic and transatmospheric vehicles. The fatigue and fracture behavior of materials is studied in specialized laboratories to provide practical methods for ensuring structural integrity. Specialized facilities are also used to study the behavior of materials under extreme conditions of high and low temperature, pressure or vacuum, and electron radiation.

The Structural Dynamics Division conducts research on aeroelasticity, unsteady aerodynamic loads, aeroservoelasticity, structural dynamics and controls for spacecraft, and landing and impact dynamics for aircraft safety and ground handling. Analytical methods are developed for calculating aeroelastic deformation and instabilities, for active control of dynamic behavior of aircraft and spacecraft, and for dynamic stresses and strains in large space structures. Unique facilities are employed in experimental studies of unsteady aerodynamics, aeroelastic behavior, dynamics of aircraft under simulated landing and crash conditions, and dynamic response and control of large space structures.

The Structural Mechanics Division conducts research on structures and mechanics for advanced aircraft, spacecraft, and automated construction of the space station. Research is conducted on aerothermal loads and high-temperature structures to support technology development for hypersonic vehicles and advanced launch systems. Analytical methods are developed to predict stresses and strains in complex aerospace structures, behavior of composite structures, thermal responses of structures, and aerothermal loads. The division develops new structural systems for aircraft and advanced computational methods for structural analysis and design.

The Acoustics Division conducts research on the generation and propagation of aircraft noise and seeks to understand the relationships between unsteady aerodynamics, structural dynamics, and noise generation by the interaction of fluids with solid surfaces. This research is directed toward predicting and reducing the noise from helicopter rotors, conventional and advanced aircraft propellers, and turbofan engines. Research is conducted on the propagation of noise from its source through the atmosphere and through aircraft structures.

The Interdisciplinary Research Office develops methodologies for aircraft and spacecraft design which will provide a means of understanding and quantifying interactions among multiple engineering disciplines. The goal is to control and exploit these interactions for improved vehicle performance and increased efficiency of the design process. This research has focused on the development of algorithms and techniques for integrating strength and stiffness designs of large-aspect-ratio wing transport aircraft and of rotorcraft. The methodology has been developed for the optimization of space antenna dish shapes subjected to thermal loadings. Controls, structures, and structural dynamics have been integrated for use in the design of space station type structures.

Significant accomplishments have been made in 1989 in all areas of research within the Structures Directorate. The Acoustics Division has studied the generation of and reduction methods for noise from vehicle types that range

from helicopters to hypersonic cruise. The Materials Division has shown important results in the development of advanced polymers, fibrous and metal matrix composites, and new metal alloys and methods for their fabrication. The Structural Dynamics Division has made contributions to the understanding and prediction of the dynamic behavior of both aircraft and spacecraft and to the safety of both with their work on tires and landing gears. The Structural Mechanics Division has done significant work to optimize the design of new aircraft structures made with advanced composites, to determine the loads on and response of hypersonic vehicle structures, to find methods for allowing these hypersonic structures to withstand the high heat loads, and to develop methods for the robotic assembly of future large space structures. The Interdisciplinary Research Office has led in the development of methods for the integrated optimization of vehicle design. The following highlights will briefly discuss some of the most important accomplishments of the year.

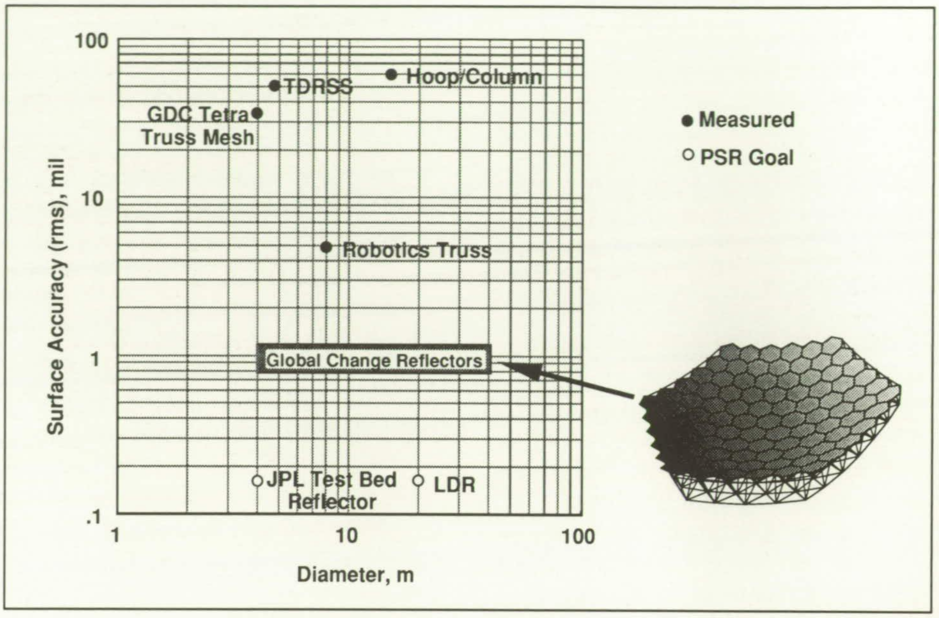

Reflector surface accuracy. (GDC stands for General Dynamics Convair; TDRSS is Tracking and Data Relay Satellite System; PSR is precision segmented reflector; and LDR is large deployable reflector.)

Experimental Measurement of Robotic Assembly Truss Upper Surface Accuracy

Proposed deep-space and Earth science missions will require large, accurate trusses to support highly precise reflective surfaces. An 8-m-diameter, two-ring planar tetrahedral truss having 102 2-m-long members and 31 nodes has been fabricated for use in an experiment to demonstrate the robotic assembly of large space structures. The variation in the truss member lengths was found experimentally, and each truss member was placed in a known location in the assembled truss. Convergent close-range photogrammetry was employed to locate the spatial coordinates of the 19 upper surface nodes. A total of 25 data photographs of the truss were taken at two different elevations as the truss support platform was rotated through 12 radial positions. A least-squares triangulation and resection routine was performed on the photographic data, providing spatial coordinates and measurement precisions for the upper surface nodes. These coordinates were then converted and scaled to a global coordinate system.

The measured root-mean-square (rms) accuracy of the displacements normal to the upper surface of the truss was found to be 5.4×10^{-3} in. (the precision of the individual measurements was $\pm 0.96 \times 10^{-3}$ in.), showing that precise measurement of the surface accuracy of large truss structures is achievable using low-cost, noncontacting techniques. The figure shows that this structure demonstrates a significant improvement in the measured surface accuracy over that of deployable mesh reflectors previously developed for space communication applications. Based on this experience, the construction of parabolic reflector trusses having rms surface accuracies of 1×10^{-3} in. is thought to be possible using standard fabrication tolerances and machining techniques. It also may be possible to fabricate trusses having the very high surface accuracies required for use in optical-quality applications such as precision reflector support trusses.
(K. Chauncey Wu, 43111)

Advanced Turboprop En Route Noise Test

Development of the advanced turboprop has led to concerns for en route noise. Advanced turboprops generate low-frequency, periodic noise signatures that can propagate from cruise altitudes and be audible on the ground. The assessment of en route noise is difficult due to the variability of received noise levels resulting from atmospheric propagation and the uncertainty in predicting community response to the relatively low-level (as compared to airport operations) en route aircraft noise signatures. In response to the en route noise issue, especially the expressed concerns of the Society of Automotive Engineers (SAE) A-21 Aircraft Noise Committee, NASA and the Federal Aviation Administration (FAA) have developed an Aircraft En Route Noise Technology Program. This program consists of noise measurements, atmospheric propagation tests, and subjective response research. The En Route Noise Test is part of the overall program funded by NASA and the FAA.

The objective of the En Route Noise Test was to study the influence of turbulence scattering and refraction due to wind and temperature gradients on the propagation of propfan noise from cruise altitudes. The En Route Noise Test was performed at the White Sands Missile Range during April 1989 and consisted of flying a test airplane over a ground microphone array (shown in the first figure). The test airplane was Lewis Research Center's Gulfstream II, which has an advanced turboprop mounted on its left wing. The test matrix included level passes over the microphone array at altitudes of 2000 ft to 30,000 ft above ground level, Mach numbers from 0.5 to 0.77, and propfan rotational tip speeds from 620 ft/sec to 840 ft/sec. Weather parameter profiles were measured up to an altitude of 40,000 ft. A linear microphone array was used so that array processing could be used in the data analysis to be able to investigate with a high level of confidence the results of a single overflight. The data plot (second figure) is an example of an ensemble-averaged time history with confidence bounds.

Advanced turboprop test airplane.

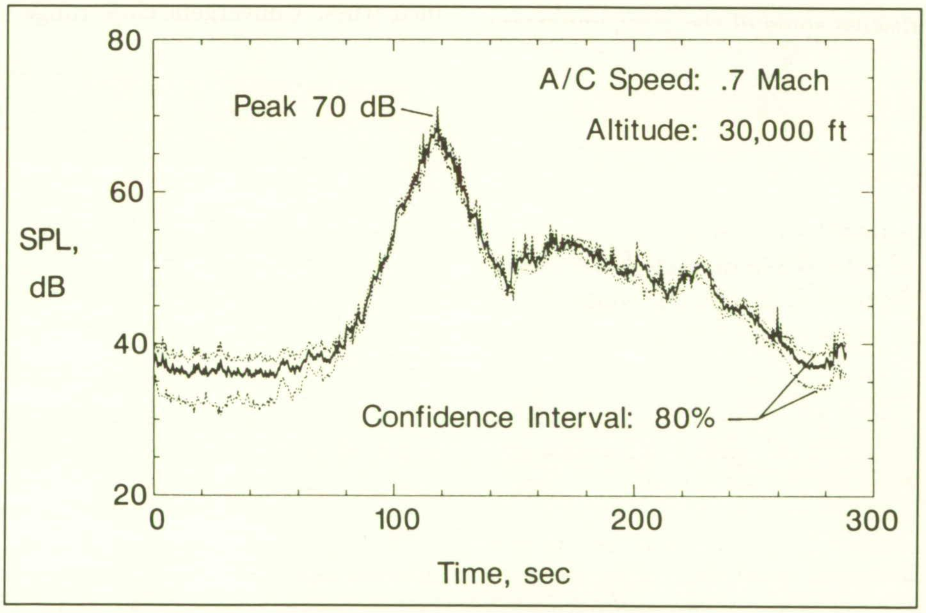

Example of ensemble-averaged time history for Mach 0.7 and 30,000-ft altitude overflight.

Data collected in the En Route Noise Test will be used to validate acoustic propagation models. Spatial and temporal variability and their relationship to time of day and weather parameters will be investigated. In addition, acoustic data recorded in the test will be used to investigate the subjective response to propfan noise.
(William L. Willshire, Jr., 45270)

Hypersonic Fluctuating Loads in Scramjet Engine Model

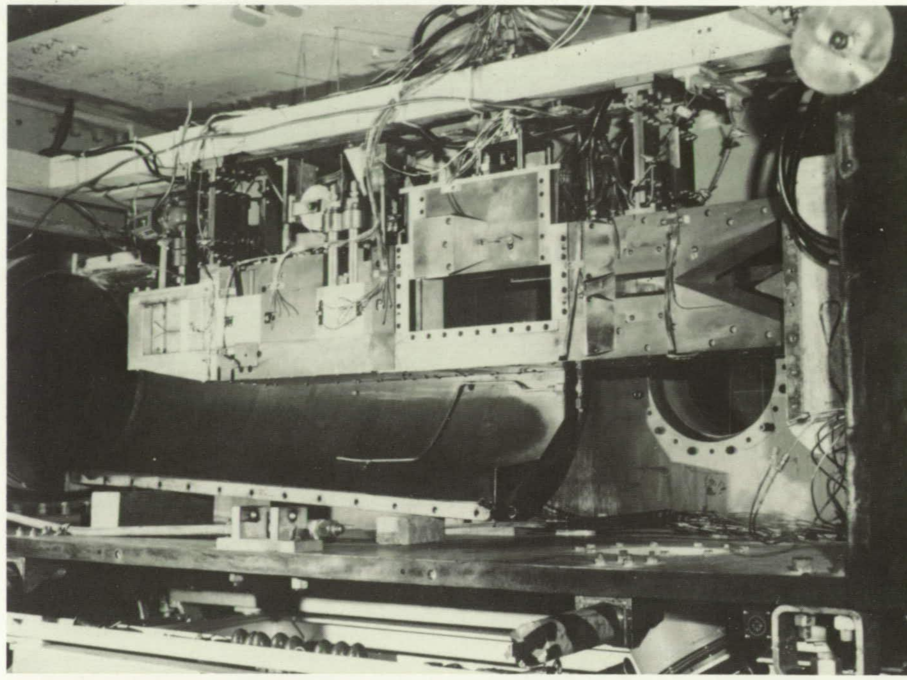

JHU/APL National Aero-Space Plane B-1 engine model installed in Combustion-Heated Scramjet Test Facility. L-88-10,681

Two critical problems for supersonic combustion ramjet (scramjet) engine design are the control of the combustion process to prevent aerodynamic instabilities that can lead to an engine unstart, and the quantification of the fluctuating pressure loads generated by the combustion process, turbulent boundary layers, and shock/boundary-layer interactions. Fluctuating pressure measurements in scramjet engines are of interest from the standpoints of combustion instability onset and structural design of engine components. The purpose of this work is to develop measurement technology for fluctuating pressure loads in the high-speed, hostile environments of scramjet engines.

A scramjet engine model designed by the Johns Hopkins University (JHU) Applied Physics Laboratories (APL) was installed in the Combustion-Heated Scramjet Test Facility at Langley Research Center, as shown in the figure. An array of eight piezoresistive pressure sensors was installed in the top wall of the scramjet model. During a typical test, a 34-sec time history was recorded. The test period began when a steady-state heat release was achieved by the combustion of gaseous hydrogen in the combustor section. Changes in the boundary pressure fluctuations were measured along the top wall of the model as the engine operating parameters were manipulated. In particular, changes in the boundary-layer pressure fluctuations just upstream of the combustor section were measured when the fuel flow rate underwent a step increase.

The pressure time histories at two sensor locations upstream of the combustor section showed clear evidence of significant changes in overall pressure levels associated with combustion noise propagating upstream through the boundary layer. The measured peak-to-peak pressure fluctuations at these sensors indicated an increase in level from 12 dB to 19 dB resulting from a step increase in the fuel flow rate.

Also, it was demonstrated that the time evolution of an engine unstart (i.e., the destabilization of the inlet diffuser flow by an increased back pressure in the combustor) could be tracked by comparing synchronized time histories at the various sensor locations. This measurement technology is important for the continued development of scramjet engine design technology.
(Tony L. Parrott, 45273)

Numerical Prediction of Sound Generated by Shock Vortex Interaction

The passage of turbulence through shock waves in supersonic

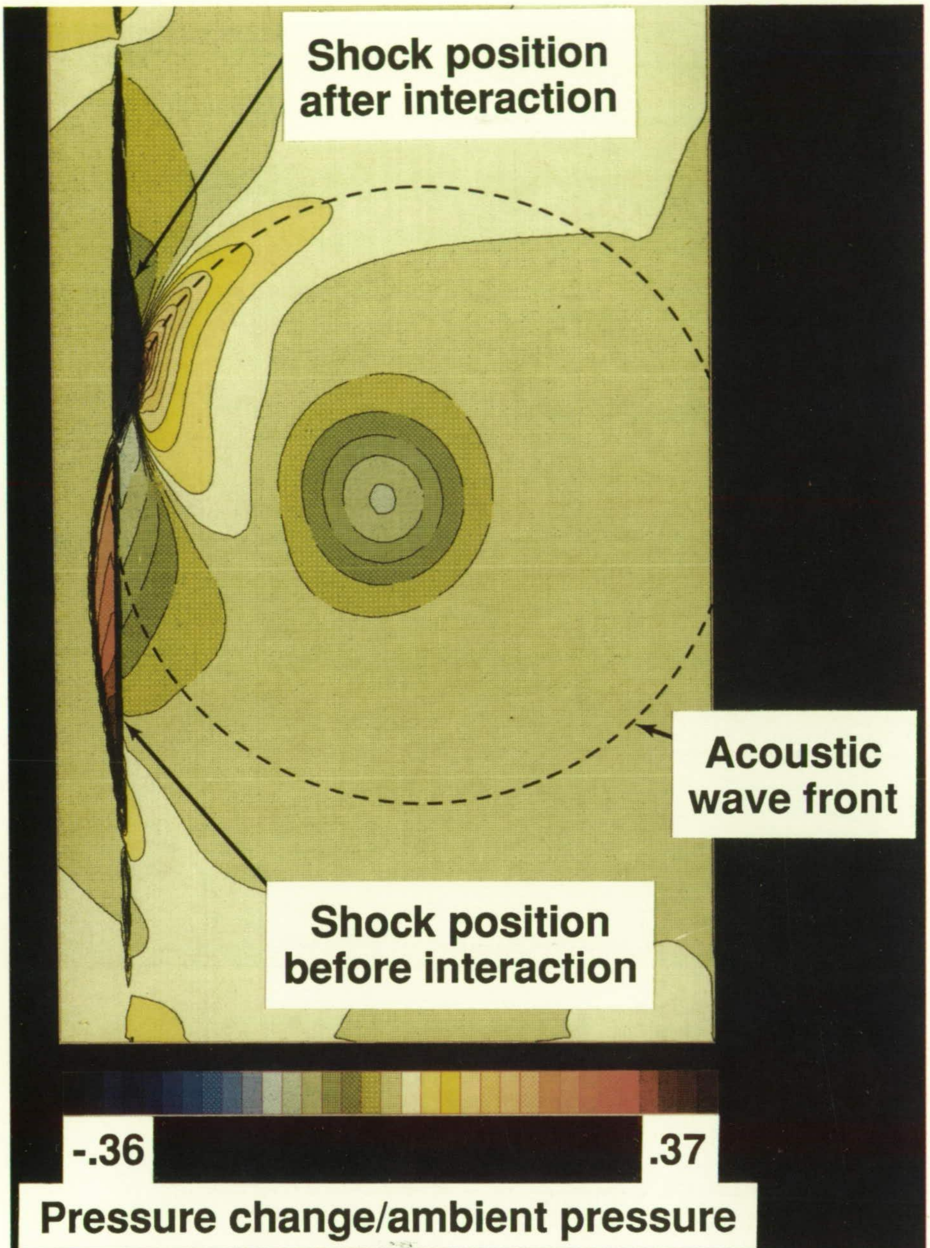

Pressure contours downstream of shock after interaction with vortex.

jet plumes is known to generate shock-associated noise, one of the several mechanisms for supersonic jet noise. This particular mechanism was modeled by the passage of a vortex through a normal shock. After an initial Mach 1.1 flow field was established, a vortex was superimposed on the flow upstream of a stable normal shock in a duct and allowed to convect downstream with the flow to the duct outlet. The Euler equations, which govern the dynamics of inviscid flow, were solved on a grid of 132 points in the axial direction and 122 points in the normal direction with a second-order-accurate finite volume technique. This numerical method was chosen because shocks are captured as a part of the solution. One of the benefits of shock capturing is that it also allows situations where the shock vortex interaction produces secondary shocks to be investigated.

The contours in the figure show the change in pressure downstream of the shock after interaction with a strong vortex. The heavy lines in the figure represent the location of the shock before and after the interaction. The dashed circular region indicates the position of the vortex. The deflection and splitting of the shock is seen in this figure as well as the formation of two distinct pressure regions at the points of maximum shock excursion. The pressure region indicated by the solid lines represents an increase in pressure from the preinteraction state; the region indicated by long dashed lines represents a decrease in pressure. Analysis of the wave front shows that it travels at the local speed of sound and is therefore a sound wave. The acoustic wave front is shown for illustrative purposes by a dashed circular arc passing through the compression and expansion regions.
(Kristine R. Meadows, 43624)

Supersonic Jet Noise Laboratory

Recently the supersonic Jet Noise Laboratory at Langley Research Center was upgraded with a SUE (sudden expansion) propane burner to increase the facility's 1000°F electric heat capability to afterburning-type temperatures. An

increasing body of evidence exists which suggests that these elevated temperatures produce density differences that drive absolute jet instabilities. This type of instability, whose amplitude grows temporarily, is responsible for rapid plume mixing behavior in hot jets. Both sound and optical emissions from supersonic jets depend heavily on the mixing behavior of the jet, and accurate understanding of the physical principles underlying the physics of this mechanism is essential to the development of predictions for these emissions. This new heated capability will enable more accurate prediction of fighter aircraft acoustic loads and community noise for the commercial supersonic transports.

The supersonic Jet Noise Laboratory has the capability of aeroacoustic measurements (i.e., flow field diagnostics and acoustic and thermal imaging) under continuous-flow conditions in both the subsonic and supersonic flow regimes. The maximum jet Mach number of this facility is 2.2 with flow temperatures reaching 4000°R. The facility is anechoic, permitting both near- and far-field acoustic measurements. Model nozzles include single, coannular, and twin configurations with both round and non-round exit geometry. Shock-free supersonic Mach 1.5 and Mach 2.0 elliptic nozzles have been designed and studied in this laboratory. The facility also has a low-temperature secondary stream (1000°F to 2 lbm/sec) which when combined with the propane burner flow permits the study of mixed nozzle flows that emulate the AST/VCE (Advanced Supersonic Transport/Variable-Cycle Engine) requirements. Both primary and secondary flow streams independently are capable of supplying 23 lbm/sec air at a pressure ratio to 12 with the propane burner. Both air and fuel delivery systems are completely computer automated.

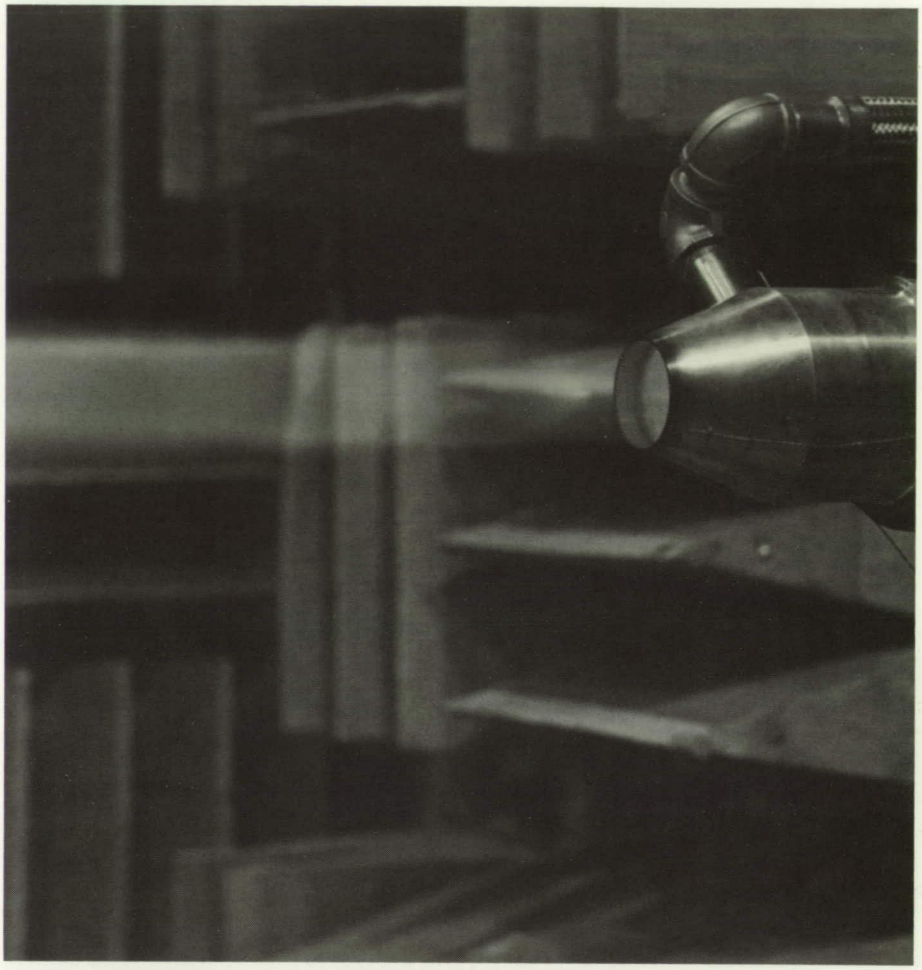

Heated Mach 2 axisymmetric jet, $T_0 = 2600°F$. L-88-09842

Diagnostic laboratory capabilities include the automated computerized use of conventional supersonic pitot and static pressure probes, hot-wire and hot-film anemometry, dynamic wall and free-field sensor arrays, laser anemometry, imaging radiometry, Fourier transform/infrared spectrophotometry, and phase-averaged schlieren with digital image processing.
(John M. Seiner, 46276 and James C. Manning)

Easy-to-Process, Tough Composite Matrices From Bisacetylenes and Bismaleimides

High-performance thermosetting and thermoplastic polyimides are under extensive experimental and developmental evaluation for a great number of aerospace structural applications because of their high glass transition temperatures T_g's, excellent mechanical performance, and ability to withstand harsh environments, such as heat, moisture, and chemicals. The poor processibility and lack of damage tolerance

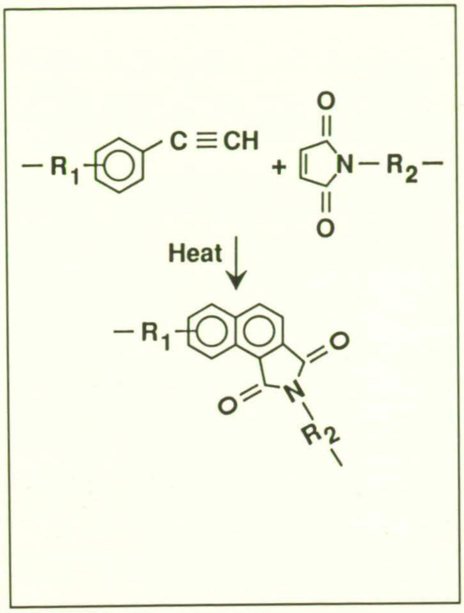

Chemistry of high-performance addition-type thermoplastic polymers.

of these materials, however, have seriously inhibited their widespread use in fabricating large aerospace structures.

Synthesis research at Langley Research Center has provided a means to overcome the limitations previously found in polyimides. Acetylene-containing oligomers (triple bonds) have been shown to react with maleimides (double bonds) in an addition-type polymerization (no volatiles generated) leading to a linear polymer structure with good toughness. This novel chemistry, illustrated in the figure, has been demonstrated in resin, composite, and adhesive forms. The polymer that has been studied to the greatest extent has been designated LaRC-RP80. This new material exhibits ease of processing and a high level of toughness while maintaining a respectable T_g, compared to a commercial bismaleimide (BMI). This polymer displays exceptional thermo-oxidative stability, absorbs very little moisture, and retains good thermal/mechanical properties in wet environments. Because of the fundamental nature of this chemistry, it can be used to obtain any number of new polymers with a very desirable combination of properties.

(Ruth H. Pater, 44277)

Effect of Fiber/Matrix Interface Strength on Properties of Titanium Metal Matrix Composite

Recent interest in hypersonic flight vehicles has required the development and characterization of materials capable of retaining high stiffness and strength at temperatures in excess of 550°C. One of the most promising classes of materials is titanium-based metal matrix composites.

A [0/90/0] laminate with continuous silicon carbide fibers (SCS-6) reinforcing a titanium matrix (Ti-15-3) was selected as a model material for characterization. One panel was subjected to 1000°C

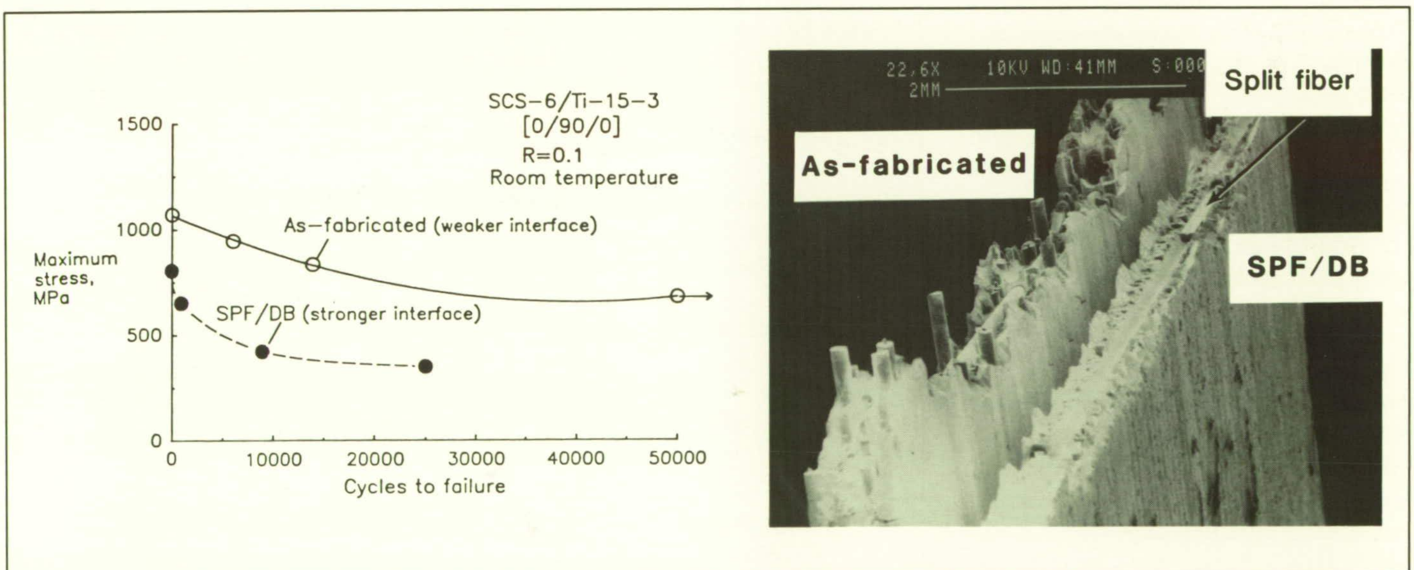

Comparison of as-fabricated and SPF/DB mechanical behavior and failure modes.

for 1 hr to simulate the temperature cycle that the material would see during a superplastic forming/diffusion bonding (SPF/DB) process. Another panel was left in the as-fabricated (ASF) condition. The composite showed a 9-percent increase in elastic Young's modulus, a 25-percent decrease in tensile strength, and a 30-percent decrease in failure strain as a result of exposure to typical SPF/DB conditions. Furthermore, the fatigue life (shown in the figure) for the SPF/DB specimens was approximately 50 percent lower than for the ASF specimens. The fracture surface of the ASF specimens was very irregular with significant fiber pullout as compared to the planar fracture surface of the SPF/DB specimen in which fibers were flush with the surface. These features suggest that the fiber/matrix interface is stronger after the temperature cycle. A matrix crack growing toward a fiber with a stronger fiber/matrix interface is more likely to fracture the fiber rather than deflect along a weaker crack path such as an interface disbond. This results in a more "notch-sensitive" material that will have a lower strength and fatigue life. Microstructural examinations of the fiber/matrix interphase regions also support the conclusion that the interface strength has increased.

Additional tests showed that the SPF/DB matrix material has a higher modulus and strength than the ASF material; this would allow higher thermal residual stresses to be present in the SPF/DB composites, which would also contribute to a higher interface bond strength. Therefore, the strength reduction exhibited by the composite is due to both a stronger fiber/matrix interface bond and an elevation of the residual radial compressive stresses around the fiber. The fiber properties were unaffected by the temperature cycle.

This study shows that a typical SPF/DB thermal process cycle can result in a significant reduction in the tensile strength and the fatigue life of a composite despite the fact that both the matrix and fiber/matrix interface strengths are increased. In short, a stronger fiber/matrix interface may not always have a desirable effect on the performance of a composite. In general, a strong fiber/matrix interface is less desirable when designing a composite material system with a stronger, stiffer matrix.

(W. S. Johnson, 43463, R. A. Naik, and W. D. Pollock)

High-Aspect-Ratio Configuration Optimized for Aeroelastically Tailored Wingbox

Tailored composite structures can enable advanced airframe configurations. A high-aspect-ratio, forward-swept wing configuration was selected for study, and three wingbox models with different interior structural configurations were developed. The wingbox models are shown on the left side of the figure. An integrated multidisciplinary procedure consisting of an aerodynamic analysis with aeroelastic corrections, a structural analysis, and a structural optimization algorithm was used for this study. Minimum-weight wingbox structures that satisfy the loading conditions and design constraints were obtained.

Optimized weights for the two-spar, four-spar, and multispar/multirib wingboxes are shown

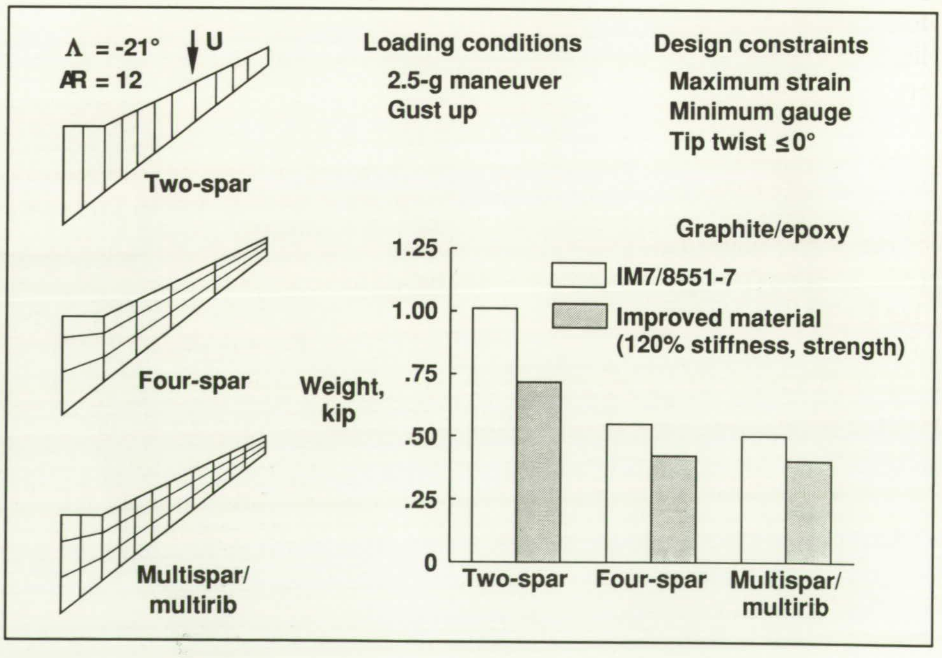

Weight comparison for wingbox configurations.

on the right of the figure. Results are presented for wingboxes modeled with IM7/8551-7 damage-tolerant graphite/epoxy material and for wingboxes modeled with an improved material having stiffness and strength properties that are 20 percent greater than the respective properties for the IM7/8551-7 material. The results show that the conventional two-spar wingbox is the heaviest of the wingboxes studied. This wingbox satisfies all requirements using thick tailored cover panels. The four-spar and multispar/multirib wingboxes are approximately 45 percent and 50 percent lighter, respectively, than the two-spar wingbox. These wingboxes combine an efficient internal structure with tailored cover panels to achieve feasible lightweight designs. The four-spar wingbox appears to be the best of the wingboxes studied because it has approximately the same weight as the multispar/multirib wingbox but is a much simpler design than the multispar/multirib wingbox. The results of this study show that the four-spar wingbox is significantly lighter than the conventional two-spar wingbox for this high-aspect-ratio wing configuration and indicate that new, structurally efficient wing internal structure concepts are possible by exploiting the benefits of composite materials.

(M. J. Shuart, 43170, R. T. Haftka, and R. L. Campbell)

Damage of Thick Reinforced Plastic Materials by Low-Velocity Impact

Epoxy reinforced with small graphite fibers (Gr/Ep) is stronger, stiffer, and less dense than aluminum; thus, it has great potential for aerospace applications. In order to reduce structural weight, NASA is interested in using Gr/Ep cases in the solid rocket motors of the Space Shuttle and in new, advanced launch systems. Thick Gr/Ep material would be needed to replace the 0.5-in.-thick steel of the solid motor cases of the Space Shuttle. However, dropped tools, errant stones, hail, and other debris can seriously damage thin sheets of Gr/Ep. Experiments revealed that the energy to damage thick Gr/Ep plates is much greater than that to damage thin sheets, but still less than that to damage conventional metal plates. Thick plates exhibited total crushing; whereas, thin sheets exhibited widespread splintering and delamination. An investigation was made to understand how the damage develops in the thick plates, perhaps leading to a more impact-resistant material. The impacts were simulated by pressing smooth hemispherically shaped indenters against a 1.4-in.-thick Gr/Ep plate that was cut from a prototype motor case that was filament wound.

Examinations of the damaged plates by scanning electron microscopy revealed matrix shear failure beneath the contact site. This type of shear failure is typical of compression failure in other materials. The shear failure of the matrix caused intense deformations that broke the fibers. The shear and compressive stresses that would cause this damage were calculated

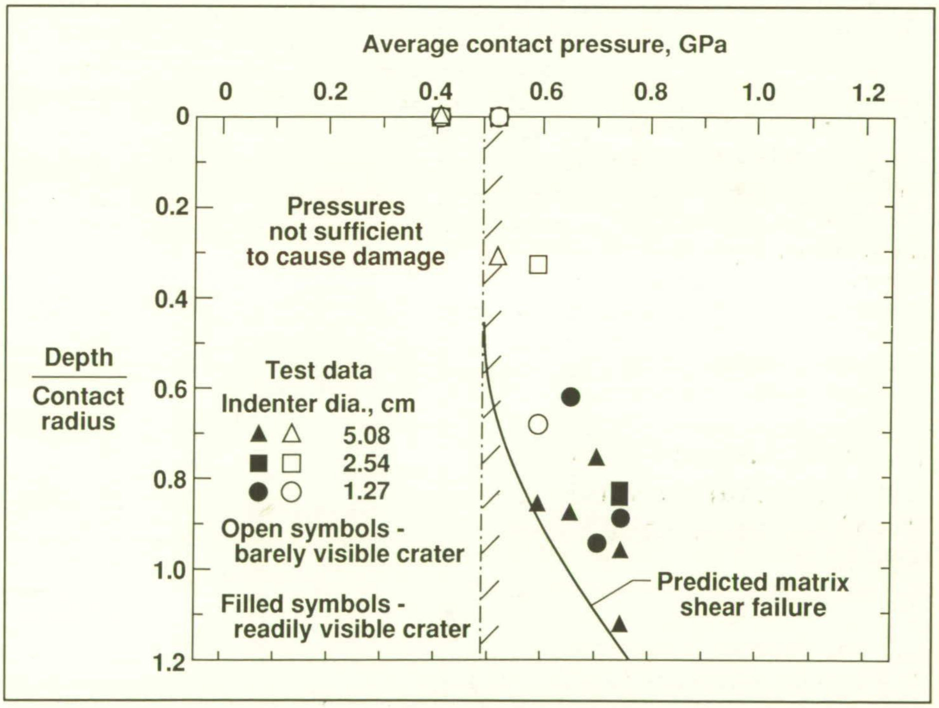

Depth of damage due to low-velocity impact.

using the theory of elasticity. The analysis predicted fiber compression failure on the surface at the center of the contact site at a pressure of 0.487 GPa. The matrix shear failures were predicted to occur beneath the surface at the center of the contact site at approximately the same pressure. With increasing pressure, each type of damage spreads, but the matrix shear failures extend much deeper than the fiber compression failures. Thus, the fibers broken by matrix shear failure are the most critical. The maximum depth of broken fibers caused by matrix shear failure is plotted in the figure for various contact pressures and indenter diameters. The depths are normalized by contact radius so that the results are independent of indenter diameter. The curve is the analytical result for matrix shear failure, and the symbols are the experimental results. The theory and experiments agree well. The open and filled symbols differentiate between barely visible and readily visible surface damage. The Gr/Ep is damaged at pressures below that at which the damage can be detected. These results indicate that the resistance to impact of a thick Gr/Ep plate can be improved by increasing the shear strength of the epoxy.
(C. C. Poe, Jr., 43467)

Improved Stress Corrosion Characterization With Breaking Load Test Method

Stress corrosion cracking (SCC) of aluminum alloys has long been recognized as a significant contributor to environmentally assisted failures in structural applications. SCC continues to be a major factor in establishing the service lifetimes of commercial structural aluminum alloys and will certainly be a consideration in the development of emerging advanced aluminum alloys. The breaking load test method, which was developed cooperatively with Alcoa Laboratories, offers an improved accelerated technique for quantifying resistance to stress corrosion. The method provides more information with fewer specimens and shorter exposure times than conventional tests and is more sensitive to small performance differences among resistant materials. The method utilizes data from tensile tests performed on smooth specimens after exposure to static stress and a corrodent. The degree of stress corrosion attack is indicated by comparing the post-exposure strength with the original tensile strength. Test results can be statistically evaluated to determine probabilities of survival and threshold stress levels for SCC and can be evaluated by fracture mechanics principles to describe SCC damage as equivalent flaw size.

Testing of aluminum alloy 7075 aged to high-, medium-, and low-stress corrosion resistant tempers resulted in ratings that were consistent with those determined by currently accepted test methods, but were obtained in approximately one-third the time and with an order of magnitude fewer specimens. Development of an ASTM standard test method is currently under way based on the results of this program. The threshold stresses presented in the bar chart for powder metallurgy (PM) alloy 7091 and ingot metallurgy (IM) 7075 demonstrate the sensitivity of the method and its application for evaluating both conventional and advanced aluminum alloys.
(Marcia S. Domack, 43126)

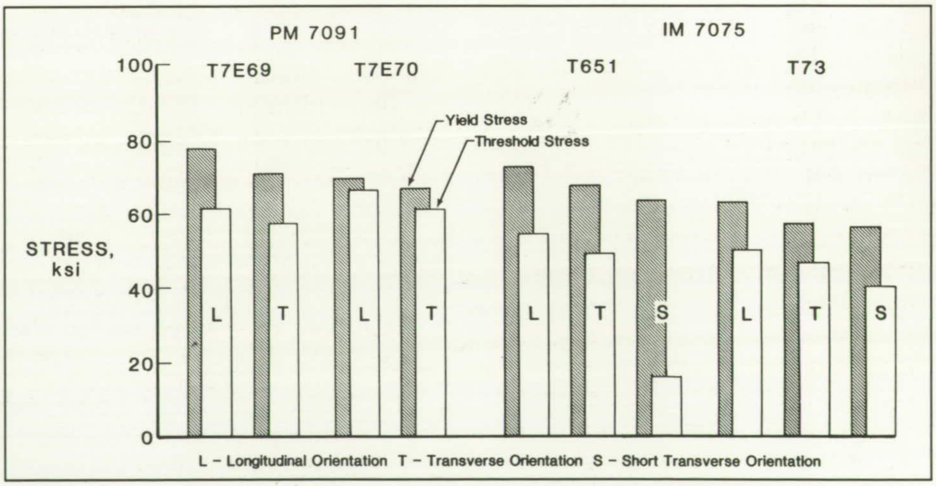

Threshold stresses for PM and IM alloys.

Inexpensive Method for Calculating 3-D Stress-Intensity Factors

Surface or corner cracks emanating from bolt holes are among the most common types of cracks which

occur in aircraft structures. The knowledge of how fast these cracks may grow is used to set aircraft inspection intervals to find cracked components before failure. The stress-intensity factors for a crack are used to make these life calculations. Over the last decade, the stress-intensity factors for three-dimensional crack configurations subjected to tension, bending, and pin loadings have been calculated using a three-dimensional (3-D) finite-element method employing from 10,000 to 15,000 degrees of freedom. These solutions were obtained on the supercomputers (STAR-100 and VPS-32) at the Langley Research Center using in-house computer codes. Concurrently, several investigators in the United States and elsewhere have been developing the line-spring or slice-synthesis models for analyzing three-dimensional crack configurations. These models are quasi-three-dimensional models based on two-dimensional stress-intensity factor solutions for edge and through cracks. The earlier line-spring models were quite inaccurate, but improvements made in two-dimensional analyses and the determination of model constants from the three-dimensional analyses have greatly improved the accuracy and versatility of these simple models.

As part of the NASA/Chinese Aeronautical Establishment Cooperative Program on Fatigue and Fracture Mechanics, established in 1986, a study was undertaken to compare the three-dimensional stress-intensity factor solutions from the finite-element method (FEM) with those being developed at the Beijing Institute of Aeronautical Materials using a 3-D weight-function method (WFM). The weight-function method is a slice-synthesis model with very accurate weight functions for edge cracks and through cracks. One of the many comparisons made between the two methods is shown in the figure. Here the stress-intensity correction factors F_{cn} for a corner crack at a notch in a plate are plotted against the angular location around the crack front. The crack was a quarter-circle at the edge of a notch with a notch-radius-to-plate-thickness r/t ratio of 1.5. Comparisons are made for various crack-depth-to-plate-thickness a/t ratios. The two methods agreed well (within approximately 3 percent), except in the boundary-layer regions (0° and 90°, respectively). (Neither solution is accurate at the boundary layer.) The curves show the results of closed-form equations developed to be used in damage-tolerant calculations.
(J. C. Newman, Jr., 43487)

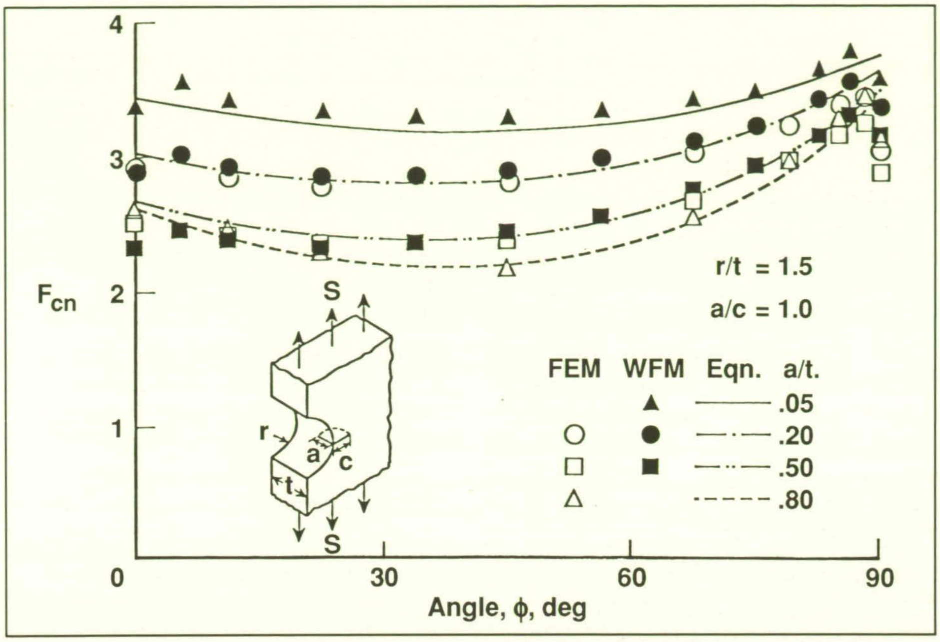

Correction factors to 2-D stress intensity solutions for 3-D crack configurations illustrated in figure. (Quarter-circular crack front; $\phi = 0°$ to $90°$.)

Superior Mechanical Properties of Powder Metallurgy Aluminum Alloy Sheet

Inherent low cost, low density, and ease of fabrication have made aluminum alloys important commercial materials for aerospace structures. Aluminum alloys with improved properties and higher temperature capabilities required for advanced aircraft applications are currently being made through powder metallurgy (PM) techniques. An alloy development program, which was conducted under contract to Langley Research Center, has demonstrated that 2XXX series powder aluminum alloys with novel chemistries and excellent strength and toughness can be produced in a commercial, pilot-scale (145 lb billets) operation. Alloy powders from this pilot-scale study were used in a

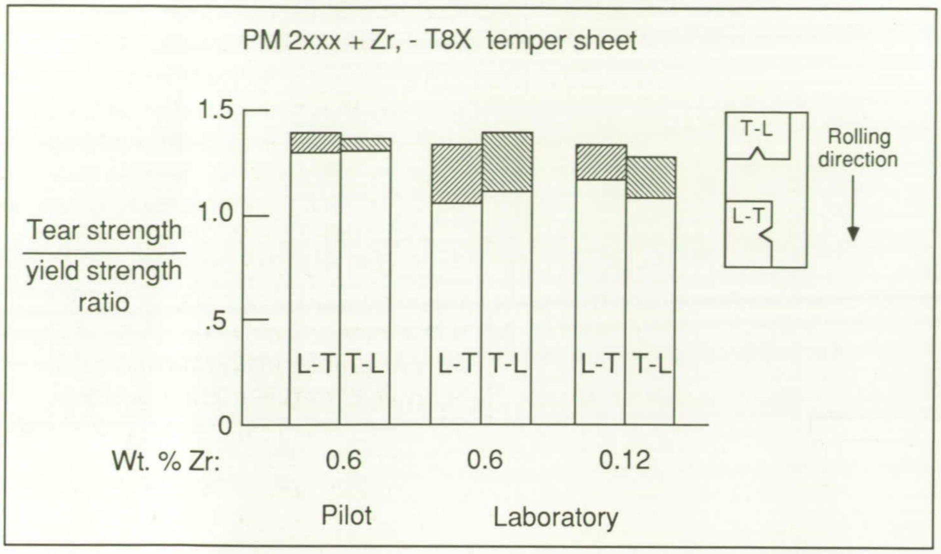

Toughness of laboratory- and pilot-processed PM aluminum alloy sheet.

Langley in-house, powder consolidation and sheet fabrication program to determine whether the laboratory operation could produce advanced alloy sheet with properties equivalent to those of alloys produced in the pilot studies that were superior to ingot metallurgy (IM) produced material. Over 50 sheets of PM 2XXX series aluminum alloy with Zr additions (for improved toughness) have been produced at Langley. The powder was consolidated in a Langley-designed vacuum hot press, forged, and hot-rolled into sheet.

Good agreement was obtained between Langley laboratory-scale and pilot-scale PM-produced alloy microstructures and bidirectional tensile properties. Kahn-Tear tests were used to measure sheet toughness. The normalized tear strength/yield strength ratio (a measure of toughness) of the laboratory sheet was in close agreement with values obtained from pilot-scale sheet as shown in the figure.

This study demonstrates that aluminum powder metallurgy sheet produced on a 1-lb or 2-lb laboratory scale can be utilized for advanced alloy synthesis and fabrication process development. Also, a small in-house research facility will permit inexpensive and relatively fast screening of innovative rapid solidification powder metallurgy aluminum alloy compositions.

(O. R. Singleton and W. Barry Lisagor, 43140)

Mixed-Mode Delamination Testing

Failures in composite structures often develop as delaminations between plies. Typically, such delaminations initiate and propagate under the combined influence of normal and shear stresses. Therefore, tests of delamination resistance should account for the effects of combined tensile normal stress (mode I) and sliding shear stress (mode II). Various approaches have been used to develop tests with such combined stresses. Unfortunately, however, several different types of specimens are usually needed to generate delamination data over a desired range of mixed-mode combinations. These data from different specimen types can be influenced by different test variables and analysis procedures. As a result, a new test apparatus has been developed which allows a single specimen type to be used over a wide range of mode I/II ratios as well as pure mode I and mode II delaminations.

This new mixed-mode bending (MMB) test simply combines the mode I double cantilever beam (DCB) test and the mode II end notch flexure (ENF) test. This new test is achieved by adding an opening-mode load to a mid-span loaded ENF specimen, as shown in the figure. This additional load separates the arms of the split laminate as in a DCB test. The relative magnitudes of the two applied loads determine the mixed-mode ratio at the delamination front. By applying these two loads through a lever and hinge apparatus as shown, the test can be conducted by using a single load. The position of this load on the lever determines the mixed-mode delamination ratio. Pure mode II loading occurs when the applied load is directly above the specimen mid-span. Pure mode I loading can be achieved by removing the lever and pulling up on the hinge.

The MMB test has been successfully used to measure the delamination fracture toughness of a graphite/PEEK (polyetheretherketone) composite over the full range of combined mode I and II loadings.

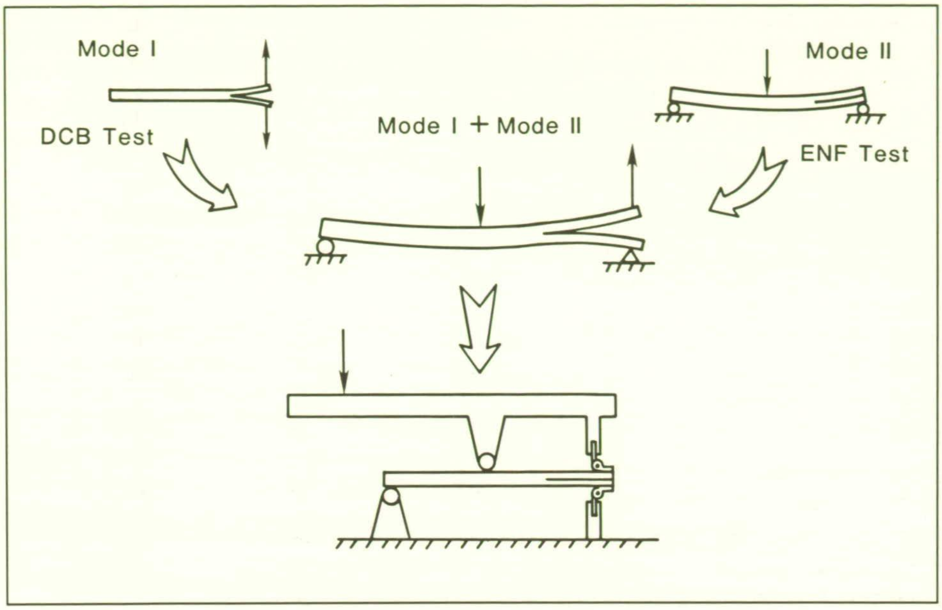

Mixed-mode bending concept for delamination testing.

In the future, it will be applied to other composites and will be extended to cyclic testing.
(J. H. Crews, Jr., 43457 and James R. Reeder)

New Option for Nonlinear Analysis in STAGS Computer Code

Nonlinear problems for the static analysis of shell structures often have more than one solution for a given load. Identifying and computing more than one numerical solution for a fixed set of input data is much more difficult than accounting for only one solution. Until now, general-purpose finite-element codes for structural analysis have not attempted to compute multiple solutions. Numerical analyses have been implemented with the assumption that each problem has a single solution path as a function of load. This solution path can be nonlinear, but it must be unique.

A new option has been incorporated into the STAGS (Structural Analysis of General Shell Structures) general-purpose shell code which discards the assumption of a unique solution path. The new ET (equivalence transformation) option derives a small set of coupled cubic equations in unknown modal amplitudes of eigenvectors of the tangent stiffness matrix while retaining all the degrees of freedom of the original finite-element model. The transformed problem is mathematically equivalent to the original problem. The new option has been applied to the postbuckling analysis of cylindrical shells. A plot of nondimensional load λ as a function of end shortening for a cylindrical panel is shown in the figure. Three separate solutions appear in the neighborhood of the point marked ET. Older versions of the STAGS code and other finite-element codes are inefficient or break down as the analysis proceeds along the solution path from the origin toward the point marked ET. The new ET version of STAGS computes three solutions for

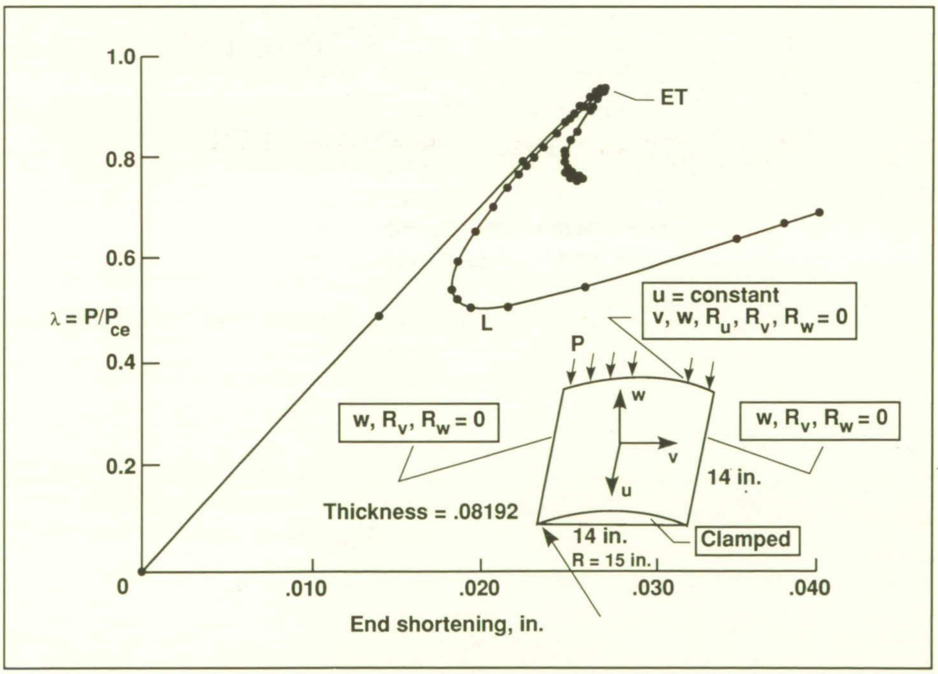

Nondimensional load-shortening curve for curved panel.

certain values of the load including solutions on the path marked *L* in the figure.
(G. A. Thurston, 43178, C. Rankin, and F. Brogan)

Improved Performance of Al-Li Alloy by Novel Chemistries

Lightweight Al-Li alloys have significant potential for structural applications in aircraft and aerospace vehicles. Current alloys require an intermediate stretch prior to heat treatment (T8 condition) in order to achieve peak strength. This need for an intermediate stretch precludes its use in advanced forming processes such as superplastic forming (SPF). Previous research indicated that comparable strengths might be achieved in aluminum alloys by the minor addition of alloying elements, without the need for an intermediate stretch (T6 condition).

Research was conducted to determine the effects of minor additions of cadmium (Cd), tin (Sn), or indium (In) on the mechanical properties and microstructure of baseline aluminum alloy 2090. These elements were added to promote nucleation of strengthening phases in the alloy. Of the three additions, the indium was most effective in increasing the age-hardening response of the baseline alloy, resulting in a peak hardness of approximately 82 on the Rockwell B scale. The yield strength of the indium-modified alloy was approximately 71 ksi, which was at least 9 ksi greater than the other three alloy variants and equal to the yield strength of the baseline alloy subjected to a 6-percent stretch prior to heat treatment. The ductility of the indium-modified alloy was higher than the other three alloy variants, with a total elongation of approximately 8 percent. The high strength of the indium-modified alloy is attributed to a threefold to fourfold increase in number density of specific strengthening precipitates and a significant increase in the homogeneous distribution of these precipitates, when compared to the baseline alloy.

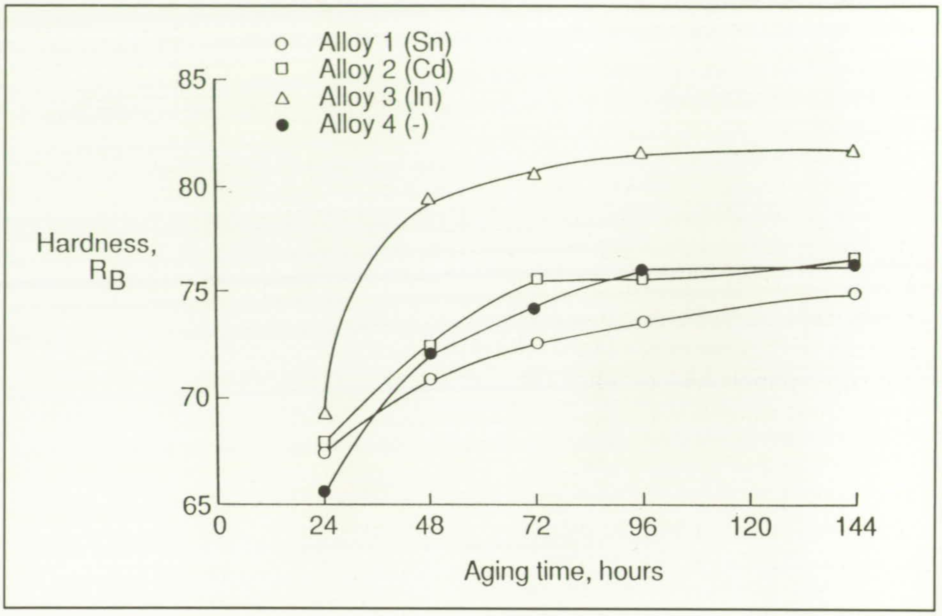

Al-2.3Cu-2.3Li-0.15Zr-X alloys aged at 160° C.

This research has demonstrated that the indium-modified alloy is capable of achieving comparable strength and higher ductility when compared to the baseline alloy subjected to a 6-percent intermediate stretch; this permits use of the indium-modified alloy in superplastic forming applications for the production of net shape parts.
(Linda B. Blackburn, 43133)

Sound Transmission Loss of Integrally Damped, Curved Panels

The sound transmission characteristics of integrally damped, curved panels have been investigated in a joint program with the United States Air Force to reduce aft-equipment bay interior noise levels in B-1B bombers. The curved panels were mounted on a specially designed supporting frame that was installed as a partition between two adjacent reverberant rooms. A sound source in one of the rooms provided high levels of broadband noise. The transmission loss characteristics of the test panels were determined from the difference in the measured sound pressure levels in each of the rooms. Sound transmission loss measurements were conducted for 13 different panels, 3 of which are discussed here. The panels were 32 in. high with an arc length of 52 in. and a curvature radius of 90 in. The baseline panel

was an undamped aluminum panel with riveted skin and frames, typical of the B-1B aft-equipment bay walls. The second panel had a layer of damping materials constrained within aluminum skins and rivet-bonded skin-frame attachments. The third panel, representative of the aft-equipment bay door of the B-1B, was made of composite fiber materials and contained a damping septum within its honeycomb core. All three panels had roughly the same total weight.

The variation of transmission loss with frequency for the three panels is shown in the figure. The damped aluminum panel exhibits a higher transmission loss than the undamped aluminum panel over the entire frequency range except in the vicinity of the ring frequency (630 Hz). Because the composite panel had a lower ring frequency (315 Hz), it was found to have a 5 dB to 7 dB increase in sound transmission loss relative to that of the damped aluminum panel in the 630 Hz and higher one-third octave bands. To investigate the effect of temperature on the sound transmission loss, because the B-1B aft-equipment bay is located close to the engine exhaust, the panels were heated to approximately 180°F and tested again. However, no noticeable change in the sound transmission loss characteristics was observed. It was concluded that advanced concepts of integral skin and structure damping and integration of composite and honeycomb materials improve the sound transmission loss characteristics of large aircraft components with the potential of reducing aircraft interior noise levels.
(Ferdinand W. Grosveld, 43686)

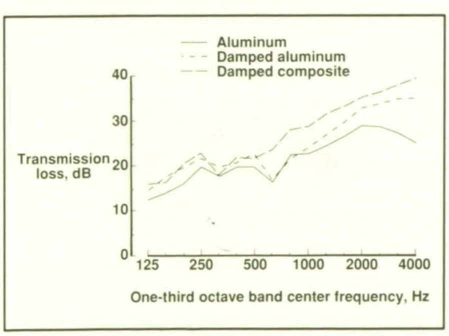

Measured noise transmission loss of aircraft panels.

Vectorized Lanczos Eigensolver for Parallel/Vector Supercomputers

The vibration and buckling analyses of large flexible space structures and the next generation of aircraft, such as the supersonic transport vehicle, will require the judicious use of high-speed computer resources. The need for an efficient, reliable eigensolver for the solution of these very large problems is the motivation for this research.

An algorithm based on the basic Lanczos method has been analyzed and was previously implemented on a 20-processor parallel computer. To test the eigensolver on a high-performance supercomputer, vibration analysis of a high-speed transport model, as shown in the figure, was implemented on a CRAY-2. This model, which was used in the preliminary design studies of this vehicle, is composed of 2386 two-, three-, and four-noded elements with 4518 degrees of freedom.

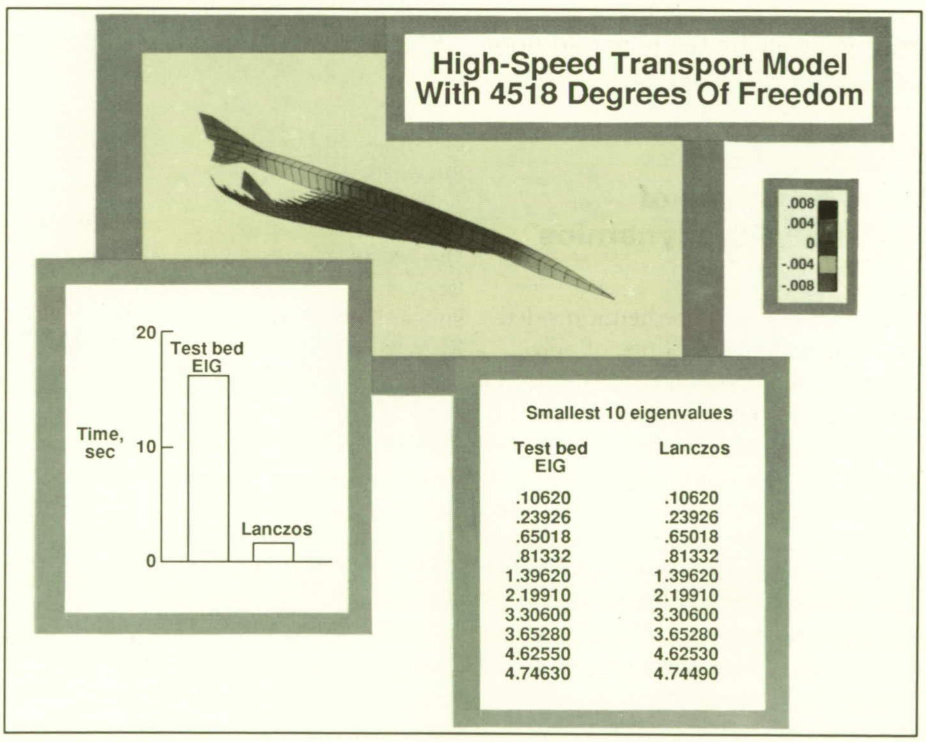

Test bed EIG	Lanczos
.10620	.10620
.23926	.23926
.65018	.65018
.81332	.81332
1.39620	1.39620
2.19910	2.19910
3.30600	3.30600
3.65280	3.65280
4.62550	4.62530
4.74630	4.74490

Vectorized Lanczos vibration analysis algorithm developed to exploit CRAY-2.

L-88-11,710

The Lanczos algorithm, which was optimized to exploit the vector capability of the CRAY-2 supercomputer, found the 10 smallest eigenvalues and eigenvectors of the high-speed transport in less than 2 sec. The results agreed with those found using a subspace iteration method (labeled EIG) which took more than 17 sec for the analysis. The Lanczos eigensolver has been installed in the CSM (computational structural mechanics) test bed to provide a general-purpose capability for performing large-scale vibration and buckling analysis. Using algorithms that exploit the high performance of the newest supercomputers, the analyst can now solve in a few seconds large-scale structural problems that took hours to perform in the recent past.
(Susan W. Bostic, 42910)

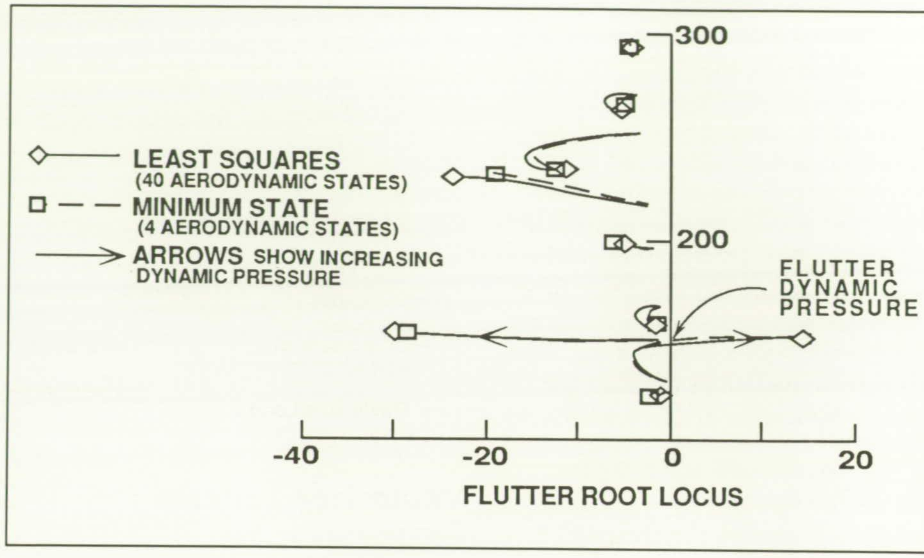

Comparison of aeroelastic behavior with aerodynamic approximation method.

Low-Order Aeroservoelastic Equations Using Minimum-State Approximations of Unsteady Aerodynamics

One of the key ingredients needed to integrate the disciplines of aerodynamics, structural dynamics, and control theory is the ability to accurately transform the aeroelastic equations of motion into a state-space form. A strong motivation for using mathematical representations in state-space form is the availability of efficient linear system algorithms for aeroservoelastic analysis and for design of control systems. Currently, the transformation of the aeroelastic equations relies on the use of rational functions of the Laplace variable to approximate the elements of the reduced frequency-dependent unsteady aerodynamic forces. However, this approach has the disadvantage of significantly increasing the number of governing equations. There is, of course, always a tradeoff between how well the rational function approximates the aerodynamic forces and the desire to keep the state-space model small.

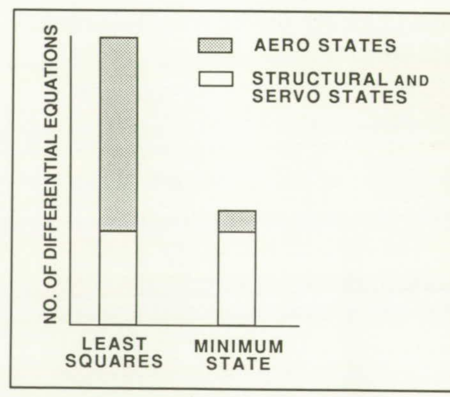

Reduction in aerodynamic states using Minimum-State Method.

By applying physical weighting to the various aerodynamic data terms according to their importance in subsequent analyses, the Minimum-State Method (MSM) was found not only to yield very accurate aeroservoelastic state-space models but also to provide the lowest-order models as compared to other common methods. The physical weighting procedure introduces a measure of importance which allows the aerodynamic approximation to be improved at some reduced frequencies based upon physical properties without actually enforcing equality constraints at the specified points. This measure of importance is based upon partial derivatives of selected open-loop parameters with respect to the weighted term at a specified design flight condition.

Using the MSM with the physical weighting procedure, the total size of a typical time-domain aeroservoelastic model can be effectively reduced by 50 percent. The first figure contains a comparison of dynamic-pressure root locus plots using both the MSM and the more classical Least-Squares Method (LSM) for an aeroelastic model represented by 10 elastic modes. As

can be observed, the models behave in a similar fashion in that the differences are quite small throughout the frequency and dynamic pressure ranges of interest including the flutter condition. The second figure indicates that the MSM model needed only one-tenth the number of aerodynamic states used by the LSM. The benefits in using the MSM include significant computer time savings for control design and analysis tasks, more realizable optimal control laws, and the ability to perform near real-time simulations of the aeroservoelastic equations.
(Mordechay Karpel and Sherwood Tiffany, 42832)

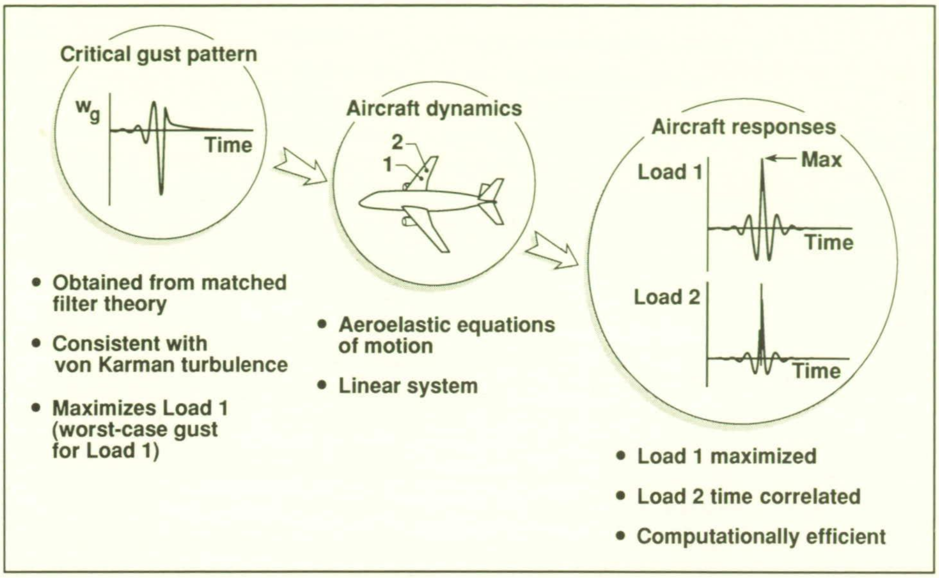

Time-correlated gust load responses to critical gust pattern.

Novel Approaches for Determining Maximized and Time-Correlated Gust Loads

Aircraft manufacturers have recently encouraged the Federal Aviation Administration to investigate alternative means of complying with the regulations that relate to aircraft gust loading. Recent investigations have shown that novel applications of the Matched Filter Theory (MFT) and the Random Process Theory (RPT) to the analysis of gust loading on linear aeroelastic systems are possible alternatives. These approaches have been found to allow an analyst to predict the maximized (worst-case) gust load, the corresponding time-correlated loads, and the critical gust pattern that produces them.

MFT was originally applied in the field of signal processing for the design of an electronic filter that maximized the detection of a returning radar signal. In the current application to linear aeroelastic systems, MFT is used to determine a critical gust pattern (a time history of vertical gust velocity) which produces the worst-case deterministic response of a chosen load quantity and time-correlated responses of other load quantities. The figure shows, in the upper left, a critical gust pattern produced by MFT. This gust pattern has a finite probability of occurring in turbulence described by the von Karman power spectral density function. This critical gust pattern is then applied analytically to the flexible airplane depicted in the center of the figure, and the dynamic loads at multiple locations on the wing are computed. As an example, two load time histories are shown on the right side of the figure; Load 1 response represents the maximized gust load resulting from the critical gust pattern, and Load 2 response represents one of the many time-correlated loads. MFT guarantees that, in response to all other equiprobable gust patterns, the value of Load 2 at any value of time will never exceed the maximum value shown in the upper part of the figure. It was further proved in this investigation that the time-correlated gust loads computed by MFT were theoretically identical to auto- and cross-correlation functions of RPT. Thus, auto- and cross-correlation functions of RPT may be interpreted as time-correlated gust loads.

Both approaches are computationally fast and provide new analysis options for directly computing time-correlated dynamic loads for linear aircraft applications. In addition, the MFT and the RPT approaches are general enough to be applied to a variety of dynamic-response problems, such as taxi, landing, and maneuver loads in addition to gust loads.
(Anthony Pototzky, Thomas Zeiler, and Boyd Perry III, 42840)

Supersonic Far-Field Boundary Conditions for Transonic Small-Disturbance Theory

Modifications have been made to the Computational Aeroelasticity Program–Transonic Small Disturbance (CAP-TSD) code which improve its accuracy for low supersonic free-stream flows. The CAP-TSD code was developed for aeroelastic analysis of complete aircraft configurations in the transonic speed range. The modifications made consist of implementing more accurate far-field boundary conditions that were derived using the method of characteristics (MOC). To determine the new far-field boundary conditions, the MOC was applied to the two-dimensional steady full-potential equation, and then, small disturbance assumptions were made which were consistent with those in CAP-TSD. The mathematical result was a simple boundary condition that easily is solved computationally.

To assess the new supersonic boundary conditions, calculations were performed for the F-5 fighter wing. The F-5 wing, which is approximately 4 percent thick, has a leading-edge sweep of 31.9° and a taper ratio of 0.28. Calculations were performed at a free-stream Mach number of 1.05 and an angle of attack of 0°, for the wing oscillating in pitch at a reduced frequency based on a root semichord of 0.1. The figure shows a comparison of unsteady upper surface pressure coefficient $\tilde{C}_p$ distributions located at 49 percent semispan. The results are plotted along the streamwise x direction, which is nondimensionalized by the local chord c. These results were calculated with a very small sectional grid that contained 109 × 62 points and was five chord lengths square. When the original boundary conditions in CAP-TSD are used, the unsteady pressures are in poor agreement with the experimental data. Using the new boundary conditions brings the calculated unsteady pressure distributions into very good agreement with experiment.

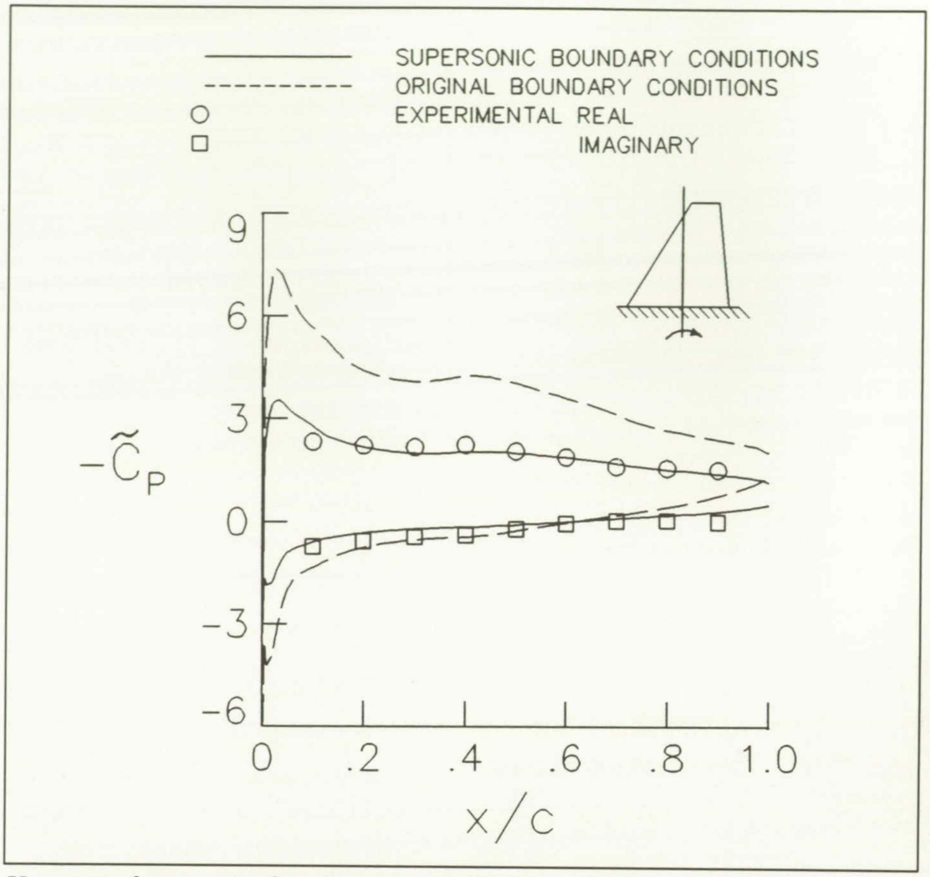

Upper-surface unsteady pressure distributions showing improvement in solution when supersonic boundary conditions are used.

The results presented demonstrate that the supersonic boundary conditions allow the use of small computational grids for supersonic free streams without losing solution accuracy. Because smaller grids can be used, the computational cost is also reduced.

(Michael D. Gibbons and John T. Batina, 42276)

Transonic Flutter Characteristics of Composite A-6 Wing

Because the A-6 Intruder airplane is an important part of the United States Navy's air arm and will be used for many years to come, a new composite structure wing to improve fatigue characteristics and to remove flutter placards for certain external store configurations is being developed. This new design included modifications based on results of an earlier flutter test in the Transonic Dynamics Tunnel (TDT). To verify that this modified design has acceptable flutter speeds, an experimental

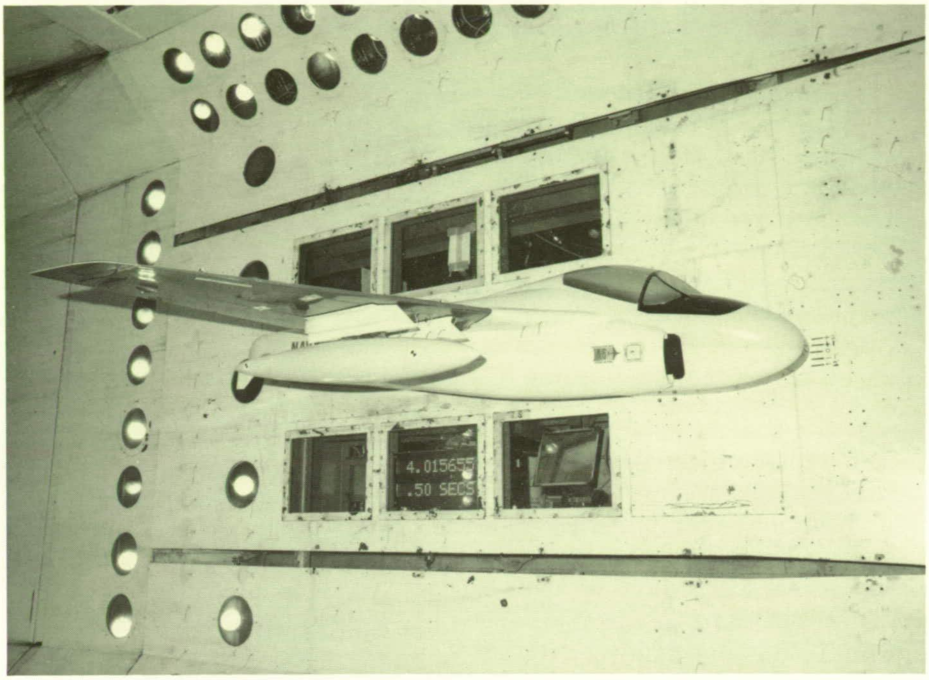

A-6 model in Transonic Dynamics Tunnel. L-87-5780

study was undertaken to determine its transonic flutter characteristics.

A 1/4-size dynamically scaled aeroelastic model was tested in the TDT to determine the flutter characteristics of the wing with and without external stores. The store configurations that were tested were selected from those most commonly used and having the most impact on flutter. Fuel tanks internal to the wing structure were remotely filled with water to determine internal fuel effects on flutter.

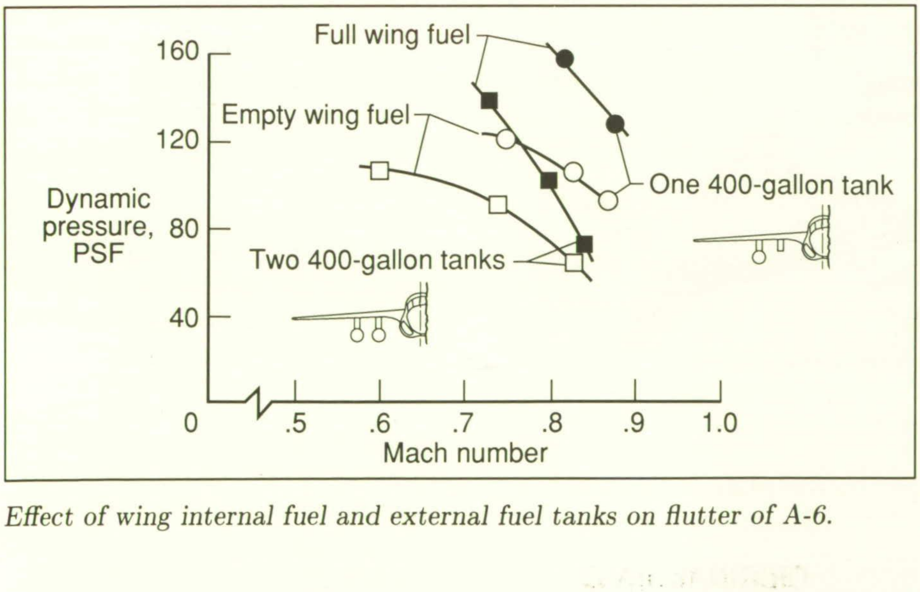

Effect of wing internal fuel and external fuel tanks on flutter of A-6.

A total of 37 configurations were tested at transonic Mach numbers. Based on flutter analyses adjusted by the wind tunnel test results, there is substantial indication that the full-scale aircraft will be flutter free. Flutter results obtained for two configurations, namely one with a single 400-gal fuel tank attached to the outboard pylon position and one with tanks attached to both under-wing pylons, are shown in the figure. The dual-fuel-tank configuration has a lower flutter boundary than the single-fuel-tank configuration. Also shown is the effect of internal wing fuel. The empty wing fuel case was found to be more critical than the full wing fuel case. The large amount of flutter data obtained has contributed significantly to the available information on the effect of store configuration variables on flutter.

(Stanley R. Cole, 41267 and José A. Rivera, Jr.)

Unsteady Euler Algorithm Based Upon Dynamic Unstructured Grid Methodology

An algorithm has been developed to solve the unsteady Euler equations for unsteady aerodynamic analysis of complex aircraft configurations. The algorithm uses a finite-volume spatial discretization on an unstructured grid made up of tetrahedra. The unstructured grid methodology was used to allow the treatment of complex aircraft geometries. The flow solver involves a multistage Runge-Kutta time-stepping scheme to march the Euler equations in time. A significant aspect of the present capability

is the dynamic mesh algorithm that is employed for problems involving static or dynamic deformation of the aircraft. The dynamic mesh algorithm is a general procedure that can move the original mesh to maintain alignment with the instantaneous surface of the aircraft and can treat realistic motions and aeroelastic deformations of complex aircraft configurations.

To demonstrate the capability, calculations were performed for a supersonic fighter configuration. The grid that was used contained 13,832 nodes and 70,125 tetrahedra. Instantaneous pressure coefficient C_p contours on the aircraft surface are shown in the figure; these contours are due to the fighter oscillating harmonically in a complete-vehicle bending mode. The free-stream Mach number was 2.0, the angle of attack was 0°, and the reduced frequency based on wing tip semichord was 0.1. These contours indicate that during the first half of a cycle of motion when the aircraft bends up, there is a significant increase in the level of flow compression (red-white contours) along the nose and the forward part of the canopy, as well as in the outboard part of the wing. During the latter half of a cycle when the aircraft bends down, the opposite situation occurs; the pressure levels decrease along the nose and canopy, and a considerable amount of flow expansion (blue-green contours) takes place on the aft outbound region of the wings.

The results presented demonstrate that time-accurate inviscid flows now can be computed for complex aircraft configurations undergoing realistic motions or aeroelastic deformations.
(John T. Batina, 42268)

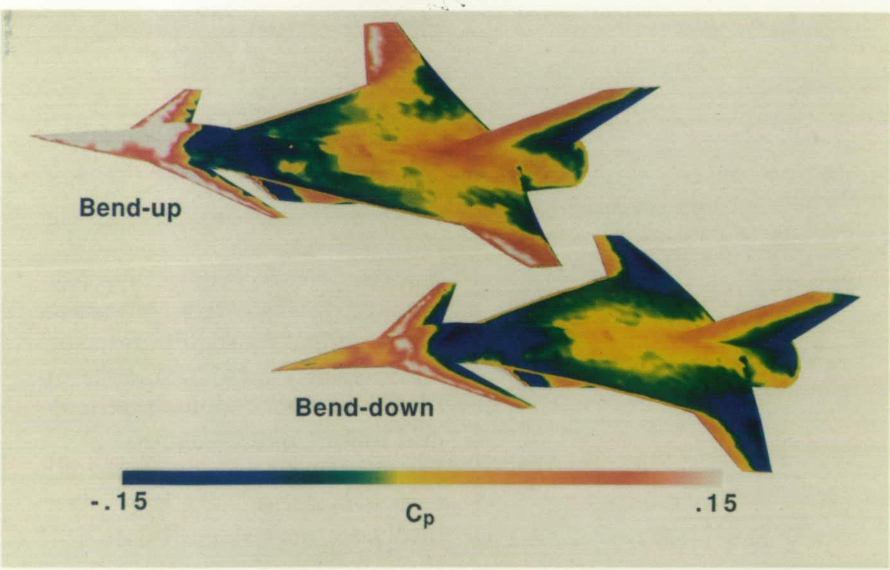

Instantaneous pressure coefficient contours for fighter undergoing harmonic bending oscillation.

Honeycomb Panel Weight Reduction by Improved Intracell Buckling Coefficient

Honeycomb panels play an important role in aircraft structures. For areas with low loading indexes, the compressive load-carrying capability of minimum gauge face sheets becomes an issue. This situation arises when high-strength materials are used by the structural designer to satisfy strength criteria at the cell level shown in the upper left of the figure. This local buckling phenomenon is called intracell buckling. Existing work indicates that the commonly used design equations for intracell buckling are very conservative for low ratios of face sheet thickness to cell size t/s. The objective of this research is to find realistic prediction methods for intracell buckling at low t/s ratios.

Finite-element models of honeycomb panels were developed which included the face sheets and honeycomb core. Buckling loads of the structure were then determined for various ratios of face-sheet thickness to cell size. This approach allowed calculation of the intracell buckling coefficient based upon critical load and known geometry, fixity, and material constants.

Results indicated that the buckling coefficient is not constant for varying t/s ratios as is assumed by the design equations. Rather, the results showed an obvious relationship between buckling coefficient and the relative bending stiffness between face sheet and core structure. As the bending stiffness of the face sheet decreases with smaller thickness, the amount of edge restraint provided by the core in-

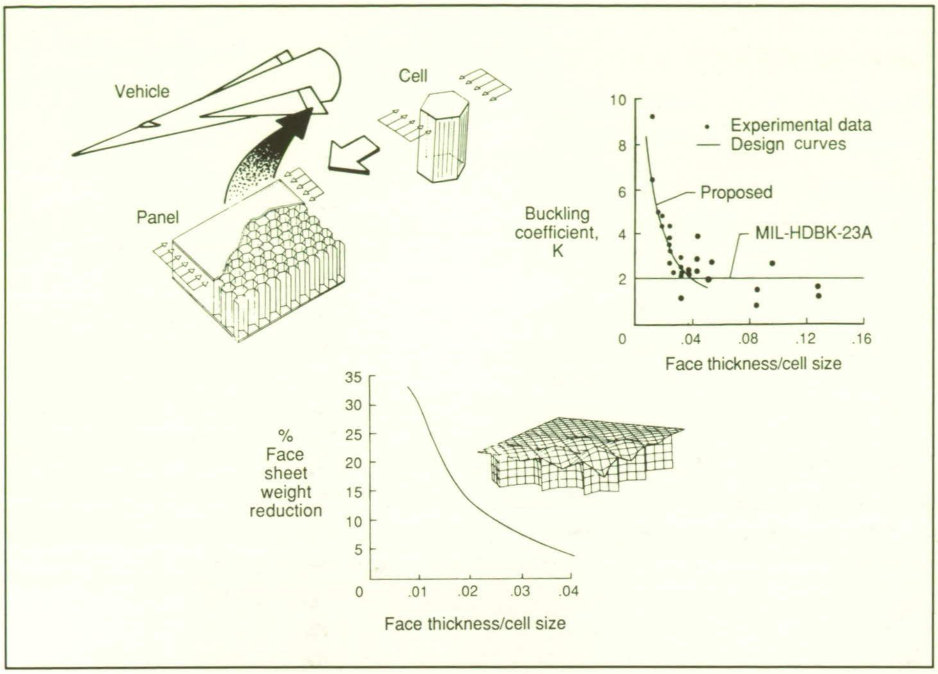

Effect of assumed buckling coefficient on honeycomb panel weight.

creases. Therefore, the buckling coefficient K increases, which results in higher critical loads. The same trend of increasing K with a decreasing t/s ratio is observed in the experimental data shown in the upper right of the figure for $t/s < 0.04$.

Current intracell buckling design equations, such as the one shown from *Structural Sandwich Composites MIL-HDBK-23A*, ignore the interaction between face sheet and core when predicting buckling loads. The analytical results of the lower part of the figure show that reductions of up to 30 percent on face-sheet weight are possible when using buckling coefficients based on relative stiffness between the face sheet and the core.

The majority of experimental work which is the basis for design equations was carried out in the early 1950's. Additional tests are needed on modern honeycomb materials to validate a design approach for low t/s ratios.
(R. Franklin Vause and Donald R. Rummler, 45185)

Corduroy Texture Solution to Space Shuttle Tire Spin-Up Wear Problem

Spin-up wear damage to the Space Shuttle tires was an initial problem at the Kennedy Space Center (KSC) Shuttle Landing Facility. Research was undertaken to define a texture modification for the touchdown zones of the KSC Shuttle Landing Facility which would reduce spin-up damage to an acceptable level while maintaining adequate cornering friction when wet.

A variety of texture modifications were investigated at the Aircraft Landing Dynamics Facility (ALDF) and on the KSC runway. The modifications included smooth concrete; longitudinal corduroy with spacing of 4, 4.5, 5, and 7 blades per in.; and 4.5-blades-per-in. corduroy with transverse grooves. Tests were conducted on the ALDF to investigate the spin-up wear and cornering behavior of the smooth, smooth-grooved, and 4.5-blades-per-in. corduroy (both grooved and ungrooved). The Instrumented Tire Test Vehicle (ITTV) was used at KSC to evaluate the differences between the various blades-per-in. corduroy that had been cut into the existing KSC runway. The ITTV was then used at the Aircraft Landing Dynamics Facility to compare the KSC data with the 4.5-blades-per-in. corduroy texture that was cut into the ALDF track. Additionally, a simulated rollout was performed at the ALDF to predict the wear for spin-up on the 4.5-blades-per-in. ungrooved corduroy surface and subsequent rollout on the KSC texture.

Test results showed that the spin-up damage caused by the 4.5-blades-per-in. ungrooved, corduroy surface was no worse than that caused by a smooth, ungrooved surface (the minimum possible except for lake bed landings). The ITTV tests at KSC showed that the 4.5-blades-per-in. ungrooved corduroy was preferred over the other blade spacings, and the ITTV tests at Langley Research Center showed that the Langley corduroy data were comparable to KSC data, thus validating the wear predictions for the KSC landings on the modification. Wet friction on the corduroy surface was acceptable at 70 percent of the dry KSC surface value. The figure shows

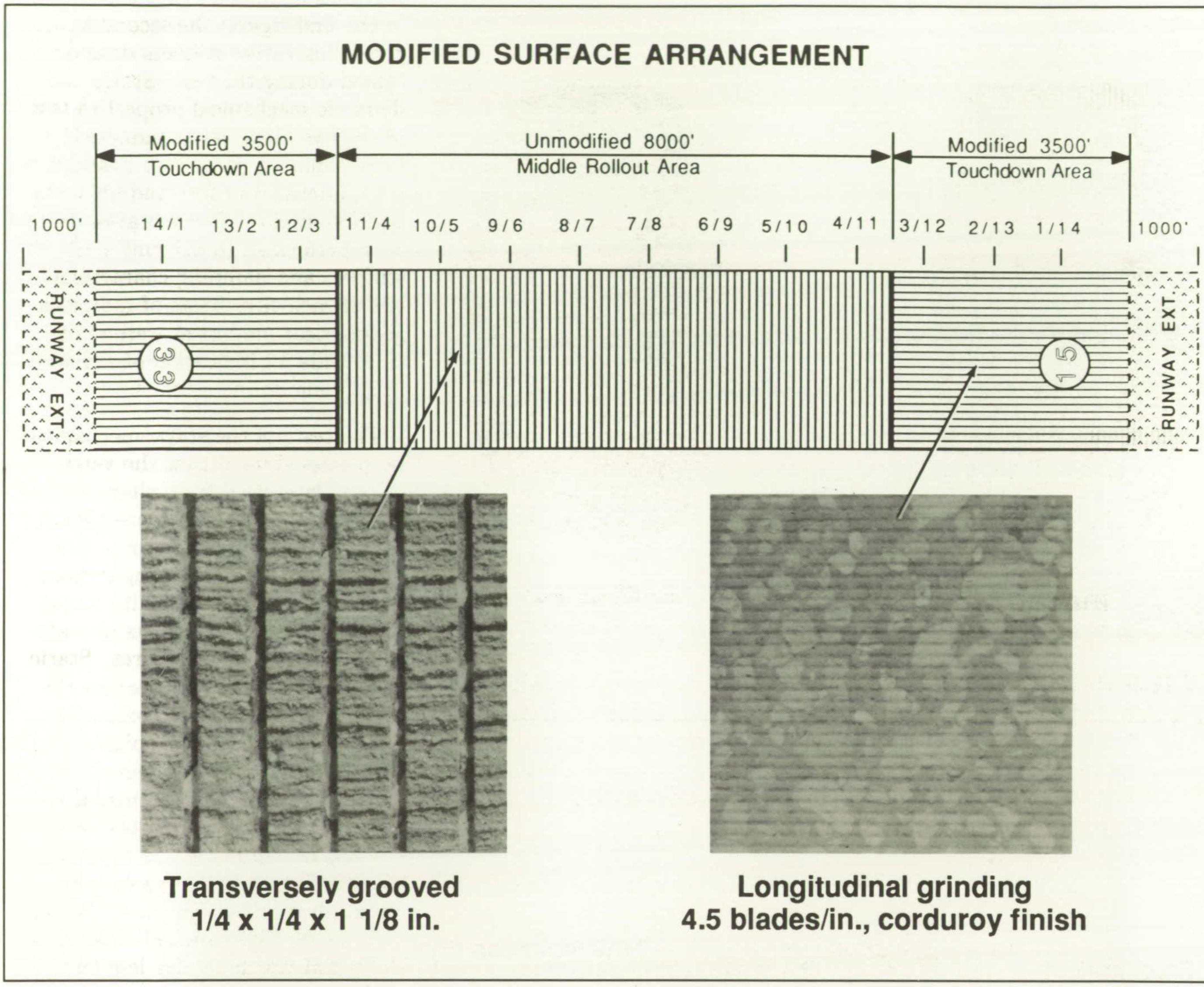

NASA KSC Shuttle Landing Facility. L-88-2524

details of the runway lengths with the corduroy modification texture.

The wear and friction benefits of the new corduroy surface should translate into improved safety margin for the Space Shuttle at present crosswind limits, or a crosswind capability increase of 3 knots to 5 knots at present safety margins.
(Robert H. Daugherty, 41309 and Sandy M. Stubbs)

Mechanical Properties of Aircraft Radial Tires

Although the aircraft landing gear industry in the past has been hesitant to consider the use of radial-ply tires, projected needs for future aircraft landing operations have indicated that it may be desirable to use these tires. Consequently, a research study was undertaken to determine the data base of information needed to establish the validity of using radial tires in airplane applications.

To this end, the mechanical properties of 30 X 11.5—14.5 (30 in. is tire outside diameter, 11.5 in. is tire section width, and 14.5 in. is wheel bead seat diameter) type VIII, radial-ply aircraft tires have been determined from tests conducted at the Aircraft Landing Dynamics Facility. These results have been compared to those obtained for bias-ply tires of conventional design. Pho-

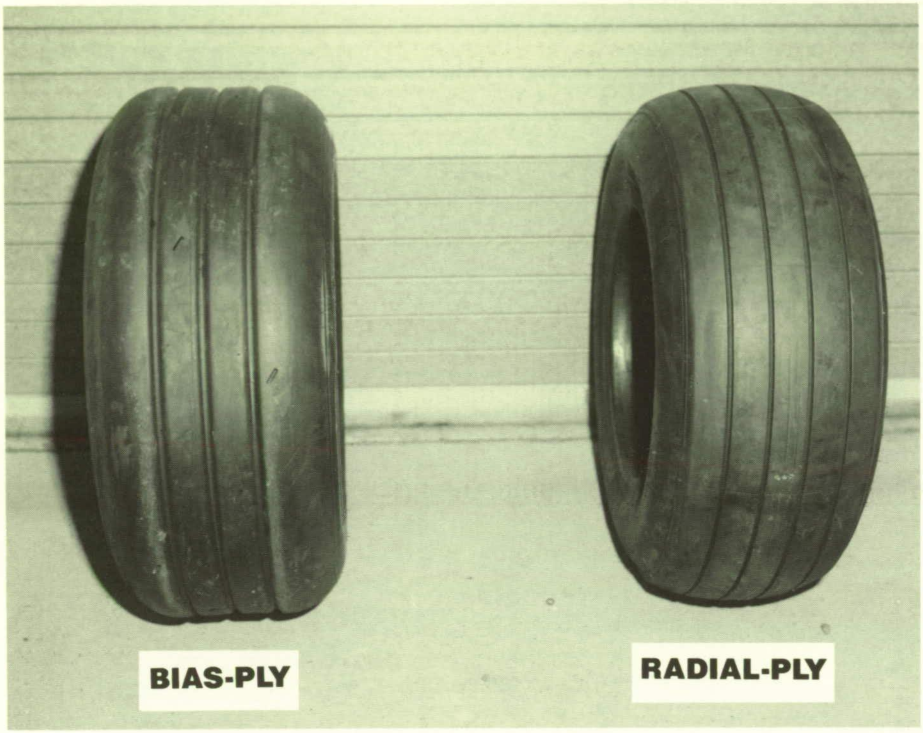

30 X 11.5—14.5 bias-ply and radial-ply tires. L-86-10,087

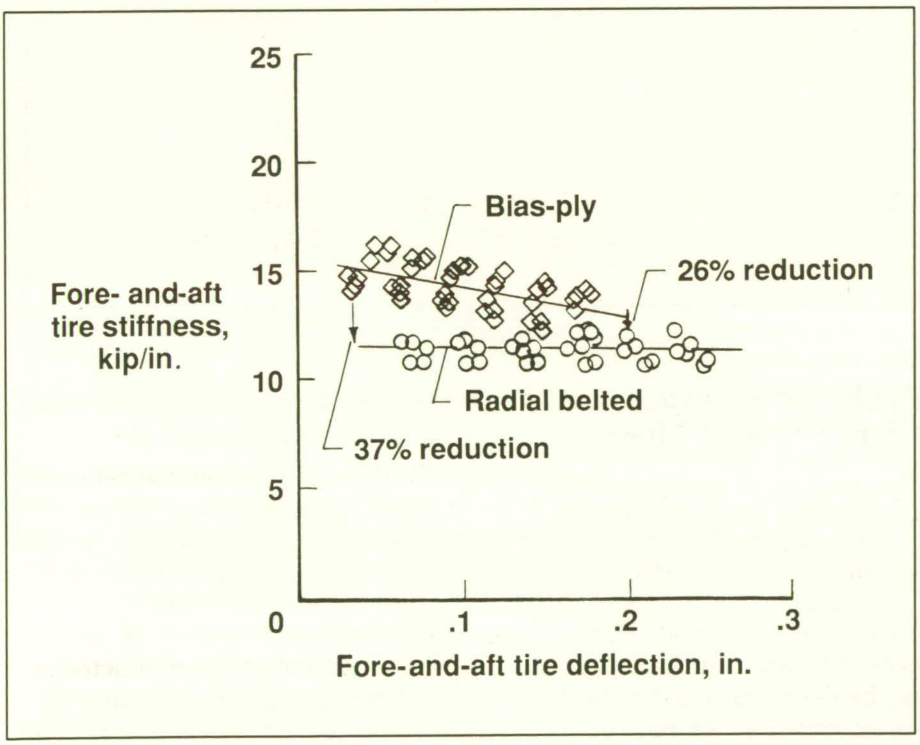

Static fore-and-aft tire deflection, in. (30 X 11.5—14.5, type VIII, aircraft tires).

tographs of the two tires are shown in the first figure; the second figure gives illustrative stiffness data obtained during the test. Static and dynamic mechanical properties tests of the two tires were conducted at rated inflation pressures. Static vertical, lateral, and fore-and-aft tests and fore-and-aft free vibration tests were performed to determine the stiffness and damping characteristics of each tire. Tests of footprint geometrical properties were made to provide an indication of tire hydroplaning characteristics.

The tests of the static mechanical properties showed that the vertical and lateral stiffness characteristics of the radial tire were similar to those of the bias-ply tire, thus indicating that the landing dynamics of aircraft equipped with radial tires would be the same as aircraft equipped with bias-ply tires. Static fore-and-aft stiffness values for the radial-ply tire were approximately 30 percent less than the bias-ply tire. This reduced stiffness of the radial tire could be detrimental to the dynamics of antiskid braking systems designed for bias-ply tires. The static hysteretic loss of the radial-ply tire was less than that for the bias-ply tire; this indicates that the radial tire generates less heat during normal operation and, therefore, runs cooler. The nearly circular shape of the radial-ply tire footprint at its rated inflation pressure may interfere with the improved hydroplaning potential associated with higher inflation pressures characteristic of this type of tire.

These test results mark the first significant step in determining the data base needed to ensure the safe use of radial-ply tires in aircraft landing gear applications.
(Pamela A. Davis, 41307 and Mercedes C. Lopez)

Integrated Aerodynamic Load/Dynamic Optimization of Helicopter Rotor Blades

As part of a Center-wide activity at Langley Research Center to improve helicopter rotor blade design procedures by accounting for discipline interactions, an integrated aerodynamic load/dynamic design optimization procedure has been developed for helicopter rotor blades. The procedure combines the helicopter analysis code CAMRAD with the optimization program CONMIN. The procedure accounts for variations in airloads due to changes in design variables and is a significant step toward the ultimate Langley goal of integrating all appropriate disciplines in rotor blade design optimization. The optimization problem is formulated to minimize blade weight and 4/rev vertical hub shear. Constraints are imposed on natural frequencies (to avoid resonance), autorotational inertia (to provide for safe landing in the event of engine failure), and centrifugal stress. The design variables include blade stiffnesses at the root, root chord, taper ratio, radius of gyration at the root, and magnitudes of nonstructural masses located spanwise.

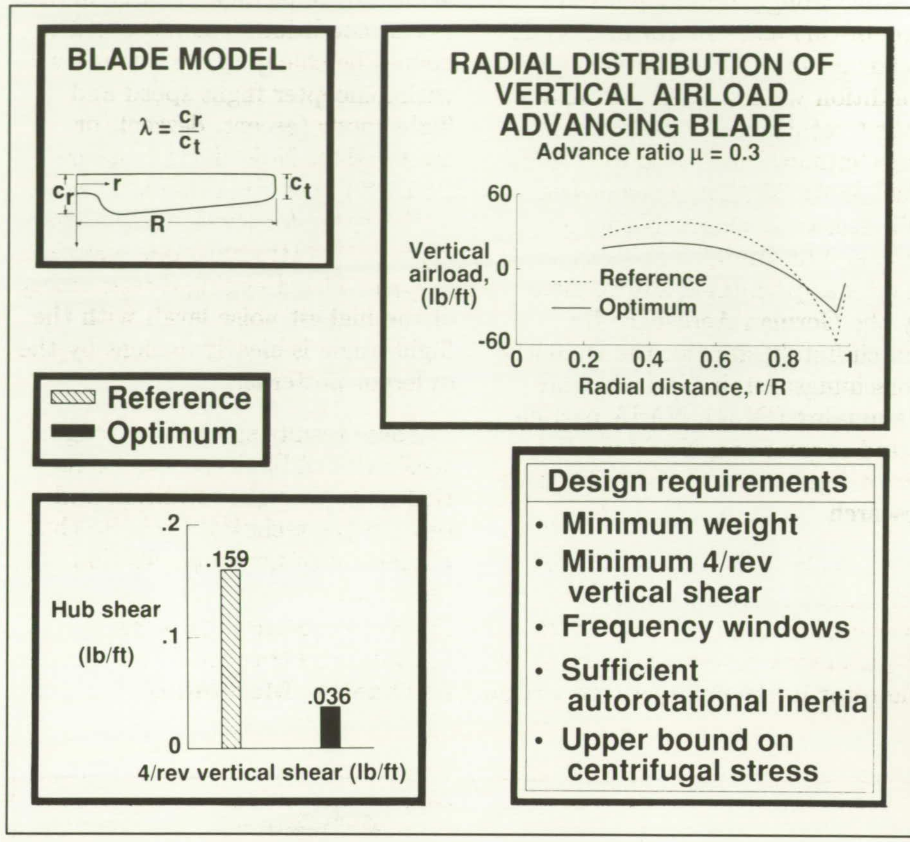

Integrated aerodynamic load/dynamic optimization of helicopter rotor blades. L-89-4874

The procedure was applied to a wind tunnel model of a rotor blade. The optimization procedure yielded a blade design with a 10.6-percent reduction in weight and a 77.6-percent reduction in hub shear from that of the reference (baseline) blade design. Reduction of hub shear is achieved when any of the following occur: blade natural frequencies move away from the excitation frequencies; mode shapes become more nearly orthogonal to the forcing function; or blade harmonic airloads are reduced. The extent to which the optimization process reduced the airloads was investigated because this was the unique feature of the procedure. A large reduction in the amplitudes of the spanwise and azimuthal vertical airload distributions after optimization was found. As shown in the figure, the vertical airload for the advancing blade ($\psi_i = 90°$) was reduced significantly along the entire span of the blade. (The negative value of the airload near the tip is caused by the large negative angle of attack due to the downward twist of the blade.) The airload at the tip is zero because the theory assumes that the blade has drag but no lift outboard of a certain radial location near the tip. **(Joanne L. Walsh, 42806, Aditi Chattopadhyay, and Michael F. Riley)**

Directionality of Helicopter Impulsive Noise

High levels of helicopter impulsive noise occur when helicopter rotor blades meet the tip vortices previously shed into the rotor's wake. This interaction noise, called blade-vortex interaction (BVI) noise, is a major cause of community noise problems and an important factor in helicopter noise certification procedures.

The strongly directional radiation of this noise source and its dependence on the helicopter flight condition were studied during a recent rotor noise experiment in the German/Dutch Acoustic Wind Tunnel (DNW, Duits-Nederlandse Windtunnel/Deutsch Niederlandischer Windkanal). The experiment was performed and funded by the German Aerospace Research Establishment, the Deutsche Forschungsanstalt für Luft- und Raumfahrt (DLR). NASA participated as part of a NASA-DLR Letter of Agreement on rotor acoustics research.

The noise radiation pattern of this impulsive noise source was measured in a large plane under (both upstream and downstream of) the rotor in the open jet test section of the DNW facility. A large matrix of test conditions was measured to define the changing directionality with helicopter flight speed and flight mode (ascent, descent, or level flight). Noise level contours for an 80-knot condition are shown in the figure for three different rotor flight angles (tip-path-plane angle α_{TPP}). The changing directionality of the highest noise levels with the flight angle is clearly evident by the different patterns.

These results show the strong sensitivity of blade-vortex interaction noise to flight condition and provide the technical basis for the refinement of noise certification procedures.
(Ruth M. Martin, 43631, Robert E. Grandle, and Michael A. Marcolini)

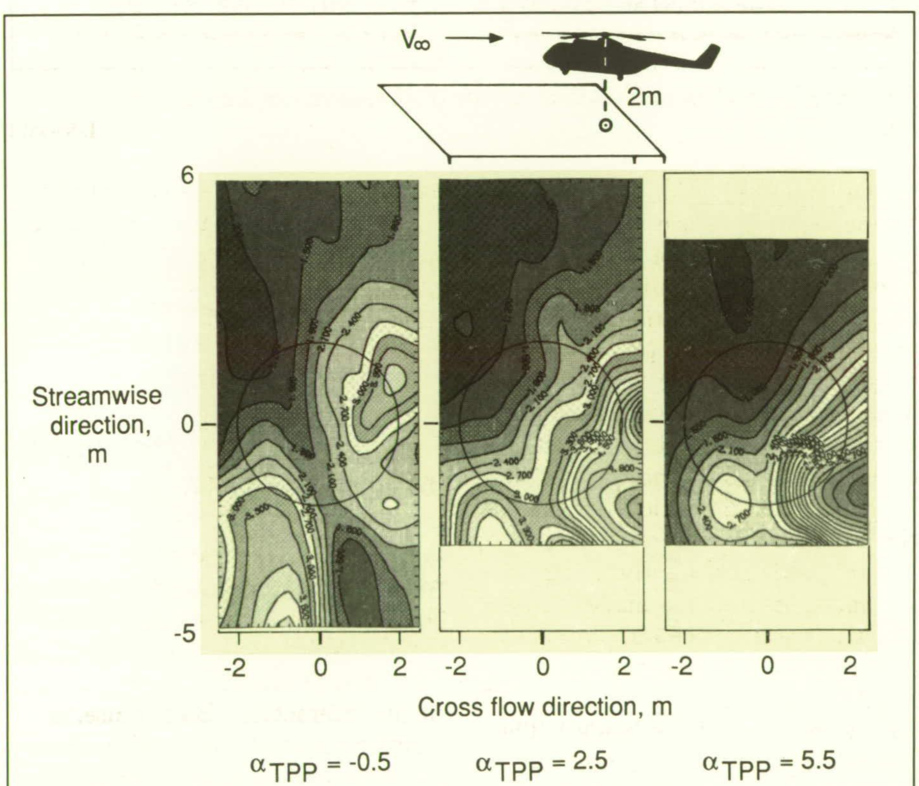

Variation of rotor impulsive noise directivity with flight angle.

Reduction of Rotor Blade-Vortex Interaction Noise Using Higher-Harmonic Pitch Control

Blade-vortex interaction (BVI) is the source of one of the most objectionable types of helicopter noise. This impulsive noise is due to aerodynamic interaction of the rotor blades with previously shed blade tip vortices. In-house analytical studies showed that decreases in blade lift and/or vortex strengths should reduce the intensity of the interactions and thus noise. Based on this concept, the use of higher harmonic control of blade pitch angle, historically studied as a means to reduce helicopter vibration, should offer potential for noise reduction.

A test (shown in the first figure) was conducted using the Aeroelastic Rotor Experimental System (ARES) in the Transonic Dynamics Tunnel (TDT). The ARES used an articulated four-bladed 110-in.-diameter rotor with untwisted blades of rectangular planform. A unique sound power measurement technique was developed for the test because of the TDT reverberance and Freon environment. Using a specially developed open-loop control system, prescribed higher harmonic pitch motion was superimposed on the normal blade pitch for a broad range of rotor operating conditions. It was found that the pitch control could significantly increase or decrease the noise depending on the control amplitudes and phases. A control input of particular interest was a four-per-revolution collective blade pitch motion giving a $-1°$ amplitude at 60° blade azimuth. This pitch control corresponds to a pitch being minimized near the predicted BVI

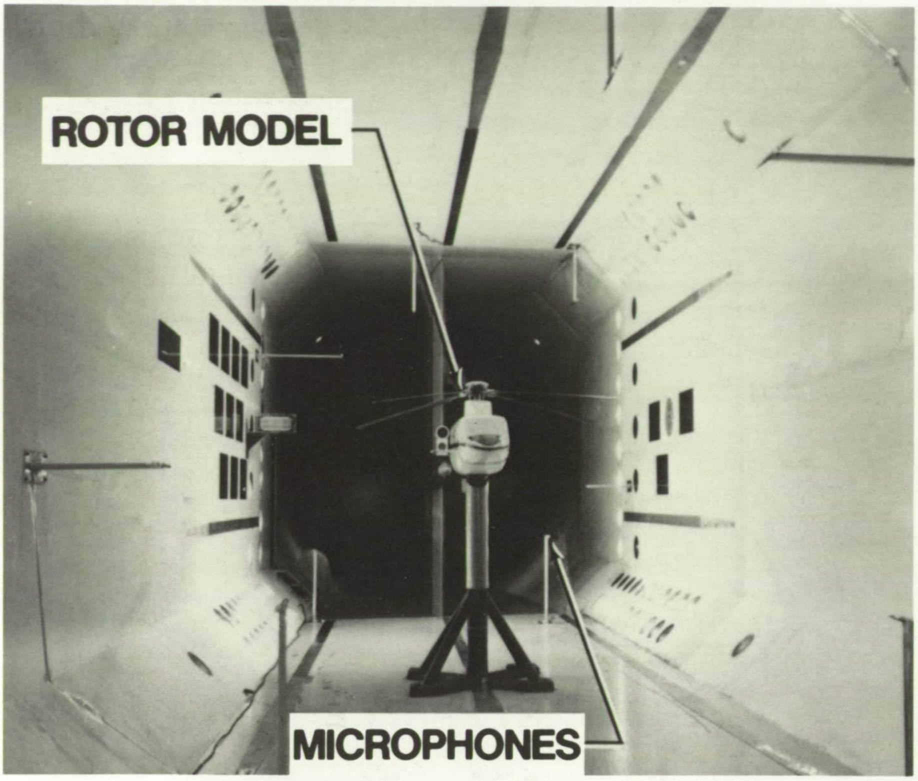

ARES noise test in TDT.

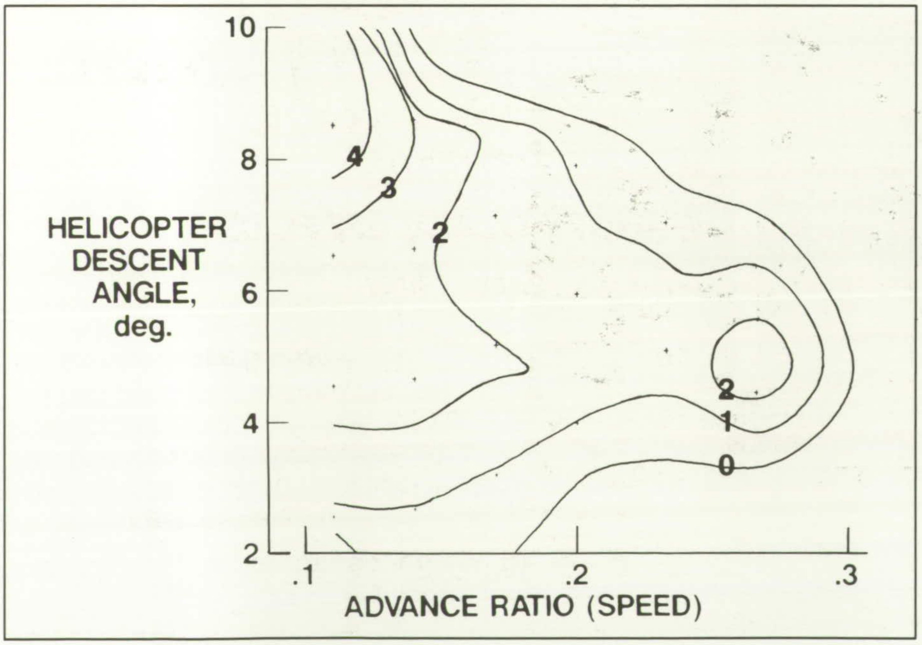

Reduction in BVI noise level (dB).

locations. The second figure shows a contour plot of the noise reductions found when this pitch control was used. The dB level reductions shown are the differences of spatially averaged noise levels between the control and no-control cases in which the flight conditions are matched. Helicopter descent angles were calculated using model test conditions and full-scale fuselage drag data. The advance ratio is the forward speed divided by the rotor tip speed. The flight range shown is for descending flight conditions typical of a landing approach. The noise reductions (up to 4.7 dB) are greater for the lower speeds at which, without controls, BVI noise is the most severe. The results show the noise reduction concept to be viable. The effects of higher harmonic pitch controls on vibration and noise directivity remain to be addressed.

(Thomas F. Brooks, 43634, Earl R. Booth, Jr., and William T. Yeager, Jr.)

Important Contributors to Vibratory Response Identified by Test of Helicopter Airframe

Excessive vibration is the most common technical problem to arise as a "show stopper" in the development of a new rotorcraft. With only a few exceptions, these vibration problems are identified during the flight test phase of development. Vibration predictions have not been relied on by the industry during design because of deficiencies in current vibration analysis methods. With a view toward establishing a capability in the industry to fully

utilize vibration analysis during design, the Langley Research Center has under way a program, designated DAMVIBS (Design Analysis Methods for VIBrationS), with the overall objective of establishing the foundations for developing a superior design analysis capability for vibrations. Among the many activities under the DAMVIBS program is one aimed at identifying those difficult components that are important contributors to airframe vibratory response and which require more detailed finite-element representation.

Typically, only the primary structure is represented fully (stiffness and mass) when forming the finite-element model (FEM) of an airframe. There are many components (e.g., transmission, engines, and stores) and secondary structures (e.g., fairings, doors, and access panels) which are represented only as lumped masses. To isolate the effects of each component on overall vibratory response, multiple ground vibration tests are being conducted.

The initial effort in this area was conducted by Bell Helicopter Textron utilizing an AH-1G helicopter airframe. Ground vibration tests were conducted on a total of eight aircraft configurations with each configuration representing a progressive removal of a suspect component until only the primary airframe structure remained. At each stage, analyses were performed using an existing FEM of the airframe modified to reflect the specific configuration tested. An illustrative result is given in the figure which shows the importance of secondary panels and canopy glass on airframe response at the higher frequencies. These difficult components studies on the AH-1G helicopter represent the first such studies conducted on

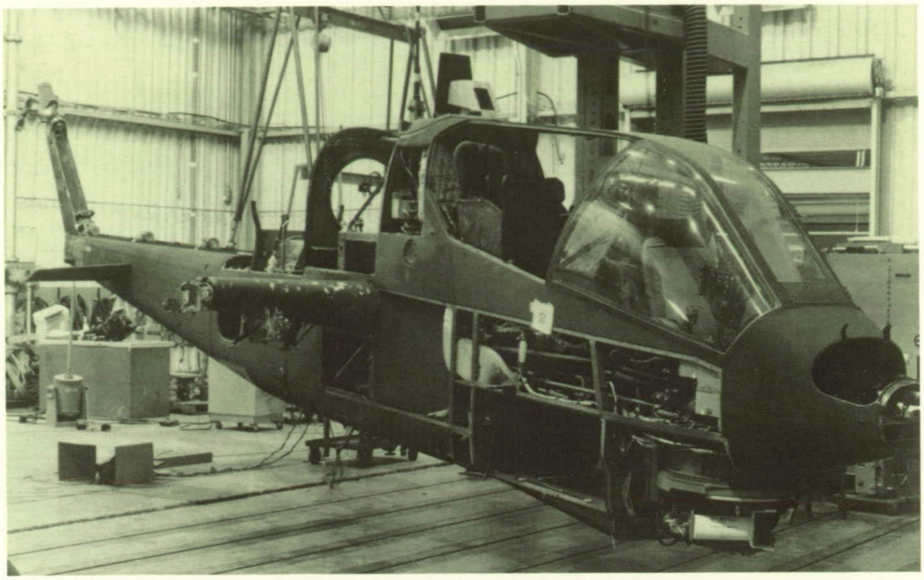

Stripped-down helicopter airframe used in ground vibration test. L-89-7126

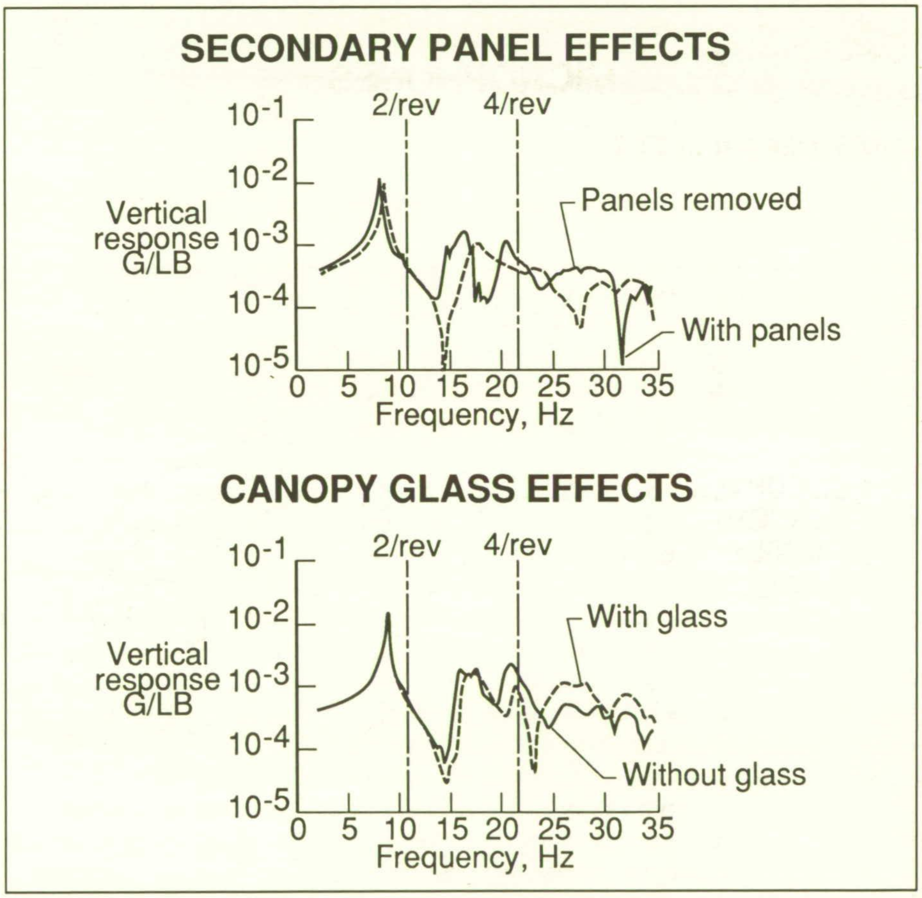

Effect of secondary panel and canopy glass on vertical response.

an airframe structure with additional tests to be performed on both metal and composite airframes.
(Raymond G. Kvaternik, 41228)

Low Dielectric Polyimide Films and Coatings

Polymer	Diamine Ar	Dielectric constant at 10 GHz
6FDA + $DDSO_2$	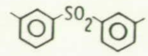	2.86
6FDA + 4,4'-ODA	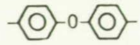	2.79
6FDA + 3,3'-ODA	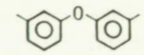	2.73
6FDA + APB	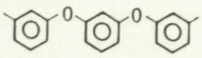	2.67
6FDA + 4-BDAF	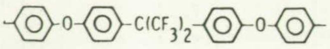	2.50
6FDA + 3-BDAF	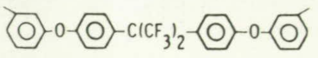	2.40
6FDA + 4,4'-6F	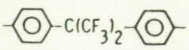	2.39

Dielectric properties of fluorine-containing polyimides.

High-performance polyimide films and coatings are currently being exploited by the electronic circuit industry. To be useful for such applications as interlevel insulators, passivant overcoats, or substrate components, a polymeric material must be an excellent insulator. The dielectric constant of commercial polyimides presently used as state-of-the-art materials by the electronics industry ranges from 3.2 to 4.0 depending on moisture content.

Structure/property relationship studies of highly insulative, low dielectric aromatic polyimides are being conducted in the Materials Division at Langley Research Center. Dielectric constants below 3.0 have been achieved through the reduction of both dipolar and chain-chain interactions and through several other mechanisms used to increase the free volume of the polymer. Particularly low dielectric constants in the range of 2.4 to 2.6 have been achieved by the additional incorporation of fluorine atoms into the polymer backbone. The polyimides containing fluorinated alkyl groups in the polymer structure show excellent resistance to moisture, and, therefore, there is little effect on the dielectric constant when the polymer is exposed to high levels of humidity. These aromatic polyimides are highly suitable as film and coating materials for applications in which thermal stability, high electrical insulation, and resistance to moisture are required.
(Anne St. Clair, 44242)

Benefits of Sonic Boom Shaping

Studies have indicated that the distribution of the volume and lift of a supersonic transport may be manipulated in order to shape the pressure-time signature of the resulting sonic boom which reaches the ground. Proper shaping of the sonic boom will reduce adverse human response. People exposed to sonic booms from a supersonic transport would be located both indoors and outdoors, and, therefore, it is necessary that an assessment of the benefits of shaping include the sound transmission characteristics of typical buildings. Because, from a human perspective, the most fundamental attribute of a sound is loudness, this characteristic was chosen as the basis for estimating the potential benefit of sonic boom shaping. Using a well-developed theory of loudness, calculations were performed for a range of those parameters which describe a conventional N-wave sonic boom and a shaped sonic boom as heard outdoors. In addition, estimates of the noise reduction provided by typical residential buildings enabled loudness to be calculated for the same sonic booms as would be heard indoors.

The figure illustrates the calculated loudness values for a range of sonic booms heard outdoors and indoors, with windows either open or closed. The first column in the figure contains data for an N-wave, which is characterized by a rapid rise in pressure to the peak, followed by a relatively slow decrease in pressure, and an abrupt return of pressure to ambient. The other columns in the figure contain data for a range of shaped booms, which are characterized by a rapid rise to the initial shock amplitude and a

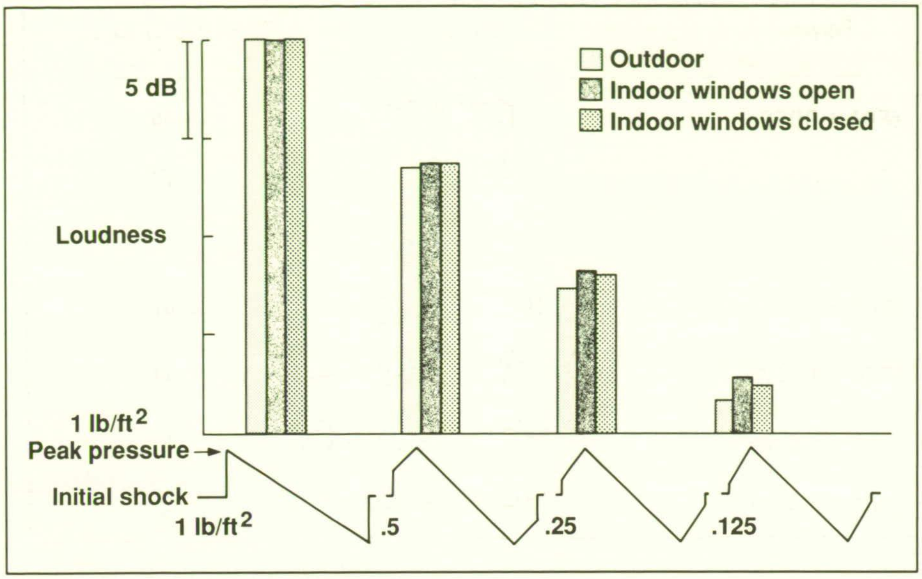

Loudness of sonic booms heard indoors and outdoors.

more gradual rise to the peak pressure. For the shaped booms, the initial shock amplitudes range from 0.125 lb/ft^2 to 0.5 lb/ft^2. For illustrative purposes, the rise time of the initial shock and the peak pressure have been held constant for all the boom signatures. The calculated values of loudness for the shaped booms are shown relative to the loudness of an N-wave heard under the same conditions, indoors or outdoors. The results indicate that substantial reductions in loudness can be achieved through shaping, even for signatures having the same peak pressure. Furthermore, these reductions are found to be of similar magnitude for observers located either indoors or outdoors. Based on these predictions, it is clear that the loudness of a shaped boom may be reduced by reducing the initial shock amplitude.
(Kevin P. Shepherd, 43583)

Reduction of Circumferential Gap Heat Loads by Discrete Longitudinal Gap Fillers

The gaps between reusable surface insulation tiles on the Space Shuttle cause local flow disturbances that have been studied extensively on flat surfaces. Important parameters (including gap width, gap length, and flow angularity) and their effects on local and total heat transfer rates have been identified. However, the effect of surface pressure gradients, which occur naturally on curved surfaces, have not been quantified. In general, pressure gradients would cause greater flow ingestion into the tile gaps and augment the aerothermal loads. Consequently, many of the Space Shuttle tile gaps are filled to circumvent this problem, but this approach costs in weight and labor. The objective of this study was to

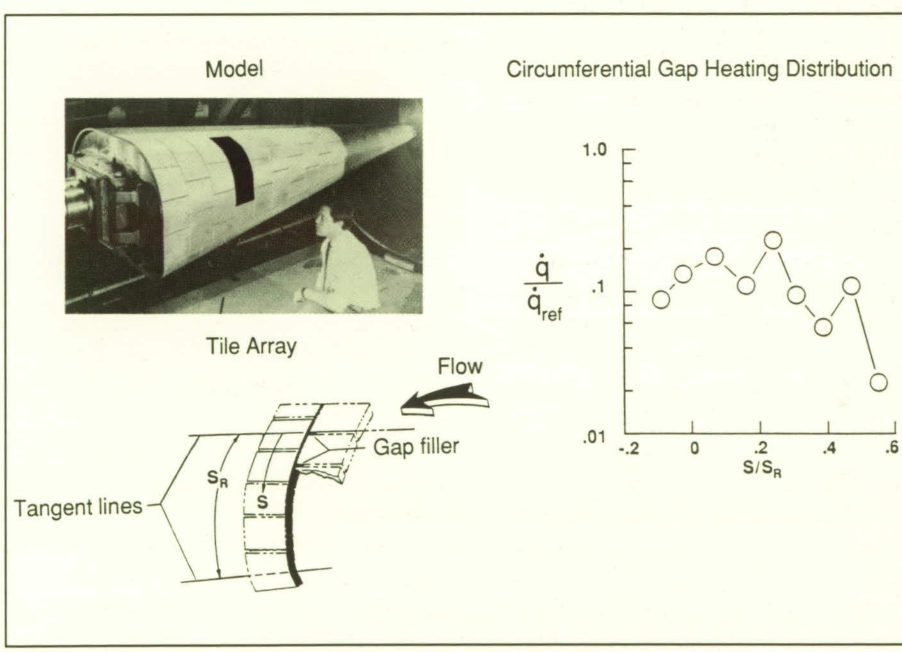

Effect of discrete gap filler for Space Shuttle tiles (Mach number = 6.6 and angle of attack = 10°).

determine experimentally the gap heat transfer rates and effect of gap fillers in reducing the heating rates.

The Curved Surface Test Apparatus has been developed as a generalized test model for the 8-Foot High-Temperature Tunnel (8-Foot HTT). The model is representative of the forward portion of a lifting body, and the complex, three-dimensional flow field around this body has been defined experimentally and analytically. An extensive array of simulated tiles was installed over the aft portion of one side of the model as shown in the figure. Thin-wall, metallic heat-transfer tiles were installed in the location (highlighted in black) adjacent to pressure-instrumented solid tiles to determine the aerothermal loads in the tile gaps. The instrumented circumferential tile gap of interest is also illustrated in the figure. Tests were at Mach 6.6, a total temperature of 3400°R, Reynolds numbers of 0.4 to 1.5 × 10^6/ft, and angles of attack of 7°, 10°, and 13°, which provided a pressure gradient range. Discrete gap fillers, such as those illustrated in the longitudinal gaps that provided a continuously open circumferential gap, allowed the effect of gap fillers to be assessed.

Heat transfer rates and pressures were obtained on the surface and at gap half depth to identify the effect of pressure gradient on the gap aerothermal loads. Discrete gap fillers provided insight into the mechanisms that resulted in the increased heating rates. The most significant result of the study was that the longitudinal gaps, which are more closely aligned with the external flow than the circumferential gaps, tend to channel the flow into the circumferential gaps. This increased flow raises the gap heat transfer rates. When the longitudinal gaps are blocked as illustrated, the circumferential gap heating relative to the no-gap filler reference circumferential heating rate $\dot{q}_{ref}$ is reduced by an order of magnitude as shown in the graph in the figure.
(L. Roane Hunt, 41352)

ENSA in Good Agreement With Mach 11.68 Compression Corner Data

The Euler/Navier-Stokes Analyzer (ENSA) is a space-time finite-element formulation of the compressible Navier-Stokes equations with the dependent variables written in terms of a scalar entropy function. This formulation enforces the second law of thermodynamics and provides improved solution stability and accuracy in the presence of flow phenomena with high entropy production, such as shock waves, heat transfer, and chemical reaction. The improved stability of this formulation eliminates the need for addition of an implicit artificial viscosity term. The resulting set of equations is solved through a Galerkin/least-squares algorithm with a nonlinear discontinuity capturing operator. The algorithm uses any mixture of quadrilateral and triangular elements in an unstructured mesh and incorporates a domain decomposition algorithm that permits explicit or implicit subdomain treatment.

Comparison of the ENSA computed wall data for Mach 11.68 flow over a 15° compression corner is shown in the figure. The wall temperature is constant at 540°R, and the Reynolds number is based on free-stream conditions and the 17.4-in. length from leading edge to corner. The computations were done

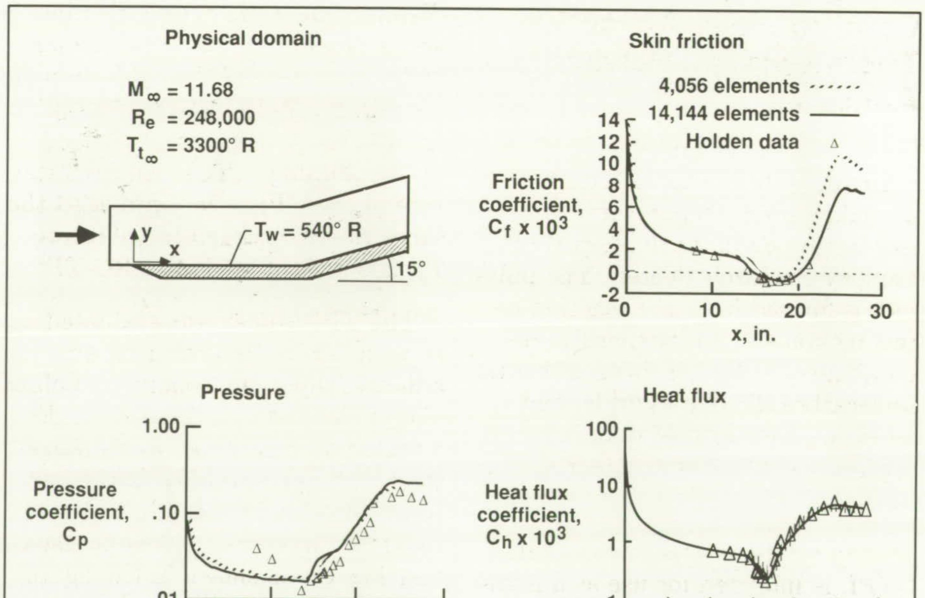

Comparison of predictions with experimental data.

with mesh sizes of 4,056 and 14,144 elements, each with the mesh compressed near the wall. The results show that the computational values for the wall quantities of friction, pressure, and heat flux coefficients agree closely with the measured experimental values. The effect of increased mesh size is only significant in the downstream skin friction coefficient prediction, where there are no experimental data.

The ENSA was successfully demonstrated in an environment with shock waves and strong temperature gradients. These results were obtained with an entropy formulation of the governing equations, a finite-element solution algorithm, and no explicit artificial viscosity.
(T. J. R. Hughes and George C. Olsen, 41354)

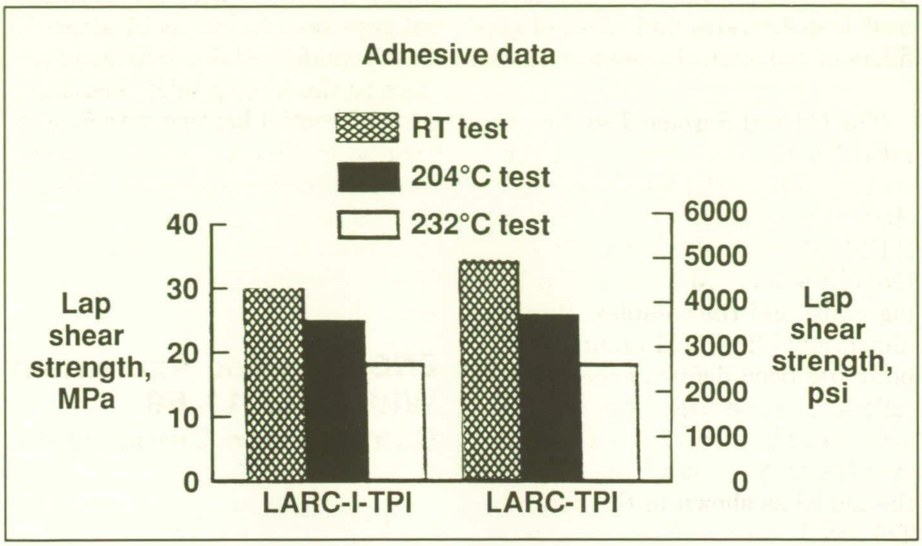

Lap shear strength data for LARC-I-TPI and LARC-TPI.

LARC-I-TPI, New Commercially Attractive Thermoplastic Polyimide Adhesive

LARC-TPI is a commercially available, high-temperature, thermoplastic polyimide developed at Langley Research Center. The polymer is formed from the reaction of two monomers, an inexpensive dianhydride, 3, 3′, 4, 4′-benzophenonetetracarboxylic dianhydride, and an expensive diamine, diaminobenzophenone, which is a potential carcinogen.

A new adhesive material, LARC-I-TPI, is intended for use as a high-temperature, high-performance adhesive for future aerospace applications. The polymer has other potential applications; however, this work focuses on its adhesive properties. Being very similar in chemical structure to LARC-TPI, the isomer provides similar properties and is potentially less expensive to produce and therefore commercially attractive. The TPI-isomer was formed from an inexpensive diamine, meta-phenylene diamine, and a potentially inexpensive dianhydride, 4, 4′-isophthaloyldiphthalic anhydride. Molecular weight control of this polymer was achieved by endcapping. The chemical structure of the TPI-isomer provided the same glass transition temperature T_g, 260°C, as that for LARC-TPI.

The TPI-isomer was evaluated as an adhesive by preparing an adhesive tape and bonding titanium alloy (Ti-6Al-4V) adherends under a variety of conditions to optimize the bonding procedure. Lap shear strength tests were conducted at room temperatures (RT's) of 204°C and 232°C. As shown in the figure, strengths were similar for both adhesive systems. In addition, the results, not shown here, for a 72-hour water boil exposure indicated a moderate improvement in strength retention for the TPI-isomer over that of the LARC-TPI.

This new polymer retains the excellent adhesive and thermoplastic properties of LARC-TPI, but eliminates the expense and potential carcinogenicity of the diamine used in its preparation. These beneficial modifications were achieved by employing the molecular design technique of interchanging chemical units within a polymer structure.
(Donald J. Progar, 44256 and J. Richard Pratt)

Total Dose and Dose Rate Effects for Electron Irradiation of Thermoplastics

Graphite fiber-polymeric materials are lightweight, stiff, dimensionally stable, and reformable (if they are thermoplastic). Therefore, these materials are attractive for

C-3

space applications; however, they must also be stable in radiation environments, such as geosynchronous Earth orbit (GEO), particularly if they are to serve for long-term missions.

A study has been conducted to determine and explain the effects of total absorbed doses and absorbed dose rates on tensile properties for electron irradiation of one example of the advanced thermoplastics, a polyetherimide. The kinetics of the molecular structural changes were studied using electron paramagnetic resonance (EPR), and the findings were related to the changes in the tensile properties of the material for total doses from 0.001 MGy to 100 MGy at dose rates of 0.1 MGy/hr to 100 MGy/hr from 100 keV electrons. As seen from the figure, the total dose threshold for large changes in tensile elongation to failure is approximately 2 MGy; the shaded areas are the 1-σ uncertainty bands about the data points, each of which is an average for six specimens. The decrease in elongation is due to crosslinking of molecular chains. There is no variation of the tensile properties with dose rate because the rate of radical creation exceeded the rate of radical decay for all the dose rates studied. The present results lend increased confidence in results obtained from accelerated-life testing. Two total doses for 30 years are highlighted, one for a low Earth orbit (LEO) and one for geosynchronous Earth orbit.
(E. R. Long, Jr., 44249 and S. A. T. Long)

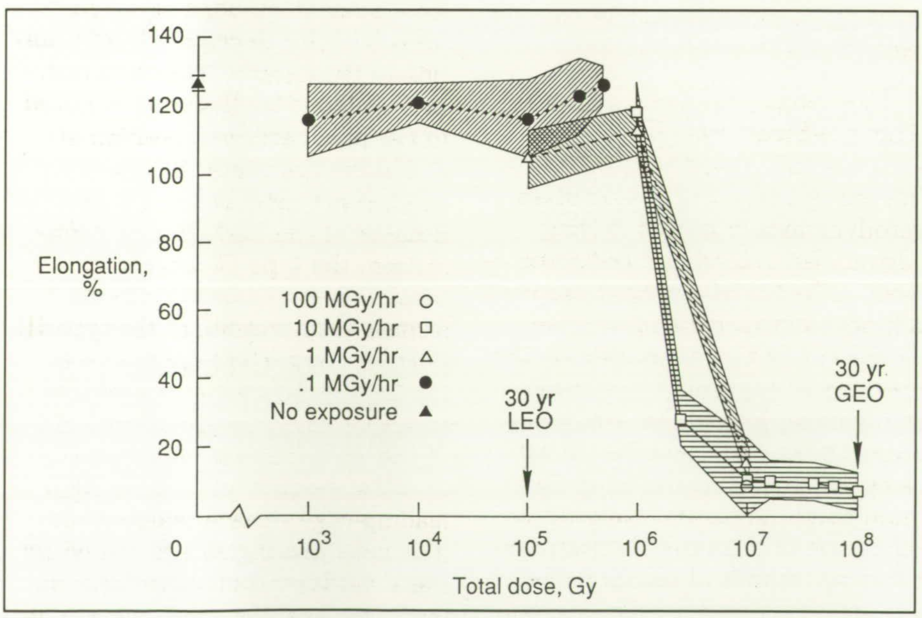

Elongation to failure of irradiated polyetherimide for four dose rates.

Interface Between Unstructured and Structured Meshes Identified by Heat Flux Indicator

Computer simulation of high-speed viscous flows is obtained by solving the compressible Navier-Stokes equations using the finite-element method. To capture steep gradients in the flow variables that are present near shocks and thin boundary layers, an adaptive unstructured remeshing method is employed in which a new mesh is created based on error indicators from a numerical solution on an earlier mesh. The application of the current remeshing method for a simple viscous flow, where the inviscid region is discretized in an unstructured manner using a mixture of quadrilateral and triangular elements and the viscous region is discretized in a structured manner using only quadrilateral elements, is illustrated in the upper left figure.

A structured boundary-layer mesh is required because of turbulence modeling requirements and, to some extent, limitations of the numerical procedures. The magnitude of the heat flux vector is used to identify the boundary-layer edge as shown in upper right figure, and tangential velocity is used as an error indicator to generate an adaptive structured mesh in the boundary-layer region. Quadrilateral elements are chosen in the boundary layers because the elements can accommodate the high-aspect ratios that are required for mesh optimization. Hypersonic Mach 11.68 flow over a 15° compression corner, as shown in the lower left of the figure, is used to demonstrate the procedure. The inviscid region that includes a strong compression shock is discretized using density as an error indicator. A portion of the mesh (lower right of the figure) indicates the adaptive structured boundary-layer mesh and the unstructured mesh. The results showed good comparison of the aerodynamic heating with either

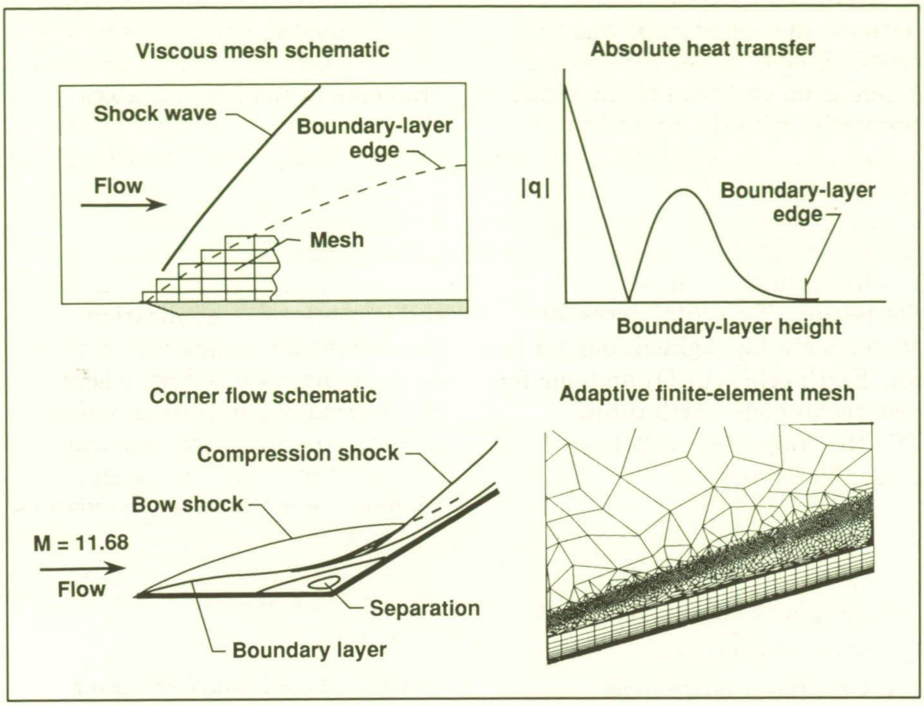

Boundary-layer edge indicated by zero heat flux.

experimental or other analytical results. This method reduces the number of elements in the boundary layer by identifying the boundary-layer edge and adapting the mesh to the flow physics.

(Gururaja R. Vemaganti and Earl A. Thornton, 41349)

Heat Transfer/ Deformation Coupling Demonstrated by LIFTS Analyzer

The design of leading edges for hypersonic vehicles that experience intense stagnation point pressures and heating rates depends on accurate prediction of the aerodynamic flow, the structural temperature response, and the structural deformations and stresses. Significant coupling occurs among the aerodynamic flow field, structural heat transfer, and structural response creating an interdisciplinary interaction. Understanding the fluid-thermal-structural interaction is important for the design of leading edges to survive such severe aerothermal environments.

The Langley Integrated Fluid-Thermal-Structural (LIFTS) analyzer is used to investigate the interdisciplinary interaction of an aerodynamically heated leading edge under a simulated test environment. The LIFTS analyzer employs a finite-element method to solve the Navier-Stokes equations for the flow solution, the energy equation of the structure for the temperature response, and the equilibrium equations of the structure for the structural deformation and stresses. A schematic of a proposed experimental setup of an 0.25-in.-diameter, 3-in.-long, 0.1-in.-thick leading edge is shown in the upper left of the figure. The leading edge is initially exposed to the undisturbed Mach 5.25 flow (position A) behind the oblique shock generated by the free-stream Mach 8 flow. After 1 min, the leading edge is raised instantaneously to the predetermined position B to produce the type IV shock-shock interference pattern that results in a supersonic jet impingement normal to the leading-edge surface, causing intense stagnation point pressure and heating rate.

The fluid analysis is first performed to predict the flow behavior and aerothermal loads on the leading edge when it is at the position A. An adaptive mesh refinement technique is used in the fluid analysis to minimize the number of unknowns. The finite-element flow model and flow Mach numbers are shown in the lower left of the figure. The predicted aerodynamic heating rate is in excellent agreement with the Fay and Riddell solution as shown in the upper right of the figure. This heating rate causes the leading-edge temperature to increase nonuniformly resulting in the leading-edge bending upward (as shown in the centered right portion of the figure). As mentioned, the deformed leading edge is raised to the predetermined position B at 1 min to produce the type IV shock-shock interference pattern. Because of the leading-edge deformation, the type IV interference pattern does not occur. The deformed shape results in the type III interference pattern (as shown in the figure). The heating rate distribution shown in the lower right of the figure reflects this type III interference pattern and the high leading-edge surface temperature. The peak heating rate is caused by the shear-layer/boundary-layer interaction, and the minimum heating rate is at the nose of the leading edge where the temperature is maximum.

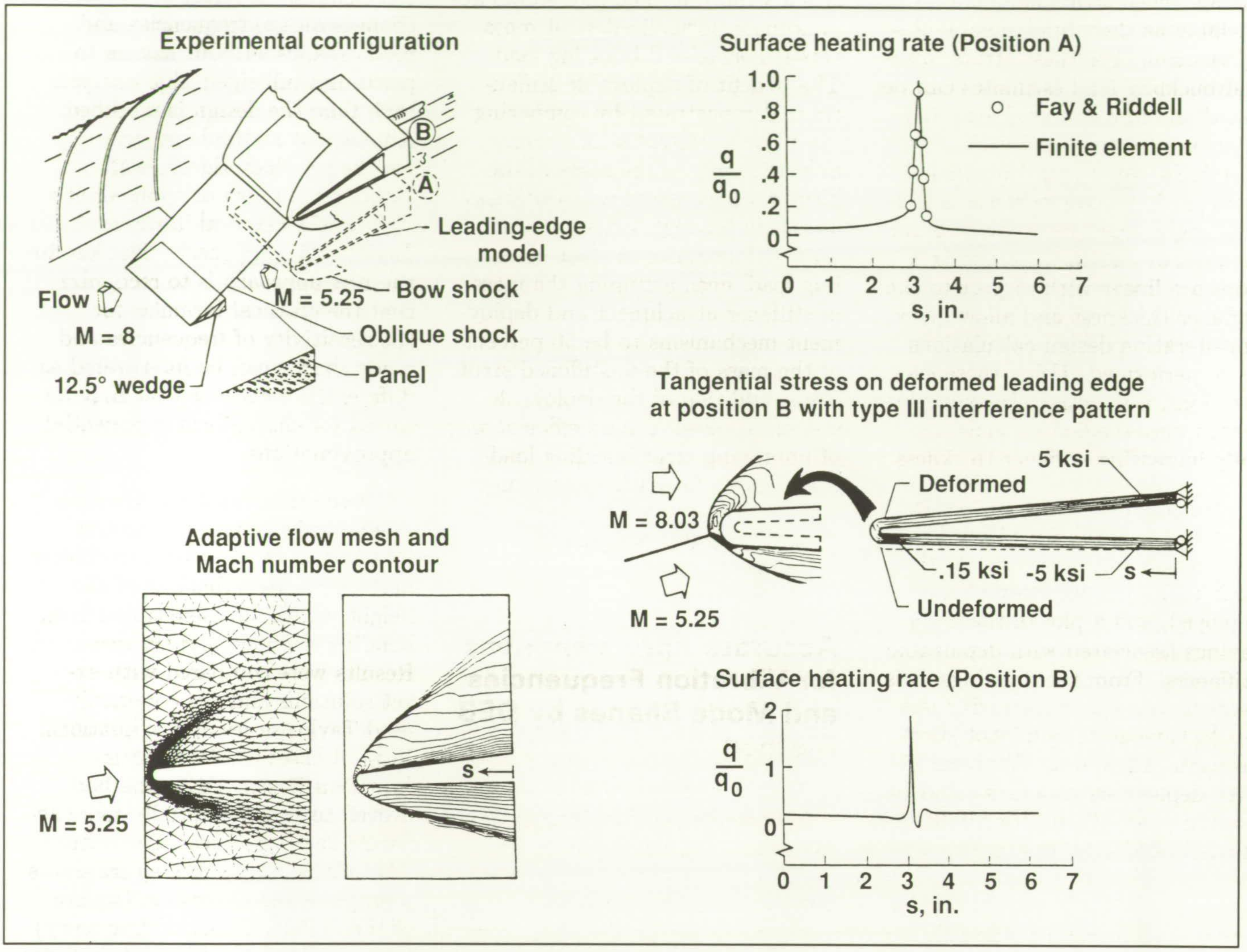

Fluid-thermal-structural analysis of leading edge.

The demonstration has shown the capability of the integrated fluid-thermal-structural analysis approach to provide solutions to complex aerothermostructural behavior and the interdisciplinary interaction. The integrated fluid-thermal-structural result underlines the importance of the interdisciplinary interaction that must be taken into account in the design and testing of the aerodynamically heated leading edges subjected to shock-shock interference loading.
(Pramote Dechaumphai, 41357)

Deployable Stiffeners for Slender Space Truss Struts

The design of large space structures is primarily driven by stiffness as opposed to strength considerations. This consideration, along with the need to minimize packaged volume for efficient transport to orbit, encourages the use of very long slender truss struts. However, many large space structures are also required to withstand significant loads due to thermal gradients, spacecraft operations, and attitude control maneuvers. Consequently, the stability of these slender struts becomes a design concern. A deployable stiffener concept, which allows high buckling loads to be achieved without sacrificing packaging efficiency, has been developed for truss struts.

Extensive numerical analysis of Euler column buckling and local stiffener buckling was performed to determine design rules that ensure

that stiffened struts exhibit Euler buckling as their fundamental stability mode. For these struts, mass and buckling load estimates can be based on cross-sectional area and moment of inertia calculations, respectively. Assuming thin-walled cross sections, approximate expressions were determined for area and moment of inertia. These expressions are linear with respect to the stiffener thickness and allow quick, first-iteration design calculations to be performed. Using these expressions, mass versus buckling load trends were studied by monotonically increasing stiffener thickness.

The figure shows an isometric view of a portion of a stiffened strut, cross-sectional views of the strut with stiffeners stowed and deployed, and a plot of the mass savings associated with deployable stiffeners. From the drawings, it is evident that the stowed stiffeners would have an insignificant effect on packaged volume. Thus struts with deployable stiffeners could be used in place of simple cylindrical struts in any erectable or deployable space structure. The plot shows approximate normalized strut mass versus normalized buckling load. The benefit of deployable stiffeners is demonstrated by comparing the mass of a strut with deployable stiffeners to the mass of the strut with increased wall thickness. The mass savings are significant for large increases in strut buckling load, even assuming the mass of stiffener attachment and deployment mechanisms to be 50 percent of the mass of the unstiffened strut. Thus, addition of the deployable stiffeners allows a more efficient way of improving strut buckling load than simply increasing the strut wall thickness.
(Mark S. Lake, 43114)

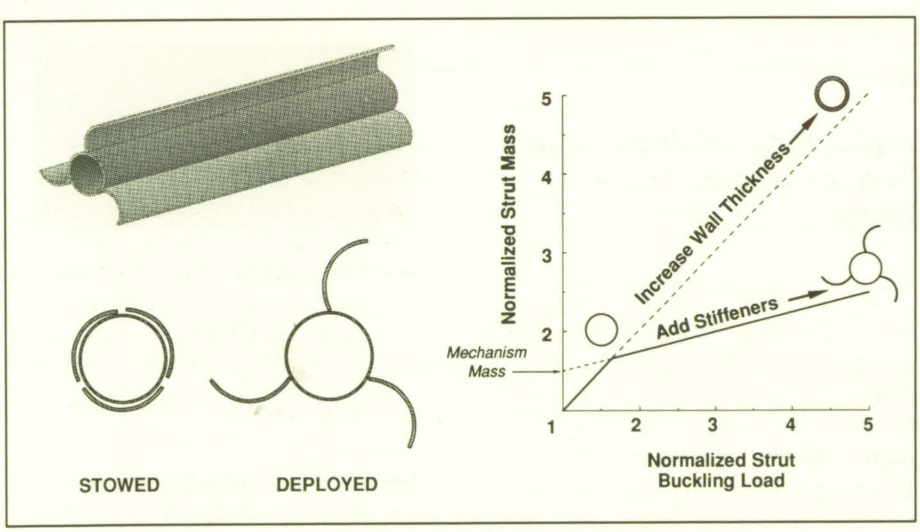

Deployable stiffeners that permit significant increase in strut buckling load with small mass and stowed volume penalties.

Accurate Approximations for Vibration Frequencies and Mode Shapes by DEB Method

In optimization for structural dynamics, it is highly desirable to calculate the effect of design changes on the frequencies and mode shapes without having to perform a full eigenvalue analysis each time the design is modified. An efficient method has been developed which significantly extends the range of applicability beyond the classical linear or Taylor series approach. The key to the new approach is to recognize that the classical formulas for the sensitivity of frequencies and mode shapes can be interpreted as differential equations that may be solved for closed-form exponential approximations.

These approximations were derived, implemented, and tested. The test cases involved a cantilever beam with perturbations of the height, width, cross-sectional area, bending stiffness, and tip mass. Results were compared with exact solutions and the commonly used Taylor series approximations. In most cases the Differential-Equation-Based (DEB) method proved to be substantially more accurate than the linear approximation. For example, the figure shows a graph of the eigenvalue (square of the first fundamental frequency) versus the height of the beam H for values perturbed from the nominal value of 5.0 in. For as much as a 50-percent increase in H, the new approximation is within 2 percent of the exact solution. Similar results were seen for perturbation studies of the other variables and the same trends occurred for approximating frequencies of the second bending mode. The DEB method approximates mode shapes with a similar degree of accuracy.

An outstanding advantage of the DEB method due to its increased accuracy is that iterative design, particularly in optimization, will

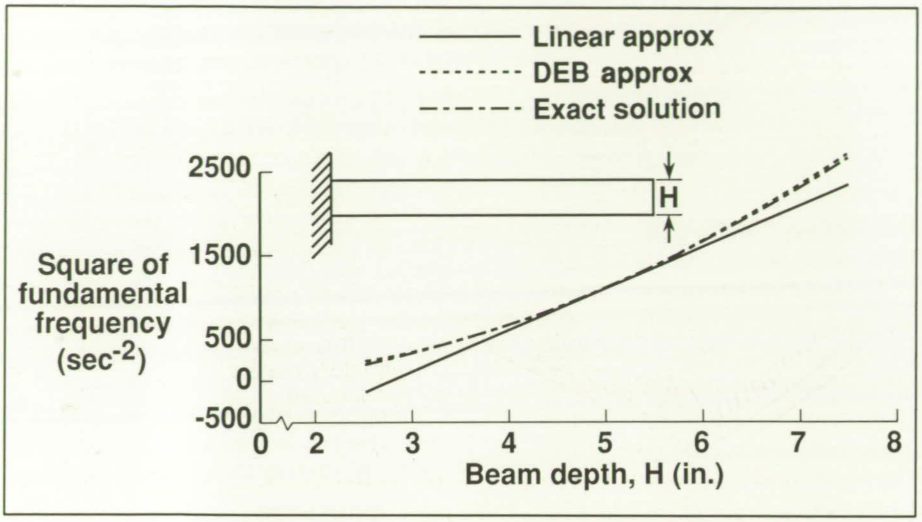

Comparison of DEB and linear approximations of frequency for perturbation of beam depth.

not require reanalysis as often, therefore saving computer time. **(Jocelyn I. Pritchard, 42805 and Howard M. Adelman)**

Surface Machining of Thin 3-D Orthogonal Carbon-Carbon Composites

Woven three-directional (3-D) orthogonally reinforced carbon-carbon (C-C) composites offer significant advantages over typical 2-D reinforced C-C composites in terms of the much higher interlaminar strengths achieved as a result of the through-the-thickness (z-direction) reinforcement. However, several areas of concern exist. One concern is that the flexural moduli of 3-D orthogonal C-C composites tend to be low relative to typical 2-D composites. Another concern is that the loop ends of the "z" reinforcing fibers present a rough external surface, and removal of these loops may be desirable to achieve aerodynamic smoothness. Finally, the z-loops may, in any event, be destroyed during preparation of the surfaces for application of oxidation-resistant coatings or by the coating application itself.

A study was conducted to determine what effect removal of the z-loops by machining has on mechanical properties. Interlaminar shear and across-ply tensile strengths remained high while flexural strength and modulus were greatly improved. The figure shows a plot of flexure strength versus modulus for several 3-D preform styles with and without the z-loops machined from the C-C surface. The reason for the higher properties after machining is that the test-specimen thickness used in the stress calculations no longer includes the thickness contribution from the essentially non-load-bearing z-loops. The flexural moduli, however, are still lower than the modulus of the 2-D reference material; this is because of the inherently lower in-plane fiber volume fraction of the 3-D reinforcement architecture.

This study shows that light machining of 3-D orthogonal C-C composites may be an acceptable

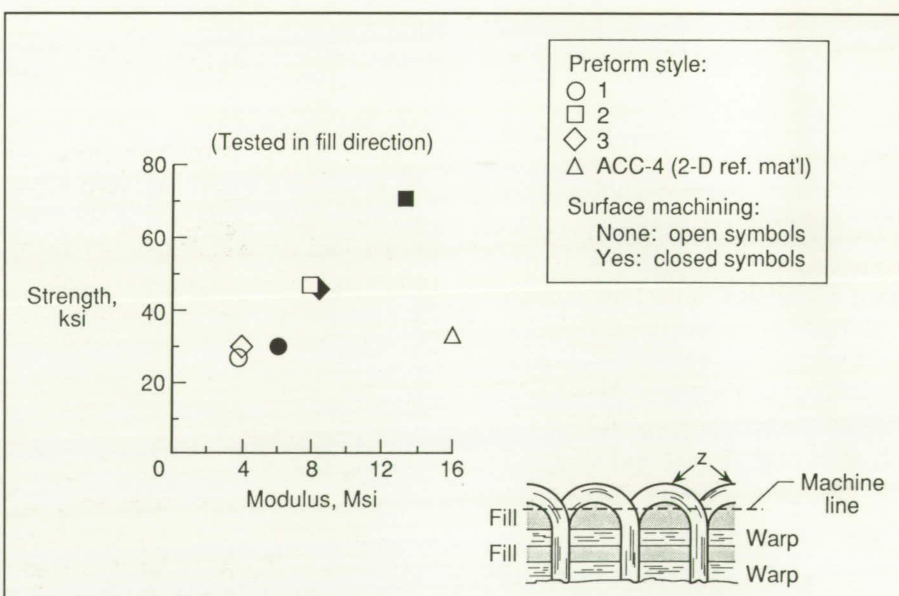

Effect of light surface machining on flexure performance of thin 3-D orthogonal carbon-carbon composites.

approach for preparing surfaces for coating and for improving surface smoothness. These results also imply that unmachined 3-D orthogonal C-C composites may possibly be conversion coated (a process that converts the loop to a carbide) without significantly degrading mechanical properties. **(P. O. Ransone, 43503)**

Development of Carbon/Carbon Heat-Pipe Structure

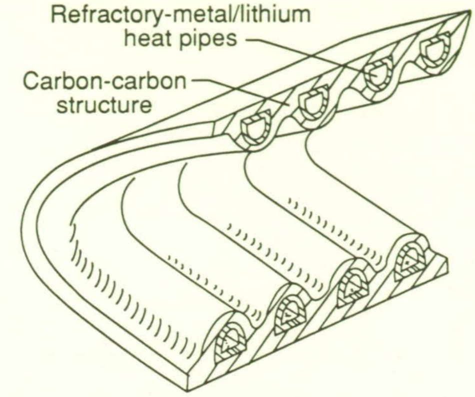

Carbon-carbon/refractory-metal heat-pipe leading edge.

Future hypersonic vehicles such as the National Aero-Space Plane (NASP) will experience high heating rates that will cause temperatures to exceed the maximum structural reuse temperature of carbon-carbon. (Currently carbon-carbon is limited by its oxidation protective coating to temperatures below 2800°F.) This study is to extend the maximum heat flux capability of carbon-carbon structures by using embedded heat pipes and thereby provide a simple, reliable, fail-safe, potentially lighter alternative for the nose cap and wing leading edge of NASP.

The design philosophy of the present concept utilizes the high specific strength of carbon-carbon at elevated temperatures to accommodate the thermal/structural loads. This philosophy also uses very thin refractory-metal D-shaped, heat pipes (5 mil thick), embedded within the structure (as shown in the figure) to transport the stagnation heat aft where it can be rejected by radiation. The heat pipes could be sized and spaced close enough so that in the event of a failure, the ablation protection afforded by the carbon-carbon would be sufficient to enable a safe reentry. The preferred method of construction would be to fabricate, fill, and check out the individual heat pipes, embed them in a 2-D layup of carbon-carbon prepreg, and process (pyrolyze and densify) as would be done for a typical carbon-carbon component.

Two-dimensional thermal/structural analysis indicates the feasibility of the concept. Reaction rate studies of refractory metals (molybdenum, tungsten, and tantalum) indicate that tungsten is the least reactive with carbon; because of its very high thermal conductivity and low coefficient of thermal expansion, tungsten is the leading candidate for a container for the lithium working fluid. Tungsten tubes (0.03 in. thick) have been successfully embedded within 2-D carbon-carbon prepreg and pyrolyzed and densified three times without any noticeable damage to the composite. The proposed concept can extend the use of conventional carbon-carbon structure to withstand much higher local heating rates (such as those predicted for the wing leading edge of NASP) by significantly reducing peak stagnation temperatures. Also, the current concept offers an ablative/fail-safe capability in the event of a heat pipe failure. **(Charles J. Camarda, 45436 and Philip O. Ransone)**

Increase in Heat Transfer Rate Amplification by Coalesced Multiple Shock-on-Lip

Hypersonic airbreathing engine performance is maximized when the oblique shock waves used to compress the external air flow intersect the engine cowl, i.e., shock-on-lip. These oblique shock waves emanate from the vehicle nose and engine inlet ramps, and their number is dependent on the vehicle design and mission. The purposes of this investigation were to determine the heating rate distribution resulting from two oblique shock waves coalescing at their intersection point with the blunt bow shock wave from a cylindrical leading edge;

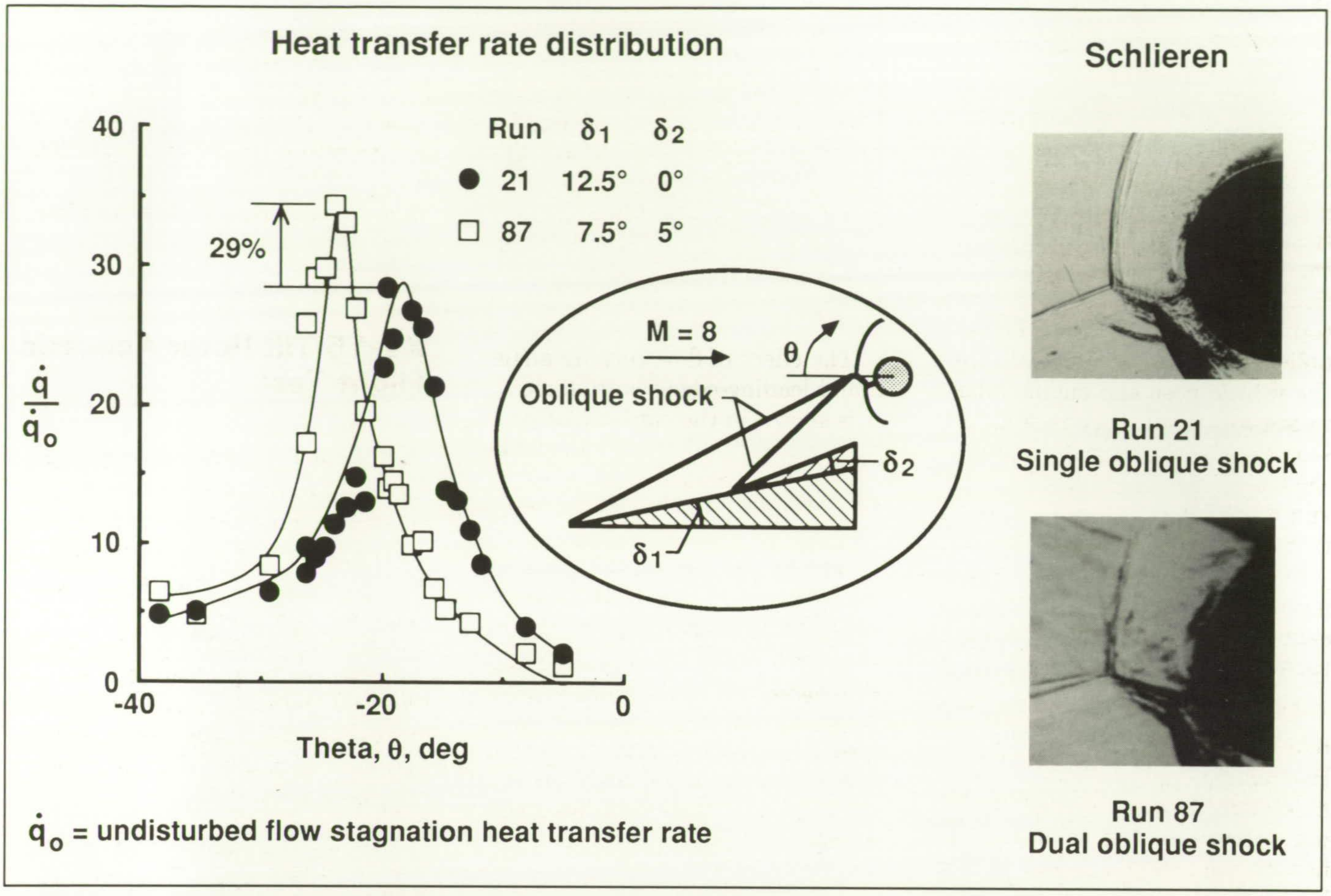

Comparison of interference heating from single and dual oblique shocks.

the peak heat transfer rate amplification above the undisturbed (no oblique shock wave) stagnation heat transfer rate; and the change from a single oblique shock interaction.

A cooperative experimental study was conducted with the Calspan-University of Buffalo Research Center (CUBRC) in the Calspan 48-Inch HST (Hypersonic Shock Tunnel) using an existing shock interference model. The wedge shock generator was modified to accommodate a second wedge to generate the second oblique shock wave. The Mach 8 free-stream flow was turned through a 7.5° wedge angle and then through a 5° wedge angle to obtain a total turning angle of 12.5°; this total turning angle corresponds to the flow turning angle of the single oblique shock interaction. The wedges and cylinder were positioned to allow the two oblique shock waves to coalesce at their intersection point with the bow shock wave from the cylinder as shown in the center of the figure.

Schlieren photographs of a single and dual shock-shock interaction, which results in supersonic jet interference patterns, are shown on the right of the figure. The local heat transfer rates $\dot{q}$, normalized by the undisturbed stagnation point heat transfer rate $\dot{q}_o$, are plotted as a function of angular position θ from the undisturbed flow stagnation point. The distributions are similar, thus indicating that the supersonic jet interference pattern is essentially unchanged. The location of the peaks differs by approximately 4° because the flow behind the dual shock has a higher pressure than that of the single oblique shock wave. Most importantly, the peak heat transfer rate amplification ratio increases 29 percent from 28 to 36 because of the higher pressure recovery.

(Michael S. Holden, Christopher E. Glass, 41350, and Allan R. Wieting)

Acceptable Levels for Cowl Leading-Edge Loads

Hypersonic airbreathing engine performance is maximized when the oblique shock waves used to compress the external air flow intersect the engine cowl, which creates a shock-on-lip condition. This condition is shown schematically in the top portion of the figure. These oblique shock waves emanate from the vehicle nose and engine inlet ramps and create a supersonic jet shock wave interference pattern that impinges on the leading edge and amplifies the pressure and heat transfer flux. The objective of this parametric study has been to determine the effect of cowl leading-edge sweep and flow deflection angle on the peak heat transfer flux.

The design or reference heat flux to a 1/8-in. radius, unswept cowl leading edge for Mach 16 flight at a dynamic pressure of 2000 lb/ft^2 was determined analytically. The flow turning angle δ is assumed to be 10° for this reference condition. The peak heat fluxes for other flow turning angles were predicted with the EASI (Equilibrium Air Shock Interference) code, which has been calibrated on experimental data at Mach 8 to Mach 16. The effect of leading-edge sweep Λ was determined by assuming that the peak heat flux varies with the $(\cos \Lambda)^{2.2}$ as shown experimentally by Glass.

The effect of flow turning angle δ and leading-edge sweep angle Λ is shown in the carpet plot on the right of the figure. The filled symbol represents the reference heat flux or NASP (National Aero-Space Plane) design condition of 70,000 Btu/ft^2/sec, which is five times the maximum level in the Space Shuttle main engine. For the NASP, the flow deflection angle is expected to be in the 5° to 8° range, which would reduce the reference heat flux up to 25 percent. Sweeping the leading edge 45° would reduce the reference heat flux an additional 45 percent, for a total reduction of 70 percent. The resulting heat flux would then be approximately 28,000 Btu/ft^2/sec, which is still severe but more acceptable. However, sweeping the leading edge will create either a spherical tip or a notch that would still be subjected to the higher heat flux.

(Christopher E. Glass, 41350)

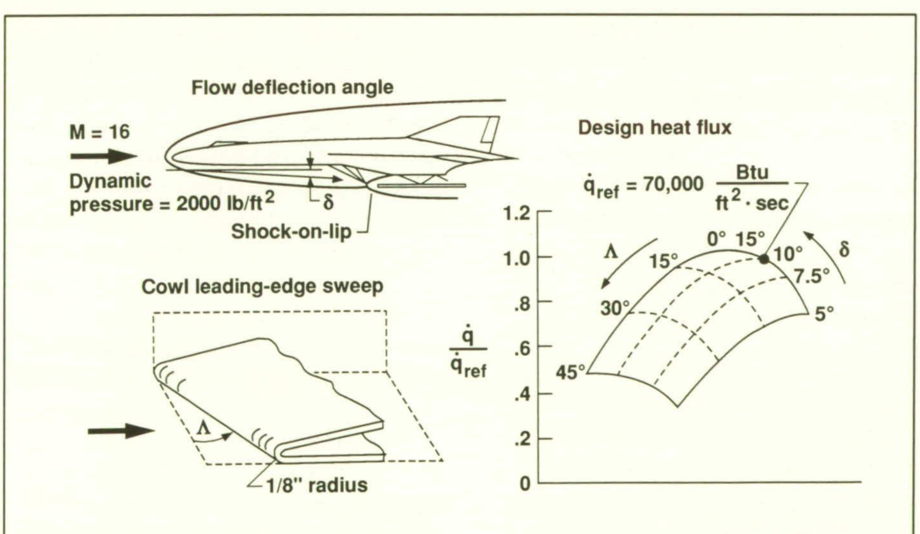

Shock wave interference heating for swept cowl.

XV-15 Tilt Rotor Acoustic Flight Test

The tilt rotor type aircraft has a high potential for use as an inter-city commuter aircraft. One problem that must be addressed and solved is the acoustic impact of such operations on the nearby community. In order to begin to understand the problem and to validate present acoustic prediction programs, a high-confidence-level, accurate data base of a tilt rotor vehicle was needed.

Langley Research Center, jointly with Bell Helicopter Textron, conducted flight noise tests on the XV-15 tilt rotor aircraft. These flight tests were conducted in September 1988. The tests consisted of hovers, level flyovers, ascents, and descents.

The aircraft was repeatedly flown over a 20-element microphone array to provide ensemble-averaged overhead and sideline acoustic measurements. The data discussed herein are preliminary results based on single microphone measurements. For these data, the aircraft was at an altitude 250 ft and approximately 30° above the horizon with respect to the microphone position. A time history and narrowband analysis for the aircraft flying at 130 knots in the airplane mode (nacelle tilt = 0°) was done. The

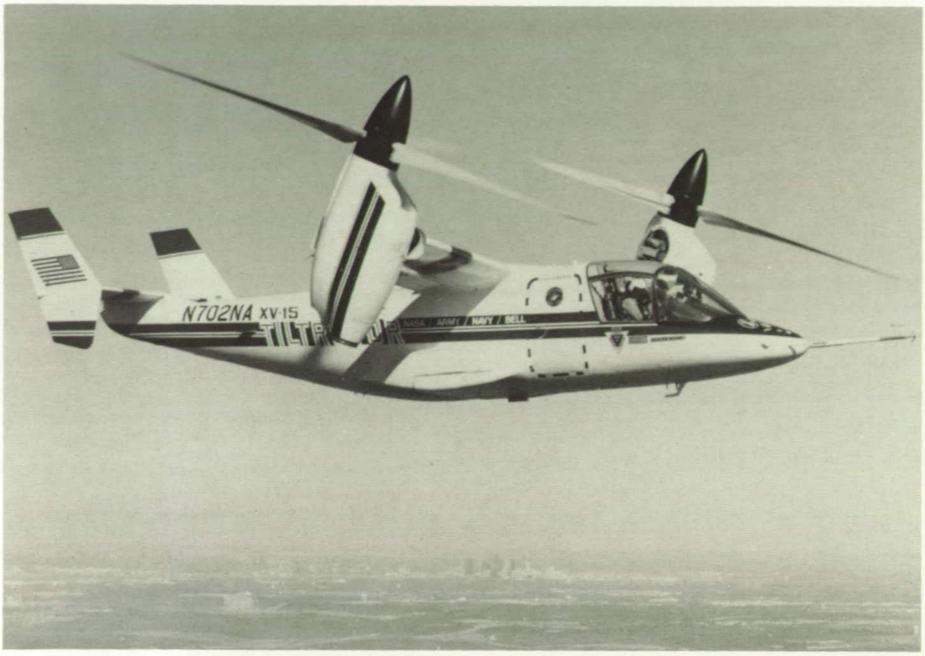

XV-15 tilt rotor in approach configuration. L-88-11,720

time history is typical of a quiet turboprop aircraft. The narrowband spectrum shows only three harmonics and indicates an OASPL (overall sound pressure level) of only 92 dB. Then for comparison, a time history and corresponding narrowband analysis for the aircraft flying in the helicopter (approach) mode (nacelle tilt = 85°) at 90 knots was performed. This time history is typical of a helicopter with indications of an impulsive content in the acoustic signal. The impulsive signal is seen in the narrowband analysis as a strong harmonic content. A scalloped shape is typical of the helicopter blade-vortex interaction (BVI) noise harmonics that usually occur in a frequency range of 900 Hz to 1500 Hz and are present in these data. The richness of harmonic content above 1000 Hz, evident in the approach data, would give rise to higher annoyance in this mode. The OASPL for the approach configuration is 101 dB.

The tilt rotor aircraft is relatively quiet when operating in the airplane mode; however, when operating in the approach mode, the noise level increases significantly due to the impulsive content of the acoustic signal. Because the approach mode is most critical to community acceptance, the high noise levels could present problems at many heliports.
(Otis S. Childress, Jr., 45278 and David A. Conner)

Community Noise Annoyance to Advanced Turboprop Aircraft

Advanced turboprop (ATP) aircraft are expected to have one of three propeller configurations: single-rotating propeller (SRP), counterrotating propellers with an equal number of blades on each rotor (n × n CRP), or counterrotating propellers with an unequal number of blades on each rotor (n × m CRP). The harmonic tonal content of ATP noise occurs at frequencies higher than those generated by conventional propeller aircraft but lower than the frequencies of tones in conventional jet aircraft noise. Each propeller configuration also has unique noise characteristics due to differences in harmonic content and tonal directivity patterns. The ATP aircraft will come into general usage only if their noise meets standards of community acceptability currently applied to conventional aircraft. An experiment has been conducted to compare the annoyance of flyover noise from ATP aircraft having different propeller configurations with the annoyance of conventional turboprop and jet aircraft flyover noise.

The Aircraft Noise Synthesis System was used to generate 40 realistic, time-varying simulations of ATP takeoff noise. Of the 40 noises, 8 represented SRP configurations, 12 represented n × n CRP configurations, and 20 represented n × m CRP configurations. In the experiment, 64 subjects judged the annoyance of the synthesized ATP takeoffs along with recordings of five conventional turboprop takeoffs and five conventional jet takeoffs. Each of the noises was presented at three sound pressure levels to the subjects in an anechoic listening room.

Analyses of the judgments examined the effects on annoyance of blade passage frequency, tone-to-broadband noise ratio, propeller configuration, and aircraft type. For example, the figure compares the annoyance responses to ATP aircraft with different propeller configurations and the annoyance responses to conventional turboprop

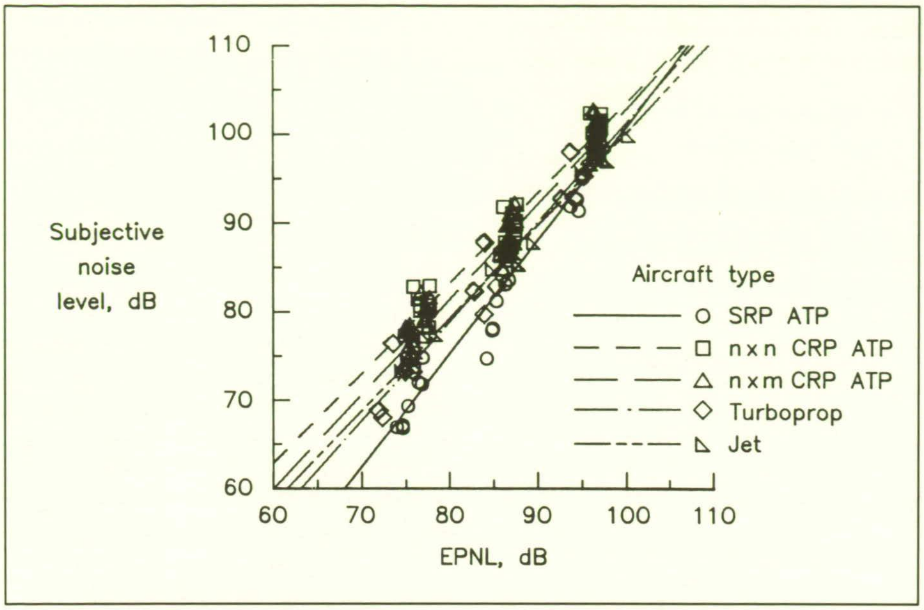

Comparison of annoyance responses using effective perceived noise level (EPNL).

and jet aircraft. Although there appear to be small differences among each of the five aircraft types, regression analyses indicated that no statistically significant differences exist in annoyance response between the CRP advanced turboprops and the conventional turboprops and jets. The SRP advanced turboprops were found to be slightly less annoying than the other aircraft types. The annoyance prediction ability of current noise measurement and correction procedures was also examined. The addition of duration corrections and corrections for tones above 500 Hz to the noise measurement procedures improved prediction ability.

(David A. McCurdy, 43596)

Minimization of Controller Energy by Structural Optimization

Performance requirements for future spacecraft necessitate the use of active controls to augment vibration damping. Unlike conventional system design, active structure design allows the freedom to change both the controller and the structure. The objective of this research is to develop physical insight into the structural optimization process which will maximize the system efficiency.

An interdisciplinary design was conducted by embedding structural weighting matrices into a conventional multivariable control synthesis method known as Linear

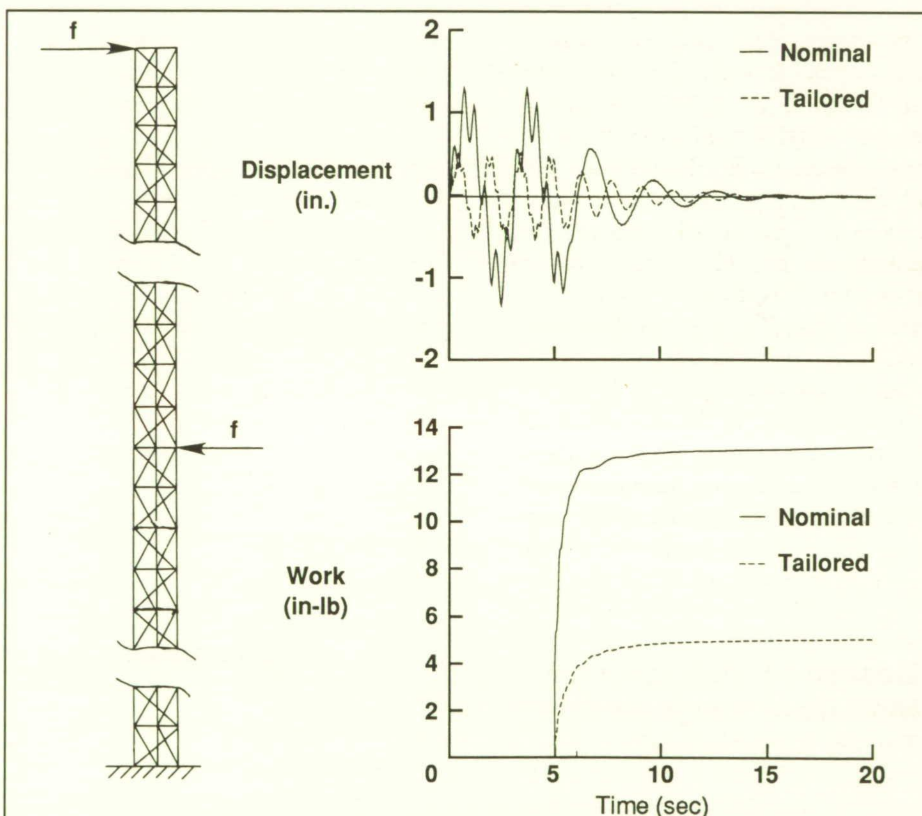

Closed-loop truss-beam response (top) and actuator work used for vibration suppression (bottom).

Quadratic Regulator (LQR) design. Embedding of the structural matrices into the LQR control design enabled the closed-loop cost function to be expressed analytically in terms of only structural quantities and two scalar gains. The closed-form solution provided substantial physical insight into the optimal tailoring objective. For minimization of the structures kinetic and potential energy and the work of the controller, the appropriate tailoring objective is to maximize a quantity related to the structural vibration frequencies cubed.

The figure shows a 54-bay truss beam excited by unit impulse forces. A seven-mode controller was designed for the nominal structure and for an optimized design that maximized the previously mentioned objective while maintaining the same weight as the original design. The closed-loop performance of both designs met the performance requirement of attenuating the vibration amplitude to a threshold level within 10 sec after the controller was activated. However, the optimized design consumed 56 percent less energy than the nominal design. The physical insight provided by the closed-form solution enabled an optimization objective to be derived which is simple enough to be applied early in the design process of future spacecraft.
(W. Keith Belvin, 44319)

Design of Hybrid-Scale Models of Large Space Truss Structures

Verification of structural dynamic properties for large spacecraft, such as Space Station *Freedom*, represents a significant research challenge. Ground tests of such spacecraft are limited due to their large size and the effects of gravity. Furthermore, flight tests are difficult and costly. Thus, verification is limited to component and subassembly tests, with analytically synthesized results used to predict the fully mated vehicle performance. The use of dynamically scaled models offers an attractive possibility to alleviate these limitations.

An approach for designing hybrid-scale models of large space truss structures has been developed by Langley Research Center under a combined in-house and contractual effort. This approach provides a scale model design using realistically scaled hardware with a size suitable for ground testing in existing test facilities. This approach employs classical distorted scaling techniques (used extensively in wind tunnels) to accomplish different scale factors for the truss structure components, appendages, and payloads. Using this technique, a hybrid-scale model of Space Station *Freedom* has been developed under contract by Lockheed Missiles and Space Company.

The model has the overall size of a 1/10-scale model, but has the dynamic characteristics of a conventional 1/5-scale model (upper portion of figure). Detailed studies have shown that hybrid scaling laws can be applied to all components of the *Freedom* Station, and analyses have validated these laws by comparisons with full-scale predictions (as shown in the lower portion of the figure). Based on current designs of Space Station *Freedom*, this model has planform dimensions of approximately 30 ft by 50 ft, weighs approximately 4000 lb, and has a fundamental vibration frequency of 1 Hz. Assembly and ground testing of this model in various configurations will occur in a large high-bay test facility at Langley Research Center.
(Paul E. McGowan, 44350)

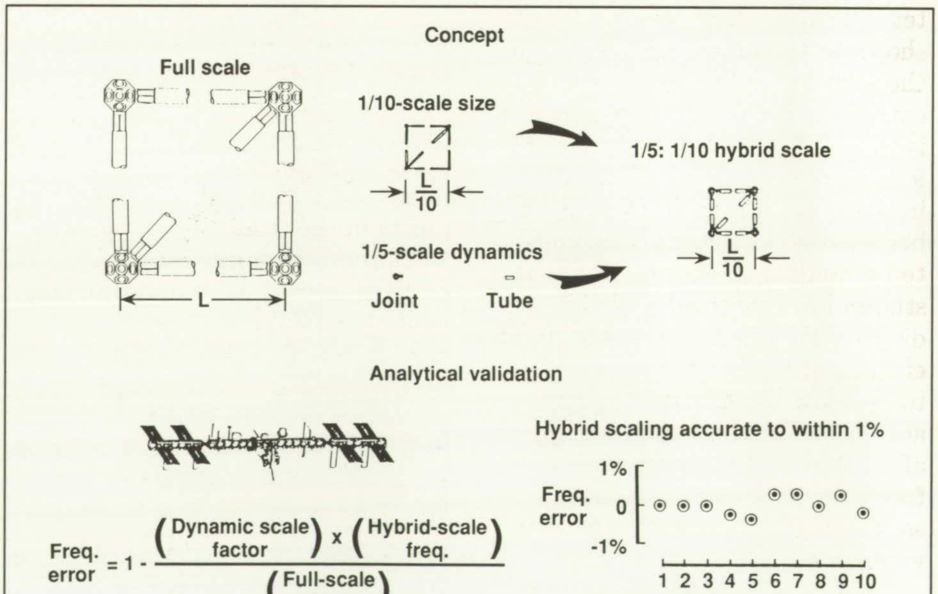

$$\text{Freq. error} = 1 - \frac{\left(\text{Dynamic scale factor}\right) \times \left(\text{Hybrid-scale freq.}\right)}{\left(\text{Full-scale freq.}\right)}$$

Hybrid scaling concept and analytical validation.

Development of Member Exchange Procedure for Improving Surface Accuracy in Truss Reflector Structures

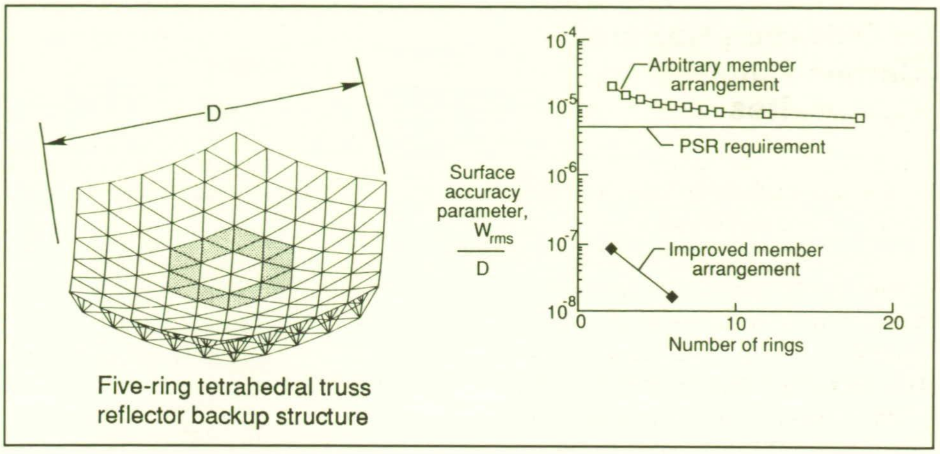

Member exchange procedure applied to two- and five-ring tetrahedral truss reflector structures.

Many current and future space missions have requirements for large electromagnetic reflectors for applications ranging from communications antennas to advanced, space-based telescopes. The diameters for these reflectors range from 10 m to more than 50 m. One of the major requirements in designing reflectors of this type is that the surface must be highly accurate. Communication antennas might have surface accuracy requirements in the 10-mil range, but astronomical instruments capable of detecting infrared wavelengths would have surface accuracy requirements of less than 1 mil.

One candidate for the reflector backup structure, especially for larger diameter reflectors, is a truss structure. Shown in the left-hand side of the figure is a five-ring tetrahedral truss in which a ring is shown as the highlighted region on the surface. For trusses, a major contributor to the surface distortion is the manufacturing error in the lengths of the individual members in the truss. Errors in these member lengths are generally assumed to be random in nature. Previous studies have assumed probability distributions for the member length errors and used statistical methods to estimate the effects on surface accuracy. These studies have generally found that the achievable surface accuracy is of the same order as the length accuracy of the individual members.

A study conducted at Langley Research Center and Virginia Polytechnic Institute and State University has taken a different approach to the problem. First, it is possible to accurately measure the length errors in each of the members in a truss reflector. Then, it is possible to analytically predict, for a particular arrangement of members, the surface distortions for the truss. The next obvious question is, "Which arrangement of members produces the most accurate surface?"

An analytical, optimization procedure has been developed to answer this question. The procedure involves the trial-and-error evaluation of the surface distortion for many different member arrangements in the truss. This approach would be very computationally costly if carried out using standard analysis methods. To reduce this cost, a technique has been developed using an influence-coefficient for the effect of each member on the distortion at each top surface, truss joint. Then the total distortion at a surface joint due to all members is just the sum of the influence-coefficients. This technique reduces the cost of an evaluation from thousands of arithmetic operations to a few dozen. Typically, thousands of these evaluations are required to produce a new, optimum arrangement of members.

The technique has been applied to several example trusses of the type shown in the figure. The plot shows three sets of surface accuracy data as a function of number of rings in the reflector. With an arbitrary arrangement of members, the surface accuracy of the reflector fails to meet a requirement of the ongoing Precision Segmented Reflector (PSR) study at Langley Research Center. For the two- and five-ring cases, the member exchange procedure is able to improve the surface accuracy by approximately two orders of magnitude and easily meet the PSR requirement. This procedure makes it possible to substantially improve the performance of a reflector with a given set of members or, alternatively, to accept larger member length errors from a cheaper manufacturing process and still achieve the surface accuracy requirement.

(W. H. Greene, 43122)

Performance Evaluations of Oxidation-Resistant Carbon-Carbon Composites

Carbon-carbon composites have attractive high-temperature structural properties and are, therefore, being considered for use as hot structural materials for advanced hypersonic vehicle airframes; unfortunately, if unprotected, these composites are subject to rapid oxidation. One goal of current research is to develop improved, more oxidation-resistant carbon-carbon (ORCC) composites. An important first step, described herein, is to identify those material parameters having a significant effect on the performance life of ORCC composites in representative vehicle mission environments. The approach employed consisted of evaluating the oxidation performance of numerous state-of-the-art ORCC materials protected with silicon-based coatings in the multiparameter environmental simulators of the Materials Division. Time-varying conditions of temperature and pressure (representative of those that might be experienced on an advanced aerospace vehicle designed to operate in both cruise and orbital modes) are depicted in the first figure. A repeated sequence of these profiles, mixed with intermittent humidity exposures, was performed until the specimens lost 75 g/m^2. Results of these oxidation tests are depicted in the second figure for materials obtained from LTV Aerospace and Defense Company, Science Applications International Corporation (SAIC), HITCO Fabricated Composites Division, and Chromalloy Research and Technology Division (CRT) of Chromalloy American Corporation.

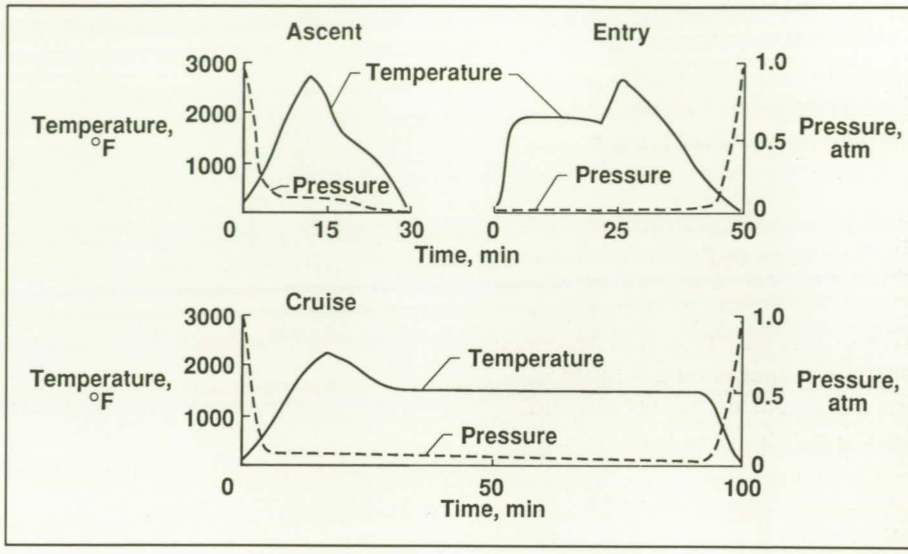

Mission simulation test environment.

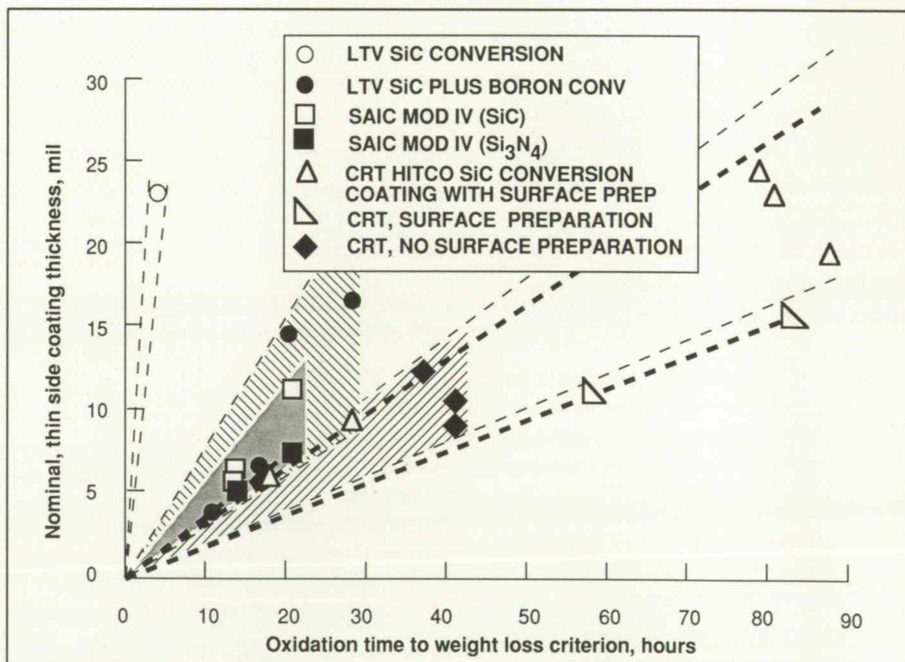

Comparative performance of coated carbon-carbon.

The predominant failure mode observed for most specimens was coating separation. Another major finding is that boron in some concentration is essential for good coating performance. Also, there is no significant difference in performance between silicon nitride- and silicon carbide-based coatings produced by chemical vapor deposition. Overcoat glazes can have a positive beneficial effect, and substrate surface preparation is important for good coating adherence and, hence, increased longevity. These data suggest fruitful directions to be taken to develop improved forms of ORCC composites.
(D. M. Barrett, 43505)

Systems Engineering and Operations Directorate

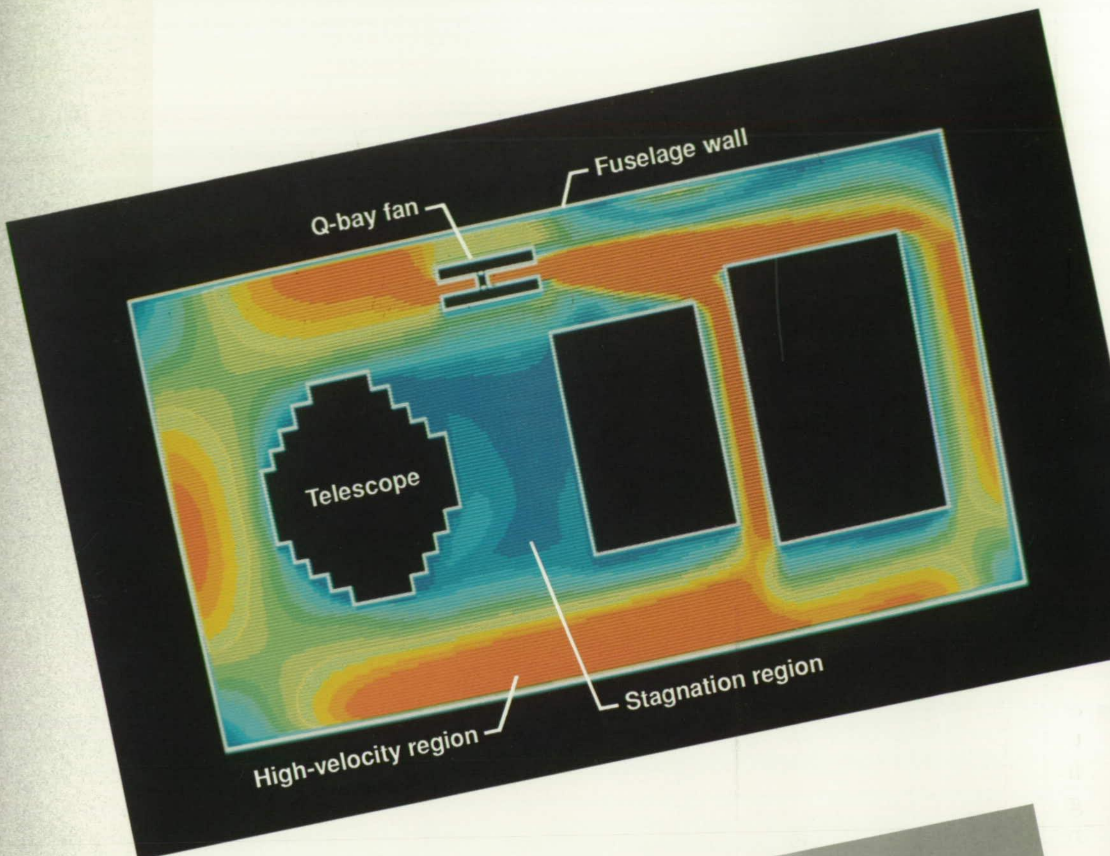

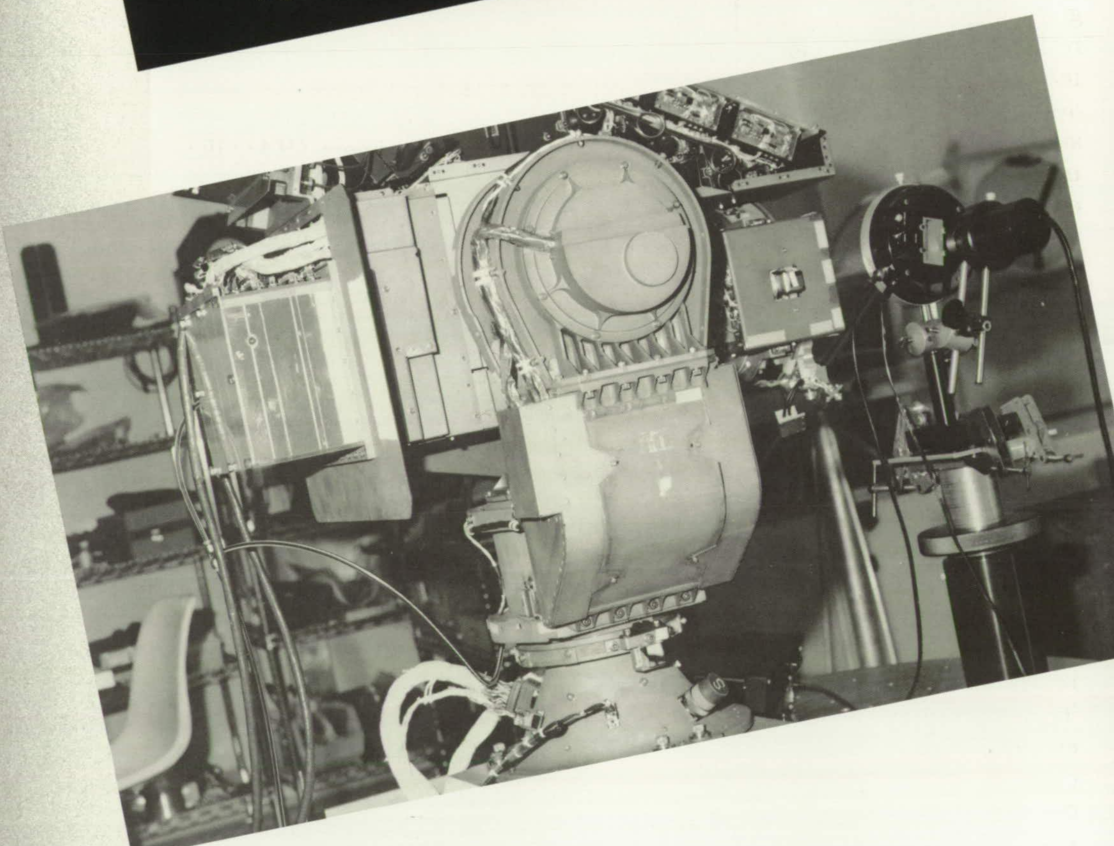

The function of the Systems Engineering and Operations Directorate is to support ongoing aeronautical and space research at Langley Research Center. This work force is divided into five divisions with specific support functions. The Systems Engineering Division is responsible for structural, mechanical, thermal, electrical, and aeronautical systems engineering functions required to provide flight hardware and research models for aerospace research applications and technology. The Facilities Engineering Division is responsible for engineering and design of aerospace research and development equipment and institutional facilities for aeronautical and space research, such as special handling equipment, model supports, and special test equipment. The Fabrication Division is responsible for developing and fabricating aeronautical and aerospace research hardware related to ground support equipment as well as research facilities test equipment. This division provides developmental manufacturing technology and electronics technical support, including communications systems and instrumental hardware. The Operations Support Division is responsible for providing the technical, mechanical, electrical, and maintenance services for research and institutional facilities. This division operates laboratory equipment and wind tunnels and collects, records, and interprets test data. The Systems Safety, Quality, and Reliability Division has overall responsibility to ensure the safety of operation of all aerospace and ground facilities as well as to ensure that the aerospace hardware and the ground research equipment meet all quality and reliability standards. This division also manages the environmental health program for the Center and inspects the construction of major modifications to the many unique research facilities. In addition to the five divisions, the Facilities Program Development Office is responsible to the directorate.

The Systems Engineering and Operations Directorate made significant contributions to numerous space, aeronautical, and facility programs during the past year. Major accomplishments in support of the space program included a Gas Response Test conducted to verify the performance of the Halogen Occultation Experiment (HALOE) instrument. This test required the design and development of an extensive facility. Additional support to HALOE included the development of a manifold system to ensure a vacuum over the lifetime of the photovoltaic detectors, the development of a technique to measure optical microcontamination, and the vibration testing of the HALOE instrument.

In support of the Center's aeronautical programs, a Lear 28/29 aircraft was equipped with an instrumented wing glove to study wave instabilities and disturbances in the transition from laminar to turbulent flow. In addition, an Integrated Helmet and Display Sighting System (IHADSS) developed by Honeywell was installed on the Langley Research Center Boeing 737 aircraft to assess the feasibility of performing safe and accurate manual approaches and landings under visual meteorological conditions (VMC) for possible application to future aircraft without cockpit windows or acceptable forward vision during the landing sequence. Extensive studies were conducted in support of the National Aero-Space Plane (NASP) Program including seal development and the fabrication of lightweight high-temperature sandwich panels. Also, approximately 95 wind tunnel and free-flight models were designed and fabricated. In addition, the operation and maintenance for the Center's research facilities were provided by the directorate. In support of the 8-Foot High-Temperature Tunnel, the transpiration-cooled Mach 7 nozzle was tested to determine the cooling flow capabilities and to validate analytical flow predictions.

Because of the unique requirements of some of the aerospace research performed at the Center, both engineers and technicians are involved in applied research in solving engineering and fabrication problems. These problems relate to the support hardware and software necessary to provide the experimental systems requested by research. The following contributions represent typical engineering fabrication research and technology development highlights in the Systems Engineering and Operations Directorate.

Lear 28/29 Natural Laminar Flow (NLF) Wing Glove Structural Testing

A Langley Research Center Lear 28/29 aircraft was equipped with an instrumented wing glove to study wave instabilities and disturbances in the transition from laminar to turbulent flow. Previous studies used hot-film sensors and pressure belts mounted directly to the wing surface. However, a linear spanwise distribution of sensors was not possible because upstream sensors would influence the transition region downstream. Measurements of streamwise disturbance growth patterns were accomplished with an 0.25-in.-thick foam core and fiberglass-faced glove. This glove was bonded directly to a 6-ft-wide portion of the wing surface. Hot-film and temperature sensors were flush-mounted on the glove surface, and wires and tubing were routed through the internal foam core to specific attachment junctions. Structural integrity of the sandwich construction and surface warpage in the vicinity of pressure tubing due to thermal effects were areas of primary concern.

Test panels were constructed in a manner identical to the proposed glove construction. Testing was in accordance with the following specifications: ASTM C393, "Flexure Test of Flat Sandwich Construction;" ASTM C297, "Tension Test of Flat Sandwich Constructions in Flatwise Plan;" ASTM D1876, "Peel Resistance of Adhesives (T-Peel Test);" ASTM C203-85, "Breaking Load and Flexural Properties of Block-Type Thermal Insulation;" and ASTM D790-86, "Flexural Properties of Unreinforced and Reinforced Plastics and Electrical Insulating Materials."

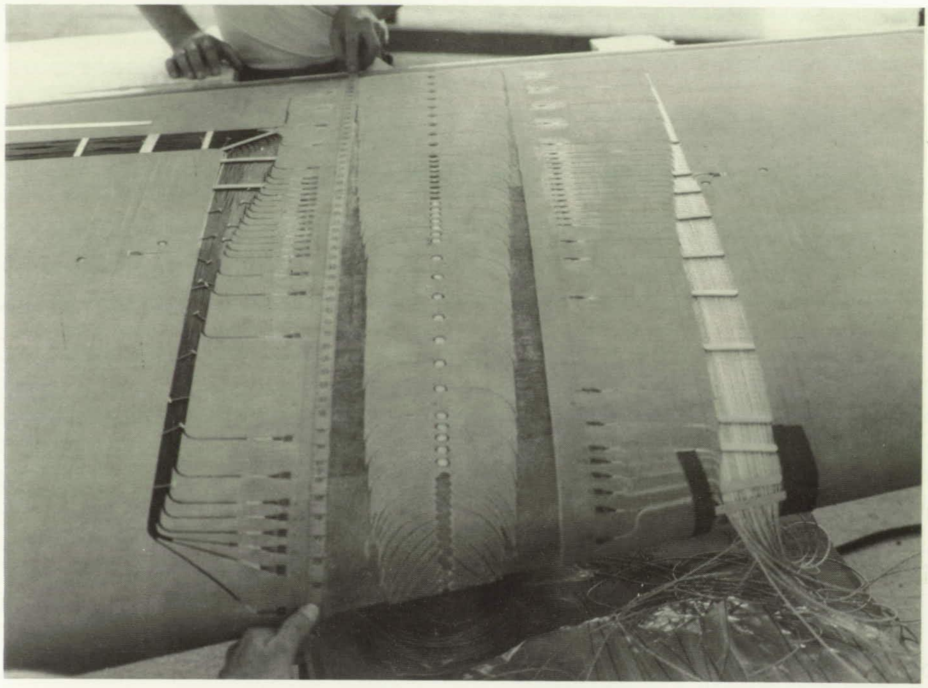

Instrumented wing glove.

Test results verified that the glove could withstand expected flight loading conditions and wing design bending loads and deflections. Additionally, thermal expansions and contractions of the multilayer assembly and internal tubing and wiring would not increase surface waviness beyond the 0.002-in. per 2-in. length specified design criteria.

The first flight of the aircraft was in February 1989, and more than 20 flights have been successfully completed. The glove has remained structurally sound with no apparent surface warpage or joint debonding. **(Mark Lord, 47119)**

Finite-Element Method for Large-Amplitude, Two-Dimensional Panel Flutter at Hypersonic Speeds

Panel flutter is the self-excited oscillation of a plate in a supersonic or hypersonic flow. Panel flutter differs from wing flutter in that the aerodynamic forces resulting from the flow act only on one side of the panel. In the framework of small deflection (linear) structural theory, a critical value of the dynamic pressure λ_{cr} exists, above which the panel motion becomes unstable and grows exponentially with time, and below which any disturbance to the panel decays. Because of the recent interest in flight vehicles that operate in the hypersonic regime, a finite-element method for determining the large-amplitude limit-cycle

dynamic pressure λ_1 of panels using nonlinear, hypersonic, third-order piston theory aerodynamics has been developed.

In actuality, it is well known that the panel not only bends but also stretches due to large-amplitude vibrations. Such membrane tensile forces in the panel provide a limited stabilizing effect of the "hard spring" type that restrains the panel motion to a bounded amplitude for limit-cycle oscillations with increasing amplitude as the dynamic pressure increases. The external skin of a flight vessel can, thus, withstand velocities beyond linear critical value.

The finite-element equations for panel flutter result in a damped eigenvalue problem in the configuration space; as such, they do not conform to standard eigenvalue solution algorithms. Thus, the proposed approach transforms the eigenvalue problem from the configuration space to a state space resulting in a more standard form of the eigenvalues and eigenvectors. As the dynamic pressure increases monotonically from 0 ($\lambda = 0$ corresponds to *in vacuo* large-amplitude free vibration), the skewed symmetric aerodynamic influence matrix perturbs the symmetric stiffness matrix resulting in two of the eigenvalues approaching each other until they coalesce.

Results for displacement ratios c/h equal to −0.6, 0.0, and +0.6, respectively, are shown in the figure, in which the real part of the eigenvalue approaching positive values for a fixed dynamic pressure determines the critical dynamic pressure. These results were obtained using the third-order-piston theory for the system geometry. The Mach number times aspect ratio Mr and mass μ/M are noted in the figure. Unlike the linear aerodynamic theory finite-element results, the sign of the displacements affects the coalescence of the modes.
(Carl E. Gray, 47236, C. Mei, and C. P. Shore)

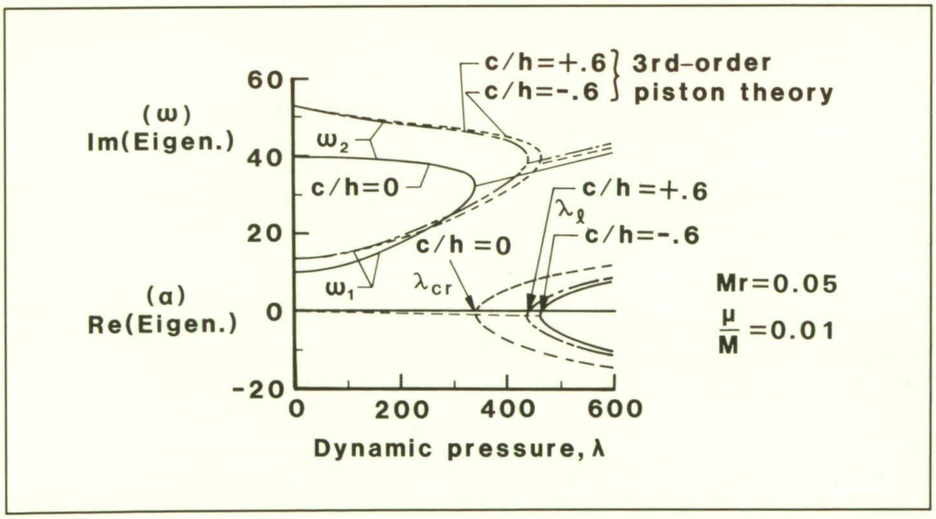

Variation of eigenvalues with nondimensional dynamic pressure.

Monte Carlo Simulation of Reentry Plasmas

A new procedure for the treatment of weakly ionized gases with the Direct Simulation Monte Carlo (DSMC) method has been developed. The current DSMC method accounts for nonequilibrium in the translational and internal modes, dissociation, and ionization. The new procedure takes advantage of ambipolar diffusion concepts to determine the behavior of charged particles in the flow. As the lighter electrons begin to diffuse out of the flow, a charge separation and corresponding electric field are produced. The effect of the electric field is to retard the diffusion of the electrons and enhance the diffusion of the ions. This process is known as ambipolar diffusion. In the new procedure, a cell electric field is calculated by equating the diffusion velocity of the ions with that of the electrons in the cell. The charged particles then are moved under the influence of that electric field. This procedure is a more physical treatment of electron mobility than was available in previous DSMC simulations. In the earlier simulations, charged particles were constrained to move as ion-electron pairs.

The prediction of electron temperature is one of the important parameters that is dependent on the method of modeling charged particles in the flow. The electron temperature is directly related to the level of ionization in highly energetic flows because electron impact ionization is significant. Also, the electron temperature has a large impact on the amount of radiation in the flow. The figure is a comparison of electron temperature through a shock wave in air at 10 km/sec and 0.1 torr for both methods. The

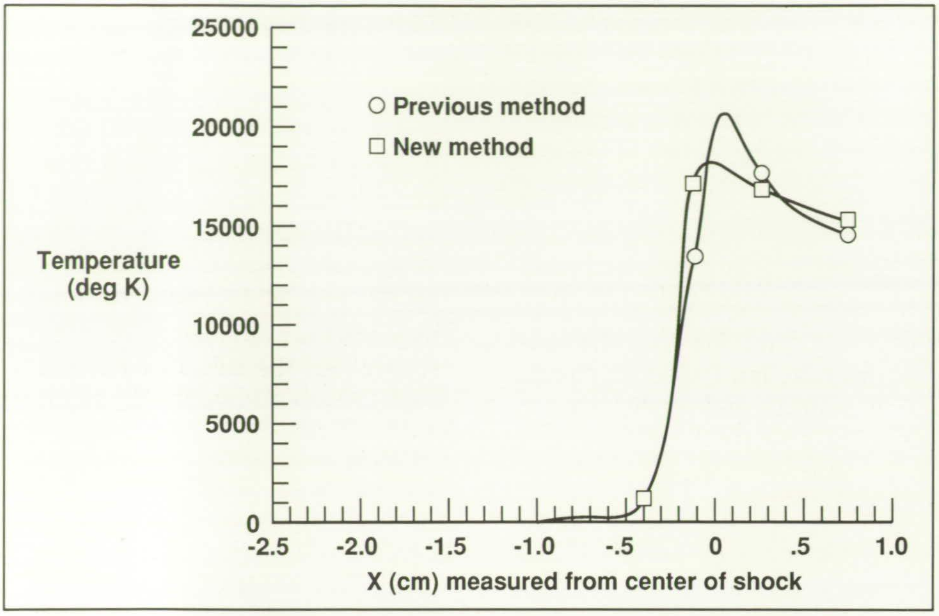

DMSC results for electron temperature through reentry shock wave.

figure shows a significant difference between the new method and the previously employed method results. The new method predicts a lower peak temperature and more diffusion of high-temperature electrons into the shock. This prediction is consistent with the enhanced electron mobility. The lower temperature results in the prediction of less total ionization and less radiation. **(Ann B. Carlson, 47050)**

Structural Analysis of Thermal Insulation Retainer Assembly

A detailed structural analysis of an insulation retainer, the thermal barrier clamp assembly (TBCA), which holds foam insulation around the fan drive shaft of the National Transonic Facility wind tunnel has been performed to determine the regions of high stress. This insulation retainer assembly consists of two roughly semicircular stainless-steel bands that are placed around the insulation on the shaft and then connected together with the two clamp assemblies at 0° and 180°. Each clamp assembly consists of four stiff stainless-steel bars. Two bars are attached with screws to the fore and aft ends of each stainless-steel band. Seven bolts are used between the bars at each clamp assembly to clamp the bands together.

The most significant loading that the TBCA is subjected to is a centrifugal force due to the rotation of the shaft. As the retainer band deforms under the centrifugal loading (as shown in the figure for a deformed geometry plot), it tries to assume an oval shape. This shape occurs because the concentrated mass at the clamp bars causes large radially outward inertia loads at these locations. The band is constrained from moving inward, however, by the insulation and the shaft, but it is free to move radially outward. Under the centrifugal loading, various regions of the band will be compressed against the insulation while other regions will be pulled away. Accounting for this

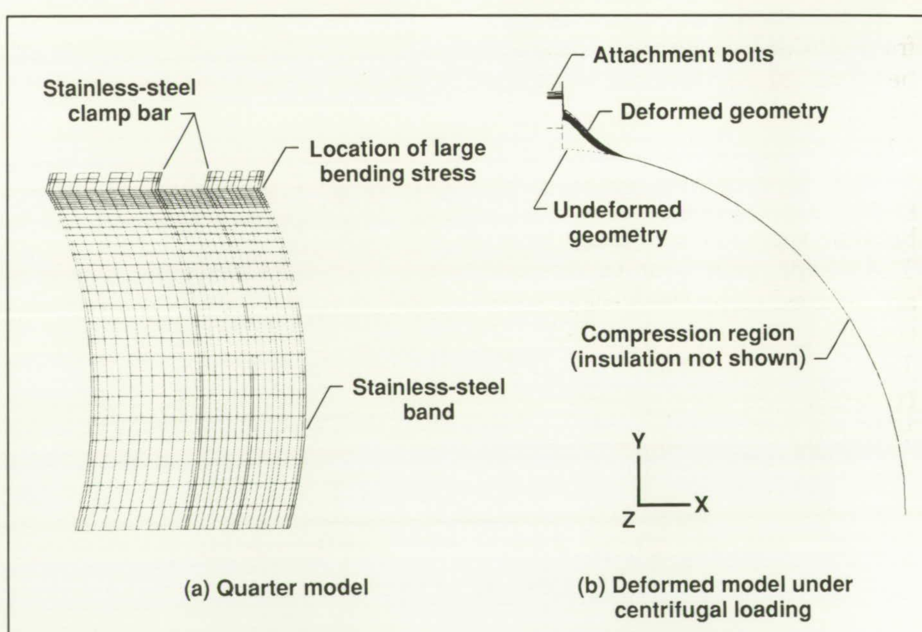

Finite-element model of TBCA.

variable contact region significantly complicates the analysis.

Another complication in the analysis is the mechanism by which the band carries this nonuniform centrifugal load. Because the band is thin, its resistance to the transverse centrifugal load only occurs after it has rotated radially outward. Accurately representing the stiffness of the band and accounting for the changing contact region under load requires a nonlinear finite-element analysis. Accordingly, the geometric nonlinear analysis capability of the Engineering Analysis Language (EAL) finite-element program was used. The EAL handles the deflection-dependent stiffening of the band directly. However, modifications to the geometric nonlinear analysis procedures were required to handle the variable contact. A modification was made to allow the direct inclusion of a nonlinear (piecewise linear) relation between any two degrees of freedom in the model.

From the analysis results and from intuition, it was clear that bending stresses in the band near the clamp bars were high. It was also clear that these stresses were strongly influenced by the detailed geometry and contact pattern between the band and clamp bar. These large cyclic bending stresses are believed to be the mechanism that initiated the failure of the TBCA.

(Carl E. Gray, 47236 and William H. Green)

Fluid Flow Analysis for Convective Thermal Control of Flight Experiments

A method for thermally analyzing convectively cooled flight experiments has been applied to the Lidar Atmospheric Sensing Experiment (LASE). This technique utilizes a fluid flow analysis code to optimize fan-forced air circulation patterns and predict air velocities in thermally critical areas. Predicted air velocities from the fluid analysis were used to calculate forced convection coefficients for the flight experiment. These convection coefficients were used in a finite-difference thermal analysis code to describe the response of the aircraft internal air temperature and heat loss for the experiment during transient flight profiles.

Two-dimensional flow models of the LASE primarily were used to detect areas of stagnation. The figure shows an optimized LASE lower hatch fan flow model with few stagnation regions and excellent circulation. Three-dimensional flow models provided an accurate way to predict air circulation speeds throughout the aircraft equipment bay (Q-bay) and verify the results of the two-dimensional cases. Analysis results indicated that the average air circulation speed along the Q-bay walls was approximately one-half of the originally assumed value. Consequently, additional fans are being considered to improve the air circulation in these areas.

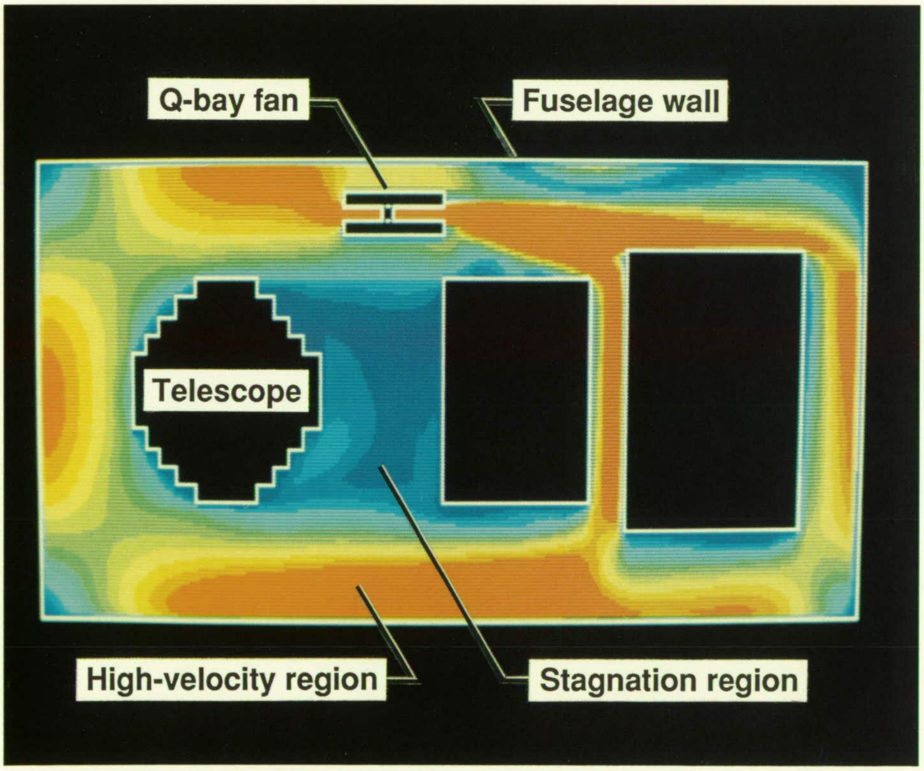

LASE lower hatch fan flow model. L-89-03017

ORIGINAL PAGE
COLOR PHOTOGRAPH

Considering the complexity of convectively cooled experiments, this analysis proved to be an effective modeling technique for predicting component surface temperatures and aircraft internal air temperatures in flight.
(Brian D. Killough, 47047)

Gas Response Test Apparatus for HALOE Instrument Performance Verification

A Gas Response Test apparatus has been designed, fabricated, and implemented to verify the accuracy of prediction models of the Halogen Occultation Experiment (HALOE) multichannel gas filter correlation instrument. The HALOE instrument measures stratospheric trace gases important to the further understanding of the chemical and dynamical interactions of the upper atmosphere. HALOE is one of the Upper Atmosphere Research Satellite (UARS) instruments to be launched into near-Earth orbit from a Space Shuttle in the fall of 1991. HALOE will measure hydrogen fluoride, hydrogen chloride, nitric oxide, and methane by the gas filter correlation technique; nitrogen dioxide, carbon dioxide, water vapor, and ozone are measured by a radiometer.

The apparatus employed to stimulate the HALOE response to these gases is shown in the figure. The temperature of the HALOE instrument, which is situated in the 8- by 15-Foot Thermal-Vacuum Chamber, is maintained at 10°, 20°, or 30°C in a vacuum at less than 10^{-5} torr.

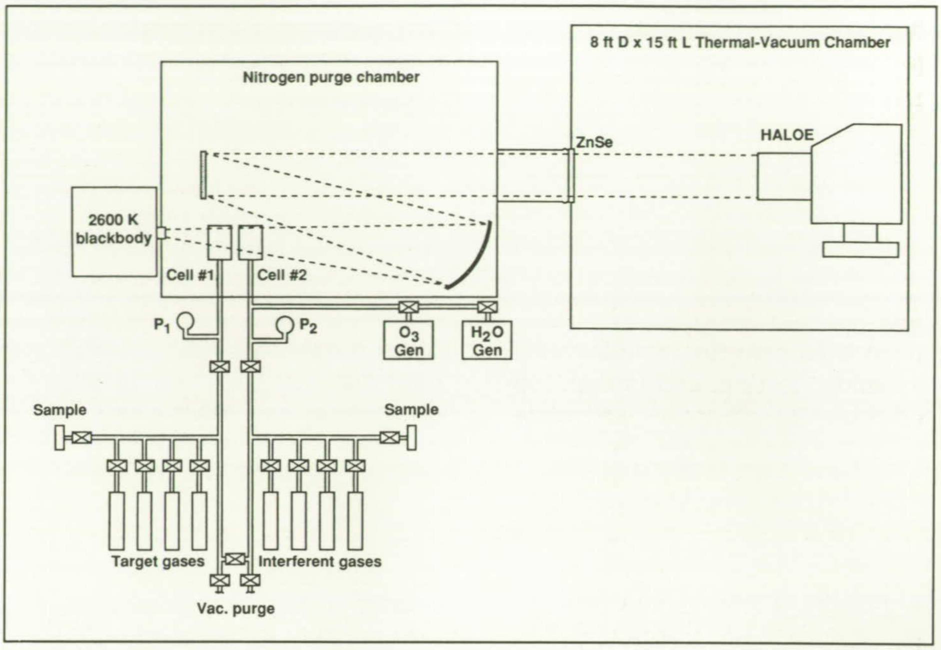

Gas Response Test apparatus.

External to the vacuum chamber is a nitrogen-purged gas response test chamber that communicates to HALOE through an 8-in.-diameter zinc selenide window. The purge chamber contains mirrors that collect and focus radiation from a high-temperature carbon block blackbody source into the 6-in.-diameter HALOE inlet telescope. Gas cells, which are situated in the blackbody radiance beam, can be filled from a gas supply/plumbing system to various subatmospheric pressures at selected mixing ratios. The gas supply bottles contain concentrations of the gases of interest; these gas concentrations are diluted in nitrogen where appropriate. The total pressure established in the gas cells is determined by pressure-monitoring instrumentation.

In operation, the HALOE instrument initially views the blackbody source with the gas cells pumped to hard vacuum. Desired premixed target gases are admitted to the cells to predetermined pressures and monitored by the pressure measuring instrumentation system. The response of HALOE then is recorded. These pressures are reduced in small steps until the gas cells again are completely evacuated. The response of HALOE is recorded at each step. Samples of the gas fill conditions are removed from the plumbing apparatus (in sample takeoff cells) and taken to a scanning Fourier transform interferometer for an independent determination of the fill condition in the target and interferent gas cells. In many cases where the spectral signatures of the gases overlap, different gases are put into each cell, so that the effect of an interfering gas (such as methane) upon the measurement of a target gas (such as hydrogen chloride) can be determined.
(A. G. Beswick, 41624)

Optical Microcontamination Measurement for Space Instruments and Assembly/Test Facilities

Microcontamination of optics and radiators in sophisticated, high-performance infrared optical systems such as the HALOE instrument occurs during manufacture, assembly, testing, and in-flight operation. The effects of particulate contamination are usually negligible, but molecular contamination of condensable volatile materials (CVM's) may exceed allowable limits. Polymerization of molecular films is a particular hazard because it stabilizes and darkens the deposited contaminant that would otherwise gradually evaporate from the surface.

A measurement technique has been developed to measure very small amounts of CVM's on the HALOE instrument, in the HALOE clean room, and in the 8- by 15-Foot Thermal-Vacuum Chamber in which testing of the HALOE instrument took place. Measurements of the residues of cleaning and wash solvents have also been made. The measurement technique is high-resolution-in-transmission spectroscopy using a Fourier transform infrared (FTIR) spectrometer.

One-in.-diameter optical witness plates of low index-of-refraction are placed in the HALOE clean room, and the strong CH_2 absorptions at 2860 and 2920 cm^{-1} are measured reliably to 0.1-percent transmission depths. Similar witness plates were placed on the HALOE instrument and in the 8- by 15-Foot Thermal-Vacuum Chamber during the extensive vacuum and gas response tests of 1989. Residues of solvent washes from the clean room and from the fore and aft shrouds of the 8- by 15-Foot Thermal-Vacuum Chamber were analyzed, as were residues from "clean" wash solvents.

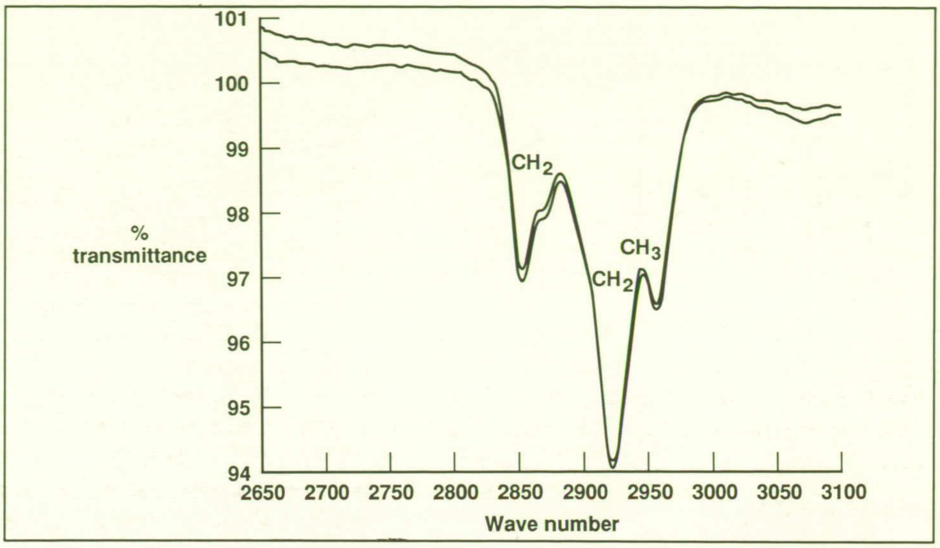

FTIR spectra of 77 K witness plate in 8- by 15-Foot Thermal-Vacuum Chamber.

The FTIR measurements of the HALOE clean room witness plates showed no CVM accumulation and, in particular, no dioctyl phthalate (a suspected CVM) deposition. The witness plates on the HALOE instrument and the 8- by 15-Foot Thermal-Vacuum Chamber witness plates maintained at ambient temperature showed no CVM accumulation. However, the witness plate held against a liquid nitrogen cold surface and the washes of the liquid-nitrogen-cooled shrouds showed very strong (6-percent to 65-percent transmission) absorption depths of CH_2. No evidence of caprolactam, a protective bagging material monomer of concern, was found. The measured residues of 50 mL of "clean" solvents were of the order of 1-percent transmission depths.

(G. A. Harvey, 45640 and J. L. Raper)

Vacuum Manifold System for HALOE Photovoltaic Detectors

The HALOE gas channel photovoltaic detectors contain thermoelectric coolers that require a vacuum for proper operation. In order to ensure a vacuum over the lifetime of the detectors, a manifold system was designed and installed on the HALOE instrument.

Each of the eight detectors is connected to the manifold system with a coiled, annealed copper tube to minimize any induced forces on the detectors. The manifold system provides for connection to the ground support equipment (GSE) vacuum pumps. Two redundant vent valves, which are included in the manifold system design, will open the detectors to the vacuum of space when the instrument is launched into orbit on the Upper Atmosphere Research Satellite (UARS).

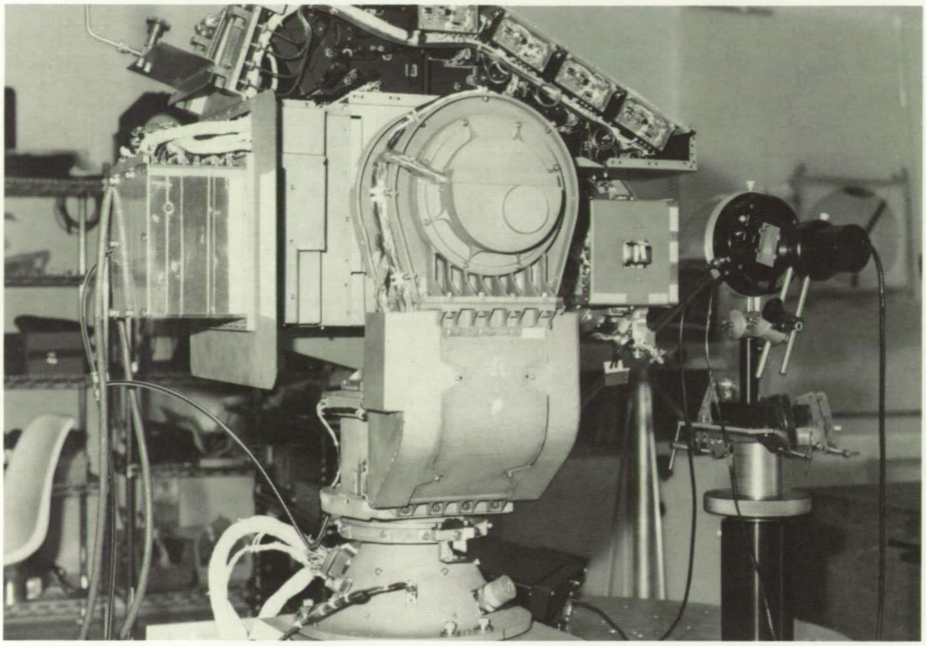

HALOE photovoltaic detector vacuum manifold assembly. L-88-04288

For instrument ground operation, the detector manifold system is evacuated with the GSE HALOE pump station. A small GSE ion pump (2 L/sec) attached to the instrument is used to maintain vacuum after the HALOE pump station is disconnected. The manifold system will be sealed and the small GSE ion pump removed prior to launch by a cold weld pinch-off of the copper-connecting tube between the pump and the manifold.

The manifold system vent valves are spring-loaded devices that use atmospheric pressure to provide the force to seat the O-ring seal. The valves open when the pressure across a piston equalizes during launch and vents the detectors to space vacuum.
(D. E. Williams, 47186)

Vibration Testing of HALOE

Concentrations of eight gases in the upper atmosphere will be measured by the HALOE, which will be flown on the STS (Space Transportation System) in the early 1990's. As part of the required structural validation for STS experiments, vibration tests were conducted to demonstrate good workmanship and obtain vibration characteristics for use in structural analysis. Of particular interest was how the vibration characteristics might change with varying levels of vibration input. These tests were performed in the Langley Engineering Vibration Test Facility.

The modal survey test was conducted by applying separately a random vibration and swept sine environment through an

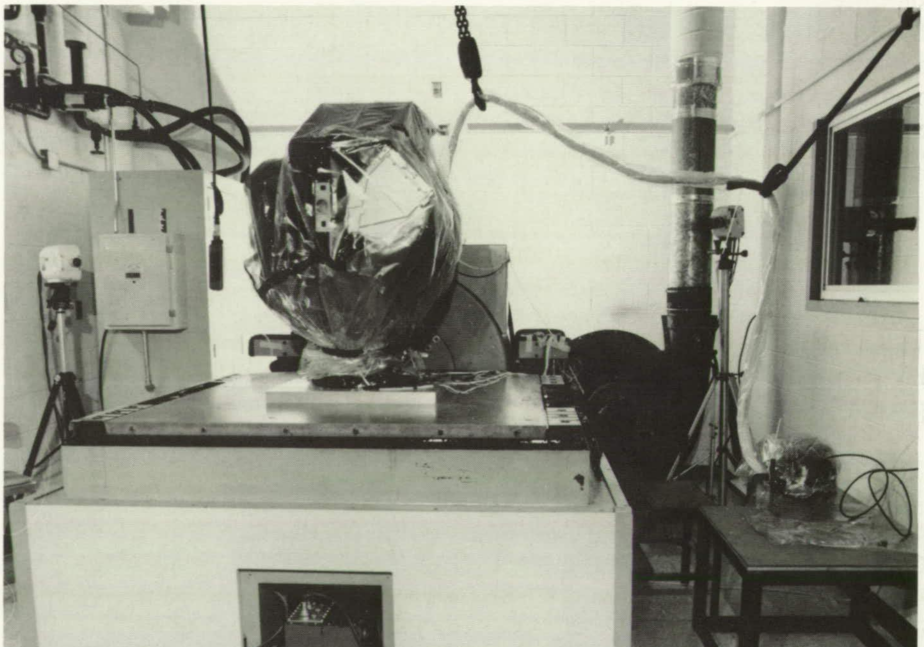

HALOE flight instrument shown on vibration test fixture. L-88-9248

electronically driven shaker to the base of the HALOE in each of three orthogonal axes. Data acquisition consisted of measuring and recording the vibration input as well as the output response at 27 locations on the HALOE. Natural frequencies, damping factors, and shapes were obtained for all HALOE structural modes below 50 Hz. Narrowband random vibrations at several levels of power were used as input to obtain information on the variation of the HALOE dynamic characteristics with increases of vibration input. Swept sine vibrations of constant amplitude were also used to confirm the results of the random input test. These sine tests were repeated with increased amplitude to study the nonlinear vibration response. An analytical model based on these test data has been used to generate loads for structural assessment.

The HALOE instrument is shown on the Unholtz-Dickie T-1000 electromagnetic shaker. A contamination protective bag covers the instrument to maintain cleanliness during vibration testing. **(Thomas C. Jones, 47037)**

Treatment of Titanium Honeycomb Core Prior to Electroplating

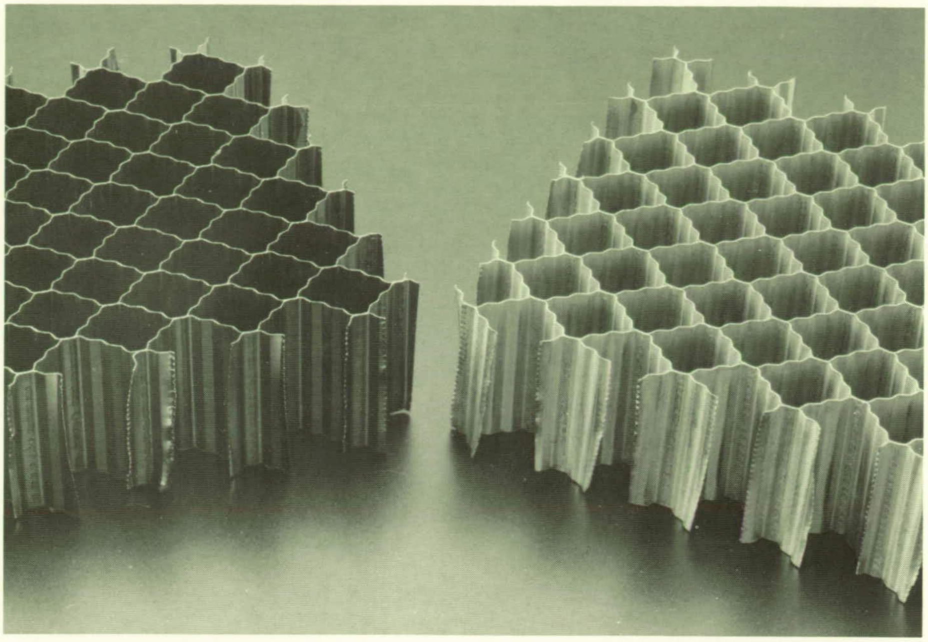

Titanium honeycomb core (left) and copper-plated post-treated (right) samples.
L-89-6866

A requirement of the National Aero-Space Plane (NASP) Program has been to fabricate lightweight high-temperature titanium aluminide honeycomb core (HC) sandwich panels that have specific properties at elevated temperatures as well as joining characteristics that will enable the panels to be efficient structural components. A joining process called enhanced diffusion bonding, which relies on a combination of brazing and solid-state diffusion to promote bonding, has been employed to develop the titanium aluminide honeycomb core sandwich panels.

To enable the successful joining of these sandwich panels, a solution of sodium bichromate and hydrofluoric acid in conjunction with reverse electrical current has been used to apply a conversion coating on the titanium honeycomb core and to keep it active and receptive to electroplating. Electroplated metals such as nickel, nickel tungsten, nickel cobalt, acid copper, alkaline copper, and silver have been applied in thicknesses of 0.000050 in. to 0.005 in. with good bonding and adhesion characteristics. By using selective masking techniques, these metals can be applied in the desired areas. The figure shows one sample that has been plated with acid copper on the edges and one piece of HC that was not plated.

The solution of sodium bichromate and hydrofluoric acid can treat other titanium alloys such as Ti-14Al-21Nb, Ti-3Al-2.5V, and Ti-15V-3Al-3Cr-3Sn, while having the same bonding characteristics as the titanium aluminide.
(Michael L. Kelley, 44535)

Correlation of Measured and Predicted Flow Rates and Pressure for Mach 7 Transpiration-Cooled Nozzle

For the transpiration-cooled Mach 7 nozzle used in the 8-Foot High-Temperature Tunnel (8-Foot HTT), a flow test was conducted for three components: the converging section, the nozzle, and the spool

piece. The objective of these experiments was to determine the cooling flow capabilities of these components. Test results were used to validate analytical flow predictions for the Mach 7 nozzle arrangements of complex flow passages.

The Mach 7 nozzle is composed of 6,800 platelets ranging in thickness from 0.006 in. to 0.06 in.; each platelet is fusion bonded together to form the nozzle. A typical platelet is shown in the figure. The platelets have complex flow-metering passages that allow very precise distribution of coolant. Throughout the nozzle, these flow passages vary in both flow area and length and make it a challenge to precisely calculate flow rates through the platelets. The analysis methodology consisted of solving the one-dimensional, adiabatic, steady-flow representation of the energy equation. In order to accurately calculate the flow rates, irreversible energy losses due to frictional and geometrical effects needed to be considered. When assessing the frictional effects, it is standard practice to calculate the Reynolds number using the hydraulic diameter D_h equal to $4A/p$, where A and p are the flow cross-sectional area and wetted perimeter, respectively. For flow in a duct for nonstandard cross sections, one should replace D_h by D_{eff}. The term D_{eff} is defined as the product of δ times D_h where δ is a geometric correction factor determined from laminar-flow calculation (also applicable for turbulent flow) for the particular geometry of the duct. When performing calculations for a rectangular flow duct, an uncorrected value of D_h can be as much as 23 percent greater than corrected values, which results in underpredicting the friction factors.

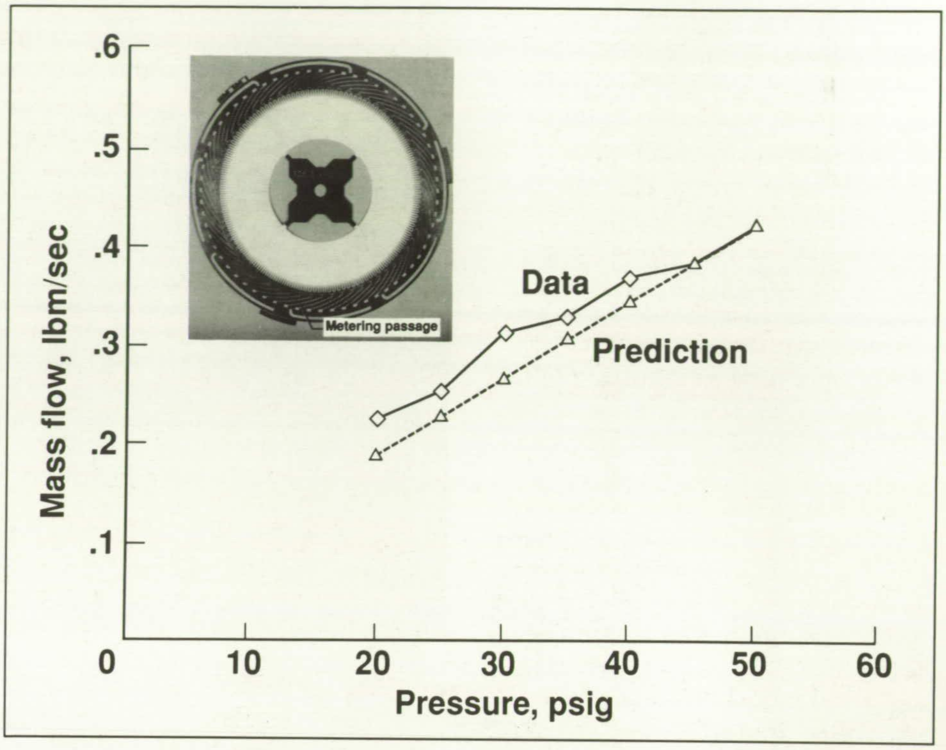

8-Foot HTT transpiration-cooled nozzle flow prediction and measurement comparison.

Also shown in the figure is a comparison of analytical and measured results for flow rates versus pressure for a section of 160 platelets near the throat region. Thus, using the geometric correction factor provides analytical results that are in good agreement with measured data. The analysis was instrumental in locating nozzle manufacturing defects. The initial flow rate measurements for a portion of the converging section were one-half the predicted rates indicating the possibility of defects in the nozzle. This defect was determined to be improper surface etching. The converging section was re-etched resulting in nozzle transpiration flow rates that were in better agreement with analysis. **(Carlos R. Miro, 47249 and James W. Mayhew)**

Improvements in Casting Procedures for Stycast

With the increased worldwide interest in hypersonic flight over the past few years, Langley Research Center has been performing an intense study of heat transfer and heat concentrations on hypersonic aircraft. Many of the wind tunnel models used to complete such studies are fabricated at Langley using an epoxy casting resin system (Stycast) capable of withstanding 500°F for extended periods and 1000°F for brief periods. Stycast basically is formulated for an electrical insulating material and is not intended for model fabrication. The casting process has been plagued for years with problems, such as gas voids, shrink distribution, and voids caused by unknown phenomena.

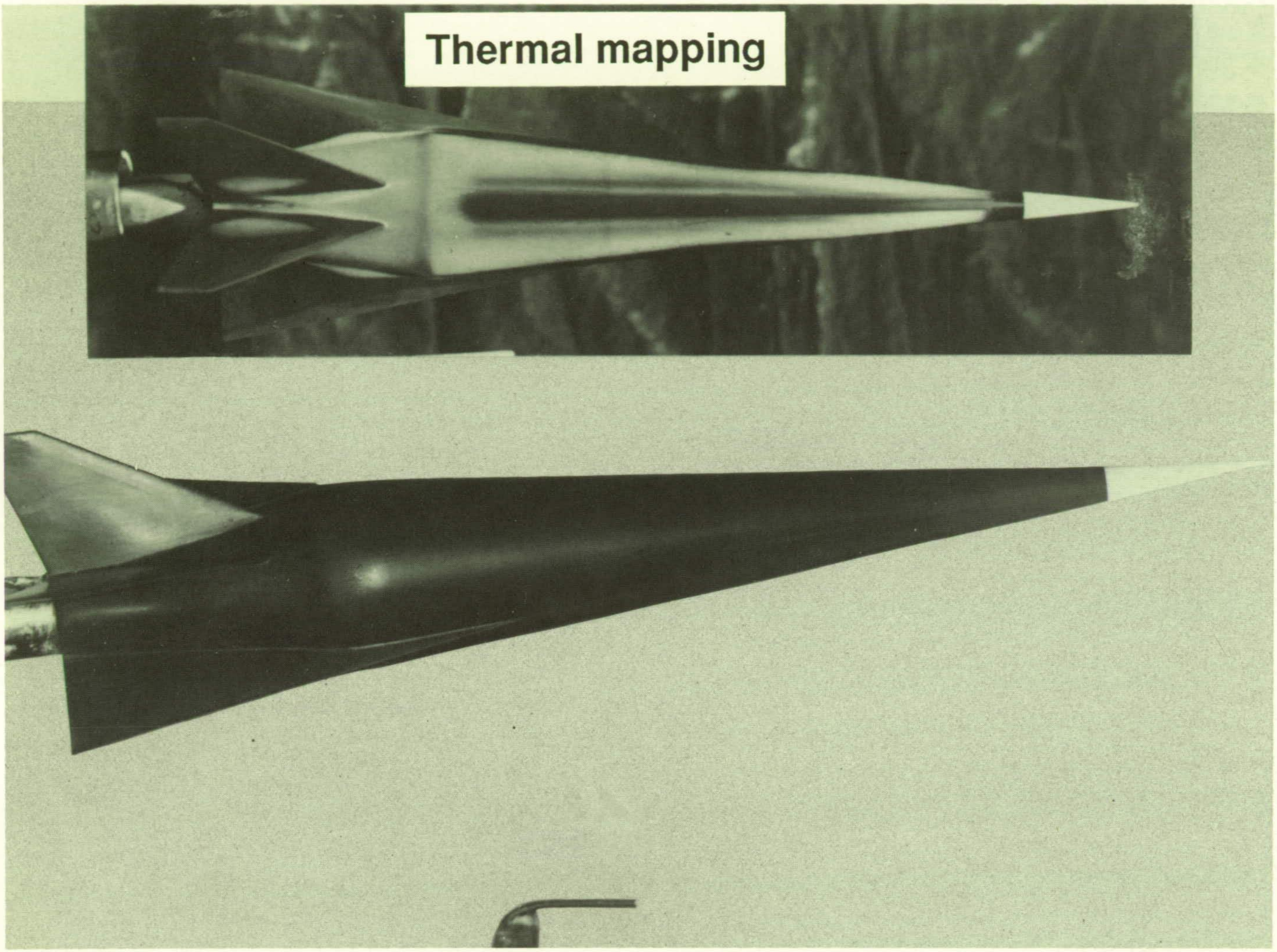

L-88-6497

Aerodynamic/aerothermodynamics National Aero-Space Plane Technology Maturation Plan 3.1.2 accelerator concept (Mach Number = 6, in air; Reynolds number = 7 × 10^6/ft; wing cone = 6 °; and angle of attack = 10 °).

A recent effort in the development of new casting procedures has spawned the ability to pour near-perfect castings. Specifically, research was done experimenting with combinations of resin vacuums, pouring temperatures, and pressure injection. This development enables model-making technicians to mold more complex shapes such as super-thin-wing and tail cross sections. In addition, the quality of castings eliminates costly repair and cleanup procedures. Major advancements in this area have made it possible to meet the influx of requests for such models.

(Robert C. Evans, 45480 and Glenn D. Ormsby)

Technology Utilization Program

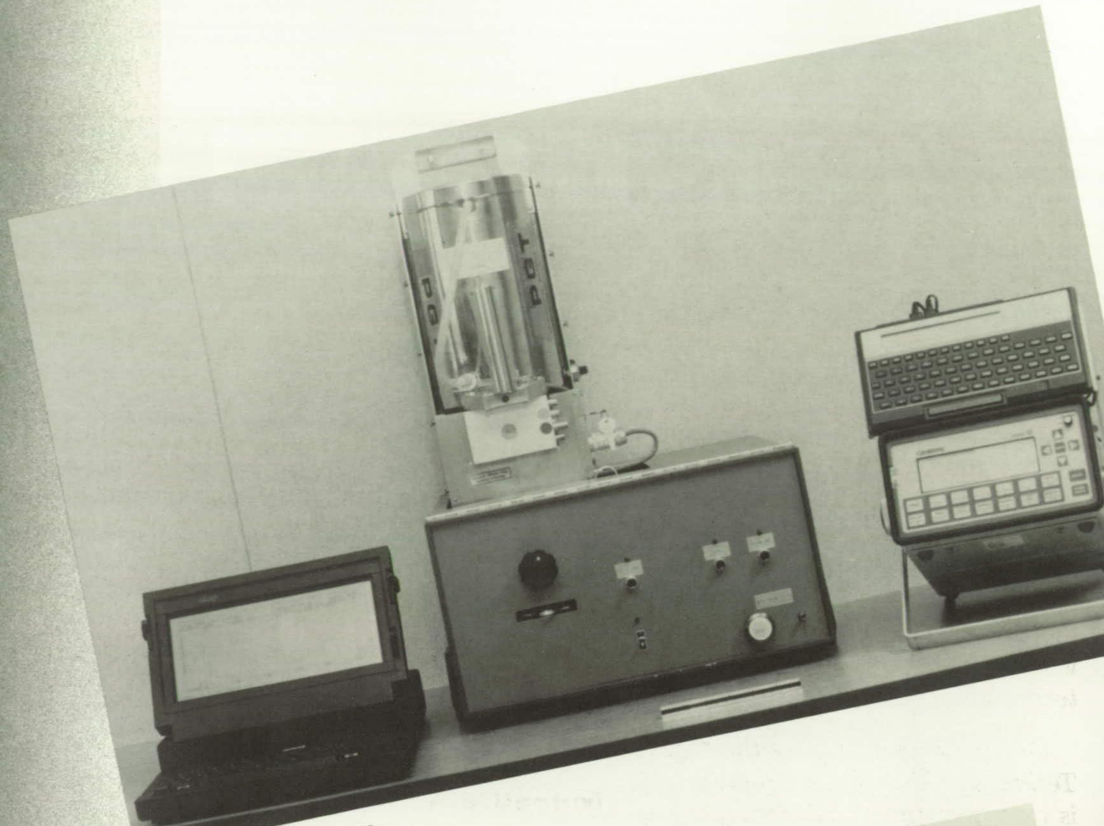

EMPAX system.

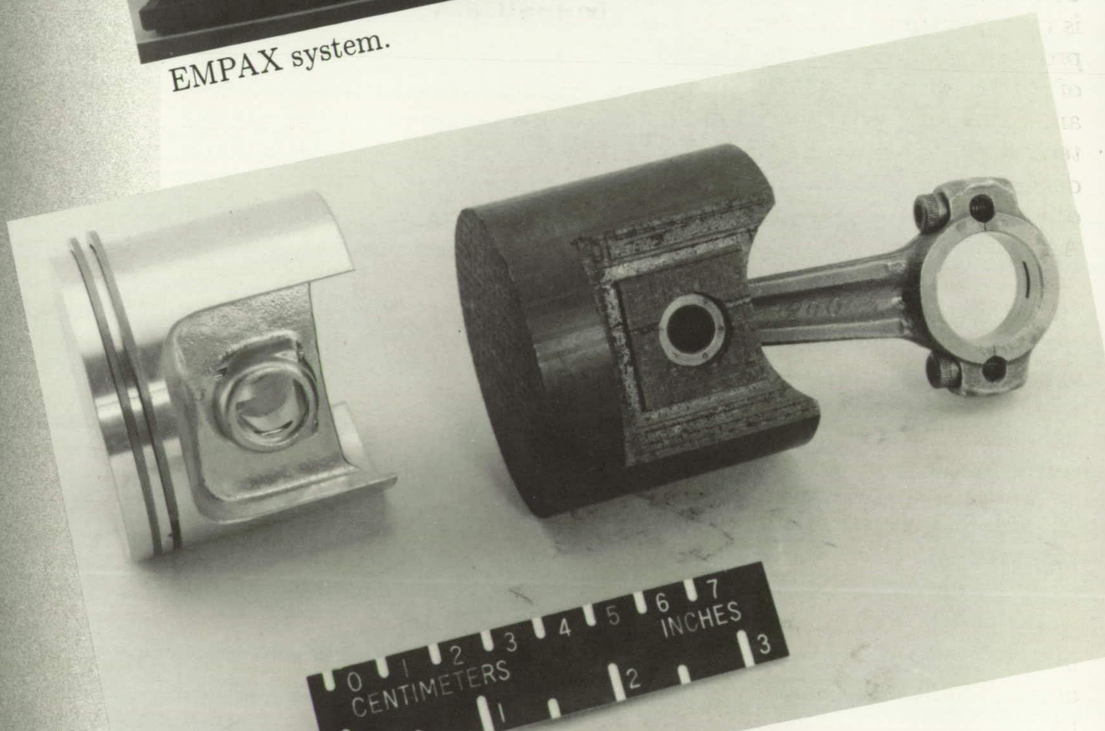

ORIGINAL PAGE
BLACK AND WHITE PHOTOGRAPH

One of the Congressionally mandated responsibilities of NASA is to promote economic and productivity benefits to the Nation by facilitating the transfer of aerospace-generated technology to the public domain. NASA's means of meeting this objective is its Technology Utilization Program, which provides a link between the developers of aerospace technology and those in either the public or private sectors who might be able to employ the technology productively.

One important facet of the NASA Technology Utilization Program is its applications engineering projects, which involve the use of NASA expertise to redesign and re-engineer extant aerospace technology to solve problems delineated by federal agencies or other public-sector institutions. Applications engineering projects originate in various ways; some stem from requests for NASA assistance from other government agencies and some are generated by NASA engineers and scientists who perceive possible solutions to public-sector problems through the adaptation of NASA technology. Additionally, NASA employs a multidisciplinary applications team that maintains a liaison with public-sector agencies, medical and public-health institutions, professional organizations, and academia to uncover significant problems in diverse fields such as health care, public safety, transportation, environmental protection, and industrial processes which might be amenable to solution by the application of NASA technology.

A significant achievement in technology transfer in 1989 involved the acceptance by the Environmental Protection Agency of the EMPAX (Environmental Monitoring with Portable Analysis by X-ray) system. This unique system permits in situ monitoring of toxic waste sites (or water reservoirs) for detecting the presence of hazardous inorganic pollutants.

Nuclear Fuel Quantity Measurement System

One of the persistent problems in the aviation industry relates to the Fuel Quantity Gauging (FQG) systems aboard aircraft. The feasibility of a nuclear gauge for fuel quantity measurement aboard aircraft has been demonstrated recently. The gauging system is based on the attenuation of low-energy gamma rays in the fuel column between a collimated radiation source and a collimated colinear detector. Modeling studies with weak Am^{241} (59.5 keV) radiation sources indicate that it is possible to continuously monitor the fuel quantity in aircraft tanks to an accuracy of better than 1 percent.

Currently, the Airlines Electronic Engineering Committee (AEEC) is coordinating an industry-wide study of aviation fuel properties as a first step toward the improvement of fuel quantity measuring systems. Langley Research Center is a major participant in this comprehensive study. The AEEC has been providing Langley with aviation fuel samples from airports throughout the world over a period of 12 months since August 1988. The Langley effort examines the variation of the fuel mass absorption characteristics as affected by season and geographical origin of the samples. For a nu-

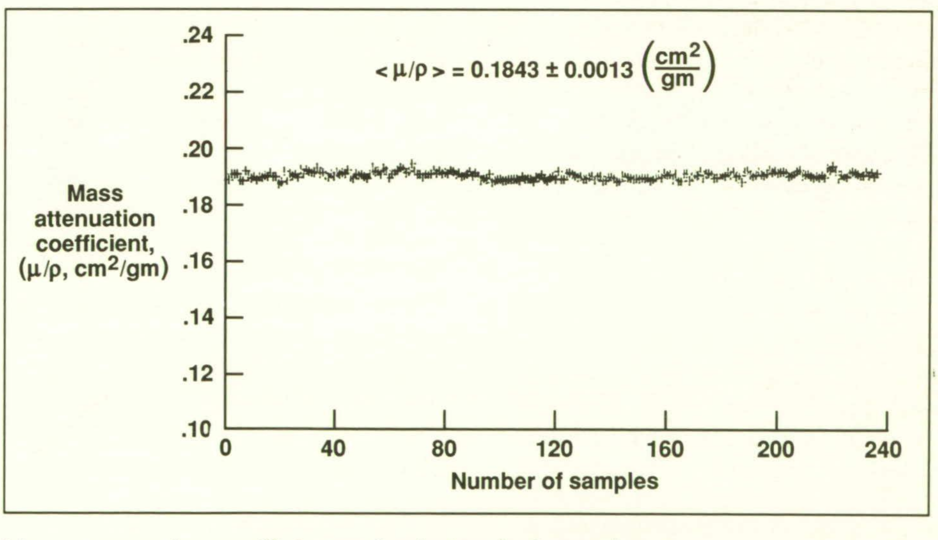

Mass attenuation coefficients of aviation fuel samples.

clear fuel gauge system to function reliably, the mass attenuation coefficient μ/ρ values for all fuels must remain constant.

As a result of the analysis of 250 fuel samples to date, it has been found that there is considerable variation in the linear attenuation coefficient μ and the density ρ values; however, the μ/ρ values for all samples are essentially constant at $0.1843 + 0.0013$ cm^2/gm. The figure clearly shows the uniformity of μ/ρ for all of the fuel samples received. From these results, it is concluded that a measurement of μ when the tank is full should permit a direct determination of the fuel density. When coupled with a measure of the fuel volume, at any time, the fuel mass aboard may be determined.
(Jag J. Singh, 44760)

CAD/CAM of Orthopedic Shoes

Approximately 10 million pairs of orthopedic shoes are manufactured annually in the United States. The design and manufacture of these shoes is a labor-intensive and highly skilled process. Unfortunately, the number of skilled shoemakers is declining rapidly. At the same time, the number of people needing these shoes is increasing. This growing disproportion between supply and demand is being reflected in increased costs and longer delivery times. The current cost of a pair of orthopedic shoes ranges from \$500 to \$800, and delivery times can be 90 days or more.

The use of more automation in the custom-shoe industry would help to solve this problem. Currently, computer-aided design and computer-aided manufacturing (CAD/CAM) are being used in the design and manufacture of off-the-shelf shoes, particularly by those companies making specialized recreational footwear, but these techniques have not been used in custom-shoe manufacture because of added complexity and the unique nature of these shoes.

In 1985 a workshop supported by the National Institute of Handicapped Research recommended the development of a cost-effective CAD/CAM system for orthopedic shoes. In the same year a developmental program was initiated by the Veterans Administration (VA), with technical and financial support from NASA, to produce a CAD/CAM program that would automate most of the design and some of the manufacture of custom-made shoes. This CAD/CAM program was to be based on NASA-developed computer programs, such as NASCAD (NASA Computer-Aided Design), APT (Automatically Programmed Tool), RIM (Relational Information Management), and CLIPS (C Language Integrated Production System). After approximately 4 years of development work, this "CAD/CAM for Orthopedics" Program is nearly completed.

In addition to the NASA-developed computer programs, the "CAD/CAM for Orthopedics" Program includes several custom-developed programs to provide capabilities not found in the NASA computer programs. Currently the CAD/CAM program accepts foot-shape data from a commercially available three-dimensional (3-D) surface scanner; displays and rotates a tiled, 3-D wire frame model of the scanned foot; accepts and displays other personal and medical data on that person; and provides a capability for interactively modifying (by using eight different types of operations) the foot data set to produce a tiled wire model of the analogous shoe last. This program also provides the numerical code necessary to machine the shoe last on any commercially available three-, four-, or five-axis milling machine; verifies that the shape of the last is, within dimensional tolerances, the shape of the last model; produces a data file that provides the information required by a commercially available software system that is currently being used in the shoe industry to produce patterns for the cutting of leather for shoe uppers; and provides the numerical code necessary to machine a mold of the shoe innersole on any commercially available three-, four-, or five-axis milling machine. This program runs on a Sun 3/260 workstation.

Other participants in this CAD/CAM development program included North Carolina State University and the University of Missouri-Columbia. This program will be turned over to the VA in early 1990 for operational tests at one of their orthopedic shoe clinics.
(Franklin H. Farmer, 42490)

Ambulatory Fetal Heart Monitor

Nonportable fetal heart monitors are commonly employed in doctors' offices and hospitals to detect fetal heart-rate (FHR) patterns. Abnormal patterns can reveal fetal problems such as hypertension, prolonged asphyxia, and decreased

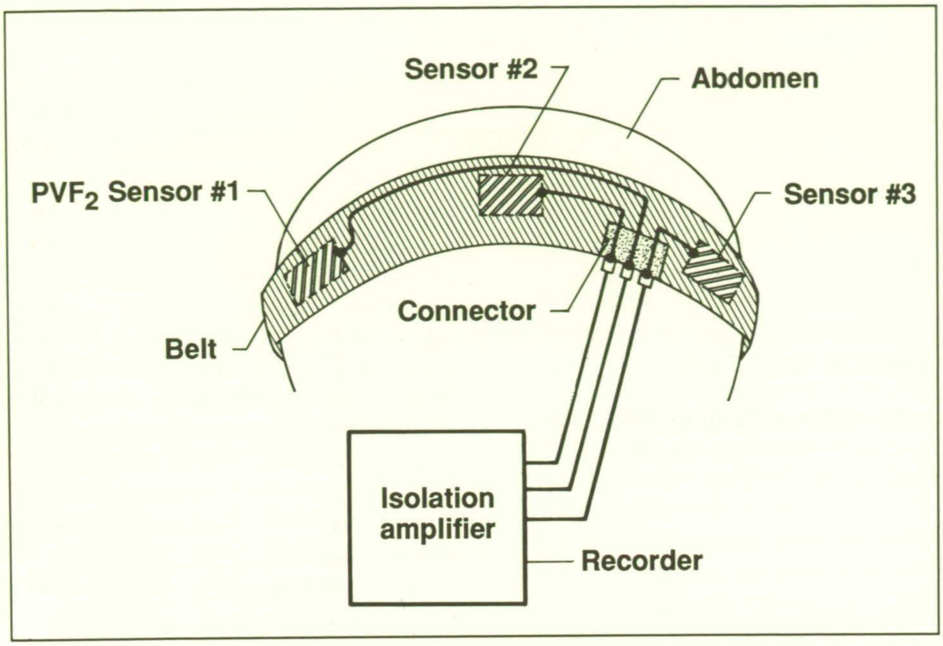

Experimental arrangement of sensors in fetal heart-rate monitor.

uterine blood flow. An ambulatory system is needed to monitor the FHR continuously and detect fetal responses to the daily activities of the mother. Of particular concern is the use of alcohol, drugs, and tobacco, as well as exposure to viral and bacterial pathogens and other toxins. The monitor should recognize abnormal patterns and warn the mother to seek medical help.

The problems faced in the development of an ambulatory monitor have been more complex than might be expected. The clinical monitor could not be miniaturized and coupled to a portable power source because movement of the mother generates strong background signals that overwhelm the relatively weak acoustic emissions of the fetal heart. Dr. Donald A. Baker of the Holy Family Medical Clinic, Spokane, Washington, requested that NASA technology be applied to the solution of this problem.

The approach to this problem has been to design and build a specialized acoustic sensor using a piezoelectric polymer film, polyvinylidene fluoride (PVF_2), as the sensing element and to develop a signal-processing algorithm based on signature analysis and time-delay estimation techniques. The PVF_2 is minimally sensitive to rigid-body motion noise because it has a low surface mass density. A better signal-to-noise ratio has simplified the signal-processing requirements. Multiple sensors are being used (shown in the first figure) to determine the location of the fetal heart and thus provide information on the position of the fetus. The data processing algorithm is being developed in conjunction with Dr. Jack Stoughton of Old Dominion University.

Clinical testing of the system at EVMS (Eastern Virginia Medical School) has recently been initiated. The fetal heartbeat of 120 beats per minute has been detected, and two fetal heart tones have been resolved: one at 30 Hz and one at 50 Hz (much lower than the published frequency of 100 Hz to 125 Hz). Also, a fetal kick and a subsequent heartbeat have been recorded (shown in the second figure), which indicates that the system can also provide data for the classic test of fetal well-being, the fetal nonstress test.
(Allan J. Zuckerwar, 44658)

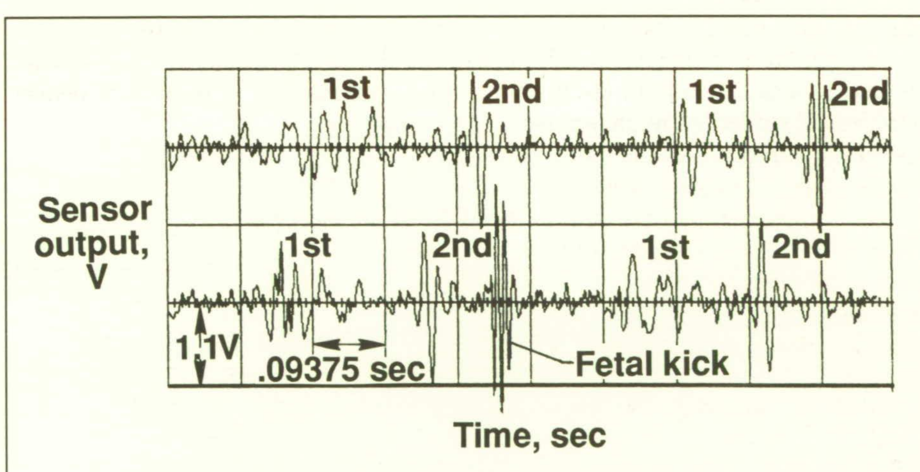

Time history of fetal heart tones (39th week of term).

NASA
National Aeronautics and Space Administration

Report Documentation Page

1. Report No. NASA TM-4150	2. Government Accession No.	3. Recipient's Catalog No.
4. Title and Subtitle Research and Technology 1989 Langley Research Center		5. Report Date February 1990
		6. Performing Organization Code
7. Author(s)		8. Performing Organization Report No. L-16657
9. Performing Organization Name and Address NASA Langley Research Center Hampton, VA 23665-5225		10. Work Unit No.
		11. Contract or Grant No.
12. Sponsoring Agency Name and Address National Aeronautics and Space Administration Washington, DC 20546-0001		13. Type of Report and Period Covered Technical Memorandum
		14. Sponsoring Agency Code

15. Supplementary Notes

16. Abstract

The mission of the NASA Langley Research Center is to increase the knowledge and capability of the United States in a full range of aeronautics disciplines and in selected space disciplines. This mission will be accomplished by performing innovative research relevant to national needs and Agency goals, transferring technology to users in a timely manner, and providing development support to other United States Government agencies, industry, and other NASA centers. This report contains highlights of the major accomplishments and applications that have been made during the past year. The highlights illustrate both the broad range of the research and technology activities at NASA Langley Research Center and the contributions of this work toward maintaining United States leadership in aeronautics and space research. For further information about the report, contact Dr. Richard W. Barnwell, Chief Scientist, Mail Stop 105-A, NASA Langley Research Center, Hampton, Virginia 23665, (804) 864-6062.

17. Key Words (Suggested by Authors(s)) Research and technology, Aeronautics, Space, Structures, Materials, Electronics, Flight systems, Technology utilization, Engineering, Aerodynamics	18. Distribution Statement Unclassified—Unlimited Subject Category 99

19. Security Classif. (of this report) Unclassified	20. Security Classif. (of this page) Unclassified	21. No. of Pages 227	22. Price A11

NASA FORM 1626 OCT 86

NASA-Langley, 1990

For sale by the National Technical Information Service, Springfield, Virginia 22161-2171